STRUCTURAL ANALYSIS

OF

THE NORTHERN WESTERN DESERT OF EGYPT

by

MOHAMED GHARIB EL-MALKY, B.Sc.(Hons.), M.Sc.

A thesis submitted for the degree of Doctor of Philosophy of the University of London and the Diploma of Membership of Imperial College

JANUARY 1985

Structure Geology Section,
Department of Geology,
Royal School of Mines,
Imperial College,
London S.W.7

ABSTRACT

A structural analysis of the Northern Western Desert of Egypt has been carried out by studying large, intermediate and small scale structural features. These include field study of Gaa-Abu Rawash village area, photogeological study of Abu Rawash area, Landsat imagery study, palaeotectonic analysis and geophysical study.

A theoretical model was constructed on the basis of the field data and the derived theoretical rose diagrams were used for interpreting the fracture patterns of Abu Rawash village pericline as well as the aerial photographs' fracture traces.

During the course of the research, new techniques of fracture trace analysis have been developed. These techniques have been effectively applied in order to get a filtered representation of more than one quantitative fracture aspect which is amenable for any structural study in a chosen area.

The most prominant trends of lineaments, which were interpreted from the Landsat images, are ENE and NNE. These lineaments have been analysed in light of a compiled theoretical rose diagram which was constructed on the basis of both field data theoretical model and a theoretical model derived by Price (1974), making use of the available subsurface data.

Palaeotectonic and geophysical analyses were applied for the purpose of detecting concealed structures on regional and local scales.

Many geophysical techniques have been used, such as filtering, continuation, second vertical derivative, reduced to the pole and pseudogravity in the analysis of the gravity and aeromagnetic maps. The different approaches of this study proved to be very useful in locating some strike-slip faults with different relative sense of movements. Some of these geophysical lineaments coupled with ENE and WNW mapped fold structures were used to define the block framework of the study area. This block framework has been identified on the compiled map of surface lineaments (interpreted from Landsat images). The structural significance of such framework has been discussed in light of simple shear model of deformation.

The fold structures present in the studied area have been discussed during the course of this study where some possible mechanisms for their establishment have been put forward by the author.

Generally, this study throws much light on the long debated structural framework of Egypt.

ACKNOWLEDGEMENTS

I wish to express my deepest gratitude to Professor N.J. Price for his help, encouragement, support and advice throughout the research. His critical reading of the manuscript was also most appreciated.

I am very grateful to Dr. J.W. Norman for his help and advice during the course of Landsat images interpretation as well as reading of the manuscript.

My gratitude goes to Dr. D.R. Cowan for providing useful computer programs, help and advice during the course of geophysical study.

Immense thanks are due to Dr. J.W. Cosgrove for his useful discussions and help during the field study.

Many thanks go to the authorities of the Egyptian Government for their financial support during the course of this study.

Special thanks to the authorities of the Military Survey of Egypt for providing the aerial photographs used in this research.

Thanks also go to the authorities of AMOCO Oil Company of Egypt for supplying aeromagnetic data for a part of the Western Desert of Egypt.

I am very much indebted to Professors S. Omara, B. Issawi (Geological Survey of Egypt), A. Sabri (Ain Shams University), Y. Abdelhady (Cairo University), H. Elkhashaab (Faculty of Science, Sohag) and A. Hasanein (Al-Azhar University) for their help and support during the course of this study.

I am also very grateful to many people and colleagues for helping in various ways during the

research, particularly Dr. M. Critchley and Dr. J.N. Park. Also, thanks go to Soumayyah Haber for the typing of this thesis.

Finally, special thanks are due to my wife and sons (Khaled and Amre) for their patience, encouragement and great support throughout the period of the research.

This thesis is dedicated to my parents who supported me in all aspects of my life.

TABLE OF CONTENTS

		PAGE NO.
Title Page		i
Abstract		ii
Acknowledgements		iii
Text Contents		v
List of Figures		ix
List of Plates		xv
List of Tables		xvi

Text Contents

Chapter		
I	Introduction	
	1.1 Location	1
	1.2 Purpose of This Study	1
	1.3 Summary of Definitions and Abbreviations	6
II	General Geological Setting	
	2.1 Introduction	11
	2.2 Structural Elements	11
	2.2.1 Elements of Regional Structures	19
	2.2.2 The Structural Elements of Egypt	26
	2.2.3 The Structural Elements of the Western Desert	42
	2.2.4 The Nile Delta	58
	2.2.5 Origin of the Depressions	60
	2.2.6 Basalt Occurrences	61
	2.3 Stratigraphy	62
	2.4 Geologic History	88
III	Field Study of Gaa-Abu Rawash Village Area	
	3.1 Introduction	94
	3.2 Purpose of Study	94
	3.3 Previous Work	98
	3.4 Basic Concepts	102

Chapter		Page No.
	3.4.1 Fracture Phenomena	102
	3.4.2 Relationships Between Folds, Faults and Fractures	108
	3.5 Field Study	108
	3.5.1 Introduction	108
	3.5.2 Field Data of Abu Rawash	110
	3.5.2A The Study of the Attitudes of the Outcrops	113
	3.5.2A.1 Interpretation of Contoured Diagram	116
	3.5.2A.2 Flow of Ductile Materials and El-Medawara Structure	118
	3.5.2A.3 El-Medawara Structure	119
	3.5.2B The Study of the Attitude of Fractures	121
	3.5.2B.1 Structure Fracture Identification and Interpretation	123
	3.5.2B.2 Theoretical Model	131
	3.5.2B.3 Interpretation of the Contoured Diagram	134
	3.5.2B.3A Fractures Related to the Main Pericline	134
	3.5.2B.3B Fractures Unrelated to the Pericline	138
	3.5.2B.4 Directional Rose Diagram	139
IV	Aerial Photographic Study of Abu Rawash Area	
	4.1 Introduction	144
	4.2 Photogeological Interpretation	145
	4.2A Objective Factors	146
	4.2B Subjective Factors	146
	4.3 Techniques and Fracture Aspects	147
	4.3.1 Aspects of Fracture Traces	147
	4.3.1.1 Quantitative Aspects	148
	4.3.1.2 Qualitative Aspects	153

Chapter		Page No.
	4.4 Techniques of Fracture Trace Analysis	154
	4.4.1 Changes in Intensity of Fracturing	157
	4.4.2 Changes in Fracture Pattern Orientations	157
	4.4.3 Changes in Lineament and Fracture Trace Patterns	158
	4.4.4 The Integrated Technique	159
	4.5 Data Processing	161
	4.6 Statistical Analysis of the Fracture Traces of Abu Rawash	162
	4.6.1 Methods of Analysis	162
	4.6.2 Methods of Presentation	165
	4.7 Results	167
	4.8 Analysis and Interpretation of the Rose Diagrams and Histograms	177
	4.8.1 Study of Some Rose Diagrams in Light of the Field Data	179
	4.8.1B Study of Some Rose Diagrams in Light of the Theoretical Model	184
	4.8.2 Analysis of the Directional Rose Diagrams	186
	4.8.3 The Analysis of the Rose Diagram Maps	199
	4.8.4 The Analysis of Histograms Derived From the Integrated Model	206
V	Landsat Imagery Study	
	5.1 Introduction	209
	5.2 Images Used in the Study	211
	5.3 Factors Affecting the Interpretation of Landsat Images	215
	5.4 Lineaments	216
	5.5 Circular Features	219
	5.6 Preparation of Images for Analysis	221
	5.7 Landsat Images Analysis and Interpretation	221
	5.7.1 Interpretation Methods	222
	5.7.2 Detection of the Circular Features	224
	5.7.3 Handling and Presentation of the Data	224
	5.7.4 Compiled Maps of Lineaments	225
	5.7.5 Presentation of the Data	228
	5.8 Results and Interpretation	230
	5.8.1 Discussion	244
VI	Palaeotectonic Analysis	
	6.1 Introduction	258

Chapter		Page No.
	6.2 The Analysis of Regional Isopach Maps	259
	6.2.1 Principles of Interpretation	262
	6.2.2 The Basement Relief or Structure Contour Map	268
	6.2.3 Paleozoic Isopach Map	271
	6.2.4 Jurassic Isopach Maps	277
	6.2.5 Albian-Cenomanian Isopach Map	287
	6.2.6 Turonian Isopach Map	289
	6.2.7 Middle Eocene-Palaeocene Isopach Map	299
	6.2.8 Eocene Isopach Map	305
VII	Geophysical Study	
	7.1 Introduction	312
	7.2 Previous Geophysical Work	313
	7.3 Preparation of the Geophysical Data	316
	7.4 Geophysical Data Used in the Study	318
	7.5 Analytical Techniques Used in this Study	324
	7.6 Geophysical Data Processing	331
	7.7 Principle of Interpretation	333
	7.8 Results	335
VIII	Synthesis	
	8.1 Introduction	361
	8.2 Analysis of Lineament Shear Patterns	362
	8.3 Block or Lineament Framework	369
	8.4 Structural Conclusion	387
	References	391
	Appendix I: Some Results of Landsat Images Study	404
	Appendix II: Filter Coefficients of Geolphysical Data	445

LIST OF FIGURES

Figure No.		Page No.
1.1	Location Map of the Studied Area in Egypt	2
1.2	Geological Map of Abu Rawash Area	3
2.1	Geological Map of Egypt	12
2.2	Distribution of Longitudinal Dunes in Northern Part of Libyan Desert	12
2.3	Sketch of Plate Boundaries and Motions	14
2.4	Approximate Position of Plate Boundaries in the Mediterranean Area	14
2.5	The Relative Motion Between Africa, Arabia and Eurasia	15
2.6	Plate Boundaries and the Relative Motions of the Arabian, Nubian and Somalian Plates	17
2.7	Relative Motion Between the Sinai, Arabian and Nubian Plates	17
2.8	Late Cretaceous Structural Elements	20
2.9	Some Major Deep Shears of Africa	22
2.10	Orientation of the Maximum Stresses Relative to Major Deep Shears in Africa	22
2.11	Structural Sketch Map of the Arabian Peninsula and Surrounding Countries	24
2.12	Middle East Framework	25
2.13	Structures of Egypt and the Surrounding Eastern Mediterranean Countries	27
2.14	Block Diagram of the North Egypt Deformations	27
2.15	Structure Contour Map of the Western Desert of Egypt (Top Cenomanian)	29
2.16	Simplified Tectonic Map of Egypt	31
2.17	Map Showing the Main Syrian Arc System in Egypt	31
2.18	Geologic Map of Duwi Shear Zone in Egypt	36
2.19	Relation of WNW Faults to Oil Occurrences in Gulf of Suez Region	38
2.20	Main Directions of Faulting and North Sinai Folds	40
2.21	Probable Stages in Evolution of East-West Thrusts Into Gravity Faults	41
2.22	Sketch Map of Major Structural Elements of Egypt	41
2.23	Sketch of a Geological Cross Section Across Egypt	43
2.24	Sketch of Structural Block Diagram of the Northern Nile Basins	45
2.25	Main Fracture Zones in Egypt	45
2.26	Geological Map of the Western Desert of Egypt	47
2.27	Tectonic Sketch Map of the Western Desert of Egypt	50
2.28	Map Showing the Fold Structures in Egypt	52
2.29	Map Showing Surface Structure of the Northern Western Desert of Egypt	53
2.30	Maps Showing the Main NNW Undulations or Folds	54
2.31	Secondary Structures of Strike-Slip Faults	56
2.32	Tentative Tectonic Map of the Nile Delta Region	59
2.33	Top Cretaceous Fault Structures	59
2.34	Well Location Map, Northern Egypt	65
2.35	Paleogeologic Map of Pre-Carboniferous, Northern Egypt	67

Figure No.		Page No.
2.36	Marine Jurassic Isopach Map	71
2.37	Jurassic Facies (Combined Ratio) Map	72
2.38	Environments of Deposition of Oligocene in Northern Egypt, Simplified	84
2.39	Environments of Depostion of Early Miocene Sediments in Northern Western Desert, Egypt	84
2.40	Environments of Deposition of Middle Miocene Sediments in Northern Western Desert and Nile Delta, Egypt	86
2.41	Environments of Deposition of Pliocene Sediments in Northern Western Desert and Nile Delta, Egypt	86
2.42	Diagrammatic Cross Sections Showing Tentative Interpretation of Geologic Evolution of Northern Part of Western Desert, Egypt	90
3.1	Location Map of Abu Rawash Area	95
3.2	Location Map of the Studied Area	96
3.3	Geological Map of the Studied Area	97
3.4	Different Types of Fractures	104
3.5	Explanation of Patton's Model	106
3.6	Mohr-Coulomb Failure Relationship For Discontinuities in Limestone	107
3.7	Relationship Between Stresses, Folding and Possible Fractures	109
3.8	Geological Map of the Study Area	111
3.9	Geological Map of Gaa-Abu Rawash Village Area	112
3.10	S-Pole and Contoured Diagrams of the Bedding Planes	115
3.11	Sketch of a Geological Section Across the Northern Limb of Gaa-Abu Rawash Village Pericline	117
3.12	Geological Cross Section Across Gaa-Abu Rawash Village Area	117
3.13	Sketch Map of El-Medawara Structure	120
3.14	S-Pole and Contoured Diagrams of the Measured Fracture Plane Poles	129
3.15	Stereograms of Theoretical Fracture Poles (A)	132
3.16	Stereograms of Theoretical Fracture Poles (B)	133
3.17	Theoretical S-Pole and Contoured Diagrams of the Fracture Plane Poles	135
3.18	Observed and Theoretical Contoured Diagrams of the Fracture Plane Poles	136
3.19	Gaa-Abu Rawash Village Pericline (Field Data) Rose Diagram	140
3.20	Compiled Theoretical Rose Diagrams	142
4.1	Graph Showing the Relationship Between the Air Photograph Scale and the Mean Length of Linear Geological Features Detected	150
4.2	Relationship Between Bed Thickness and Distance Between Joints	152
4.3	The Orientation of the Principal Stresses and Structures Developed	152
4.4	Some Fracture Patterns	155
4.5	Fracture Patterns Associated With Folds	156
4.6	Interpreted Fracture and Bed Traces of Abu Rawash Area	163
4.7	Modified Geological Map of Abu Rawash Area	168
4.8	Location of the WNW Dextral Strike-Slip Faults	169

Figure No.		Page No.
4.9	Structural Map of Abu Rawash Area	170
4.10	Geologic Cross Section Across El-Hassana Dome	172
4.11	Geological Section Across the Giza Pyramids Area	172
4.12	Geological Cross-Section Across Abu Rawash Area	172
4.13	An Experimental Model Showing the Effects of Basement Faults on the Overlying Sedimentary Cover	176
4.14	Interpreted magnetic Trends of a Part of the Northern Western Desert of Egypt	176
4.15	Field Data and Abu Rawash Area Rose Diagrams	180
4.16	Field Data and Gaa-Abu Rawash Village Pericline Rose Diagrams	181
4.17	Field Data and El Talun-Sudr El Khamis Folds Rose Diagrams	182
4.18	First Step in Derivation of a Theoretical Rose Diagram	185
4.19	Abu Rawash Area and the Theoretical Model Rose Diagrams	187
4.20	Gaa-Abu Rawash Village Pericline and The Theoretical Model Rose Diagrams	188
4.21	El Talun Sudr El Khamis Folds and The Theoretical Model Rose Diagrams	189
4.22	Abu Rawash Area Rose Diagrams	191
4.23	Gaa-Abu Rawash Village Pericline Rose Diagrams	192
4.24	Wadi El-Talun-Sudr El Khamis Folding Rose Diagrams	193
4.25	Hassana Dome Rose Diagrams	197
4.26	Ghigiga Dome Rose Diagrams	198
4.27	Fracture Frequency Rose Diagram Map	200
4.28	Integrated Rose Diagram Map	201
4.29	Relative Fracture Energy Rose Diagram Map	202
4.30	Relative Fracture Density Rose Diagram Map	204
4.31	Average Fracture Density Rose Diagram Map	205
4.32	Integrated Histograms	207
5.1	Images of Different Contrast Ratio With Corresponding Brightness Profiles	213
5.2	Geographic Location of the Images Used in the Study	214
5.3	Average Rainfall in Millimetres and No. of Landsat Images Used in the Study	223
5.4	The Process of Digitization	224
5.5	Compiled Map of Lineaments (False Colour)	226
5.6	Compiled Map of Lineaments (From Band 7)	227
5.7	Shows the Construction of a Lineament Compiled Map	229
5.8	Histogram Showing the Lineament Frequencies With Different Class Intervals	231
5.9	Band 7 Weighted Rose Diagrams Map	233
5.10	Band 7 Integrated Rose Diagrams Map	232
5.11	Band 7 Relative Fracture Energy Rose Diagrams Map	234
5.12	Band 7 Relative Fracture Frequency Rose Diagrams Map	235
5.13	The Number of Images Used With the Relative Sun Azimuth	240
5.14	Fracture Developed During Downwarping and Parallel or Non-Parallel Uplift	242
5.15	Shows Trends of the Subsurface Basins and Uplifts	243
5.16	Shows the Construction of Theoretical Rose Diagram	243
5.17	Theoretical Rose Diagrams Based on Price's Model (1974)	245
5.18	Compiled Rose Diagrams	246

Figure No.		Page No.
5.19	Compiled Theoretical Rose Diagrams	247
5.20	Map Showing Some Circular Elliptical Features in West Cairo	252
5.21	Map Showing Some Circular or Elliptical Features in the Studied Area	253
5.22	Geological Profile Burg el Arab-Abu Rawash	255
6.1	Diagrammatic Contour Patterns for Isopach Map of Regional Negative Areas	261
6.2	Axes of Subsidence During Vertical and Tilted Sinking	261
6.3	Possible Development of Sedimentary Basins	263
6.4	Effects of Faulting On the Thickness of the Deposits	266
6.5	Shows Deposition After Faulting	267
6.6	Effects of Regional Dip, Uplift and Topographic Relief on the Thickness of Deposits	267
6.7	Northern Egypt Depth Map of Top of Basement	269
6.8	Northern Egypt Isopach Map of the Palaeozoic	269
6.9	Northern Egypt Depth Map of Top of Palaeozoic	272
6.10	Geological Cross Section L-L (Where the Top of the Palaeozoic Has Been Taken as a Datum)	272
6.11	Location Map of the Geological Cross Sections	273
6.12	Possible Basement Faults and Their Effects on the Overlying Sediments	275
6.13	Some Drape Folds	275
6.14	A Monocline Structure	276
6.15	Seismic Section	276
6.16	Unforced Fold Structure	276
6.17	Drawing Illustrating Sequential Movements and Deformation Envisioned for Dinosaur National Monument	278
6.18	Jurassic Isopach Map	279
6.19	Geological Cross Section M-L (Where the Top of the Jurassic Has Been Taken as a Datum)	281
6.20	Geological Cross Section C-C (Where the top of the Jurassic Has Been Taken As a Datum)	282
6.21	Geological Cross Section D-D (Where the Top of the Jurassic Has Been Taken As a Datum)	283
6.22	Compiled Jurassic Isopach and Lineament (I.R. Colour Composite) Map	284
6.23	Compiled Masajid Formation Isopach and Lineament (I.R. Colour Composite) Map	285
6.24	Isopach Map of Albian-Cenomanian (Top Alamein-Top Abu Roash)	288
6.25	Geologic Cross Section N-N (Where the Top of Cenomanian Has Been Taken As a Datum)	290
6.26	Geological Cross Section P-P (Where the Top of Cenomanian is a Datum	290
6.27	Geological Cross Section R-R (Where the Top of Cenomanian Is a Datum)	290

Figure No.		Page No.
6.28	Geological Cross Section L-L (Where the Lower Cretaceous is a Datum)	291
6.29	Compiled Albian-Cenomanian Isopach and Lineament (I.R. Colour Composite) Map	292
6.30	Isopach Map of Turonian	293
6.31	Top Abu Roash "C" Unit Structural Contour Map	295
6.32	Structural Cross Section (A-A) Abu Gharadig Field	296
6.33	Structural Cross Section (B-B) Abu Gharadig Field	297
6.34	Compiled Turonian Isopach and Lineament (I.R. Colour Composite) Map	298
6.35	M. Eocene-Palaeocene Isopach Map	300
6.36	Compiled M. Eocene-Palaeocene Isopach and Lineament (I.R.) Colour Composite) Map	303
6.37	Isopach Map of Eocene, Western Desert	306
6.38	Compiled Eocene Isopach and Lineament (I.R. Colour Composite) Map	308
7.1	Possible Shear Zones Interpreted From Gravity Anomalies	315
7.2	Smoothed Gravity Map of the Studied Area	319
7.3	Smoothed Aeromagnetic Map of the Western Desert of Egypt	320
7.4	Smoothed Aeromagnetic Map of the Nile Delta	321
7.5	Some Features of Aeromagnetic Maps Which Define Aeromagnetic Lineaments	334
7.6	Prominent Aeromagnetic Lineament Cutting Rocks Adjacent to the Coastal Batholith in British Columbia	334
7.7	Detection of Possible Shears Across Folded or Faulted Region	336
7.8	Shearing of Folded and Faulted Regions	337
7.9	Lowpass Filtered Gravity Map of Western Desert of Egypt	339
7.10	Upward Continuation of the Gravity Map of the Western Desert	340
7.11	Highpass Filtered Gravity Map of the Western Desert of Egypt	342
7.12	Second Vertical Derivative of the Gravity Map of the Western Desert of Egypt	343
7.13	Reduced to the Pole Aeromagnetic Map of the Western Desert of Egypt	344
7.14	Pseudogravity Map of the Western Desert of Egypt	345
7.15	Lowpass Filtered Aeromagnetic Map of the Western Desert of Egypt	347
7.16	Upward Continuation of the Aeromagnetic Map of W.D. of Egypt	348
7.17	Highpass Filtered Aeromagnetic Map of the Western Desert of Egypt	349
7.18	Second Vertical Derivative of the Aeromagnetic Map of W.D. of Egypt	350
7.19	Reduced to the Pole Aeromagnetic Map of the Nile Delta	352
7.20	Pseudogravity of the Aeromagnetic Map of the Nile Delta	353
7.21	Lowpass Filtered Aeromagnetic Map of the Nile Delta	354

Figure No.		Page No.
7.22	Upward Continuation of the Nile Delta Aeromagnetic Map	355
7.23	Highpass Filtered Aeromagnetic Map of the Nile Delta	357
7.24	Second Vertical Derivative of the Aeromagnetic Map of the Nile Delta	358
7.25	Rose Diagrams of Possible Geophysical Regional and Local Shears	359
8.1	Regional and Local Shears Interpreted From the Filtered Gravity Maps	363
8.2	Regional and Local Shears Interpreted from the Filtered Aeromagnetic Maps of the Western Desert	364
8.3	Regional and Local Shears Interpreted From the Filtered Aeromagnetic Maps of the Nile Delta	365
8.4	Rose Diagrams of Interpreted Geophysical Shears and Possible Maximum Compressions	366
8.5	Diagrammatic Cross Section Showing Possible Development of NNW Undulations	370
8.6	Cross Section Showing Development of Undulation as a Result of Basement Block Faulting	370
8.7	Structure Contour Map (Top Cenomanian)	372
8.8	Comparison Between Pure Shear and Simple Shear Mechanics (A). Various Phases of Simple Shear Mechanics (B and C)	373
8.9	Forces and Composite of Structures that Can Result from Wrenching Deformation	374
8.10	Geometrical Relationship Between Subsurface WNW Shears and Palaeozoic-Lower Cretaceous Basins and Uplifts	374
8.11	Compiled Map of WNW Aeromagnetic Shears and ENE Fold Structures (W.D.)	379
8.12	Compiled Map of WNW Aeromagnetic Shears and ENE Fold Structures (The Nile Delta)	380
8.13	Compiled Map of WNW Gravity Shears and ENE Fold Structures (The Study Area)	381
8.14	Compiled Map of ENE Aeromagnetic Shears and WNW Fold Structures	383
8.15	Compiled Map of ENE Gravity Shears and WNW Fold Structures	384
8.16	Block Framework Defined From Interpreted Surface Lineaments (Band 7)	385
8.17	Block Framework Defined From Interpreted Surface Lineaments (Infra-Red False Colour Composites)	386

LIST OF TABLES

Table No.		Page No.
2.1	Locations of the Poles and Angle of Rotation of Some Plates	16
2.2	The Depths of the Basement (As Encountered in Some Wells)	66
2.3	Depths of the Palaeozoic Section (As Encountered in Some Wells)	69
2.4	Generalised Stratigraphy of Abu Rawash	76
2.5	The Measured Section of Abu Roash I and II	77
2.6	Thicknesses of Upper Cretaceous	77
2.7	Stratigraphy of Abu Rawash Unit	78
2.8	Thicknesses of Palaeocene Section	81
2.9	Thicknesses of Oligocene, Miocene and Pliocene - Recent Sections	81
2.10	Thicknesses of Pleistocene-Pliocene Section	81
4.1	Numerical Computer Output of the Fracture Traces	166
4.2	Correlation Coefficients of Field Data and Aerial Photographs Rose Diagrams	183
4.3	The Prominent Trends of Abu Rawash Area Rose Diagrams	194
4.4	The Prominent Trends of Gaa-Abu Rawash Village Pericline Rose Diagrams	194
4.5	The Prominent Trends of Wadi El Talun-Sudr El Khamis Folding Rose Diagrams	194
4.6	Correlation Coefficients Between Rose Diagrams	195
5.1	Spectral Bands Used in the Study	211
5.2	Colour Composite Images and True Colours They Represent on the Ground	215
5.3	Correlation Coefficients of Some Rose Diagrams (False Colour Composite and Band 7	237
7.1	Noise Filter Coefficients (Fourth Quadrant)	318
7.2	Trends of the Gravity Map of the Northern Western Desert	322
7.3	Trends of the Aeromagnetic Data	324
7.4	Regional Trends of the Gravity Map	338
7.5	Local Trends of the Gravity Map	341
7.6	Trends of Filtered Aeromagnetic Maps of the W.D.	341
7.7	Regional Trends of the Aeromagnetic Maps of the W.D.	346
7.8	Local Trends of the Aeromagnetic Maps of the W.D.	346
7.9	Trends of the Filtered Aeromagnetic Maps of the Nile Delta	351
7.10	Regional Trends of the Aeromagnetic Maps of the Nile Delta	351
7.11	Local Trends of the Aeromagnetic Maps of the Nile Delta	356
7.12	Possible Shears on Local and Region Scales	356

LIST OF PLATES

Plate No.		Page No.
2.1	Stratigraphic Nomenclature	64
2.2	Well Log of Rabat-X1 Western Desert	68
2.3	Well Log of Abu Rawash (Abu Roash) Well No. 1	68
3.1	Minor NE-SW Fold Structure	114
3.2	Represents the Cross Warping Gaa-Abu Rawash Village Pericline	122
3.3	Shows One of the N60W Fractures	124
3.4	Represents One of the Extension Fractures Which Nearly Normal to the Axis of the Gaa-Abu Rawash Village Pericline	124
3.5	Shows Two Sets of Fractures and Their Possible Types	125
3.6	Represents a NE Minor Reverse Fault	126
3.7	Shows One of the Nearly E-W Extension Fractures	126
3.8	Shows An Extension, N35°W, Fracture, (Minor Normal Fault)	127
3.9	Shows One Set of Closed Fracture Which Trends N55°W	127
3.10	Shows One of the Shears That Trend E-W	128
3.11	Shows Some Long Tension Fractures Which Trend N10°-15°W	128
4.1	Oblique Aerial Photograph of the NW Limb of El-Talun Plunging Anticline (Gebel El-Higaf)	175

CHAPTER ONE

INTRODUCTION

CHAPTER ONE

Introduction

1.1 Location

The area under study lies between the Mediterranean Sea and the Latitude 28 00 N. It is bordered to the east by the River Nile and the eastern boundary of the Nile Delta, and to the west by the International Egyptian-Libyan boundary (Longitude 25 00 E.), (Fig. 1.1).

1.2 Purpose of This Study

The aim of this research work is to determine the structural form and evolution of N. Egypt. To this end, four main types of studies were conducted. They are:

1. Relatively local scale survey on the field of structures exposed to the W. of Cairo (Fig. 1.2);
2. Intermediate scale survey of smaller selected areas using aerial photographs;
3. Regional scale survey of the area Landsat imagery; and
4. The interpretation of these data in the light of geophysical and subsurface data.

The first three of these projects or studies are clearly intended to augment one another and enable the observations of the regional scale studies to be interpreted in light of the observations conducted at the local scale. The fourth line of study brings into consideration both new and old sets of data which help

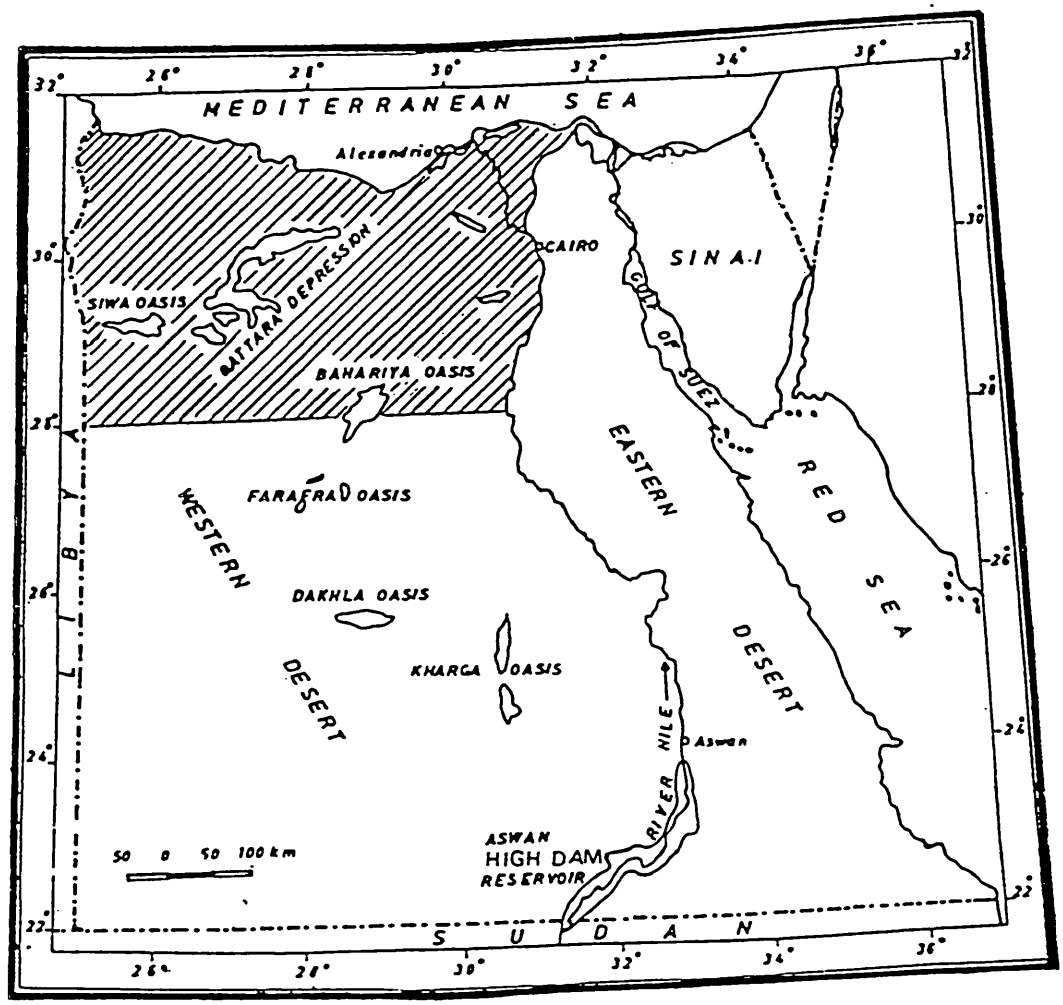


Fig. 1.1 Location map of the studied area in Egypt

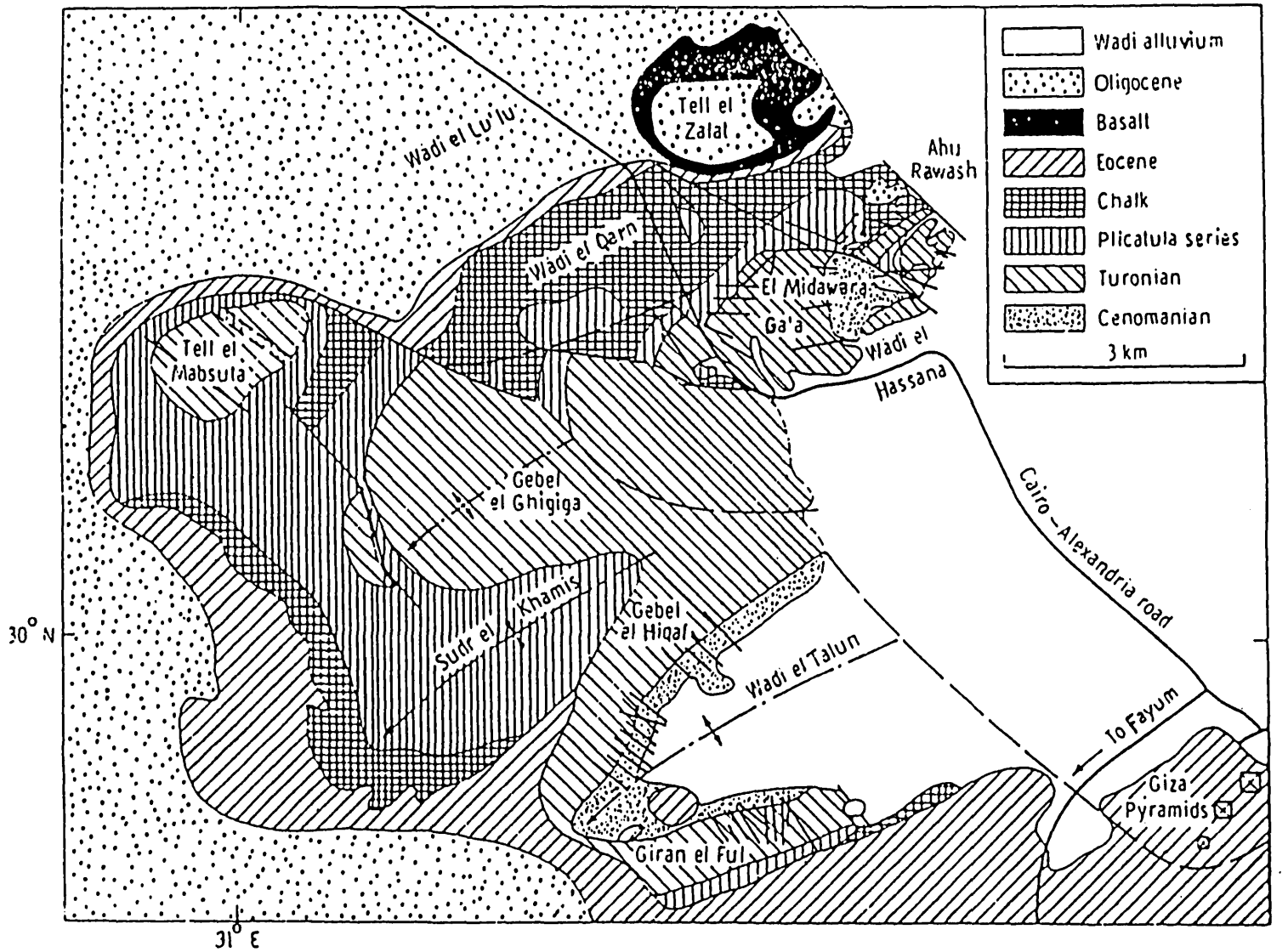


Fig. 1.2 Geological map of Abu Rawash area
(After Faris,1946, Jux,1954, and Omara,1953)

the interpretation and analysis, based on the other three studies.

1. The field study was conducted on the Abu Rawash area. This area was chosen because of its importance from the structural point of view as well as its accessibility. The Abu Rawash folds represent one of the most important structural trends in Egypt. This trend, NE - SW, is well represented at the Sinai Peninsula, Eastern Desert, and Western Desert of Egypt. It was the writer's intent to study the Faiyum, Wadi El Natrun areas and Qattara Depression, but because of the difficulties in accessibility and lack of facilities, as well as the time factor, these areas could not be satisfactorily studied. Consequently, the writer will use some of the known and mapped structures of the local area of the Abu Rawash and elsewhere to confirm or augment his regional scale studies.

This field study was conducted to establish certain relationships and to obtain data which would enable interpretation of the second phase of the study to be more readily evident.

2. <u>The analysis and mapping of the Abu Rawash aerial photographs:</u>

Many of the small fractures seen in the field are too minute to be seen on aerial photographs. For the same reason, some structures which can be seen on aerial photographs (1: 60,000) are too small and cannot be seen or easily studied on 1: 1000,000 or 1: 500,000 Landsat imagery. Hence, the aerial photographic study forms an

important link between the local field study and the regional study based on the third aspect - that is, the structural study of regional fracture traces analysis based on a study of satellite imagery.

3. The analysis and mapping of regional scale lineaments and linear features seen on Landsat imagery over the studied area:

Such elements include the tectonic style and major fracture systems and patterns as well as individual structural features such as faults and folds. The mapping of the linear features and lineaments are expected to provide clues to subsurface structures. An attempt will be made to relate these features to subsurface information in order to determine its effect on the stratigraphic and structural conditions of the area under study. This information is of two kinds. The first is based on drill hole data and comprises compiled isopach maps, and the second relates to geophysical data. This final aspect of study results in part from the author's interests in geophysics.

4. Isopach maps exist which cover most of the studied area for different stratigraphical horizons. These isopach maps are of vital importance in the interpretation of surface lineaments, for they have proved to be of great help in the determining of the cause for certain observed circular features as well as the detection of the hidden structures of the subsurface.

5. Interpretation of available geophysical data (i.e. aeromagnetic and gravity) may be used to help in

the detection of major structures or dislocations, especially within the sedimentary cover or the basement. This study is currently being carried out for the whole of the studied area and includes both local and regional structures.

In this study, the smallest observations will be considered first (i.e. the field studies) and we will then work downscale through the aerial photographic study to the analysis of fracture traces built up from the study of Landsat images. However, prior to these studies, a review of the geology of the area under investigation as it has been revealed by many authors will be presented just after the definitions and abbreviations.

1.3 Summary of Definitions and Abbreviations

1. Abu Rawash: An area which lies NW of the Giza Pyramids (Fig. 1.2) and sometimes has been written in the literature as Abu Roash or Abu Rauwash.

2. Av. F.L.: Average Fracture Length;

3. Baharia: A name of an Oasis in the N.W.D. which sometimes has been written in literature as Bahariya.

4. Band: A wavelength interval in the electromagnetic spectrum at which Landsat image is required;

5. Brightness: Magnitude of the response produced in the eye by light;

6. Computer Compatible Tape (CCT): The magnetic tape upon which the digital data for Landsat MSS images are recorded;

7. Colour Composite Image: A false colour range produced by assigning colours to three selected compounds of multi-image (e.g. Bands 4, 5 and 7);

8. Contrast Ratio (or Contrast): The ratio between the reflectance of the brightest and darkest parts of the image;

9. Detectability: A measure of the smallest object that can be discerned on an image;

10. Digital Image Processing: Computer manipulation of the digital values for picture elements of an image;

11. Drag Folds: Folds formed along wrench faults and forming a small (acute) angle with them;

12. Enhancement: The digital or photographic process which alters the appearance of an image so that the interpreter can extract more information;

13. ERTS: Earth Resources Technology Satellite (now called Landsat);

14. Fracture Trace Analysis: The branch of photogeology that applies to the recognition, interpretation and statistical analysis of the surface traces of rock fractures, detectable on any form of remote sensed imagery, or more conventionally, air photographs, and ideally includes the investigation of a sample of such features in the field;

15. Gray Scale: A calibrated sequence of gray tones ranging from black to white;

16. Image: The representation of scene as recorded by remote-sensing system;

17. Interpretation: The extraction of information from an image or aerial photograph or geophysical data;

18. IR: The infrared region of the electromagnetic spectrum with wavelengths ranging from 0.7 um to 1.0 mm;

19. I.T., (or Int. Tech.): Integrated Technique;

20. Landsat: An unmanned earth-orbiting NASA satellite that transmits multi-spectral images (in the 0.4 - 1.1 um range) to earth receiving stations;

21. L.L.: Left Lateral movement which is associated with sinistral strike-slip fault;

22. Lineament: A linear topographic or tonal feature on the terrain, images and maps that may represent a zone of structural weakness;

23. Linear: An adjective that describes the straight line nature of features on the terrain or images and maps;

24. Low sun angle images or aerial photographs: Images or aerial photographs acquired in the morning, evening or winter, when the sun is at a low elevation above the horizon;

25. MSS: Multispectral Scanner System of Landsat that acquires images at four wavelength bands in the visible and reflected IR region;

26. NASA: National Aeronautical and Space Administration;

27. N.W.D.: Northern Western Desert of Egypt;

28. Overlap: The extent to which adjacent images or aerial photographs cover the same terrain, expressed in percent;

29. Photogeology: The mapping and interpretation of geological features from aerial photographs;

30. Photogeological fracture trace: The image of a natural linear feature consisting of topographic, drainage, vegetation, soil or rock tonal alignment visible on aerial photograph and possessing the characteristics of the surface trace of a rock fracture;

31. R.Av.F.L.: Relative Average Fracture Length;

32. Remote sensing: The collection of information, mainly the electromagnetic radiation, about an object without being in physical contact with it;

33. Resolution: The ability to distinguish closely spaced objects on an image;

34. R.F.E.: Relative Fracture Energy;

35. R.F.F.: Relative Fracture Frequency;

36. R.F.L.: Relative Fracture Length;

37. R.L.: Right Lateral movement which is associated with dextral strike-slip fault;

38. Satellite: An object in orbit around a celestial body;

39. Scene: The area on the ground that is covered by an image or photograph;

40. Sidelap: The extent of lateral overlap between images or photographs acquired on adjacent flight lines;

41. Stereo model: A three dimensional mental impression produced by viewing the left and right images

or photographs of an overlapping pair with the left and right eye, respectively;

42. Stereopair: Two overlapping images or photographs that may be viewed stereoscopically;

43. Stereoscope: A binocular optical device for viewing overlapping images or diagrams to obtain the mental impression of a three dimension model;

44. Tone: Each distinguishable shade of gray from white to black on an image;

45. Vertical exaggeration: In a stereo model, this is the extent to which the vertical scale is larger than the horizontal scale;

46. W.D.: Western Desert of Egypt;

47. W.T.: Weighted Technique.

CHAPTER TWO

GENERAL GEOLOGICAL SETTING

CHAPTER TWO

General Geological Setting

2.1 Introduction

The Northern Western Desert, which occupies an area approximately 200,000 sq. km., 17% of the total area of Egypt, is almost completely covered by Tertiary and Quaternary sedimentary rocks. The area under study includes the Nile Delta and other geographical features in the area, such as the large plateau north and west of the Qattara depression (the height of which averages 250 meters above sea level), the great Qattara depression, sand dunes, the hollow of Wadi Natrun, the Faiyum depression, the Baharia Oasis, the Siwa Oasis and a part of the Great Sand Sea (Fig. 2.1 and 2.2).

This chapter presents firstly, an outline of the structural features and causes, which begin with the regional elements, moving up in scale to specific local structures. This is followed by a summary of the stratigraphy of the area, with a brief resume of the historical development of the area.

2.2 Structural Elements

In this section, structural elements are going to be described from the regional, moving up in scale to specific small areas. Consequently, this section first presents the continental or regional structural features of the Mediterranean region and East Africa. This leads

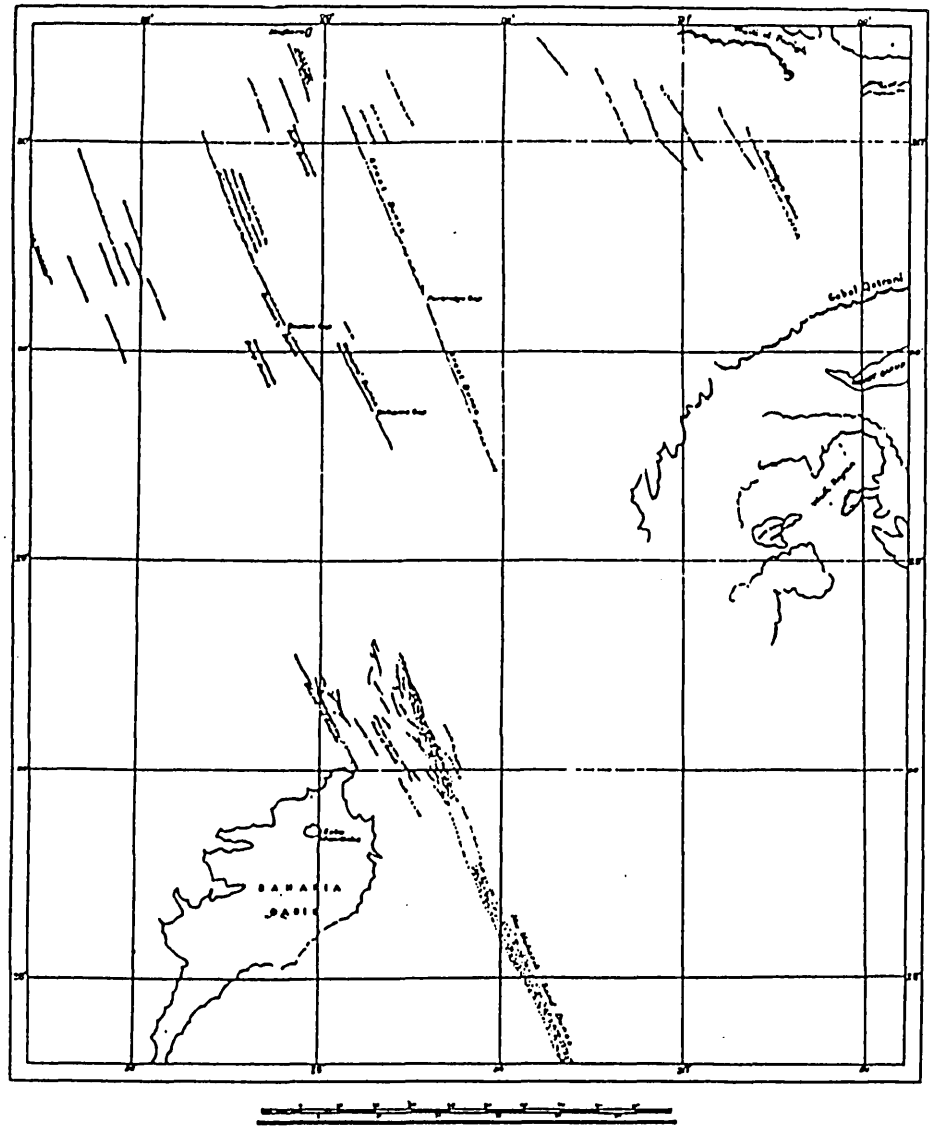


Fig. 2.2 Distribution of longitudinal dunes in northern part of Libyan desert
(After Hume,1925)

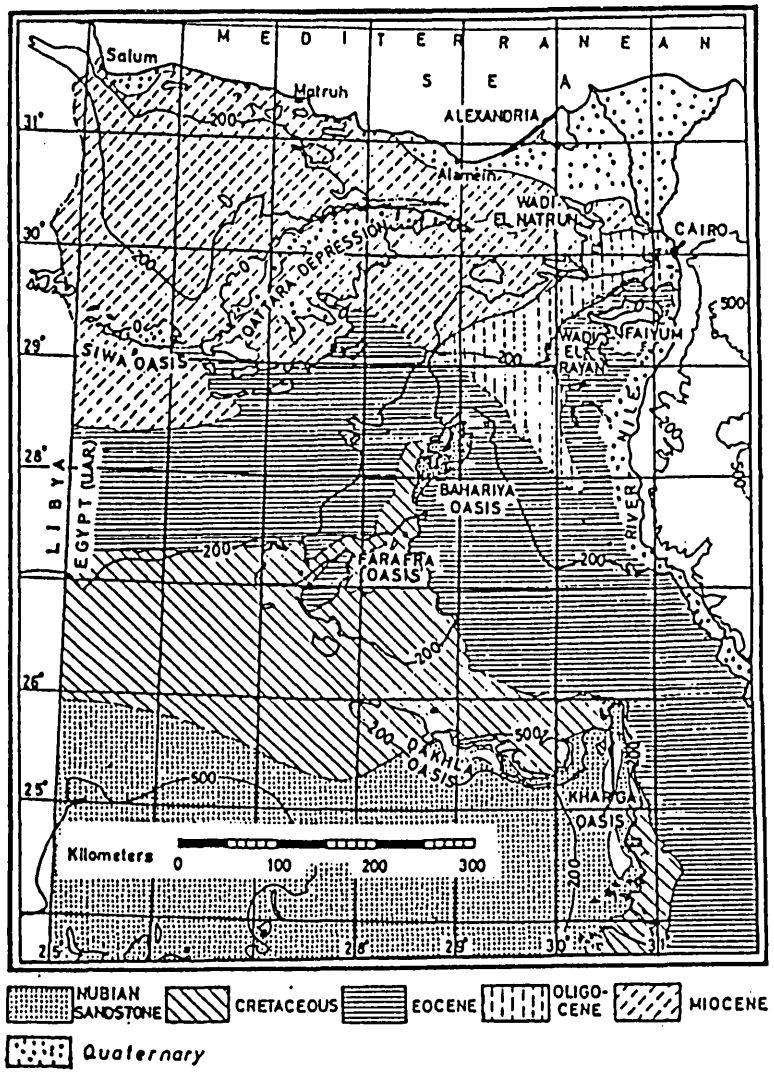


Fig. 2.1 Geological map of Egypt

to a more detailed summary of the local structures of the studied area which have been deduced or inferred by various authors, in an attempt to establish a basis on which one may rely subsequently, when a new structural analysis based on the data established is presented here..

The African plate, coupled with the Eurasian and Arabian plates, are the major units involved in major tectonics in this part of the world. The boundaries between these plates are the Azores-Gibralter ridge and its extension across North Africa, the Red Sea and the Alpide zone in Iran (Fig. 2.3).

The pole of relative motion between these plates has been located by Le Pichon (1968), as mentioned by McKenzie (1970), at 9° N, 46° W. This pole requires the motion between Africa and Eurasia to be strike-slip at the Azores, changing to overthrust south of Spain and in North Africa.

According to McKenzie (1970, 1972), the African and Arabian plates are moving northwards, (Figs. 2.3, 2.4 and 2.5), relative to the Eurasian plate. This motion is taken up on several faults at plate boundaries. The motion between African and Eurasian plates is disturbed by a relatively rapid motion of Aegean (part of Greece, Crete and part of western Turkey) and Turkish (most of Turkey and Cyprus) plates.

The seismic activity of the eastern Mediterranean, which is bounded to the south by the Unstable Shelf of Egypt, is very much greater than that of the western Mediterranean and can be attributed to the existance of

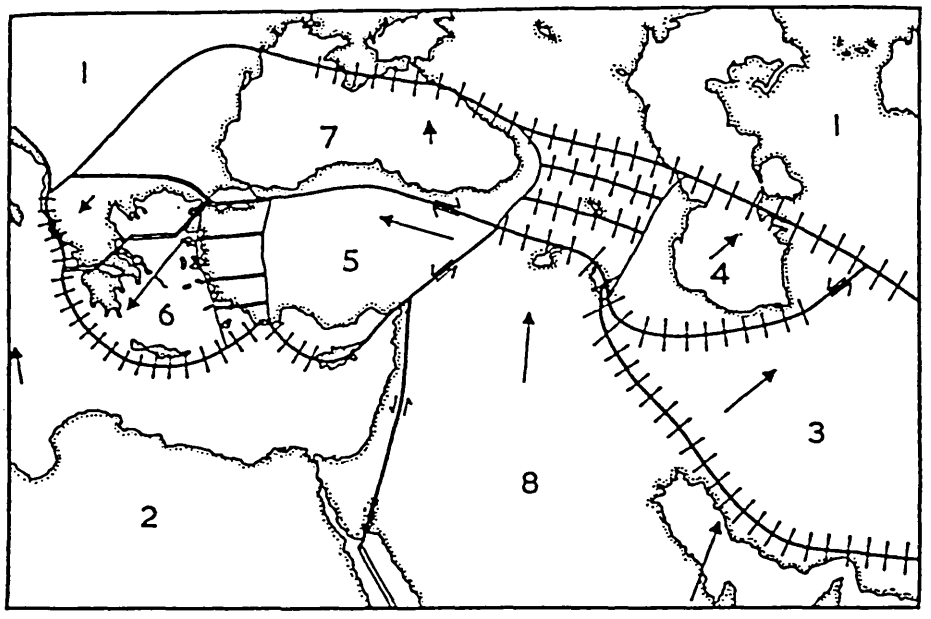


FIG.2.3 Sketch of plate boundaries and motions. The arrows show the directions of motion relative to Eurasia and their lengths are approximately proportional to the magnitude of the relative velocity. Plate boundaries across which extension is occurring are shown by a double line, transform faults by a single heavy line and boundaries across which shortening is occurring by a solid line crossed by short lines at right angles. The activity in western Turkey and in the Caucasus is due to normal faulting and thrusting respectively, but the plate boundaries shown in the figure in these regions do not correspond to individual plates and their boundaries, but only represent the general nature of the deformation. The plates are assigned the following numbers: 1 Eurasian, 2 African, 3 Iranian, 4 South Caspian, 5 Turkish, 6 Aegean, 7 Black Sea and 8 Arabian.

(After Mckenzie,1972)

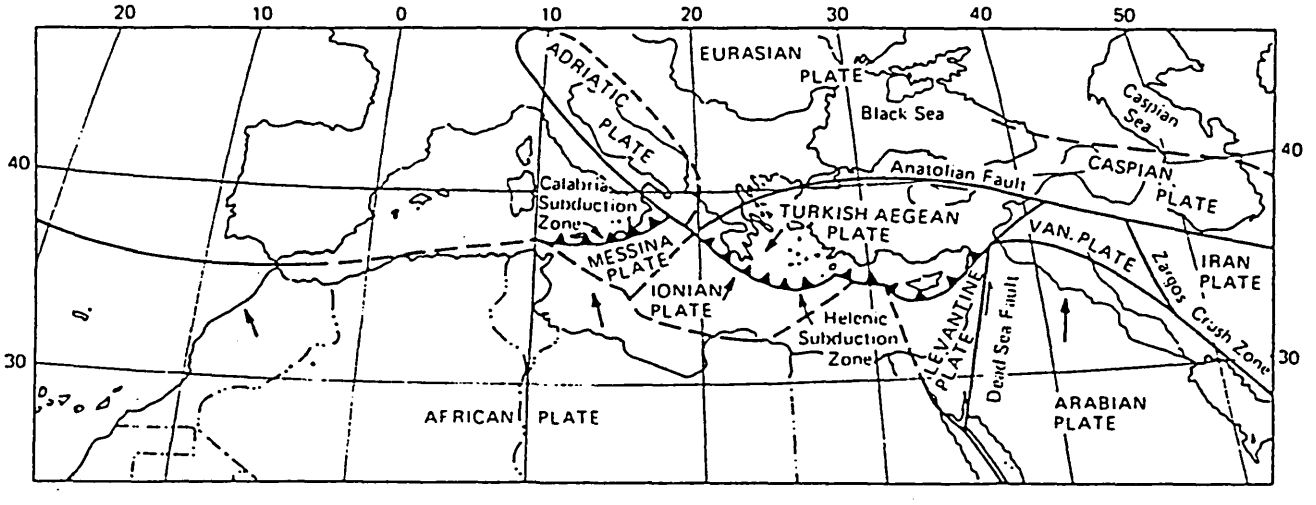


Fig.2.4 Approximate position of plate boundaries in the Mediterranean area (after Dewey *et al.*, 1973). Bold arrows refer to plate motions, relative to the Eurasian Plate. Key: ▲▲▲▲▲ = Subduction zones (triangles point in direction of dip): ═══ = oceanic ridges —— = transform faults.

(After Condie,1982)

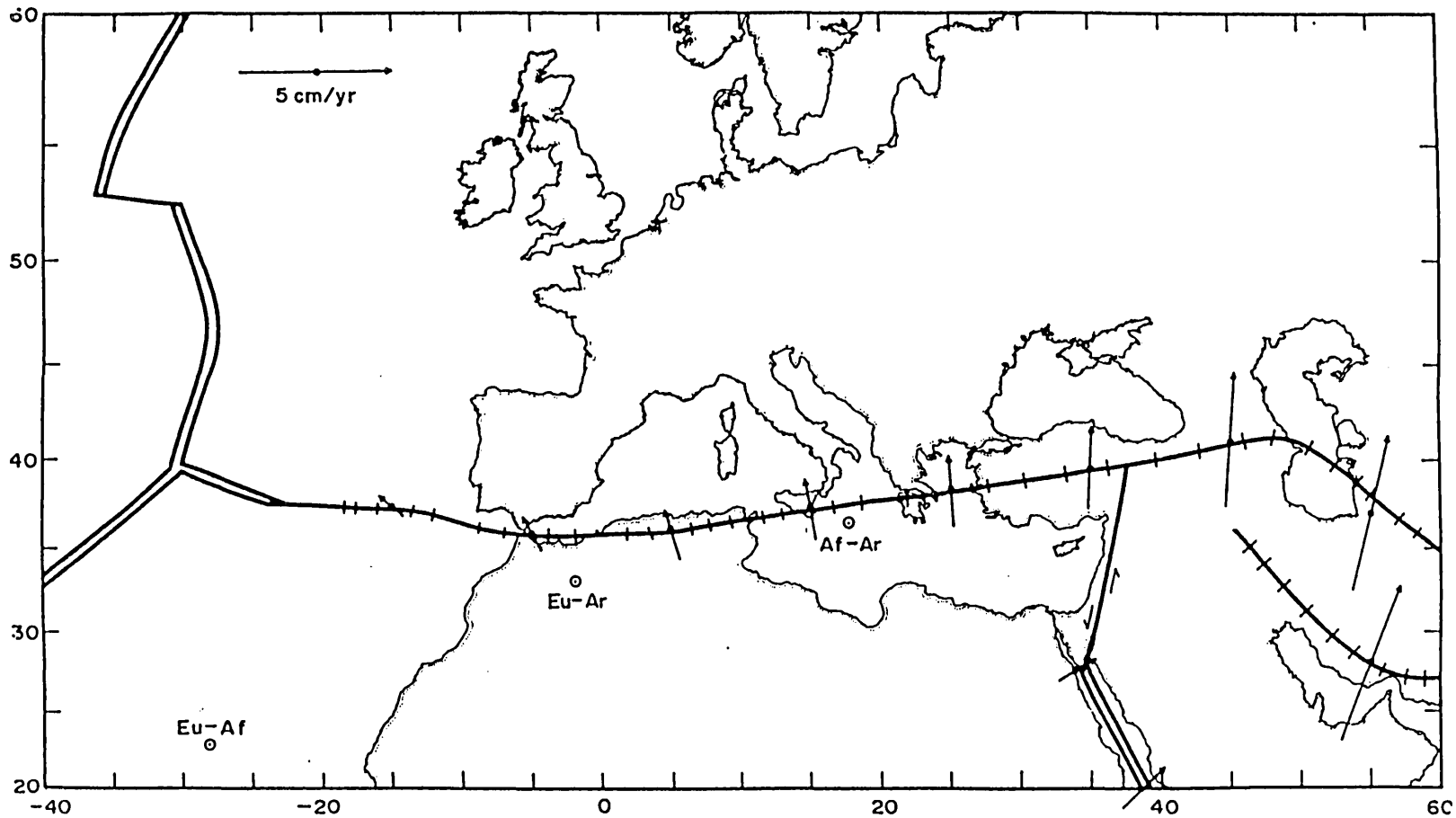


FIG.2.5 The relative motion between Africa, Arabia and Eurasia obtained from observations in the surrounding oceans. The plate boundaries are simplified to a single line in order to show the direction and magnitude of the relative motion which must be taken up by all the various motions taking place across the active belt. Extensional plate boundaries (ridges) are shown as a double line, transform faults as a single heavy line and boundaries where shortening is occurring as a solid line with short cross lines. Two boundaries are shown in Iran, but the slip vectors on each show all the relative motion between Arabia and Eurasia. The interpretation of the active processes in South-west Asia and the Mediterranean would have been extremely difficult if the motion between the three major plates in this figure had not already been obtained from oceanic magnetic lineations. The vector in the North-east Atlantic shows the scale of all the other vectors in the figure, and does not represent the motion between America and Eurasia.

(After Mckenzie, 1972)

the small, relatively rapidly moving plates, the Aegean and Turkish plates.

One may readily infer, therefore, that the structures of the eastern and western Mediterranean, as well as those of North Africa, are different.

With regard to the plate tectonics of the Red Sea and East Africa, three plates meet at the south end of the Red Sea. These are the Arabian, the Nubian and the Somalian plates. The relative motion between these plates, on one hand, and between these plates and the Sinai plate, on the other hand, are demonstrated in Figs 2.6 and 2.7 and Table 2.1 (after Le Pichon et al, 1976).

Table 2.1: Locations of the poles and angle of rotation of some plates

Plate Pair	Latitude	Longitude	Angle (degree)
+ Sinai/Arabia	32.5	-4.4	-1.7
* Arabia/Nubia	36.5	18.0	3.25
+ Somalia/Nubia	1.1	27.4	-1.35
+ Sinai/Nubia	35.5	40.9	1.75

+ Francheteau and Le Pichon

* McKenzie et al (1970)

The Red Sea trough, or Paar (Swartz and Arden, 1960) has been produced by the separation of Arabia from Africa. There is less general agreement on the time of this initial separation, however, although the Red Sea appears to be primarily a late Tertiary feature, Freund

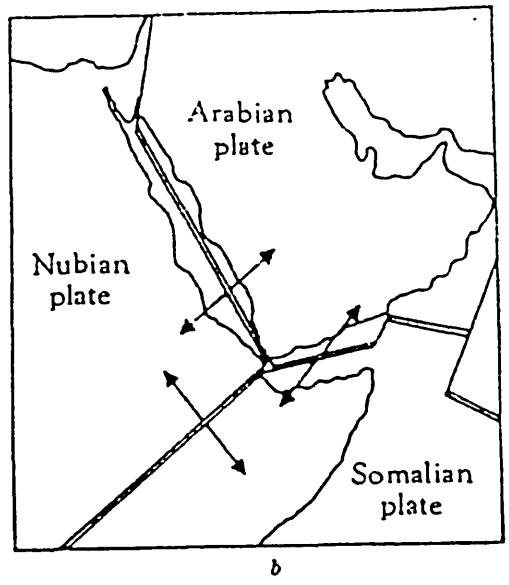


Figure 2.6: Plate boundaries and the relative motions of the Arabian, Nubian and Somalian Plates (after Mckenzie et al, 1970)

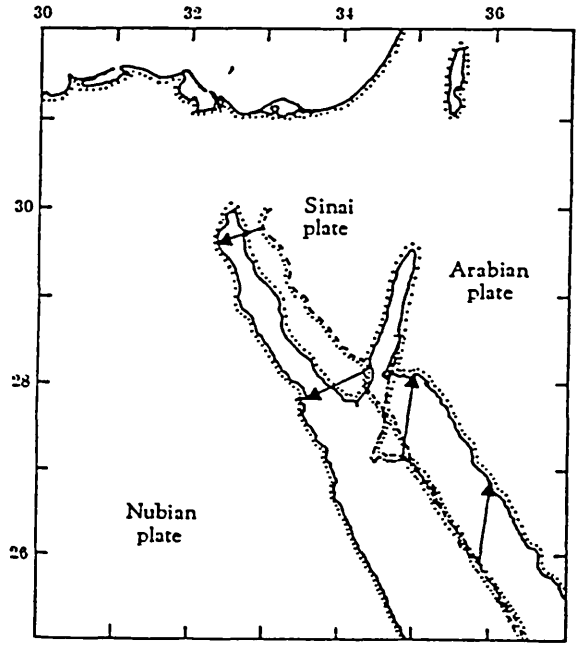


Fig.2.7 Relative motion between the Sinai plate, taken to be fixed, and the Arabian and Nubian plates is shown by the arrows.

(After Mckenzie,1970)

(1965) suggested that the separation occurred in several phases during upper Cretaceous to Pleistocene times, while others, such as Tromp (1950), believed that the graben was formed in its initial stages at the end of lower Eocene.

The extension of the Gulf of Suez takes place by normal faulting rather than by the formation of Oceanic floor. The long history of activity of many normal faults probably depends on the existance and orientation of existing basement faults (McKenzie et al, 1970).

A possible right lateral strike-slip fault along the Gulf of Suez was suggested by Youssef (1968) and Le Pichon et al (1976). Although the former believes that the horizontal offset along the Gulf of Suez is about 60 km., on field grounds, the second predicts an offset of about 33 km., on plate tectonic grounds.

Abdel-Gawad (1970), based on the assumption that the dominant movement of Sinai relative to Africa was towards the NNE but at a slower rate than the Arabian plate, proposed that the Gulf of Suez experienced a left lateral shear movement with a limited extension across the Gulf of Suez.

It was found from the field (Freund et al, 1970) and the plate tectonic studies (Le Pichon et al, 1976), that the Dead Sea region shows a post-Cretaceous sinistral strike-slip movement of 105 km.; 60 km. pre-Miocene and 40 to 45 km. post-Miocene.

2.2.1 Elements of Regional Structures

According to Sander (1981), the major structural elements of the Mediterranean region can be classified into:

1. Pre-Cambrian and Palaeozoic massifs;
2. Mobile belts;
3. Large fault troughs;
4. Platforms and shelves;
5. Basins;
6. Persistent highs and;
7. Faults.

For the purpose of this study, the most important structural elements are platforms (Fig. 2.8) and faults.

Platforms

Platforms are large (more or less elongate) areas, only slightly disturbed by orogeny, in which sedimentation was relatively uniform over extensive tracts. However, epeirogeny and faulting may have recurred at intervals. Platforms are classified into Stable and Unstable.

1. Stable platforms are characterized by a thin and incomplete sedimentary section, because subsidence was slow and intermittent.

2. Unstable platforms are those in which subsidence was relatively persistent, and the sedimentary section is thick and more or less complete, although movements along faults and minor orogeny may have caused a local hiatus.

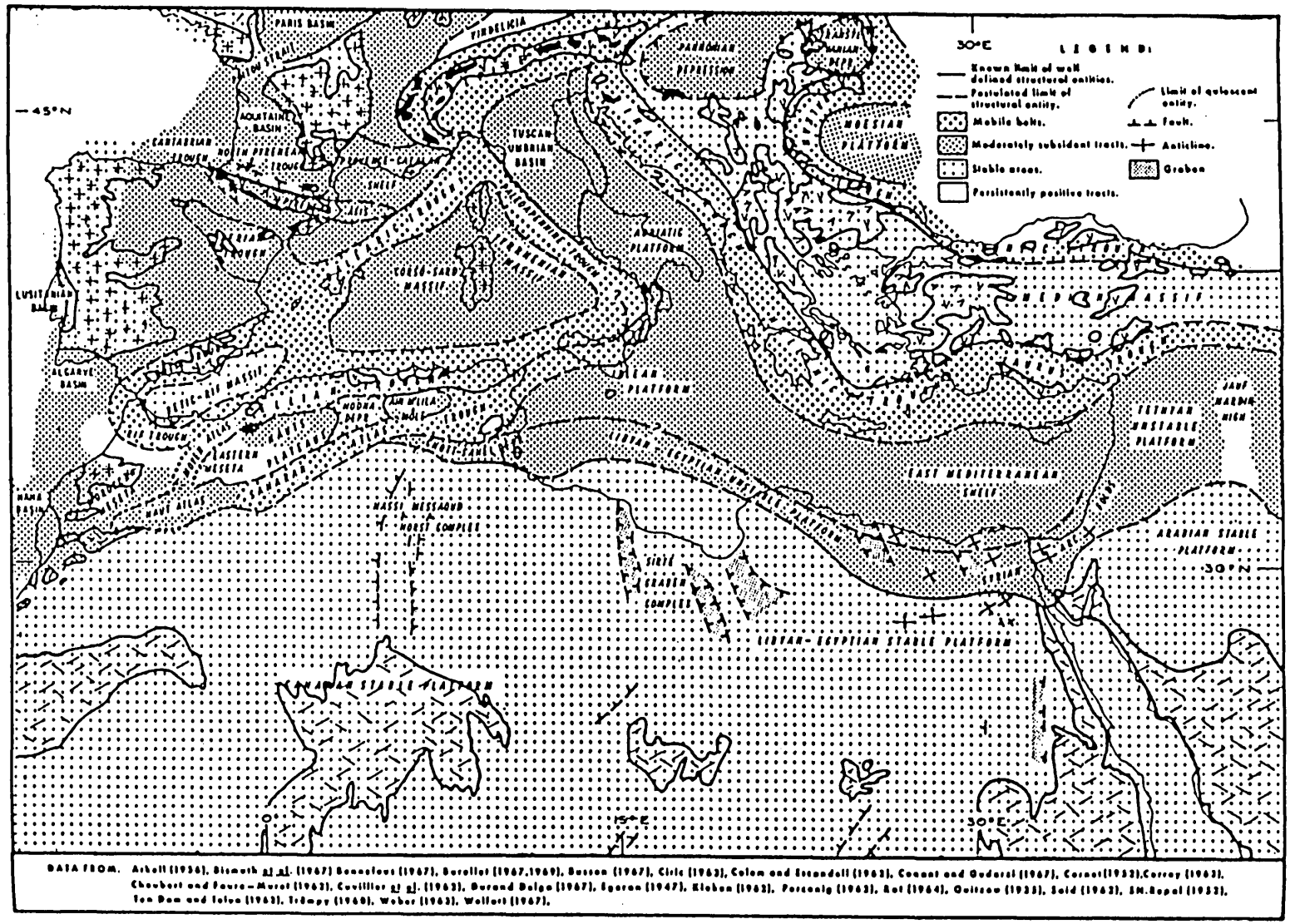


Fig. 2.8 Late Cretaceous structural elements (After Sander,1981)

The platforms of North Africa, which are the foreland of the African shield, have maintained their identity and relative stability since the end of Palaeozoic times with faulting and epeirogeny responsible for most of their deformation.

Faults

Major fault systems are significant in North Africa where they are thought to reflect ancient fracture systems in the basement. Four major trends of faulting have been mentioned by Sander (1981). Although none of them is confined to one geographic area, certain trends are more common in one locality than in another. These trends are:

1) N 85 E or nearly E-W;

2) NNE to NE;

3) NNW (parallel to the faults delimiting the Gulf of Suez); and

4) N - S faults.

Some of the faults with this trend are strike-slip faults.

Major crustal shears in Africa (Fig. 2.9) have been assumed by Moody (1966). The trends of these shears are 1) NNW trend (the Gulf of Suez trend), 2) NNE (the Gulf of Aqaba trend), 3) ENE (Qattara trend) and 4) WNW trend. The first and second pairs of these shears are thought to have been generated by nearly N - S, or meridional, and nearly E - W, or equatorial compressive stresses (Fig. 2.10), respectively. However, as it has

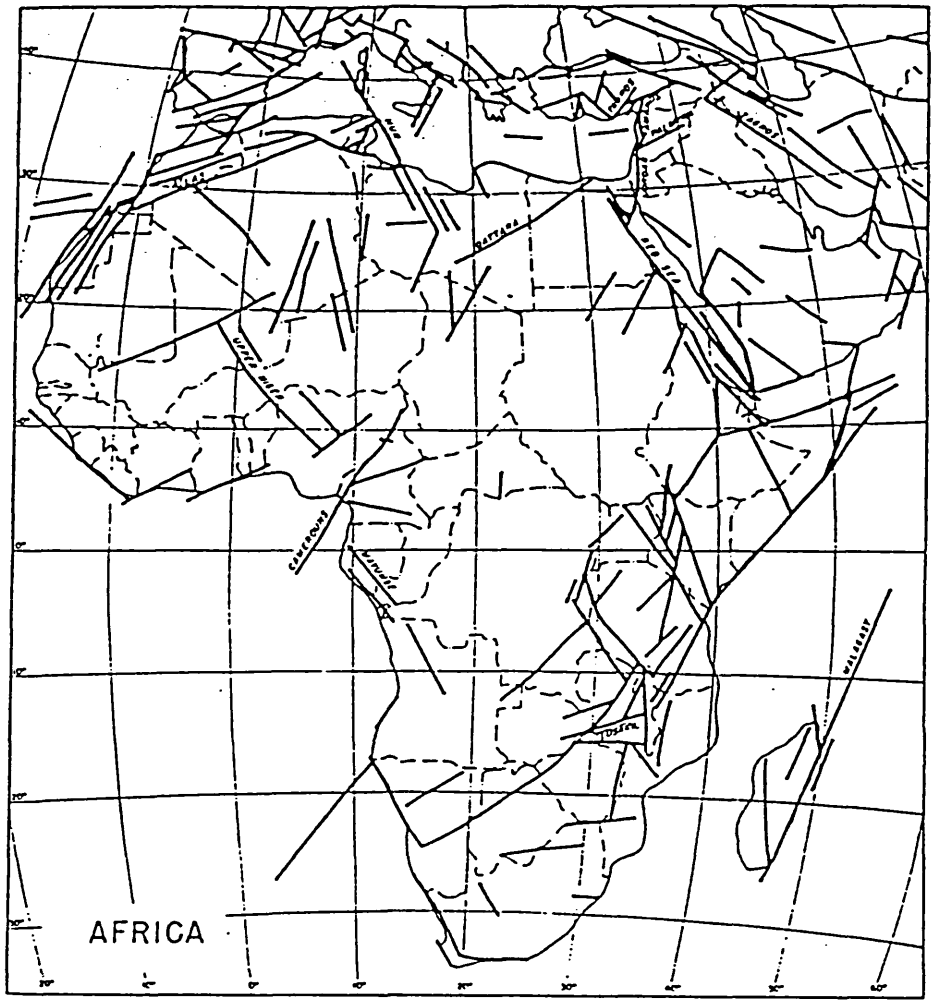


Fig. 2.9 Some major deep shears of Africa

(After Moody,1966)

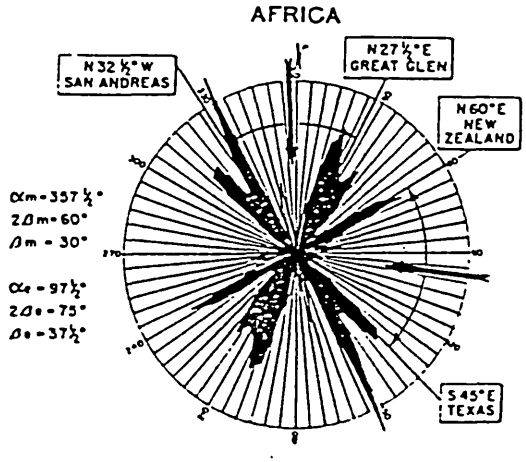


Fig. 2.10 Orientation of the maximum stresses relative to major deep shears in Africa.

(After Moody,1966)

been proved during the course of this study, the WNW and ENE (Qattara trend) shears, at least in Egypt, exhibit strike-slip lateral movements which contradict those proposed by Moody (1966) and cannot be attributed to E-W compression stresses.

Picard (1937), in his structural study on the Arabian Peninsula and its surrounding countries, (see Fig. 2.11), divided the tectonic zones into: the Arabian-Nubian nucleus (1), the unfolded zone or belt (2), zone of simple folding (3), zone of complex folding or nappes (4), the Median mass of Persia (5), and Yemen Abyssinian plateau (6), as a magmatic raised block.

With respect to Egypt, the most important zones are:

1) the Arabian-Nubian nucleus;

2) the unfolded zone (plateau like structure); and

3) the zone of simple folding (Jura folding).

The large structural elements from Picard's point of view are:

1. Epirogenetic movements;

2. Fold forming tangential forces which control the simple and complex folds of the geosyncline zone;

3. Tension forces which cut and plough-up the uplifted parts into rifts and faults.

Weeks (1952), in his work in the Middle East, classified the regional tectonic zones (see Fig. 2.12) into:

1) Stable foreland shelf; 2) Hinge belt; 3) Trough and belt of frontal folds (outside Egypt); 4) Borderland nappe zone (outside Egypt).

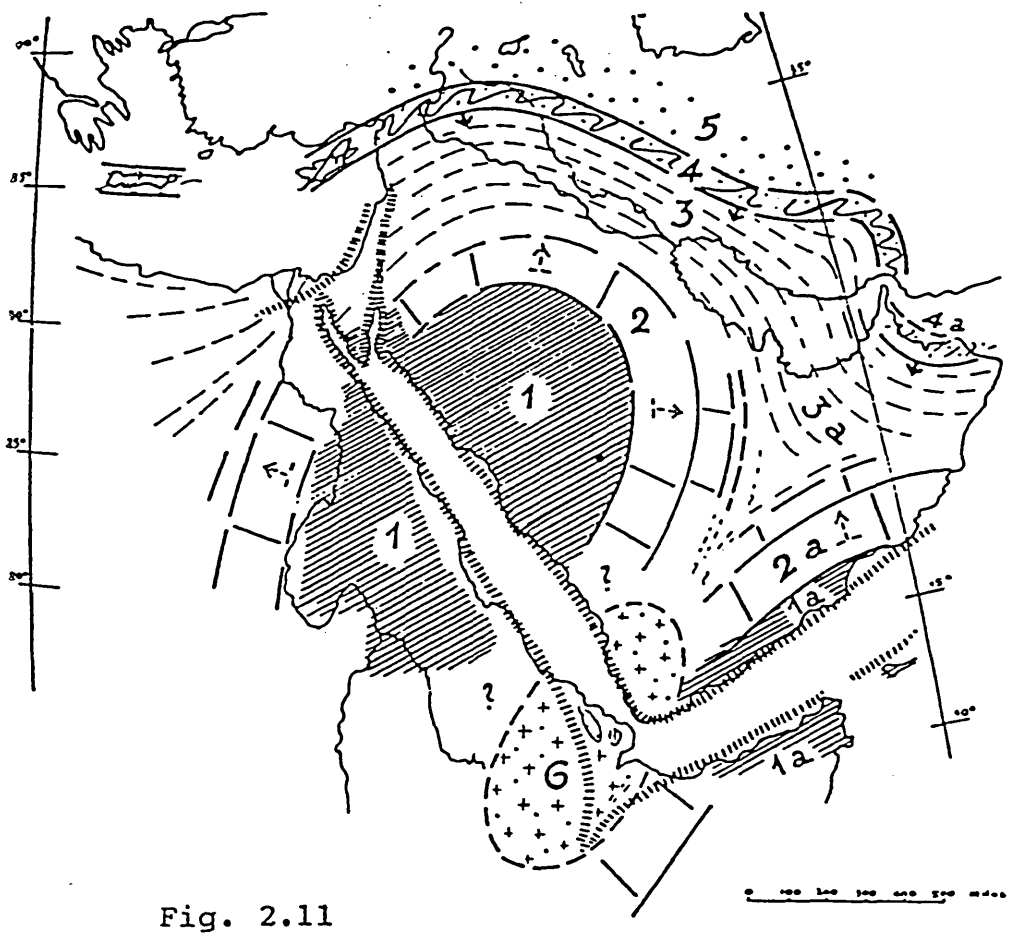


Fig. 2.11

Structural Sketch Map of the Arabian Peninsula and Surrounding Countries.

(For the purpose of clarity the younger volcanic areas have been omitted from the map.)

1. massifs:
   - 1 arabo-nubian
   - 1a arabo-somali
2. Zone "tabulaire":
   - 2 arabo-nubian
   - 2a arabo-somali
3. Zone of simpler folding (autochthonous)
   - 3a Khub al Khali
4. Zone of complex folding (nappes)
   - 4a arc of Oman
5. Median Mass ("Zwischengebirge")
6. Block of Yemen—Abessinia ("Sabea")

Rift-faultings

direction of folding-movements

dip of zone tabulaire

(After Picard,1937)

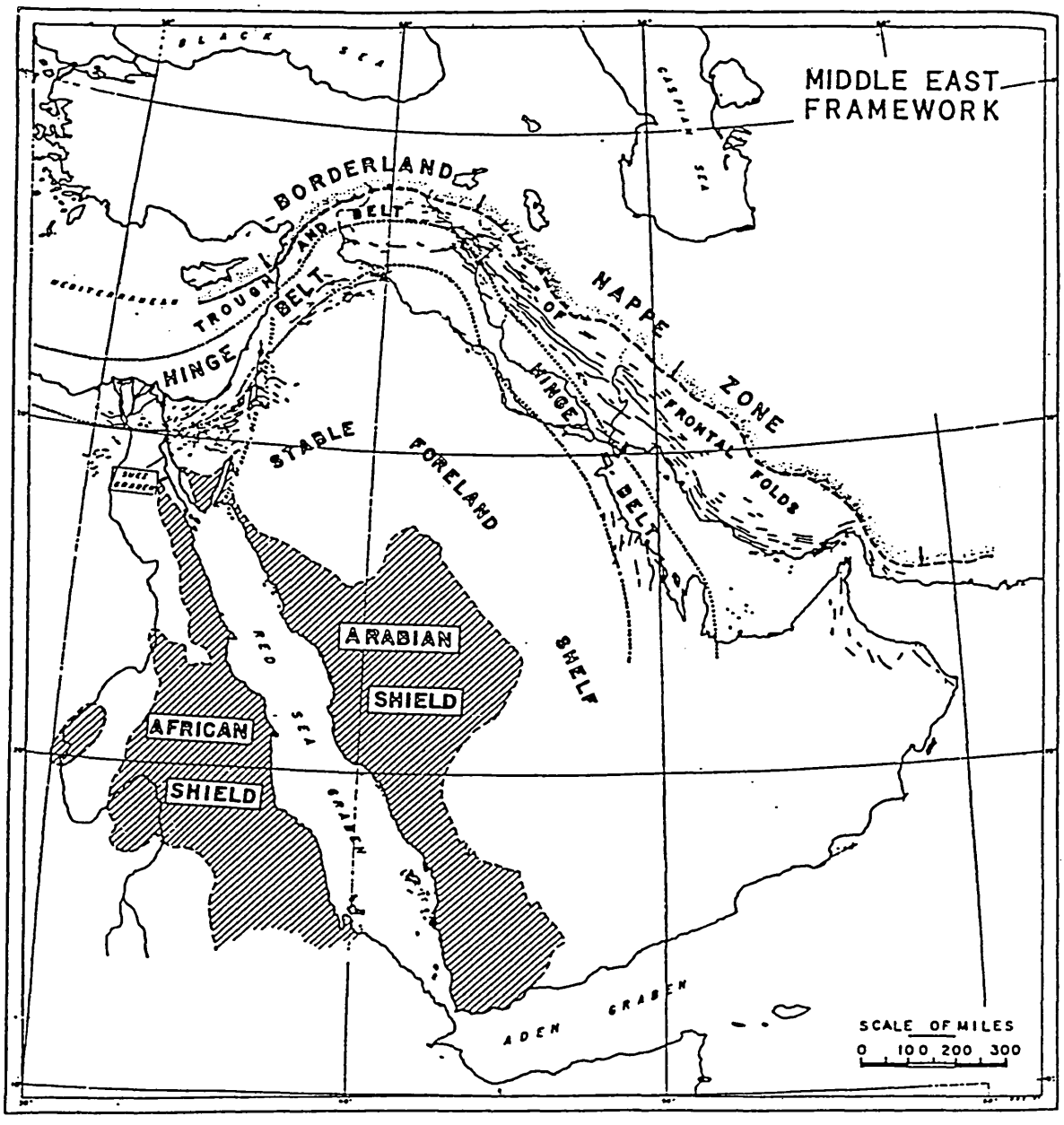


Fig. 2.12 Middle East framework (After Weeks,1952)

The structure of Egypt and the adjacent countries of the East Mediterranean, which are indicated in Fig. 2.13, were presented by Knetsch (1957).

2.2.2 The Structural Elements of Egypt

Little has been written on the structural framework of Egypt, except in works dealing with the neighbouring countries, such as Picard (1937, 1943), Henson (1951), Weeks (1952) and Knetsch (1957). Here, the structures of Egypt will be reviewed as they were discussed by different authors.

With regard to Yallouze and Knetsch (1954), Northern Egypt comprises the following (see Fig. 2.14):

1. The Syrian arc systems of folds (mobile belt);
2. Fracture zone of the Nile Delta;
3. Rift valleys;
4. Basins and swells, such as the Nile basin and Baharia swell.

Sigaev (1967) classified the structural stages of Egypt into: pre-Cambrian (lower structural complex) and platform or upper structural complex.

1. Pre-Cambian (lower-structural complex)

This lower structural complex is concerned with the pre-Cambrian geosynclinal fold sequences which constitute the crystalline basement of the platform and outcrop, where they form large domal features.

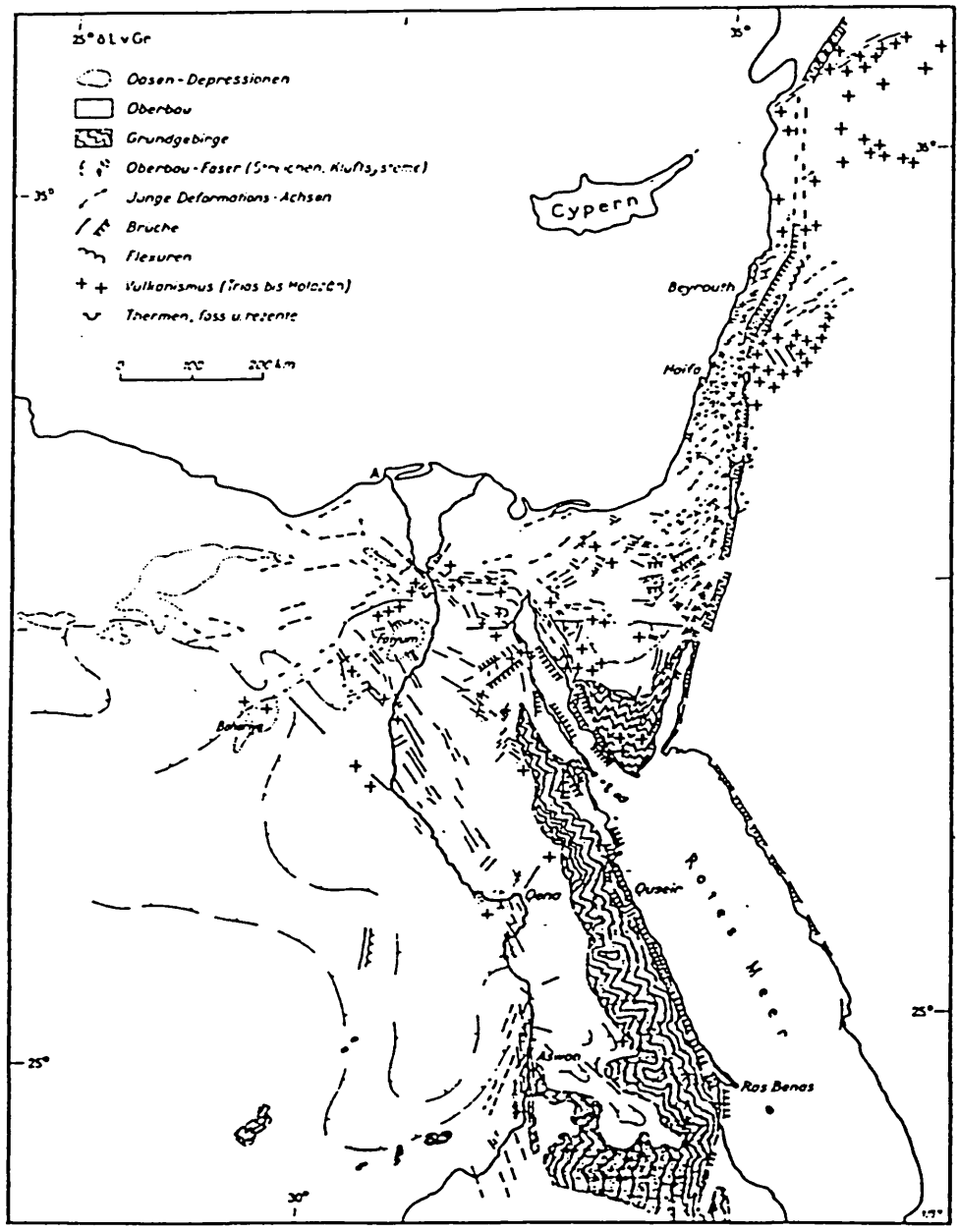


Fig. 2.13 Structures of Egypt and the surrounding eastern Mediterranean countries. (After Knetsch, 1957)

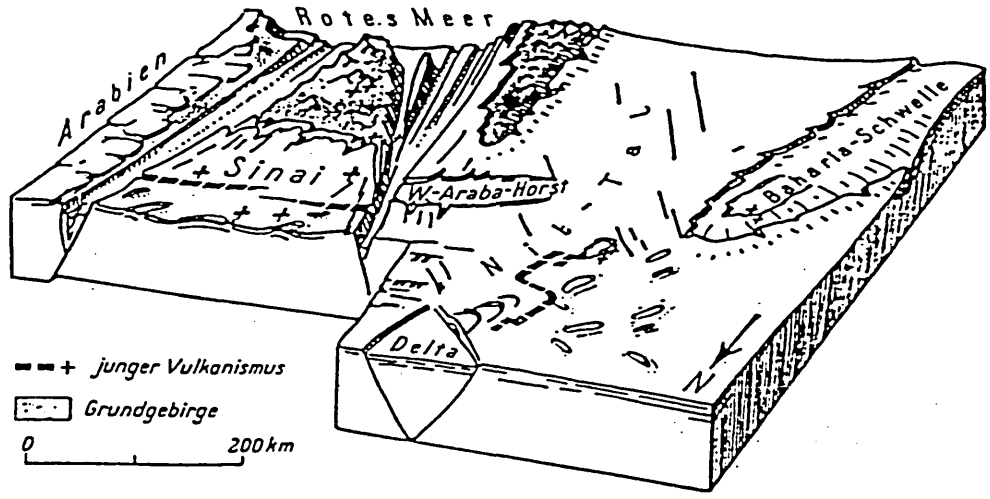


Fig. 2.14 Block diagram of the north Egypt deformations. (After Knetsch, 1957)

2. Platform or upper structural complex

The upper structural complex was divided (Sigaev, 1967) into: a) pre-Jurussic structural stage; b) Jurassic-Nubian structural stage; c) pre-Eocene structural stage; d) Eocene structural stage and e) Oligocene-Quaternary structural stage.

The pre-Eocene structural stage and even the Jurassic-Nubian structural stage, is represented by the structure contour map (Fig. 2.15) of the top Cenomanian (Sigaev, 1967). The structural trends of this map are: 1) ENE; 2) NNE; 3) NNW; 4) NW; 5) NE; 6) N - S; and 7) E - W. He suggests that the main structural trend is NW along the Mediterranean coast and in the area covered by the western boundary of Egypt, and the Abu Magharic depression between the Baharia Oasis and Faiyum depression.

The important feature of the Oligocene-Quaternary structure, as is mentioned by Sigaev (1967) are:

i) Wide development of ruptural deformation in the Oligocene-Miocene;

ii) Active basalt extrusion at the end of the Oligocene and the beginning of the Miocene;

iii) Intensive downwarping and the widening of the Gulf of Suez and Red Sea grabens in Miocene and Pliocene.

According to Picard (1937, 1943); Henson (1951); Weeks (1952); Shata (1953, 1955); Knetsch and Yallouze (1955); and Knetsch (1957); Said (1962) divided Egypt from the tectonic point of view into: 1) the Arabian-Nubian massif (shield); 2) the Stable shelf;

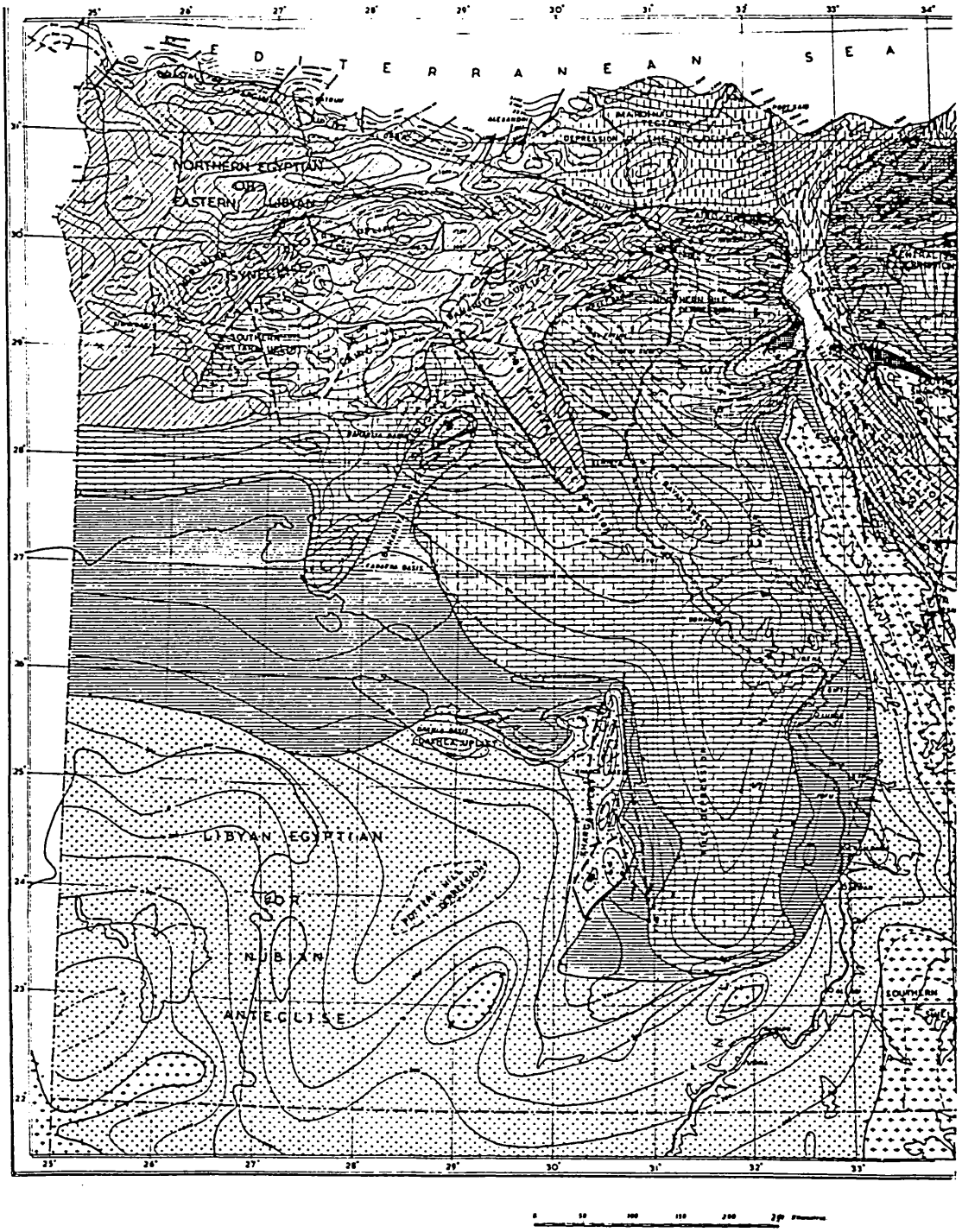


Fig. 2.15 Structure contour map of the Western Desert of Egypt, top Cenomanian. (After Sigaev, 1967)

3) the Unstable shelf; and 4) the Gulf of Suez (Fig. 2.16).

1. The Arabian-Nubian massif

The Arabian-Nubian massif is the surviving roots of old mobile belt that developed early and prior to Cambrian time. The massif is a stable tectonic unit which shows a high degree of deformation and metamorphism. Igneous intrusions, mainly acidic, are widespread and the sediments show evidence of considerable granitization. The Arabian-Nubian massif or shield represents an upwarping (Picard, 1937) which is sloping towards Arabia in the east and towards Nubia in the west.

In Egypt, this massif includes the basement rocks of southern Sinai, the Eastern Desert mountains and the southern part of the Western Desert.

2. The Stable shelf

As was noted earlier, the Stable shelf encircles the Arabo-Nubian mass, with very ill defined boundaries. It represents a relatively rigid or stable region which almost lies outside the area under investigation. The stable shelf is characterized by:

i) thin continental, epicontinental and shallow marine sediments, which cap the rigid basement. The greatest and lower part of this sedimentary section is composed of sandstone, while the smallest part, the upper part of this section, consists of shales, marls and limestone.

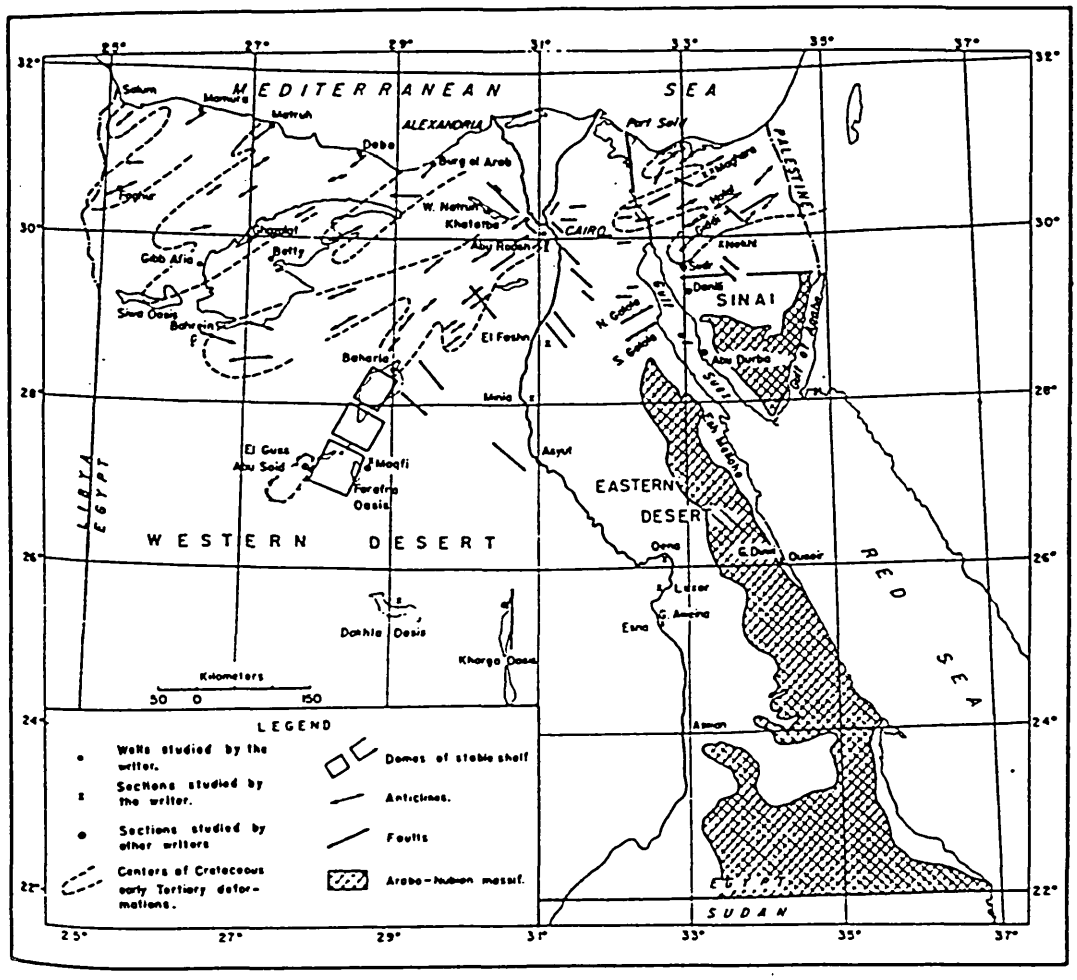


Fig. 2.16 —Simplified tectonic map of Egypt showing most of the important locations in text (modified and completed from Knetsch and Yallouze, 1955).
(After Said, 1961)

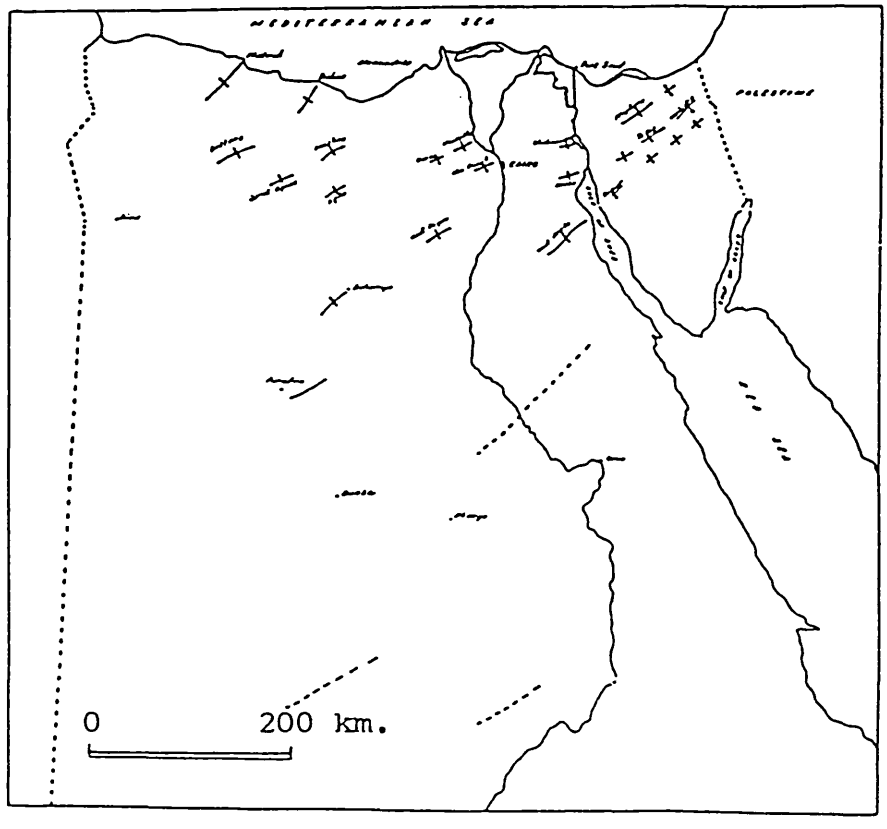


Fig. 2.17 Map showing the main Syrian Arc System in Egypt. (After Shukri, 1954)

ii) Faulting is common in this shelf. Large scale faulting, produced by crustal deformation is present. The strikes of the faults which have been reported in this shelf are: a) N - S, East African (Kharga Oasis); b) NW, Erythean (controls the extent and direction of the Gulf of Suez); c) E - W, Tethyan (Cairo - Suez road); and NE, which has been reported all around the Stable belt.

iii) Folding plays a minor role in the structure of the shelf. The folds of this shelf are drape features which result from block faulting. The sets of folds which are present in this shelf are: 1) N - S folds, Kharga Oasis - Western Desert; 2) ENE - WSW fold of Wadi Araba, Eastern Desert; 3) NW - SE folds, Eastern Desert; 4) NNW - SSE folds, Aswan area (Attia, 1955) and; 5) NE - SW folds, Dakhla Oasis - Western Desert.

3. The Unstable Shelf

The Unstable shelf constitutes the greater part of the northern Egypt, which lies between the foreland and geosyncline. This shelf is characterized by the following:

a) Variation in thickness and facies of the sedimentary section over its area;

b) Its marine sediments are predominantly calcareous and of chemical or organic origin, with some evaporites. Terrigeneous clastics are rare and of short time range, except: i) adjoining the margins of the

Stable shelf to the south, and; ii) in the neighbourhood of local elevations of the basement;

c) This shelf shows tectonic disturbances of minor order, including Germano type tectonics, diaprism and faults. According to Said (1962), the forces which acted on the subsurface to produce these features are not obvious, but are suggested to be related to infracrustal or regional faults that strike NE - SW;

d) The deformation history of this belt consists of: i) a long period of compressive movement in a form of superposed regional gentle movements, followed by; ii) a short period of predominately tensional relief.

The compressive stresses that affected the Unstable shelf began perhaps as early as Palaeozoic and continued unabated until at least the Pliocene (Said, 1962). The evidence of the compressive movements has been inferred from the subsurface data (Said, 1962) where the Triassic sediments are missed, especially in the western part of the Western Desert, indicates that this area was folded above sea level at the end of the Paleozoic. Also, the sedimentary gaps at the bottom and within the Jurassic formations in many localities suggests pre-Jurassic folding. In northern Egypt, folding continued or was renewed during lower Cretaceous (Aptian - Albian). The local folding throughout the Unstable shelf began to take place by the end of the lower Cretaceous. It seems to become stronger at or near the end of the Turonian. Folding continued either steadily or intermittently throughout the Senonian and Palaeocene. These folds are

known as the Syrian arc system, which is characterized by:

a) Asymmetric folds with NE - SW trend, where the dip of the southern flank is steeper than that of the northern one;

b) The folds are severely fractured and faulted;

c) The folds form en echelon;

d) The folds are bounded on the south or the north by high angle longitudinal reverse faults which dip towards the fold axes, with downthrown to the south or the north. Most of the faulting, such as normal and reverse, probably took place towards the end of the compression period.

Shukri (1954) mentioned the following main lines of the Syrian arc system of Egypt (see Fig. 2.17):

1) Matruh line;

2) Dabaa line;

3) Qattara line;

4) Moghra-Garet Agnes (gravity highs);

5) Khatatba line (passing through Gebel Agila, Gebel Ruzza and Khatatba (gravity highs);

6) Abu Rawash line (including Abu Rawash, Shabrawet and Moghara);

7) Baharia line (passing through Baharia and Wadi Rayan;

8) Wadi Araba line (includes Farafra Oasis, Wadi Araba and Somar). This line lies within the Stable shelf of Egypt, where the folding was formed as a result of block faulting.

The Syrian arc system of folds has been affected by younger faults, which trend NW and E - W. The studied area falls within this shelf.

4. The Gulf of Suez

The Suez Gulf or rift is situated within the Stable shelf of Egypt. It is like the other rifts in the region and represents a northern branch of the Red Sea rift. The Suez rift separates the minor plate, formed by the Sinai block, from the African plate. It is slightly arcuate with a general NW strike. Said (1962) mentioned that the Gulf of Suez has been an active zone of subsidence throughout its geological history. But Garfunkel and Bartov (1977) reported that the Suez rift was not clearly defined before late Eocene times. This rift was already well developed and sufficiently depressed to be inundated by the sea in the earliest Miocene.

On the both sides of the Gulf of Suez, Abdel Gawad (1970) recognized the following main trends: 1) NNE (Aqaba trend); 2) NW (Gulf of Suez trend); 3) WNW; 4) NE and; 5) E - W. He suggested that the NE faults in the Gebel Um Disi area (SW of the Gulf of Suez) are sinistral strike-slip faults with a lateral displacement of 7 km. In the Gebel Duwi area, (Fig. 2.18), Youssef (Said, 1962) describes large WNW strike faults and intensive deformation of the pre-Cambrian, Creteceous and Eocene strata. According to Abdel-Gawad (1969), the Duwi strucure is a WNW shear zone which intersects the Red Sea

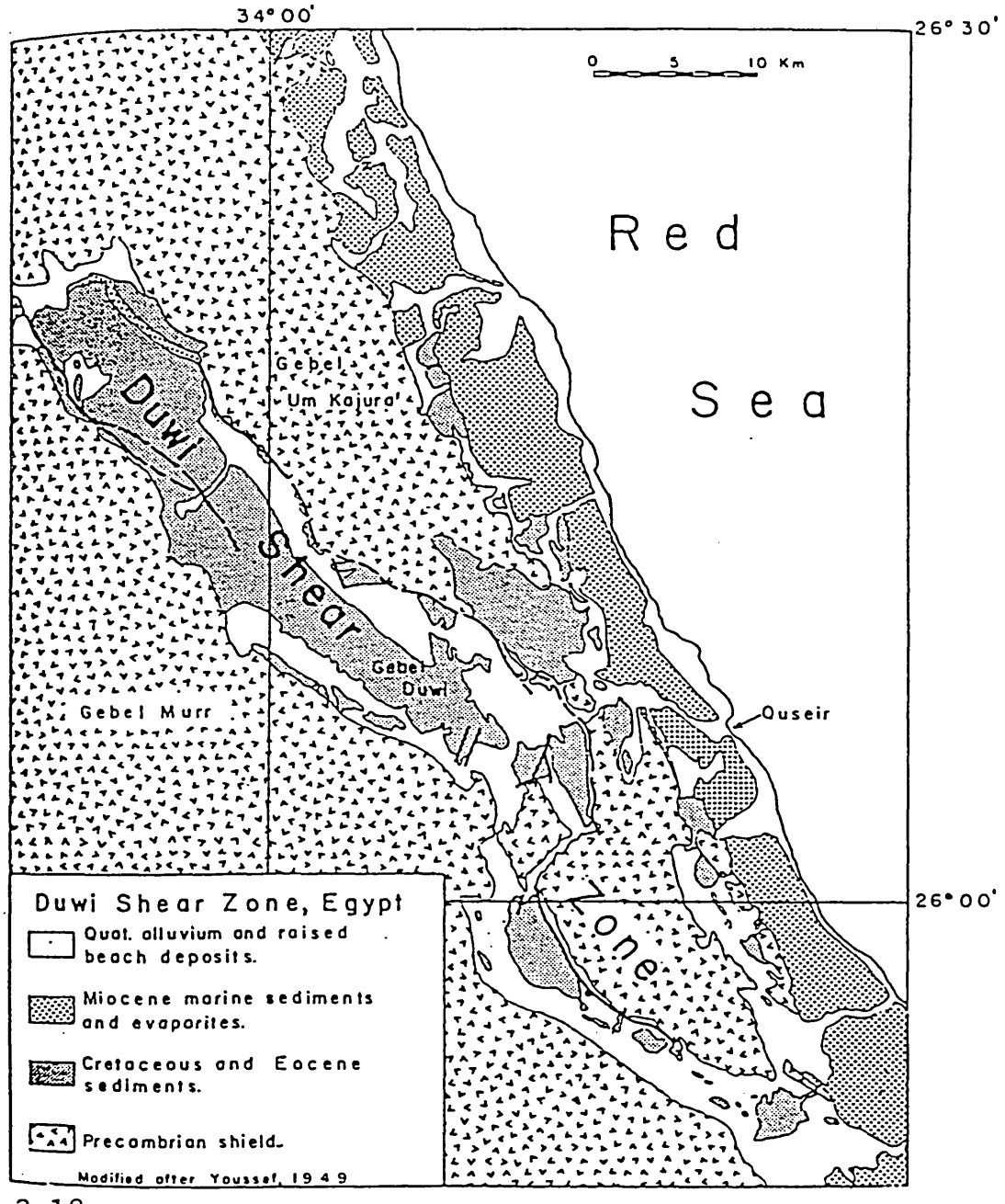


FIG. 2.18 —Geologic map of Duwi shear zone in Egypt. Wrench faults affect Precambrian shield and overlying Cretaceous and Eocene strata. Note orientation of shear zone relative to Red Sea coast and presence of marine Miocene and raised beach deposits along shear zone. Duwi structure is believed to be displaced continuation of Abu Masarib shear zone in Figure 2. Modified from Youssef (1949) and Said (1962, Fig. 16).

(After Abdel Gawad, 1969)

at 30° degrees, where the pre-Cambrian basement and overlying Cretaceous and Eocene sedimentary rocks form parallel slabs that rise in the elongate ridges of Gebel Duwi and are interrupted by NE faults. This shear was rejuvenated by the end of the Eocene and has become inactive since that time. However, the sense of the relative lateral movement along this shear zone has not been mentioned by Abdel Gawad or any of the former authors, but the present writer, based on aerial photographs' study as well as subsurface data in the Western Desert proved that these shears practice right lateral movement, dextral strike-slip faults.

In the Gulf of Suez area, some WNW faults have been located (Fig. 2.19) (Abdel Gawad, 1969).

On the southern part of the Gulf of Suez, the interpreted air photo lineaments were classified by El-Eter and Abdel Rahman (1976) into two groups as follows: 1) a. NW and NE sets; b. Northerly and Easterly sets; 2) a. WNW and NNE sets; b. ENE and NNW sets. It has been proposed that the first group can be mechanically attributed to N - S compression, while the second group may be considered as second order trends of the same compression, or may be developed as a result of slight westward deviation of the axis of the compression (Youssef, 1968), but they did not mention the sense of the relative movements along these sets of the air photo lineaments. These structural trends seem to date from the pre-Cambrian.

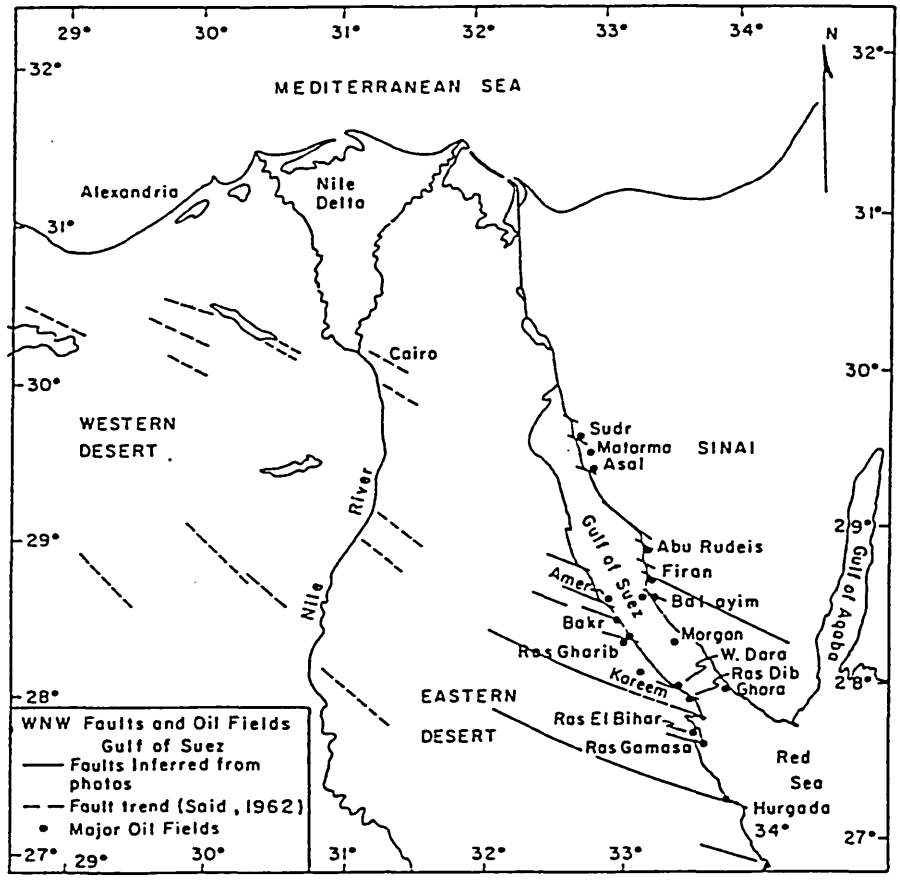


Fig. 2.19 Relation of WNW faults to oil occurrences in Gulf of Suez region. (After Abdel Gawad,1969)

Youssef (1968) grouped the main structural elements of Egypt (Fig. 2.20) under the following categories:

1) The Gulf of Suez - Red Sea (N 35 W) and the Gulf of Aqaba (N 15 E) fault trends (categories 1 and 2); these trends have been suggested to be a complementary set of shear fractures, where the maximum principal stress trends N 10 W. Much later, when this region was upwarped, the main vertical slip took place along these faults.

2) N 45 W and N - S fault trends (categories 4 and 5): These trends were assumed to form a conjugate set of shear fractures. The maximum principal stress direction was N 20 W, deviating 10° degrees to the west of the initial one (N 10 W).

3) North Sinai folds (category 6), or Syrian arc folds: The axes of these folds trend N 65 - 70 E. These folds were formed by the younger stresses where the greatest principal stress axis trends N 20 W.

4) E - W fault trends (category 3): These faults are nearly perpendicular to the initial greatest principal stress, N 10 W. These faults, as were assumed by Youssef (1968), could be thrust faults. After the erosion of the initial scarps of these faults to the level of the downthrown blocks and the deposition of late Paleozoic or Mesozoic sediments, vertical or gravity displa cements may have taken place later, along these old fractures (see Fig. 2.21). These faults were interrupted by NW en echelon faults which are considered as a surface expression of a subsurface strike-slip faults.

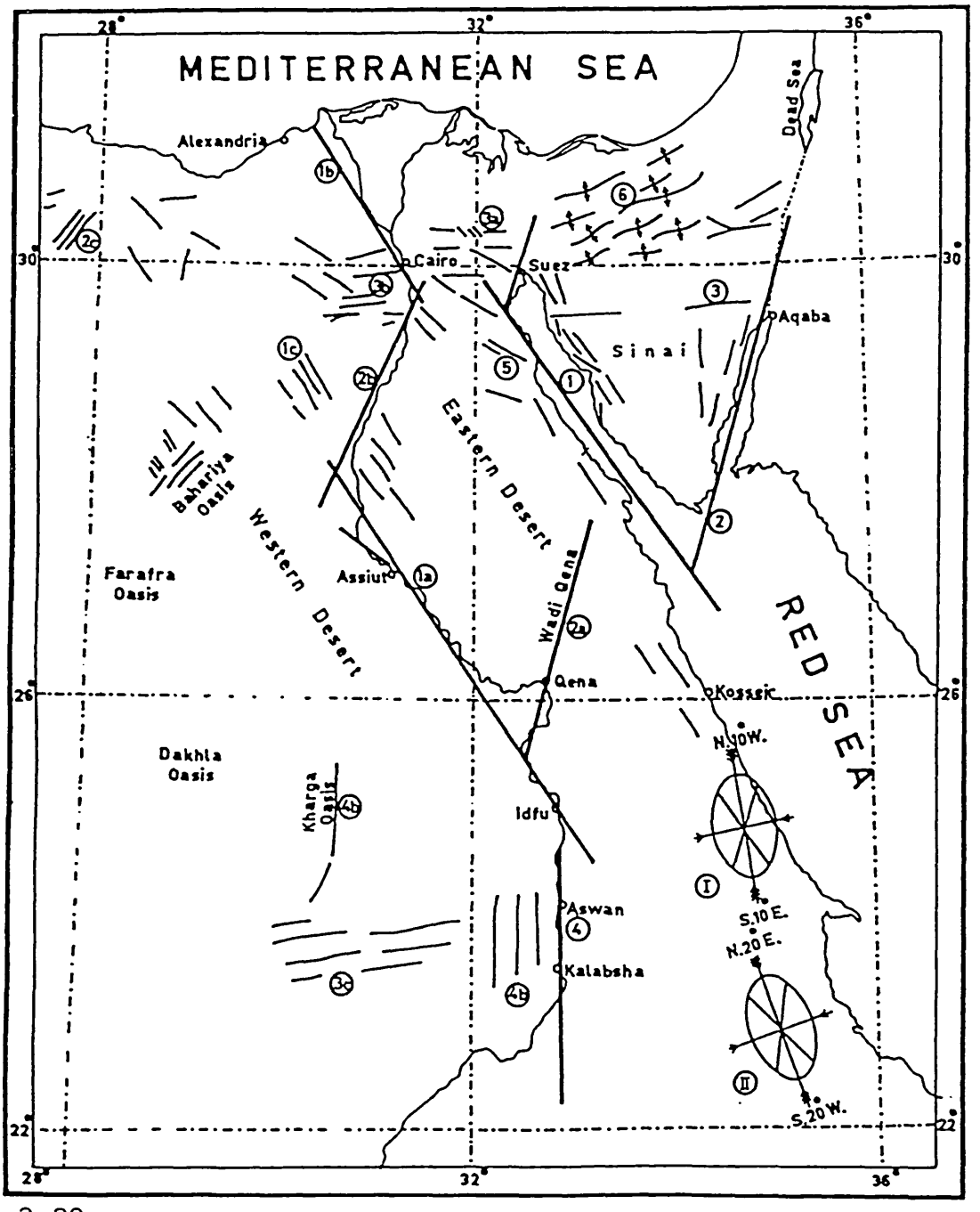


Fig. 2.20 —Main directions of faulting and North Sinai folds. 1, 1a, 1b, 1c = Gulf of Suez trend (about N. 35° W.); 2, 2a, 2b, 2c = Gulf of Aqaba trend (about N. 15° E.); 3 (Central Sinai fault), 3a, 3b, 3c = east-west trend, ancient thrusts that evolved into gravity and strike-slip faults; 4, 4a, 4b = north-south trend (deviating Gulf of Aqaba trend); 5 = N. 45° W. trend (deviating Gulf of Suez trend); 6 = North Sinai folds. I = Stress ellipse showing orientation of greatest and least principal stress axes and relation of compression to ancient fracture trends (1 and 2). II = Final orientation of stress and resulting fractures (3 and 4) after deviation from original direction in I.

(After Youssef, 1968)

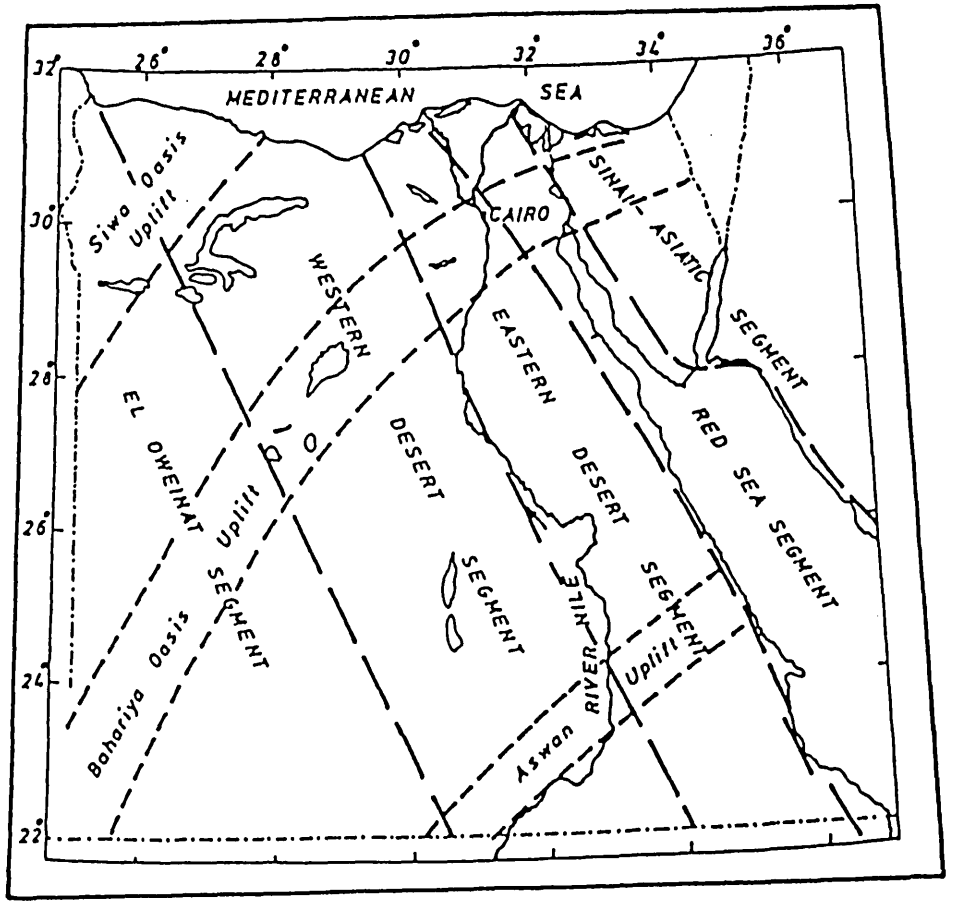


Fig. 2.22 Sketch map of major structural elements of Egypt

(After El Shazly, 1977)

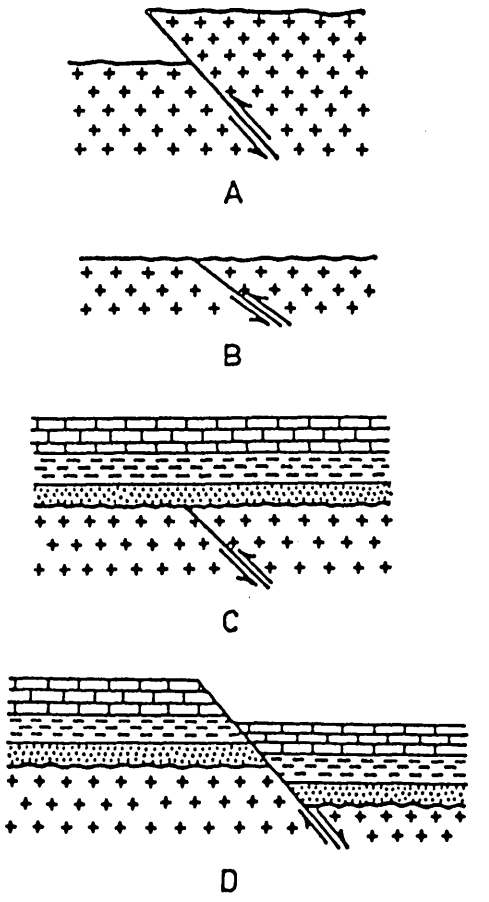


Fig. 2.21 —Probable stages in evolution of east-west thrusts into gravity faults. A = Thrust faulting in basement. B = Peneplanation of walls of thrust. C = Deposition of sedimentary sequence on peneplaned surface. Dip-slip (gravity) movement along plane of ancient thrust.

(After Youssef, 1968)

5) Folds parallel with faults (category 7): These folds are present along the Nile Valley, around the Gulf of Suez, along the Red Sea coast and the Cairo-Suez road, as well as across the Western Desert. Most of these folds are drape folds and were formed as a result of block faulting.

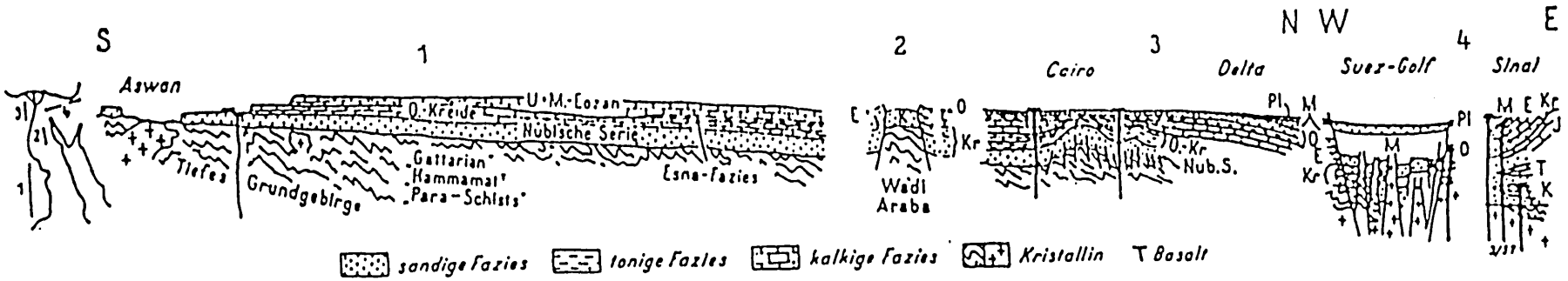
6) Folds oblique to faults (category 8): These folds have limited length and amplitude. They trend obliquely to the direction of strike-slip faults, Nile Valley (Youssef, 1968). These folds were developed as a result of movements along strike-slip faults.

El Shazly (1977) suggested that Egypt was divided into rigid crustal segments along NNW major faults since the pre-Cambrian and the latest phase of the pre-Cambrian folding have NNE or sometimes, NE axial traces (Fig. 2.22), (where the forces usually exerted from the WNW).

2.2.3 The Structural Elements of the Western Desert

The structural interpretations of the Western Desert dates back to Zittel, in 1883 (Shata, 1953), who regarded this particular area as a region of simple geological structures covered with northerly gentle dipping Tertiary strata (Fig. 2.23). Succeeding authors reported a small number of local structures, but the general attitude among them was the same as Zittel.

Recent deep drilling in the Northern Western Desert of Egypt has shown that these apparently simple areas conceal beneath the gently dipping sediments seen at the



Geologische Schnitte durch Ägypten.

Nubische Serie = Karbon bis Untere Kreide, K = Karbon, T = Trias, J = Jura, Kr = Kreide, E = Eozän, O = Oligozän; M = Miozän, Pl = Pliozän.

Fig. 2.23 Sketch of a geological cross section across Egypt. (After Knetsch, 1957)

surface a much larger number of geological structures in the form of basins and swells.

Accordingly, Yallouze and Knetsch (1954) and Sigaev (1967) divided the different tectonic regions of the Western Desert (see Fig. 2.15) into:

1) Northern Egyptian synclinal basin, where the main trends of the basins and swells it contains are ENE and NW;

2) Southern Libyan-Egyptian or Nubian large domal uplifts, where the basement structures are clearly inherited and reproduced in the Nubian blanket (Yallouze and Knetsch, 1954);

3) Nile synclinal basin, with NW trend.

It is suggested that the Nile synclinal basin has been formed as a result of the bulging of the basement of the Eastern Desert (Fig. 2.24), (Sigaev, 1967);

4) The Southern Nile basin (Yallouze and Knesch, 1954), which lies south of the Nile synclinal basin (Fig. 2.24), has a general NE axis but is somewhat crescent shaped.

Yallouze and Knetsch (1954) studied linear structures, such as fractures and drainage lines, and concluded the following:

A. The NW trending fractures and/or faults within the Northern Nile basin may be considered as tension, such as the graben and basaltic eruptions of the Eastern Desert or shears, which make a shear angle with the greatest compressional axis that produced the Baharia swell.

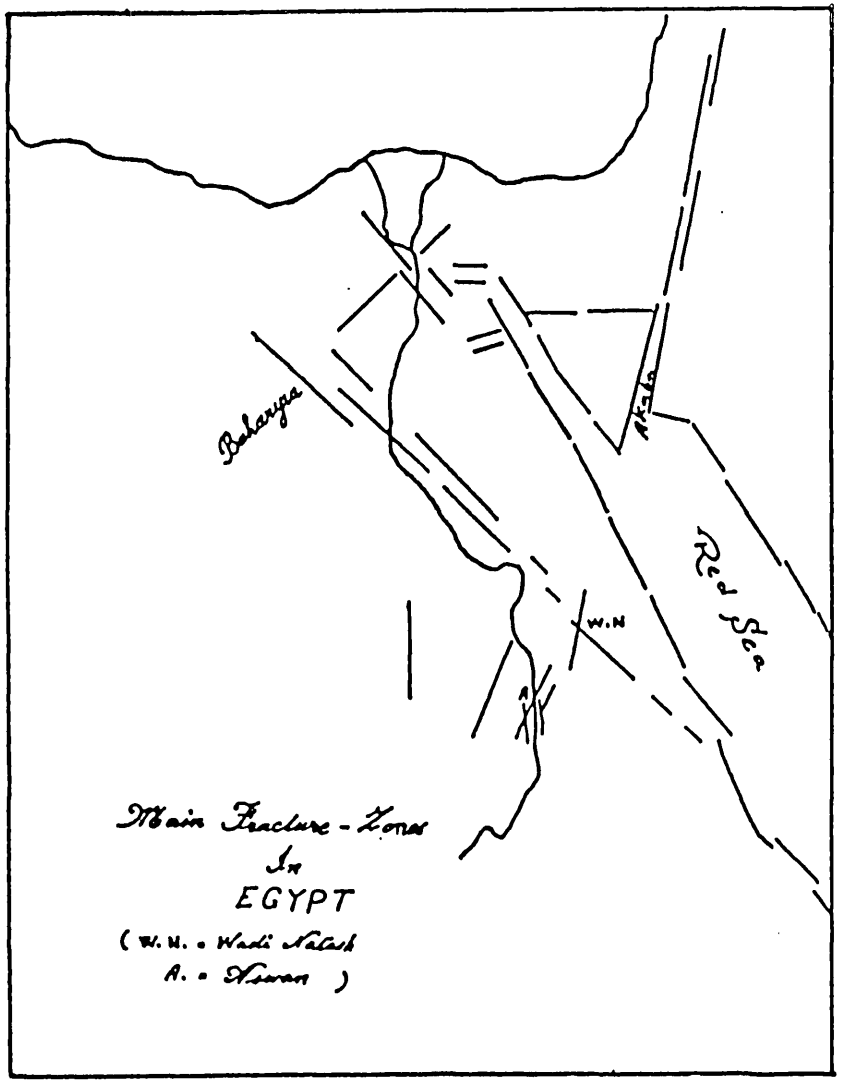


Fig. 2.25 Main fracture zones in Egypt.
(After Yallouze and Knetsch,1954)

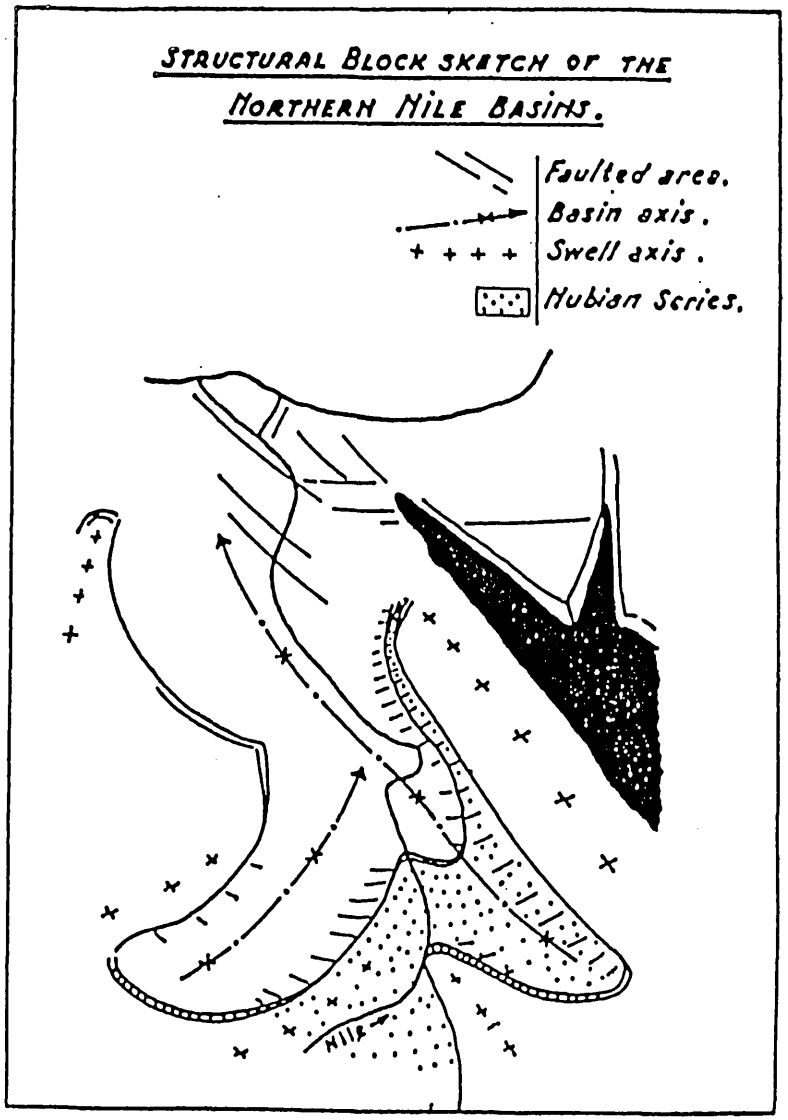


Fig. 2.24 Sketch of structural block diagram of the Northern Nile Basin.
(After Yallouze and Knetsch, 1954)

B. The Baharia swell was formed, presumably as a compressional feature.

C. The Wadi Natash- Quena - Assyut line which trends NW (Fig. 2.25), represents a structural boundary between:

a. the geoanticlinal zone of the Eastern Desert;

b. the more stable portion of the shelf in the SW, and;

c. between the Baharia swell and the folding belt in the north.

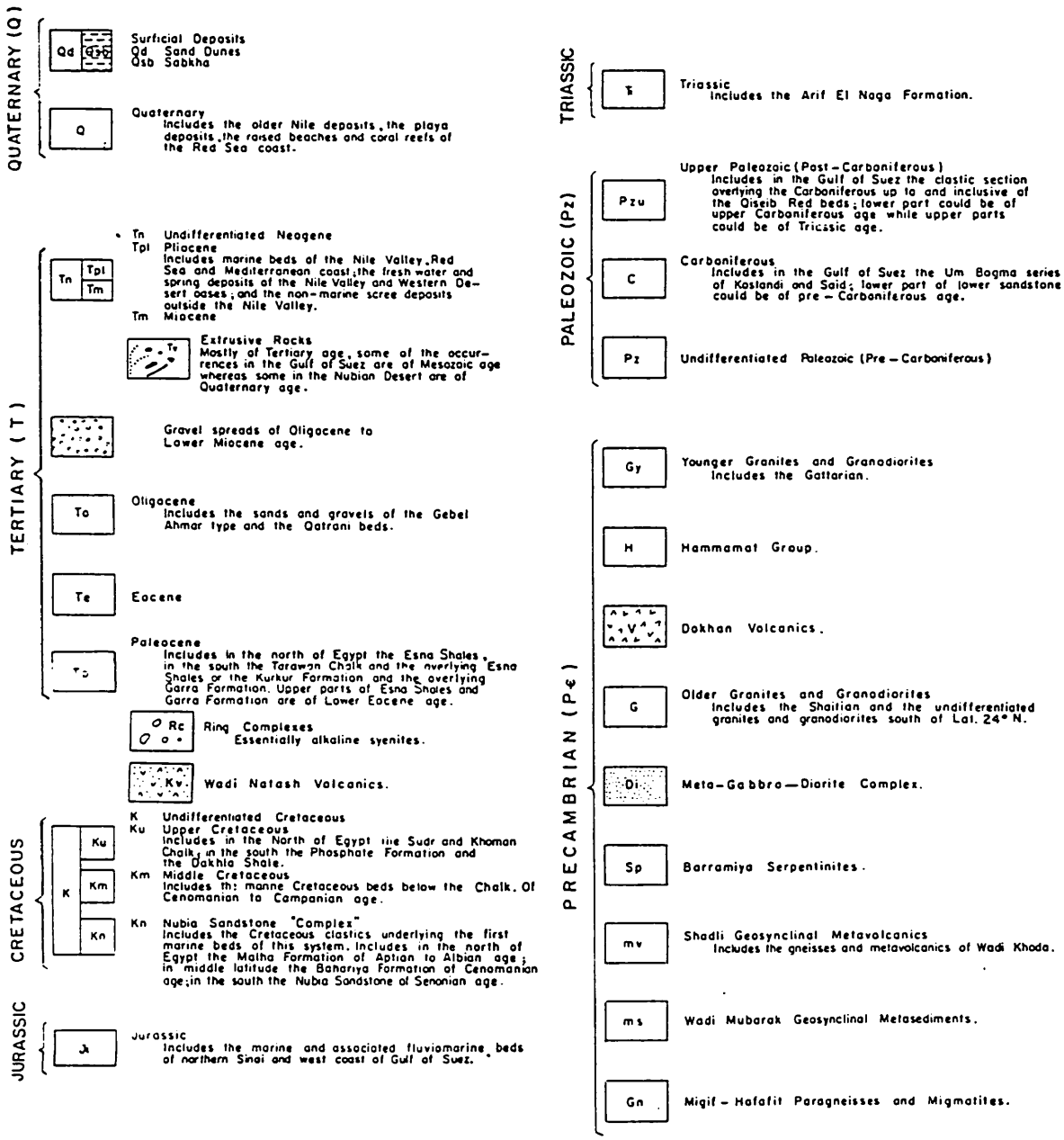
D. There is a remarkable parallelism of the major and minor structures (drainage lines and fractures). This proves that even in a composite and heterogeneous sedimentary section, the parallelism between major and minor tectonics are still preserved.

E. There are some rotation faults within the Eocene sedimentary section, where the limestones glided down over the Esna shale facies of listric (i.e. spoon shaped or shovel plane) rotational planes, but these are accompanied by no obvious tectonics.

According to Yallouze and Knetsch (1954); Sigaev (1967) and Said (1971), the structural trends of the basement in the Western Desert are: E - W, NE, N - S and NW.

a) E - W structural trends are typical for the Aswan basement (Fig. 2.26). These trends appear on the surface north and south of Cairo. They are more

The Legend of the opposite figure (fig. 2.26)



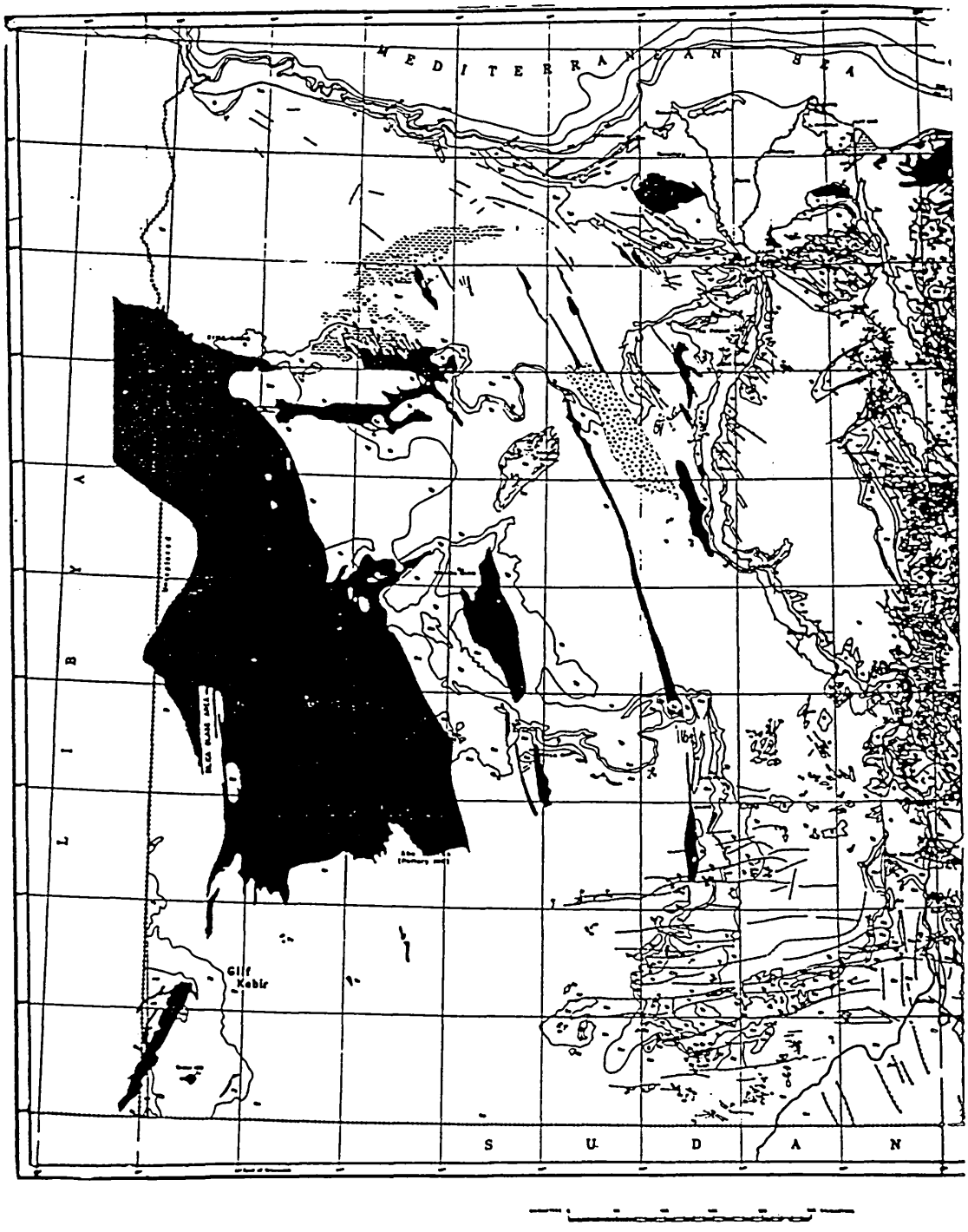


Fig. 2.26 Geological map of the Western Desert of Egypt.
(After Said, 1971)

conspicuous on the east bank of the Nile than the west bank.

b) The NE (the Gulf of Aqaba) structural trend is represented south of Aswan by great tear (shear) faults (Yallouze and Knetsch, 1954). Sometimes these faults are curved but show a general NE trend. Most of this structural trend shows also dyke-filling.

c) The N - S structural trend is thought to be present as locally slightly deviating towards NNE or NNW (Figs. 2.15 and 2.26). Some faults belonging to this trend are probably shears (Yallouze and Knetsch, 1954).

d) The shear zones of the pre-Cambrian age have been practised again and again either vertical or lateral movements during later orogenic times (Yallouze and Knetsch, 1954).

e. NW structural trends become more obvious as one proceeds further north. Some of the NW trends have been dated as post-Oligocene (Yallouze and Knetsch, 1954).

With respect to the Northern Western Desert of Egypt, the most notable episodes of tectonic disturbances, as mentioned by Said (1962), are:

1) Early Palaeozoic (Caledonian);

2) Late Palaeozoic (post lower to middle Carboniferous);

3) Late Jurassic (Nevadian);

4) Upper Cretaceous - lower Eocene (Laramide);

5) Mid to late Tertiary.

Said (1962) mentioned the following:

1. El-Khatatba - Wadi Khadish block is horst block trending NE - SW.

2. Abu Rawash block is separated from Khatatba block by NE - SW fault.

Schurmann (1974) concluded the following (Fig. 2.27):

1. The general slope of the basement surface is to the northwest.

2. The great difference in the depth of the pre-Cambrian in the Khatatba well (1,884 m.) and Wadi Natrun well (4,054 m.), as well as between Wadi Natrun well and Alam El-Buieb well (4,725 m.), is very probably attributable to ENE - WSW running step faults. These faults run approximately parallel to the fault which lies between Al-Nashfa well and Baharia well. This fault could be the boundary of an old pre-Cambrian high (Baharia - Khatatba block).

3. These ENE step faults show up flexures or warps in the outcropping younger formations.

4. This ENE trending block is cut off by the NW trending, Cairo graben.

5. This ENE old fracture line continues into the Suez and north Sinai area. The NW to NNE and NNW structural trends are relatively younger than the ENE structural trend.

6. The gravity highs trend ENE, E - W (nearly parallel to the Mediterranean coast), N - S and WNW.

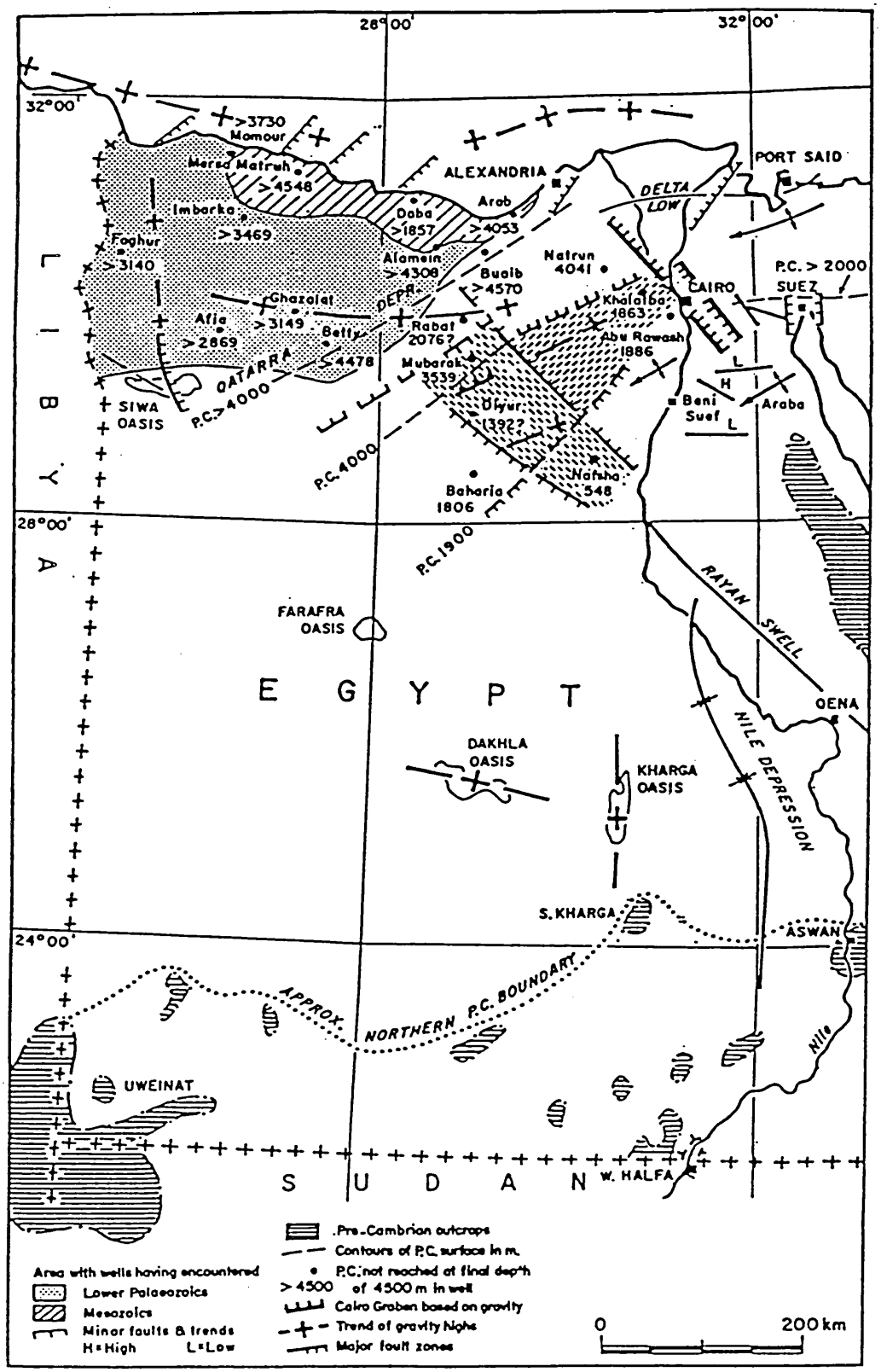


Fig. 2.27 Tectonic sketch map of the Western Desert of Egypt. (After Shurmann, 1974)

According to Shata (1953) and Said (1962), the surface and subsurface folds in the Western Desert could be classified into (Figs. 2.28 and 2.29):

1. N - S folds that affect the Palaeozoic sediments and mostly are represented in the subsurface;

2. NE - SW folds (Syrian Arc system). These folds were active during upper Cretaceous - lower Eocene.

3. NW - SE folds which affect the Oligocene and younger sediments. These folds are of secondary importance and are associated with a system of NW - SE faults which cross the Northern Western Desert of Egypt (Shata, 1953).

According to Shata (1953) and Shukri (1954), the rifting of the Red Sea and the Gulf of Suez produced a series of undulations with a NW - SE trend, which are parallel to the Gulf of Suez. These undulations are present on both sides of the Gulf (Fig. 2.30). In the Western Desert, the intensity of these undulations (or anticlines and synclines) decreases westwards.

Although there is a contradiction between Yallouze and Knetsch (1954) and other authors, such as Sigaev (1967) on the folding mechanisms of Baharia, it seems to be a general agreement between most of the authors who worked on the folding of both the Stable shelf and the Unstable Shelf, especially the Syrian Arc system of folding, that the mechanisms of the folding in the two shelves are different. However, Tromp (1949) attributed the folding of both Unstable and Stable shelves to block faulting (tilted movements of an irregularly shaped

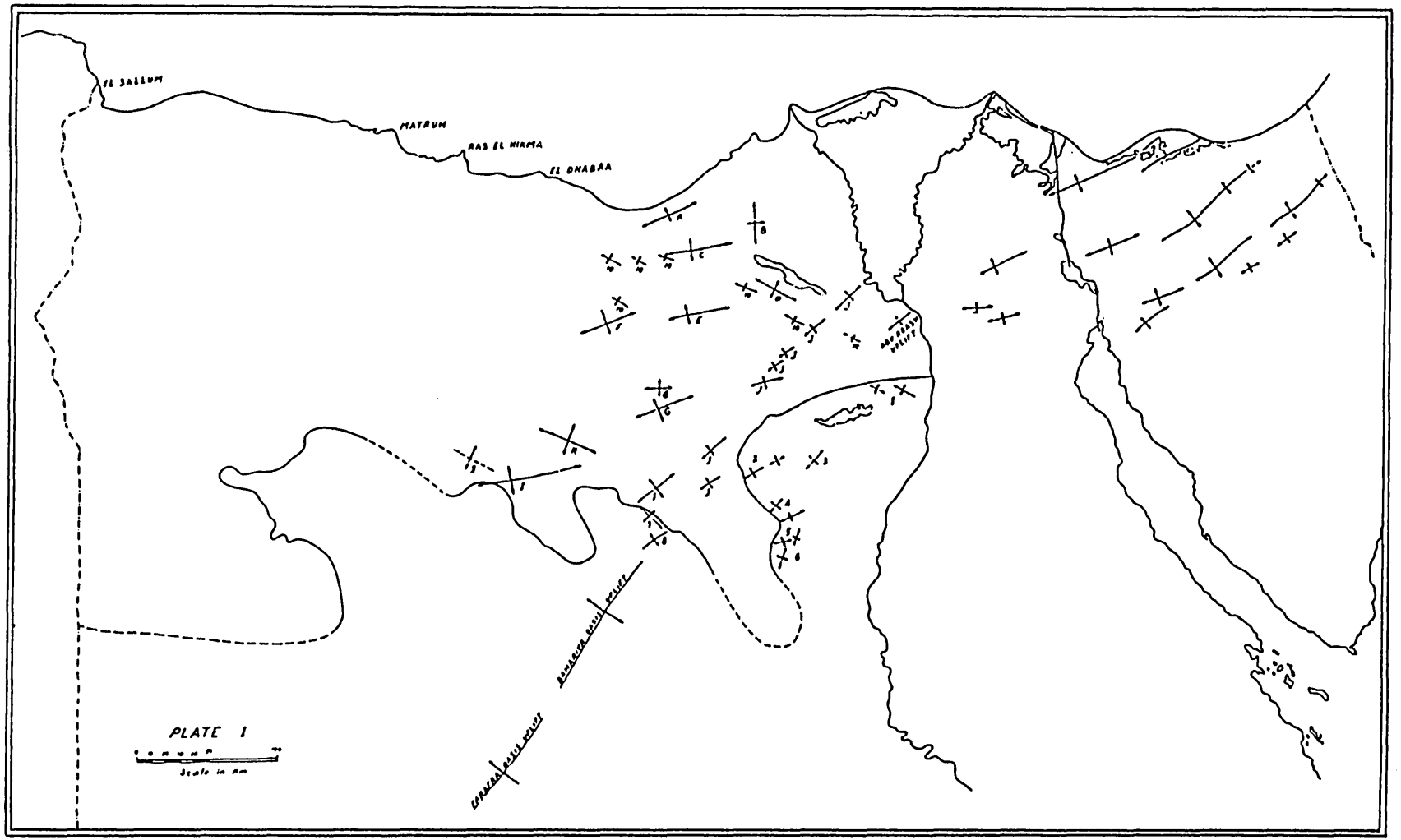


Fig. 2.28 Map showing the fold structures in Egypt. (After Shata, 1953)

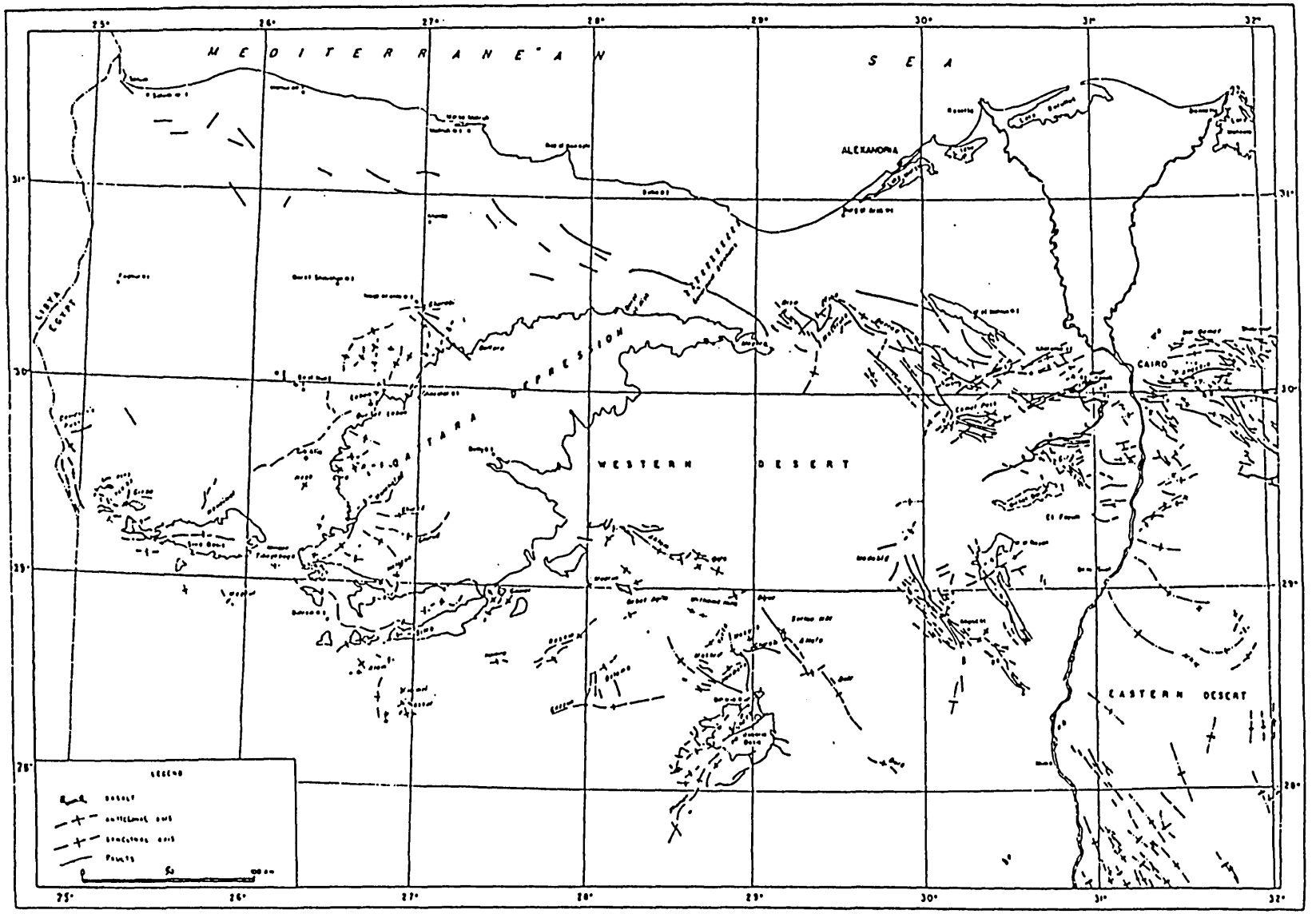
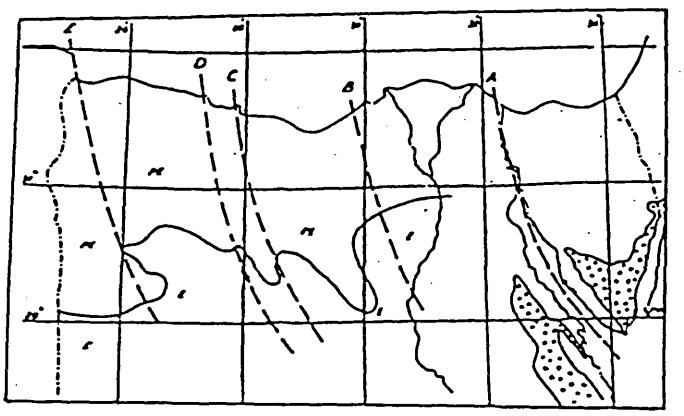
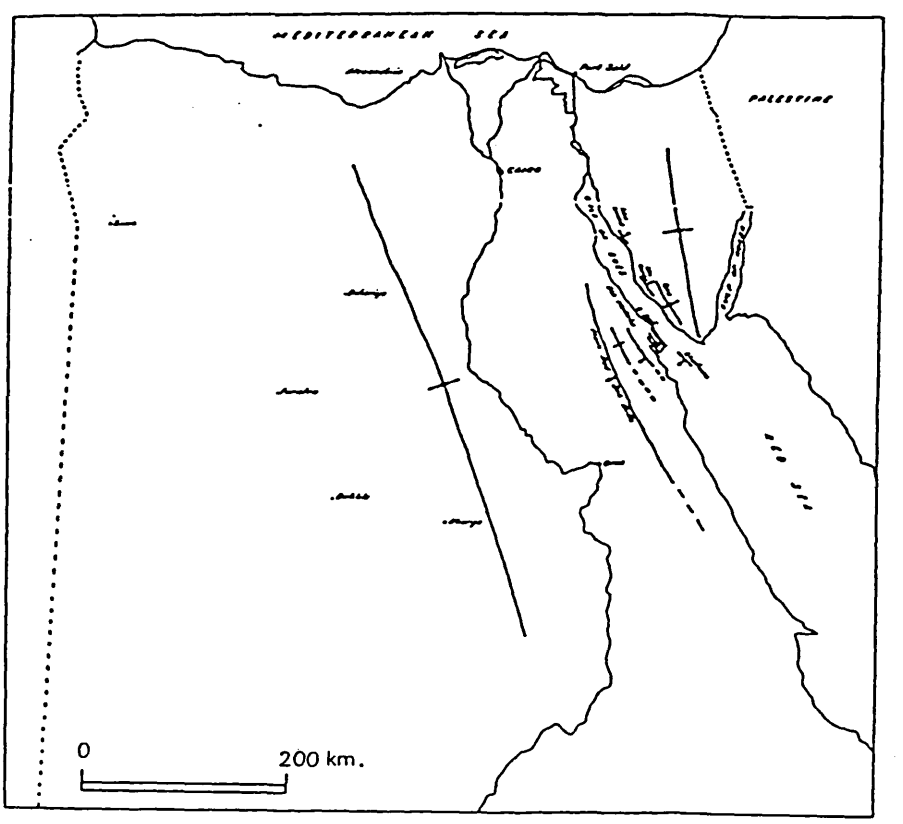


Fig. 2.29 Map showing surface structures of the Northern Western Desert of Egypt.
(After Said, 1962)



(After Shata,1953)



(After Shukri,1954)

Fig. 2.30 Maps showing the main NNW undulations or folds.

basement block). So, let us now review the mechanics of folds in both shelves in light of the previous studies.

1. Folding mechanism of the Stable shelf

The folding of the Stable shelf has been attributed to vertical movements (block faulting) by many authors (see Said, 1962).

2. Folding mechanism of the Syrian Arc system (Unstable shelf)

According to Shata (1953), Omara (1953), Knetsch (1957), Said (962), Youssef (1968), Aadland and Hassan (1972), Salem (1976) and Garfunkel and Bartove (1977), the NE - SW folds of the Syrian Arc system were formed as a result of compression, where the greatest compressional axes were oriented NW - SE, perpendicular to the axes of folding. This compression, as has been suggested by different authors, resulted from:

a) Thrusting in the subcrust that took place parallel to the axis of folding (Said, 1962; Schurmann 1974 and Salem, 1976).

b) Dragging along the contact between two blocks, as a result of strike-slip movement (Freund, 1965), (Fig. 2.31). This lateral movement resulted from the rotation of the Arabian block in the NE direction (counterclockwise). This suggestion has been criticized by Picard (1970), who mentioned that the intercontinental drifting between Africa and Arabia is of Pleistocene or even Neogene, which could hardly have caused the formation of folding, whose origin goes back as far as the early Tertiary.

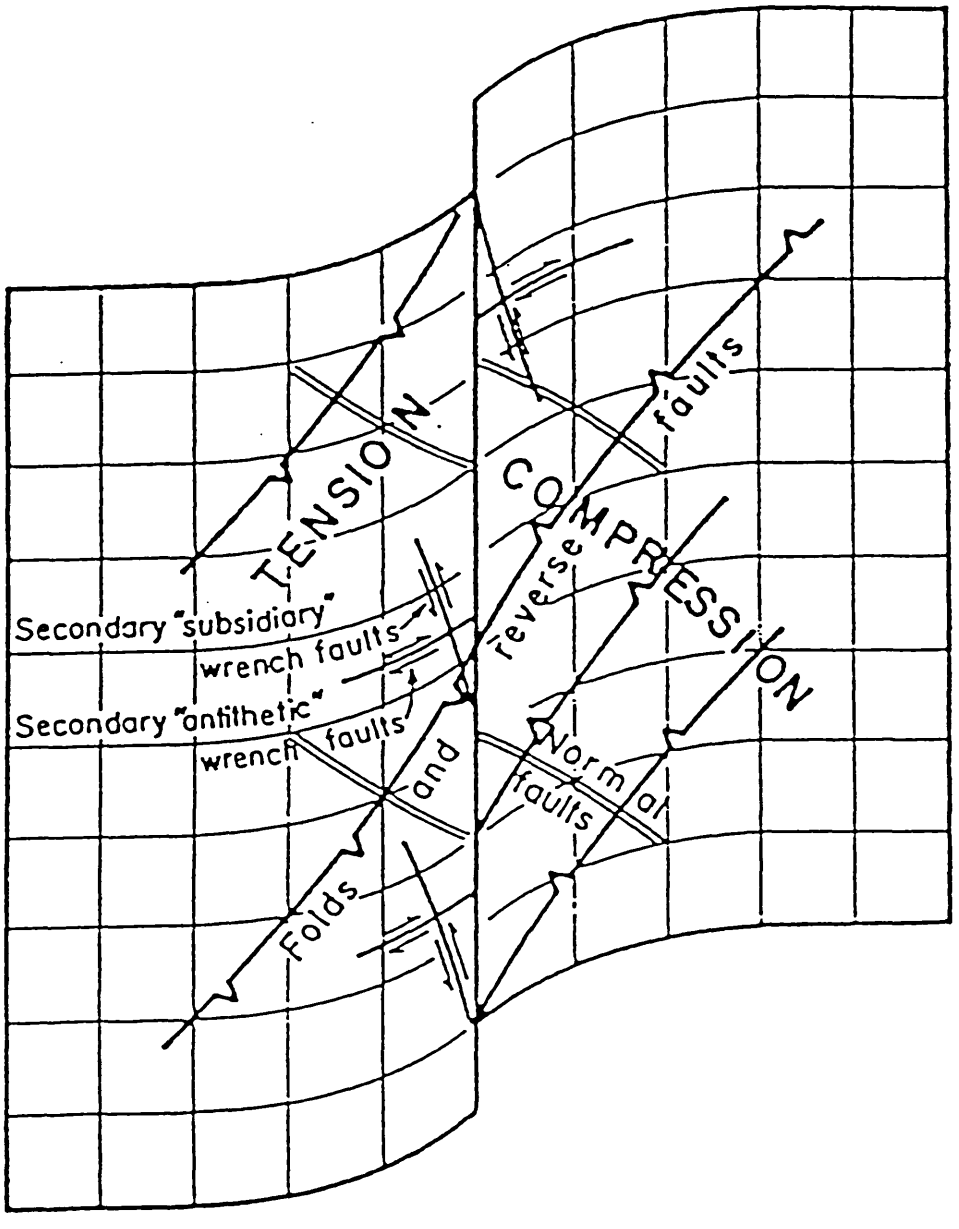


Fig. 2.31 Secondary structures of strike-slip faults

(After Frund, 1965)

According to Youssef (1968), the rotation of the Arabian plate may cause crossfolding, which resulted in the sinuous shape of north Sinai folds or Syrian arc system of folds.

El Shazly et al (1975 and 1976), in their work on the Northern Western Desert of Egypt, reported the following:

1. Some lineaments which trend nearly NW (N40-60 W) show right lateral horizontal movements.

2. Some lineaments which have N - S to NNE (N5-20E) trends show strike-slip left lateral movement or displacement. The two former trends exhibit vertical dislocation as well.

3. ENE and WNW lineaments represent important and regional faults which show no noticeable horizontal dislocation.

4. NNW (N10 - 25W) and NE lineaments show no horizontal displacement, the later trend may represent deep seated tension.

Although El Shazly et al (1974, 1975) located some lineaments, they did not demonstrate the relative horizontal sense of movement along some or few of the lineaments which have been described by them as shearing lineaments.

However, through reviewing the previous work, it was found that some of the authors have recognized or dealt with some shears without stating anything concerning the relative sense of the horizontal movements, e.g. Yallouze and Knetsch (1954). Some others described the shear

trends and their relative horizontal sense of movements, but never locate such shears or fractures on a map, such as El Shazly et al (1974 and 1975). This in fact causes a lot of trouble for anyone who intends to carry out a structural analysis of this particular area.

To this end, the author will review the next topics, which might be considered as a reflection of the structural or tectonic movements that took place over the Northern Western Desert of Egypt:

1. The Nile Delta;
2. The origin of the depressions; and
3. Basalt occurrences.

2.2.4 The Nile Delta

The Nile Delta region lies between the northern parts of the Sinai and Western Desert. It has been subjected to the same geologic events that affected the northern part of Egypt during its pre-Miocene geological history. At the end of the Oligocene, the Nile Delta began to be formed as a result of a rifting (Yallouze and Knetsch, 1954; Zein El-Din and Marzouk, 1974). By this time it had many branches. According to Zein El-Din and Marzouk (1974), the post-Oligocene faults mark the boundaries of the present Nile Delta. These faults are more or less parallel to the Gulfs of Suez and Aqaba (Shereef, 1972). The graben structure of the Nile Delta seems to be bounded to the north and south by E - W system of faults (Shereef, 1972), (Figs. 2.32 and 2.33).

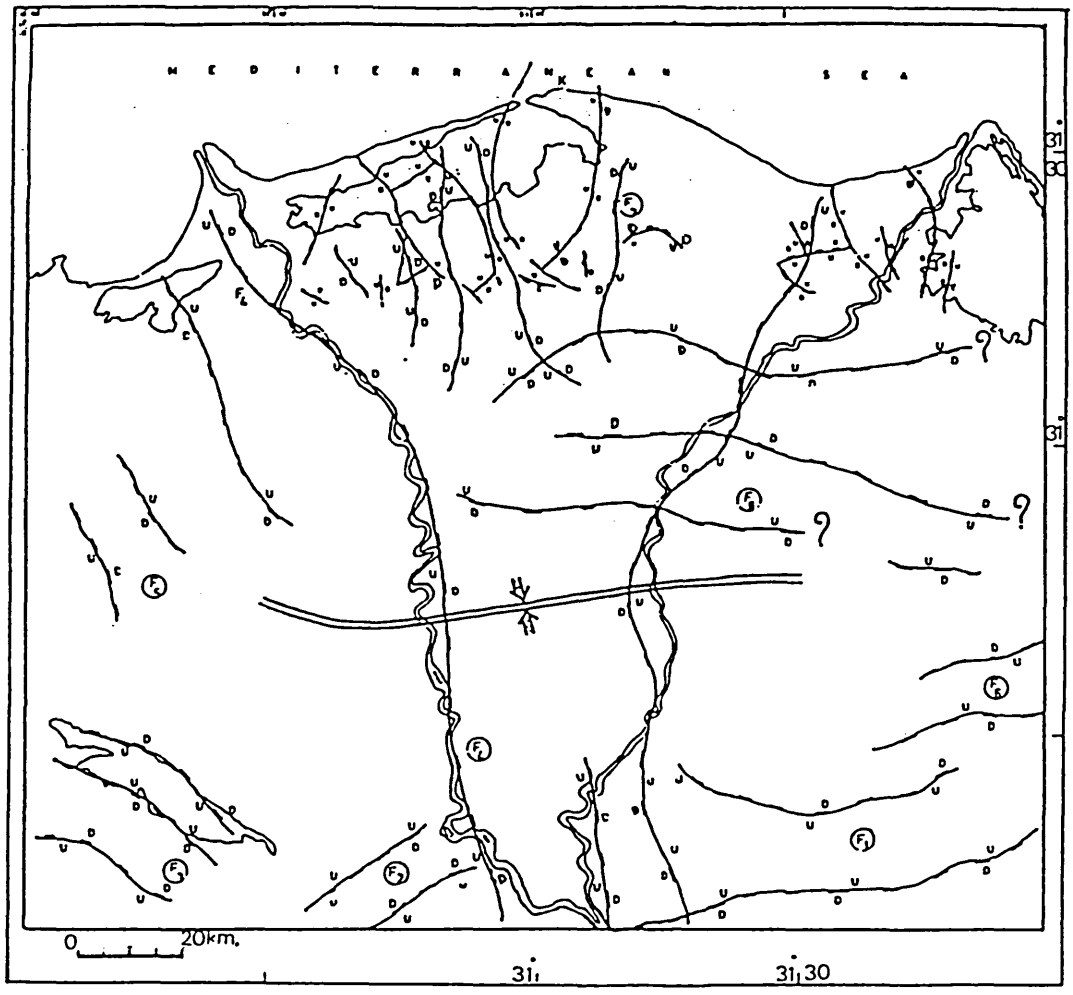


Fig. 2.32 Tentative tectonic map of the Nile Delta region. (After Shereef,1972)

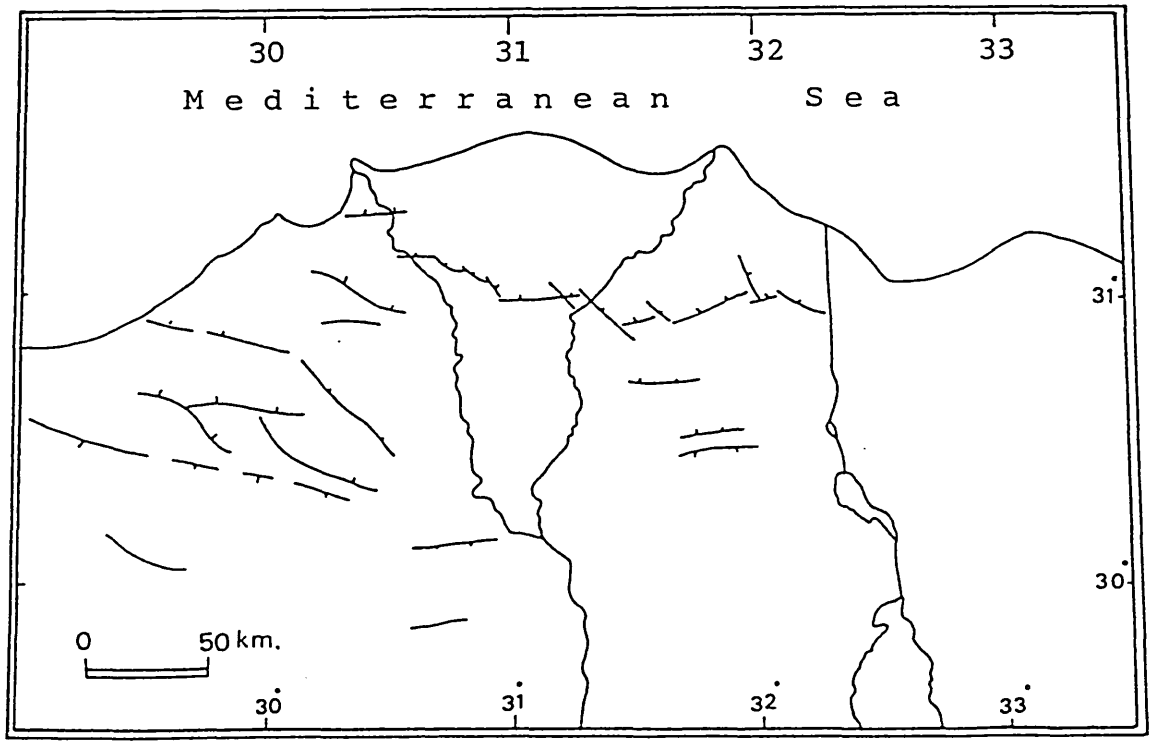


Fig. 2.33 Top Cretaceous fault structures (Conoco Delta,1976)

The Nile Delta continued its growth by rapid deposition of the Miocene-Pliocene deltaic sediments. Progressive subsidence took place in the north part of the Delta, with E - W step faulting indicated by the constantly thickening overburden.

2.2.5 Origin of the Depressions

Most of the Western Desert Depressions (Figs. 1.1 and 2.1) lie within the area under study. Some of these depressions such as Baharia and Faiyum, are completely encircled by a continuous escarpment, while others such as Qattara and Siwa form a long valley.

The different assumptions which have been offerred by various authors, as quoted by Knetsch and Yallouze (1954 and 1955) as possible reasons for the formation of these depressions are:

a) The wind erosion or corrosion (active scouring by sand carrying wind);

b) Down faulting;

c) Both down faulting and wind erosion;

d) Intensive chemical weathering in places where the structures, folds - warps - fractures - faults, permit the subterraneous water to come within reach of evaporation, creating an immense accumulation of brackish solutions which destroyed the country rocks (Yallouze and Knetsch, 1954). The decomposed materials were removed by wind.

Knetsch and Yallouze (1955) suggested the following:

A. All the Oasis depressions are localized by tectonic events or tectonic features.

The depressions seem to be preferentially developed on broad deformations, swell regions in the south and broad flexures in the north.

B. The second important factor of depression formation is water, especially leakage water from deep horizons.

C. A third main factor is the aridity which provides even slightly mineralized waters with high salt content by high evaporation figures.

D. River action might have created initial stages of depression in the south of Egypt.

2.2.6 Basalts Occurrences

The Tertiary basalt occurs (on both sides of the Nile Delta, north of Faiyum at Gebel Qatrani and Baharia Oasis) as large lava flows which are at least partially attributable to fissure eruptions, with NW, ENE and E - W orientations.

Rittmann (1954) reported the following:

a. All Tertiary volcanoes of lower Egypt were basaltic ones. Tosson (1954) found an embryonic volcano at longitude 31 17 and latitude 30 12 on the northern slope of Gebel Mokattam, near Cairo.

b. The subcrustal basaltic magma found its way towards the surface along some old structural lines of the basement complex that trend NW and ENE and which were reactivated in the Oligocene and Miocene.

c. The alignment of several eruptive centers in ENE and NW directions (Tosson, 1954) indicates the importance of these subsurface faults which extend for many kilometers.

The age of the basaltic extrusions was established (Tromp, 1950) to be Upper Oligocene and pre-lower Miocene. This basalt was attributed to the emergence and bulging of the basement around the Red Sea (Salem, 1976).

2.3 Stratigraphy

The stratigraphy of this area has, until recently, received relatively little attention. In part, this relates to the natural difficulty of studying desert areas, but in part is also attributable to the lack of sedimentational homogeneity and the scarcity of identifiable fossils within these sediments, though Blanckenhorn (1901); Beadnell (1901, 1905); Ball and Beadnell (1903); Hume (1911, 1925); Boyed (1947) and Vischer (1947) have thrown some light on this subject, as cited by Faris (1946); Omara (1953) and Said (1962).

However, since 1938 when the American oil companies began to be interested in this area as an oil prospecting region, more than sixty deep wells have been drilled. Some of them reached the pre-Cambrian. These wells gave valuable information on the Palaeozoic, Mesozoic and Tertiary sections.

As a result of this considerable interest, the published works of Shata (1953 and 1955); Amin (1961); Said (1962); Kostandi (1963); Beckman (1967); Soliman and

El-Fetouh (1970); Barakat (1970); Aadland and Hassan (1972); El Gezeery et al (1975), quoted by El Shazly (1977), and Khalid (1975) have resulted in a better understanding of the geology of the studied area.

The recently established main stratigraphic units of the subsurface and exposed sediments in the Northern Western Desert of Egypt are represented on Plate 2.1, after Aadland and Hassan (1972).

The ages of the various groups, as indicated by the previously mentioned authors (Plate 2.1) and the available subsurface data known in this area are as follows:

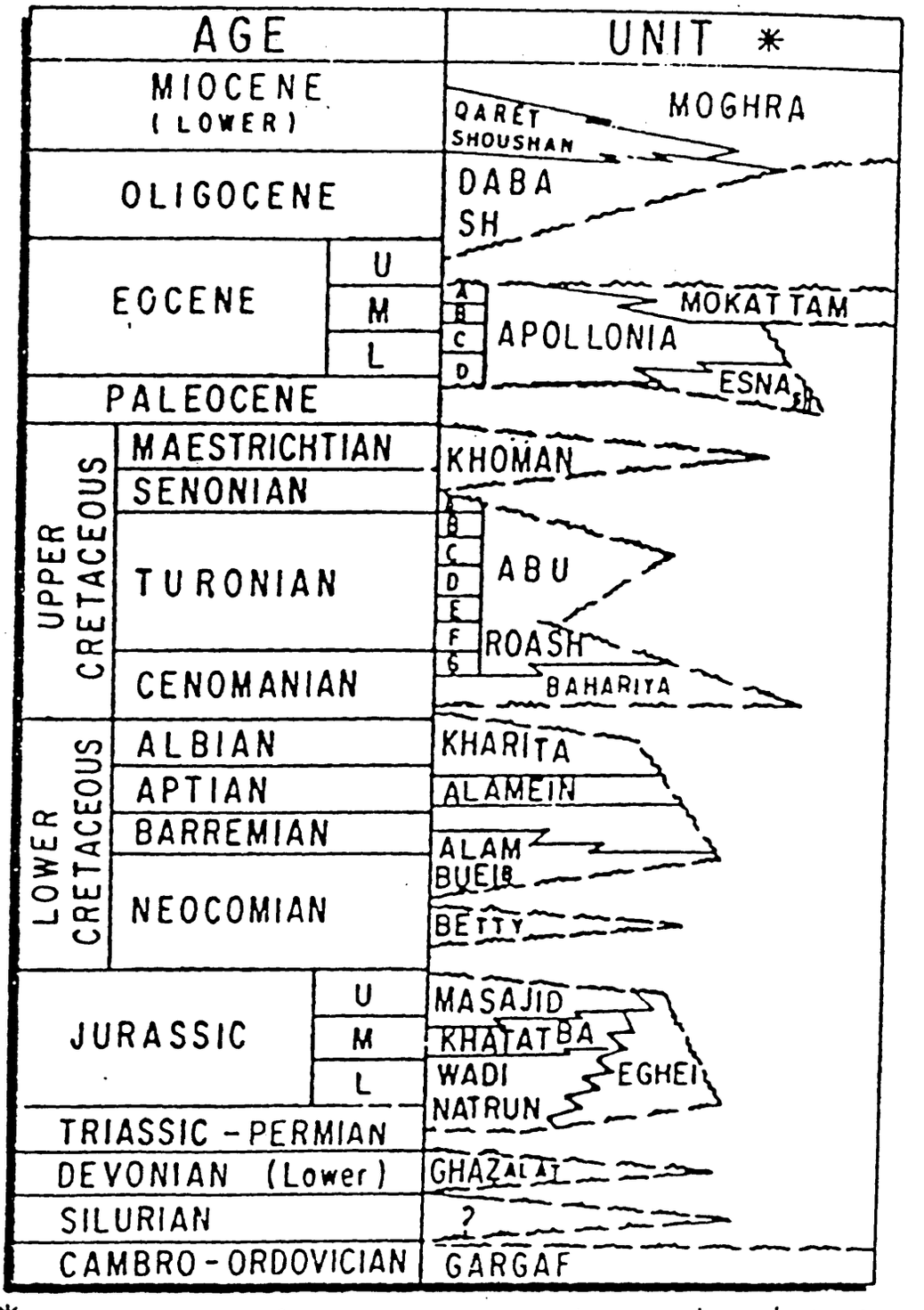
Pre-Cambrian

The pre-Cambrian is not indicated on Plate 2.1 and does not crop out in the area under study. Indeed in Egypt, the basement of pre-Cambrian crops out well to the south of the area between Aswan and the southern international boundary. It also forms the Uweinat mountains, which are located at the corner point of Egypt, Sudan and Libya (Fig. 2.27).

In the studied area, the crystalline basement is overlain by relatively thick marine and non-marine sedimentary rocks and so far is only encountered in some wells (Fig. 2.34). As indicated in Table 2.2, this basement is of late pre-Cambrian or possibly early Palaeozoic age (Beckman, 1967).

PLATE 2.1

STRATIGRAPHIC NOMENCLATURE



* Unit terms are informal and consequently have not been designated as formations, members etc

(After Aadland and Hassan, 1972)

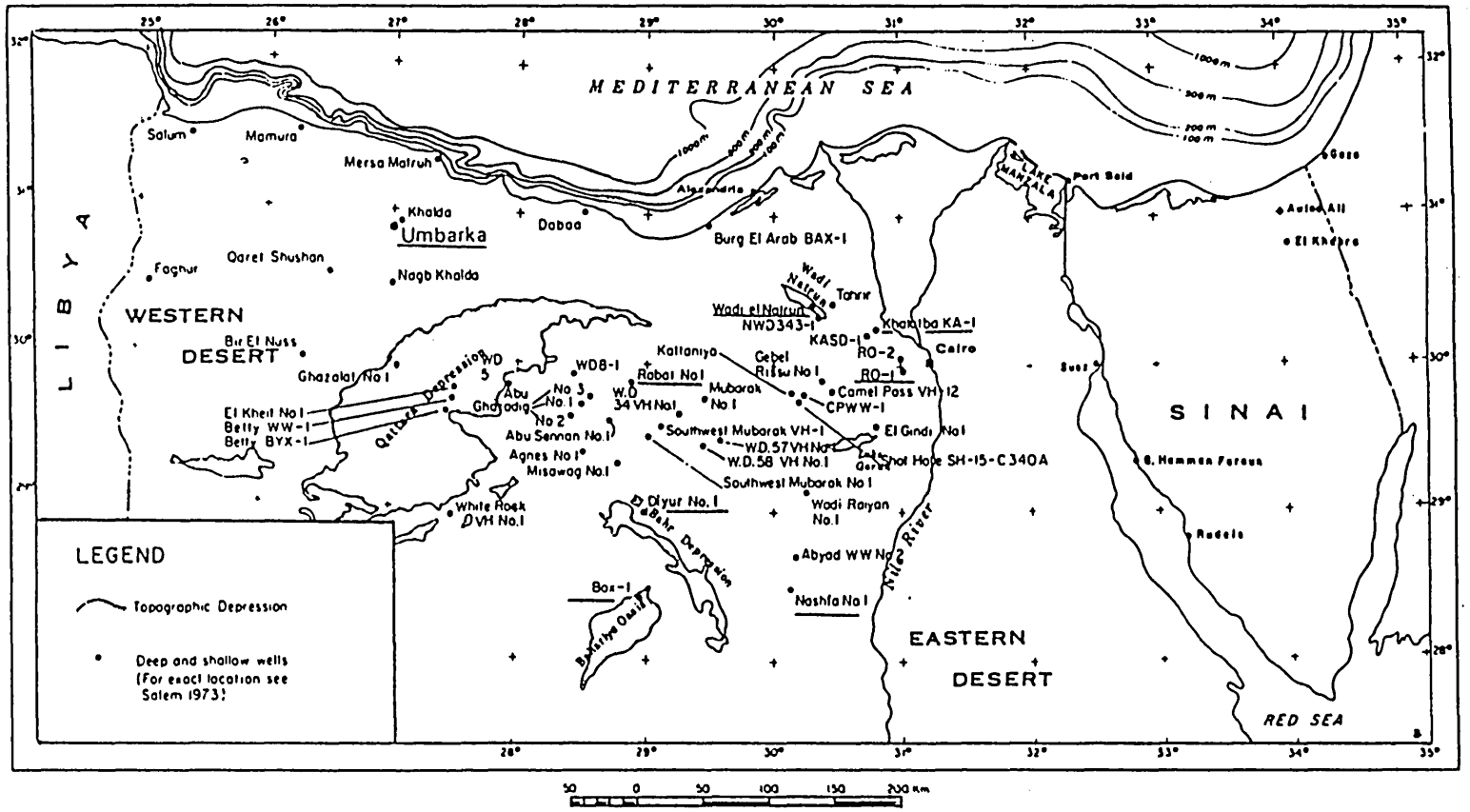


Fig. 2.34 —Well location map, northern Egypt.

Table 2.2: The depths of the basement (as encountered in some wells)

Well	Depth in m.	Bottom formation
Abu Rawash	1,886	Red Aswan granite
Al Nashfa	548	Red Aswan granite
Baharia	1,822	Andesitic to diabasic rocks
Diyur-1	1,392	Metamorphics
Khatatba	1,863	Andesitic to diabasic rocks
Rabat-1	2,076	Metamorphics
Umbarka	3,469	Metamorphics
Wadi Natrun	4,041	Weakly metamorphic sandstone

It may be inferred from this table that there is a reasonably varied thickness of sedimentary cover across the Northern Western Desert of Egypt.

Palaeozoic

The thickest Palaeozoic section is encountered near the northern end of the Egyptian - Libyan International border. The sediments of this section consist mainly of marine to continental sands and shales which range in age from Cambrian to Carboniferous (Fig. 2.35). Sandstones of questionable Silurian age, together with basaltic sills, were found in the Rabat well (Plate 2.2). The thickness of the Palaeozoic decreases from the west to the east (Beckman, 1967). In the west, at Faghur well, it attains a thickness over 1,676 meters. In Gibb Afia and Baharia wells, the thicknesses are 1,219 meters or

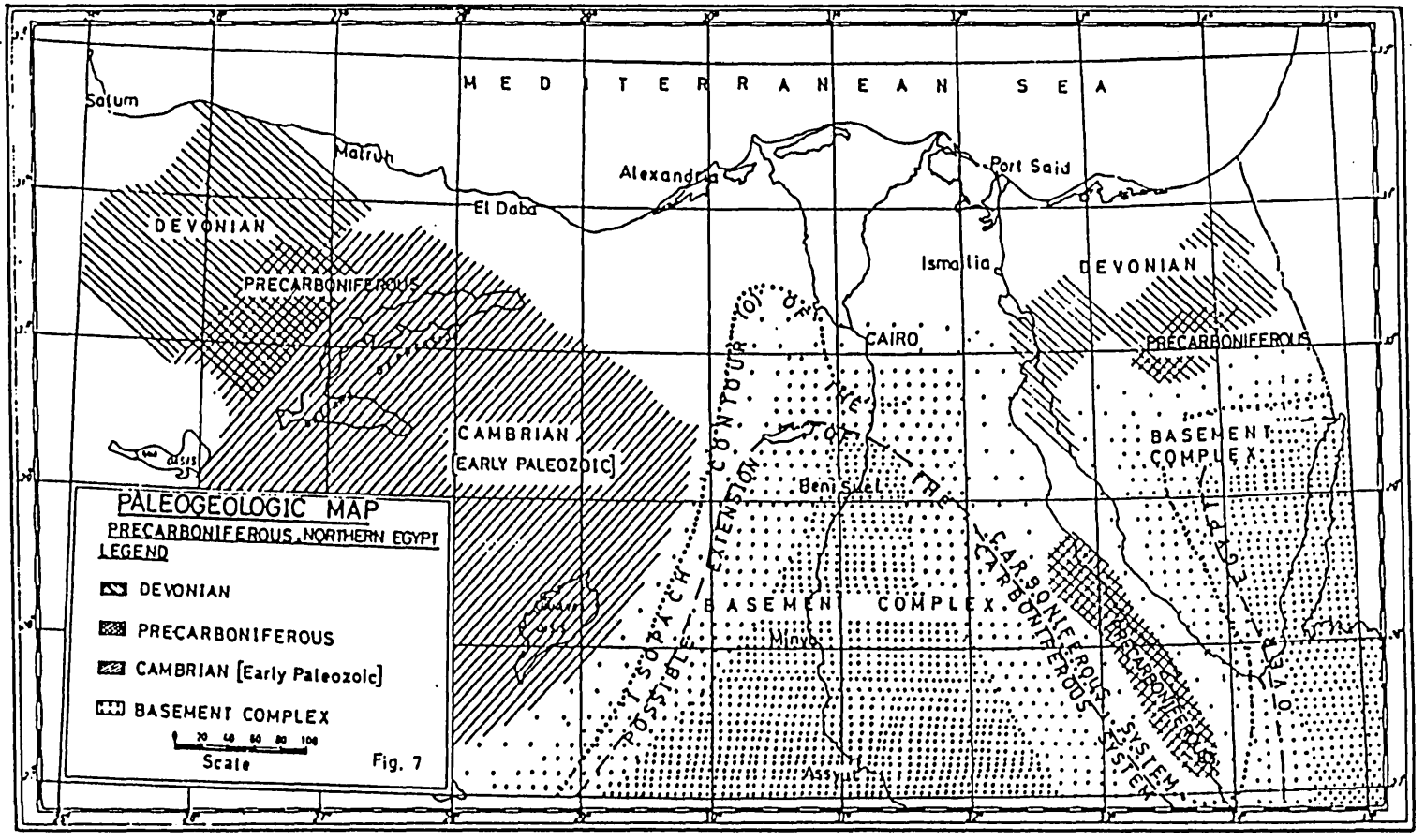
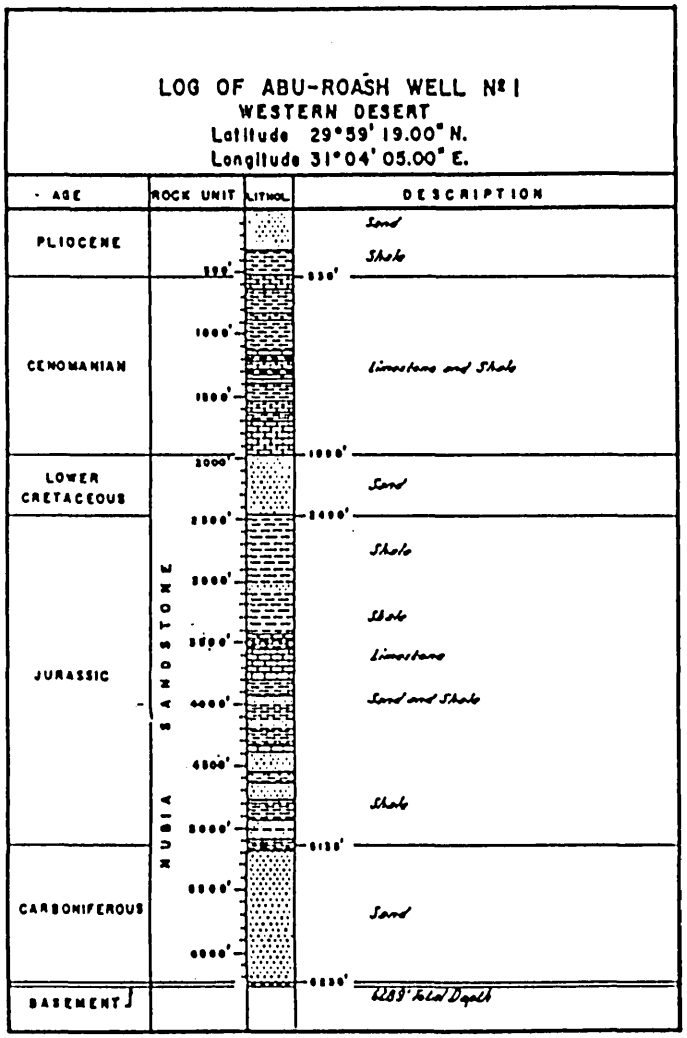


Fig. 2.35 —Paleogeologic map of pre-Carboniferous, northern Egypt.
(After Soliman and El Fetuh,1970)

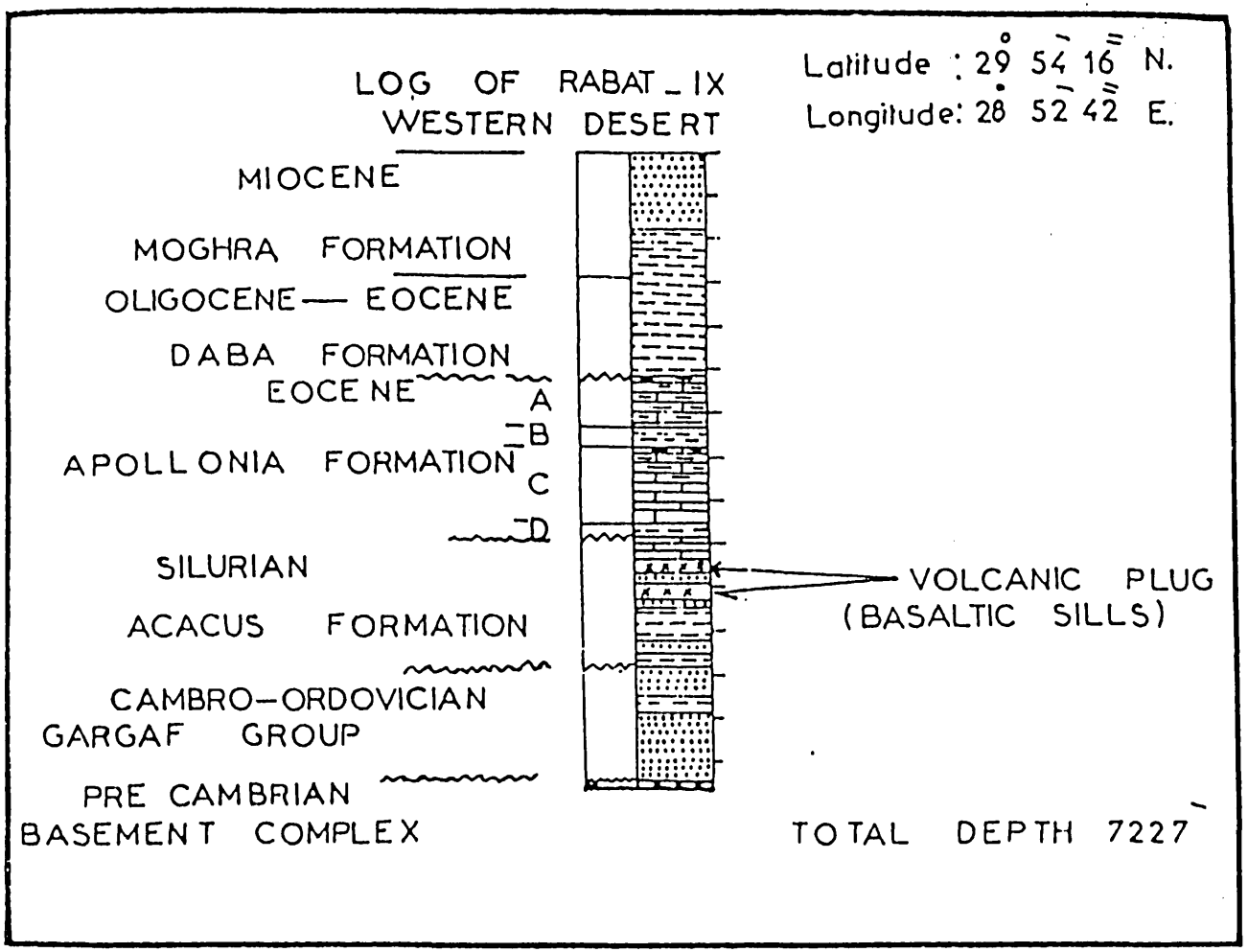
PLATE 2.3



Log of Abu Roash well No. I.

(After Said,1962)

PLATE 2.2



more, and about 853 meters, respectively. Along the longitude of Nashfa-Wadi Natrun it appears to reach a minimum and to be at least locally absent. In 1967, Beckman distinguished the following three distinct sedimentary provinces in the Palaeozoic of the Northern Western Desert of Egypt:

a) A Libyan facies with a thick marine Carboniferous-Devonian section in the west (Faghur);

b) A sandy lower Palaeozoic with Cambro-Ordovician, with no records of upper Palaeozoic in the centre at Gibb Afia, Ghazalat, Betty and Baharia;

c) An area of marine Carboniferous in the East at Khatatba and Abu Rawash.

Because of the above points, it may be inferred (although Aadland and Hassan, 1972 did not in fact draw attention to these points) that the Palaeozoic is progressively truncated from West to East by an unconformity surface thought to be related to Hereynian orogeny.

The following table shows the deep wells where the Palaeozoic section has been encountered.

Table 2.3: Depths of the Palaeozoic section

Well	Depth in metres	Bottom formation
Faghur	3,330	Old Palaeozoic
W. Faghur	3,194	Palaeozoic
E. Faghur	4,200	Palaeozoic
N. Ghazalat	3,901	Palaeozoic
Qattara Rim	3,302	Palaeozoic
Rabat	2,075	Bottom of the Palaeozoic
Gibb Afia	3,068	Cambrian
Ghazalat	3,078	Cambrian
Betty	4,463	Cambrian
Sharib	2,446	Palaeozoic
Umbarka	3,665	Bottom of the Palaeozoic
Barakat	3,847	Palaeozoic
Mamura	3,773	Palaeozoic
Abu Roash	1,810	Bottom of the Palaeozoic
Dawabis	4,147	Palaeozoic

Permo-Jurassic sediments (Eghei group)

The Permo-Jurassic sediments are widely spread in the studied area and deposited under continental conditions. A Permo-Jurassic age is assigned to those sediments because, in Diyur no. 1 the top of them was assigned a late to middle Jurassic age, based on palynological data (Khalid, 1975), while their bottom was assigned to Permian. These sediments are composed of varicoloured shales and siltstones, interbedded with continental sandstones. It is assumed by Aadland and Hassan (1972) that the thickness and distribution of this group was controlled by post Hercynian block faulting.

Marine Jurassic

The occurrence and thickness of the marine Jurassic sediments are represented in Fig. 2.36 by their isopachs. These sediments consist of three units (Aadland and Hassan, 1972; and Khalid, 1975), which are:

a) Masajid (carbonates);

b) Khatatba (shales and carbonates);

c) Wadi El-Natrun (shallow marine clastics, carbonates and evaporites).

These units together form a single marine transgression cycle. The different facies and their distribution in the area under study are represented in Fig. 2.37 (after Khalid, 1975).

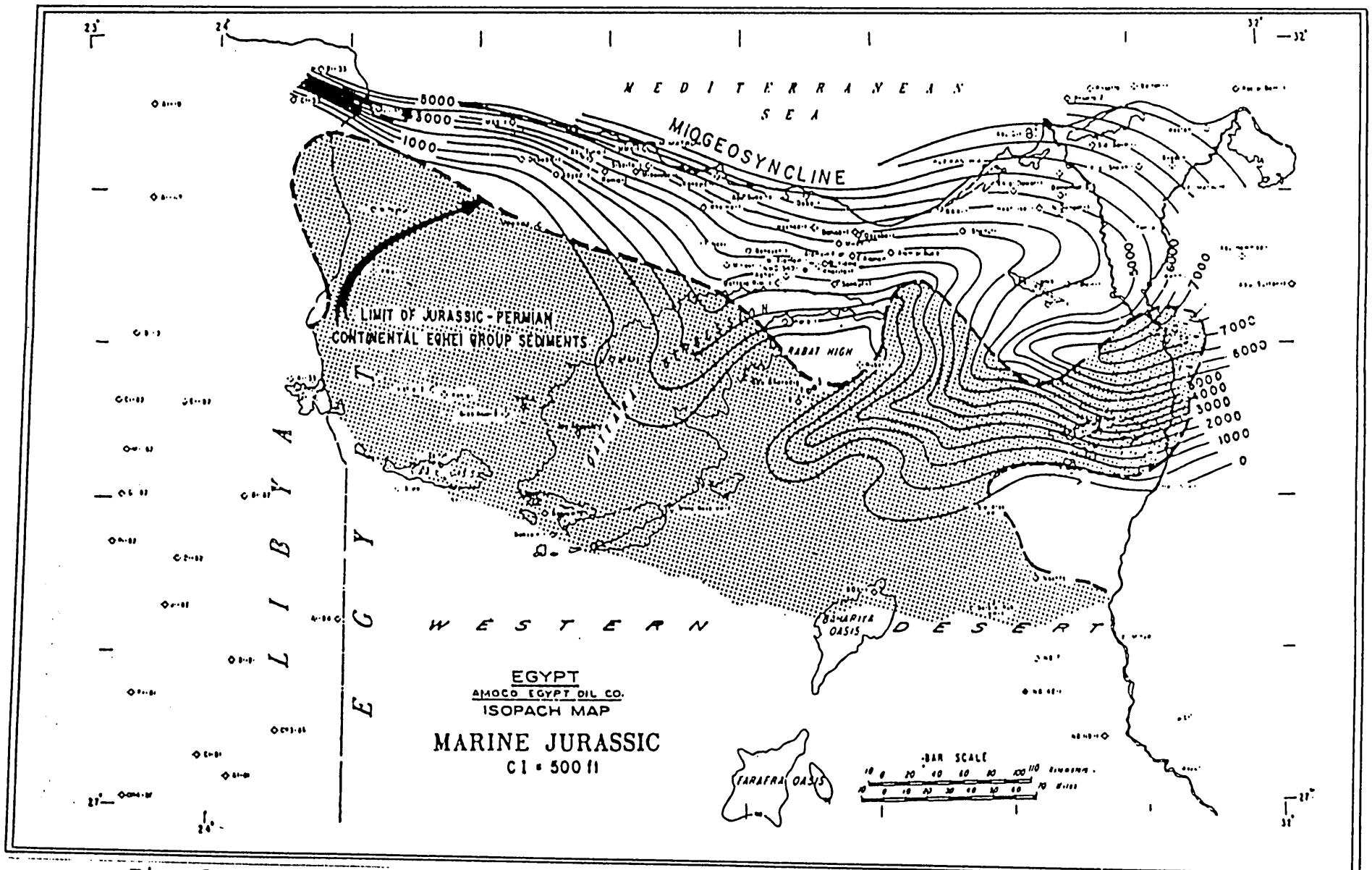


Fig. 2.36 Marine Jurassic isopach map (after Aadland and Hassan,1972)

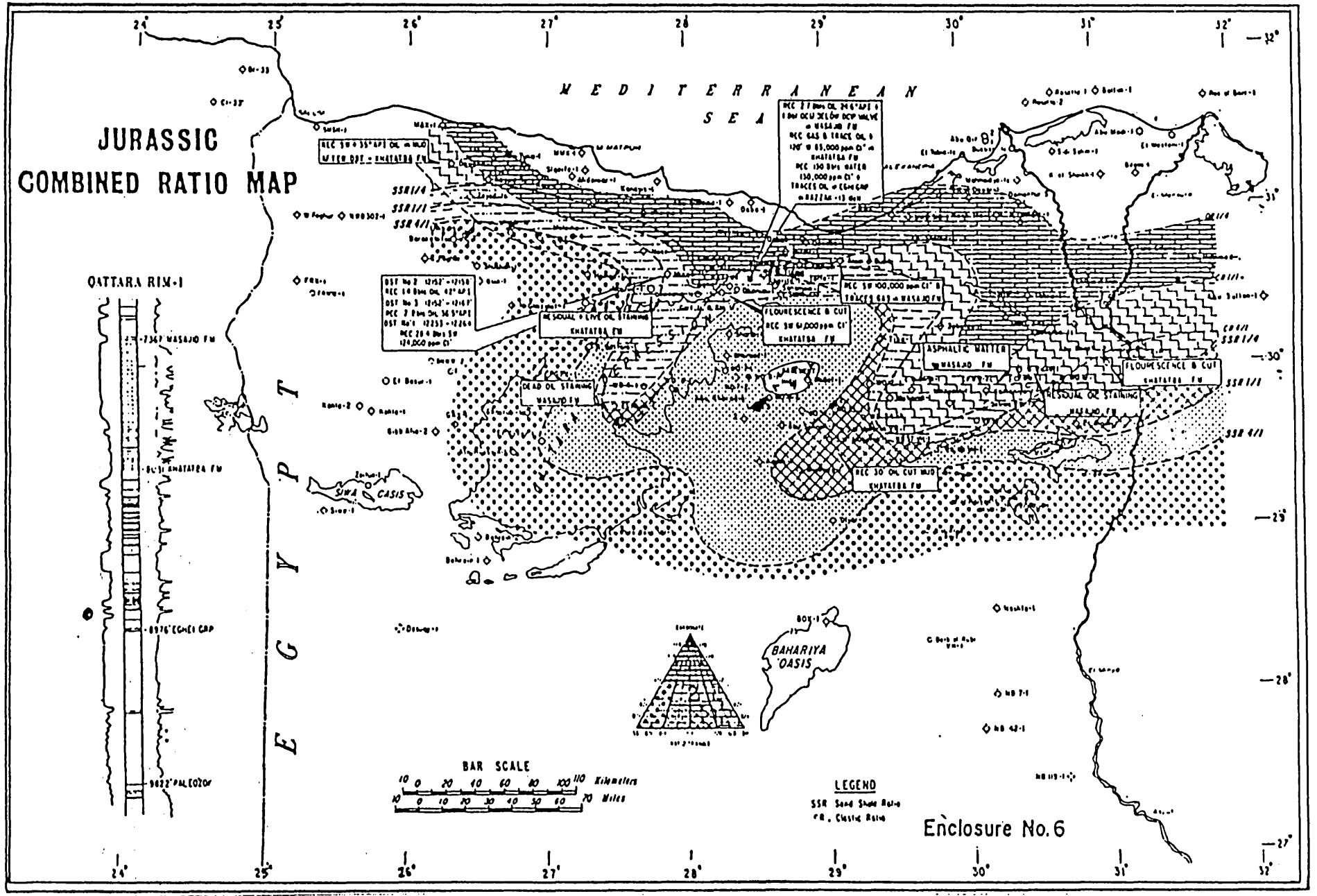


Fig. 2.37 Jurassic facies (combined ratio) map, after Khalid,1975.

Cretaceous

According to Beckman (1967), the Cretaceous is clearly the period of maximum subsidence in the Northern Western Desert of Egypt. The total thickness of the Cretaceous may be about 4,570 meters in Mersa Matruh, and is still more than 2,440 meters in the large basin which includes Mamura, Betty, Mubarak, Alamein and Burg el Arab. The Cretaceous sediments were classified into:

a) Upper Cretaceous;

b) Lower Cretaceous.

Although the boundary between the lower and upper Cretaceous is difficult to locate exactly by paleontological methods, because diagnostic fossils in the Albian and lower Cenomanian are rare, the passage from the lower Cretaceous to the upper Cretaceous is lithologically characterized in the North (Mamura to Abu Rawash) by an increase in carbonate content, further to the South by a decrease in the grain size of sands and increase in the marine fossil (Betty, Mubarak) (Beckman, 1967).

Lower Cretaceous sediments

These sediments are mainly terrigenous clastics derived from the southern shield area (Aadland and Hassan, 1972). These sediments were encountered in all the deep wells drilled in the area except at Rabat. According to Aadland and Hassan (1972), the Neocomian (Betty unit) is composed of terrigenous to marginally marine clastics, shales and rare carbonates with an early

Cretaceous depo-centre at the western sub-basin which covered most of the great Qattara depression.

The Barremian (Alam El Bueib unit) unconformably overlies the Neocomian and consists of marginal marine to deltaic sandstone, with some shale and carbonate.

The early to middle Aptian sediments are composed of shallow marine sandstone and some shales. These sediments, which overlap the Barremian and the Neocomian, were terminated near the close of the Aptian by marine carbonates and overlying shale (Alamein unti).

The Kharita unit (Albian), which consists of marginal to deltaic sandstones, some shales and rare carbonates, represents the final stage of the early Cretaceous sedimentation.

Beckman (1967) reported a gradual regression at the end of lower Cretaceous, where the basin gradually filled up with little or no deposition along its edges during Albian times.

Upper Cretaceous

The rocks of the upper Cretaceous are locally exposed at Baharia Oasis, 350 km. to the southwest of Cairo (Ball and Beadnell, 1903) and Abu Rawash.

The Cretaceous rocks which crop out at Abu Rawash, near the Pyramids of Giza, were discovered by Lefebvre, a French naval officer who visited Egypt in 1835 and was re-discovered by Schweinfurth in 1884. Since that time, the area attracted the attention of many authors such as

Blanckenhorn (1890, 1900); Sickenburger (1890); Gregory (1898); Fourtau (1889, 1900, 1903); Newton (1899); Beadnell (1901, 1902); Dacque (1903); Cuvillier (1930); Faris (1946); Omara (1953) and Jux (1954), who studied the area mainly from the stratigraphical and paleontological point of view, as cited by Said (1962).

The stratigraphy of the Cretaceous rocks of Abu Rawash is well established, either from their outcrops, as shown in Table 2.4, (after Faris, 1946) or from the sub-surface data obtained by the Standard Oil Company (1946) (see Table 2.5 and Plate 2.3).

In the sub-surface, the upper Cretaceous is divided into three units, which are:

a) the Khoman unit;

b) Abu Roash unit;

c) Baharia unit.

The thicknesses of these units are represented in Table 2.6, as measured in some deep wells at the Northern Western Desert of Egypt.

Baharia unit;

The Baharia unit is composed of shallow marine sandstones with interbeds of shales and some limestone, first marine Cretaceous unit.

Abu Raosh unit

This unit has been divided into seven members: G to A, which were deposited under shallow to open marine conditions, as shown in Table 2.7.

Table 2.4: Generalized stratigraphy of Abu Rawash
(after Faris, 1946)

Age		Series	Thickness		General Lithologic Description
Miocene-Recent					Gravel and sand deposites & alluvium (sands & gravels)
Oligocene					Bad Salt flow
EOCENE	Lower-upper Eocene		10 m	10 m	Very hard, massive, semicrystalline, dolomitic limestone
			19 m		Limestone, siliceous, interclated with sandy and clay beds
	Middle Eocene		10 m	29 m	Building stone horizon of whitish limestone sometimes becomes marly
			15 m	39 m	Massive, compact, creamish limestone
			10 m	54 m	Massive, compact, hard, grey limestone
C R E T A C E O U S	Campanian-Maastrichtian		57 m	64 m	Notice: The classic Cretaceous - Eocene unconformity varies in different structures. White chalk
	Santonian	Plicatula Series	34 m	121 m	Soft limestone, soft clays and sandy marls
	Turonian	Flint Series	34 m	155 m	White chalky limestone with interclated flint bands or concretions.
		Acteonella Series	22 m	189 m	A succession of marls and shales together with white limestone.
		Limestone Series	80 m	211 m	Hard, poorly fossiliferous limestone (dolomitized in places and chalky in others)
		Rudistae Series	26 m	291 m	Soft marls and shales
	Cenomanian	Sandstone Series	33 m	317 m	Friable sandstone (sometimes ferriginous) and shales
				350 m	

Table 2.5: The measured section of Abu Roash I and II (after S.O.C.)

Well	Abu Roash I	Abu Roash II
Date spudded	1946	1946
Latitude	29 59' N	30 01' N
Longitude	31 04' E	31 02' E
Total Depth	1918 meters	1575 metres
Elevation	92 metres	190 metres
Pleistocene - Pliocene	0 - 161 m. (161 m.)	
Miocene		
Oligocene		
Eocene - Paleocene		
Senonian		
Turonian		0 - 387 m. (387 m.)
Cenomanian	161 - 607 m. (446 m.)	387 - 744 m. (357 m.)
Lower Cretaceous	607 - 759 m. (152 m.)	744 - 877 m. (133 m.)
Jurassic	759 - 1566 m. (807 m.)	877 - T.D. (698 m.)
Undifferentiated Mesozoic /or Paleozoic		
Paleozoic	1566 - 1902 m. (336 m.)	
Basement	1902 - T.D. (16 m.)	

Table 2.6: Thickness of upper Cretaceous

Well		Thickness in metres							
	Khoman	Abu Roash							Bahariya
		A	B	C	D	E	F	G	
Abu Gharadig-1	745	233	-	-	47	159	34	220	527
Abu Sennan	501	78	115	78	96	158	32	121	175
Mubarak-1	142	221	130	66	172	170	44	260	265
S.W.Mubarak	460	180	100	65	104	119	30	204	133
W.D.8 - 1	312	143	170	70	36	-	-	-	86
Wadi Khadish-1	405	43	85	85	129	185	47	507	-

Table 2.7: Stratigraphy of Abu Rawash unit

Member	Composition	Environment
A	Shale and carbonates	deep water
B	Massive limestone	shallow water
C	Mainly shale, with some porous sandstone interbeds and limestone interclations	
D	limestones interbedded with some porous sandstone interbeds	shallow marine
E	A sequence of sandstone, shales and limestones (its top represents intra-Turonian unconformity)	shallow marine
F	Highly argillaceous carbonate sequence	open marine
G	Shale and limestone with interbeds of sandstone especially towards the base	

The Khoman unit

This unit consists of sediments which range from shale to very argillaceous limestone in the lower part (B) and thick, very fine grained chalky limestone in the upper part (A).

Locally, the thickness of the upper Cretaceous (Senonian) chalk is greatly affected by the upper Cretaceous to Eocene, Syrian Arc System of folding, which will be discussed later in this chapter.

According to Beckman (1967), the centre of the upper Cretaceous marine basin seems to have shifted gradually from north to south. Also, there is always a distinct unconformity in the Northern Western Desert between the Cretaceous and Tertiary.

Cretaceous - Eocene contact

Several authors discussed the Cretaceous - Eocene relationship in Egypt. Some of them, such as Zittel (1883) and Tromp (1949) (quoted by Shukri, 1954) mentioned that continuous sedimentation existed between the two systems.

Beadnell (1905) and Faris (1947) came to the conclusion that there is a conformable relation between the two systems in the entire region of southern Egypt. Other workers, such as Blanckenhorn (1921), quoted by Shukri (1954) and Ball (1939), said that there is an unconformable relation between the two systems. Beadnell (1902 and 1903) reported unconformable relations between the two systems at Abu Rawash and Baharia Oasis (North Western Desert of Egypt). Faris (1946) and Omara (1953) also reported an unconformable relation between the two systems at Abu Rawash. Hume (1911) and then Shukri (1954) suggested that the discontinuity of sedimentation between the two systems was controlled by the structural highs which belong to the Syrian Arc System which trends NE, while the basins separating these ridges were the sites of continuous sedimentation. Thus, these two authors believe both models, and these last expressed

views are most probably correct and have been accepted by most Egyptian geologists

Tertiary

Tertiary rocks in the Western Desert have been regionally studied by many authors, among them Beadnell (1905); Hume (1911); Shata (1955); Amin (1961); Said (1961); Kostandi (1963); Abdallah (1966); Marzouk (1970); Ouda (1971) and El Gezeery et al (1975), as cited by El Shazly (1977) and Salem (1976). The following brief summary is based on the available published subsurface and surface data.

Palaeocene

The Palaeocene in the area is represented by the Esna shale (laminated green and gray shale) of upper Paleocene (Beadnell, 1905). The thickness of the Palaeocene as it was encountered in some wells in the Northern Western Desert of Egypt is shown in Table 2.8.

Eocene

The exposed Eocene rocks (Fig. 2.1) have been divided (see Said, 1962) into the following main units: Lower, Middle and Upper Eocene.

Lower Eocene

The rocks of lower Eocene are exposed over large areas of Egypt. These sediments are represented by open or basinal marine shales and carbonates (Apollonia

Table 2.8: Thickness of Palaeocene section

Well	Abu Sennan	Abu Gharadig AG 1	Abu Gharadig AG 2	Abu Gharadig AG 3	Rabat 1	Wadi Natrun -1	WD7 -1	WD8 -1	WD32 -1
Latitude N	29 37 30	29 44 32	29 40 15	29 46 30	29 54 21	30 23 27	29 58 15	29 56 54	29 43 09
Longitude E	28 43 00	28 29 33	28 24 55	28 32 30	28 53 00	30 18 31	28 16 24	28 27 17	28 49 53
Thickness of Palaeocene in metres	15	97	82	105	107	43	216	165	152

Table 2.9: Thicknesses of Oligocene, Miocene and Pliocene - Recent sections

Well	Kharita	Shaltut	Alamein	Alam El-Buieb	Dabaa	Abu Subeiha	Faghur	Umbarka	Wadi Natrun	Khatatba	Kanayis	Rabat
Age	Thickness in metres											
Recent / Pliocene	103	7	26	14	102	34	-	-	355	-	19	-
Miocene	501	871	479	795	397	430	61	332	-	-	486	291
Oligocene	329	488	320	515	274	349	-	89	391	440	155	139

Table 2.10 Thickness of Pleistocene - Pliocene section

Well	Burg El Arab	Mersa Matruh	Abu Roash-2	Rosetta-2	Baltim	Ras El Barr	El Wastani	Abu Madi	Sidi Salem	Kafer El Sheikh
Latitude N	30 55'	31 30'	29 59'	31 37'	31 38'	31 37'	31 34'	31 26'	31 19'	31 07'
Longitude E	29 31'	27 16'	31 04'	30 32'	31 02'	31 52'	31 25'	31 23'	30 45'	31 10'
Age	Thickness in metres									
	Northern Western Desert			Nile Delta						
Pleistocene-Pliocene	128	27	161	2720	3469	2977	2919	3381	3035	4009

unit). Also, in the subsurface they are missed on the crests of the subsurface structural highs which trend NE (Salem, 1976).

Middle Eocene

Middle Eocene sediments crop out over a smaller area. These sediments consist of shallow marine carbonates and shales (Mokattam unit).

Upper Eocene

The upper Eocene, which mainly comprise marls, grits and sandstones, represents the least exposed sediments of the Eocene section in the Western Desert.

Amin (1961), quoted by Kostandi (1963), discussed the Eocene basins of sedimentation in the Northern Western Desert and stated that the lower Eocene basins and to some extent those of middle and upper Eocene reflect the effects of the late Cretaceous movements. Kostandi (1963) mentioned that the lower and middle Eocene reflect the effects of the late Cretaceous folding, while the uper Eocene reflects later movements which caused a simple pattern of folds and basins.

Oligocene

Oligocene sediments crop out north of the Faiyum depression and also at Gebel El-Ahmar, 5 km. east of Cairo. These sediments consist of cross bedded sandstones and gravels with interbedded shale and limestone. The Oligocene sediments have been encountered

in several wells in the North Western Desert (Table 2.9), where they are principally composed of terrigenous siltstone, shale and a few sandstones.

The Oligocene continental phase, quartz-chert gravels, is accompanied by volcanic activity, basalt flows (Hume, 1911). These basalt flows occur on both sides of the Nile Delta, at Baharia Oasis and in the north Faiyum desert. They form a conspicuous sheet which reaches about 25 m. thick and caps the upper Eocene rocks. These basalt flows have been considered as late Oligocene, on the basis of their relative stratigraphic position (Faris, 1946; Omara, 1953; and Said, 1962).

Shata (1955) recognized two Oligocene series. These are:

a) A fluvio-marine series which consists of alternating sandstone, shale and dolomite. These rock types crop out north of the Faiyum depression (see Fig. 2.1).

b) A continental series which is composed of dark coloured cross-bedded sandstones and crop out north and northwest Baharia Oasis.

The environments of deposition of the Oligocene are shown in Fig. 2.38, where the deltaic environment gives way to marine conditions in the Northern Western Desert.

Miocene

The lower Miocene sediments consist of sandy Moghra formation, which is part of Oligocene (Salem, 1976). At

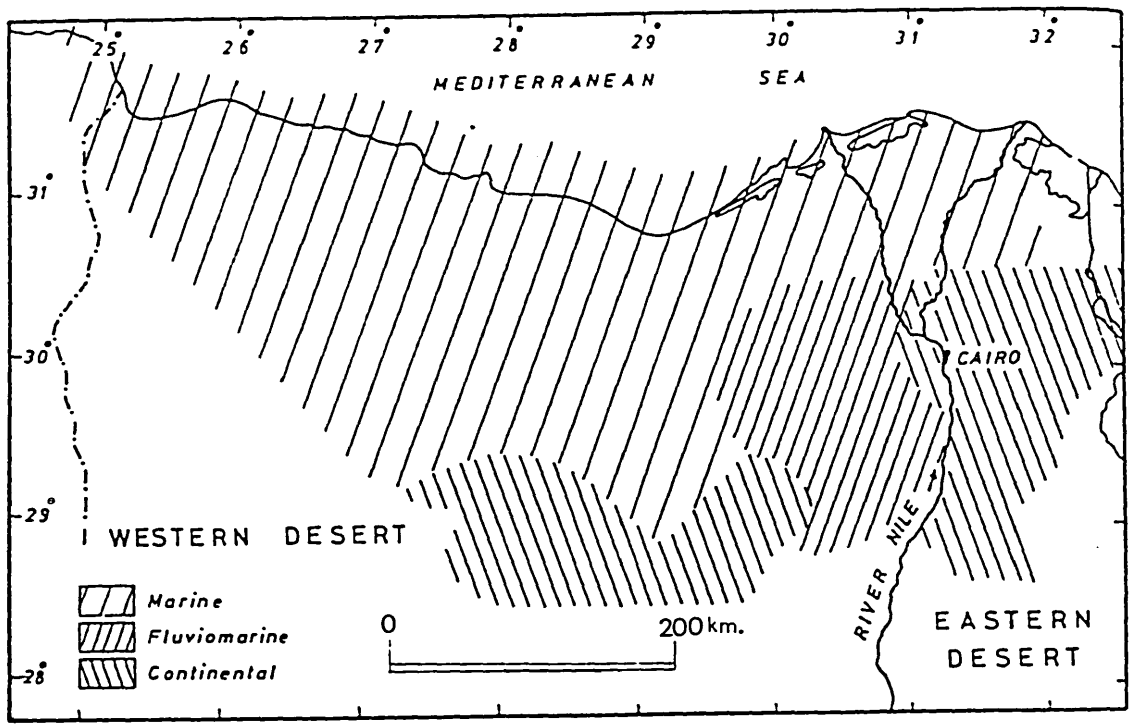


Fig. 2.38 . Environments of deposition of Oligocene sediments in northern Egypt, simplified (Marzouk, 1970).

(After El Shazly, 1977)

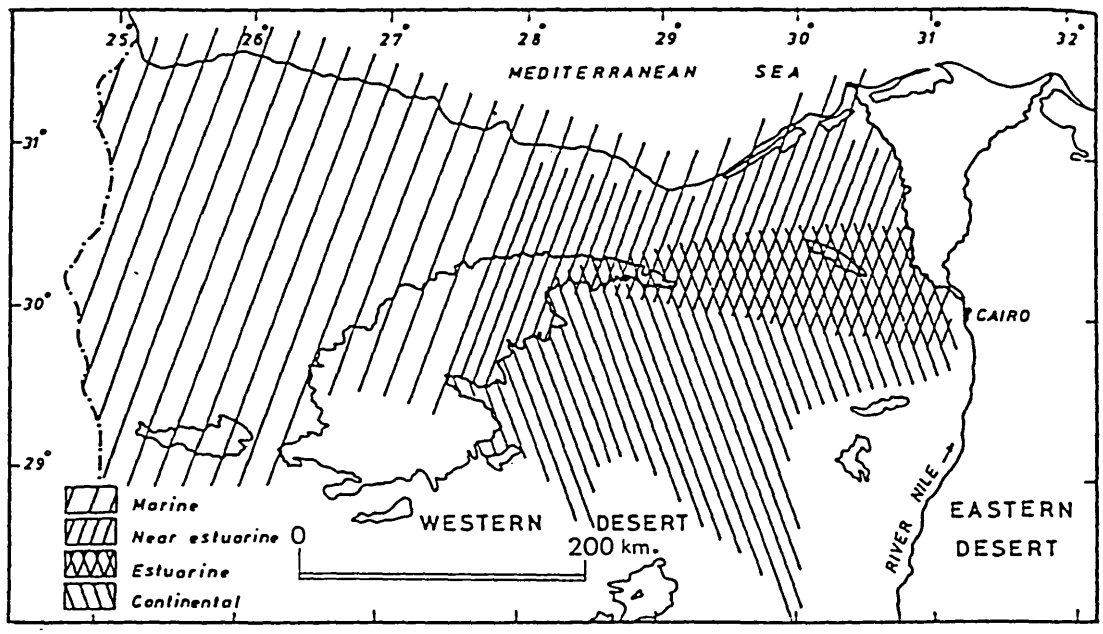


Fig. 2.39 Environments of deposition of Early Miocene sediments in northern Western Desert, Egypt (Ouda, 1971).

(After El Shazly, 1977)

El-Sallum, Qattara depression and Siwa Oasis, these sediments are mainly shallow marine facies which are represented by fossiliferous limestones and marls (Shata, 1955). The environments of deposition of the early Miocene are represented in Fig. 2.39.

In the subsurface (see Table 2.9), these sediments are composed of sandstones and shales with intercalation of limestone.

The middle Miocene sediments, termed the Marmarica limestone by Said (1961 and 1962), are predominantly carbonates. The environments of deposition of the middle Miocene sediments are represented in Fig. 2.40. In the subsurface, these sediments are composed of terrigenous deposits, especially at the Nile Delta.

According to Said (1974), as quoted by Salem (1976), the upper Miocene sediments are not present in northern Egypt.

Pliocene

Pliocene deposits are represented at Wadi Natrun by the following two shallow water series (Shata, 1955):

a) Lower series consists of black shale alternating with argillaceous sandstones;

b) Upper series represented by porcellaneous limestone, with flint, alternating with quartz sands.

The environment of deposition of the Pliocene sediments are demonstrated in Fig. 2.41.

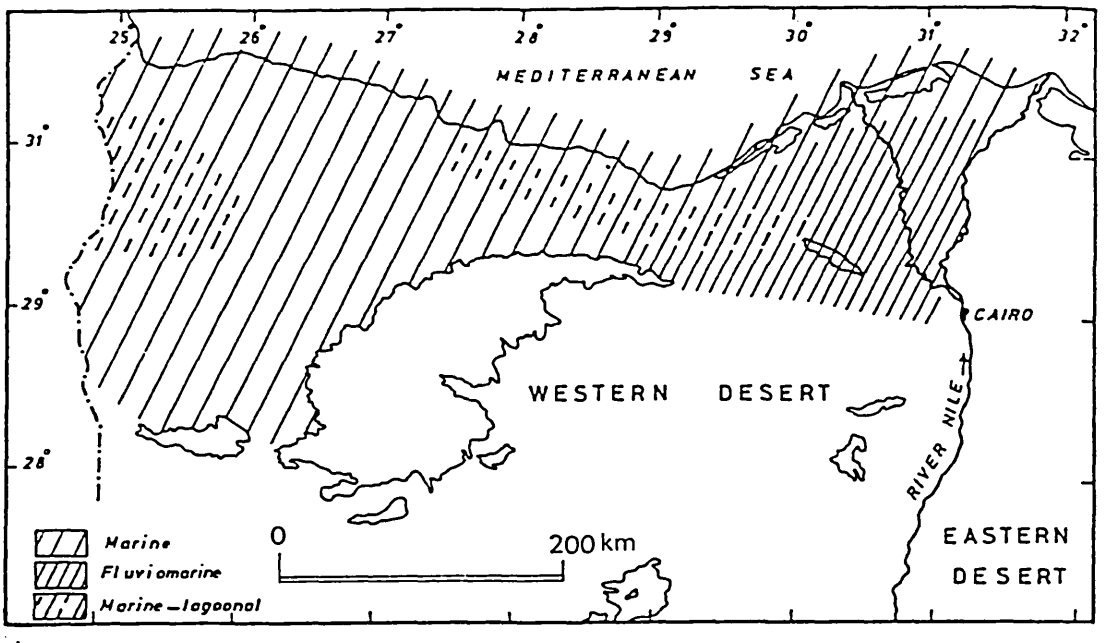


Fig. 2.40 . Environments of deposition of Middle Miocene sediments in northern Western Desert and Nile Delta, Egypt. Some environments probably extend into Late Miocene (Ouda, 1971; El Shazly *et al.*, 1975*b*). After El Shazly, 1977.

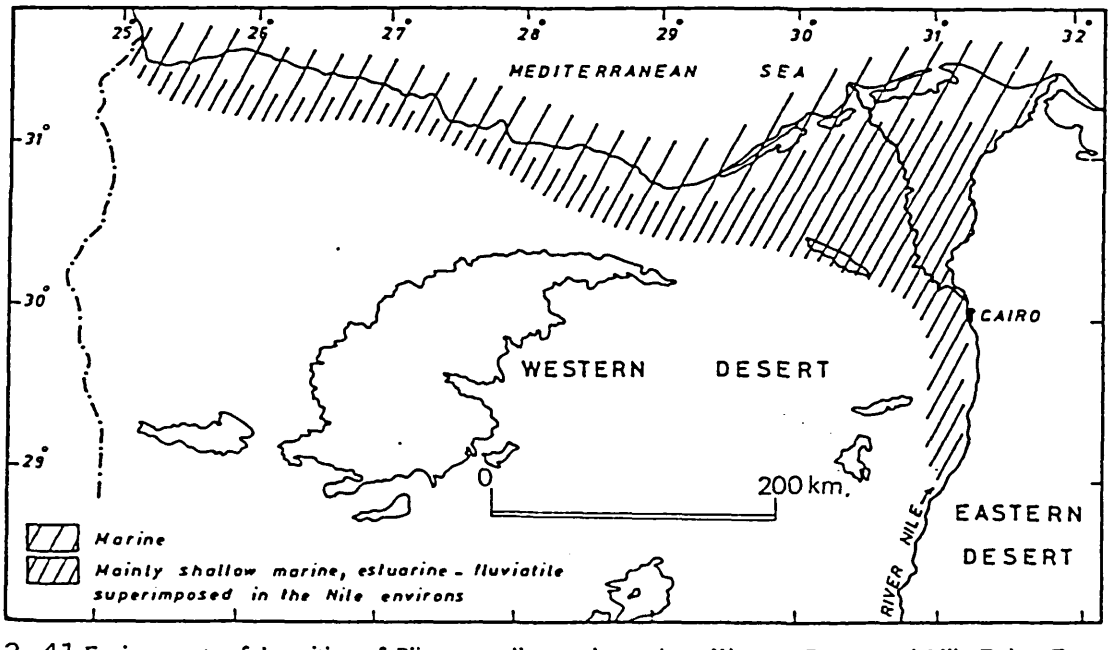


Fig. 2.41 Environments of deposition of Pliocene sediments in northern Western Desert and Nile Delta, Egypt (Ouda, 1971; El Shazly *et al.*, 1975*b*).

(After El Shazly, 1977)

Pleistocene

Pleistocene depostis constitute two series (Shata, 1955) as follows:

a) The coastal ridges, which extend for long distances almost parallel to the Mediterranean coast in the studied area are composed essentially of oolitic limestone.

Shata (1955) recognized three stages in the evolution of these ridges. These are:

i. an embryonic stage with a low lying ridge of oolite particles, which are almost loose or at least poorly consolidated;

ii. an intermediate stage to the south of the previous one, which forms a more conspicuous ridge. The depression which separates both of them is filled with salt marshes and soil;

iii. a mature stage which is represented by another line of ridges to the south of the second ridge.

These oolitic ridges have almost certainly originated from the consolidation of ancient littoral sand dunes.

b) Sand and gravel series which borders the cultivated areas.

In the subsurface, the Pleistocene and Pliocene sediments were encountered in some wells in the Northern Western Desert as well as the Nile Delta (Tables 2.9 and 2.10)

Recent

The recent deposits consist of (Shata, 1955):

a) Salt, sabakha and soil, which are mainly in the depressions and between coastal ridges;

b) Drift sand which forms longitudinal dunes;

c) Nile silt and alluvium.

2.4 Geological History

According to Beckman (1967); Soliman and A. El Fatouh (1970); Salem (1976) and El Shazly (1977), the conclusions of the structural development and stratigraphy of the Northern Western Desert of Egypt are:

1. A shallow sea covered the central part of the Western Desert in Cambra-Ordovician time. A second transgression during the Carboniferous was restricted to the northwest part of the studied area and Abu Rawash (Fig. 2.35).

2. The facies changes and the late Carboniferous-Permian volcanicity are reflections of tectonic movements and uplifting during late Palaeozoic - early Mesozoic (El Shazly, 1977).

3. The Palaeozoic sediments are more strongly folded than the overlying Mesozoic sediments (El Shazly, 1977).

4. There are so far no details of the Palaeozoic folding, but regional highs and lows may have existed.

5. A major disconformity is generally reported between the Palaeozoic and Mesozoic (Beckman, 1967).

6. A transgression took place during the Jurassic, which started from the north and northeast in the Lower Jurassic and later migrated as far west as Mamura.

7. A regression took place towards the end of the Jurassic, accompanied in some places by vertical movements and erosion. As a result of this, the upper Jurassic has variable thicknesses, and its top is often eroded.

According to Soliman and El-Fatouh (1970), later orogenic movements are evidenced in Wadi Araba (Eastern Desert), Wadi Natrun and Khatatba (Western Desert). These movements, which could have occurred at different times from pre-Carboniferous to Cretaceous in different parts of Egypt, affected the configuration and distribution of Carboniferous sediments.

According to Salem (1976), the basement rocks, together with the overlying Palaeozoic sediments were faulted during a Triassic or early Jurassic phase of extension, which created NE - SW basins which were arms of the Tethys sea. Deposition in this depressional structure (Fig. 2.42) was continued with only minor deformation until the late Cretaceous.

8. At the Cretaceous-Jurassic boundary, there is a widespread uncomformity with evidence of emergence and local uplift, particularly in the northwest (Beckman, 1967).

9. The lower Cretaceous transgression covered a surface of considerable relief and started from the north

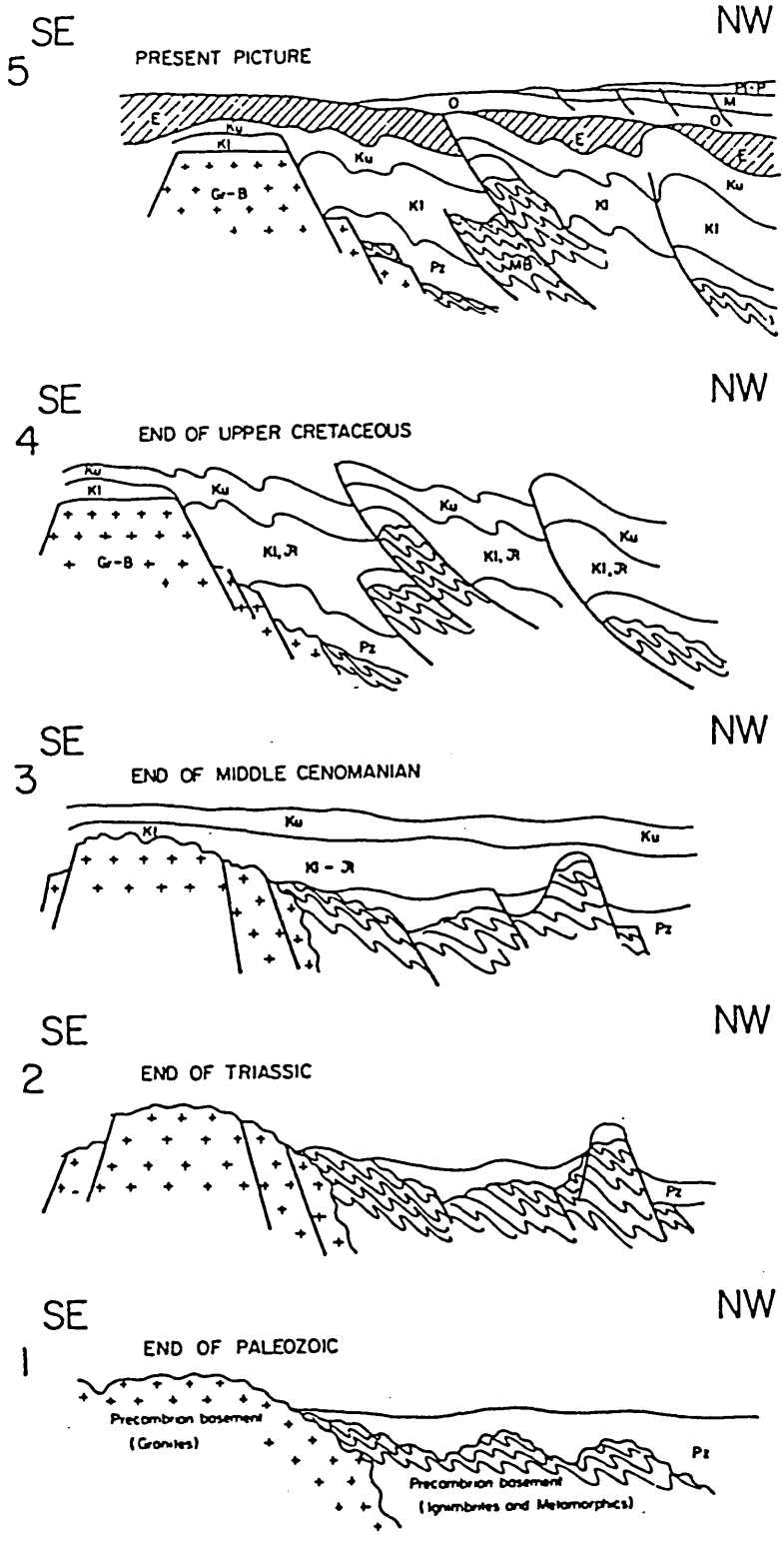


Fig. 2.42 –Diagrammatic cross sections showing tentative interpretation of geologic evolution of northern part of Western Desert, Egypt.

(After Salem,1976)

and northwest and migrated to the east and possibly south.

10. The centre of the lower Cretaceous basin received over 3,000 m. sediments at Mersa Matruh. To the south, the lower Cretaceous shales and carbonates were replaced by sands.

11. A regression, coupled with non deposition in some areas is noticed by Beckman (1967), at the lower Cretaceous (Albian).

12. The upper Cretaceous transgression started in the Cenomanian from the north to the south as far as Baharia. A second transgression, which started in the Senonian, initiated the deposition of white chalk in the north and shales further to south (beyond the limit of the studied area).

13. The Syrian Arc folding started near the end of the Turonian (Salem, 1976), or during the Senonian (Beckman, 1967) and continued intermittently into the Palaeocene and locally to the end of the middle Eocene. A widespread emergence occurred by the end of the Cretaceous (Beckman, 1967), in the North Western Desert, where there is a clear hiatus between the Cretaceous and Tertiary.

14. Palaeocene and early Eocene sediments were deposited along NE - SW elongated basins, which were separated by structural highs of the late Cretaceous rocks.

15. At the end of the lower Eocene, a regional epirogenic uplift, or updoming occurred, accompanied by considerable block faulting along an old, probably pre-Cretaceous fault zones with at least partly NE - SW trend (Tromp, 1950).

16. During the following period of regional subsidence, middle Eocene sediments were deposited.

17. General emergence, updoming, of a greater part of Egypt began near the end of the middle Eocene, probably more important even than the previous one, and became more pronounced during the Oligocene.

18. From this time onwards, great parts of south Egypt stayed more or less permanently above the sea level.

19. During the Oligocene, the NW faults became more prominent (inherited from earlier tectonic disturbances) and the regression was probably accompanied by down faulting (especially to the north of Egypt) (Salem, 1976).

20. The Oligocene - early Miocene basalts are related to the emergence and bulging of the basement around the Red Sea.

21. In the middle Miocene, a sudden shift in the river course occurred, probably due to faulting towards the east. This caused the replacement of the deltaic sediments to the west by carbonate sediments (Salem, 1976).

22. A major transgression reached its climax in the middle Miocene and ended by Alpine tectonism and uplifting during late Miocene and early Pliocene.

23. The Alpine tectonism of the late Miocene caused the development of the WNW folds (El Shazly, 1977).

24. El Shazly (1977) relates the NW, the NNE and WNW fault trends to the Alpine tectonism, initiated in the late Miocene. The NW faults exhibit right lateral movements as well as vertical displacement. But the NNE faults show left lateral displacement.

25. In late Miocene, the Mediterranean Sea acquired more or less its present form and the Nile valley assumed its identity as a result of late Miocene - early Pliocene tectonics (El Shazly, 1977).

CHAPTER THREE

FIELD STUDY

OF

GAA - ABU RAWASH VILLAGE AREA

CHAPTER THREE

Field Study of Gaa-Abu Rawash Village Area

3.1 Introduction

The structures of Abu Rawash area as a whole were thought to be representative of a major phase of structural evolutions, for folds with similar trends occur in many localities throughout Egypt. This locality, especially Gaa-Abu Rawash village area, was visited by the present writer three times, for short periods during the course of this study.

It will be recalled that such a study is the first link in the chain from local scale field investigation through air photographic interpretation to the regional study by satellite imagery.

The area studied lies about 10 km. west of Cairo and takes its name from a local area, Gaa, as well as a neighbouring village (Figs. 3.1, 3.2 and 3.3). This area is limited to the north by Wadi El-Qarn, to the south and west by the Cairo-Alexandria road and to the northeast by the village of Abu Rawash.

3.2 Purpose of Study

The aim of this field study is to determine as far as is possible, the mechanics of crustal deformation in this area and to establish those aspects of structural development which could be taken as a key for the structural evolution of large areas of the Northern Western desert of Egypt. In particular, the writer is

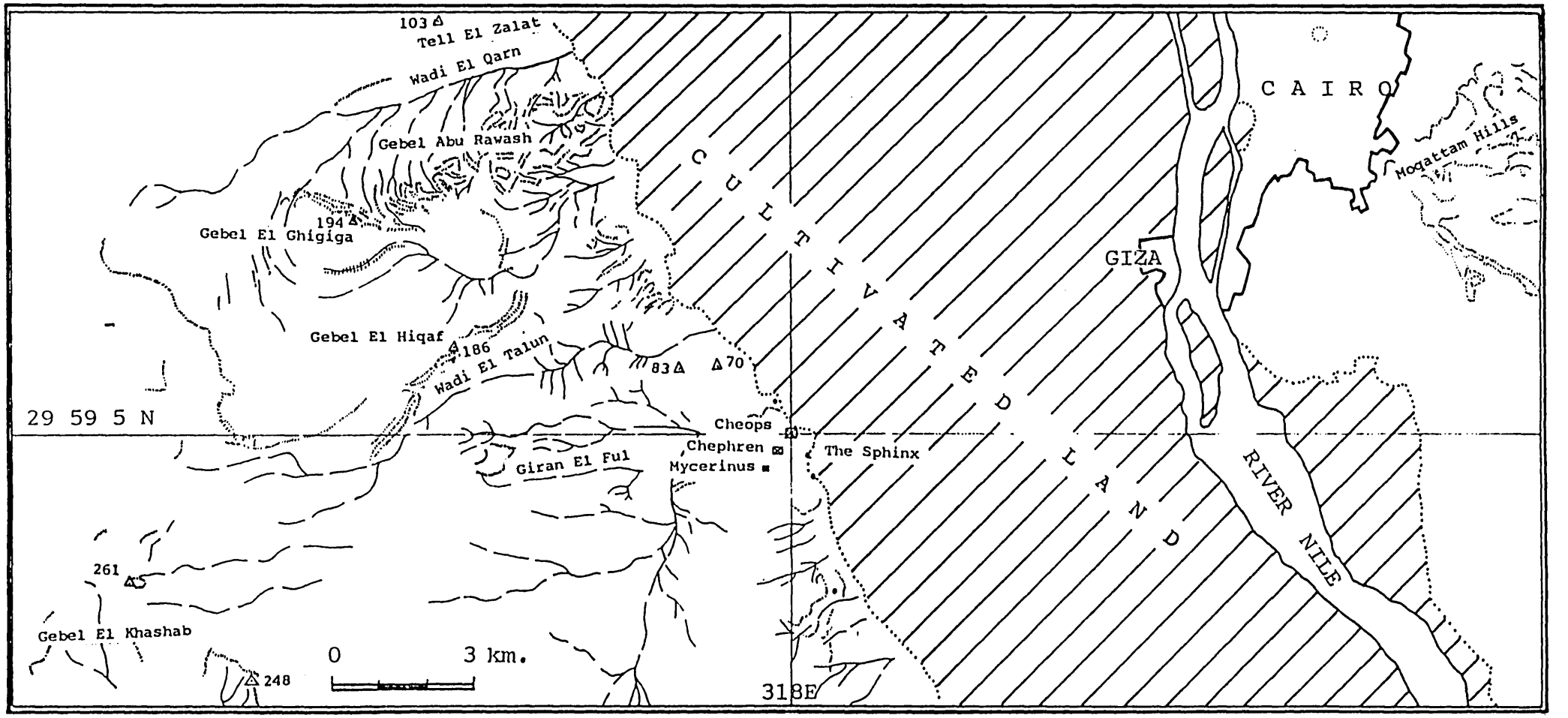


Fig. 3.1 Location map of Abu Rawash area.

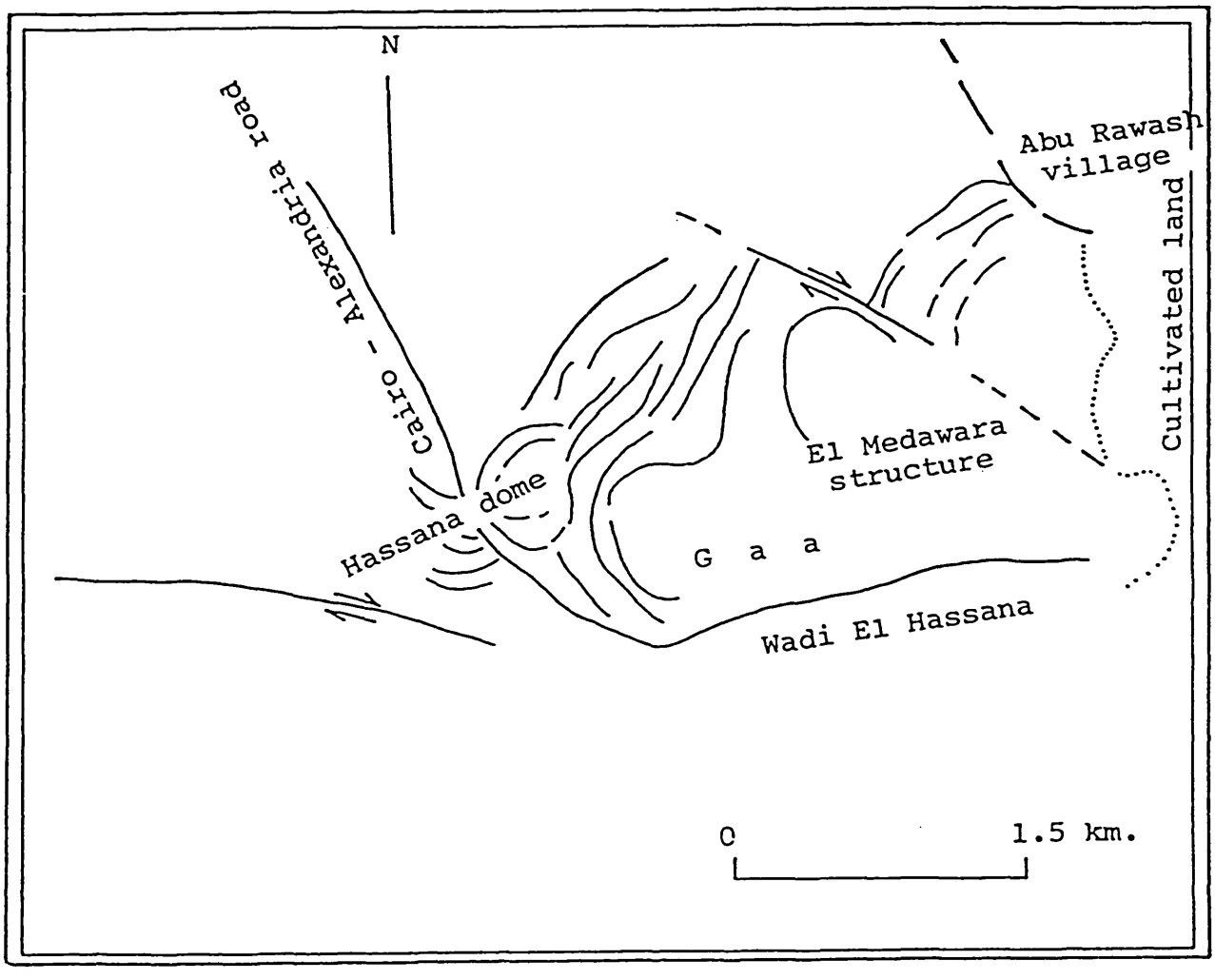


Fig. 3.2 Location map of the studied area, prepared from the aerial photographs.

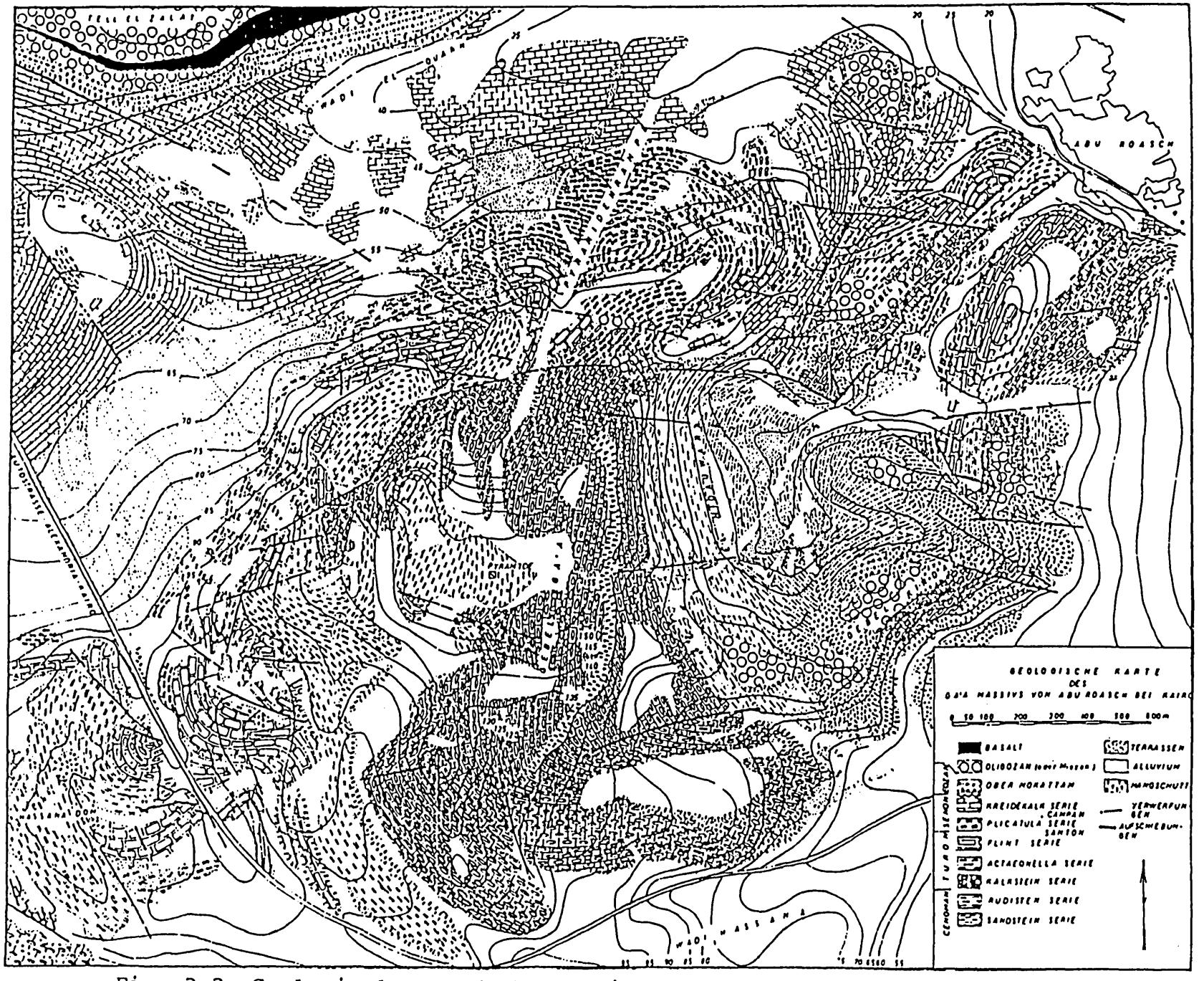


Fig. 3.3 Geological map of the studied area, after Jux (1954).

concerned with the relationship between minor fractures and the fold structures exposed in the area.

The traditional objective of such a structural study is to relate the orientation and displacements of the fractures to the stress systems which are thought to obtain during fold development and to identify trends and types of fractures which do not fit into such a pattern and which may be classified as being unrelated to the development of the fold structures. This is one of our objectives, but our main concern is how one identifies and classifies the various inter-relationships between fracture and fold trends from the fracture traces, which can be obtained from studies of aerial photographs and for satellite images.

Firstly, the traditional objective will be considered. To this end, the author will first outline the structures as already determined by previous workers.

3.3 Previous Work

Walter (1887), quoted by Faris (1946), was the first geologist who attempted a study of the Abu Rawash area, including the studied area, from the structural point of view. He attributed the Cretaceous beds outcropping on the surface to "tremendous dislocations that elevated them". Beadnell (1902) described Walter's faults or dislocations as more imaginary than real.

Abu Rawash area has been divided by Beadnell (1902) into two main regions:

a) the eastern part (Gaa dome and El Hassana dome), which represent most of the studied area;

b) the western part (Gebel El Ghigiga, Gebel El Hiqaf and Giran El Ful, which represent two anticlines separated by Sudr El Khamis syncline).

So, the studied area has been described as a domal structure, the Gaa dome (Beadnell, 1902). The centre of this dome, mainly Cenomonian clays and sandstone, is El Medawara (Gebel el Midauwara), where the hard beds of Turonian limestones form curved ridges which dip away from the centre on the NW, W and SW sides. On the NE side, these ridges end abruptly against a WNW fault, which separates El Medawara from the inclined Cretaceous rocks until Abu Rawash village. The south side is bounded by hills, where the exact disposition of the beds is not very clear but probably conform more or less regularly to the dome (Beadnell, 1902). According to him, the Gaa dome is broken and surrounded on the NW, N and E sides by a long curved fracture. The dome is also disturbed by a NNE fault, while the inclined Cretaceous rocks, until the village of Abu Rawash, are dislocated by two NE faults.

Faris (1946) considered the area of Abu Rawash to be divided into many folds, such as:

a. El Medawara centre, which represents the south western part of the studied area;

b. Abu Rawash centre, which forms the northeastern part of the area under investigation;

c. Hassana centre;

d. El Ghigiga centre;

e. Gebel El Hiqaf and Giran El Ful, or the southern centre.

The northeastern El Medawara inclined Turonian limestone (Abu Rawash centre) includes the main ridge and the quarried limestone.

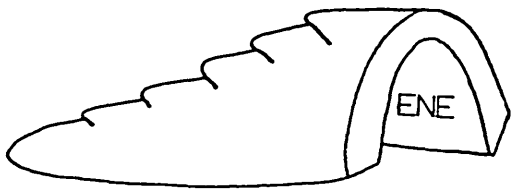
The main ridge is limited to the north by a NE trending fault which separates it from Wadi El Qarn, while to the south is limited by another NE trending fault which separates it from the quarried limestone. Generally, the dip of beds is towards the NW. According to Faris (1946), these fold structures were disturbed by faults which trend NW, NE and E - W and involved vertical displacement of two hundred meters or more, such as the NW, which separates El Medawara from its north-eastern extension until the village of Abu Rawash.

Omara (1953), in his work on the structural features of the Pyramids area, which lies completely south of the studied area, recorded the following:

i. The direction diagrams of the wadis within this particular area did coincide remarkably well with the rose diagrams derived from the trends (orientation) of the minor features.

ii. The warping of the fold axis was attributed to later compression parallel to the fold axis. Although one can argue that this warping may be referred to anticlastic effects, the presence of minor thrusts, which has been reported by Omara (1953), confirm that this

warping (cross warping) is probably the result of compression which acted parallel with the fold axis.



iii.Omara (1953) suggests, based on stratigraphic evidence, that "the main folding started at the northwest, the studied area, then migrated towards the southwest, Giza Pyramids". Generally, in the Abu Rawash area, upper Eocene and /or middle Eocene overlie uncomformably the Senonian rocks, where at the Giza Pyramid structure (fold) the Pliocene overlays uncomformably the lower upper-Eocene.

iv. The ENE folding continued during the middle Eocene but with a decreased intensity, where the dip of Eocene beds is much less than that of the Cretaceous.

Beadnell (1902) attributed the cause of this folding to N - S lateral compression.

Faris (1946) and Omara (1953) suggest lateral stresses in NW direction, perpendicular to the fold axes.

Knetsch (1958), as quoted by Said (1962), referred this folding to NW compression, which is said to be attributable to the action of a deep seated, wedge shaped, NW pointing tectonic unit that moved towards the NW. The present writer believes that the movement of the NW pointing wedge towards the NW will cause NW folds or it might cause the warping of the ENE - WSW fold axes and not the folds themselves, ENE - WSW. According to Knetsch (1958), the whole area is disturbed by faults, as indicated in his map (see Fig. 3.9).

Said (1962) inferred that this folding is a mechanical expression of deep seated infracrustal faulting, parallel to the fold axes.

With regard to El-Etr and El-Baz (1979), the actuating mechanism is probably complicated, but the maximum stresses are believed to be of vertical internal origin.

It will be argued that the presence of El-Medawara structure within the Gaa misled some workers such as Beadnell (1902) and Faris (1946) and others who described the Gaa as a dome structure.

3.4 Basic Concepts

3.4.1 Fracture Phenomena

The definition of fracture used in this study is not the same as that of Griggs and Handin (1960), who defined the fracture as a plane of no cohesion. This definition does not take into consideration those many fractures that still retain some cohesion along their planes. Because of that, the present writer considers a fracture to be a plane of discontinuity within a bed or beds of a rock mass which may have no cohesion or which may still retain some degree of cohesion.

According to the movement of the blocks of rock adjacent to the fracture plane, Griggs and Handin (1960) recognized two types of fractures; shear and extension fractures were called joints by them.

Unfortunately they did not recognize a third type of fracture which here is termed "hybrid fracture". These

fractures develop when the normal stresses acting on the potential shear plane are zero or tensile. Hence, both extension and shear occur. The hybrid fractures form a conjugate set, where the angle 2θ between this set is: $0^{o} \leqslant 2\theta \leqslant 45^{o}$ (Fig. 3.3c). The condition for the development of these fractures is that,

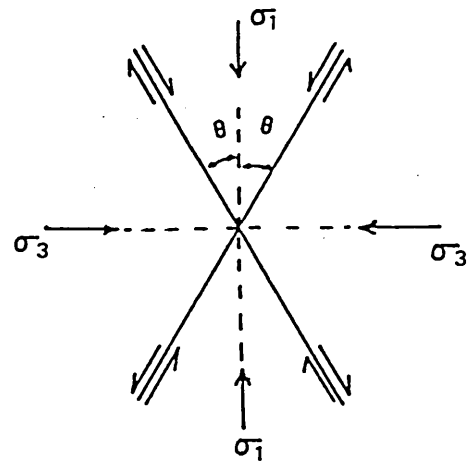
$5.4\ T \geqslant \sigma_1 - \sigma_3 > 4T$ (see Price, 1977 and Ladeira 1978).

Shear fractures

Shear fractures are initiated in a direction inclined to the axis of maximum principal stress and can occur in conjugate sets intersecting along the line of the intermediate principle stress direction. In brittle materials, the acute angle between the conjugate set is $2\theta \leqslant 90^{o}$ and bisected by the direction of the greatest principle stress (Fig. 3.4a). The condition for the development of these fractures is that the differential stress must be relatively high, so that, $\sigma_1 - \sigma_3 > 5.4T$, where $\bar{\sigma}1$, $\bar{\sigma}2$, and $\bar{\sigma}3$ are the greatest, intermediate, and least effective principle stress, respectively and T is the tensile strength of the rock.

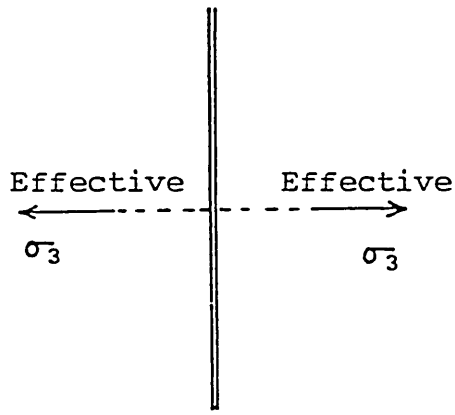
Dilation fractures

Dilation or extension fractures are formed perpendicular to the direction of the least principal stress and usually cause a volume increase in the rock mass. Because of this volume increase, they are called dilation fractures (Fig. 3.4b). The conditions for the development of these fractures is that,

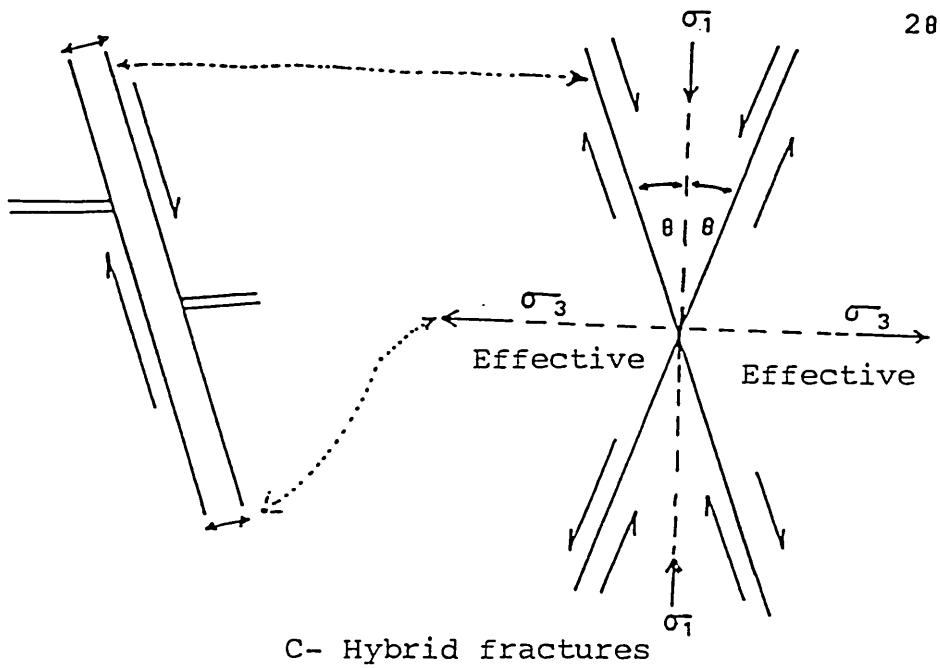


$2\theta > 45^{o}$

A- Shear fractures



B- Dilation (Extension) fractures



$2\theta < 45^{o}$

C- Hybrid fractures

Fig. 3.4 Different types of fractures.

$$P > S_3 + T$$

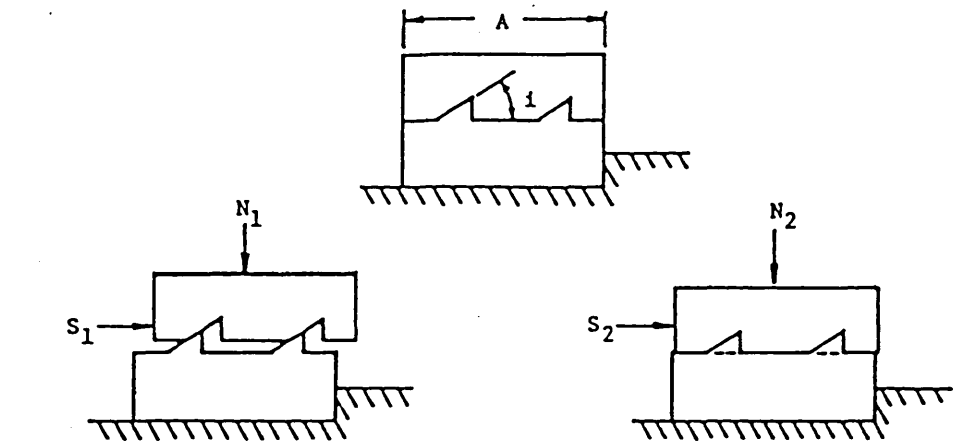
or

$$\sigma_3 > -T$$

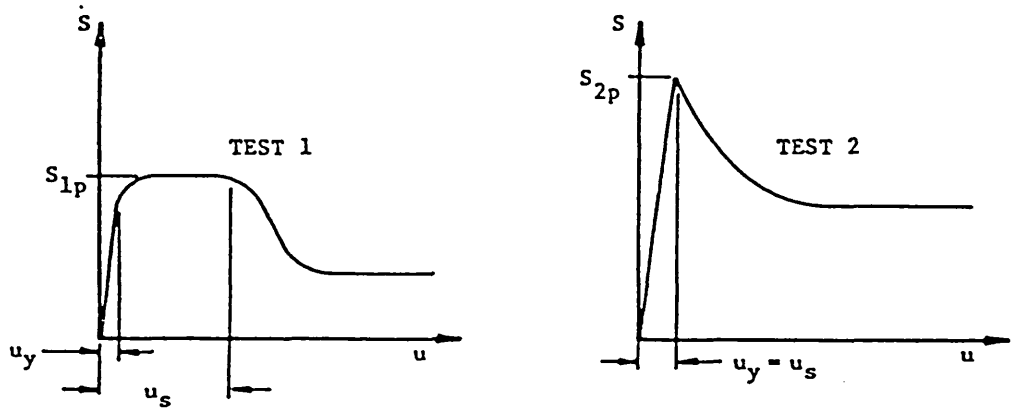
Here we assume $S - P = \sigma$, where S_1, S_2 and S_3 are the total greatest, intermediate and least principal stress, P is the pore fluid pressure and σ_3 is the least effective principal stress.

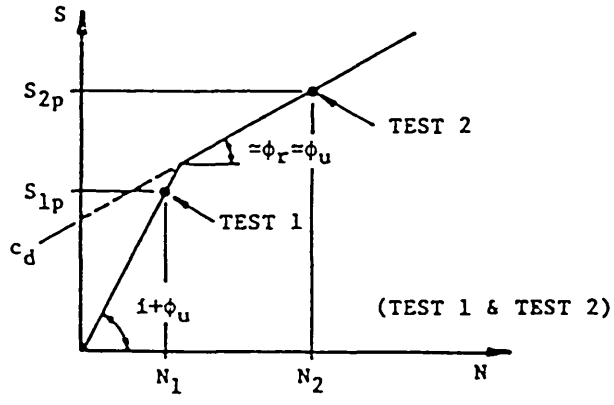
Hybrid Fractures (Dilation Shear Fractures)

Patton (1966) developed a model to explain the development of these fractures after failure of the rock mass. According to his model, these fractures develop when the normal stresses are lower than some critical value, Test 1 (Fig. 3.5b). In this case, the shear stresses initially cause elastic deformation of the asperity, the deviations of the surface from a mean plane on various scales (with undulation as largest and roughness as smallest forms of deviation), up to the yield deformation, followed by sliding of one asperity up over the other (dilation). When the resistance of the asperity is exceeded, a certain displacement shearing occurs. At normal stresses higher than critical, Test 2 (Fig. 3.5b), no dilation occurs and the asperities immediately sheared at the base. It may be possible to have dilation and shears at high normal stresses (Fig. 3.6), especially when the asperity is large (not sheared at lower stresses). Hence, these large asperities create the component of friction along the inclined sliding surfaces of the asperity at higher normal stresses.



(A)





(B)

Fig. 3.5 Explanation of Patton's model.

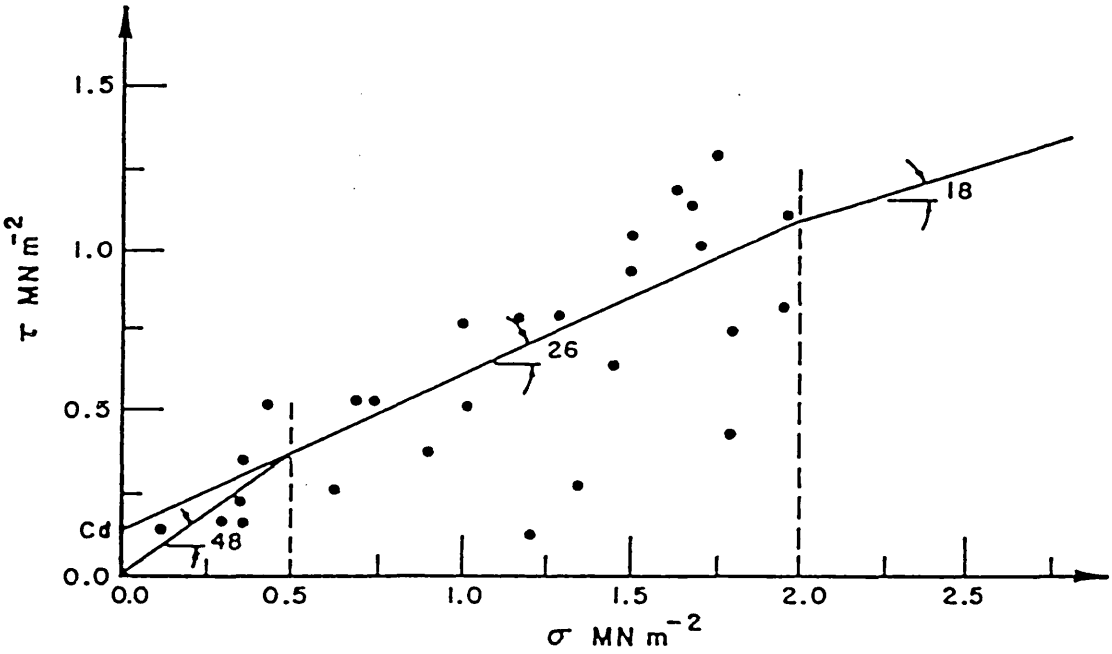


Fig. 3.6 Mohr-Coulomb failure relationship for discontinuities in limestone.

From stress analysis it follows that, as θ, the angle between the greatest principal stress and the fracture plane in a conjugate set becomes smaller, the values of the τ (shear stress) and $\bar{\sigma}n$ (normal stress) decrease and the rate of decrease of $\bar{\sigma}n$ is greater than the rate of decrease, of τ.

3.4.2 Relationship Between Folds, Faults and Fractures

Fractures and faults are related to compression and extension which develop during the folding of layered materials. As a result of folding, faulting and deformation, the orientation and magnitude of the stresses can change. From field studies, it has been established that the main sets of fractures which are found or developed in folded areas are represented in Fig. 3.7 (after Price, 1966 and Hancock and Atiya, 1979). The different orientation of the three axes of principal stresses that may be referred from the various fractures or faults are also shown in the same figure.

3.5 Field Study

3.5.1 Introduction

Fractures are a common deformational feature in rock and they will be used in this study as an aid to understanding the structural geology of the area under consideration. Certain field observations of fractures can be correlated by theoretical or experimental observations of fracture development and this enables one

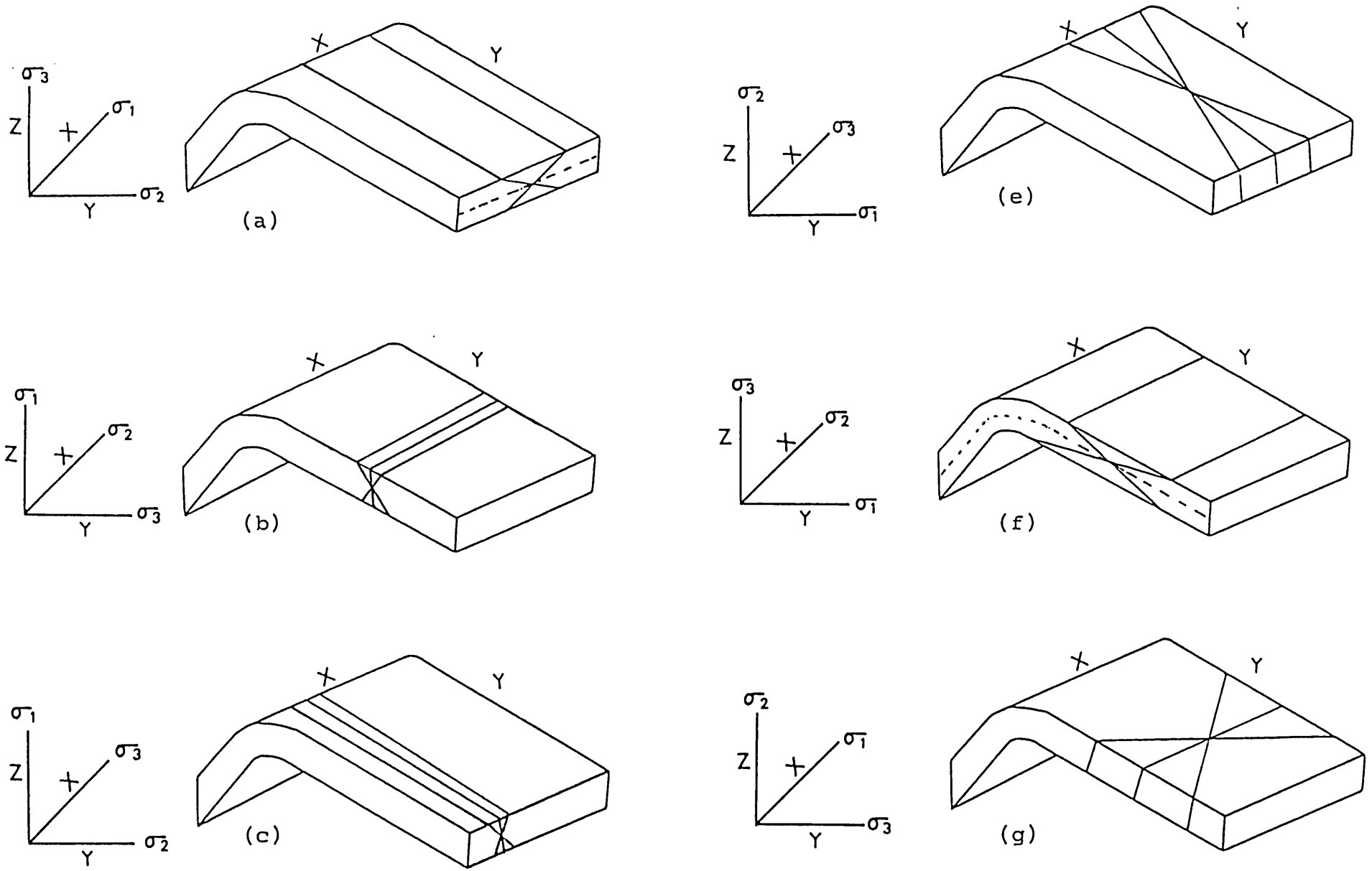


Fig. 3.7 Relationship between stresses, folding and possible fractures.

to interpret certain mechanical parameters involved in the development of fractures in and about folds.

The geological maps of the area based on the work of Faris (1946), Faris (1948), Omara (1952) and Jux (1954), and the work of Knetsch (1958) are shown in Figs 3.8, 1.2 and 3.9, respectively. Except for a number of faults, these maps show no indication regarding the geometry of the minor fractures of this area. For this reason, one of the main objectives of this study is the determination of the geometry of the flexures and orientations as well as relationships of the fractures of this area.

3.5.2 Field Data of Abu Rawash

The writer means by Abu Rawash the Gaa part or mass and its northeast extension to the village of Abu Rawash (Fig. 3.2). The Gaa rises abruptly from El-Medawara structure and forms a steep escarpment to the west. But on both northern and southern sides it is formed of a series of inclined beds.

The other part of Abu Rawash (Turonian limestones) or the northeast extension of the Gaa is arranged in step-like ridges, where a NE-SW reverse fault has been reported. These ridges are undulated and the axis of undulation is N20 - 25W - S20 - 25E.

It is quite clear from the subsurface geology of the area and from information obtained from bore holes that the rocks could be classified into three groups as follows:

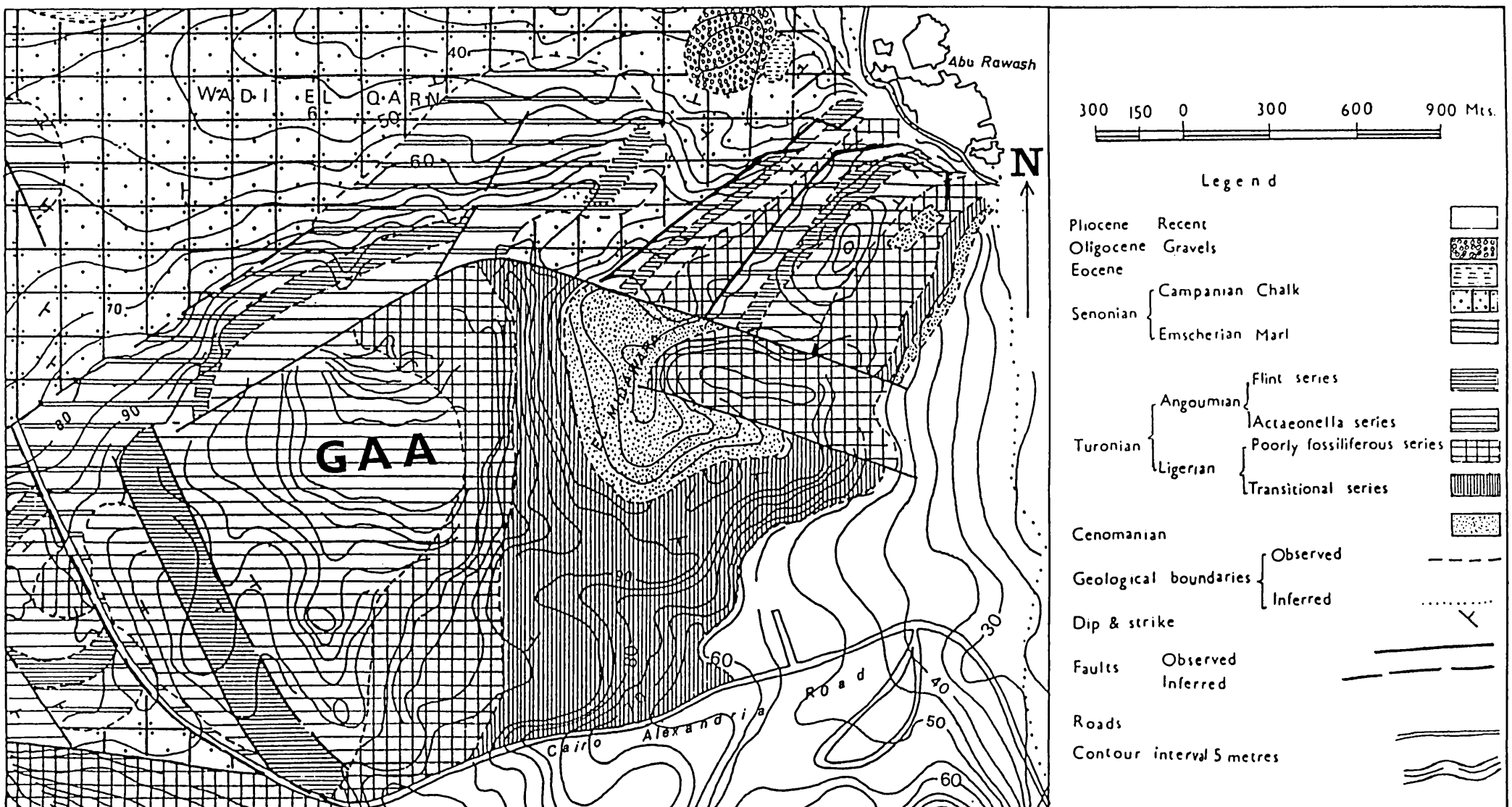


Fig. 3.8 Geological map of the study area (prepared by the present author after Faris, 1946).

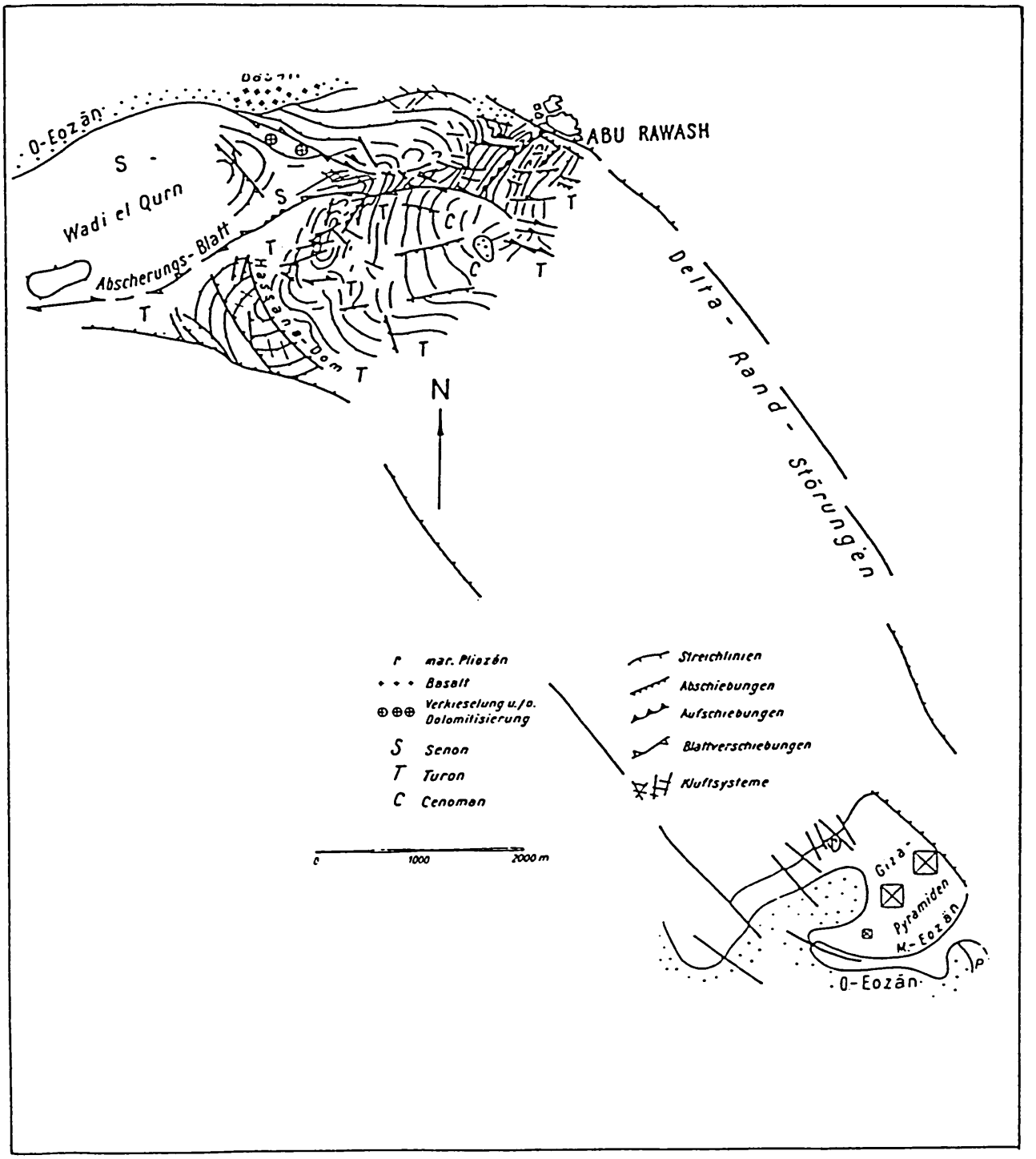


Fig. 3.9 Geological map of Gaa-Abu Rawash village area.

(After Knetsch, 1958)

a) Nubian sandstone and shale, (Carboniferous, Jurassic and lower Cretaceous);

b) Sands, sandstone, shale, clay and marl of Cenomanian;

c) Turonian limestone, with minor intercalations of shales, and Senonian massive chalk.

In this particular area, where the Nubian sandstone is thin (about 20 meters thick), the first group behaved in a ductile manner. The second group also behaved as a ductile group. Hence, it was the third group which was competent and acted as a structural control unit.

When Abu Rawash was subjected to lateral stresses, these weaker groups, especially the second one, generated a minor fold with a wave length of about 9 meters (Plate 3.1).

The present structural investigation of Abu Rawash consists of:

a) The measurements of the attitude of the outcrops;

b) The measurement of the attitude of the fractures and evidence of movement.

3.5.2A The Study of the Attitudes of the Outcrops

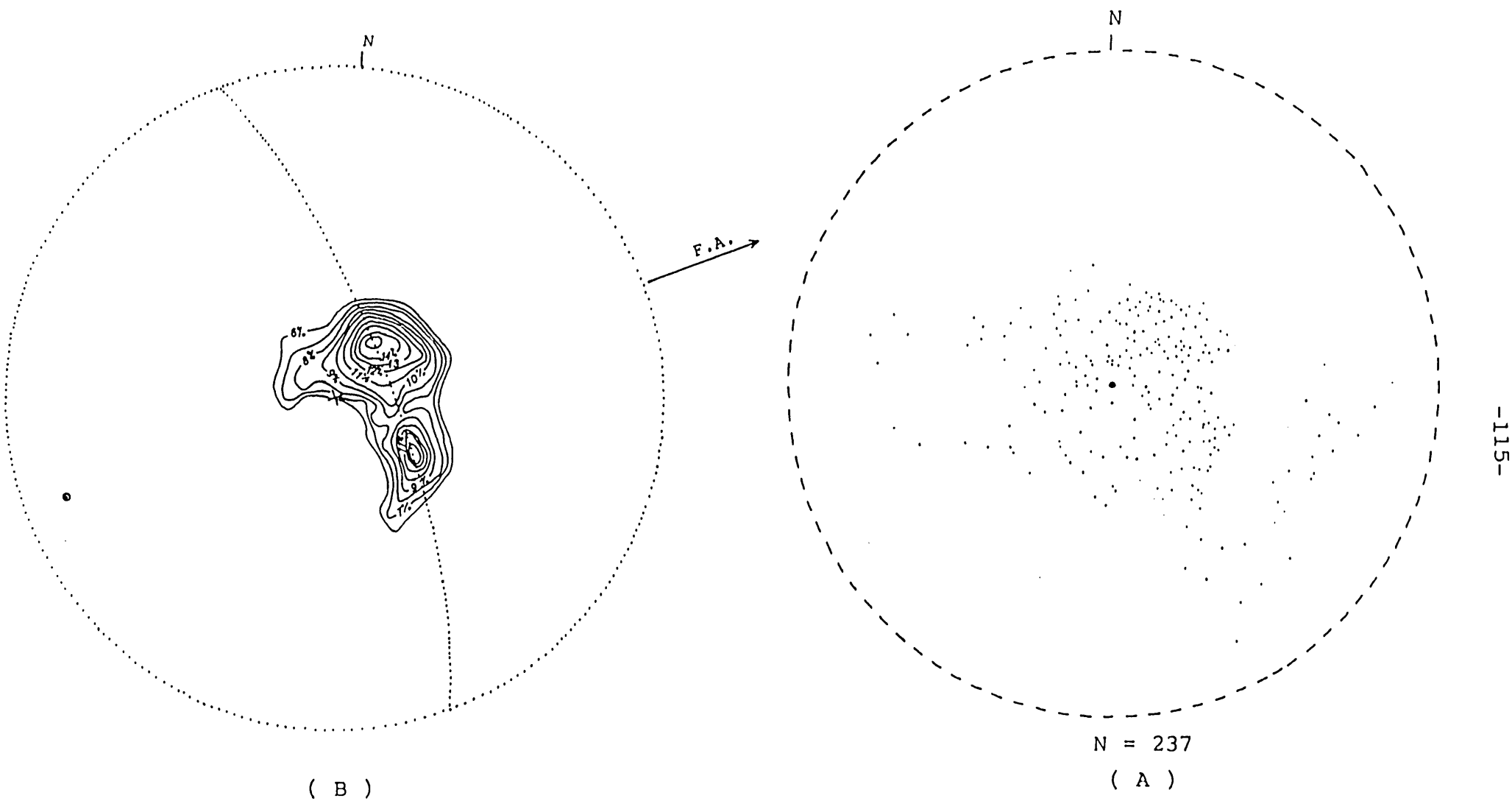
To determine the geometry of the Gaa-Abu Rawash village area (Fig. 3.3), the attitudes of the outcrops were recorded in the field. These measurements were plotted as S - poles of bedding planes on Schmidt equal area projection (Fig. 3.10a), and then contoured (Fig. 3.10b).

Plate 3.1





Minor NE —— SW fold structure.



(B)
Contoured diagram of the bedding plane poles.

(A)
S-pole diagram of the measured bedding planes.

Fig. 3.10 S-pole and contoured diagrams of the bedding planes (Gaa-Abu Rawash village area)

3.5.2A.1 Interpretation of the Contoured Diagram

The two maxima of the contoured diagram enable one to establish the orientation of a great circle (plane). Statistically, as indicated in Fig. 3.10b, the pole of this plane is the axis of the fold. This axis is trending N64E and plunges 14° degrees in the SW direction. So, the contoured diagram (Fig. 3.10b) enables one to infer that the Gaa-Abu Rawash village structure is a fold which plunges to SW.

At the entrance to the studied area near Abu Rawash village, the writer found the beds dip to the NE at about 25° degrees and where the limestone is quarried they dip at 20° degrees in the NE direction, nearly the direction of the fold axis. Because of these dip directions, the writer regards the Gaa-Abu Rawash village, or simply Abu Rawash village structure, as a pericline.

It has been shown in the previous work (Figs. 2.1, 3.3, 3.8 and 3.9) that the pericline is strongly disturbed by faults.

During the field study, it was seen that one of the NE faults which lies between the Gaa and Abu Rawash village, caused a repetition of the beds across the fault plane (reverse fault), as seen in Fig. 3.11, as well as increase of the dip of the hanging wall up to nearly 55° degrees, while the dip of the foot wall is about 30° degrees (Fig. 3.11). Another WNW fault which occurs in the area studied, represents a right hand or dextral strike-slip fault. This fault trends about N58W

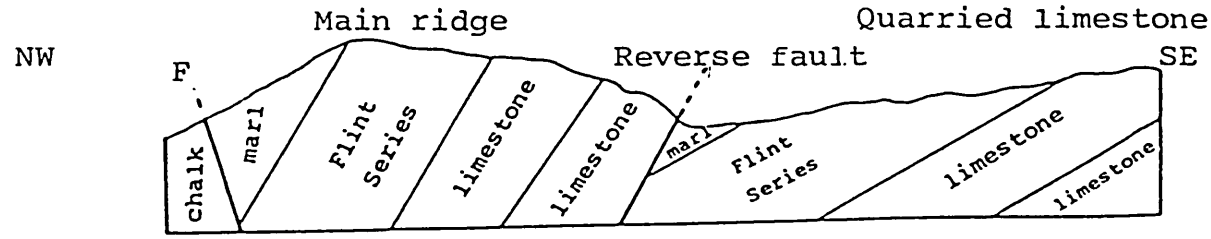
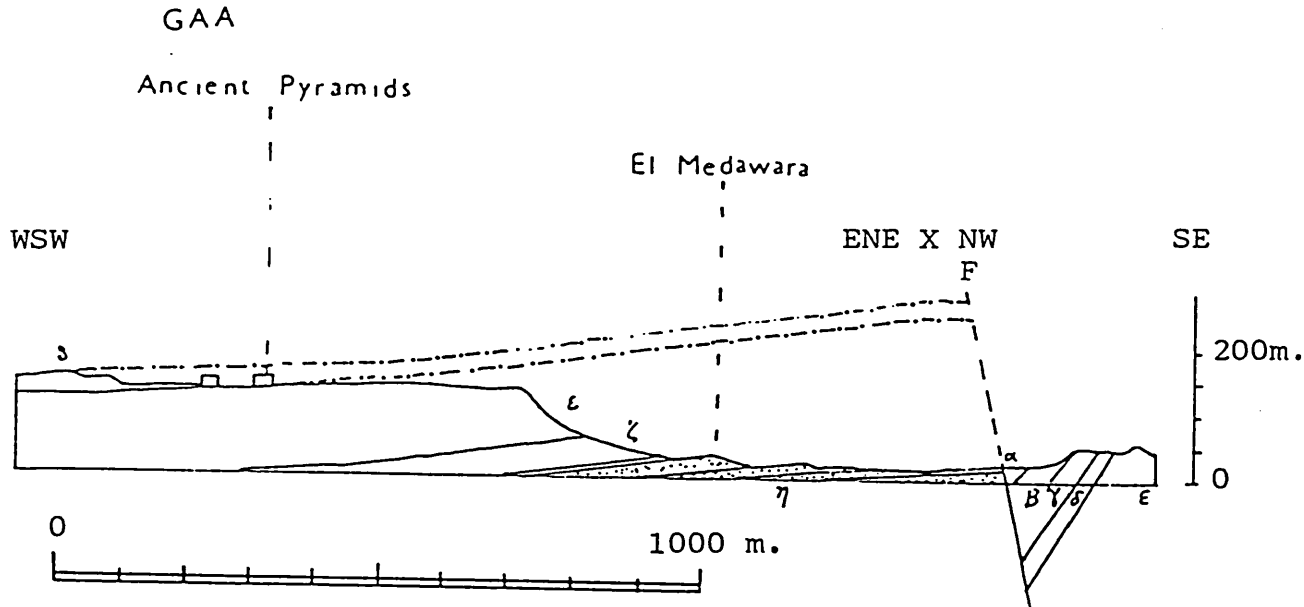


Fig. 3.11 Sketch of a geological section across the northern limb of Gaa-Abu Rawash village pericline.



∝ White chalk
β Ostrea and Plicatula bed
γ Flinty Series
δ Acteonella-Nerinea limestone
ε Hard compact and often chalky limestone
ξ Rudistae beds (alternating shales, marls and limestone)
η Clay and sandstone

Fig. 3.12 Geological cross section across Gaa-Abu Rawash village area (after Beadnell, 1902).

and separates the Gaa from the other northeastern part of the Gaa-Abu Rawash village pericline. This fault exhibits an apparent down-throw of more than 200 meters to the NE, as mentioned by Beadnell (1902) and Faris (1946), (Fig. 3.12).

Another WNW, N73W right lateral or dextral strike-slip fault, which is possibly of a regional extent, has been detected from the aerial photographs during the course of this study. This fault also has a down-throw to the NE.

These WNW right lateral strike-slip faults make an angle of about 15° degrees with each other.

3.5.2A.2 Flow of Ductile Materials and El-Medawara Structure

The rocks of the area studied are mainly of sedimentary origin, so they contained fluid inside their pores. Excess fluid pressure occurs when pores filled with fluids are deformed at a rate faster than they can escape. The clay and shales made an impervious barrier and helped increase fluid pressure during their diagenesis. These impervious barriers impede the escape of fluid from the sediment so that the pore fluid pressure build-up during gravitional compaction and becomes or may become high, as a result of tectonic deformation. In the area under study, this led to an over-pressured clay which has been intruded or injected into the fractures of the overlying Turonian limestone. Jux (1954), as quoted by Omara (1964), described the

injected clay as clay dikes. The crushed flint bands contained in limestones could be attributed to both pore fluid pressure and tectonic deformation.

3.5.2A.3 El Medawara Structure

El Medawara (or Midauwara) structure has a diameter of about 1.5 km. This structure lies in the Gaa, SW part of the Gaa-Abu Rawash village pericline. The beds, which roughly lie south of El-Medawara structure are not in conformable relation with this particular structure (Fig. 3.13). This is in contrast to the statement made earlier by Beadnell (1902). In fact, the beds which lie south and north of El-Medawara structure dip in the NW direction, so the structure was formed within the NW limb of the Gaa-Abu Rawash village pericline. This structure consists of curved ridges with very gentle dip (6° - 8° degrees) radiating from the centre of the structure, except to the south. The core of these ridges is composed mainly of Cenomanian sands and shales with dip of about 2° degrees. These Cenomanian deposits were covered by superficial sands and gravels (Fig. 3.3). The structure is present on the upthrow side of a WNW dextral strike-slip fault which has a downthrow of more than 200m. On the NE extension of the structure there is a NE reverse fault.

Accordingly, the present writer attributes this structure to diapiric intrusion which results from the migration of the ductile sediments, shales and sands, to the areas of maximum curvature during the folding

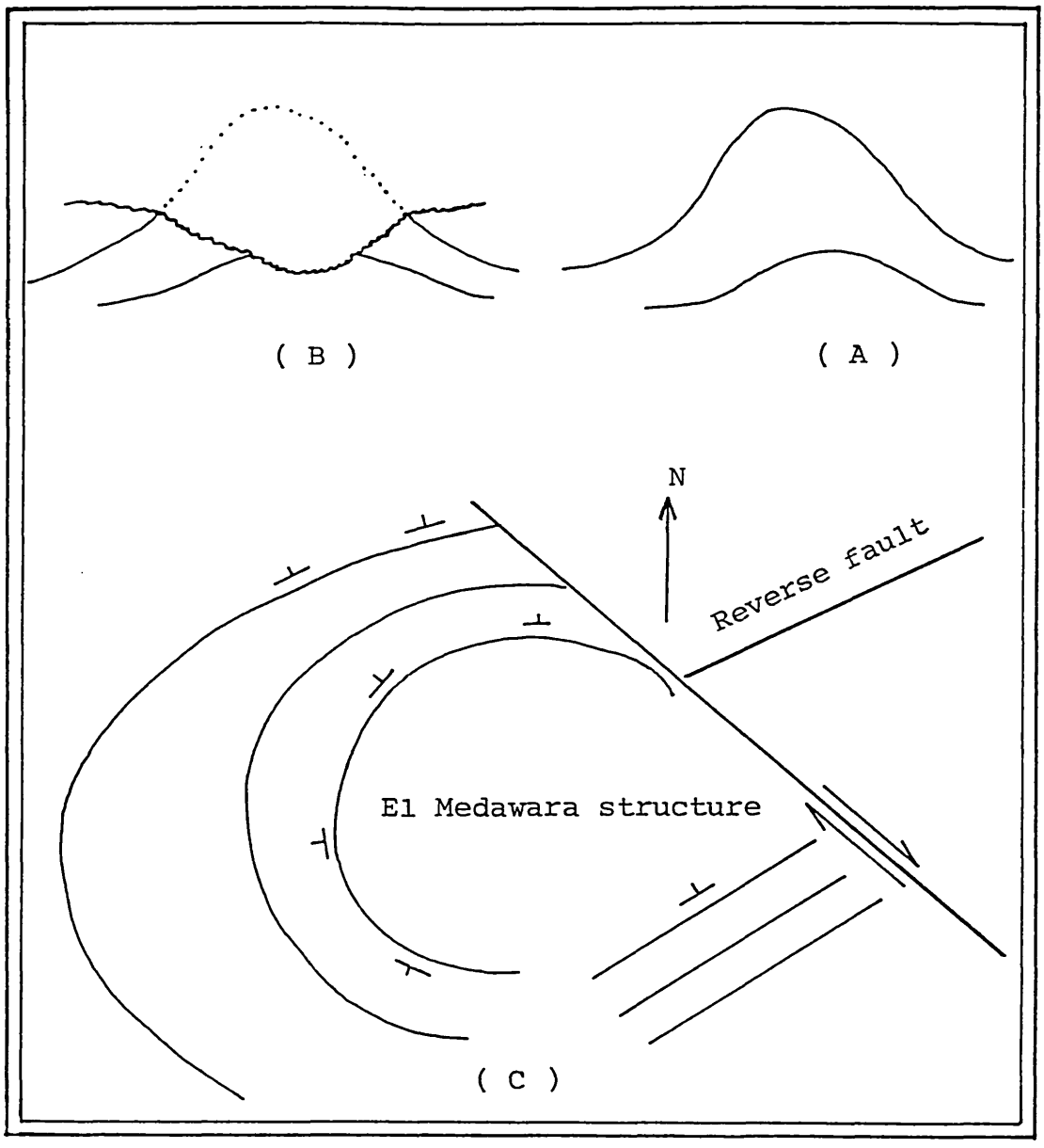


Fig. 3.13 Sketch map of El Medawara structure.

process. When these sediments became over-pressured as a result of tectonic deformation such as folding and the subsequent faulting, they pierced the overburden. After the pressure had been released, these sediments became nearly horizontal.

So, the Gaa-Abu Rawash village pericline has been disturbed by faults and diapiric structure. The other structural feature which disturbed the pericline is the cross warping (Plate 3.2). At Wadi El-Talun anticline, the cross warping is accompanied by NW minor thrusts which are normal to the fold axis. Accordingly, Omara (1953) attributed this cross warping to a compression parallel to the fold axis.

3.5.2B The Study of the Attitude of Fractures

If rock was subjected to stresses sufficient to cause failure, the type and orientation of fracture planes reflect the direction of these applied stresses.

Theoretically, the maximum shear-stress planes make an angle of 45° degrees with both the axes of the maximum and minimum principal stresses. But experimental rock deformation has shown that shear planes are often inclined about 30° degrees, relative to the direction of the greatest principal stress axis. This decrease in the shear angle, from 45 to nearly 30° degrees has been attributed, cf. Navier-Coulomb Criteria of Brittle Failure, to the angle of internal friction and expressed as follows:

$$\theta = 45^{\circ} - \phi/2$$

Plate 3.2





Represents the cross warping, Gaa - Abu Rawash village pericline.

where θ is the angle between the greatest principle stress and the shear plane and ϕ is the angle of internal friction. This angle ϕ ranges from about 30° degrees to about 40° degrees for brittle materials (especially limestone).

Plates 3.3 to 3.11 show a few examples of field structures which have been considered.

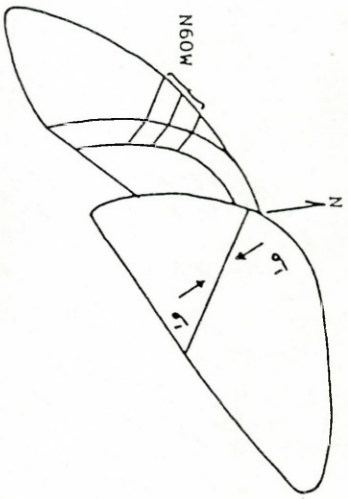
The fracture attitudes have been recorded in the field, plotted as poles on Schmidt net (Fig. 3.14a). A contour diagram was prepared from the plotted poles (Fig. 3.14b) to facilitate identification of fracture patterns. The contour intervals within the circle indicate a tendency for the fractures to form several well defined groups with different orientation, dip and contour densities.

3.5.2B.1 Structural Fracture Identification and Interpretation

Price (1966) reported that the fractures which develop in competent units in the limbs of folds remote from the crests or troughs of these folds, are usually strongly influenced by the orientation of the rock unit, so that many of fracture planes are inclined to the vertical , but are often roughly perpendicular to the surface of the rock unit in each limb. The observations in the studied areas confirm this statement, for most of the fracture planes are perpendicular to the surface of the bedding plane.

Plate 3.3

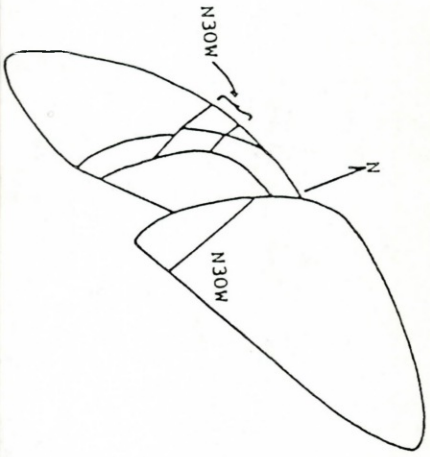




Shows one of the N60W fractures. This fracture may be a shear fracture initiated when the maximum principal stress, σ_1, was normal to the pericline axis.

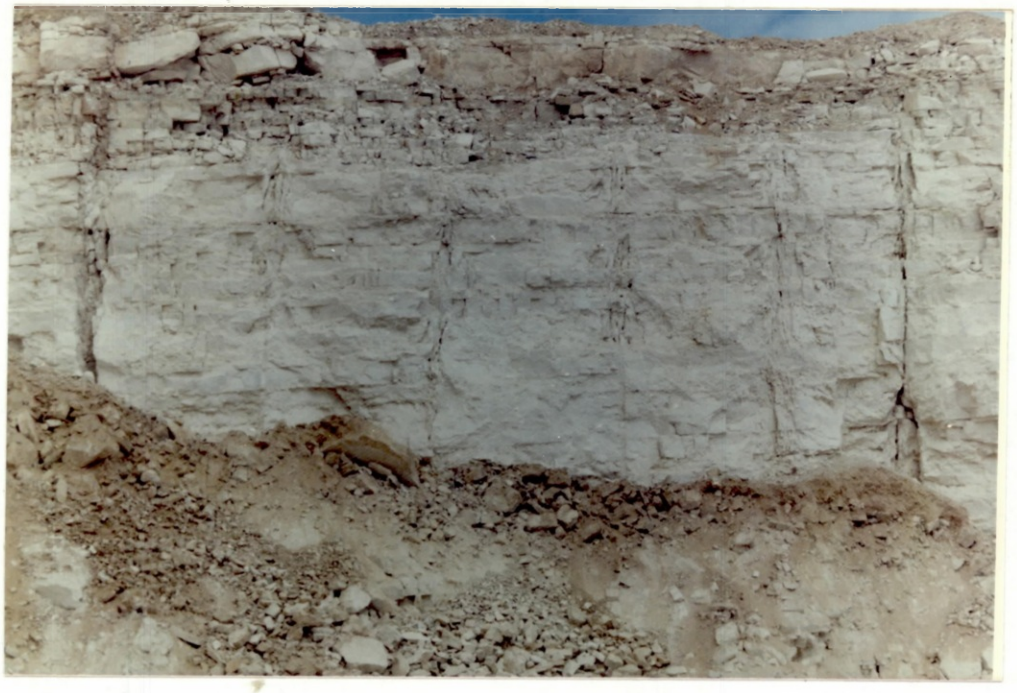


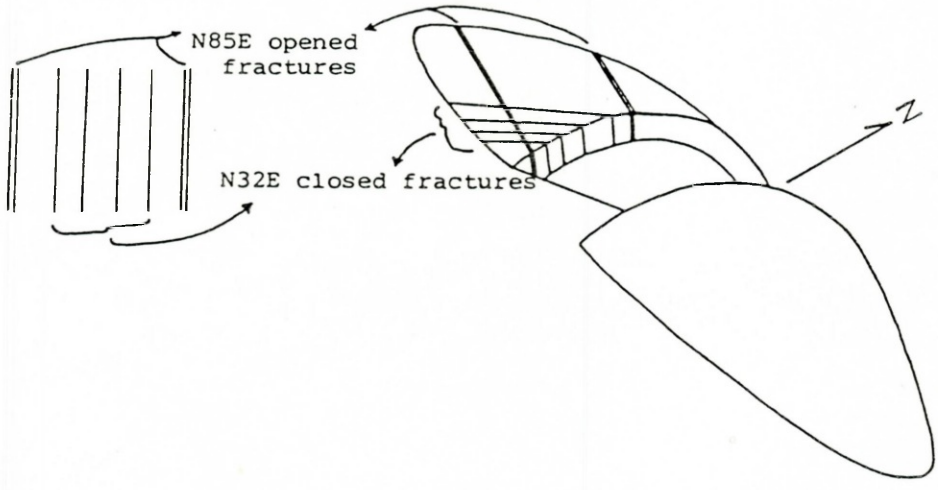
Plate 3.4



Represents one of the extension fractures which nearly normal to the axis of the Gaa-Abu Rawash village pericline. This fracture represents a normal fault.

Plate 3.5





Shows two sets of fractures. The first set represents unopened or closed fractures which have a N 32 E trend. This set could be shear fractures developed when σ_1 was parallel with the pericline axis. The other set trends N 85 E. It consists of opened fractures which could be extension fractures.

Plate 3.6



Represents a NE minor reverse fault.

Plate 3.7



Shows one of the nearly E-W (N 85 E) extension fractures. This fracture is filled with sands.



Plate 3.8

Shows an extension, N35W, fracture (minor normal fault).

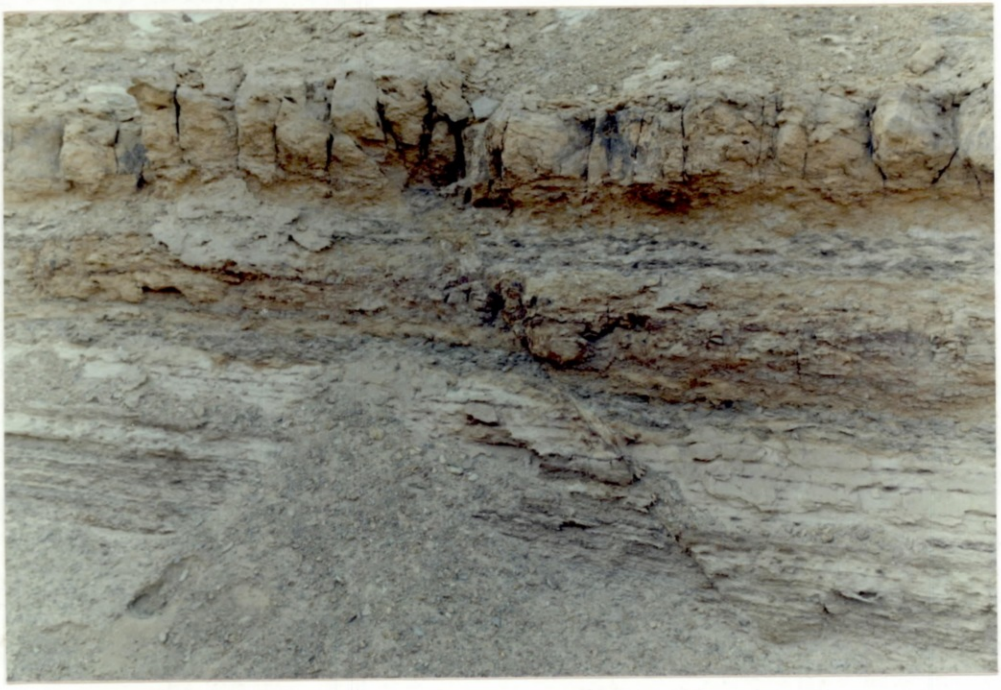
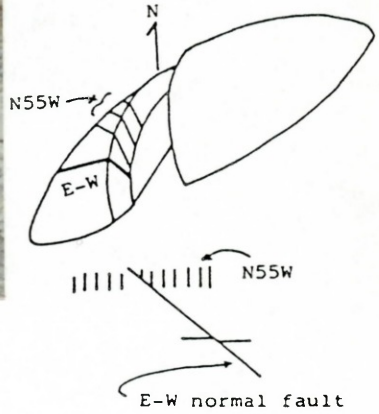


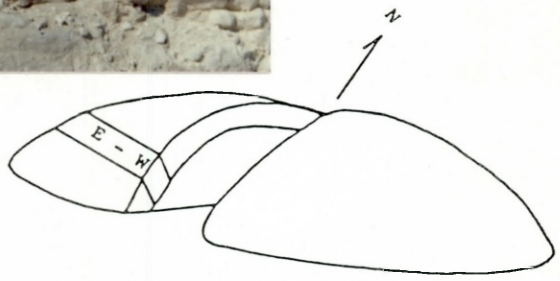
Plate 3.9



Shows one set of closed fractures which trends N55W. This fracture set, most probably, is a shear set that developed as a result of stresses normal to the axis of the pericline. these shears were disturbed by an E-W normal fault, where the shears become opened on both sides of the fault. This E-W normal fault possibly used one of the shears which developed when the maximum principal stress, σ_1, was parallel with the fold axis.



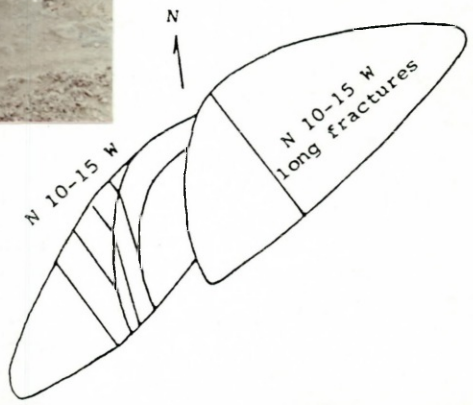
Plate 3.10



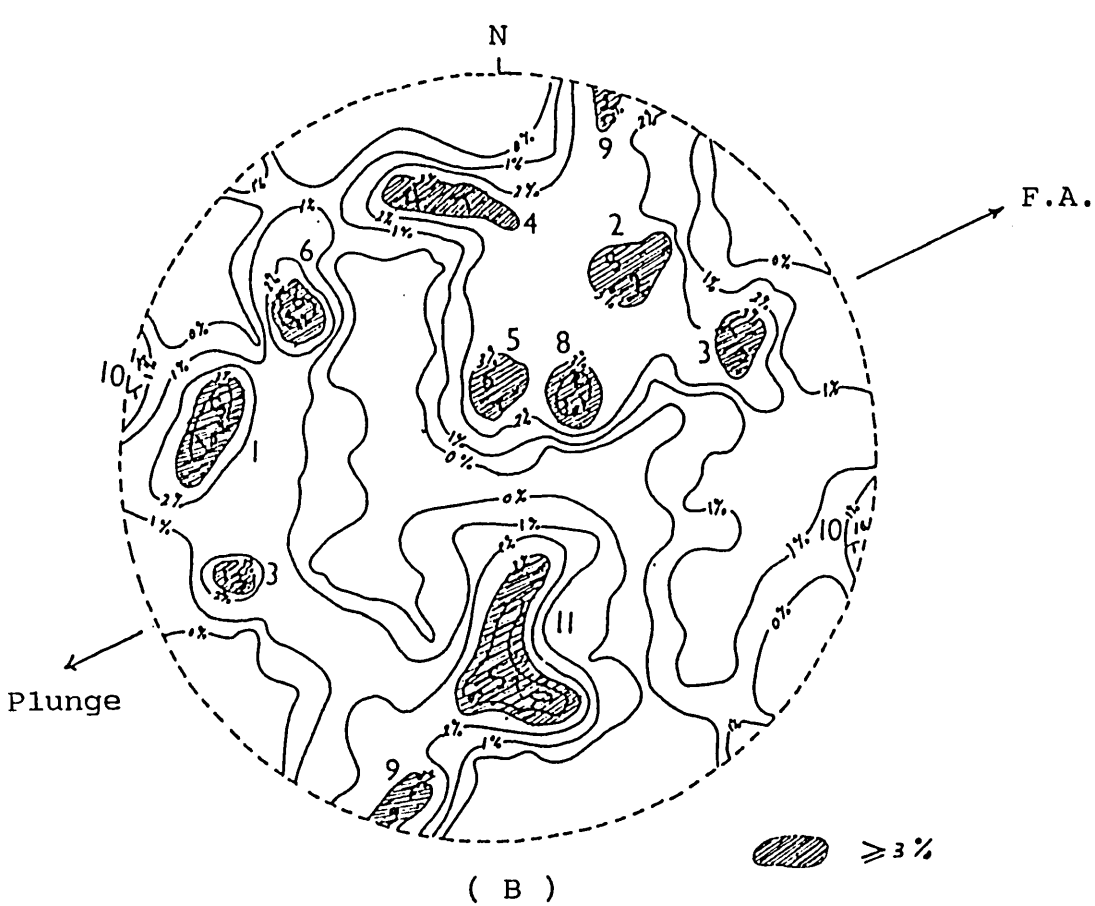
Shows one of the shears that trends E-W. This fracture may have been developed as a result of horizontal stresses, $\overline{\sigma_1}$, parallel to the pericline axis. This fracture represents a minor reverse fault.



Plate 3.11

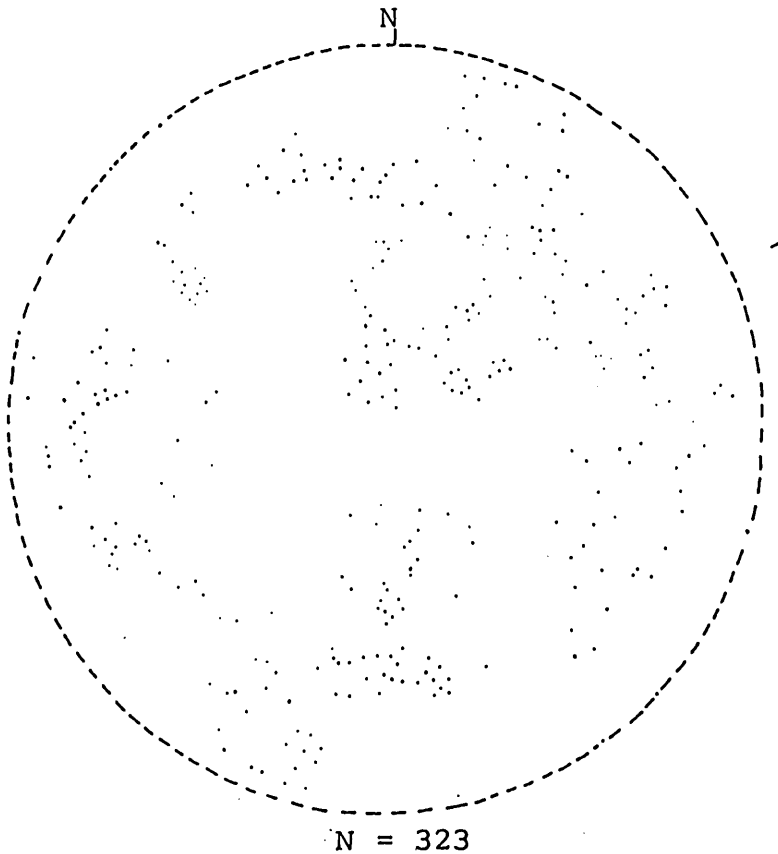


Shows some long tension fractures which trend N10 - 15W.



(B)

Contoured diagram of the fracture poles.



(A)

S-pole diagram of the measured fracture plane poles.

Fig. 3.14 S-pole and contoured diagrams of the measured fracture plane poles.
(Gaa-Abu Rawash village pericline)

Also, if one considers that the regional compressive stress axes which give rise to the fold acted normally and parallel with the fold axis, the orientation of the fractures will be influenced by the plunge of the fold axis.

In order to consider these several parameters and interpret the fracture patterns of the Gaa-Abu Rawash village area (Fig. 3.14b), a theoretical model has been made.

The model was constructed to clarify observations which relate to large areas, or whole folds, in order that the model may subsequently be applied to photo - geological and satellite imagery studies.

Before dealing with the theoretical model, one would like to make clear the following:

1) The theoretical model was carried out only on the northwest limb, as the other limb is poorly expressed and eroded.

2) The model has used a wide range of bedding plane dip.

3) The model relates to the simple concept that the fold axis is essentially cylindrical. This is almost certainly an incorrect assumption. Unfortunately, although one knows that fracture orientation is probably arranged around a domal feature, there is not sufficient information available to permit a detailed analysis of the fracture orientations such domes exhibit.

If, as is possible, the Gaa-Abu Rawash village structure represents the central part of such a dome,

then as a first approximation at least, the central part can be treated as cylindrical.

3.5.2B.2 Theoretical Model

It has been noted (Price, 1966) that the fractures which develop in the leading and trailing limbs are related to the limbs of the fold rather than to the fold as a whole. Here it is often of interest to determine the orientation of these fractures as they existed after assumed rotation and tilting of the fold axis.

In order to identify and interpret the contoured diagram of the fracture orientations observed in the field (Fig. 3.14), the following procedure was adopted:

1) Bedding planes were plotted on Schmidt area net at dip angles of 10°, 15°, 20°, 25°, 30°, 50° and 55° degrees rotation of the bedding plane about a horizontal fold axis.

2) The different ideal theoretical fractures these beds contain are shown on stereograms as poles (Figs. 3.15 and 3.16).

3) The bedding planes as well as the idealised fractures they contain were rotated about a horizontal axis perpendicular to the fold axis with an increment of 5° degrees from 0 to 25° degrees in both the clockwise and anticlockwise directions, in order to take the plunge of the pericline into account.

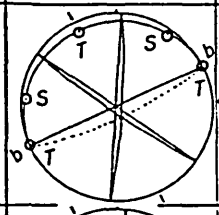
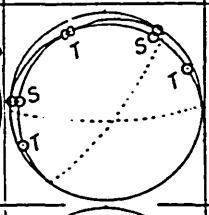
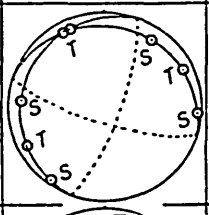
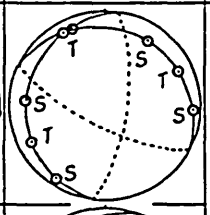
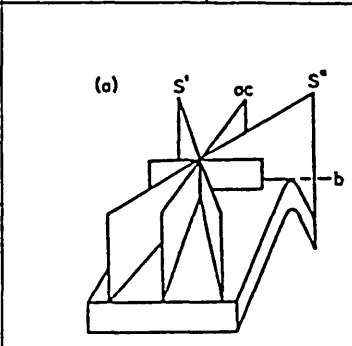
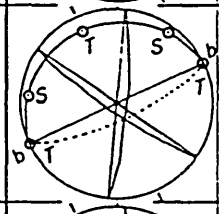
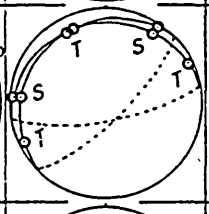
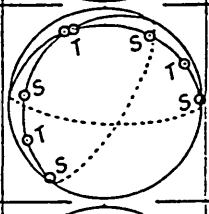
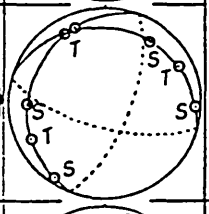
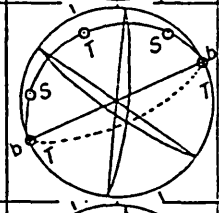
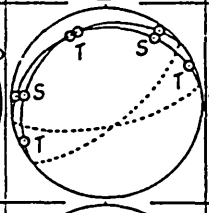
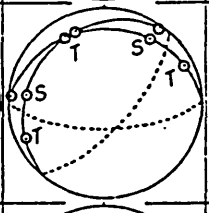
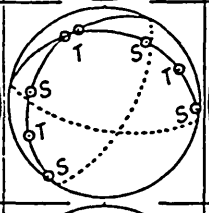
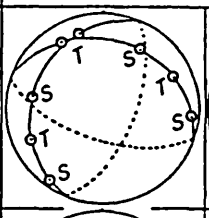
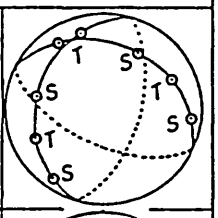
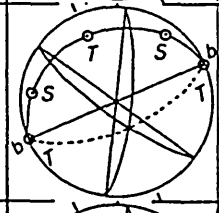
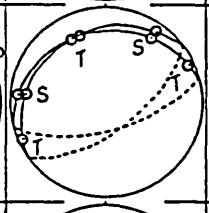
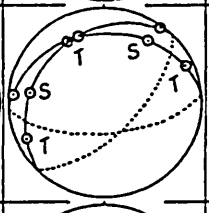
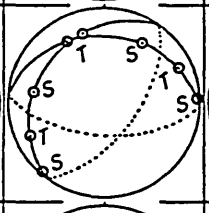
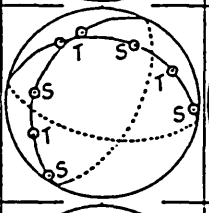
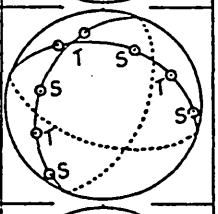
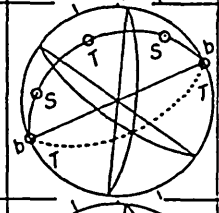
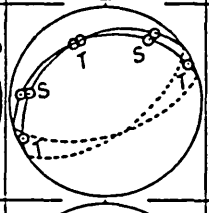
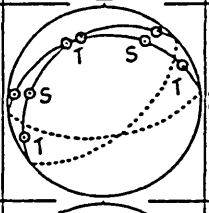
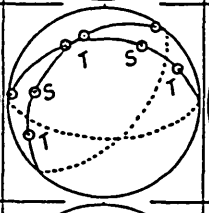
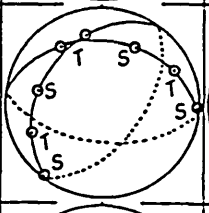
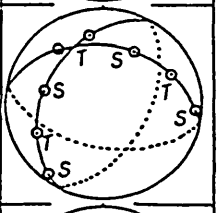
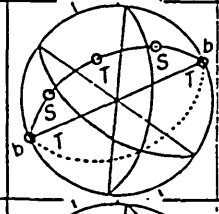
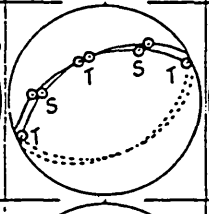
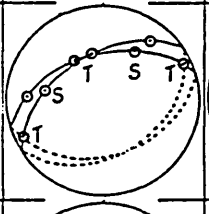
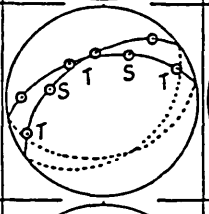
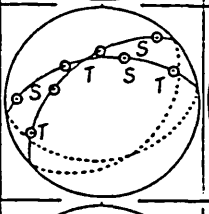
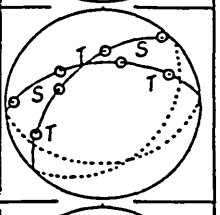
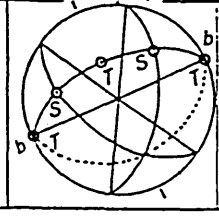
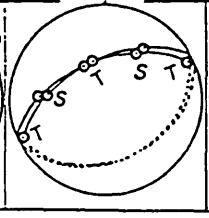
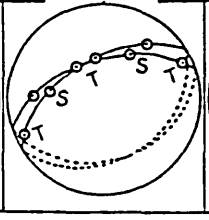
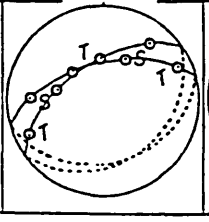
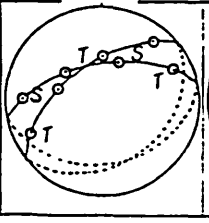
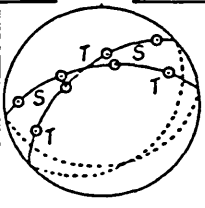
Dip of beds	Rotation in degrees (Clockwise and anticlockwise, see Fig. 3.16 b)					
	0	5	10	15	20	25
10						
15						
20						
25						
30						
50						
55						

Fig. 3.15 Stereograms of theoretical fracture poles (A) . .
(Where the shear plane makes an angle of 25 degrees with the axis of the maximum principal stress)

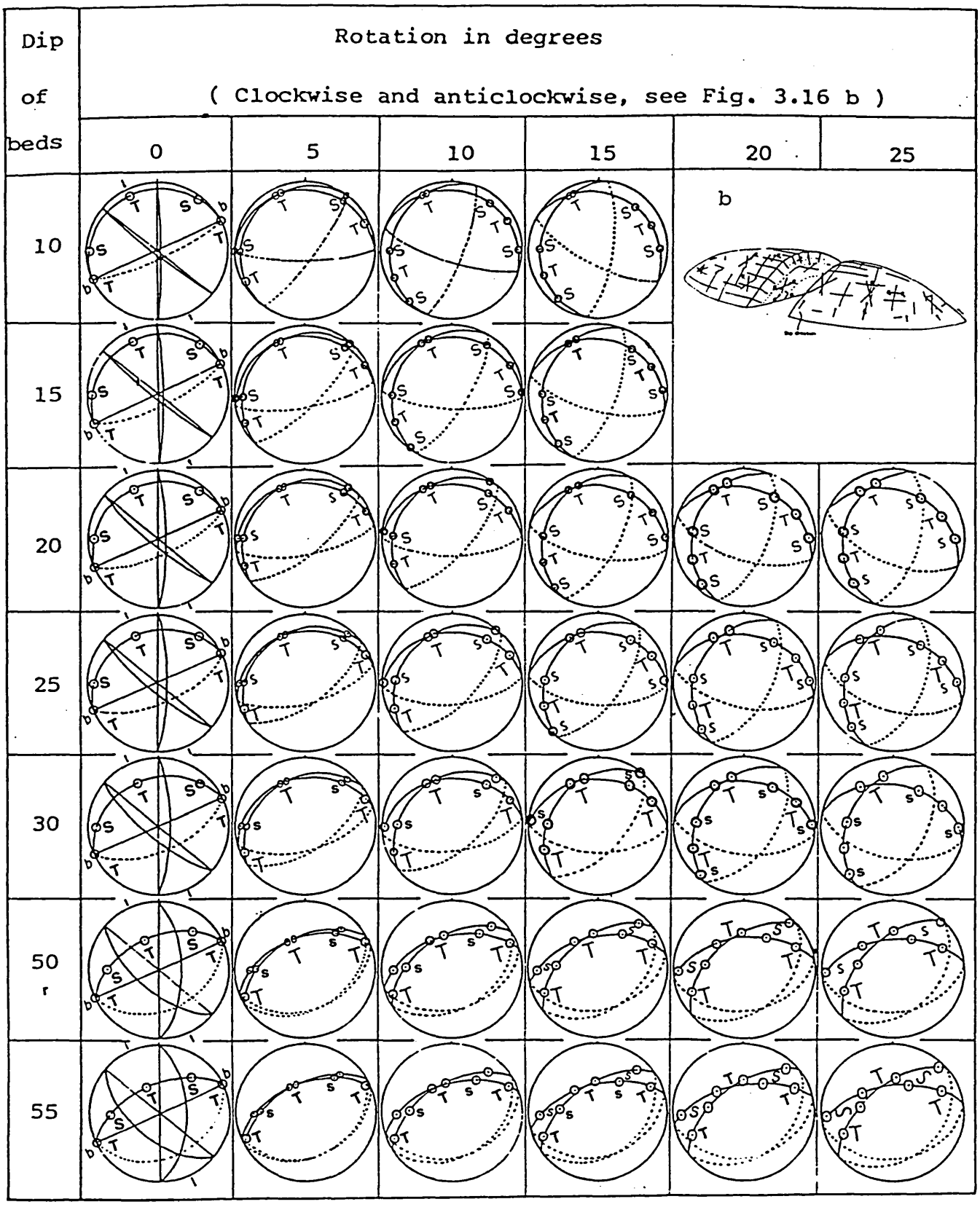


Fig. 3.16 Stereograms of theoretical fracture poles (B) .
(Where the shear plane makes an angle of 30 degrees with the axis of the maximum principal stress)

3.5.2B.3 Interpretation of the Contoured Diagram

The contoured diagram derived from field data (Fig. 3.14) is not a simple one. However, by comparing this diagram with the compiled orientations of the contoured diagram derived by the theoretical models (Fig. 3.17), it is relatively easy to classify most of the fracture maxima of this diagram (Fig. 3.14) and to infer the causes of the lack of simplicity of the contour diagram (Fig. 3.14).

In conjunction with the field studies and the theoretical model, the observed field fractures (Fig. 3.18a) were classified into the following:

3.5.2B.3A Fractures Related to the Main Pericline

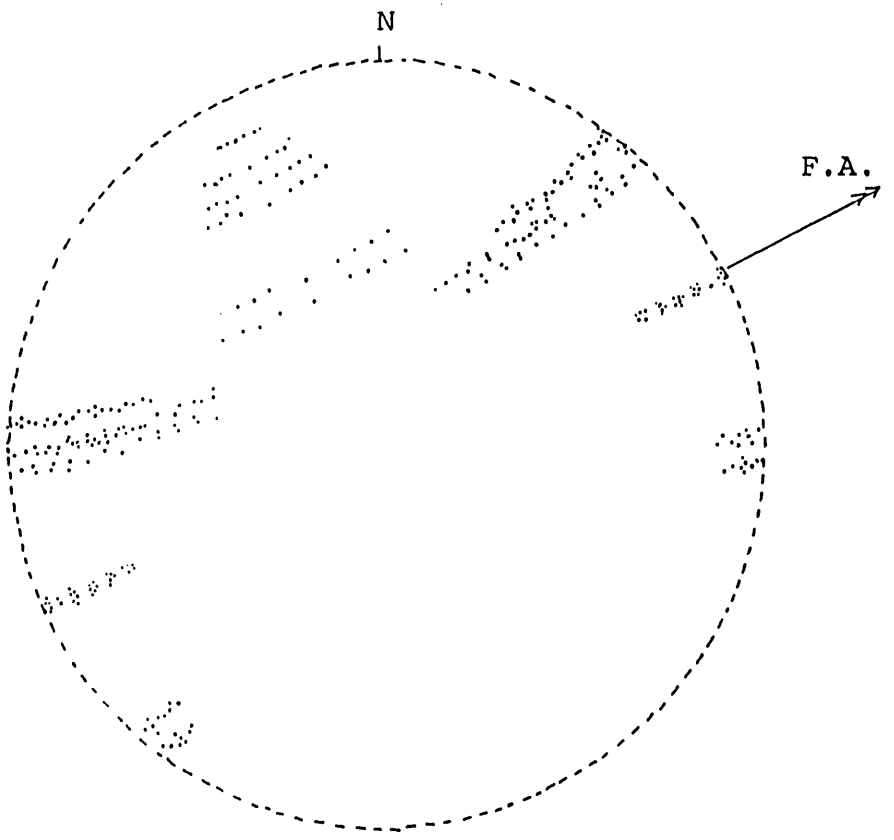
The sets of fractures shown on the contoured diagram of the field fractures (Fig. 3.18a) can be classified with respect to the contoured diagram of the theoretical model into:

a) Sets developed when the effective maximum stress ($\bar{\sigma}1$) was perpendicular to the fold axis such as:

i) Set 1: these fractures are shear fractures that strike approximately N5^{o}E, with an average dip of 65°E;

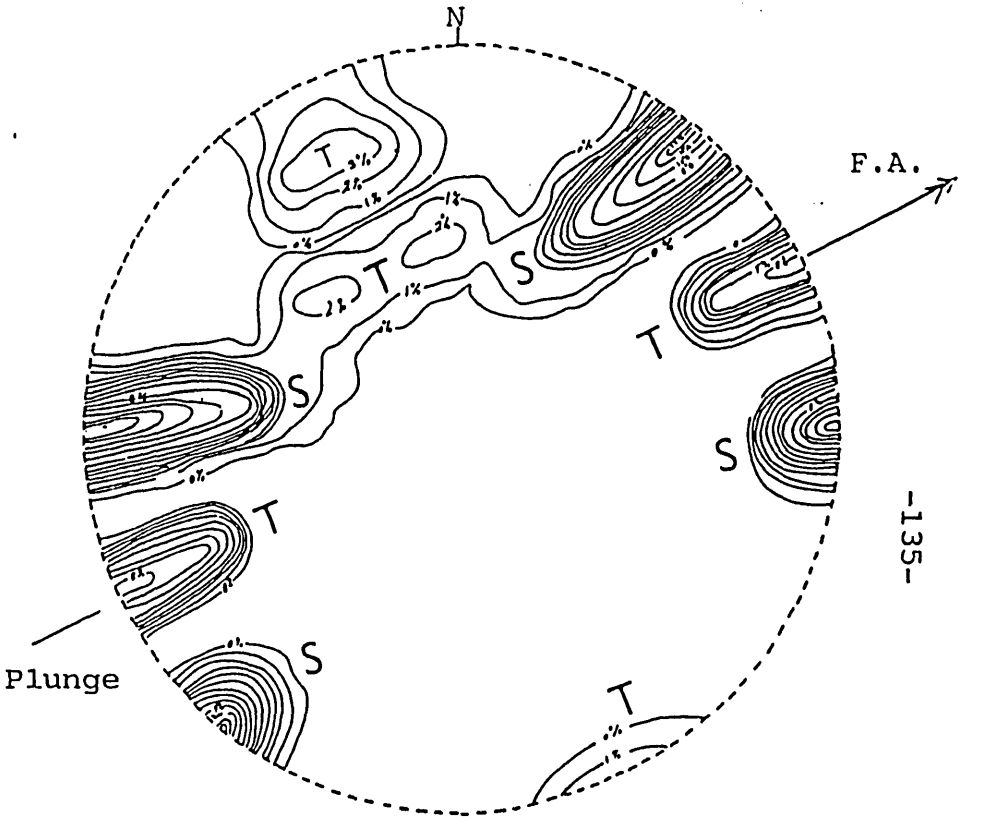
ii) Set 2: these fractures could be classified as shear fractures which strike N55^{o}W with an average dip of 50° degrees towards the SW.

Set 1 and Set 2 most probably form a conjugate set of shear fractures;



(A)

S-pole diagram of theoretical fracture poles drived from the theoretical models.

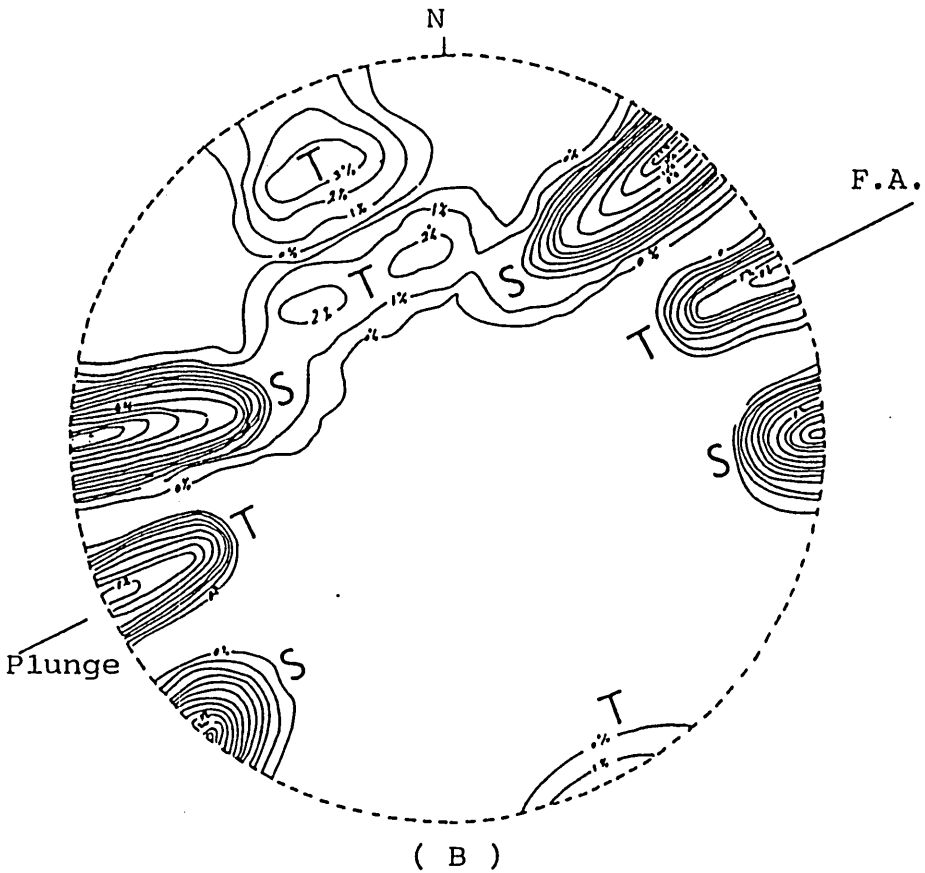


(B)

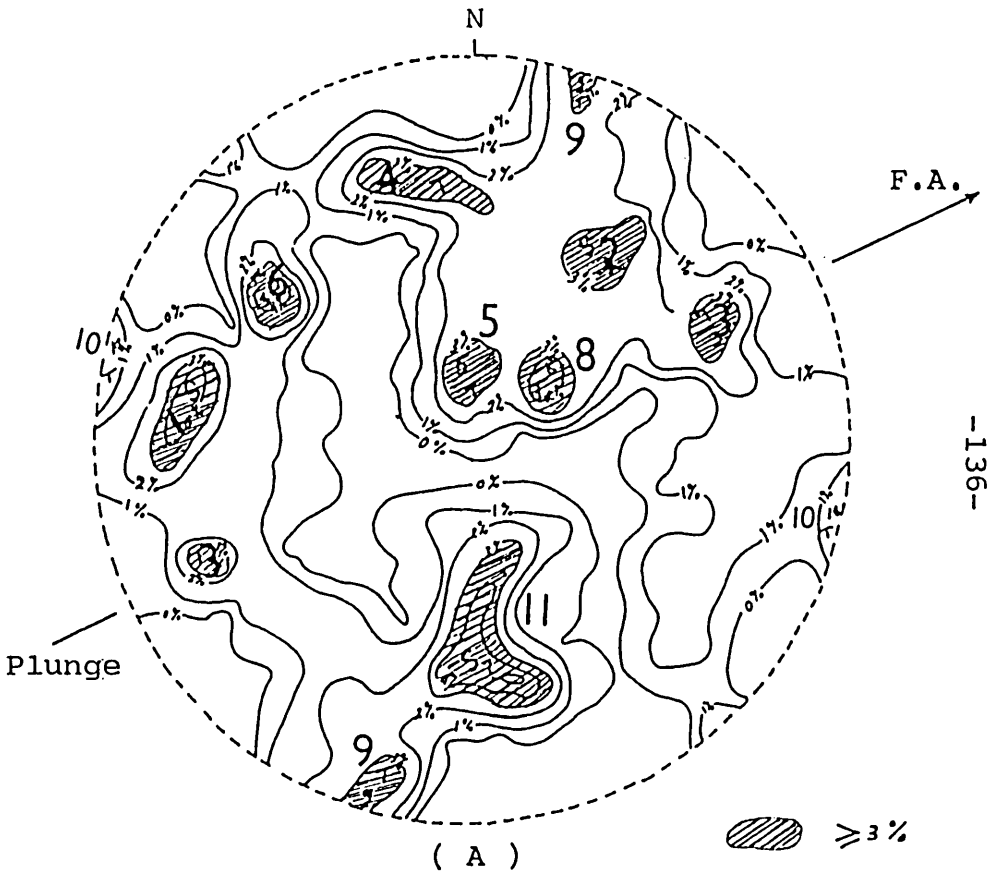
Contoured diagram of the theoretical fracture poles derived from the theoretical models.

T : Extension fracture poles S : Shear fracture poles

Fig. 3.17 Theoretical S-pole and contoured diagrams of the fracture plane poles.



Contoured diagram of the theoretical fracture poles.



Contoured diagram of the observed or measured fracture poles.

Fig. 3.18 Observed and theoretical contoured diagrams of the fracture plane poles.

iii) Set 3: these are extension fractures that developed perpendicular to the fold axis, and most probably parallel to the maximum principal stress. Their trend is nearly N25°W with an average dip of 65° degrees to the SE and 30° to the SW; these fractures are present in the shale beds, especially at El-Medawara;

iv) Set 4: these are classified as being extension fractures that trend nearly N70 - 90E with an average dip of 60° degrees to the south;

v) Sets 5 and 8: these are low angle fractures that developed nearly either parallel or normal to the pericline axis. These fractures are most probably extension fractures. They are not likely to be seen clearly in aerial photographs. So they will not be considered further.

b) It is sometimes inferred that sets of fractures developed when the effective maximum principal stress, $\bar{\sigma}_1$, acted parallel to the fold axis. Fracture sets which could be interpreted accordingly are:

i) Set 6: these fractures may be shear fractures with strike N36°E with an average dip of 55° degrees SE;

ii) Set 7: these fractures probably are shear fractures that strike N85W with an average dip of about 50° degrees nearly north.

Sets 6 and 7 could represent a conjugate set of shear fractures.

iii) Set 11: these fractures strike N75° to 95°E with an average dip of 45° degrees, roughly to the north.

Although this set is not represented in the contoured diagram derived from the theoretical model (Fig. 3.18b), it may be related to the process of folding where the maximum principal stress acted perpendicular or parallel to the fold axis.

3.5.2B.3B Fractures Unrelated to the Pericline

These fractures are represented on the contoured diagram (3.18a) and are probably not related to the main folding of the Gaa-Abu Rawash village pericline. These fractures are:

i) Set 9: these fractures are trending N73W with an average dip of 85° due to roughly, both north and south. These fractures may be related to the strike-slip fault of the same trend which has been detected from the aerial photographs.

ii) Set 10: these fractures are not well represented on the diagram and are nearly perpendicular to the previously mentioned Set 9.

The lack of simplicity of the diagrams can be attributed to a number of parameters which include:

a) The difference in the dips of bedding planes which strongly affected the fracture pattern;

b) The plunge of the pericline which is mainly to the SW and NE;

c) The different stress orientations which probably acted on the pericline throughout its development, so that stress was both normal and parallel to its axis at different periods;

d) The faulting which changed the dip of the hanging wall such as the reverse fault which has been discussed earlier. Also, the strike-slip faults may be shared in the complexity of the fracture contoured diagram.

From these analyses, one may infer that most of the fractures in the studied area could be referred to the folding process, where the stresses acted normal and parallel to the folding axis, while some other fractures might be related to a later faulting which disturbed the structure of the studied area such as the dextral N73W strike-slip fault.

With respect to the field studies, there are some major or long fractures such as those sets which are nearly E - W and N25 - 30W, which might be related to later regional stresses which happened after folding processes were complete.

3.5.2B.4 Directional Rose Diagram

The rose diagram of the Gaa-Abu Rawash village area was constructed from the field data (Fig. 3.19), with a directional class grouping of 5° degrees, in order to bring out geologically significant trends and relationships, so that these trends could be correlated with photogeologic and satellite imagery data. By comparing this rose diagram (Fig. 3.19) with compiled theoretical rose diagrams derived from the theoretical models with the same class interval (5° degrees), as

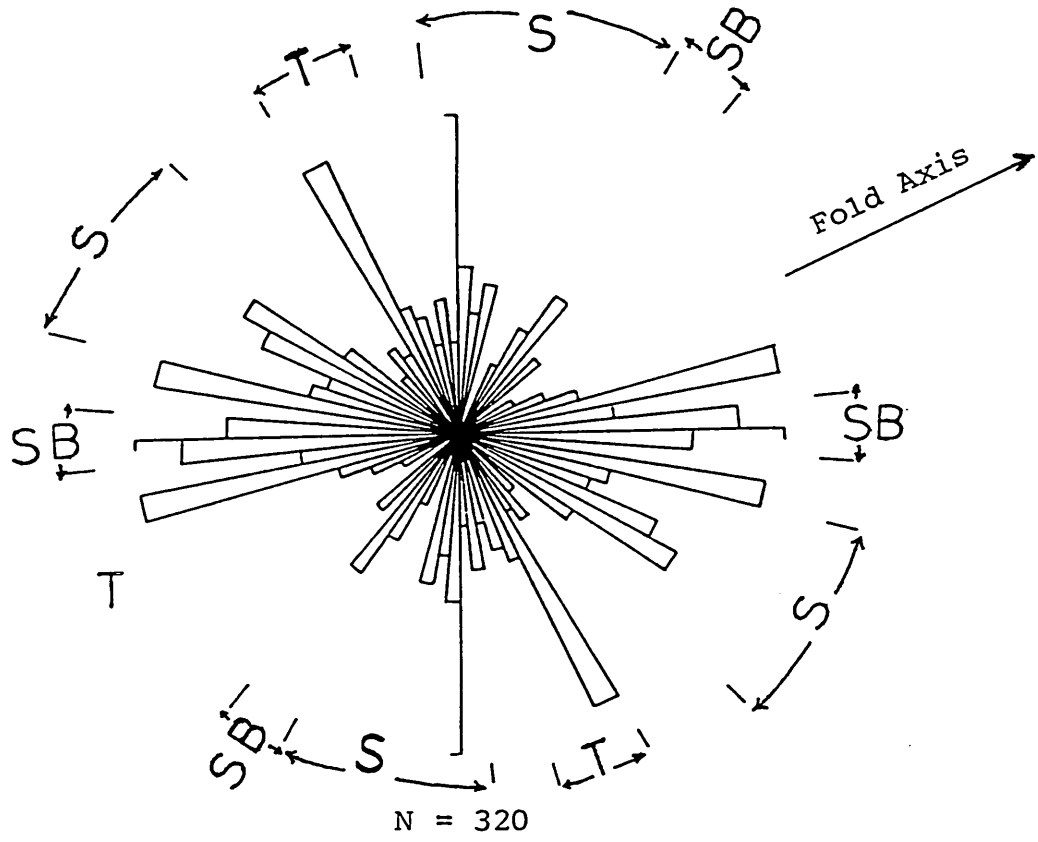


Fig. 3.19 Gaa-Abu Rawash village pericline (field data) rose diagram.

indicated in Fig. 3.20, one could classify these different class intervals into both shear, S, and extension, T, fractures, which could be developed when the effective maximum principal stress was normal to the axis of the pericline, as shown in Figs. 3.19 and 3.20.

On the other hand, if one takes into consideration that this structure has been subjected to stresses parallel to the fold axis, then one may expect shear fractures with trends of about N35 - 40E and E - W to N85W or generally nearly E - W, which is given a symbol as SB in Figs 3.19 and 3.20. So, these trends are present within the same range of the extension fractures of the Gaa-Abu Rawash village pericline.

In Conclusion

1. The Gaa-Abu Rawash village structure is a pericline with an axis trend N64E.

2. The Gaa-Abu Rawash village structure owes its origin to a folding episode that took place at the end of Upper Cretaceous, when the greatest principal stress acted normal to the fold axis.

3. When the maximum principal stress acted parallel with the fold axis, it caused the warping of the structure. The axes of the warping are nearly perpendicular to the fold axis.

4. The folding movements continued during middle Eocene.

5. The pericline is cut by some faults which either utilised existing fractures which resulted from folding,

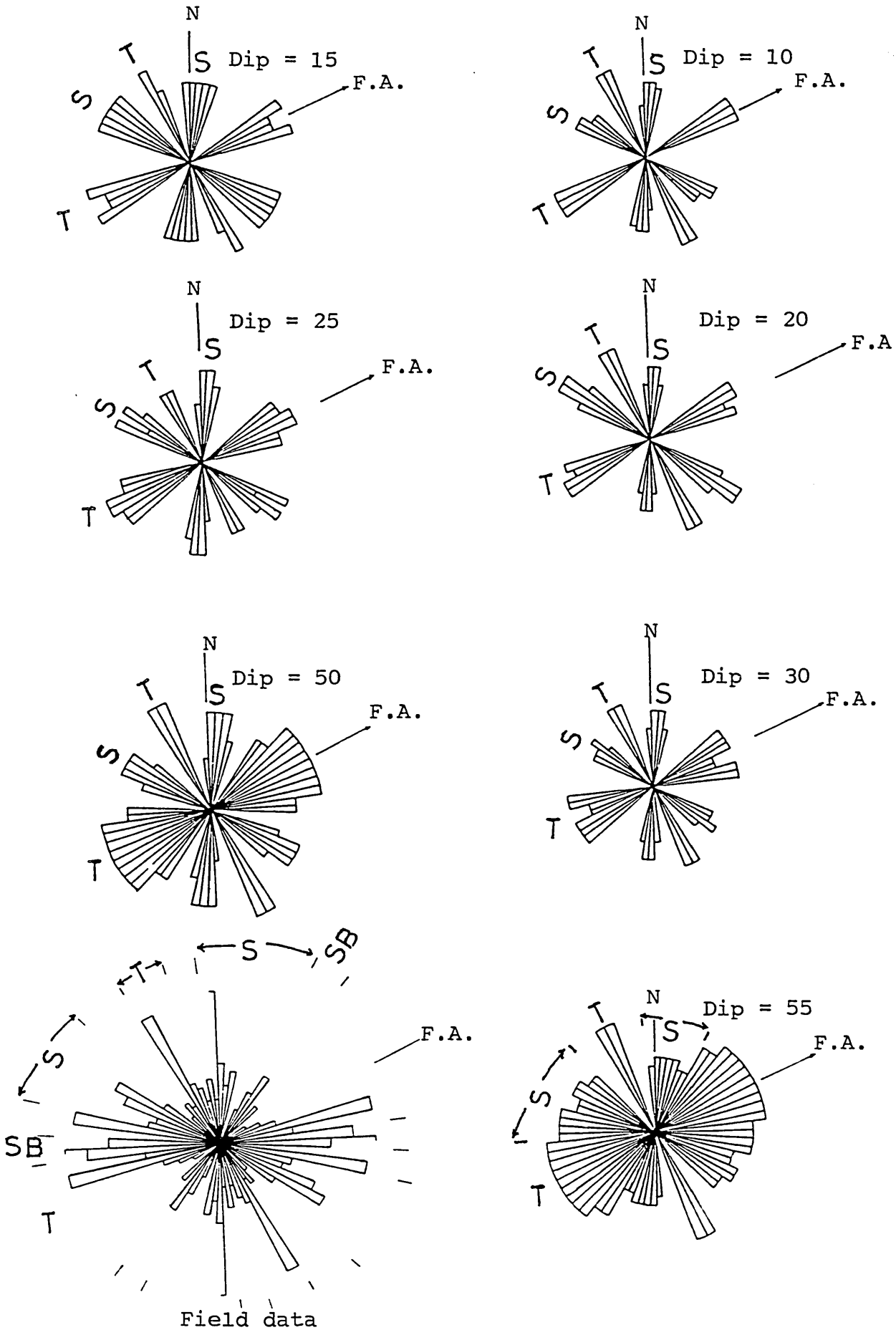


Fig. 3.20 Compiled theoretical rose diagrams.

such as NE reverse faults that are nearlv parallel to the axis of the pericline and NW faults (some of which are nearly normal to the axis of the pericline), or others resulted from later stresses such as E - W and N73W dextral strike-slip faults.

6. Most of the NW faults exhibit a down-throw towards the NE, especially the strike-slip faults. These later movements along the fault planes, which may be attributed to a deep NW basement fault, will be discussed in the next chapter.

7. Tectonic stresses led to overpressured shales and sands which flow towards the area of maximum curvature and then pierced the overburden as a diapir at El-Medawara.

8. In the Eocene, the area was most probably affected by regional stresses that caused long E - W or nearly E - W fractures.

9. The main faulting and fracturing on a regional scale, which probably began at the end of Oligocene, may have caused these NW long fractures.

10. Hydrothermal solutions flowed up the NW tensional fractures.

11. The theoretical model helps in understanding and interpreting the different sets of the fractures recorded in the field.

12. The present work has modified and contributed to the previously known information regarding this particular area.

CHAPTER FOUR

AERIAL PHOTOGRAPHIC STUDY
OF
ABU RAWASH AREA

CHAPTER FOUR

Aerial Photographic Study of Abu Rawash Area

4.1 Introduction

The aims of this study are to map photogeologically the different structures, such as folds and fractures, of the Abu Rawash area (Fig. 1.2), and to establish whether or not there is any relationship between these structures and the mapped fractures. Such structures, with lengths ranging between 150 meters to about 5 kilometers or with a diameter ranging from 300 meters to 3 kilometers, are too small to be seen or easily studied on the scales of the Landsat images: 1:1,000,000 and 1:500,000. Also during the field study one cannot have a complete view over the whole area of Abu Rawash. This comprehensive view would help in the interpretation of structural problems in this particular area. Thus, this study would, it was hoped, form an important link between field studies and Landsat analysis.

To achieve these goals, a detailed study based on stereoscope interpretation of the Abu Rawash aerial photographs and fracture trace analysis have been carried out. The stereoscopic model is of great importance for the recognition of fracture traces and the vertical magnification afforded by the stereoscope can help considerably in the discrimination of naturally occurring traces from artificial or non-geological ones. These data would be used for correlation with the field data and Landsat images.

Here, the photogeological interpretation will be correlated with the field mapping and later, fracture trace analysis map from Landsat images.

During the course of this study, new techniques have been developed and effectively applied to overcome the problems of fracture traces or lineaments interpretation, and to get a more realistic representation of the patterns of fracture traces or lineaments based on their quantitative aspects which are amended for any structural study. The advantages of these techniques will be discussed in this chapter, with a review of the other known fracture traces techniques.

The methods of presentation used in this study are histograms and rose diagrams. The relationships between some rose diagrams, including the field data, are expressed as correlation coefficients.

The fracture traces are analysed in light of the field data rose diagram and a theoretical rose diagram derived from a theoretical model based on field data.

Aerial photographs (1:60,000), produced by the Military Survey of Egypt, have been used for structural study.

4.2 Photogeological Interpretation

The aerial photograph is defined by Ray (1960) as instantaneous record of the ground details as determined chiefly by the focal length of the camera lens, the flying height of the aeroplane at the time of exposure and film and filter used. These aerial photographs may

be vertical, such as those used in this study, where the axis of the camera was pointing essentially vertically down or oblique, where the axis of the camera was tilted from vertical.

In order to obtain good results from the aerial photographs during the course of interpretation, the factors which impose considerable limits in the perception of these photographs must be given attention. These factors are: a) objective factors outside human control, and b) subjective factors, human (Ray, 1960 and Zwain, 1976).

4.2.A Objective Factors

1. The scale of the aerial photographs;
2. The quality of the aerial photographs;
3. The technique of viewing aerial photographs.

4.2.B Subjective Factors

1. Physical factors such as visual acuity;
2. Psychological factors, such as stressful situations which make perception rather difficult and the interpretation rely excessively on imagination.

Geological interpretation of aerial photographs can generally be considered as a two-step process. The first step includes the detection and identification of "objects", while the second step involves the deduction or inductive mental processing of these data in terms of geological significance.

During the field study, a preliminary photogeologic study had been carried out to reduce extensive field study. In this study, the interpretation of the aerial photographs has been carried out in two steps, which are:

a. Bedding and other structural features were recognised and interpreted.

b. The aerial photographs were examined for fracture traces.

4.3 Techniques and Fracture Aspects

Stereoscopic examination of aerial photographs is a fundamental aspect of photogeology. The unique feature of the stereoscope view is the three dimensional model of the scene which is being interpreted. This model gives the viewer a sense of reality, but with a vertical exaggeration of the relief.

In this study, the aerial photographs of Abu Rawash were examined under the stereoscope so that tonal characteristics of rocks and soil were enhanced. Also, the use of high power stereoscopy enables microfractures to be identified and plotted. This stereoscopic interpretation was recorded on transparent overlays.

4.3.1 Aspects of Fracture Traces

Fracture traces can be analysed according to their quantitative and qualitative characteristics.

4.3.1.1 Quantitative Aspects

The quantitative characteristics of fracture traces are essential for any statistical treatment from which it is hoped one may extract significant geological information. The quantitative analysis involves the azimuth, length and frequency of fracture traces.

With respect to the length and nomenclature of the fracture traces, there is a wide variety of classifications.

Permyakov (1949), quoted by Huntington (1969), and Gol'braykh et al (1966) introduced the term "Megajoint" to embrace all photogeological linears regardless of their forms, shapes and sizes, which may be related to bedrock tectonics. Other workers used the term "Megalineament" to include all fracture traces which are more than 20 miles in length.

Blanchet (1957) grouped fractures into two principal classes according to their length. The first of these had the ridiculous appallation of "Microfractures". For this, the term was used to describe fractures with lengths which range from 0.8 to 4 km. He termed fractures with length greater than 4 km., as Macrofractures. He claimed that microfractures originate within the sedimentary cover while macrofractures originated in the basement. Haman (1964) very reasonably replaced Blanchet's term "microfracture" with the term "mesofracture".

Mollard (1957) proposed the term "lineament" to cover continuous and discontinuous features with a range of length from 0.3 to 8 km.

Lattman (1958) introduced the term "fracture trace" and made two classes based on type of exposure and length of fractures. Fracture traces are features less than 1.6 km., in length, expressed continuously in the landscape as alignments of vegetation, soil tone, topographic sags, stream alignments or combinations, and are observed on individual aerial photographs. The relationship between the scale of the aerial photograph and the mean length of linear features detected is shown in Fig. 4.1 (after Norman, 1968).

A photogeological lineament is a natural linear feature consisting of topographic, vegetation or soil tonal alignments visible on aerial photograph or mosaics and which may be traced continuously for many miles. Lattman (1958) related fracture traces to joint patterns and small faults, and the lineaments be associated with deep seated basement features.

In light of what has been mentioned, one may infer that there may be a relationship between the length of the fracture traces and the structural feature, where small or medium fracture traces are controlled by local structures (relatively shallow structures) and lineaments or crustal fractures are basement controlled (relatively deep).

Generally, variability in the length of the fracture traces could also be attributed to:

1. The superficial deposits which may cover part or some parts of fracture traces;

2. Irregularities of the terrain (relief);

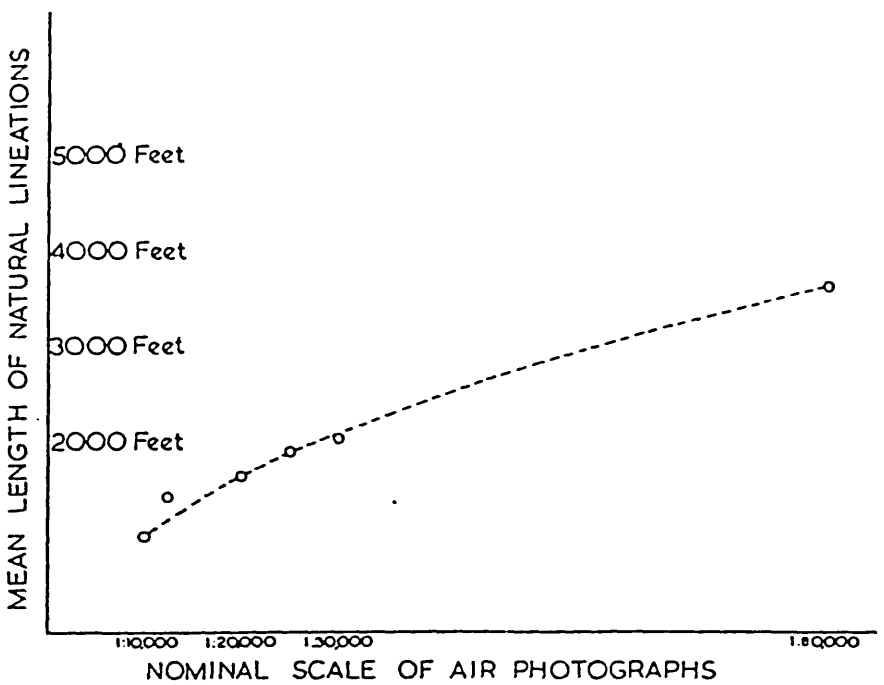


Fig. 4.1 Graph showing the relationship between the air photograph scale and the mean length of linear geological features detected.

(After Norman, 1968)

3. The geometry of the geologic structures.

A fracture trace may appear on the aerial photograph as a single trace or as many disconnected segments.

Disconnected segments enhance the frequency as well as the total length within a class interval in which they lie.

With respect to the frequency of the fractures, one can conclude the following:

a. The fracture frequency is controlled by the lithology (Price, 1966) as well as the thickness of beds, where the fractures in thin beds are much more than those in thick beds (Fig. 4.2, Ladeira and Price, 1981).

b. Deformed localities exhibit more fractures than those which are less deformed or undeformed.

c. In asymmetrical folds, the steeper limb shows more fracture traces than the other gentle (or less steep) limb. This fact has been reported by Harris et al (1960) and demonstrated during the course of this study where the fracture traces on Gebel El Higaf, the northwestern limb of Wadi Talun anticline, which dip about 32° degrees to the NW, are much longer and more frequent than those present on the other limb, Giran El Ful, with dip of about 25° to the SW, or the other limb of Sudr El Khamis syncline, with dip of about 8 - 10° degrees SE (see Fig. 4.6).

d. In anticlinal structures, the areas of maximum curvature usually contain more fractures than any other areas.

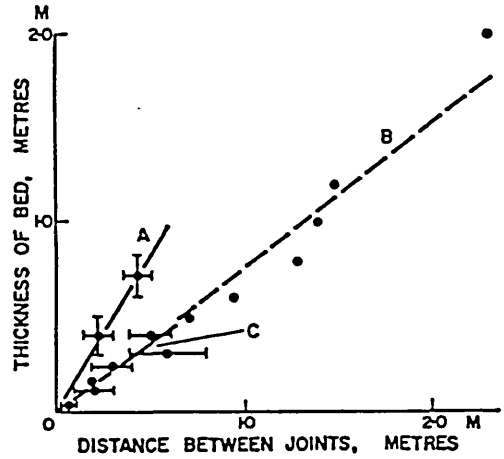
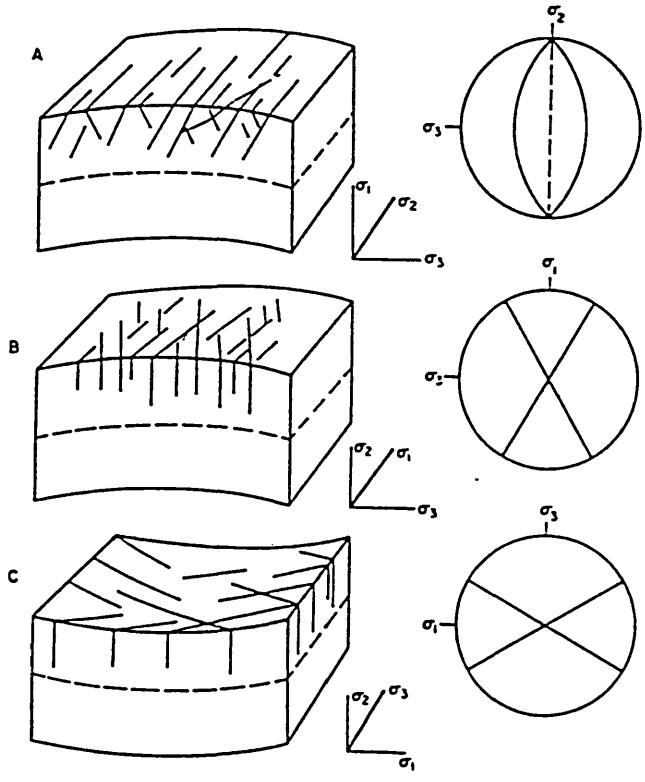


Fig. 4.2 Relationship between bed thickness and distance between joints (from data by Bogdanov, Kirollova and Novikova).

(After Price, 1966)



(a) Joints at the crest of a major anticline with the orientation of normal faults. (b) Shear joints at the crest of a major anticline with acute angle made by the joints intersected by the axial line. (c) Shear joints in the trough of a major syncline (above the neutral surface) with obtuse angle made by the joints intersected by the axial line. The orientation of the principal stresses when these structures developed and stereograms indicating their orientation are also shown.

Fig. 4.3 The orientation of the principal stresses and structures developed, after Price,1966.

e. The flat topped areas of buried draped features or salt domes have lower fracture trace density than the surrounding areas (Blanchet, 1957 and Schepis 1965).

Regarding the azimuth of the fracture traces on aerial photographs, it was found during the study that the azimuth is greatly influenced by the dip of beds which contain these fractures, especially those fractures which are inclined to the axial plane of the fold. This change in azimuth leads to a marked discrepancy when relating the fracture traces to the measured fractures in the field, in deformed localities.

In general, the orientation of the fractures is controlled by many factors, such as the relative competence of the rock units, their thickness and the size of the fold structure, as well as the degree of deformation and the orientation of the principle stress axes (see Price, 1966 and Fig. 4.3).

4.3.1.2 Qualitative Aspects

The qualitative analysis of the fracture traces is based on the shape and pattern of these fractures. The common shape of the fracture traces on the aerial photographs is rectilinear. Curvilinear, sinous and ring-like fractures were also encountered during the interpretation of the aerial photographs.

Fracture traces which show some regularity in orientation and spacing form a set and have been regarded as systematic fractures, while curved and sinous

fractures are considered as non-systematic (Hodgson, 1961).

A rock mass may contain many sets of fractures. Some of these sets may be related to each other and from a system or pattern which may be associated with other geological structures.

Fracture traces can form one or more patterns on aerial photographs, such as:

1. radial and/or concentric fracture pattern, associated with domal structures (Figs. 4.4a and 4.4b);

2. Sets of parallel fracture traces which are related to fold structures (Figs. 4.4c and 4.4d), or shear fractures (Fig. 4.3);

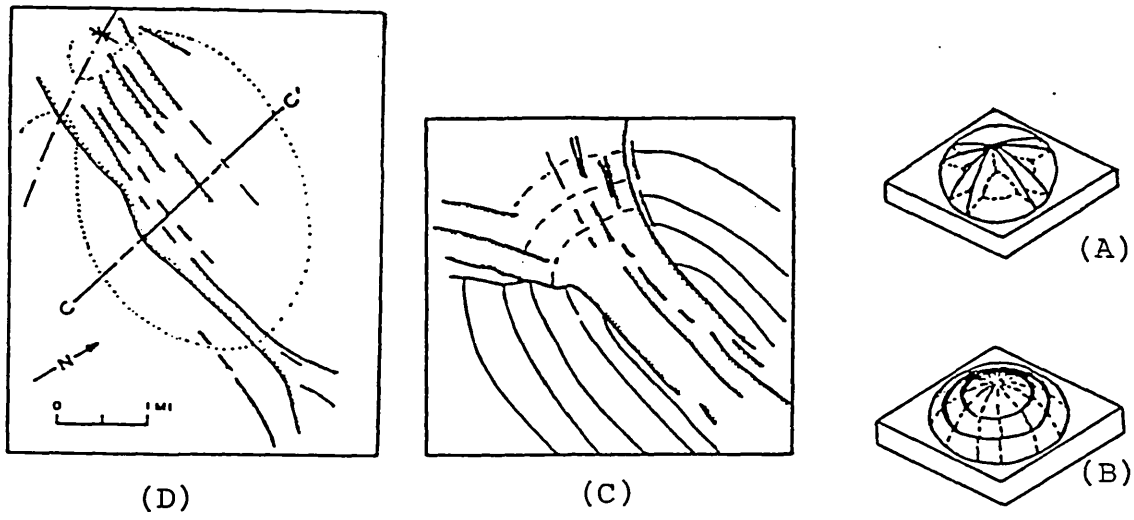
3. orthogonal fractures trace pattern of normal faults which is represented in Fig. 4.4e;

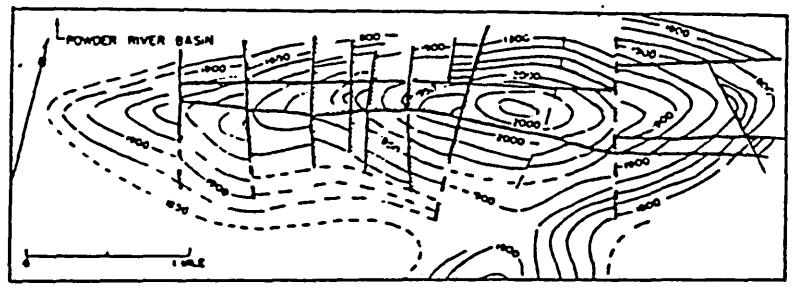
4. a set or zone of en echelon tension fractures, which is related to shearing (Fig. 4.4f);

5. various fracture patterns frequently associated with fold structures are shown in Fig. 4.5.

4.4 Techniques of Fracture Trace Analysis

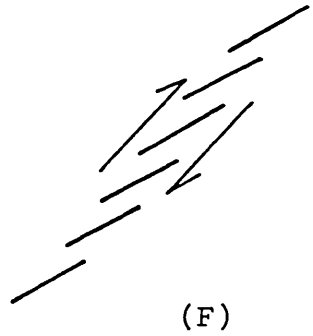
All workers who have used fracture trace analysis for the detection of subsurface structures have assumed that the presence of a structural discontinuity in the subsurface will manifest itself in the surface fracture pattern as some type of anomalous behaviour (Blanchet, 1957; Mollard, 1957; Haman, 1961, 1964; Saunders, 1969; Norman, 1976).





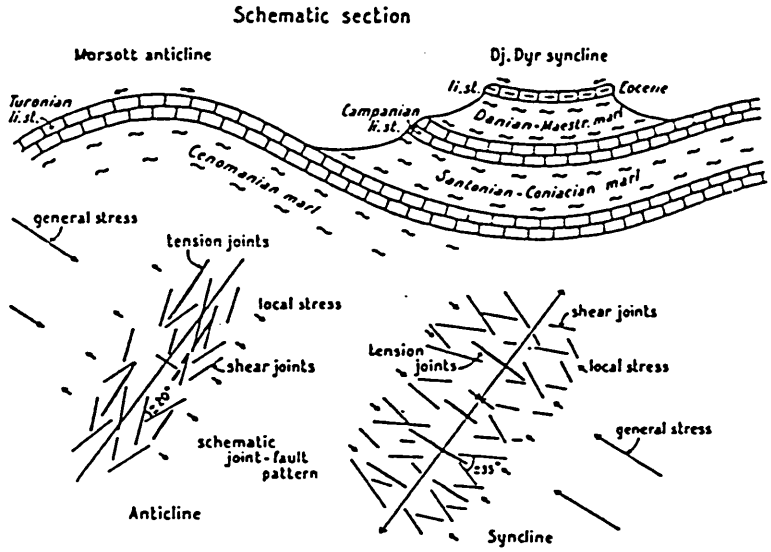
(E) —*Big Muddy anticline, Wyoming*

(After Wisser, 1960)



(F)

Fig. 4.4 Some fracture patterns.



(After De Sitter,1964)

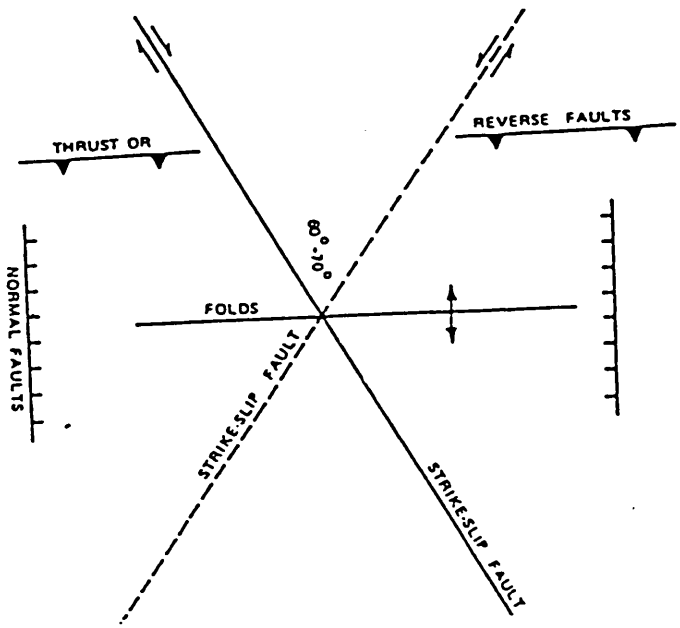


Fig. 4.5 Fracture patterns associated with folds.

Hence, one can use such changes in the intensity and orientation of fracture traces to detect subsurface structures.

4.4.1 Changes in Intensity of Fracturing

Blanchet (1957) established a technique based on changes in intensity of fractures and detected a subsurface reef structure. Firstly, all fracture angular frequency were investigated to define the regional fractures. Then, the area was studied for deviation from these regional directions. A contour map of the residual spatial frequency was prepared. This map shows a remarkable decrease in the intensity of the fractures over a dome-like feature (reef).

4.4.2 Changes in Fracture Pattern Orientations

Hobbs (1911) noticed that fracture (lineament) patterns change across zones which vary in quality of expression because of differences in tectonic behaviour of individual blocks of the basement rocks. Permyakov (1949), quoted by Huntington (1969), proposed a method [rule of the parallelogram] to detect the local tectonic features. In this method, the two major rays of local fracture frequency rose diagrams are used to construct a parallelogram. From this geometry, the trend, length and amplitude of the structure could be determined (Huntington, 1969). This technique has been applied on the fracture traces of the studied area where folding structure are present, but unfortunately it has failed to

produce meaningful conclusion. This failure could be attributed to differences in the degree of deformation of different regions as well as lack of understanding of the possible mechanisms of the observed fracture systems or patterns (see Norman and Partridge, 1978).

4.4.3 Changes in Lineament and Fracture Trace Patterns

Shults (1969), quoted by Podwysocki and Gold (1979), and 1971), mentioned that lineament directions are expressed as joints in most outcrops of platform areas, but those joints which are not related to lineament directions are commonly associated with a local tectonic feature.

Haman (1964) also differentiated between "fracture traces" and lineaments which are present over passive structure, reef. After the analysis of both of them, independantly, he found an increase in fracture traces and decrease in lineaments over the reef. He attributed this result to some basic differences in the genesis and mechanics of propagation of fracture traces and lineaments.

The mechanism of propagation is still in question. Numerous hypotheses have been suggested, including earthtides, earthquakes (Blanchet, 1957), downward setting of unconsolidated deposits into bedrock joints caused by a groundwater piping or leaching mechanism (Mollard, 1957), fatigue theory, tectonic effects, isostatic adjustment, frictional drag along the bedding planes between rock units coupled with downwarp and

uplift (Price, 1966 and 1974) and net decrease in various forms of potential energy stored in the rock; decrease in potential energy equals kinetic energy (Secor, 1969).

It is quite clear from the previous discussion that there are neither standard methods of fracture traces or lineaments interpretation nor standard techniques for their analysis. However, until now the different quantitative aspects are mostly used for visual correlation, or analysed individually, compared and conslusion drawn. In reality, these quantitative aspects such as azimuth, length and energy are not only critical in the perception process during interpretation, but also may be directly related to geological patterns such as structural fabrics and uniform deformation. So, any new technique which considers more than one of the quantitative aspects of fracture traces or lineaments would be much better than any of the previous techniques, and in the meantime overcomes the problems of fracture traces or lineaments interpretation, which has been mentioned earlier in this chapter and also has been discussed by Huntington, J.F. and Praiche, A.P. (1978). This new technique is called by the author an "Integrated Technique for the Analysis of the Fracture Traces or Lineaments".

4.4.4 The Integrated Technique

Integrated technique means the application of more than one quantitative fracture aspect, or more than one band with different wave lengths to get filtered

integrated representation of these aspects which are amenable for any structural study in a chosen area.

Based on the theorem of addition of probabilities, the application of such integrated technique allows one to make certain conclusions, e.g. if two methods used with probabilities of P_1 and P_2 respectively, then the application of two methods together gives a new conclusion with probability $P_{1,2}$, which can be written as:

$$P_{1,2} = P_1 + P_2 - P_1P_2$$

if $P_1 = P_2 = 0.5$, then $P_{1,2} = 0.75$.

This means the application of two quantitative aspects of fracture traces gives a conclusion which is much more realistic than the application of only one aspect.

This technique could be summarised in the following steps:

1. The data obtained from different aspects are normalized with respect to the corresponding standard deviation, Si.

2. A cross correlation matrix $\hat{R}$ is prepared. Each element $(r_{i,j})$ of this matrix is calculated as follows:

$$r_{i,j} = (1/S_iS_jn) \sum_{k=1}^{n} (X_{ki}-X_i)(X_{kj}-X_j)$$

where X_i is the average of the corresponding quantitative aspect and X_{Ki} is the value of the corresponding (K) quantitative aspect.

3. The solution of the following equation yields L number of filter coefficients (h_i):

$$(\hat{R}-\lambda_{max}I)h = 0$$

where R' is the cross correlation matrix, I is the identity matrix, λ_{max} is the maximum eigen value of the matrix R' and h is the eigen vectors corresponding to λ_{max}.

4. The final result is a combined or integrated value obtained from the L aspects as follows:

$$F_K = \sum_{i=1}^{L} X_{Ki} \cdot h_i$$

where F_K is the integrated value, h_i is the ith filter coefficients.

4.5 Data Processing

The subject of this study mainly concerns those fractures and patterns which are manifest on aerial photographs. Computers are ideally suited to the many iterative operations, such as fracture trace analysis, which are time consuming for the geologist. Hence, after the aerial photographs had been interpreted, all fracture traces were digitized with respect to certain fixed direction on an overlay, such as the North direction.

The digitized data of every overlay or structure has its own file name. Under this name, the file with all its information such as scale, serial number, location was stored to facilitate the reproduction of these raw data at any required time. These new data were used for the calculation of the azimuths and lengths of the mapped fracture traces.

4.6 Statistical Analysis of the Fracture Traces of Abu Rawash

The object of this study is to examine the pattern and distribution of the fracture traces of Abu Rawash area as manifested on aerial photographs and interpret geologically these patterns in an attempt to find out the relationships between these patterns and the different geological structures present.

The analysis and interpretation of a bed rock fracture is simpler than the analysis of multiplicity of highly varied fracture traces and trace patterns which occur on the compiled map (Fig. 4.6). Consequently, for the purpose of this investigation, it is thought easier to consider the fracturing of Abu Rawash area by beginning with the small fracture measured in the field and already studied, and then progress upwards to the larger fracture traces.

In order to see if the interpreted fracture traces possess local and/or regional characteristics, an examination of their directional properties will be made.

4.6.1 Method of Analysis

The fracture traces of Abu Rawash were analysed by computer program ROSES. This program was modified after Critchly, M., 1981. Data for this analysis in the form of digitized fracture traces has been taken from the

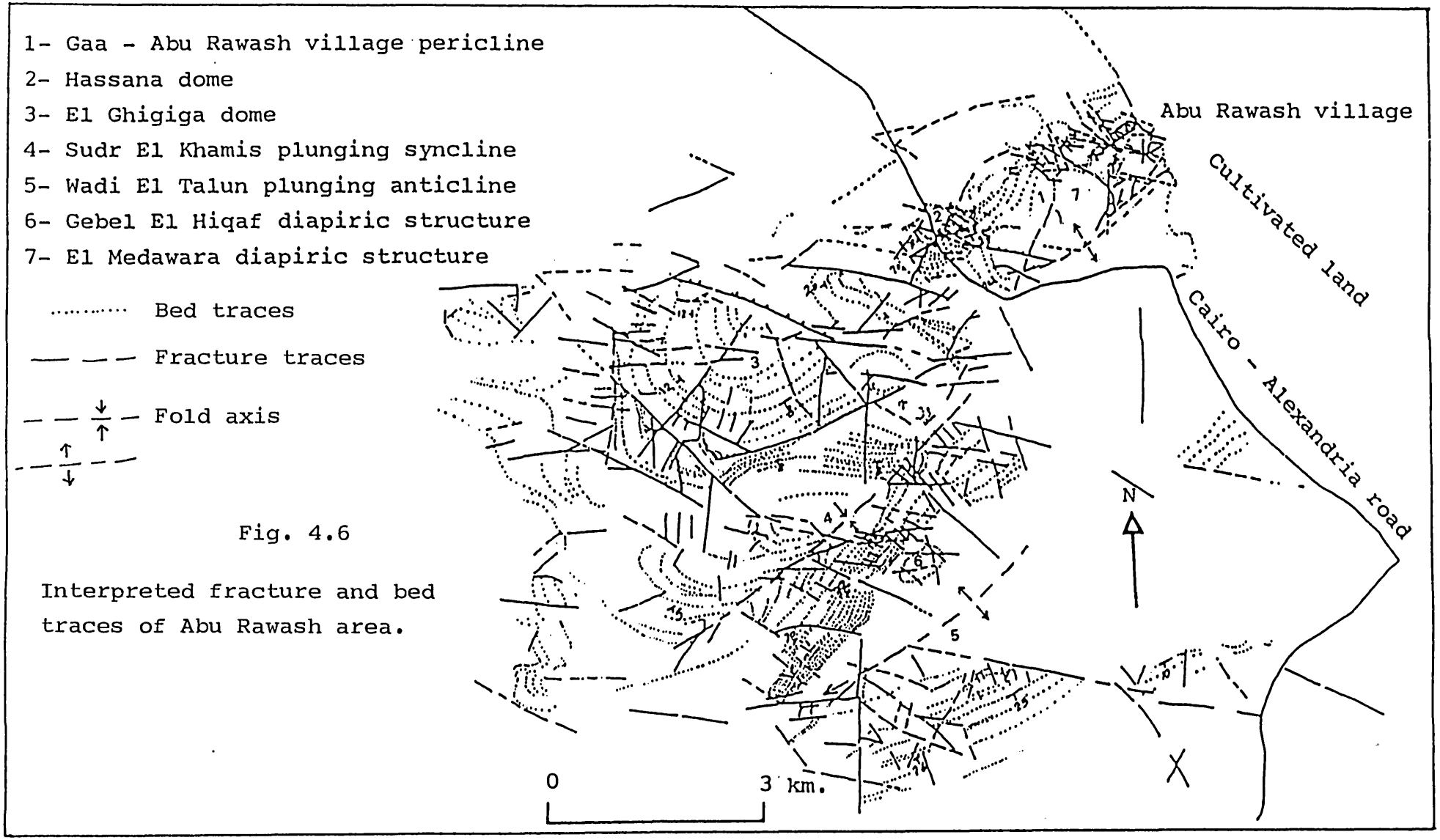


Fig. 4.6

Interpreted fracture and bed traces of Abu Rawash area.

1:60,000 compiled map (Fig. 4.6). This map has been interpreted stereoscopically from the aerial photographs of Abu Rawash district. For the purpose of checking, the digitized fracture traces were reproduced.

Statistical analysis was performed on the whole fracture traces present on Fig. 4.6 and for each single structure occurring on the compiled map. The present writer located roughly the borders of each structure represented on the map, so the fractures within these borders are likely to be more readily amenable to interpretation than if all the fracture traces for the whole area were to be represented on one diagram. The following statistics were calculated:

1. Fracture frequency and relative or percentage fracture frequency;

2. Fracture length and relative or percentage fracture length;

3. Average fracture length and relative or percentage average fracture length;

4. Fracture energy and relative or percentage fracture energy;

5. Integrated representation of 1, 2 and 4;

6. Integrated representation of 1, 3 and 4.

The directional and density (fracture length) statistics are commonly used in fracture trace analysis (Norman, 1976).

Integrated representation and fracture energy are new terms which have been introduced during the course of this study, for the purpose of generating an enhanced

comprehensive representation of different quantitative aspects or enhancing certain sets of fracture traces or patterns repectively.

Some measures of the energy associated with a fracture set can be obtained by finding the product of the multiplication of the square of the manifested length and the number of individual fracture traces within the same class interval with respect to the north direction.

4.6.2 Methods of Presentation

The computer output of the fracture traces are presented numerically in the from of tables such as Table 4.1, or graphically in the form of rose diagrams (where the number of the fracture traces "N" is written on the bottom right hand corner) and histograms. Class intervals of 5° and 10° degrees were used in this study.

Histograms are used in this study, either to show a visual comparison between relative fracture frequency, relative fracture length, relative fracture energy and relative average fracture length, or to show the homogeneity of the structural trends all over the studied area. Also, rose diagram maps were prepared to present the general patterns of the fracture traces over the area under study.

These graphical representations achieved the initial aims of the statistical analysis carried out in this study. These initial aims are:

1. To bring out geologically significant trends and relationships;

Table 4.1 Numerical Computer Output of The Fracture Traces

A 1001 ABU RAOSH RIDGE

SEARCH SECTOR (DEGREES) FROM	TO	NO. OF FRACTURES ACTUAL	NO. OF FRACTURES RELATIVE	LENGTH OF FRACTURES ACTUAL	LENGTH OF FRACTURES RELATIVE	FRACTURE ENERGY ACTUAL	FRACTURE ENERGY RELATIVE	FRACTURE LENGTH AVERAGE
0	5.0	1.0	1.2	14.0	3.3	14.0	.8	14.0
5.0	10.0	1.0	1.2	5.0	1.2	5.0	.3	5.0
10.0	15.0	0	0	0	0	0	0	0
15.0	20.0	2.0	2.4	9.0	2.1	18.0	1.1	4.5
20.0	25.0	2.0	2.4	11.0	2.6	22.0	1.3	5.5
25.0	30.0	3.0	3.7	15.0	3.6	45.0	2.7	5.0
30.0	35.0	1.0	1.2	7.0	1.7	7.0	.4	7.0
35.0	40.0	1.0	1.2	5.0	1.2	5.0	.3	5.0
40.0	45.0	0	0	0	0	0	0	0
45.0	50.0	0	0	0	0	0	0	0
50.0	55.0	0	0	0	0	0	0	0
55.0	60.0	3.0	3.7	29.0	6.9	87.0	5.1	9.7
60.0	65.0	0	0	0	0	0	0	0
65.0	70.0	4.0	4.9	26.0	6.2	104.0	6.2	6.5
70.0	75.0	3.0	3.7	14.0	3.3	42.0	2.5	4.7
75.0	80.0	3.0	3.7	10.0	2.4	30.0	1.8	3.3
80.0	85.0	4.0	4.9	22.0	5.2	98.0	5.2	5.5
85.0	90.0	0	0	0	0	0	0	0
90.0	95.0	4.0	4.9	25.0	6.0	100.0	5.9	6.3
95.0	100.0	7.0	8.5	29.0	6.9	203.0	12.0	4.1
100.0	105.0	7.0	8.5	40.0	9.5	280.0	16.6	5.7
105.0	110.0	3.0	3.7	16.0	3.8	48.0	2.8	5.3
110.0	115.0	5.0	6.1	25.0	6.0	125.0	7.4	5.0
115.0	120.0	1.0	1.2	8.0	1.9	8.0	.5	8.0
120.0	125.0	3.0	3.7	13.0	3.1	39.0	2.3	4.3
125.0	130.0	7.0	8.5	32.0	7.6	224.0	13.2	4.6
130.0	135.0	3.0	3.7	6.0	1.4	18.0	1.1	2.0
135.0	140.0	2.0	2.4	2.0	.5	4.0	.2	1.0
140.0	145.0	1.0	1.2	8.0	1.9	8.0	.5	8.0
145.0	150.0	2.0	2.4	5.0	1.2	10.0	.6	2.5
150.0	155.0	5.0	6.1	26.0	6.2	130.0	7.7	5.2
155.0	160.0	2.0	2.4	9.0	2.1	18.0	1.1	4.5
160.0	165.0	0	0	0	0	0	0	0
165.0	170.0	1.0	1.2	6.0	1.4	6.0	.4	6.0
170.0	175.0	1.0	1.2	3.0	.7	3.0	.2	3.0
175.0	180.0	0	0	0	0	0	0	0
TOTALS		82.0	100.0	420.0	100.0	1691.0	100.0	151.2

2. To obtain a summary of the data and to establish the extent of any homogeneity that may exist.

4.7 Results

a) Mapping of the structures of Abu Rawash

The strong differences which exist in the erosional resistance of the sedimentary rocks of Abu Rawash caused the typical banded patterns and structures formed by these rocks to be readily recognized on the aerial photographs.

This mapping was very useful in the detection of the sense of movement of one of the major faults in the studied area. This fault has been located in the geological maps of the area, but none of the previous authors recognized the sense of its movement (Fig. 4.7).

On the aerial photographs and the interpre—ted map (Fig. 4.8), the drag of beds along the fault plane gives a good indication about the sense of the movement of this fault. So, it is a dextral strike-slip fault which also experienced a vertical movement with a down throw side on the E, towards the Nile valley.

The different structures which have been mapped using the aerial photographs are represented in Fig. 4.6. Comparison of this map (Fig. 4.6) with those published by previous authors (Figs. 1.2 and 4.9) shows how the shape, size and geometry of the different structures are clearly and accurately expressed in Fig. 4.6. These structures have been checked during the field study and the dip of

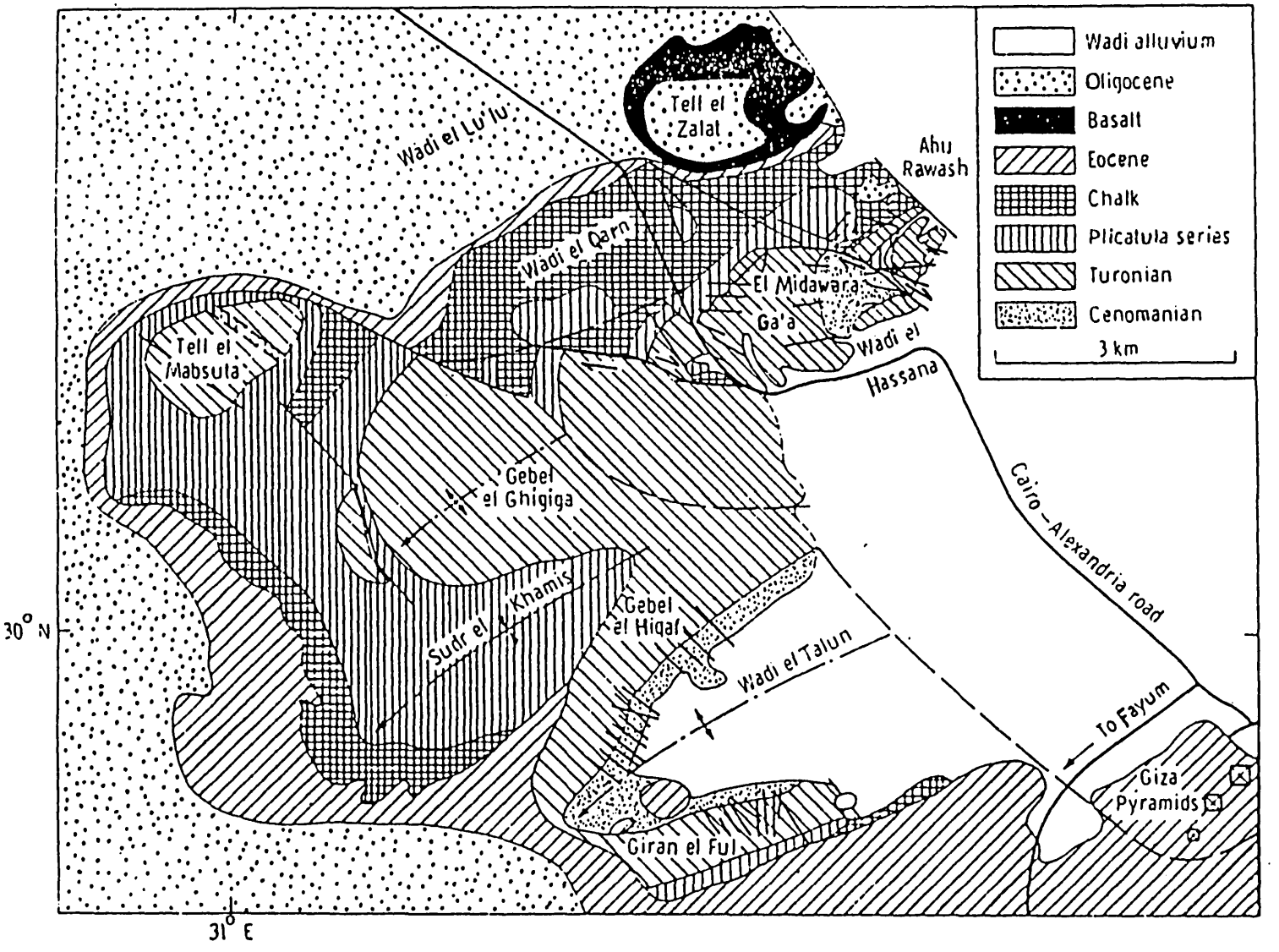


Fig. 4.7 Modified geological map of Abu Rawash area by El Malky.

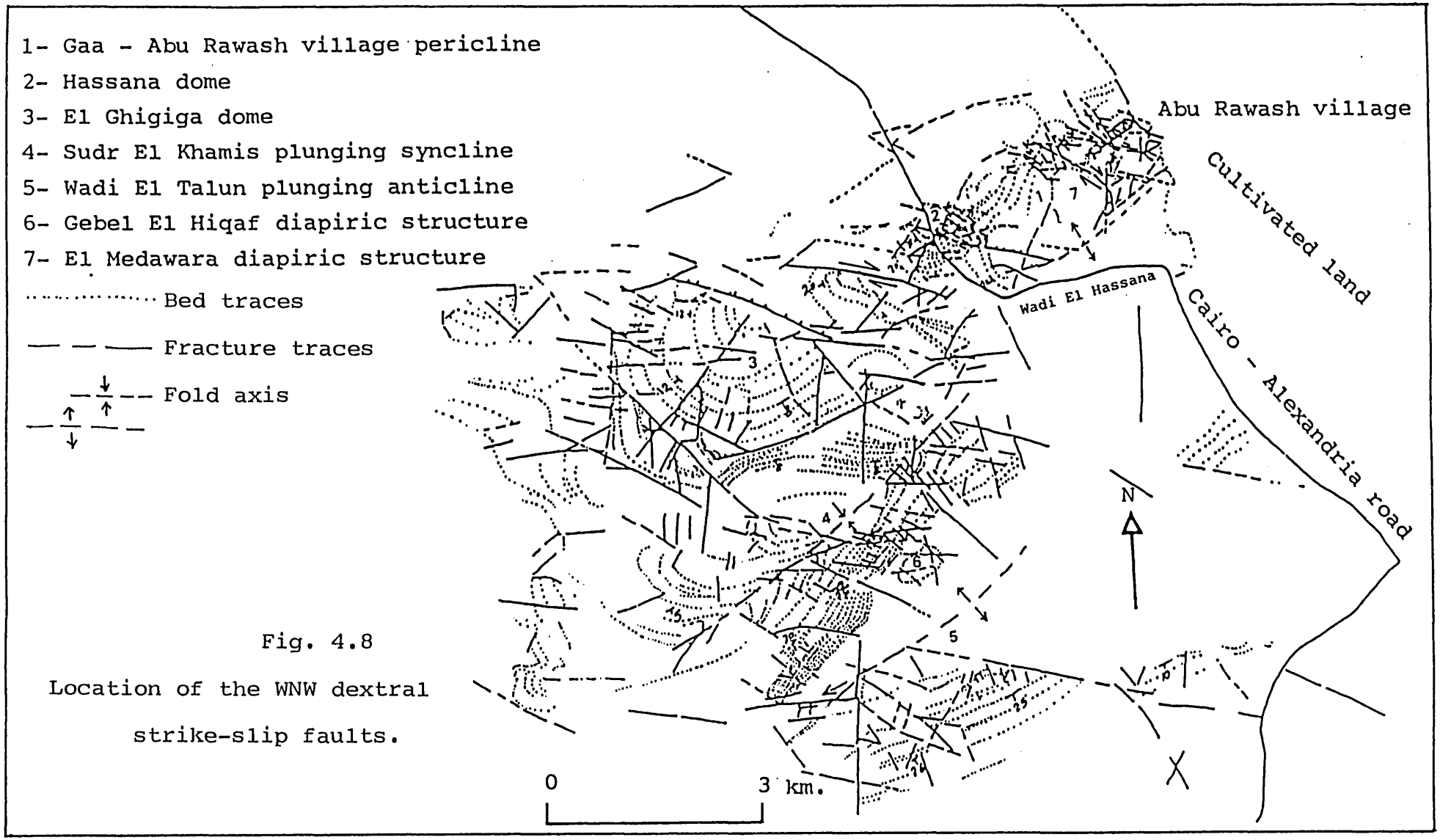


Fig. 4.8

Location of the WNW dextral strike-slip faults.

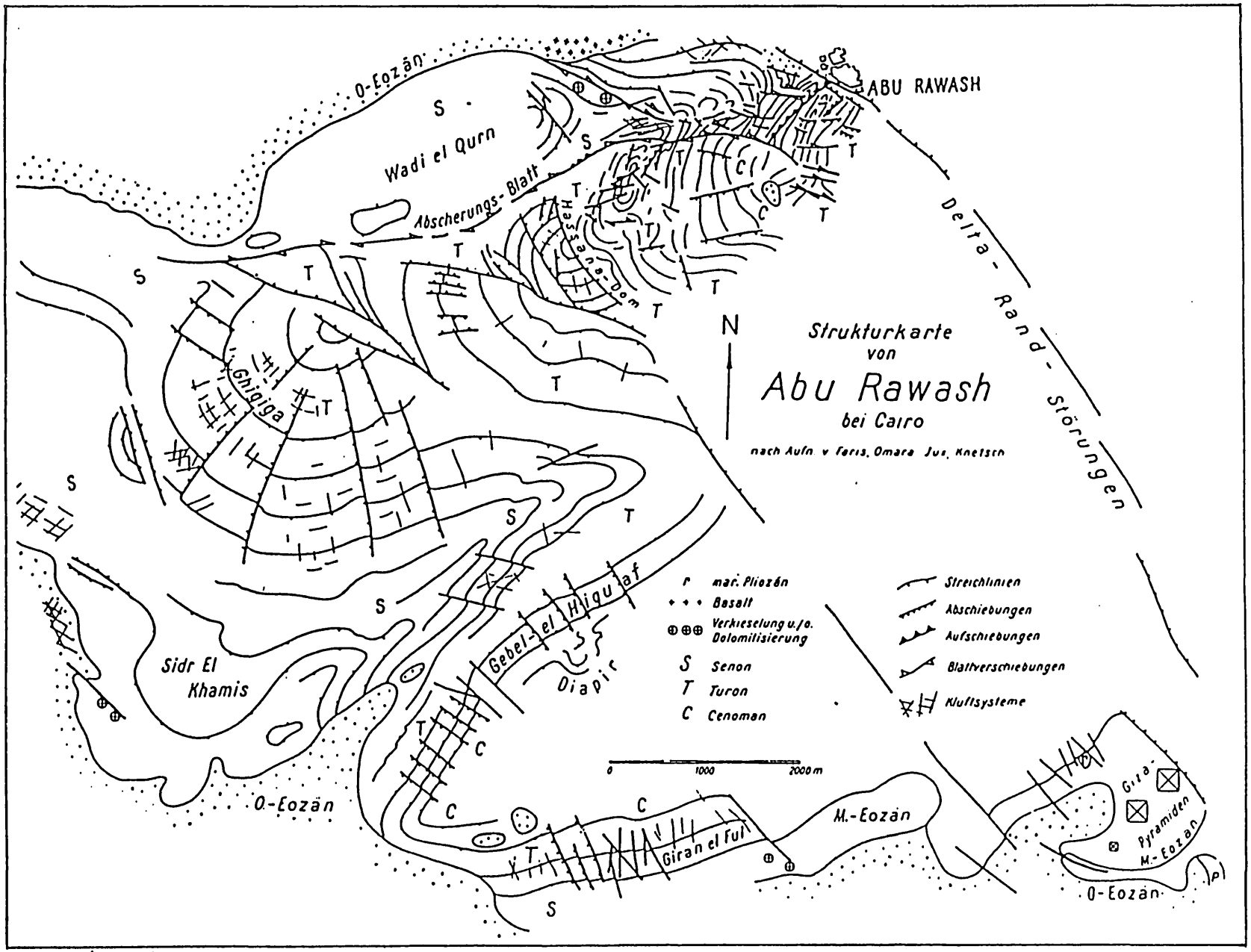


Fig. 4.9 Structural map of Abu Rawash area, after Knetsch (1958).

beds was measured, wherever possible, and displayed in Fig. 4.6. These structures are:

1) Gaa-Abu Rawash village pericline

This pericline with N64°E axis has been discussed in the previous chapter.

2) El Hassana dome

This structure is a relatively small domal structure which could be easily seen in the field and on the aerial photographs. The structure can be seen clearly in the field from the south on the way to Alexandria, where the bedding traces are well represented and beds dip away from the centre in all directions, while from the north the structure is less remarkable. The dip of the beds, as measured in the field, ranges from about 22° to 32° degrees.

The domal structure is disturbed obviously by a NW-SE fault which runs along the Cairo-Alexandria road, where one can see the structure on both sides of the road in the field and on the aerial photographs (see Fig. 4.10, after Beadnell, 1902).

3) El Ghagiga dome

This domal structure is represented in Fig. 4.6 by bedding traces in a form of nearly half a circular arc, which is limited on the northeast side nearly along its diameter by a WNW fault. The domal structure is bounded also at its southwestern end by a NW fault. At the top

α White Chalk.
β Ostrea and Plicatula bed.
γ Flinty Series.
δ Acteonella-Nerinea limestone.
ε Hard compact and often chalky limestone.
ξ Rudistae beds, alternating shales, marls and limestone.
η Clay and sandstone.

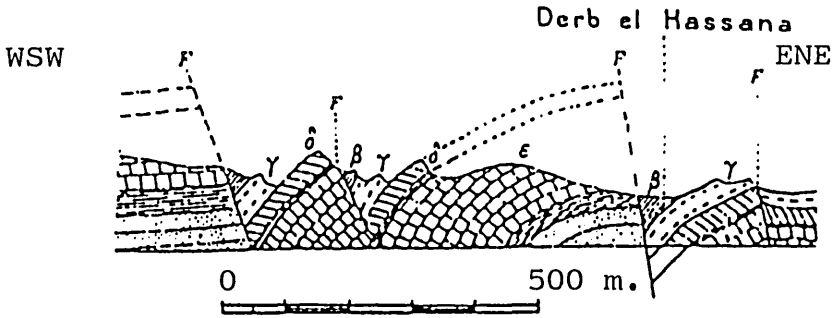
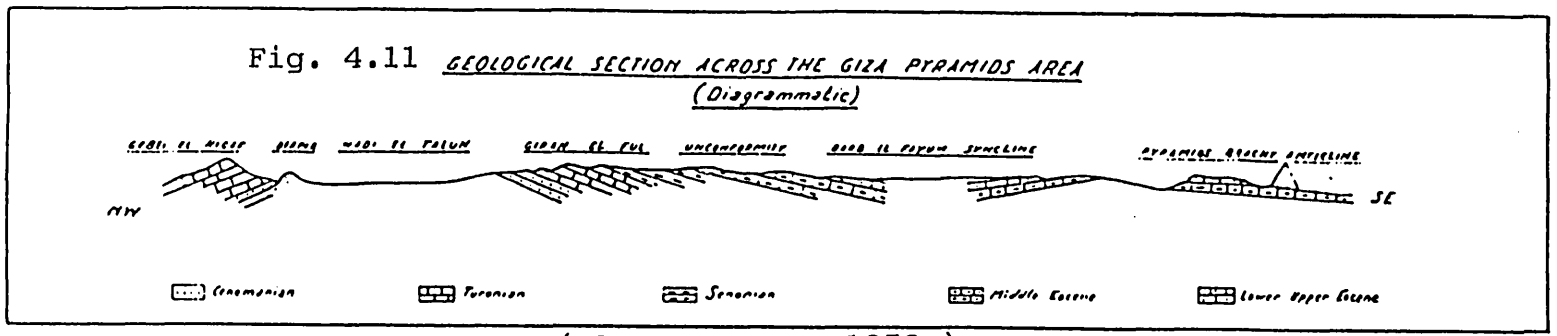


Fig. 4.10 Geological section across El Hassana dome (after Beadnell,1902)



(After Omara, 1953)

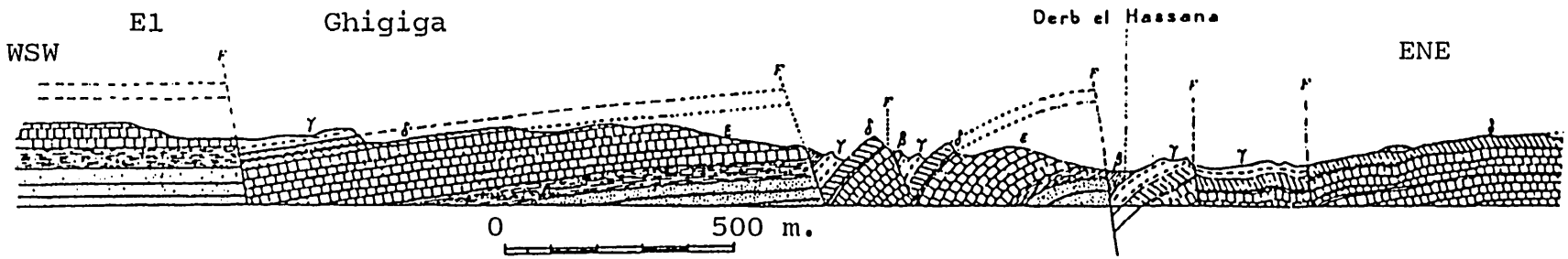


Fig. 4.12 Geological section across Abu Rawash area , after Beadnell (1902).

of this domal structure, the dip is about 4° degrees, while away from the top the dip ranges from 8° - 12° degrees.

4) Sudr El Khamis plunging syncline

The syncline is represented on the aerial photographs as well as in Fig. 4.6 by a V shaped bedding traces that point towards the NE. This syncline, which trends ENE - WSW, is narrow in the NE but becomes wider to the SW in the direction of the plunge. The bedding traces of the NW limb are curved, while that of the other limb are linear. The dip of beds, as has been recorded by Beadnell (1902) and Faris (1946), ranges from 8° - 12° degrees and becomes about 5° degrees in the south of the structure where the Eocene rocks are present.

5) El Talun plunging anticline

This anticline trends ENE($N70^{o}E$) and plunges to the SW. The core of this anticline, called Wadi El Talun, is cut by a V shaped valley which points roughly towards SW. This valley, which was formed by the erosion of the core of the anticline, is flanked by low hills where the two limbs of the anticline crop out. The northern and southern limbs are called Gebel El Higaf and Giran El Ful, respectively.

On the aerial photographs, these two limbs are represented by elongated ridges which strike roughly NE and are disturbed by NW - SE thrusts or cross faults. These faults have displacements which are small and range

from 1 to 5 meters (Omara, 1953) and caused the stepping down of the outcropping beds in the direction of the plunge, as is shown on the oblique aerial photograph of the NW limb, Gebel El Higaf (Plate 4.1).

The NW limb, Gebel El Higaf, dips northwest at 30° to 32° degrees (Omara, 1953). The SE limb, Giran El Ful, dips at about 25° degrees to the southeast (measured in the field).

At the SE end of Gebel El Higaf, NW limb of El Talun anticline, a diapiric structure is present where the Cenomanian sandstones and clays pierced the core of the anticline in this area (see Fig. 4.11). This diapiric structure has been reported in the field by Omara (1953).

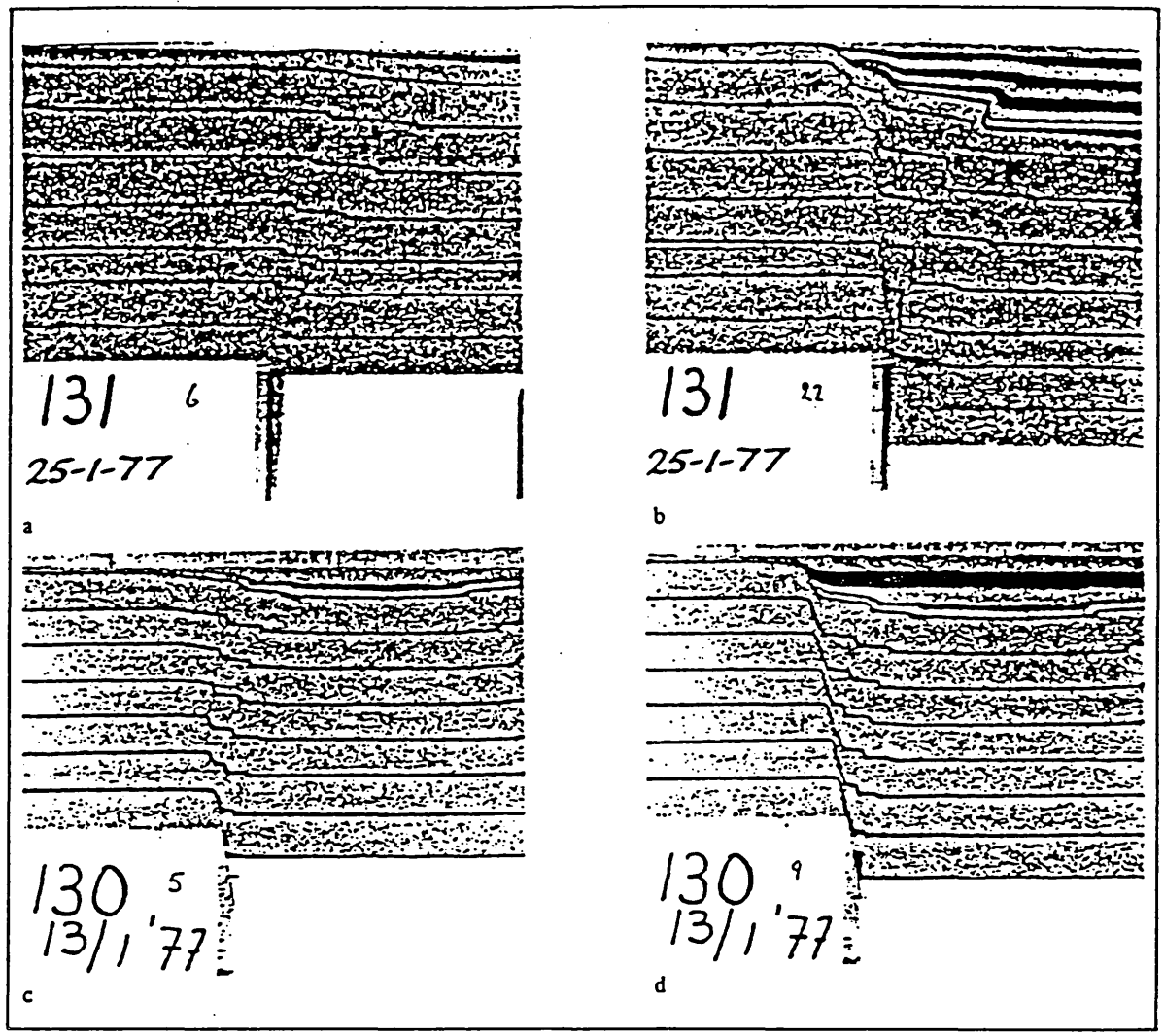
On the aerial photographs, this diapiric structure has an oval shape. The short and long lengths of this structure, as has been measured on the aerial photograph, are 360 and 660 meters respectively.

The outcrops, or the structures of Abu Rawash area are disturbed by faults, where most of the NW faults experienced a down throw on the NE side of these faults (Beadnell, 1902). Thus, the outcrops are stepped down towards the Nile Valley (Fig. 4.12 after Beadnell, 1902). Although no one pays any attention to the cause of this structural feature, the stepping down of the outcrops, the present writer (based on Horsfield's experimental approach (1977), as indicated in Fig. 4.13) attributes the stepping down of the outcrops to a NW basement-controlled faulting. This basement-controlled faulting may be related to the rifting of the Red Sea.

Plate 4.1

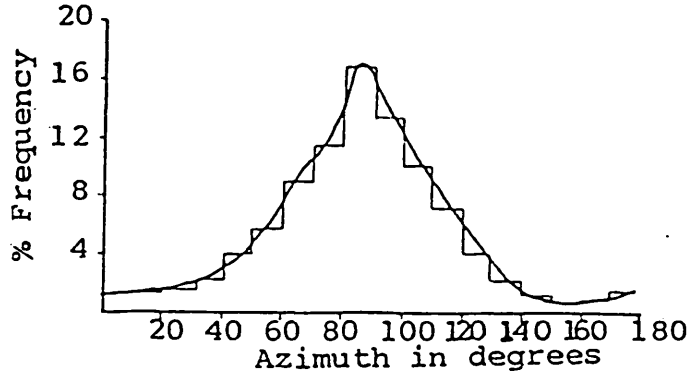


Oblique aerial photograph of the NW limb of El Talun plunging anticline (Gebel El Hiqaf), after Omara(1953).



4.13 An Experimental Model Showing the Effects of Basement Faults on the Overlying Sedimentary Cover

(After Horsfield,1977)



4.14 Interpreted magnetic Trends of a Part of the Northern Western Desert of Egypt

(After Meshref and El-Sheikh,1973)

The analysis of the aeromagnetic trends, on a part of the northern Western Desert of Egypt which includes the studied area, shows that the prominent trend is nearly E - W and the ENE trends represent noise, which is imposed on the nearly E - W signal (Fig. 4.14), (Meshref and El Shiekh, 1973). Accordingly, the main trend of the basement is nearly E - W.

Aadland and Hassan (1972) said that the Cretaceous NE and NW fault pattern was modified in early to middle Eocene by strong, nearly E - W folds and faults. However, one can conclude that nearly E - W trends were inherited from the basement as a regional trend. This E-W trend could be related to the northward movement of Africa towards Europe during late Eocene till the present (Smith, 1971, as quoted by Windly, 1977).

So, on a scale such as that which is used in this study (1:60,000), one can expect both local and regional trends to be represented as fracture traces.

It is evident that in a desert condition, structural study even of a relatively complicated region such as Abu Rawash area may be interpreted satisfactorily by the use of aerial photographs, provided there is an element of field checking.

4.8 Analysis and Interpretation of the Rose Diagrams and Histograms

The object of the analysis and interpretation of the different directional rose diagrams and histograms is to examine the patterns and distribution of the fracture

traces of Abu Rawash area as manifest on aerial photographs and to find out the relationships between these patterns and the different geological structures present in this particular area.

The only information concerning bed rock fractures (mapped in the field), fracture traces and lineaments (mapped on air photographs) is the directional frequency of the various sets. So, the correlation between the frequency rose diagrams of both the field data and data interpreted from air photographs will be based on the rays contained in these diagrams.

The analysis of the directional diagrams will be conducted on the following bases:

1. The study of some of the integrated and the relative fracture frequency rose diagrams in light of rose diagrams derived from the field data and the theoretical model;

2. The study of the individual rose diagrams in terms of the prominent rays or class intervals;

3. The analysis of the individual rose diagram maps.

4. The analysis of histograms derived from the integrated rose diagram;

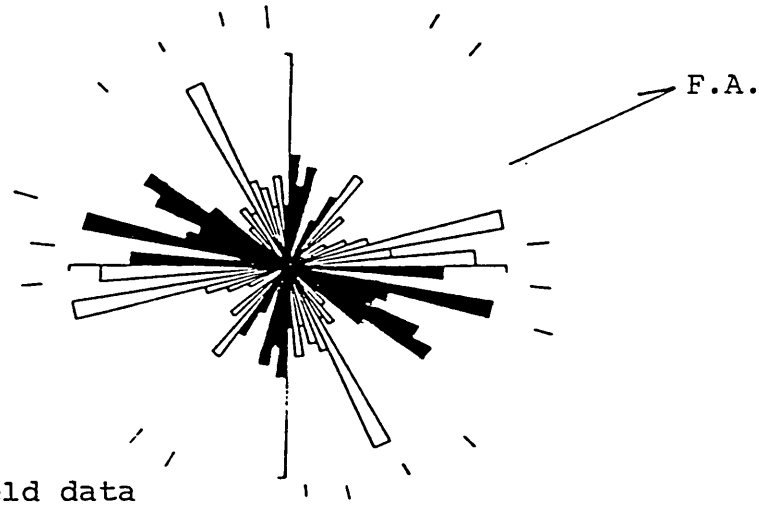
Before discussing the directional rose diagrams, one would like to make clear that the graphical output of both the directional rose diagram and the relative or percentage rose diagram are the same, because the writer used automatic scaling. However, they differ in their numerical content.

4.8.1A Study of Some Rose Diagrams in Light of the Field Data

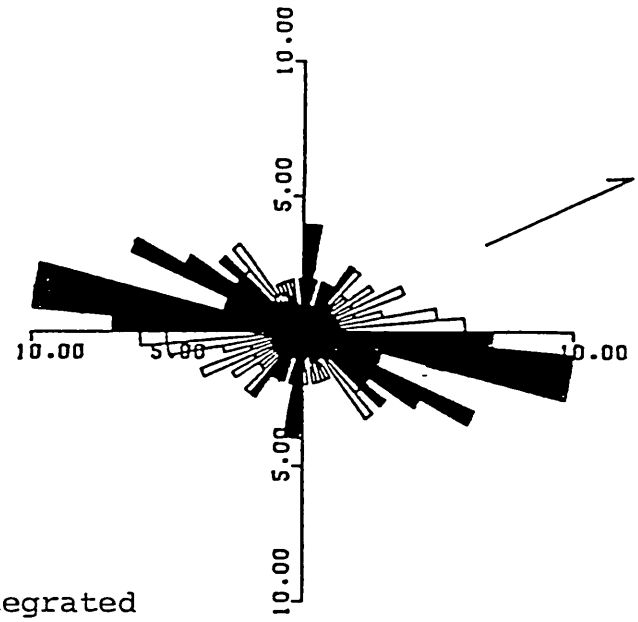
The integrated and relative fracture frequency rose diagrams of Abu Rawash area, Gaa-Abu Rawash village pericline, or Abu Rawash village pericline and Wadi El Talun-Sudr-El Khamis plunging anticline and syncline were visually and numerically (in a form of correlation coefficients) compared with the rose diagram derived from the field data in order to interpret the different class intervals of these rose diagrams, in terms of possible shear and tension fractures, and to find out the relationship between these rose diagrams.

The results of this study are represented in Figs. 4.15, 4.16 and 4.17, where the shear fractures have the black colour (or S) and the tension fractures have the white (or T) one. Also, the NW shear fractures are well developed relative to the N - S to NNE shear fractures.

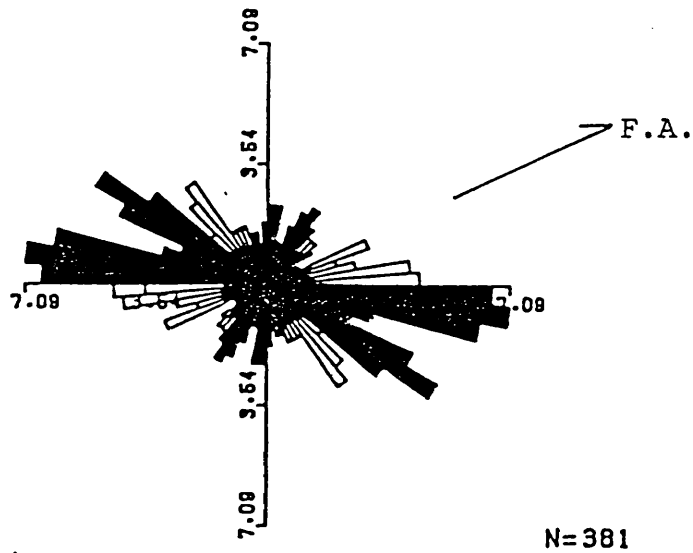
Numerical comparisons of the integrated rose diagrams and the relative fracture frequency rose diagrams with the rose diagram derived from the field data are represented as correlation coefficients in the following, Table 4.2.



A- Field data

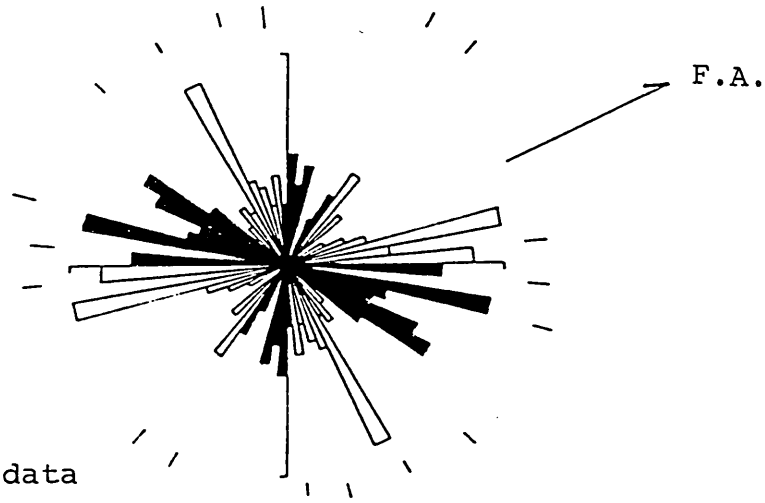


B- Integrated

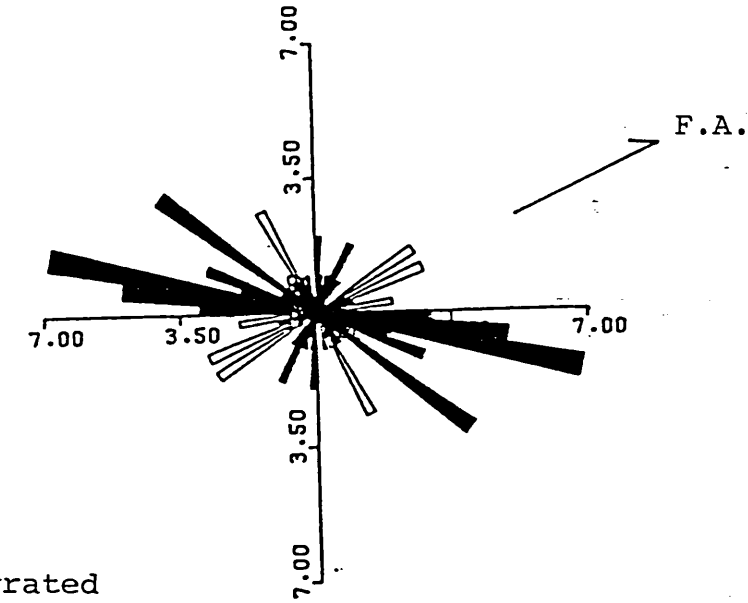


C- Relative fracture frequency

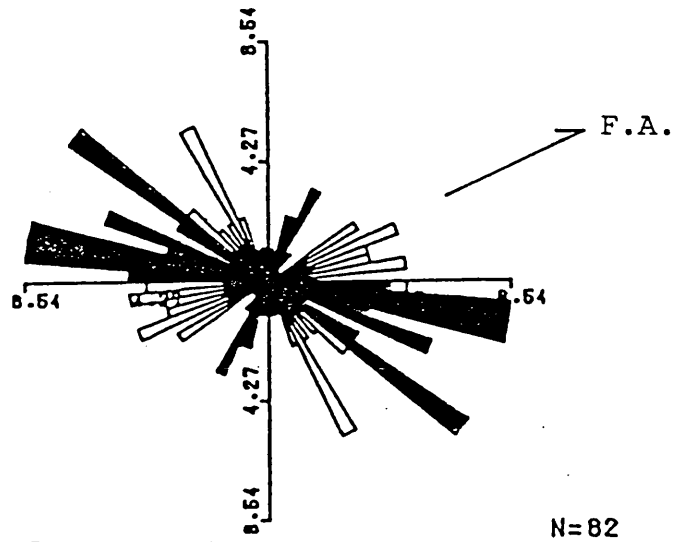
Fig. 4.15 Field data and Abu Rawash area rose diagrams.



A- Field data

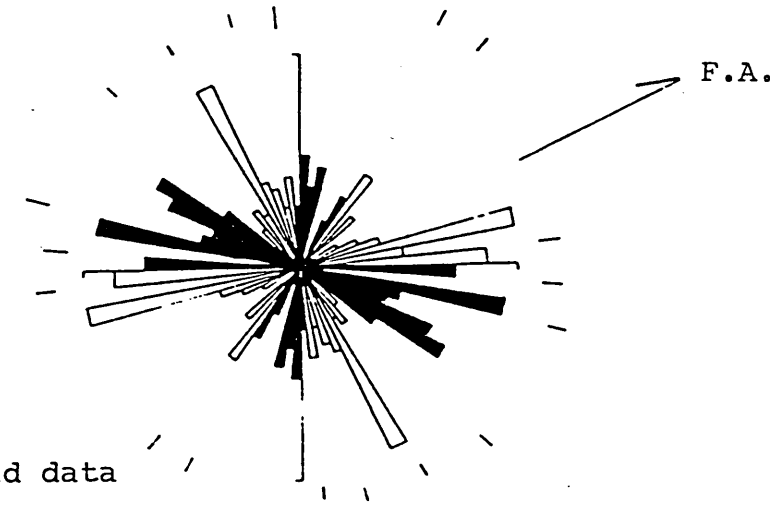


B- Integrated

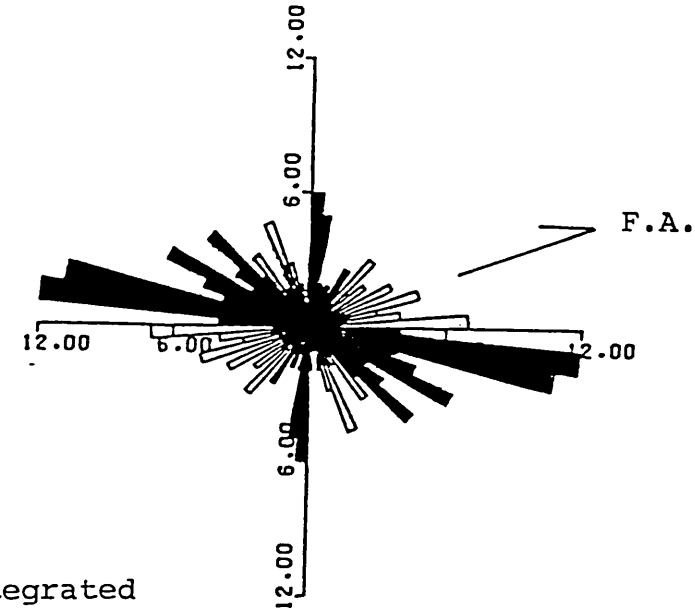


C- Relative fracture frequency

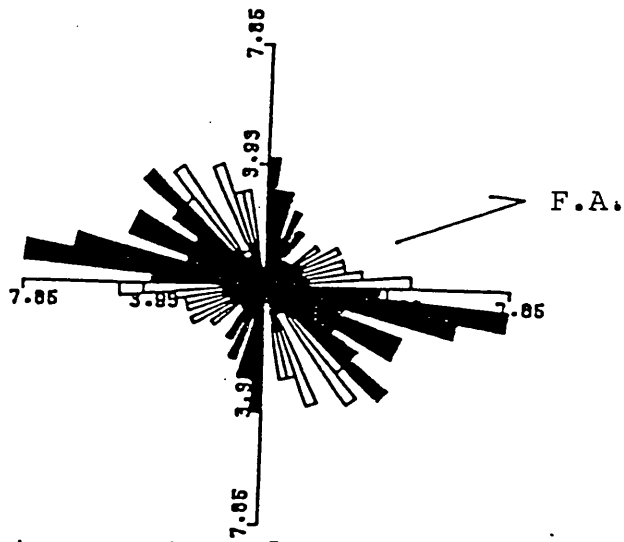
Fig. 4.16 Field data and Gaa-Abu Rawash village pericline rose diagrams.



A- Field data



B- Integrated



C- Relative fracture frequency

Fig. 4.17 Field data and El Talun-Sudr El Khamis folds rose diagrams

Table 4.2

Correlation Coefficients of Field Data and Aerial Photographs Rose Diagrams

Locality	Class interval 5°		Class interval 10°	
	Field Data/ Aerial ph. R.F.F.	Field Data/ I.T. Data	Field Data/ Aerial ph. R.F.F.	Field Data/ I.T. Data
Abu Rawash Area	0.469	0.451	0.511	0.441
Abu Rawash village pericline	0.291	0.326	0.566	0.501
W. Talun-Sudr El Khamis	0.245	0.279	0.465	0.594

R.F.F. = Relative or Percentage Fracture Frequency
I.T. = Integrated Technique

This table demonstrates the following:

i. The correlation coefficients are greatly affected by the class interval.

ii. Regarding the class interval of 5° degrees, one can notice the following:

a. The rose diagram which best fits the field data rose diagram is found to be the relative fracture frequency rose diagram of Abu Rawash area.

b. The poorest fit is found between the field data and Wadi Talun-Sudr El Khamis fold structures rose diagrams.

iii. The correlation coefficients of 10° degrees class interval reveal the following:

a. The best fit with respect to the field data rose diagram is found to be: 1) the integrated rose diagram of Wadi El Talun-Sudr El Khamis fold strucutes and 2) the relative fracture frequency rose diagram of Gaa-Abu Rawash village, or simply, Abu Rawash village pericline.

b. The poorest fit with the field data rose diagram is found to be the integrated rose diagram of Abu Rawash area.

The numerical comparisons show that the class intervals of 10° degrees gives more realistic results than the expected class interval of 5° degrees. This criterion is supported by the results of the theoretical rose diagrams derived from the field data for the purpose of interpreting aerial photograph's rose diagrams, which will be dealt with in the next section (Fig. 4.18).

4.8.1B Study of Some Rose Diagrams in Light of the Theoretical Model

The theoretical models of the previous chapter have been used to construct theoretical rose diagrams which could be compared with directional, integrated and relative fracture frequency rose diagrams derived from the interpreted fracture traces of Abu Rawash aerial photographs. The first step to construct these theoretical rose diagrams is indicated in Fig. 4.18. These theoretical rose diagrams were compared with the integrated and relative fracture frequency rose diagrams of Abu Rawash area, Gaa-Abu Rawash village pericline and Wadi El Talun-Sudr El Khamis plunging anticline and

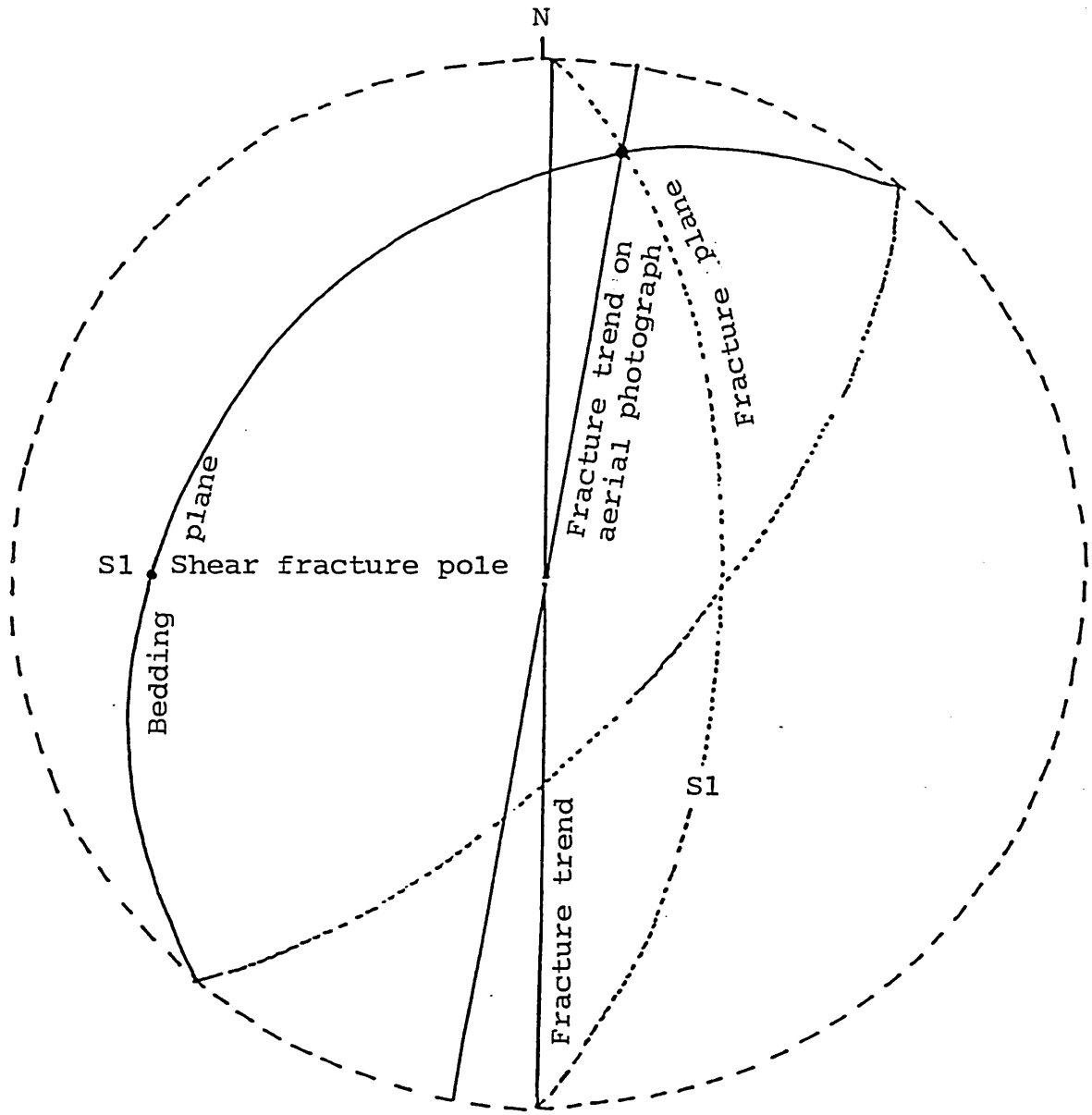


Fig. 4.18 First step in derivation of a theoretical rose diagram.

syncline to interpret the different class intervals of these rose diagrams in terms of possible shear and tension fracture and to find out which theoretical model fits these interpreted fracture traces.

The results of this study are represented in Figs. 4.19, 4.20 and 4.21, where the shears have the black colour (or S) and the extension fractures have the white (or T) one. The best fit between the theoretical model and data interpreted from the aerial photographs is found in the following:

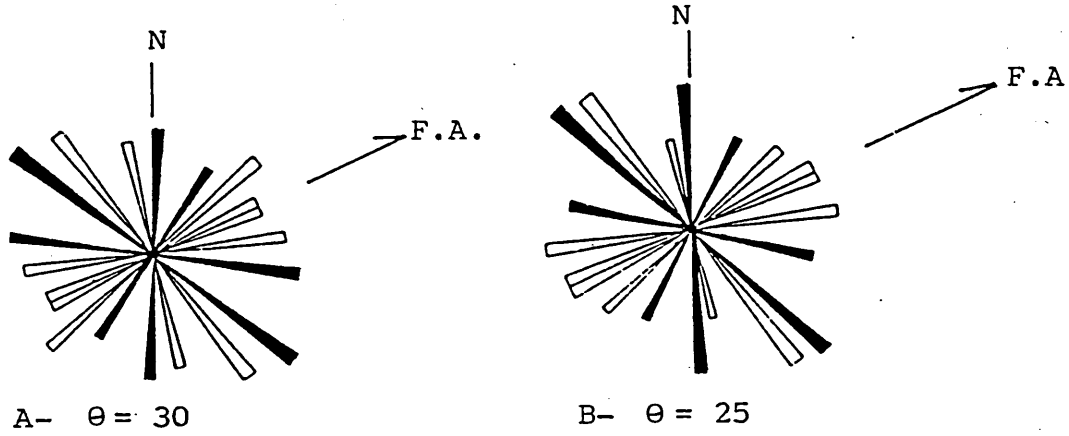
a. A fold structure, where the limbs dip 30° degrees, the amount of plunge is 20° and the shears make an angle of either 25° or 30° degrees, with the principal stress axis.

b. A fold structure, where the limbs dip 30° degrees, the amount of plunge is 15° degrees and the shears make an angle of either 25° or 30° degrees with the principal stress axis.

It is also possible to fit both the aerial photographs fracture traces with a theoretical model when the dip of the limbs of the fold is 25° degrees, with both the same plunge and shear angles.

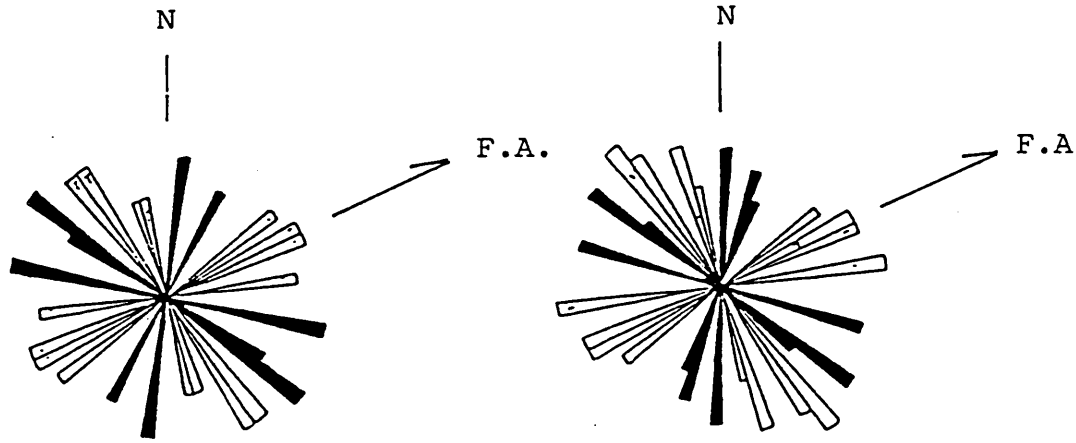
4.8.2 Analysis of the Directional Rose Diagrams

A. The directional rose diagrams of Abu Rawash area (contains all fracture traces interpreted from the Abu Rawash aerial photographs); the Gaa Abu Rawash village pericline and Wadi El Talun-Sudr El Khamis plunging anticline and syncline are represented in Figs 4.22, 4.23



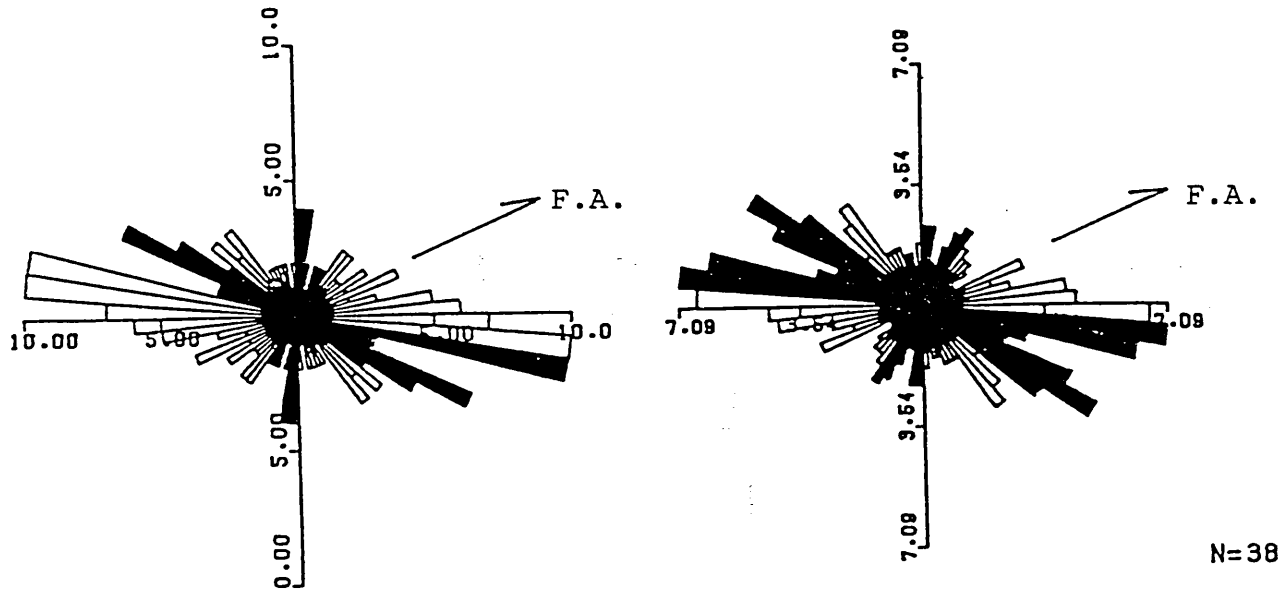
A- θ = 30 B- θ = 25

Theoretical rose diagrams (Dip = 30, Rotation = 20)



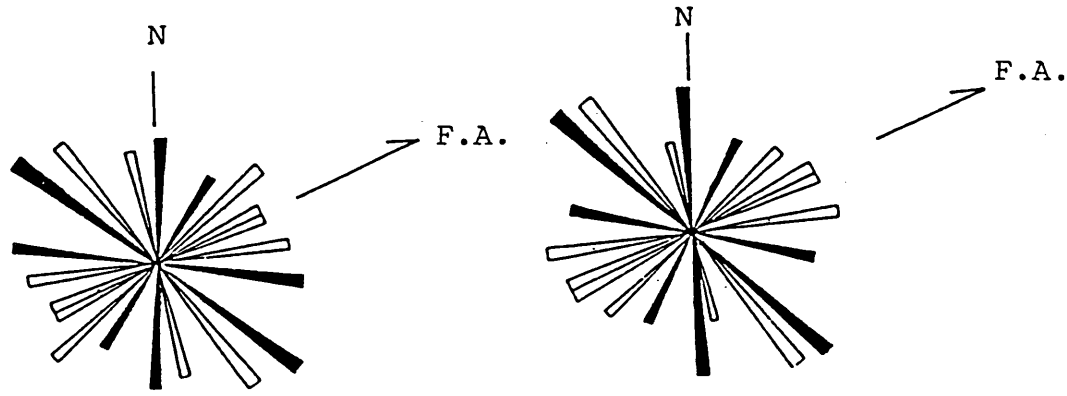
C- θ = 30 D- θ = 25

Theoretical rose digrams (Dip = 30, Rotation = 15)



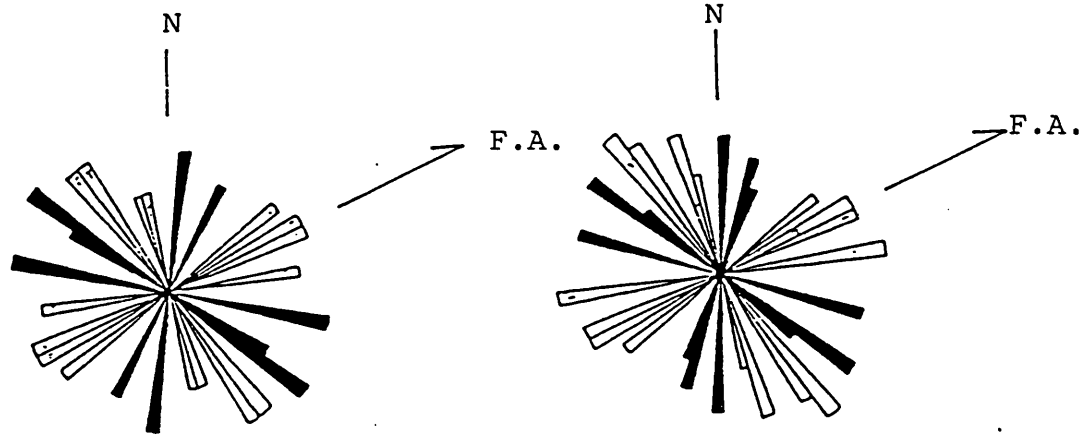
E- Integrated F- Relative fracture frequency

Fig. 4.19 Abu Rawash area and theoretical model rose diagrams.



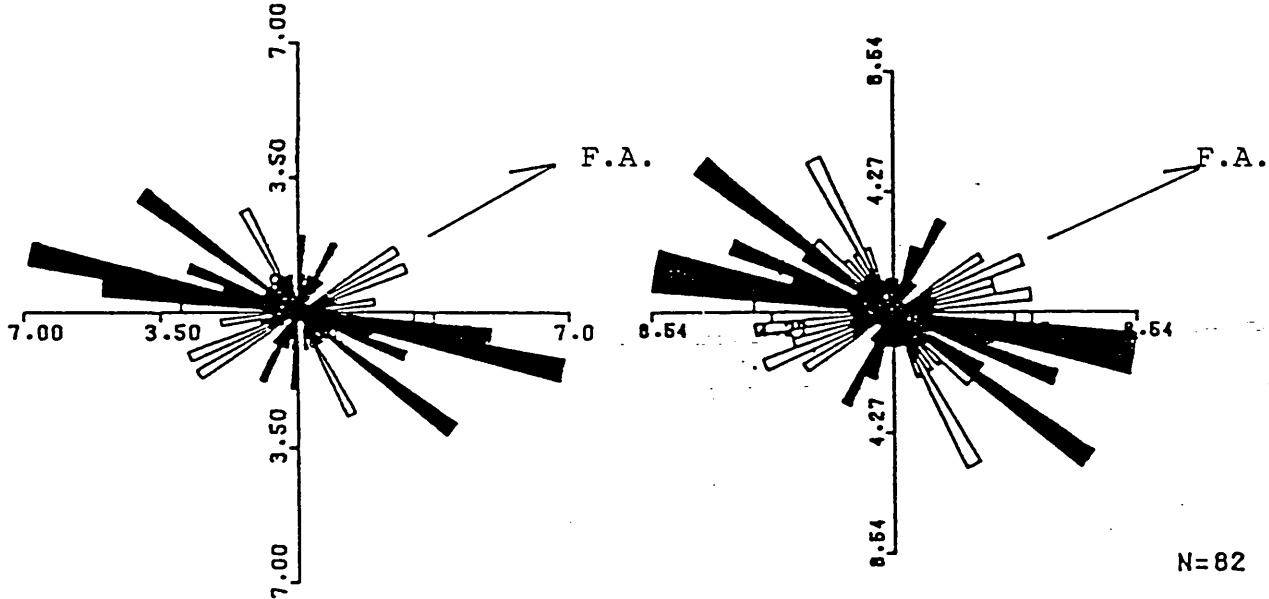
A- θ= 30 B- θ= 25

Theoretical rose diagrams (Dip = 30, Rotation = 20)



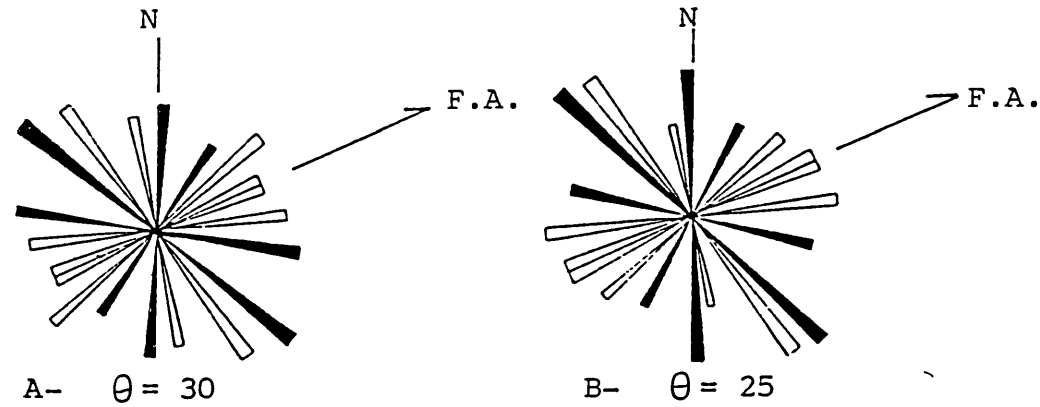
C- θ= 30 B- θ= 25

Theoretical rose diagrams (Dip = 30, Rotation = 15)



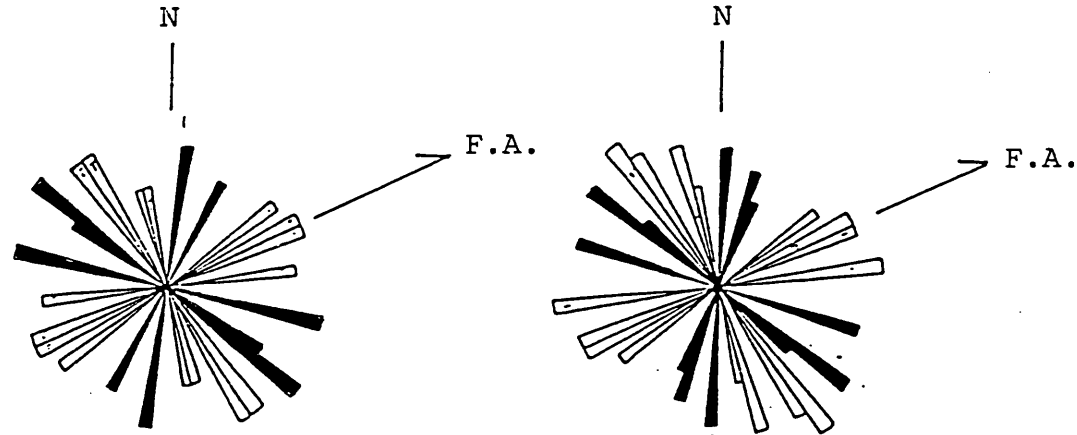
E- Integrated F- Relative fracture frequency

Fig. 4.20 Gaa-Abu Rawash village pericline and theoretical model rose diagrams.



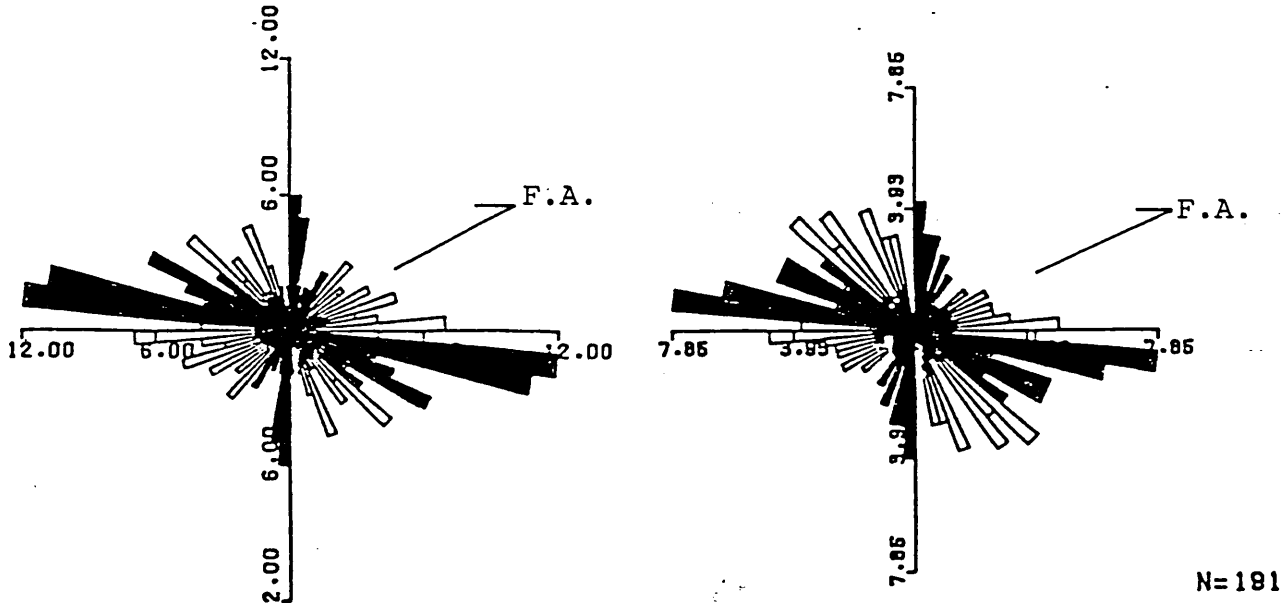
A- θ = 30 B- θ = 25

Theoretical rose digrams (Dip = 30, Rotation = 20)



C- θ = 30 D- θ = 25

Theoretical rose diagram (Dip = 30, Rotation = 15)



E- Integrated F- Relative fracture frequency

Fig. 4.21 El Talun Sudr El Khamis folds and the theoretical model rose diagrams.

and 4.24. The different class intervals were interpreted with the help of the theoretical model into shears (black colour, or S) and extension (white colour or T). The prominent rays or class intervals of these diagrams are shown in Figs. 4.22, 4.23 and 4.24, and are summarized in the Tables 4.3, 4.4 and 4.5.

The analysis of Figures 4.22, 4.23 and 4.24 shows the following:

1. The N - S shears are poorly or not represented in the relative fracture frequency rose diagrams, but have a relatively great weight in average fracture length rose diagrams. This means that these fractures are few in number but relatively long fractures.

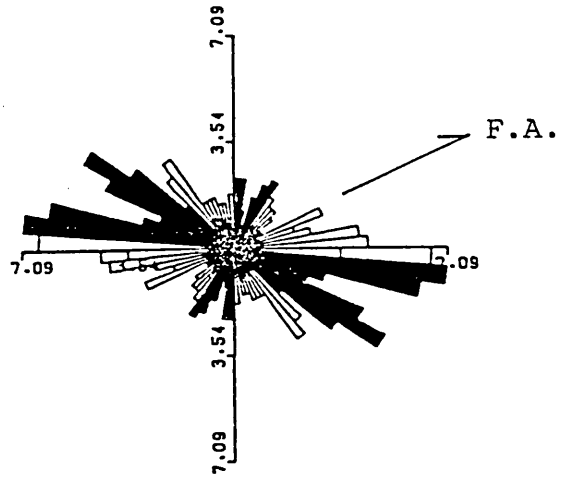
2. Some ENE extension fractures are few in number but relatively long.

3. Some WNW fractures, especially in Fig. 4.23D are relatively very short in length.

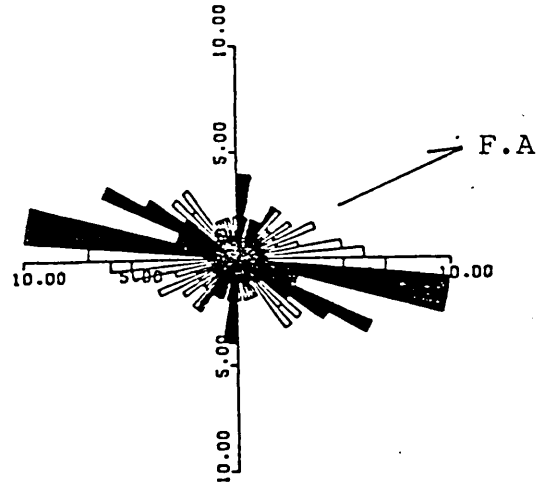
4. With respect to the field study and Figure 4.6, as well as the previous regional work, one can say that the relative fracture energy rose diagrams reflect the fault trends which are present in the studied area.

5. The integrated rose diagrams are much better than any other diagram because they still represent those fracture traces which are relatively long but few in number.

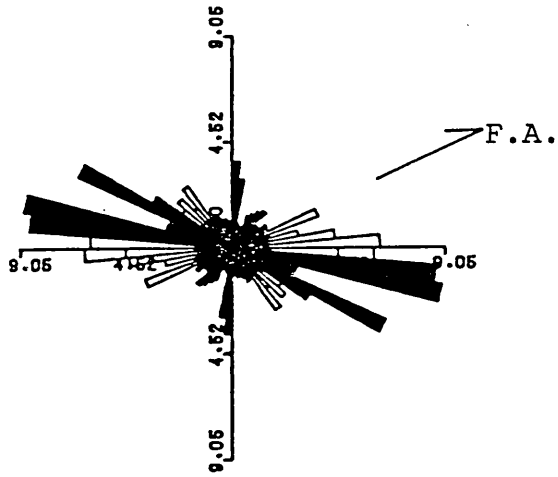
6. The average fracture length rose diagrams show those fracture traces which are ill represented or obscured in both frequency and density rose diagrams.



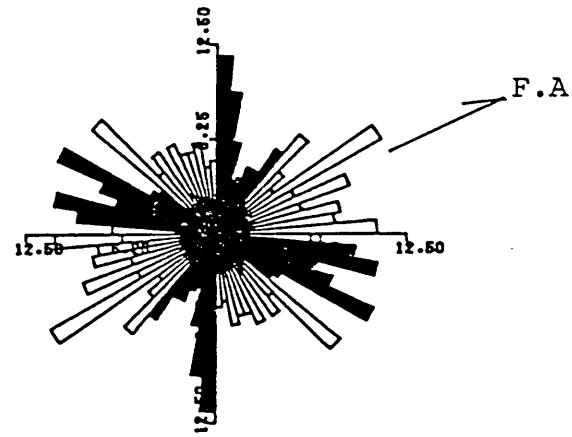
A- R.F.F.



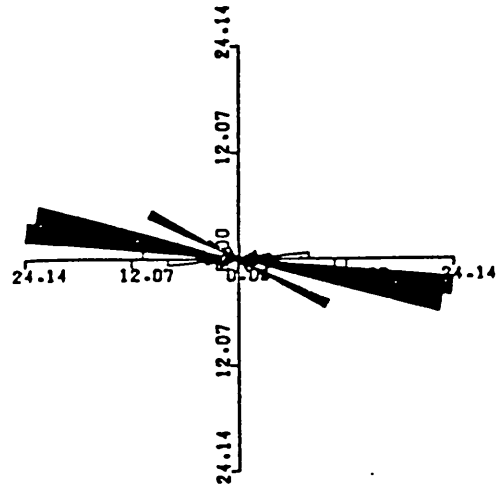
B- Integrated



C- R.F.L.



D- Av.F.L.



E- R.F.E.

Fig. 4.22 Abu Rawash area rose diagrams.

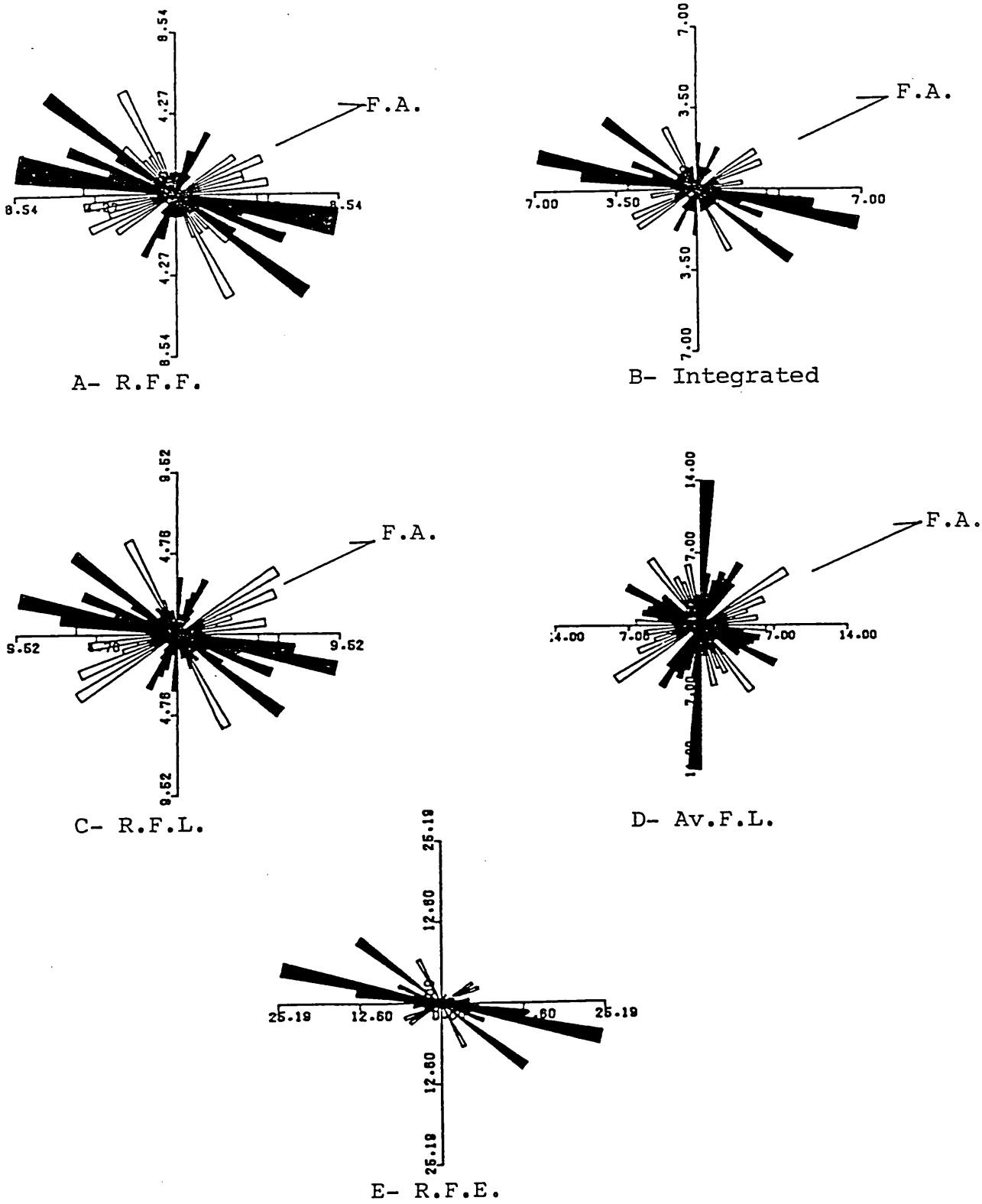


Fig. 4.23 Gaa-Abu Rawash village pericline rose diagrams.

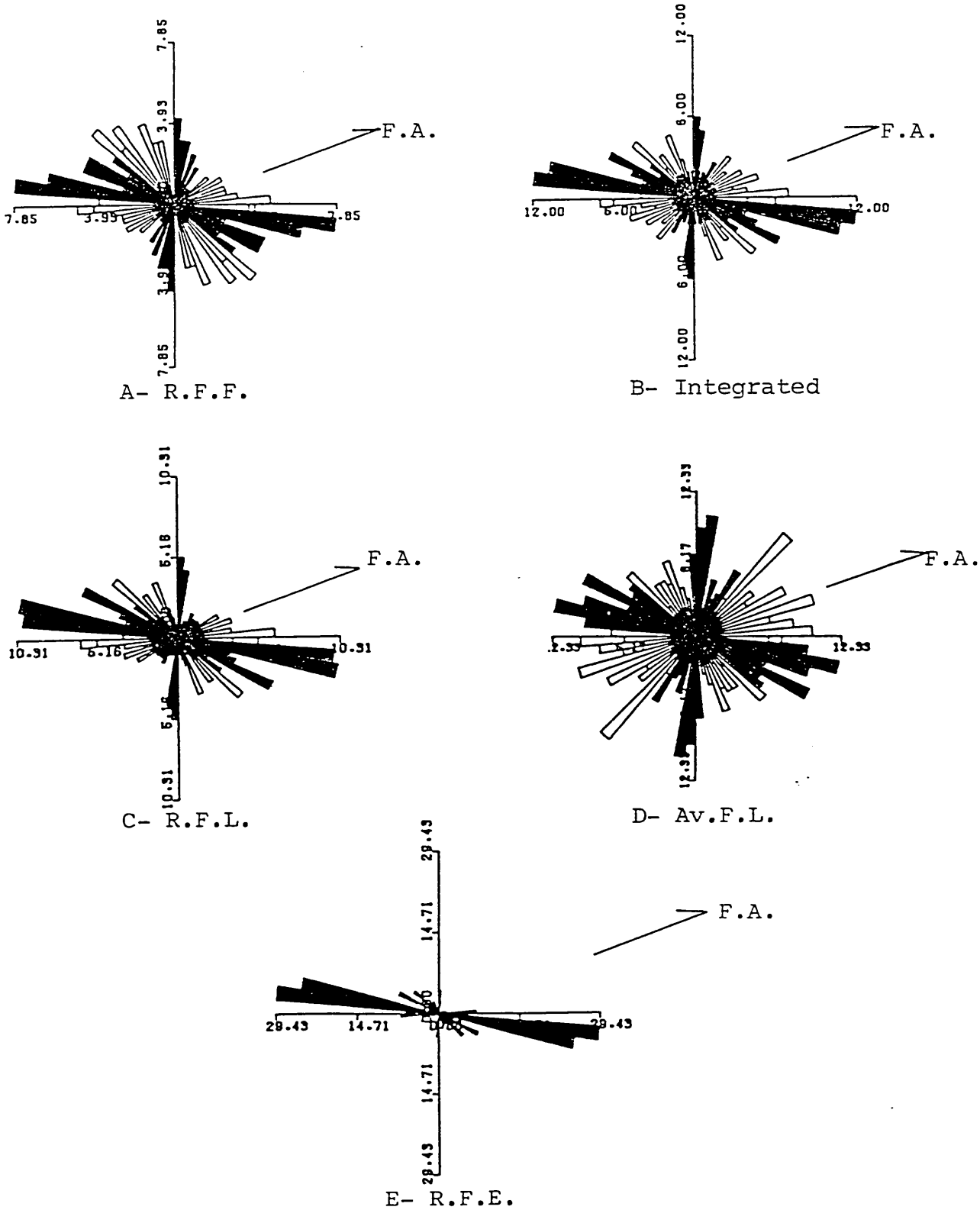


Fig. 4.24 Wadi El Talun-Sudr El Khamis folding rose diagrams.

Table 4.3

The Prominent Trends of Abu Rawash Area Rose Diagrams

Abu Rawash Area (Fig. 4.25)		R.F.Frequency Rose Diagram	%	Integrated F.F. Rose Diagram	%	R.F. Length Rose Diagram	%	Av. F. Length Rose Diagram	%	R.F. Energy Rose Diagram	%
Prominent Directions	1	N80 - 85W	7.1	N75 - 80W	8.1	N75 - 80W	9.0	N55 - 60E	4.9	N80 - 85W	24.1
	2	N85 - 90W	6.6	N80 - 85W	8.1	N80 - 85W	8.7	N 0 - 5E	4.6	N75 - 80W	23.2
	3	N75 - 80W	6.3	N85 - 90W	7.0	N60 - 65W	7.2	N60 - 65W	4.5	N55 - 60W	11.1
	4	N55 - 60W	5.8	N60 - 65W	7.0	N85 - 90E	6.3	N75 - 80W	4.3	N85 - 90W	10.8
	5	N60 - 65W	4.7	N85 - 90E	6.0	N85 - 90W	6.0	N45 - 50W	4.2	N60 - 65W	8.7
	6			N80 - 85E	5.0			N85 - 90W	4.2	N85 - 90E	7.9
				N55 - 60W	5.0						

Table 4.4

The Prominent Trends of Gaa-Abu Rawash Village Pericline Rose Diagrams

Gaa Abu Rawash Village Pericline (Fig. 4.26)		R.F.Frequency Rose Diagram	%	Integrated F.F. Rose Diagram	%	R.F. Length Rose Diagram	%	Av. F. Length Rose Diagram	%	R.F. Energy Rose Diagram	%
Prominant Directions	1	N75 - 85W	17.0	N75 - 80W	13.0	N75 - 80W	9.5	N 0 - 5E	9.3	N75 - 80W	25.2
	2	N50 - 55W	8.5	N50 - 55W	9.3	N50 - 55W	7.6	N55 - 60E	6.4	N50 - 55W	16.1
	3	N25 - 30W	6.1	N80 - 85W	9.3	N80 - 85W	6.9	N35 - 40W	5.3	N80 - 85W	13.2
	4	N65 - 70W	6.1	N55 - 60E	5.6	N55 - 60E	6.9	N60 - 65W	5.3	N25 - 30W	7.6
	5	N65 - 70E	4.9	N65 - 70E	5.6	N65 - 70E	6.2	N30 - 35E	4.6	N65 - 70W	7.0
	6	N80 - 85E	4.9	N25 - 30W	5.6	N25 - 30W	6.2	N65 - 70E	4.3	N65 - 70E	6.1
	7	N85 - 90W	4.9	N65 - 70W	5.6						
				N85 - 90W	5.6						

Table 4.5

The Prominent Trends of Wadi El Talun-Sudr El Khamis Folding Rose Diagrams

Wadi El Talun Sudr El Khamis Folding (Fig. 4.27)		R.F.Frequency Rose Diagram	%	Integrated F.F. Rose Diagram	%	R.F. Length Rose Diagram	%	Av. F. Length Rose Diagram	%	R.F. Energy Rose Diagram	%
Prominent Directions	1	N80 - 85W	7.9	N80 - 85W	9.2	N75 - 80W	10.3	N75 - 80W	5.3	N80 - 85W	29.4
	2	N75 - 80W	6.3	N75 - 80W	8.4	N80 - 85W	10.0	N40 - 45E	5.0	N75 - 80W	25.2
	3	N45 - 50W	5.2	N85 - 90E	5.3	N60 - 65W	6.7	N60 - 65W	4.6	N60 - 65W	8.0
	4	N60 - 70W	9.4	N60 - 65W	5.3	N85 - 90E	6.2	N70 - 75E	4.5	N85 - 90E	6.8
	5	N35 - 40W	4.7	N 0 - 5E	4.6	N45 - 50W	5.4	N 5 - 10E	4.5	N45 - 50W	5.8
	6	N85 - 90E	4.7	N45 - 50W	4.6	N 0 - 5E	5.2	N70 - 75W	4.3	N 0 - 5E	4.2
	7	N 0 - 5E	4.2	N 5 - 10E	3.8	N 5 - 10E	4.3	N85 - 90E	4.3	N20 - 25W	2.3
	8	N20 - 25W	4.2	N70 - 75E	3.8	N65 - 70W	4.0	N80 - 85W	4.1		
	9			N20 - 25W	3.8						
	10			N65 - 70W	3.8						

R.F. = Relative Fracture or Percentage
F.F. = Fracture Frequency
Av.F.= Average Fracture

Comparison of rose diagrams

The numerical comparisons between most of the rose diagrams of each structure have been summarized in the following table.

Table 4.6

Correlation Coefficients Between Rose Diagrams (Aerial Photographs)

Locality of the Rose Diagrams	R.F.F./ R.F.L.	R.F.F./ R.Av.F.L.	R.F.F./ R.F.E.	R.F.L R.F.E.	R.Av.F.L./ R.F.E.
Abu Rawash area	0.899	0.323	0.825	0.912	0.440
Abu Rawash village pericline	0.922	0.328	0.845	0.854	0.211
Hassana dome	0.913	0.753	0.711	0.880	0.550
El Ghigiga dome	0.926	0.345	0.792	0.872	0.337
W.Talun-Sudr El Khamis folds	0.901	0.542	0.736	0.867	0.487

R.F.F. = Relative Fracture Frequency

R.F.L. = Relative Fracture Length

R.F.E. = Relative Fracture Energy

R.Av.F.L. = Relative Average Fracture Length

This table demonstrates the following:

1. An excellent relationship is found between i) relative fracture frequency and relative fracture length rose diagrams, ii) relative fracture length and relative fracture energy rose diagrams and, iii)

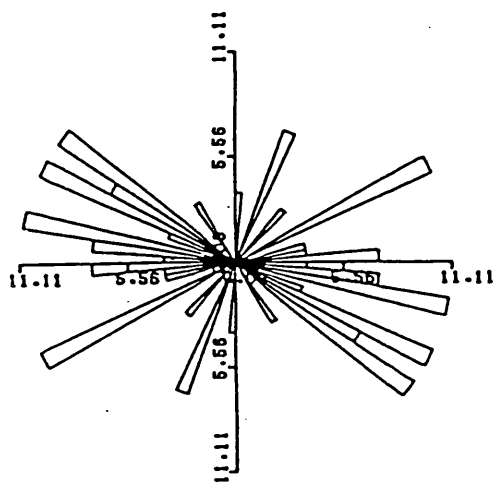
relative fracture frequency and relative fracture energy rose diagrams.

2. A relatively poor relationship is found between i) relative average fracture length and relative fracture energy rose diagrams and ii) relative average fracture length and relative fracture frequency and in turn, relative fracture length rose diagrams.

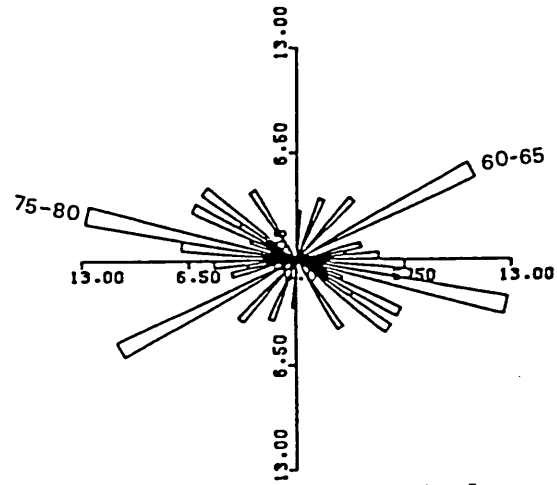
B. The domal structure directional rose diagrams of both El Hassana and El Ghigiga are represented in Figs. 4.25 and 4.26, where the prominent trends are clearly shown.

In this analysis, only the integrated and relative fracture energy rose diagrams were considered. The former rose diagrams give comprehensive views of more than one quantitative fracture aspect, while the latter rose diagrams, relative fracture energy, present fault trends. These fault trends will enhance or have enhanced the fracture traces of the same class interval. So, comparing the integrated rose diagram with the relative fracture energy rose diagram will locate the class intervals which have been enhanced due to faults.

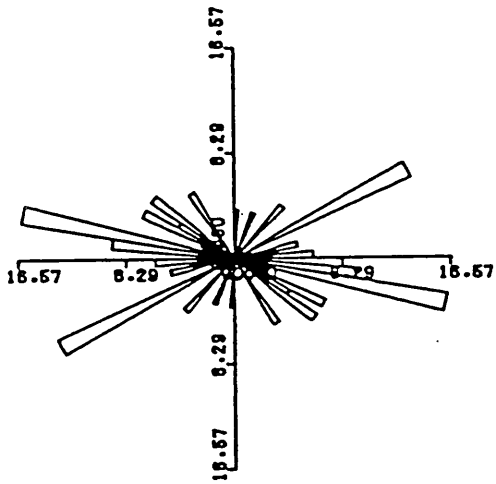
With respect to the relative fracture energy rose diagram of El Hassana dome (Fig. 4.25E), the prominent trends are N75^{o} - 80°W and N60^{o} - 65°E. According to what was mentioned before, these two trends will enhance the fracture traces of the same class interval as indicated in Fig. 4.25B. This means that the fracture



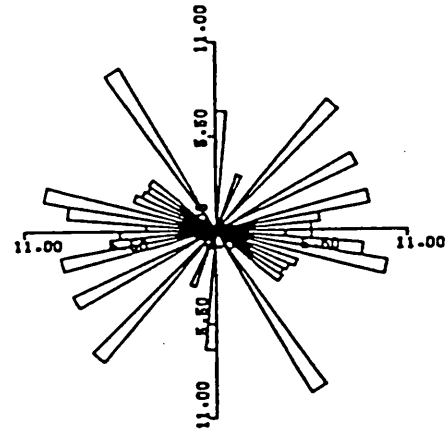
A- R.F.F.



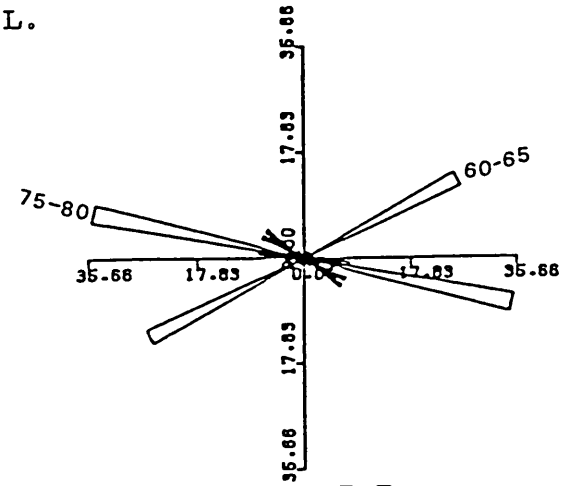
B- Integrated



C- R.F.L.

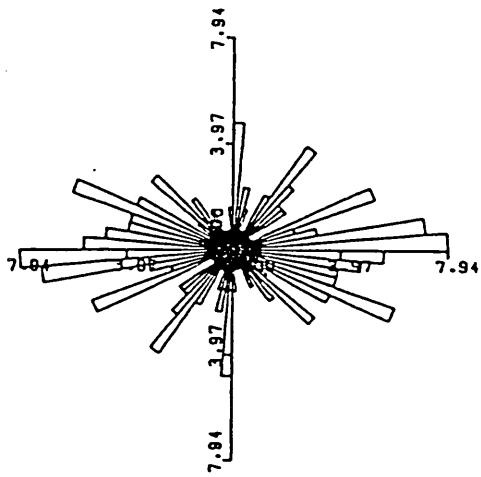


D- Av.F.L.

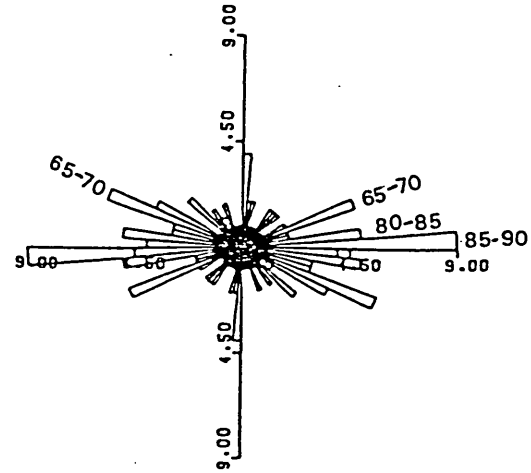


E- R.F.E.

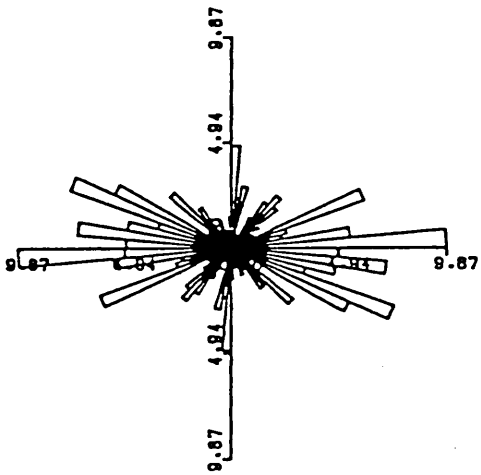
Fig. 4.25 Hassana dome rose diagrams.



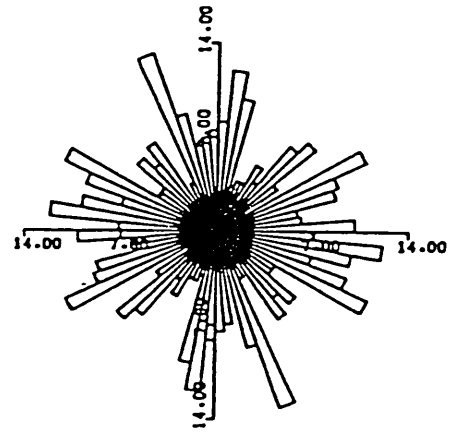
A- R.F.F.



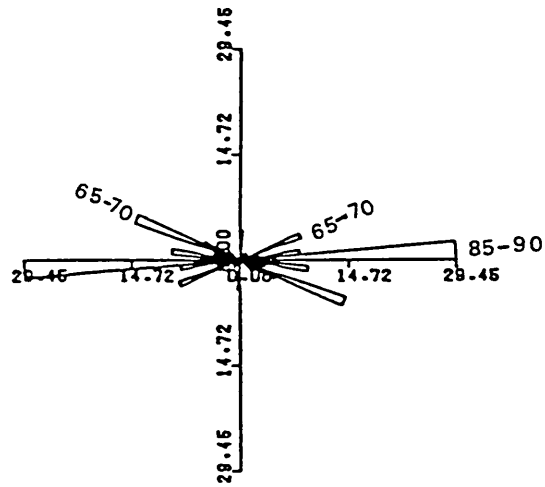
B- Integrated



C- R.F.L.



D- Av. F.L.



E- R.F.E.

Fig. 4.26 Ghigiga dome rose diagrams.

trace pattern of Fig. 4.25B is a radial pattern, and the anomaly in both N60° - 65°E and N75° - 80°W class intervals is due to faults.

Applying the same principles to the integrated and relative fracture energy of El Ghigiga dome, one can fairly say that the fracture pattern of Fig. 4.26B is a radial pattern. But the fault trends, as indicated in Fig. 4.26E, enhanced the fracture traces of the same class interval as shown in Fig. 4.26B.

4.8.3 The Analysis of the Rose Diagram Maps

In this analysis, the directional class intervals and the percentage of these class intervals were considered.

a. Fracture frequency and integrated rose diagram maps

The analysis of these two rose diagram maps (Figs. 4.27 and 4.28) shows the following:

i. The prominent trends are generally NW.

ii. The N - S fractures increased towards the SW, where the folding structure of both Sudr El Khamis syncline and Wadi El Talun anticline lie (Fig. 4.28).

iii. The NE or ENE fracture traces decreased towards the SW.

iv. Nearly E - W fracture traces increased towards the SW, where the Eocene beds are present.

b. Relative fracture energy rose diagram map

The analysis of this map (Fig. 4.29) shows:

1- Gaa-Abu Rawash village pericline
2- Hassana dome
3- Ghigiga dome
4- Talun-Sudr El Khamis folds

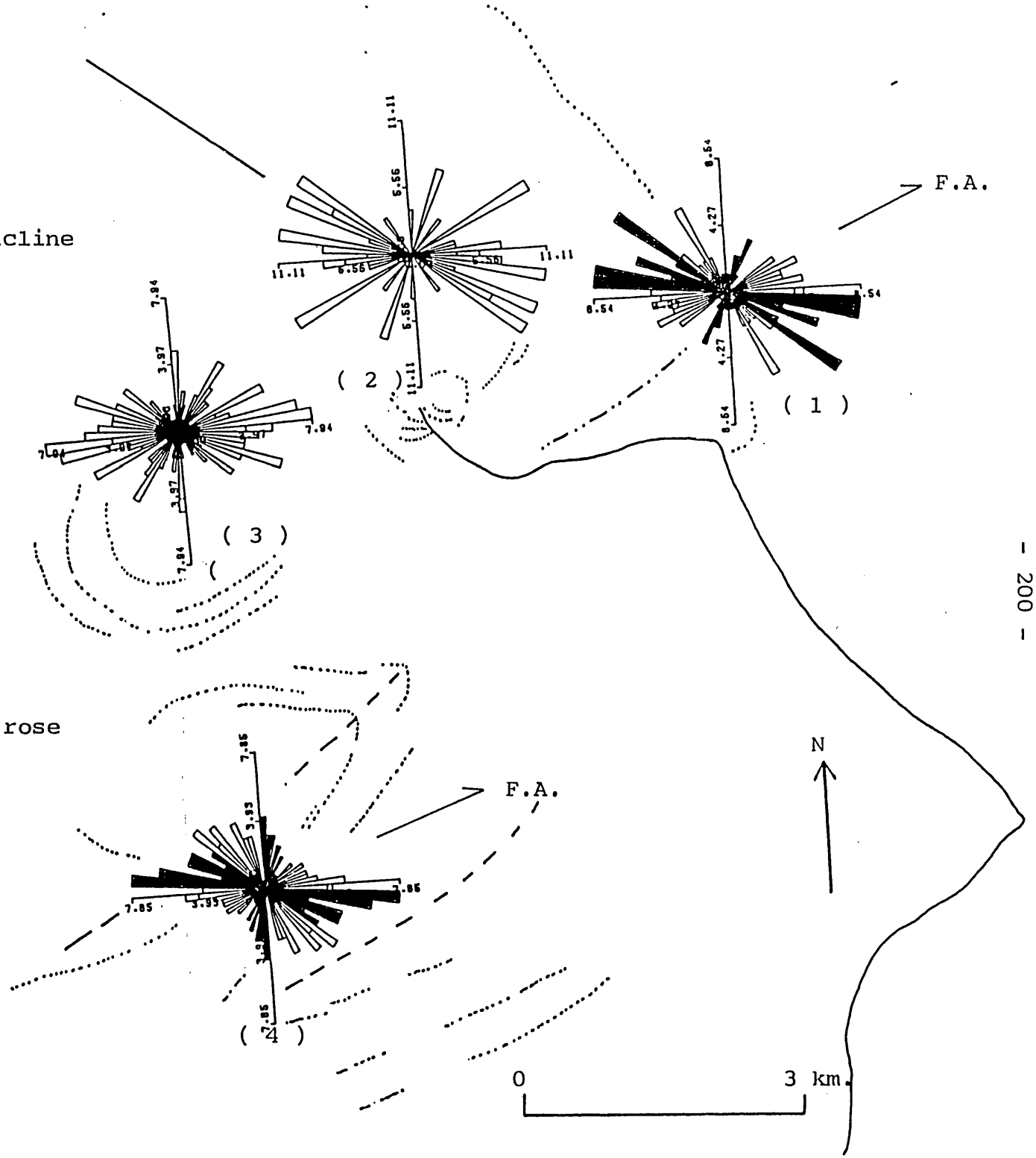


Fig. 4.27

Relative Fracture Frequency rose diagram map.

1- Gaa-Abu Rawash village pericline
2- Hassana dome
3- Ghigiga dome
4- Talun-Sudr El Khamis folds

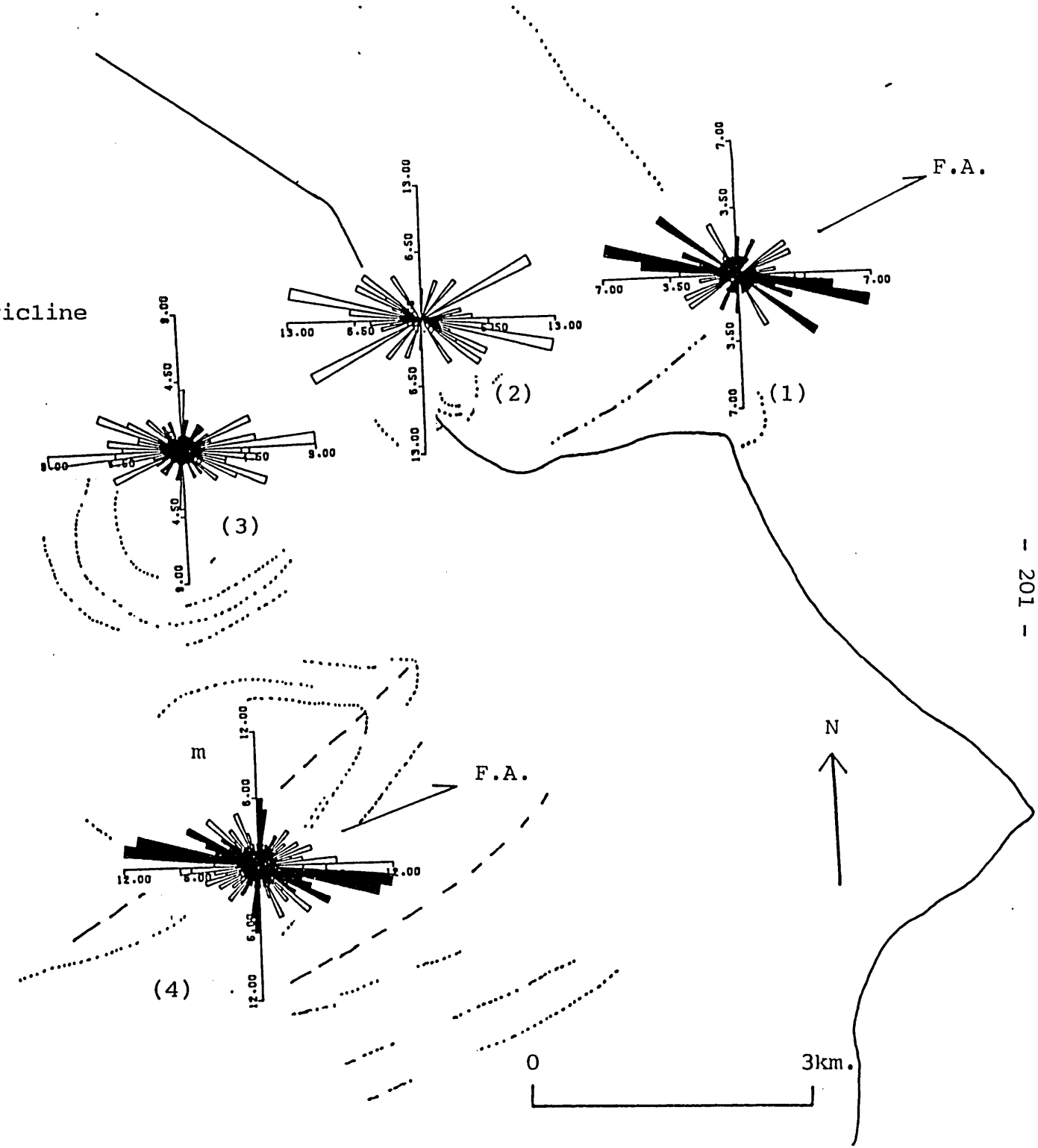


Fig. 4.28

Integrated rose diagram map.

1- Gaa-Abu Rawash village pericline
2- Hassana dome
3- Ghigiga dome
4- Talun-Sudr El Khamis folds

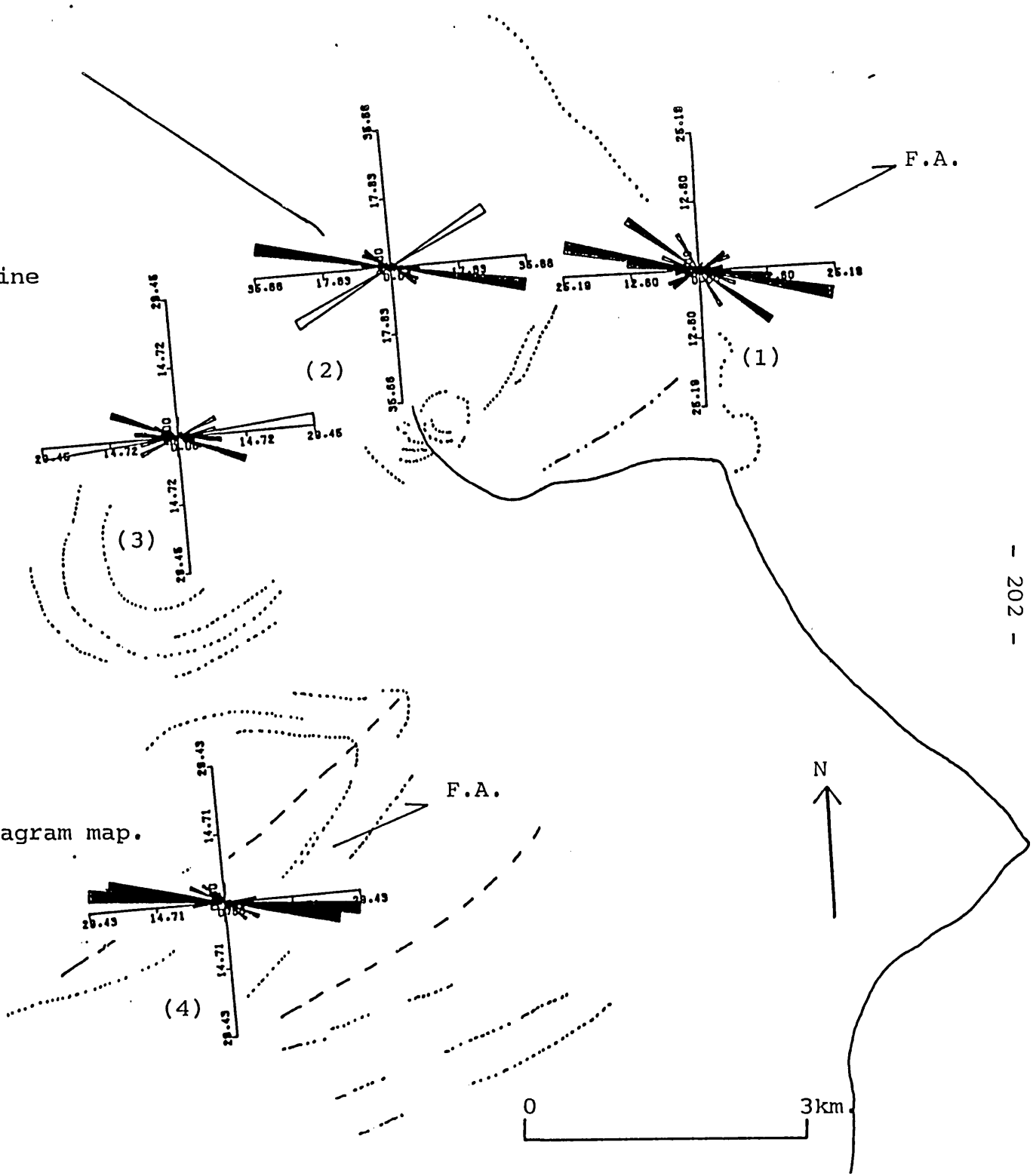


Fig. 4.29

Relative fracture energy rose diagram map.

i. The WNW fracture traces have the maximum fracture energy (the prominent trend).

ii. The fracture energy of the N - S fracture traces, or the N - S trend increased towards the SW.

iii. The fracture energy of the NE or ENE fracture traces decreased or dies out towards the SW.

c. Fracture density rose diagram map

The results of the analysis of this map (Fig. 4.30) are:

i. The tension fractures (white colour or T) become short in length towards the SW.

ii. The N - S shear fractures (black colour or S) become long in length towards the SW; El Hassana dome has been excluded.

iii. Nearly E - W trend becomes long in length towards the SW.

iv. $N50^{o}$ - $55^{o}W$ shear that fractures (black colour or S) are longer in the NE area (Gaa-Abu Rawash pericline) than in the SW area (at El Talun-Sudr El Khamis folds).

v. The NNE shear fractures (black colour or S) become very short in length towards the NE (at Gaa-Abu Rawash village pericline).

d. Average fracture density rose diagram map

The analysis of this map (Fig. 4.31) confirms or corrects the results of the analysis of the previous map

1- Gaa-Abu Rawash village pericline

2- Hassana dome

3- Ghigiga dome

4- Talun-Sudr El Khamis folds

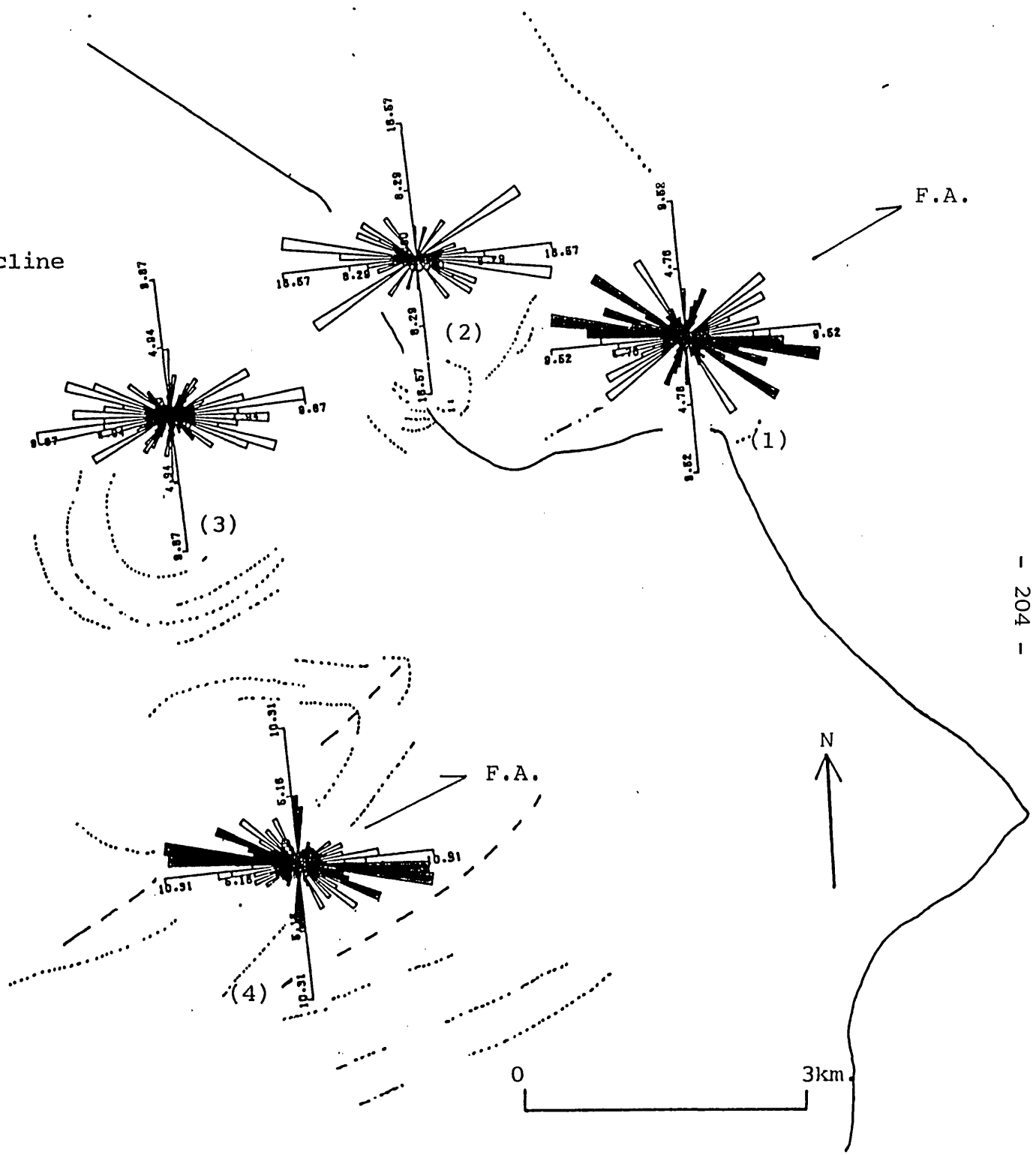


Fig. 4.30

Relative fracture density rose diagram map.

1- Gaa-Abu Rawash village pericline
2- Hassana dome
3- Ghigiga dome
4- Talun-Sudr El Khamis folds

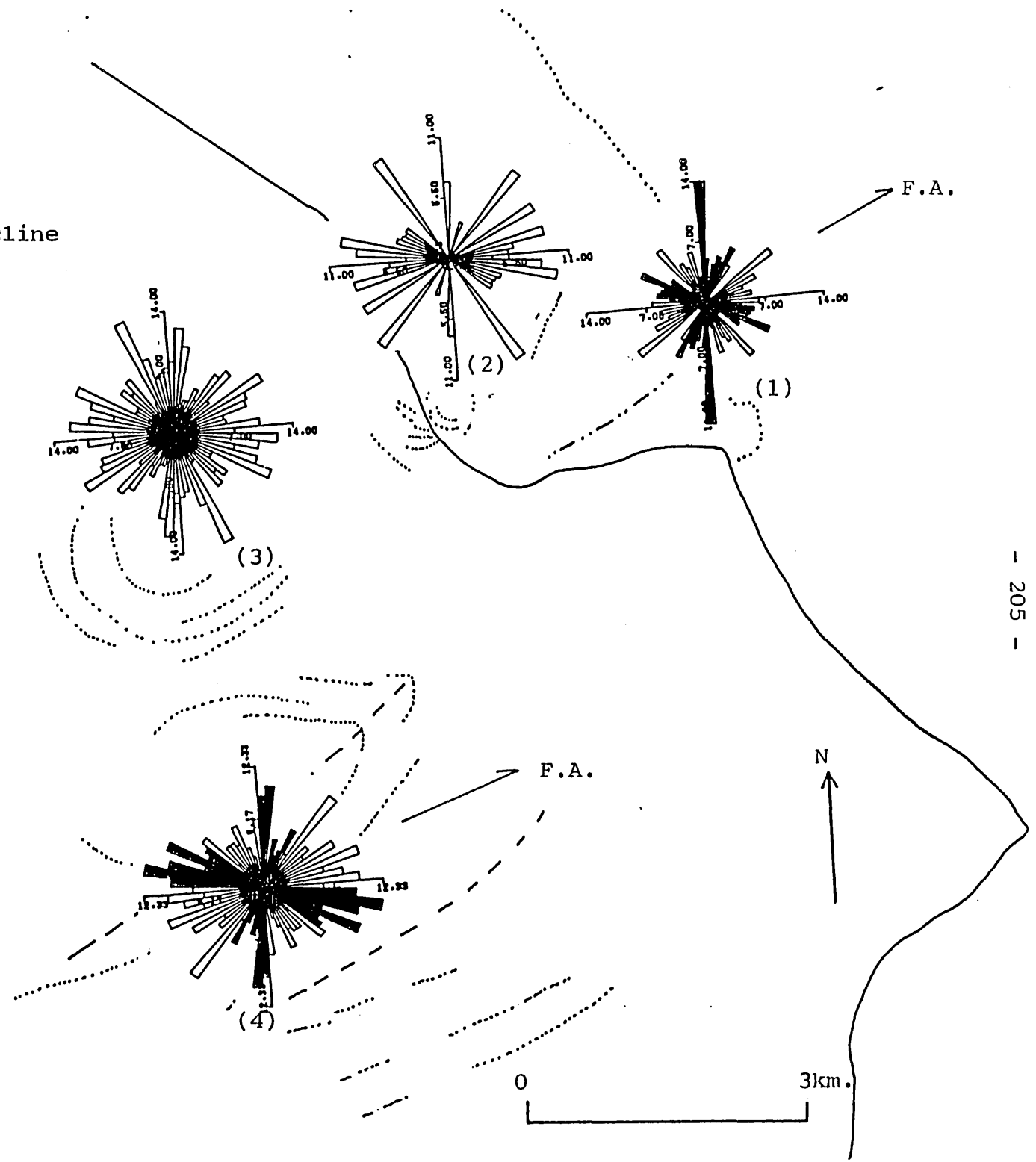


Fig. 4.31

Average fracture density rose diagram map.

(Fig. 4.30). The analysis of this map (Fig. 4.31) demonstrates the following:

i. The WNW to nearly E - W fracture traces are longer in the SW area (at El Talun-Sudr El Khamis folds), than in the NE area.

ii. The N - S shear fractures in the NE area (Gaa-Abu Rawash village pericline) are few but relatively long with respect to those in the SW at Wadi El Talun-Sudr El Khamis plunging folds.

iii. The NE tension fractures in the SW area are few but relatively long with respect to the NE area.

iv. The NW shear fractures at the SW area are relatively few but longer than those in the NE area.

v. The diagrams of the map, as shown in Fig. 4.31, have a good relationship to the structures present in the studied area.

vi. The diagrams of both Gaa-Abu Rawash village pericline and Wadi El Talun-Sudr El Khamis plunging folds, anticline and syncline respectively, reflect the geometry of these structures where the longitudinal fracture traces parallel to the fold axis, are generally longer than the cross fracture traces.

4.8.4 The analysis of Histograms derived from the integrated model

The histograms, which have been prepared from the integrated data (Fig. 4.32) show the following:

a. In the studied area, the deformation is heterogeneous.

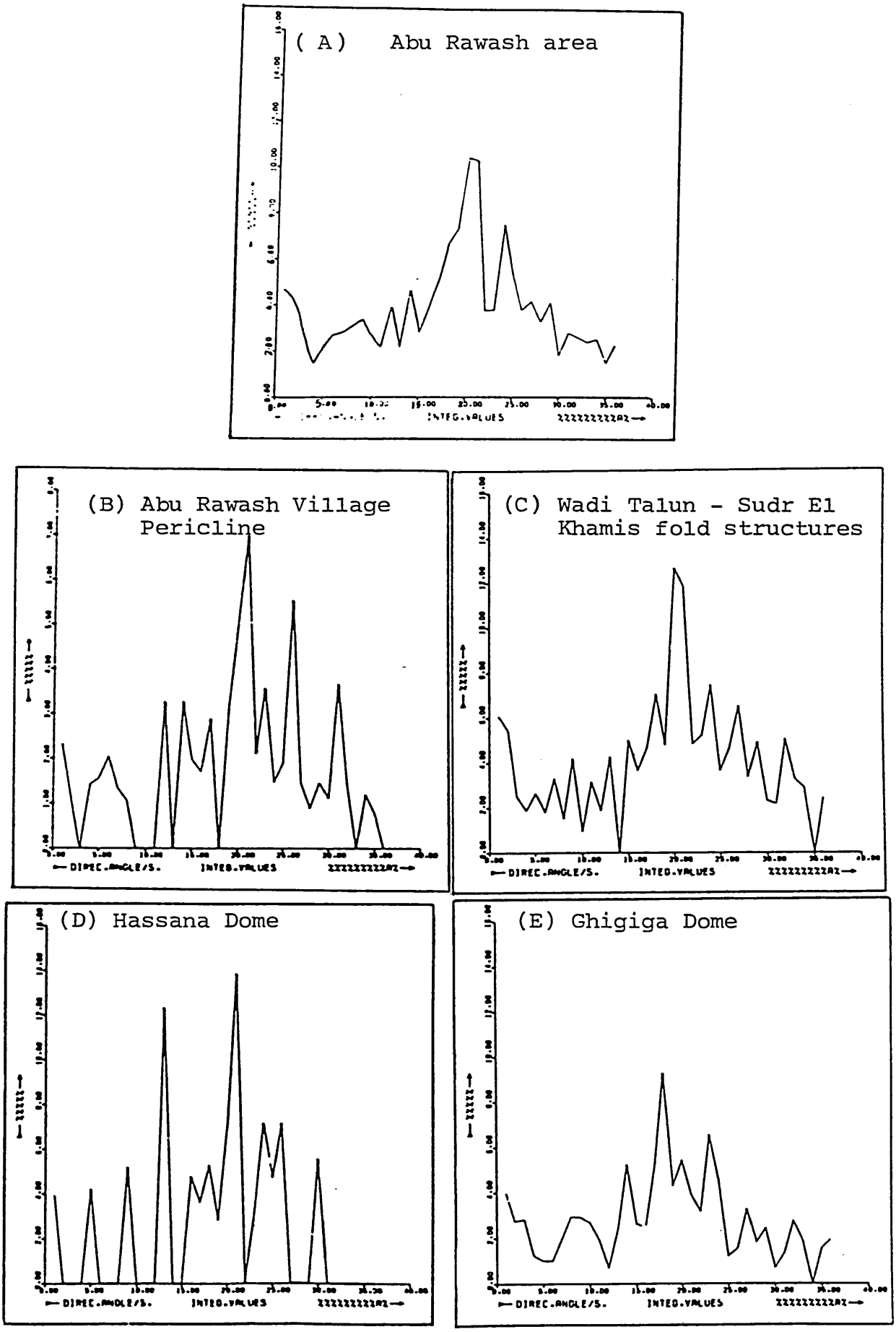


Fig. 4.32 Integrated Histograms.

b. The domal structures (Fig. 4.32D and E) become more obvious.

c. These domal structures (Fig. 4.32D and E) are disturbed to some extent by their neighbouring structures (Fig. 4.32b and c, respectively).

d. The histogram of the whole area (Fig. 4.32a) is quite different from other local structures presented in the same figure.

CHAPTER FIVE

LANDSAT IMAGERY STUDY

CHAPTER FIVE

Landsat Imagery Study

5.1 Introduction

The study presented in this chapter examines the potential and usefulness of satellite images in a structural analysis of the Northern Western Desert of Egypt.

This study is concerned with identification of lineaments, patterns and some circular or elliptical features which are manifest on Landsat images of various scales and different bands and their relationship to structural and stratigraphic anomalies.

Straight and curved alignments or tonal contrast are identified from various bands as probable fractures and herein defined as lineaments. Most lineaments appear as tonal variation or contrast and portray no obvious evidence of movement, either vertical or horizontal. These lineaments may be propagated vertically from their point of origin towards the surface throughout the geological history.

Some lineaments transect major geologic features such as mountain ranges and basins, without any significant change in their azimuth. These lineaments might be related to geodynamic forces connected with plate tectonics. Alternatively, some local structures such as folds, old impact or other phenomena may be related to or outlined by the azimuth directions of certain regional sets of lineaments. Sometimes these

lineaments have been coincident with magnetic lineaments whose source may be associated with deep-seated basement rocks and/or basic dykes.

The factors affecting the interpretation of Landsat images, including such objective, subjective and seasonal factors have been considered during the course of this study. But as we shall see, the sun azimuth seems to cause, or in part causes, a misrepresentation of the NW lineaments. To overcome the problem of incorrect representation, a Weighted Technique was applied to give, to a certain extent, weight or enhance those misrepresented rays or class intervals.

The methods of presentation and statistical analysis are much the same as in the aerial photographs' study.

The structural analysis of lineaments or fractures was undertaken empirically by comparing the lineaments with published experimental and theoretical models, especially Price's theoretical model (1974), coupled with a model derived from the field data as well as the trends of the basins and uplifts of the different isopach maps, which will be analysed in the next chapter. This analysis was used in broader interpretation of the structural history of the Northern Western Desert during the upper Cretaceous and the end of the Miocene. These analyses will be verified in the next three chapters.

Circular features detected during the course of this study have been related to mapped structures, such as synclines and anticlines, or the basins and uplifts of the isopach maps or gravity anomalies.

It was noticed in the literature that the principal points of the compass, such as the cardinal or cardinal subdivision points, have been used to express the approximate structural trends. So the writer here indicated the trends by both the compass points as well as the principal points of the compass (as an approximation).

5.2 Images Used in this Study

The electromagnetic radiation which is reflected or scattered by an object is detected by remote-sensing systems at different wave lengths or spectral bands which are shown in the following table.

Table 5.1

Spectral Bands Used in the Study

MSS Band	Colour	Wave Length UM	Colour Normally Used for Projection
4	Green	0.5 - 0.6	Blue
5	Red	0.6 - 0.7	Green
6	Photo 1R	0.7 - 0.8	Red
7	Photo 1R	0.8 - 1.1	Red

Variation in intensity of the electromagnetic waves are expressed as variations in brightness on the black and white images. This brightness could approximately be determined by the magnitude of the response produced in

the eye by visible light. The image contrast can be defined as follows:

$$C_r = \frac{B_{max}}{B_{min}}$$

where C_r is the image contrast ratio, B_{max} is maximum brightness of the scene and B_{min} is minimum brightness of the same scene (Fig. 5.1).

The spatial resolution of the Landsat images ranges from about 200 to 250 metres. Smaller features can be detected, such as canals, where the contrast is optimum (Sabins, 1978).

In this study, the standard 70mm negatives derived from the computer compatible tape (CCT) as a direct production of MSS were used to produce the 1:1000,000 images of the different spectral bands. These images were photographically enhanced (contrast enhancement) by the author, using a scanning device at the Departmental Photography Section, but they lack the advantages of digital enhancement techniques. The later techniques require the presence of the computer compatible tapes which were not available to the writer. The geographical locations of these images are represented in Fig. 5.2.

The colour composite images (1:500,000) were also used in the study. These images are a combination of bands 4, 5 and 7, respectively. These images have the spectral colour characteristics of an infra-red (IR) colour photograph. The following table shows the colour signature of the composite images on the ground (Sabins, 1978).

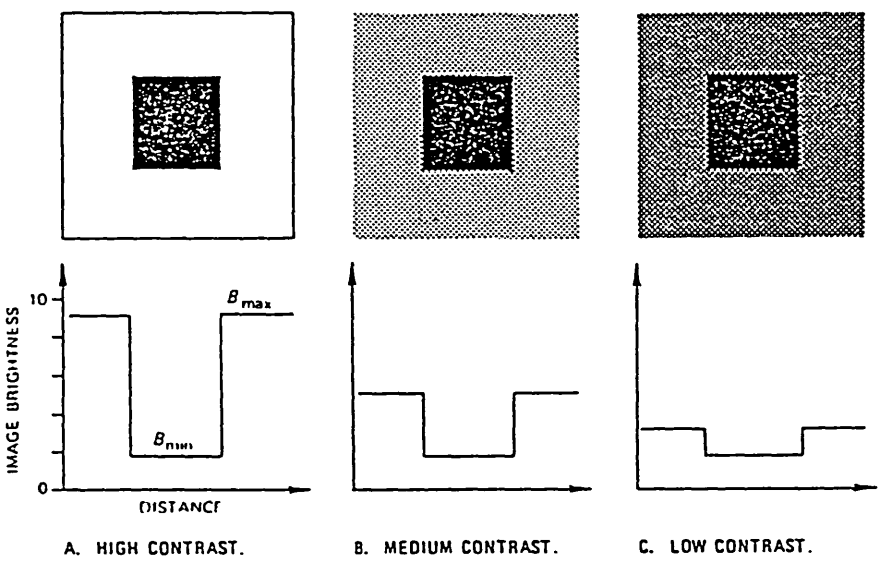


Fig. 5.1 Images of different contrast ratio with corresponding brightness profiles.

(After Sabins, 1978)

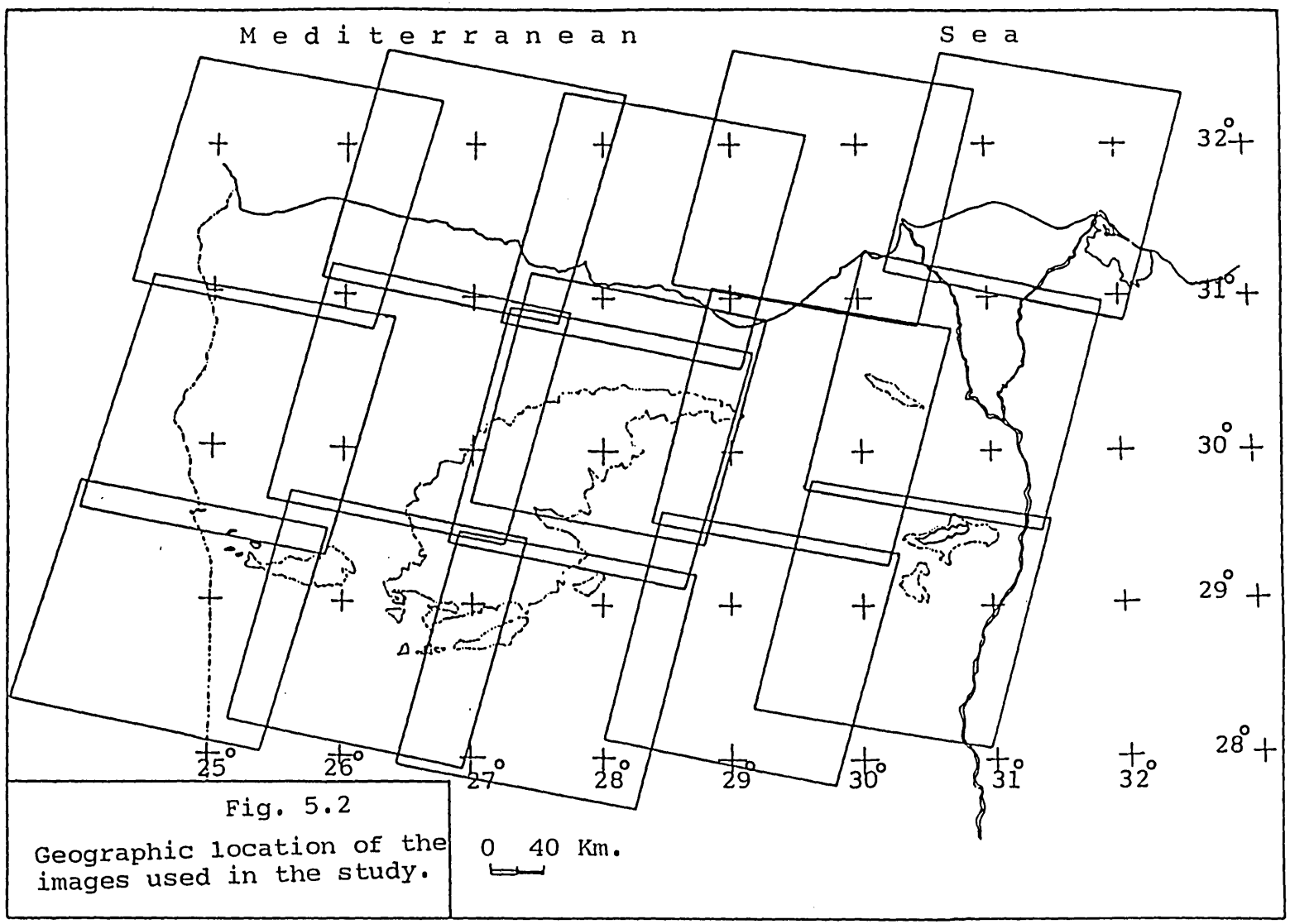


Fig. 5.2

Geographic location of the images used in the study.

Table 5.2

Colour Composite Images and True Colours They Represent On the Ground

Objects' Colour On the Ground	Colour On False Coloured Images
Vegetation	Red
Water	Dark blue
Suspended sediments	White to light blue
Red beds	Yellow
Limestone	Blue
Bare soil	Blue
Eolian sand (dunes)	White to yellow
Cities (urban)	Blue
Clouds and snow	White

5.3 Factors Affecting the Interpretation of Landsat Images

Several factors which influence or control image interpretation have been discussed by Chukwu-Ike (1977) and Al-Khatib (1981). These factors have been considered during the course of interpretation and generally classified into:

1. Objective factors, such as scale of an image, resolution, quality of images and techniques of image viewing;

2. Subjective factors, such as psychological factors, physiological factors, human bias and repetitive interpretation;

3. Seasonal factors, such as sun angle and azimuth, soil moisture, temperature, rainfall, cloud coverage and winds and dust storms.

5.4 Lineaments

Lineaments are one of the most prominent geological features interpretable from Landsat images. Hobbs (1904, 1912), quoted by O'Leary et al (1979), defined lineaments as the significant lines of landscape which reveal the hidden architecture of the basement rocks. Sonder (1938), quoted by O'Leary et al (1979), gave the lineament the following meaning: "The lineament of a region denotes a definite direction which is contained in the tectonics, jointing and the relief." O'Leary, Friedman and Pohn (1979) define the lineament as a mappable simple or composite linear feature of a surface whose parts are aligned in straight or slightly curving relationship and which differs distinctly from the patterns of adjacent features and presumably reflects a subsurface phenomenon. Lineaments are manifest at the surface in many diverse ways, as by single large faults or groups of faults subparallel with the lineament trend, by en echelon alignment of oblique fault and fold belts, by large monoclines and by juxtaposition of alignments of contrasting structures and lithologies. These are commonly, but not necessarily, expressed topographically. Some lineaments appear to be defined by lines of igneous intrusive or extrusive centres or alignments of ore bodies or brine springs. Others are revealed by regional

gravity and magnetic patterns related to subsurface rocks.

On the images, the lineaments show up as a geomorphic expression such as straight stream valleys and aligned segments of valleys, or tonal expression such as straight boundary between areas of contrasting tone or a stripe against a background of contrasting tone. Differences in vegetation, moisture content and soil or rock composition account for most tonal contrasts. When lineament is covered by sediments, the clarity of the feature on the images diminished. Lineament traces commonly are interrupted or discontinuous. This discontinuity could be attributed to:

1. burial by younger sediments;

2. local effects in the younger sediments, caused by repeated movements along continuous deep or concealed lineament;

3. topography of the terrain (relief);

4. strike-slip faults with a limited vertical component of movements at the present surface produced topographic relief less detectable than that commonly produced by normal faults;

5. defects in the standard production of satellite images, caused by misrepresentation of their, or some of their original digital values.

Generally, digital image enhancement which is outside the scope of this study, modifies the image or distorts the original digital values of the standard

image or production to give a good visual impact on the viewer.

With respect to the length of the lineaments, Lattman (1958) suggested the terms "lineament" and "mega lineament" for fracture traces over one mile (>1.6 km.) and twenty miles (>32 km.) in length, respectively. El ETR (1976) proposed a length ranging from 10 km. up to 100 km. and over 100 km. for lineament and mega-lineament, respectively.

On the basis of their length, lineaments were classified by Wertz (1976) into:

a. Continental (>500 km. in length);

b. Regional (50 km. - 500 km. in length);

c. Local (5 km. - 50 km. in length).

But Katterfeld (1979) classified lineaments as: global, regional and local. Furthermore, he considered that global and regional lineaments are parallel sets, while local ones are non-systematic and can be referred to local tectonic disturbances.

The present writer does not agree with those authors who classify the lineaments into regional or local, depending upon their manifest length on the images. The writer's experience during this study confirms that some regional lineaments may be disrupted or partially concealed or destroyed because of later tectonics and accompanied structures, along with the other causes previously mentioned. Also, if the sedimentary section has a competency comparable with that of the underlying basement, then fracture in the basement may be propagated

up into the sedimentary section. But, if the sedimentary section is less competent than the basement, then the structures in the sedimentary cover would differ from those of the basement. So the writer believes that classification of the lineaments either as local or regional must depend on or be supported by local or regional structural features from surface or subsurface geology or geophysical studies.

5.5 Circular Features

Circular and elliptical features are common in Landsat images. Their cause or origin are often uncertain.

Oval features of different sizes could be attributed (Dolivo-Dobrovol'sky and Strelnikov (1976) to:

1. folded belts framing volcano-plutonic system;
2. development of structures related to metamorphic and ultrametamorphic transformation and connected with the latter; these structures are larger than those connected with volcanic plutonic structures;
3. regions of inherited geoanticlinal development.

According to Peterson (1976), concentric arcs are associated with large domes and basins while ellipsoidal arcs are associated with grabens. In his view, the concentric and ellipsoidal features represent cone-shaped fractures caused by vertical forces; the intersection of a cone with the surface of the earth could form a circle or ellipse depending on the type of the cone and orientation of the cone and the intersection surface.

It has been quoted by Smith (1976) that the arcuate structures may be referred to:

1. meteoric impact which exerts control on later structure through tectonic heredity (Gallant, 1963; Cohenour and Sharp, 1968);

2. doming as a result of igneous intrusion and later collapse (Longwell, 1948 and Makin, 1960);

3. dragfolds along major strike slip-faults (Albers, 1967);

4. tectonic heredity from the crystalline basement.

Rowan and Wetlaufer (1975, quoted by Sabins (1978), assumed the circular and elliptical features of Nevada to be centres of igneous activity.

Chukwu-Ike (1977) attributed some circular features to domal structures and intrusions.

Circular features with large diameters ranging from tens to many hundreds of kilometers may be attributed to meteoric impact (Norman, Price and Chukwu-Ike, 1977).

Norman (1980) referred some circular features with a radius ranging from 5 - 10 kilometres to the following:

1. drape feature over resistant high igneous feature occurs at the boundary of the sedi-ments with the basement;

2. hydration of the anhydrite to gypsum causes an increase in the volume of 63%, to produce domes.

Al-Khatib (1981) attributed some small circular features, with radius ranges from 0.5 to 2.0 km. possibly to diapiric structures, while relatively large circular features with radius ranges from 10 to 30 km. to a

surface manifestation of a persistant basement topography and as a second possibility, to a salt diapirs of great size.

5.6 Preparation of Images for Analysis

The lineament interpretation presented here was obtained using images in form of prints.

A clear, smooth overlay was placed over each print on which one could trace or record the inferred lineaments. Attention was paid to handling images properly, avoiding their folding or artificial scratching or other defects which might later be mistaken for natural features.

5.7 Landsat Image Analysis and Interpretation

In the present study, Landsat images were interpreted in much the same manner as small scale aerial photographs or mosaics. The "eye-brain system" was used to search for simple patterns of features which are interpreted in terms of geology.

There are some advantages and disadvantages of Landsat images that should be emphasized:

1. Linear features caused by topography may be enhanced or suppressed on Landsat images according to their orientation, relative to the sun azimuth. Linear features trending normal or at high angle to the sun azimuth are enhanced by shadows and high lights. Those parallel to the azimuth are visually suppressed and difficult to recognize.

2. Linear features parallel to the MSS scan lines are difficult to recognize.

3. Repeated coverage of Landsat enables one to select images taken in that season which provides optimum information.

In this study, most of the images are free from cloud, which are particularly abundant in the rainy season (Fig. 5.3).

Differences of soil moisture along a lineament overshadow tonal differences. So relative humidity or soil moisture enhances tonal contrast and causes the lineament to be easily detected.

5.7.1 Interpretation Methods

During the course of interpretation, images were handled in different ways according to their size. Large size images (1:500,000) were laid down on the table and interpreted by looking at them from short or relatively long distances. Sometimes, the writer used different colour transparencies as well as the light table to enhance the tonal contrast of these images.

Small size images (1:1000,000) were held with an inclination away from the viewer and in different directions at angles ranging from 15° to 45° degrees.

Interpreted lineaments, which appear as linear tonal variations (even those which exhibited no obvious evidence of movement) were detected by these methods under suitable illumination conditions.

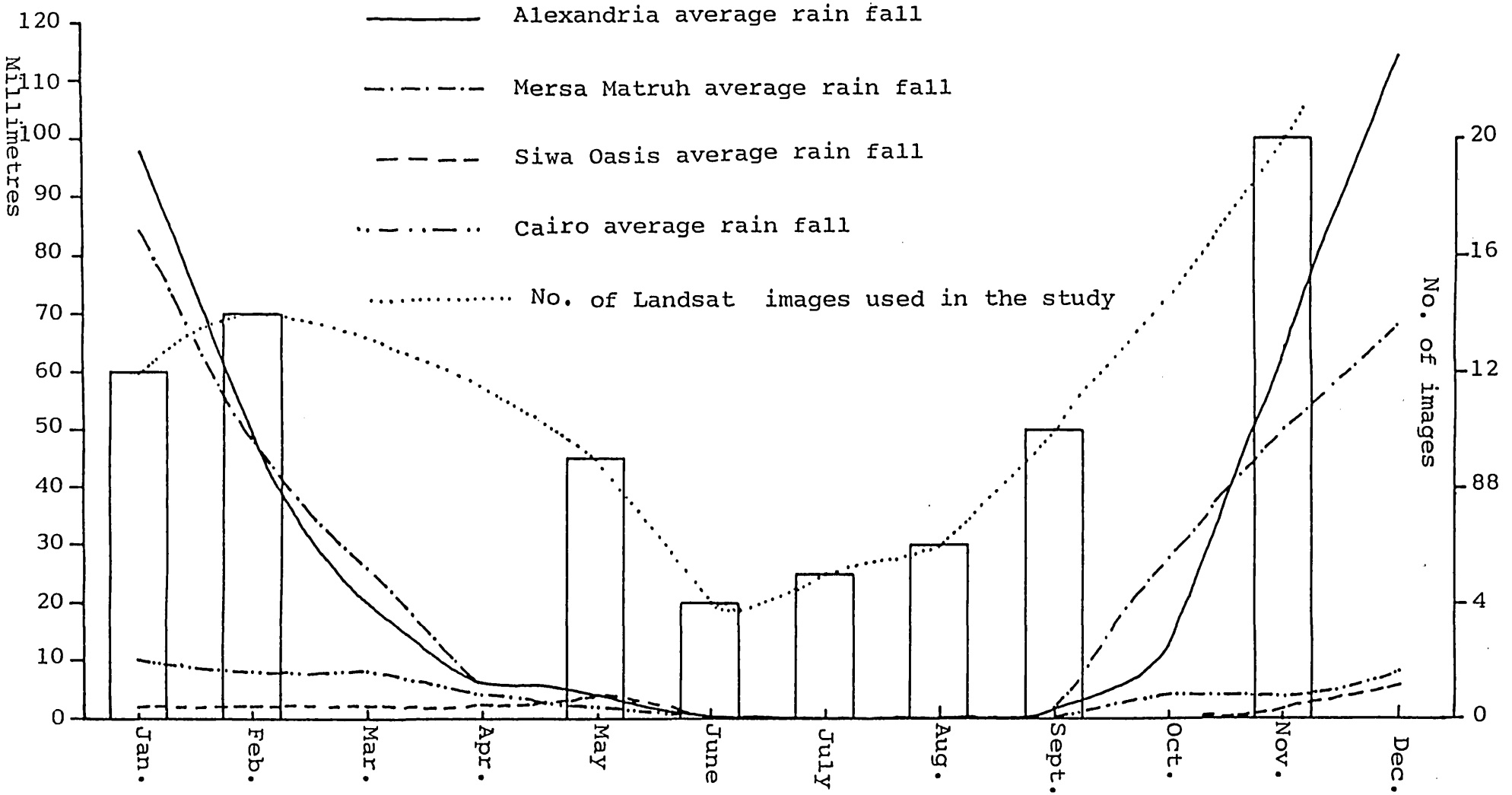


Fig. 5.3 Average rain fall and No. of Landsat images used in the study.

5.7.2 Detection of the Circular Features

The detection of circular or elliptical features in this area often required a considerable effort because these features usually have faint tonal contrast delineating their circumference.

These circular features, which have not been reported before, are potentially very important for this territory, as a region in which oil prospecting is active.

5.7.3 Handling and Presentation of the Data

Because of the large amount of information obtained from Landsat images, a data processing system was used. The D-Mac digitizer has been used to convert a graphical or photographically recorded image into a numerical form. In this study, the lineaments, as well as the fracture traces, have been digitized, using the technique described below:

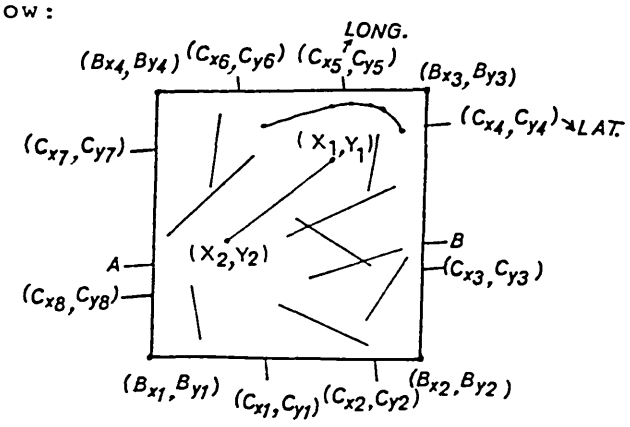


Fig. 5.4: The process of digitization

1. After the interpretaion of each image, the frame of the image was drawn and the different annotations were recorded on the overlay.

2. Each overlay was fastened on the table of the digitizer and covered by another tracing paper.

3. The latitude points A and B were used to define the x axis.

4. Each lineament was defined by two points: (x_1, Y_1) and (x_2, y_2), and marked on the top tracing paper to avoid any missing or repetition of lineaments. Curved lineaments were divided into straight segments, as shown on the top right corner of Fig. 5.4.

5. After digitizing of all the lineaments, the border corner coordinates were digitized as: (B_{x1}, B_{y1}) and (B_{x2}, B_{y2}), then (B_{x2}, B_{y2}) and (B_{x3}, B_{y3}), and so on.

6. To identify the geographical location of the image, eight longitude and latitude points were digitized and typed.

7. Each overlay was stored in the computer under a certain file name, and then, in order to check the process, the data was re-plotted and the original and re-plotted lineaments were compared

5.7.4 Compiled Maps of Lineaments

The maps (Figs. 5.5 and 5.6) were prepared as follows:

1. The frame of each interpreted overlay was marked.

2. Each image was located on the studied area map according to the latitudes and longitudes of its corners.

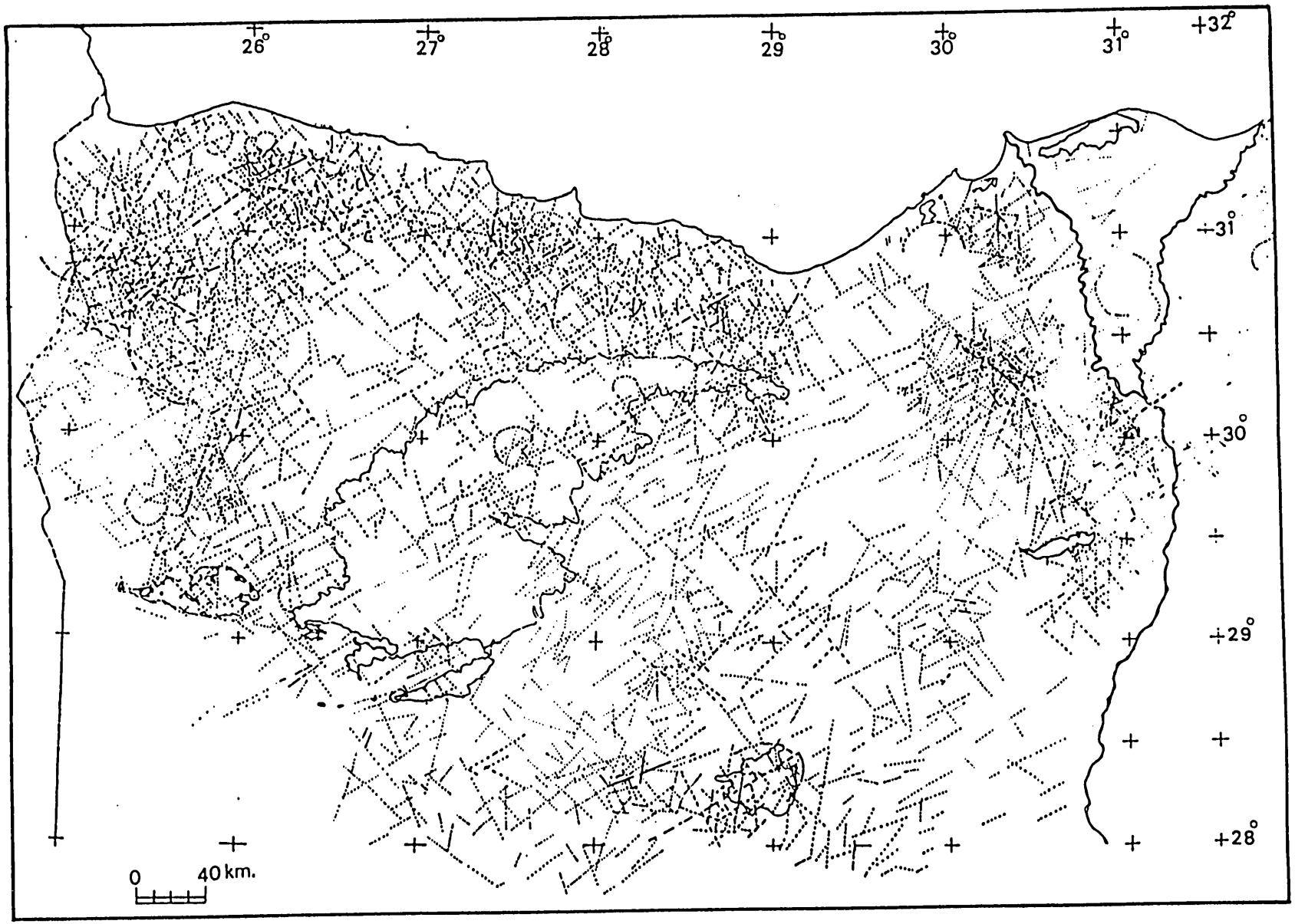


Fig. 5.5 Compiled map of lineaments (False colour composites)

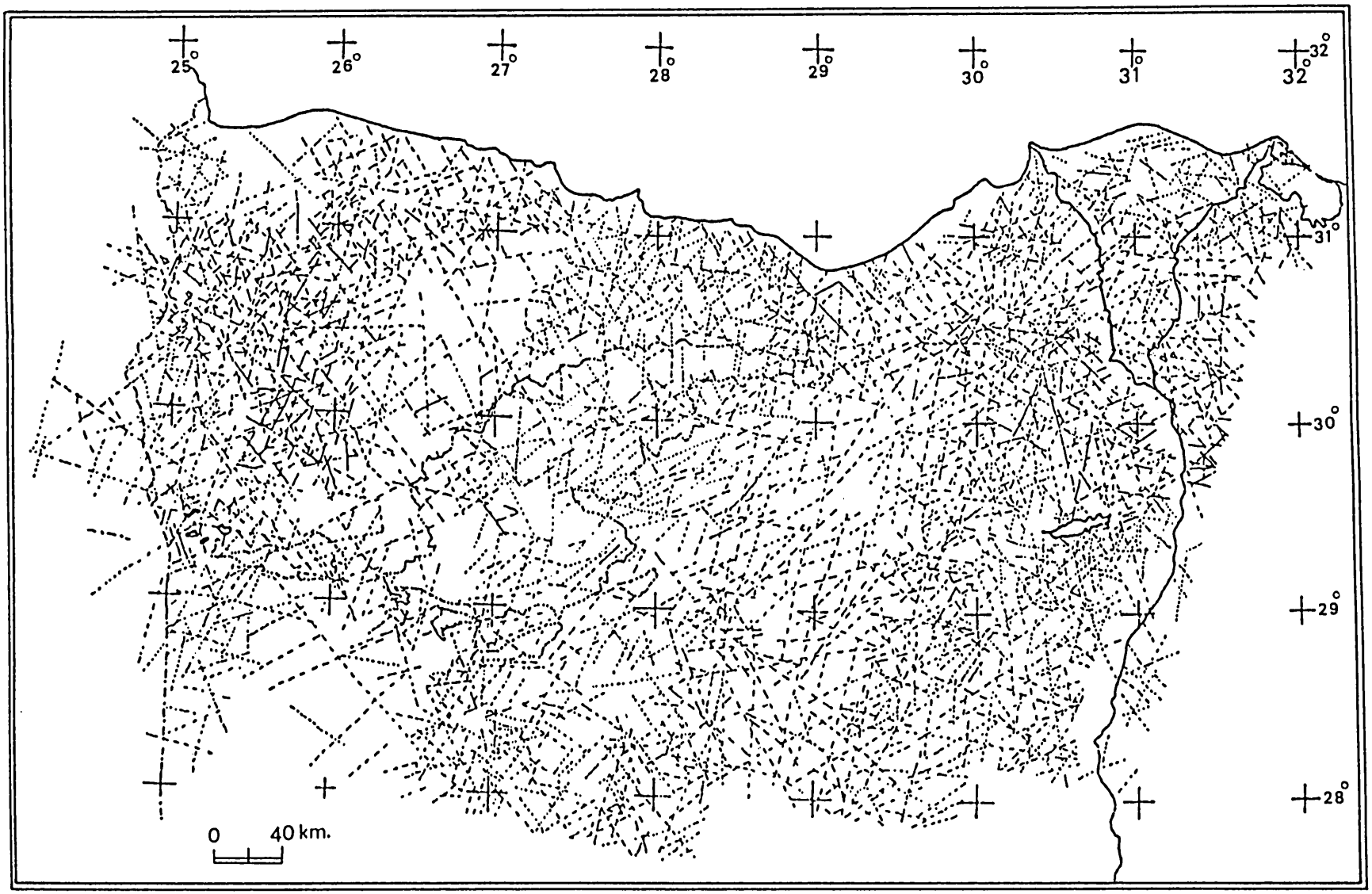


Fig. 5.6 Compiled map of lineaments (Band 7)

Thus, the different orbit paths were constructed (Fig. 5.7).

3. Each overlay was fitted along each orbit path, then the adjacent orbit paths were fitted together.

4. Any mismatch was distributed proportionally along the entire area, which is covered by the image on the map.

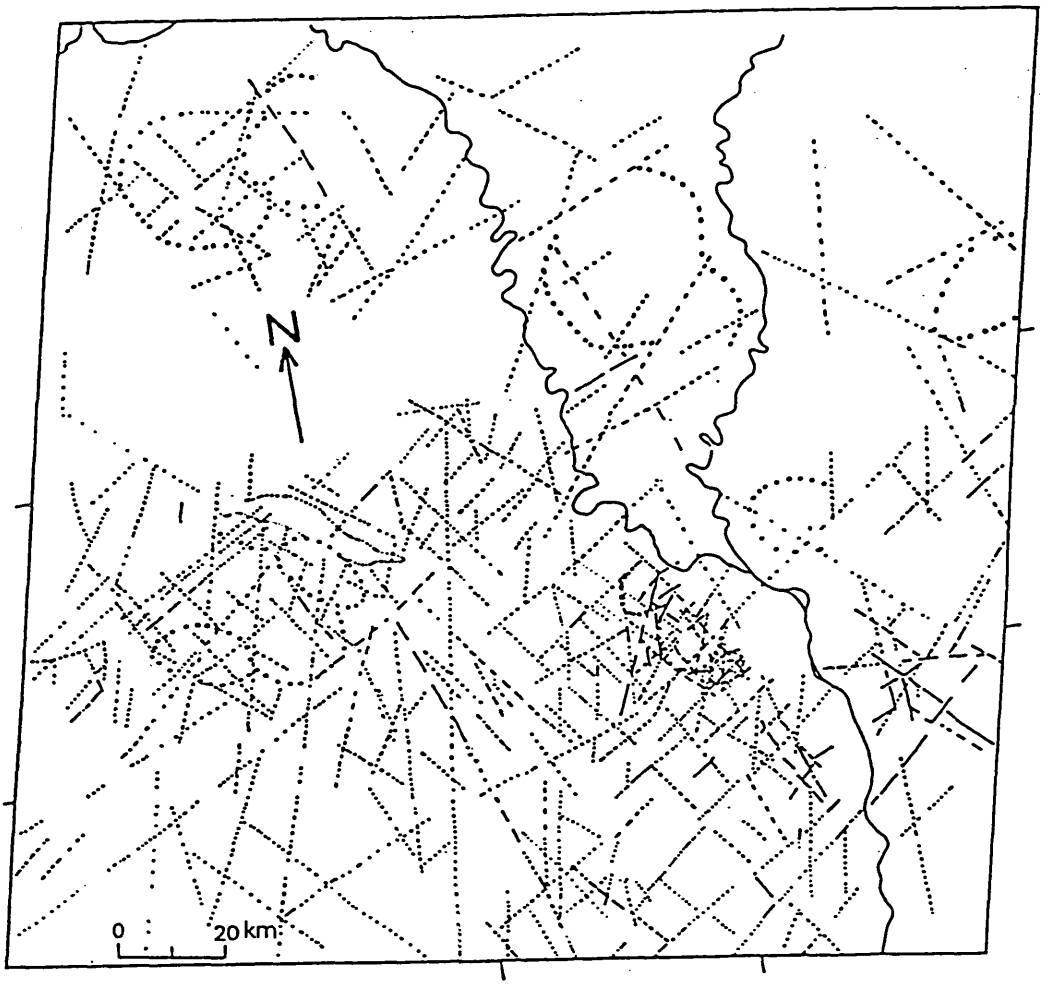
5. A transparent sheet was laid over the fitted overlays and all the lineaments were drawn, as well as the longitudes, the latitudes, and any other geographical features.

The compiled maps of lineaments (Figs. 5.5 and 5.6), with different lengths, directions and patterns were prepared from the overlays of the colour composite images (scale 1:500,000) and band 7 images (scale 1:1000,000), respectively.

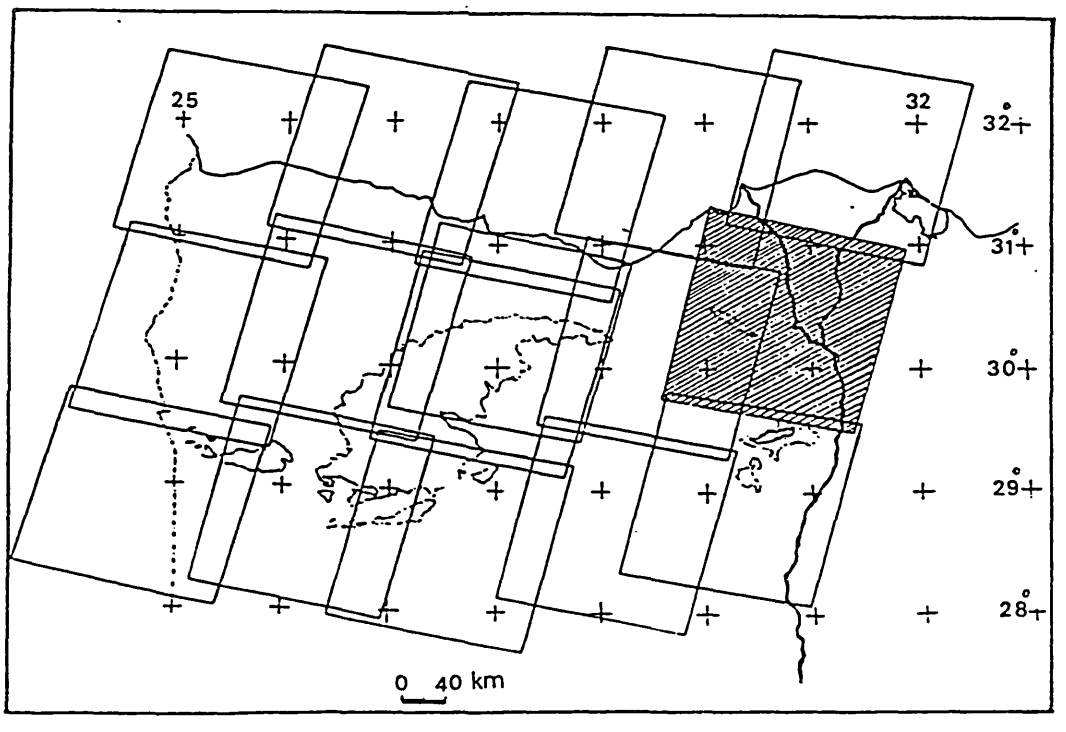
5.7.5 Presentation of the Data

The formats which were used to display the directional data in the aerial photographs' study of Abu Rawash area, such as rose diagrams and histograms, have been used in this chapter.

The statistical analysis of the interpreted lineaments are exactly the same as those of the interpreted fracture traces aerial photographs study. The computer printouts are similar to those of the fracture traces, but the directional or numerical content is different.



(A) Interpreted lineaments.



(B) The location of the interpreted lineaments

Fig. 5.7 shows the construction of a lineament compiled map.

In order to overcome, as far as was possible, the problem of misrepresentation of the NW lineament which may be caused by sun azimuth or other effects, a "Weighted Technique", based on the same principles as the integrated technique, was established to give some weight to those rays or class intervals which are not well represented. In this technique, the fracture frequency, fracture length and average fracture length were considered instead of fracture frequency, fracture length and fracture energy, which have been used in the integrated technique.

A class interval of 10° degrees was selected in rose diagrams to smooth the results and to avoid or eliminate unwanted noises (Fig. 5.8).

Rose diagrams were located and represented on maps, "Rose diagrams maps", (here the writer follows the description of such maps used by Huntington (1975), in order to present the general pattern of lineaments and to show the geographical variations of the directional data.

5.8 Results and interpretation

The outcomes of the statistical analysis, in the form of rose diagrams, are shown here in Figs. 5.9 to 5.12, which represent rose diagram maps of Band 7, 1:1,000,000) Landsat images. The rest of the results are shown in Appendix I, as rose diagram maps of the other 1:500,000 and 1:1,000,000 Landsat images used in this study.

The orientations in these diagrams are classified as shears, tension and shear and/or tension. It is

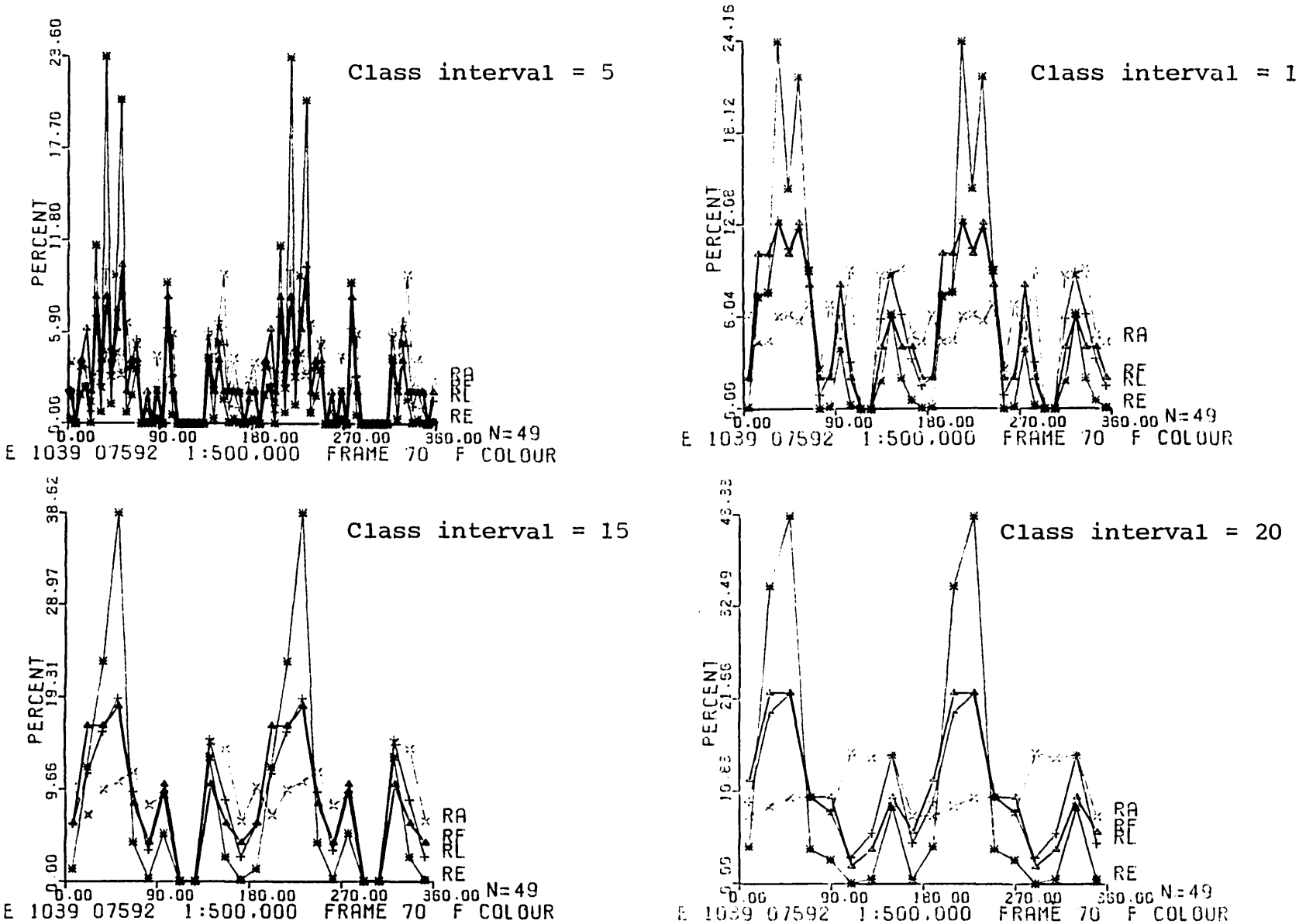


Fig. 5.8 Histogram showing the lineament frequencies with different class intervals.

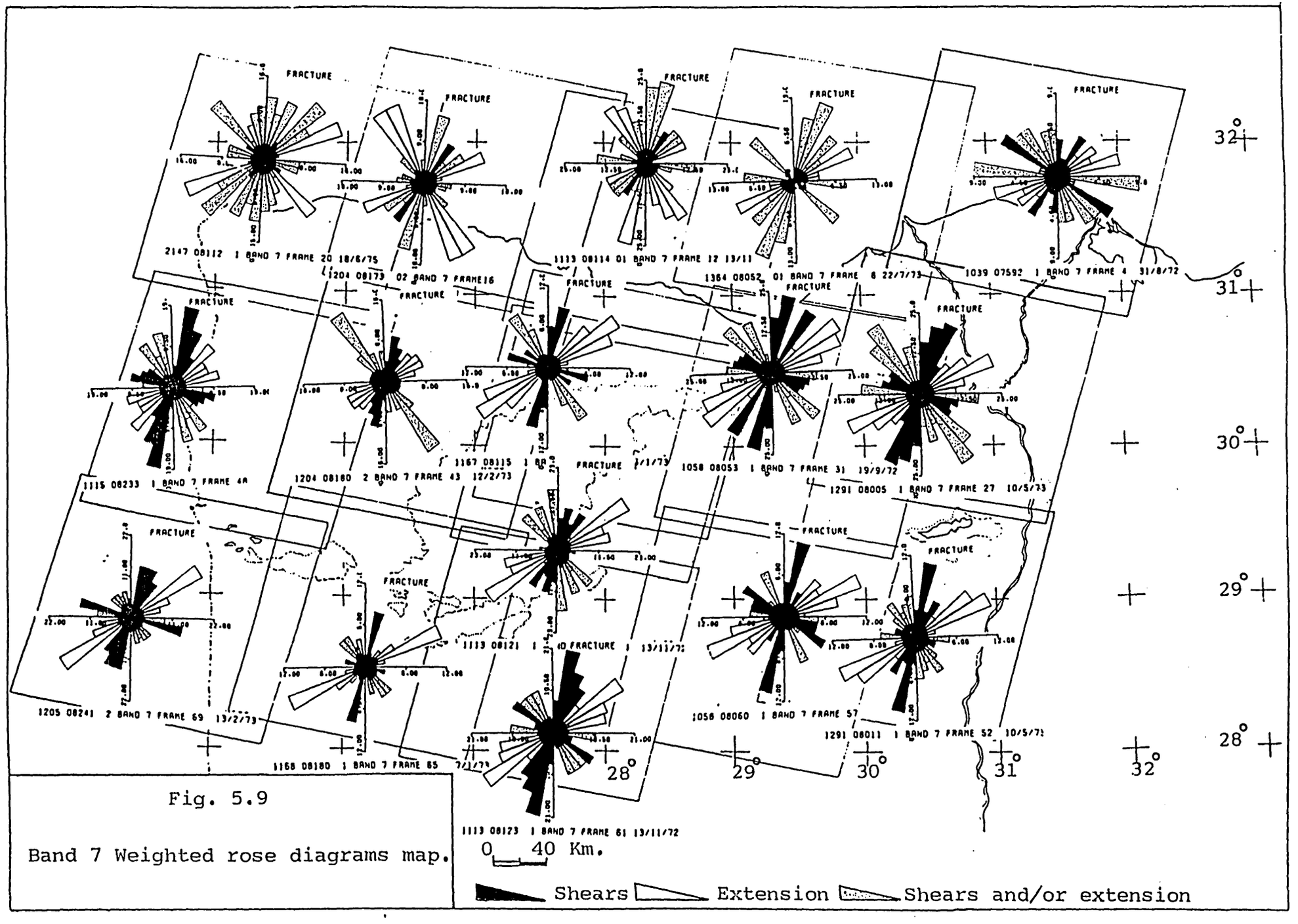


Fig. 5.9

Band 7 Weighted rose diagrams map.

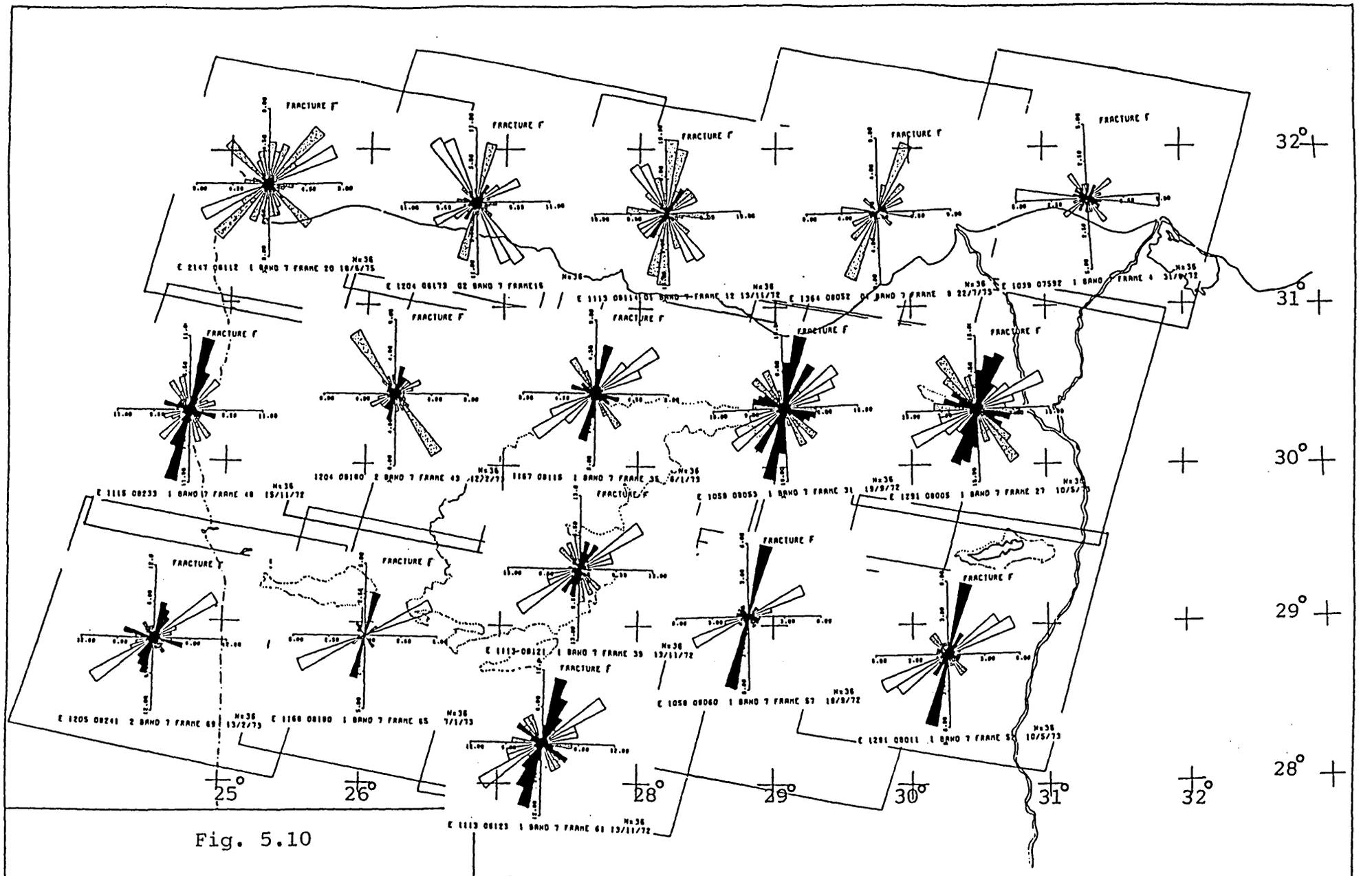


Fig. 5.10

Band 7 Integrated rose diagrams map.

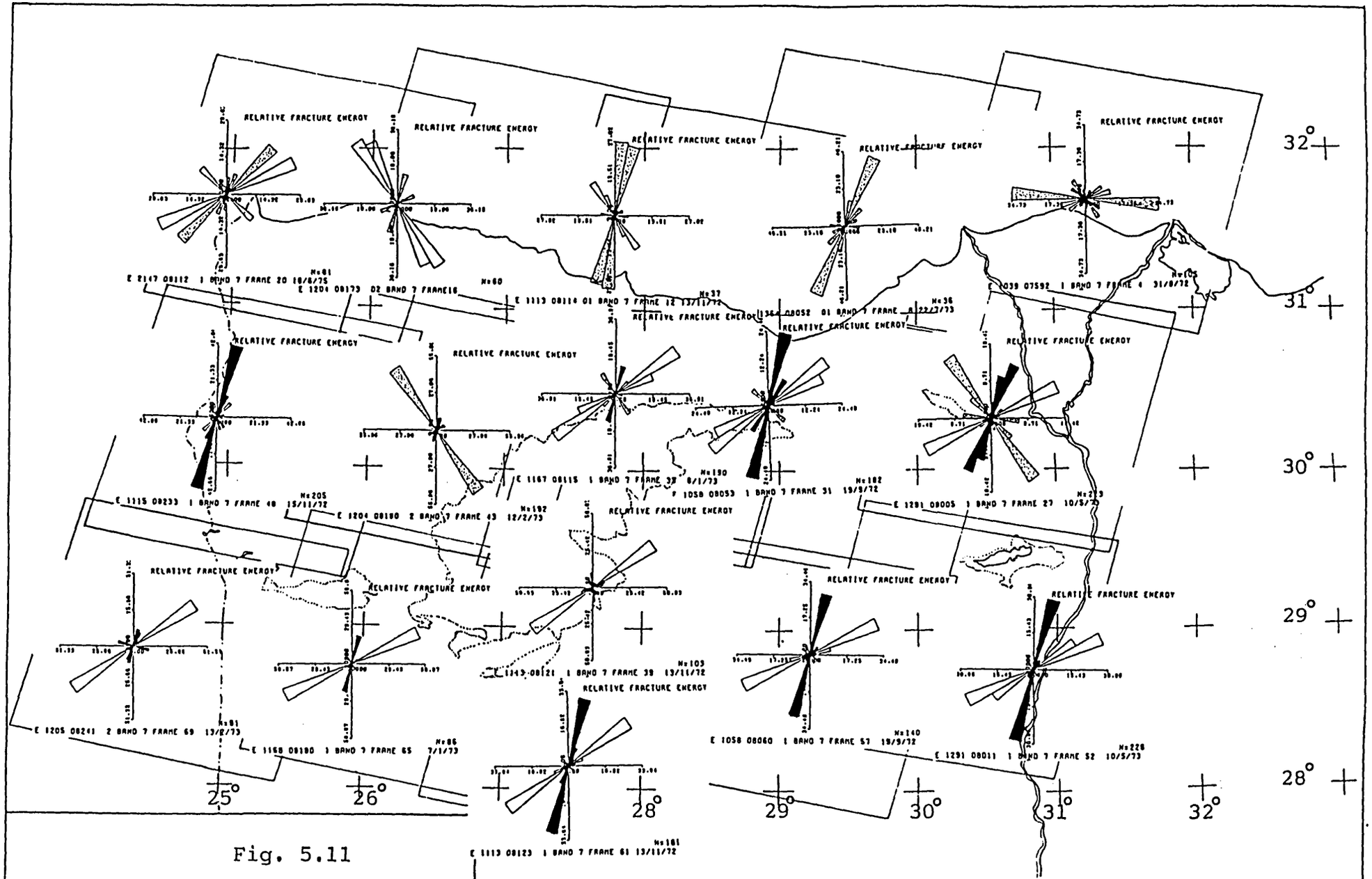


Fig. 5.11

Band 7 Relative fracture energy rose diagrams map.

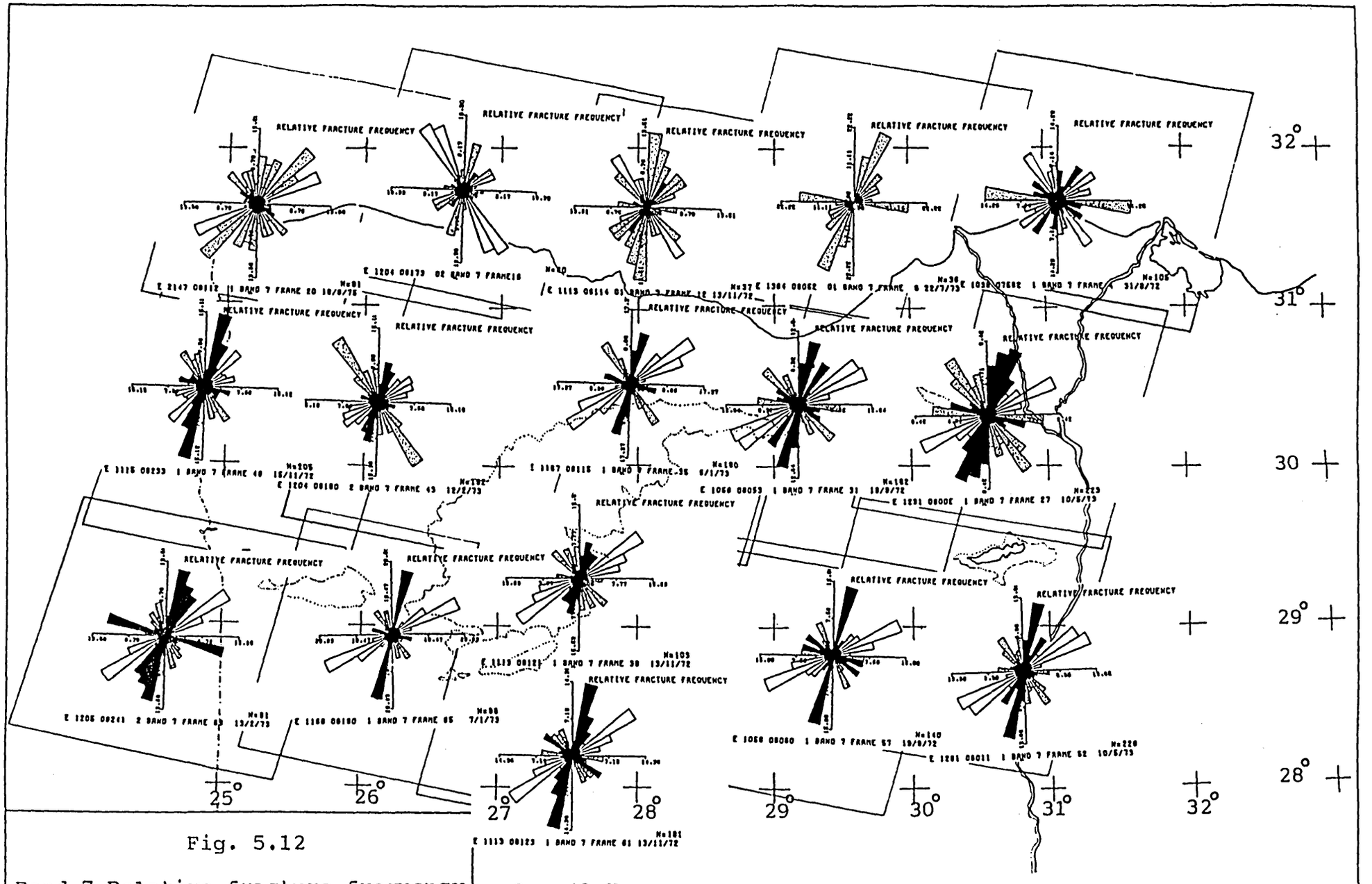


Fig. 5.12

Band 7 Relative fracture frequency rose diagrams map.

emphasized that there is no Landsat evidence for this classification. However, as will become apparent, it is possible to use a theoretical approach that permits such classification. This will be discussed later in this chapter and further verification will be adduced in Chapters VI, VII and VIII.

The relationship between relative fracture frequency (see Chapter IV for definition), relative fracture length and relative average fracture length rose diagrams are expressed in Table 5.3 as correlation coefficients. Generally, the correlation coefficients between relative fracture frequency and relative fracture length range between 0.84 to 0.977. This means the relationship between them is excellent. The relatively low correlation coefficients, especially between relative average fracture length and both relative fracture frequency and relative fracture length rose diagrams indicate that the interpreted lineaments are few in number, but they are relatively long.

Unlike the correlation between the directional data of the field and aerial photographs (Abu Rawash village pericline), the correlation between field and Landsat images rose diagrams on the one hand, and between aerial photographs and Landsat images rose diagrams on the other, indicates an extremely poor correlation. However, (in most cases), the correlation coefficients between aerial photographs and Landsat images rose diagrams are relatively higher than those between the field and Landsat images directional data.

Table 5.3

Correlation Coefficients of Some Roses (False Clolour Composite and Band 7)

Infra-red False Colour Composite				Band 7			
Frame No.	Correlation Coefficients			Frame No.	Correlation Coefficients		
	R.F.F./ R.F.L.	R.F.F./ F.Av.F.L.	R.F.L./ R.Av.F.L.		F.F.F./ R.F.L.	R.F.F./ R.Av.F.L.	R.F.L./ R.Av.F.L.
70	0.904	0.459	0.702	4	0.871	0.065	0.422
71	0.814	0.588	0.882	8	0.879	0.362	0.687
72	0.950	0.649	0.728	12	0.852	0.769	0.931
73	0.926	0.528	0.624	16	0.951	0.432	0.584
74	0.943	0.462	0.616	20	0.873	0.360	0.648
80	0.969	0.492	0.585	27	0.922	0.393	0.633
81	0.944	0.441	0.563	31	0.971	0.554	0.617
82	0.932	0.332	0.568	35	0.977	0.306	0.397
83	0.970	0.570	0.485	39	0.840	0.474	0.739
84	0.975	0.312	0.391	43	0.944	0.112	0.315
85	0.961	-0.108	0.589	48	0.954	0.273	0.423
90	0.901	0.646	0.739	52	0.968	0.148	0.230
91	0.973	0.251	0.390	57	0.943	0.128	0.380
92	0.937	0.317	0.485	61	0.958	0.420	0.557
93	0.978	0.475	0.506	65	0.904	0.144	0.440
-	-	-	-	69	0.877	0.445	0.679

R.F.F.: Relative fracture frequency rose diagram

R.F.L.: Relative fracture length rose diagram

R.Av.F.L.: Relative average fracture length rose diagram

The dominant trends of the directional data in the different rose diagram maps, except weighted rose diagram

maps, with their percentages, are represented in Appendix I.

Here, the rose diagram maps (Figs. 5.9 to 5.12) will be considered. However, the writer presented a complete set of rose diagram maps of infra-red colour composite and the rest of Band 7 images in Appendix I to demonstrate to the reader how the directional data have been summarised, enhanced and weighted in this study.

The most clearly defined trends of the rose diagram maps (Figs. 5.9 - 5.12), as indicated in compass points and the principal compass points are:

1. Set 1: N60^{o} - 70°E (ENE) of Figs. 5.9, 5.10, 5.12) and most of the rose diagrams of Fig. 5.11;

2. Set 2: N0^{o} - 20°E (nearly N - S to NNE) of Figs. 5.9, 5.10, 5.12) and most of the rose diagrams of Fig. 5.11);

These two directions swing few degrees (up to 5° degrees) either to the north or the east.

3. Set 3: N10^{o} - 30°W (NNW), most of the rose diagrams of Figs. 5.9, 5.10 and 5.12;

4. Set 4: N60^{o} - 70°W (WNW), some of the rose diagrams of Figs. 5.9 and 5.12 and few of the rose diagrams in Fig. 5.10;

These NW trends locally swing few degrees (up to 5°) to the north or the west.

5. Set 5: N80^{o} - 90°W - N80^{o}W - 90°E (nearly E-W), most of the rose diagrams of Figs. 5.9, 5.10 and 5.12 and few of the rose diagrams of Fig. 5.11;

6. Set 6: N40° - 60°W (NW), Figs. 5.9 and most of the diagrams of Figs. 5.10 and 5.12;

7. Set 7: N40° - 60°E (NE), Figs. 5.9, 5.10 and 5.12;

Set 8: N20° - 30°E (NNE), most of the rose diagrams of Figs. 5.9, 5.10 and 5.12.

One of the surprising discoveries using Landsat images is the persistent occurrence of ENE and NNE trending lineaments. These lineaments, though they vary in number, lateral extent and clarity of expression, occur over the whole of the studied area. The ENE trending lineaments shown up on Landsat images are much larger than those on aerial photographs. This ENE trend coincides with the trend of the Syrian Arc System of folding in Egypt.

The dominance of generally NE trends over NW and E-W trends could be attributed to the following:

a. the sun azimuth, NW, which enhances NE trends but causes lineaments oriented parallel or nearly parallel with it to be difficult to detect (Fig. 5.13);

b. lineaments parallel with the nearly E - W scan lines exhibited on Landsat images tend to be obscured;

c. for low sun angle up to 40° with the horizon, images show better photographic contrast as well as good visual impact than those images of high sun angle;

d. nature of the terrain, such as the presence of NW sand dunes, which cause difficulty in the detectability of NW lineaments;

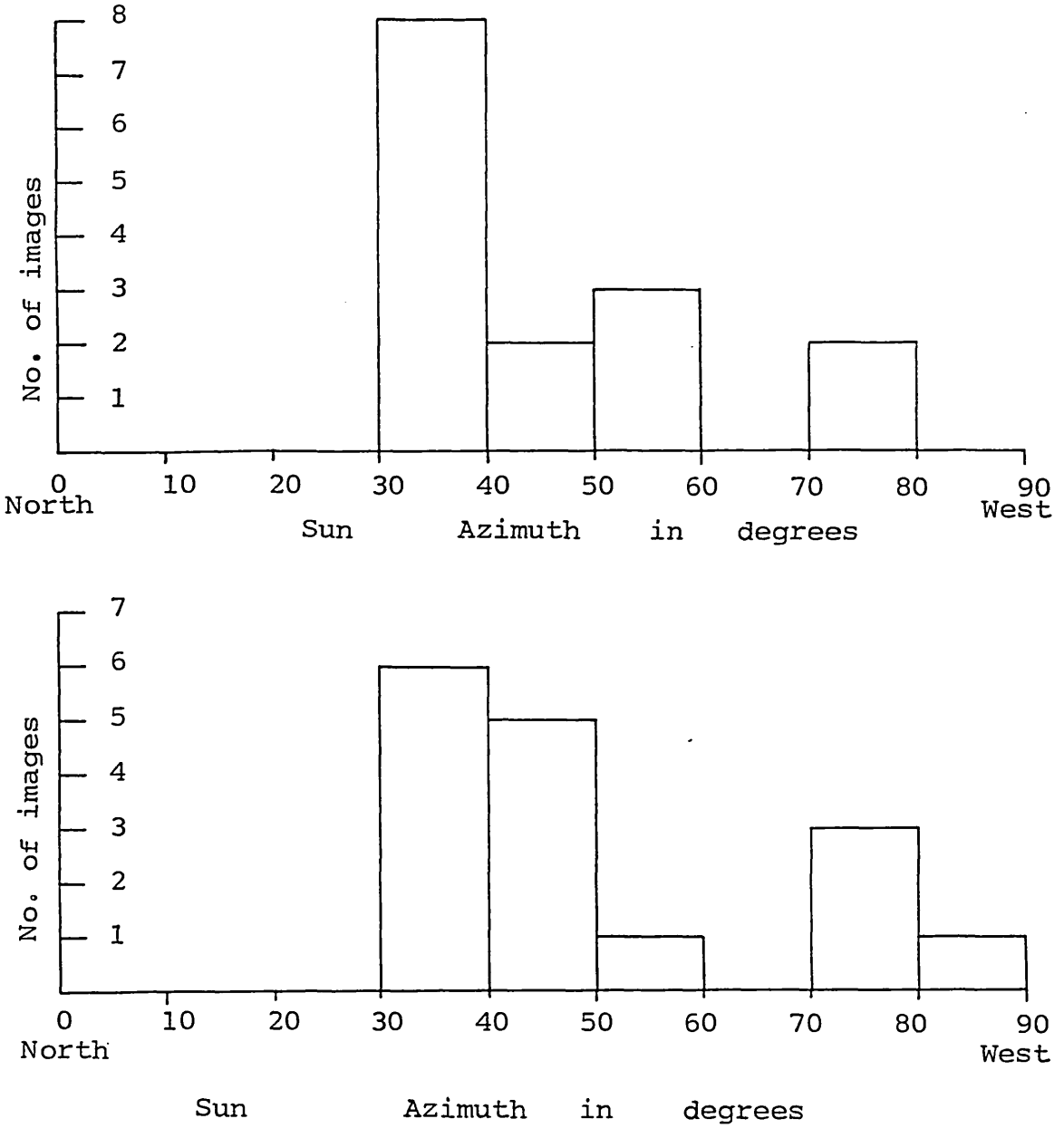


Fig. 5.13 The number of images used with the relative Sun azimuth.

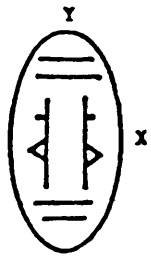
e. the tectonic stresses which cause the bc fractures to be more prominant than the ac ones (Price, 1966).

These NW and nearly E - W lineaments are well represented on the aerial photograph rose diagrams.

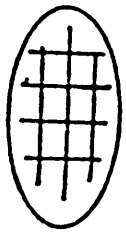
Based on a theoretical model derived by Price (1974), the possible fracture patterns that may develop in undeformed sediments as a result of downwarp and the concomitant de-watering of the sediments, followed subsequently by uplift, are represented on Fig. 5.14. In order to construct the theoretical rose diagrams, the trends of the basins have been determined (making use of the available isopach maps which will be discussed in the next chapter), as shown in Fig. 5.15 The procedures for the construction of final theoretical rose diagrams, amenable for the interpretation of the rose diagram maps (Figs. 5.9 to 5.12) are as follows:

1. The orientations of the basins and uplifts have been defined, using the available isopach maps of the next chapter (Figs. 6.18, 6.23, 6.24, 6.30, 6.35, and 6.37), as indicated in Fig. 5.15.

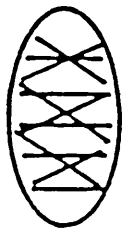
2. The possible fractures which seem to be developed during downwarping and subsequent uplifting (Fig. 5.14) were located with respect to north, where it is assumed the conjugate shear fractures make an angle of 50° - 60° degrees (see Fig. 5.16 as an example). Any changes in the directions of the basins of the same isopach map have been considered during the construction of the theoretical rose diagram. Thus, the different



A. Fractures developed during downwarping



B. Fractures developed during parallel uplift



C. Fractures developed during non-parallel uplift

Fig. 5.14 Fractures developed during downwarping and parallel or non-parallel uplift.

(After Price, 1974)

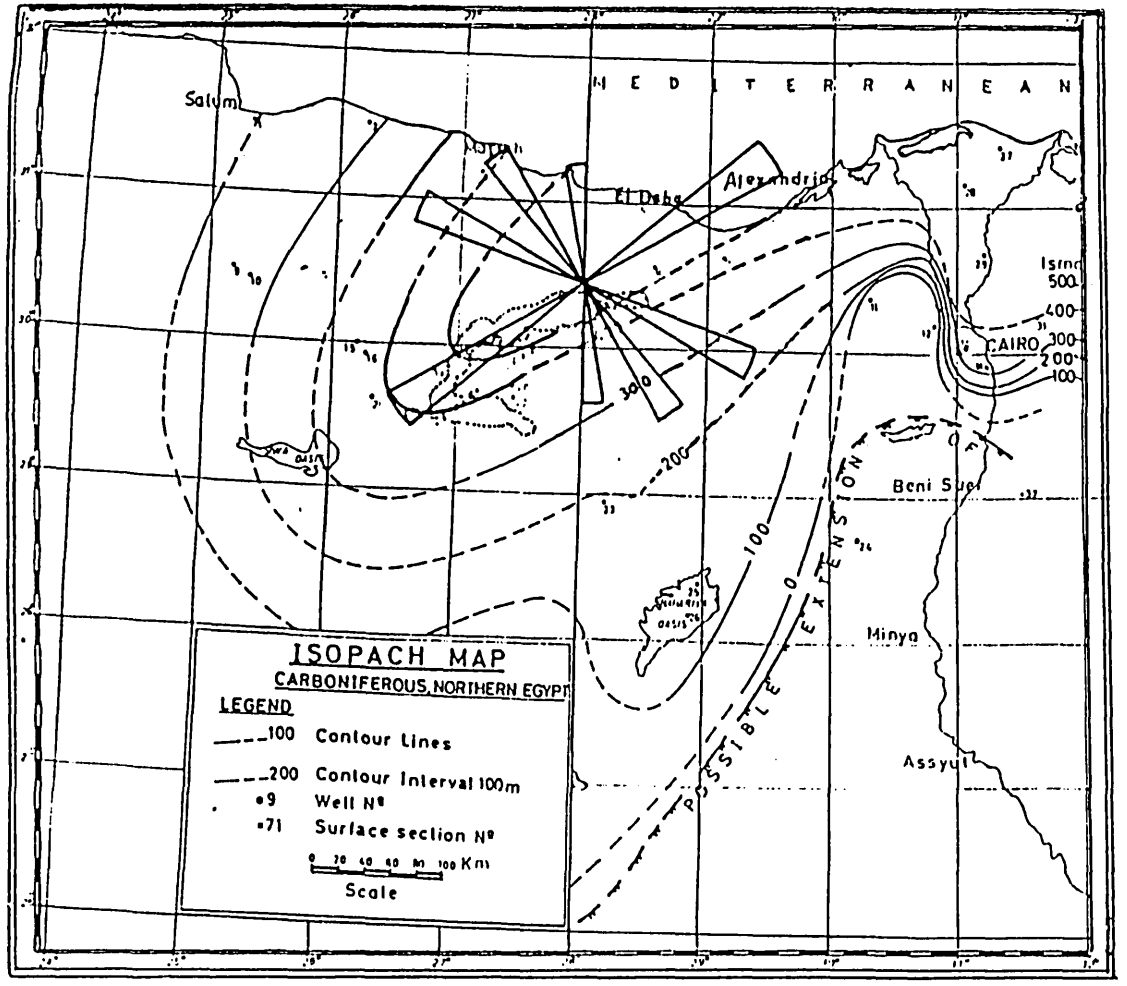
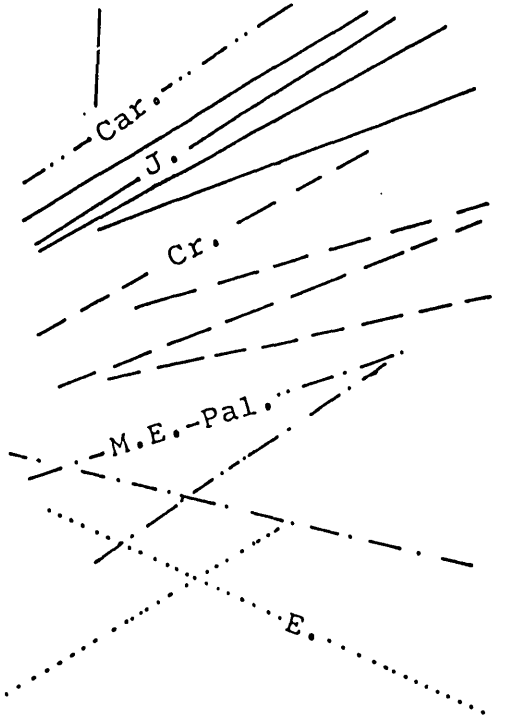


Fig. 5.16 shows the construction of theoretical rose diagram.



Car. = Carboniferous
J. = Jurassic
Cr. = Cretaceous
M.E.-Pal. = Middle Eocene - Palaeocene
E. = Eocene

Fig. 5.15 shows trends of subsurface basins and uplifts (see chapter VI)

theoretical rose diagrams presented in Fig. 5.17 were constructed.

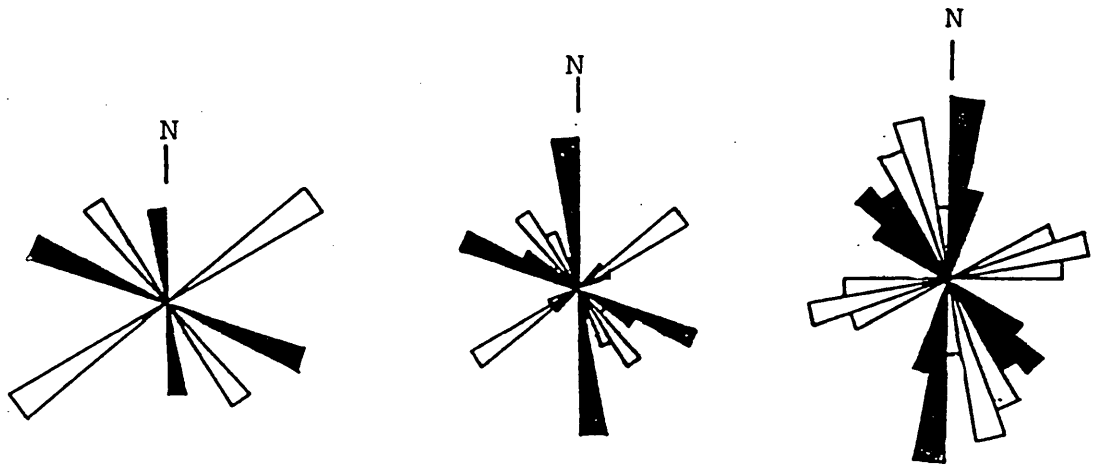
3. Rose diagrams in Fig. 5.17 A to E and F were compiled to give two rose diagrams (Fig. 5.18A and B, respectively).

4. Rose diagrams in Fig. 5.18A and B were compiled consequently with the rose diagram derived from the field data (Fig. 5.18C) to give the two final theoretical rose diagrams presented in Fig. 5.19A and B for the Northern Western Desert (including the Nile Delta) and along the Mediterranean Coast, respectively (where the shear, tension and shear-tension are represented by black, white and dotted rays, respectively. Accordingly, the different class intervals of the rose diagram maps (Figs. 5.9 to 5.12) were classified into probable shears, tension and shear-tension fractures as indicated on the rose diagram maps as black, white and dotted rays, respectively.

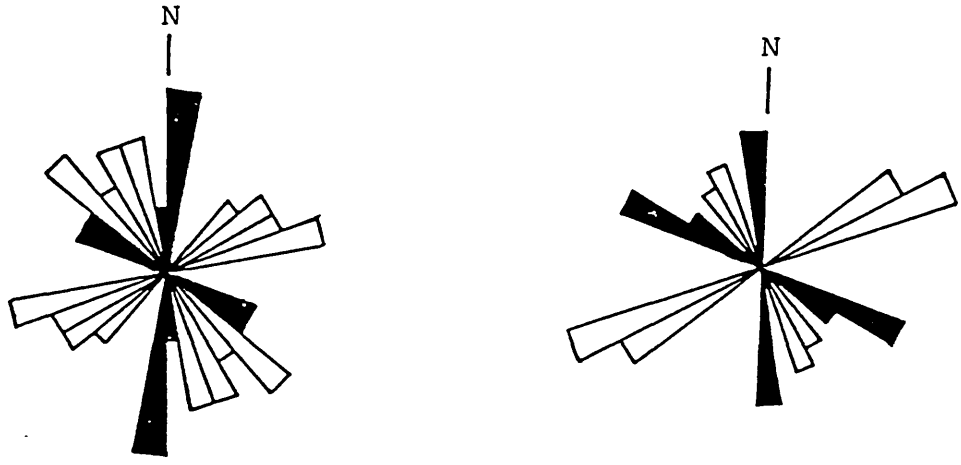
5.8.1 Discussion

The area under study has been subjected to tectonic stresses which worked on it at various intervals and with different trends throughout geological time. Generally, tectonic events are necessary for clear structural interpretation of lineaments and understanding their relationship to local structures present in the area.

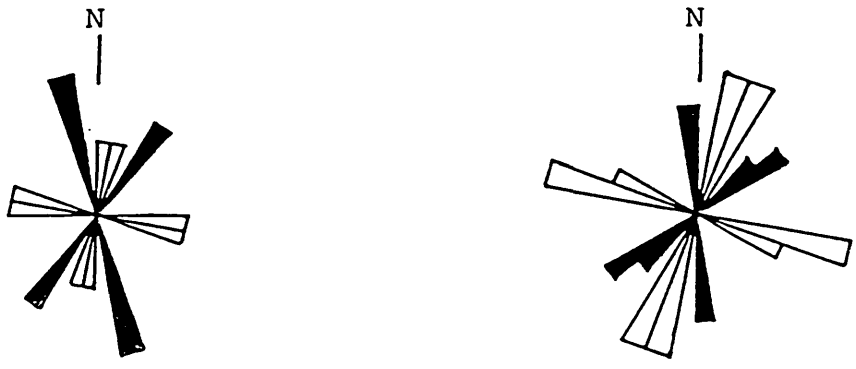
The present writer believes that lineaments would be meaningless until their origin and/or relationship to other structural features present in the area is



(A) Carboniferous (B) Jurassic (C) Cretaceous



(D) M. Eocene - Palaeocene (E) Eocene

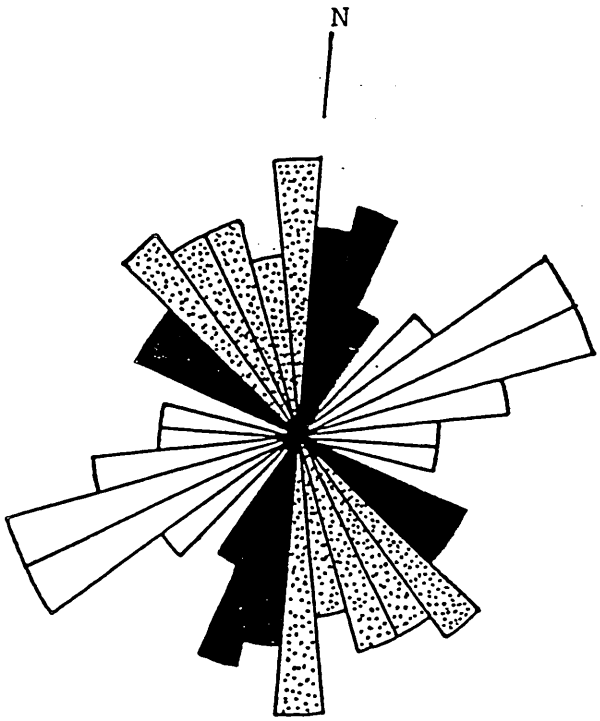


a- M. Eocene-Palaeocene b- Eocene

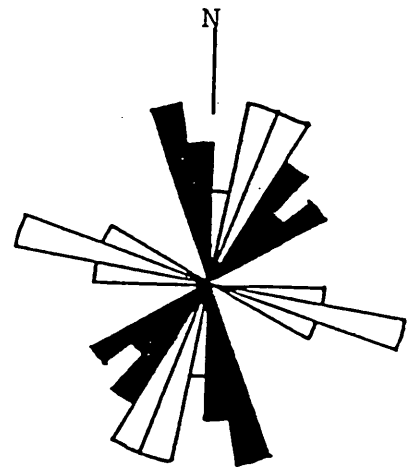
(F) Rose diagrams along the Mediterranean coast.

Black = Shears White = extension fractures

Fig. 5.17 Theoretical rose diagrams based on Price's model (1974).

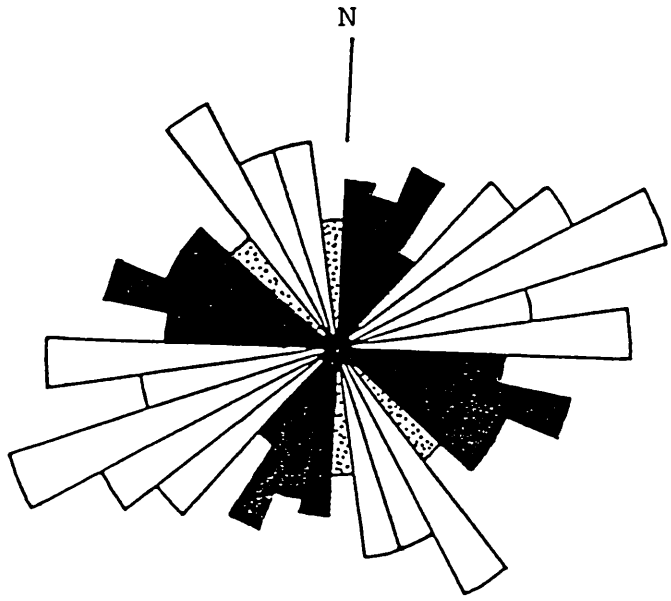


A) Compiled theoretical rose diagram across the Northern Western Desert of Egypt.



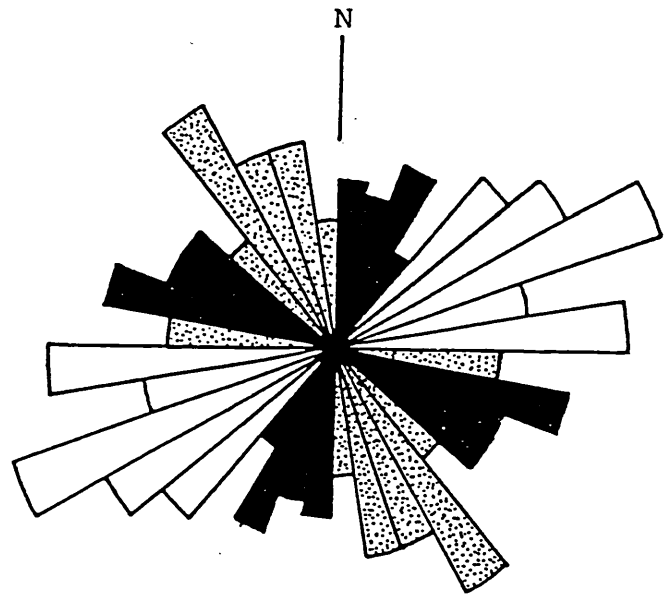
B) Compiled theoretical rose diagram along the Mediterranean coast.

Black = Shears
White = Extension
Dotted = Shears and/or Extension



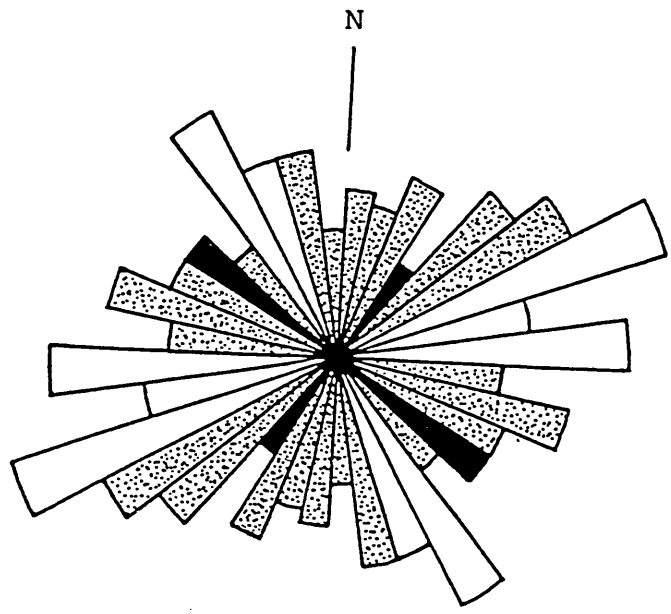
C) Compiled rose diagram derived from the field data theoretical model (Dip = 30).

Fig. 5.18 Compiled rose diagrams.



A) Compiled theoretical rose diagram across the Northern Western Desert of Egypt (compiled from Price's and field data models, see Figs. 5.18 A and C.

Black = Shears
White = Extension
Dotted = Shears and/or Extension



B) Compiled theoretical rose diagram along the Mediterranean coast (based on Price's and field data models, see Figs. 5.18 B and C.

Fig. 5.19 Compiled theoretical rose diagrams.

established. So let us review the tectonic events of the area as proposed by earlier workers. Said (1962) suggested the area has been subjected to:

1. long periods of predominantly compressive movements, followed by;

2. short, but active periods of predominantly tension relief.

Youssef (1968) suggested that the more ancient compression was oriented N10^{o}W and caused the formation of the Gulf of Aqaba and Gulf of Suez trends as a conjugate set of shear fractures. The second, younger one was directed N20W and led to the development of relatively new fractures, with trends deviate 10° - 15° relative to the old fractures (Gulf of Aqaba trend and Gulf of Suez trend) and also gave rise to the Syrian Arc System of folds (with axes trending N70^{o}E).

According to El Shazly (1977), the Alpine tectonism which initiated in late Miocene is represented in the Northern Western Desert of Egypt by open folds which trend WNW and major faults, which trend WNW, NNE and NW. The NW faults exhibit right lateral horizontal movements as well as vertical displacements. As for the concensus of earlier workers, as will be seen later, the following are conclusions with which the present author also agrees (see Chapter VIII).

1. During the Mesozoic, especially the upper Cretaceous, the tectonic stresses were oriented (N20^{o}-30°W) until the Oligocene.

2. During late Miocene-Pliocene, the tectonic compression was directed NNE (nearly N20 - 30E).

Let us now consider the analysis in more detail, dealing with the structural history of lineaments or fractures and folding during upper Cretaceous and late Miocene, because the evidence which has been deduced in the next two chapters supported this analysis.

Structural history of lineaments or fractures and folding (during upper Cretaceous and late Miocene

Invoking Price's explanation for the development of fold structures (unpublished work) and the formation of fractures during post-compressional uplift (1966), the following sequence of events is thought to be responsible for the development of folds and the formation of lineaments in the Northern Western Desert of Egypt:

1. During the upper Cretaceous

a. During upper Cretaceous, the maximum tectonic stress (S_1) was oriented approximately N20° - 30°W and the intermediate tectonic stress (S_2) was vertical. Folds which trend N60° - 70°E (ENE) (Syrian Arc System) were developed when pore fluid pressure was high and the total stress was below the limit required for shear failure conditions. These stresses possibly caused concomitant development of relatively minor faults. This phase of folding was continued up to Eocene.

b. During the post-compressional uplift which most

probably occurred by the end of Eocene, when S_1 and S_2 still retained their earlier orientations, it suggested a conjugate set of shear fractures developed at N0° - 10°E and N50° - 60°W, Set 2 (see Figs. 5.9, 5.10 and 5.12) and Set 6, respectively (see Figs. 5.9, 5.10 and 5.12).

c. Development of shear fractures caused a change in the horizontal stresses so that the release of residual stresses in N20° - 30°W (S_1 direction) tending to reduce S_1 and increase S_3. At this stage, vertical load due to gravity took on the role of the maximum principal stress. Further uplift of sediments caused the horizontal stresses to become tensile and extension fractures, or lineaments developed at N20° - 30°W (NNW), Set 3 (see Figs. 5.9, 5.10 and 5.12) and N60° - 70°E (ENE), Set 1 (see Figs. 5.9 to 5.12). The ENE fractures or lineaments are the most frequent. According to Price (1966), the bc fractures are generally the most common fractures in rocks that have been uplifted by post-tectonic compression. Thus, the lineaments or fractures of Set 1 (ENE) could be considered here as bc fractures.

d. The volcanicity (which is manifest by basaltic flows and hydrothermal activity) followed the land emergence (which occurred towards the end of the Oligocene) and made use of the tension fractures developed, Set 1 (ENE) and Set 3 (NNW).

2. At the Miocene

a. During the upper Miocene, S_1 was directed nearly N20° - 30°E and S_2 was vertical. Folds with trend of nearly N60° - 70°W (WNW) were probably developed.

b. During post-compressional uplift, when S_1 and S_2 retained their orientations, a conjugate set of shear fractures might have developed at nearly N - S and N50° - 60°E, possibly Set 2 (Figs. 5.9, 5.10 and 5.12) and Set 7 (Figs. 5.9, 5.10 and 5.12), respectively.

c. Further uplift, probably by the end of Miocene - early Pliocene, led to the development of two sets of extension fractures at N20° - 30°E and N60° - 70°W, Set 8 (Figs. 5.9, 5.10 and 5.12) and Set 4 (Figs. 5.9 and 5.12).

Circular and/or elliptical features

The interpretation of Landsat images revealed some circular or elliptical, sometimes semi-elliptical, features with variable sizes. These features have almost uniform faint tonal contrast which are usually difficult to detect. These features are commonly disconnected along their circumferences. Such features, which are shown on Figs. 5.20 and 5.21 have been interpreted from infra-red colour composite images. Some of these features have been recognized during the interpretation of the images of the different spectral bands used in this study.

The sizes of these oval features, short diameter, range between 4 to less than 50 kilometres.

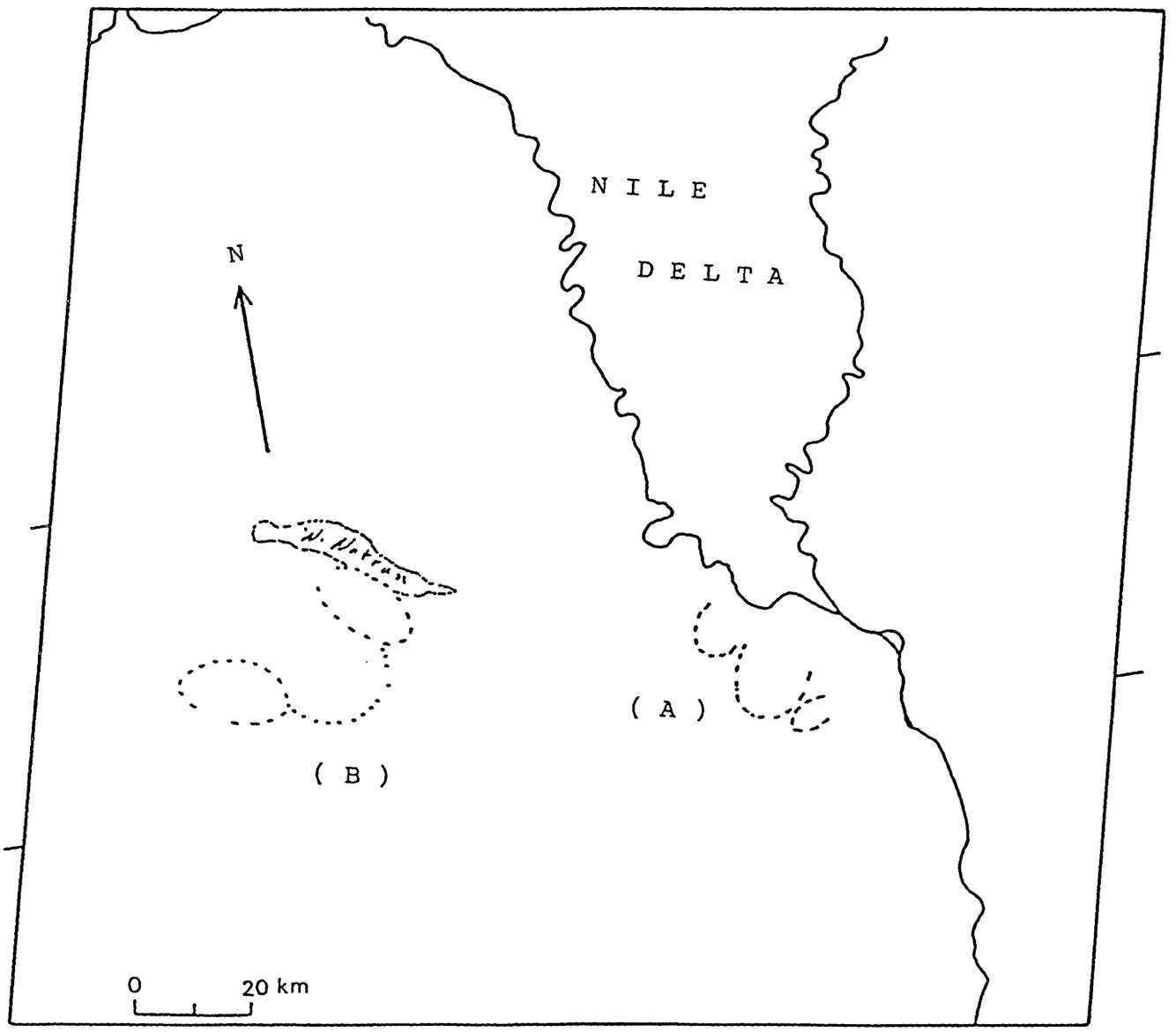


Fig. 5.20 Map showing some circular or elliptical features west Cairo.

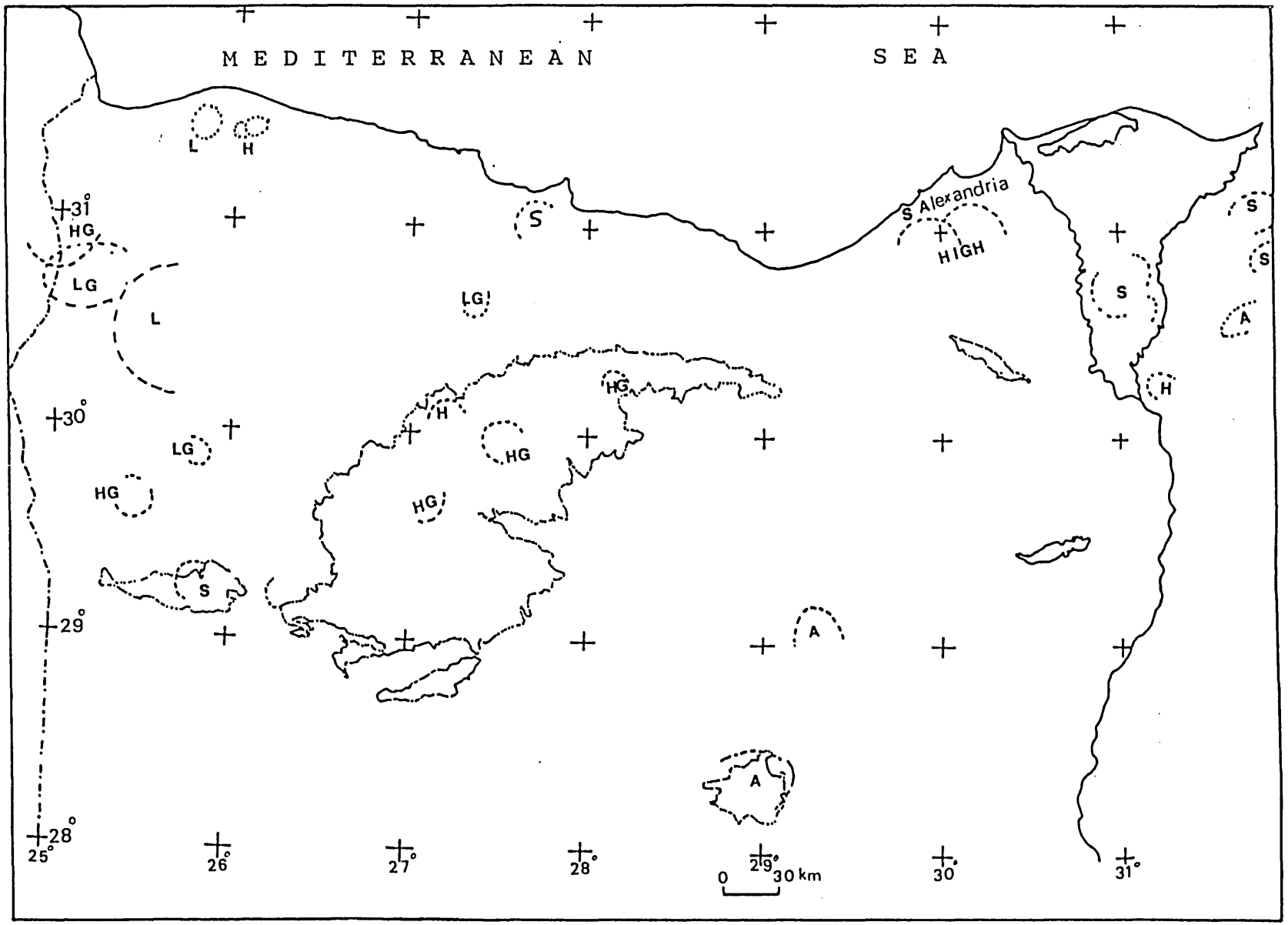


Fig. 5.21 Map showing some circular or elliptical features in the studied area.

In order to reveal the structural significance of these circular features, it was thought reasonable to relate them to the mapped structures (by former authors) and the geophysical data (see Chapter VII). The comparison of these elliptical or circular features with the geological maps (Figs. 2.28 and 2.29) show the following:

I: On Figure 5.20

A. These features reflect the ENE folding of Khatatba, subsurface, and Abu Rawash, surface. The area is structually high, as shown in Fig. 5.20.

B. These features which lie south of Wadi Natrun represent the WNW folding (Fig. 2.28).

Generally, the radial pattern (see Chapter IV) of lineaments of this particular area, Wadi Natrun, which has been noticed during the course of the interpretation of lineaments (Figs. 5.5 and 5.6) reflects the structure of the area as represented in Fig. 5.22.

II: On Figure 5.21

A. Features represent syncline structures, marked by letter S, as shown on Figs. 2.15 and 2.29.

B. Features reflect anticline structures, marked by letter A.

C. South Alexandria circular features represent a structurally high area (see Fig. 6.35). Accordingly, these features probably represent either drape fold structures or local domal structures.

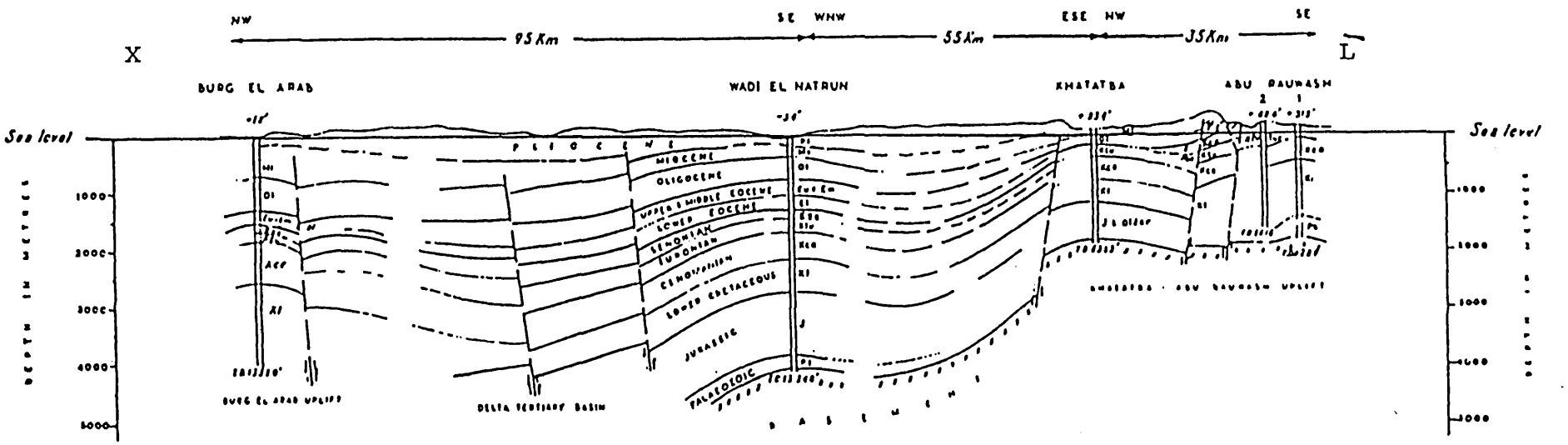


Fig. 5.22 Geological profile Burg El Arab - Abu Rawash (after Kostandi,1963)
See Fig. 6.11 for the location (X - L)

D. North Faghur features show structurally low or synclinal feature (see Fig. 2.15).

E. Other elliptical features which are marked by HG or LG reqresent structurally high or structurally low, res-pectively, on the gravity maps which will be presented in chapter VII.

In conclusion

1. It seems likely, from the compiled lineament maps (Figs. 5.5 and 5.6), that lineaments played an important role in shaping the Mediterranean Coast, the River Nile and other topographic features present in the studied area.

2. The geographical variations of the directional data of lineaments could be attributed to several factors, such as lithology, structural events, geological setting and those factors (subjective and objective) which affect the process of interpretation.

3. Although Price, in 1966, was dealing with the development of relatively small joints, it has been proved in this study (as it will be verified later in the next chapters) that Price's explanations are still valid to cover relatively large fractures such as lineaments.

4. Landsat images proved to be helpful in locating some surface and subsurface structures.

5. Changing of the direction of tectonic compression during the geological history of deformation may cause difficulty in the analysis of the fractures,

especially in the field and may lead to contradictory conclusions.

6. The theoretical models were very helpful in the analysis of lineaments.

CHAPTER SIX

PALAEOTECTONIC ANALYSIS

CHAPTER SIX

Palaeotectonic Analysis

6.1 Introduction

The object of this chapter is to obtain information on the tectonic history of the Northern Western Desert of Egypt through the analysis of some isopach maps in successive sequence (as well as a few structure contour maps) with the help of some geological cross sections. These isopach maps reflect the effects of basement block movements on the thickness of the sediments and the structural development of the studied area. If deposition appear to be controlled in extent and configuration by basement blocks, presumably this stratigraphic control is the result of reactivation of movement of the basement blocks and weakness zones controlling paleotopographic conditions.

Indeed, several periods of movements on existing fractures could occur and the principal stress directions and their magnitudes could be different for each event.

Stratigraphic lineaments were selected according to Gallagher and McGuire (1979), where the thickness contours abruptly change direction or when they form linear contour patterns (as a boundary between thin and thick areas of the same stratigraphic unit) which probably reflect basement block boundaries.

Comparing the stratigraphic lineaments (subsurface lineaments) or criteria, or their trends with surface lineaments which have been interpreted from Landsat

images or their trends, indicates whether the surface lineaments have, or have not, stratigraphical control. Such a control occurs if the paleotopographic conditions were the result of paleostructures generated by tectonic reactivations.

Subsurface maps used in this study are regional, so they exhibit a simple, or even very simple, thickness contours and in turn, a simple pattern of subsurface lineaments or fractures. Under these circumstances, it is possible to make use of Price's theoretical model (1974), where basins seem to have elliptical forms, coupled with post compressional uplifting (Price, 1966), as theoretical approaches for the analysis of stratigraphic lineaments.

Firstly, the analysis of the regional isopach maps, especially in terms of basins and uplifts they exhibit was considered where possible mechanics of Palaeozoic and upper Cretaceous folding were discussed.

6.2 The Analysis of Regional Isopach Maps

The available isopach maps of the studied area were assembled from data available in the literature. The subsurface and surface sections were taken as control points for contouring the isopach maps. Generally, the deep wells which have been drilled in the studied area are few relative to its areal extent and this shortage of the subsurface data affects the accuracy of the contouring process.

Thickness contours, coupled with subsequent compaction, enable the relief of the bottom of a series being studied to be established as it would be if the top of the series were horizontal. Study of these isopach maps in historical succession makes it possible to judge how the form and deposition of sectors or zones, with different degrees of subsidence, have changed with time. The advantages of the analysis of such maps are:

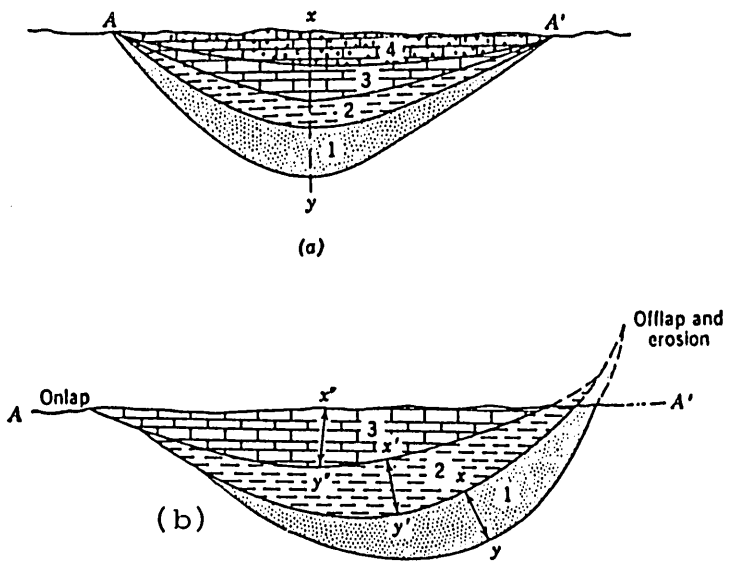
1. The contour patterns of the isopach map enable the major tectonic units in which sedimentation occurred to be identified (Fig. 6.1).

2. The analysis of a series of these maps enables the time, the position of deformation and, in special cases, the magnitude of tectonic movements, epeirogenic and/or orogenic to be established.

3. The analysis of the isopach maps shows either subsidence was continuous in a vertical direction during the deposition of several units (Fig. 6.2a) or the axes of subsidence migrate from one unit to the next as a result of tilting (Fig. 6.2b).

4. The zero contour line of an isopach map of marine sediments represents the limit of either the shoreward deposits or the seaward erosion subsequent to deposition.

5. Abrupt change in the trend of the contours of the isopachous map may be attributed to either a fault or nose (which might be formed as a result of a plunging fold).



Subsidence. (*a*) Gradual sinking along axis *xy* during deposition of units 1, 2, 3, and 4. (*b*) Migration of axes of submergence. Uplift after deposition of bed 1, during deposition of bed 2, and before deposition of bed 3.

Fig. 6.2 Axes of subsidence during vertical and tilted subsidence.
(After Bishop,1960)

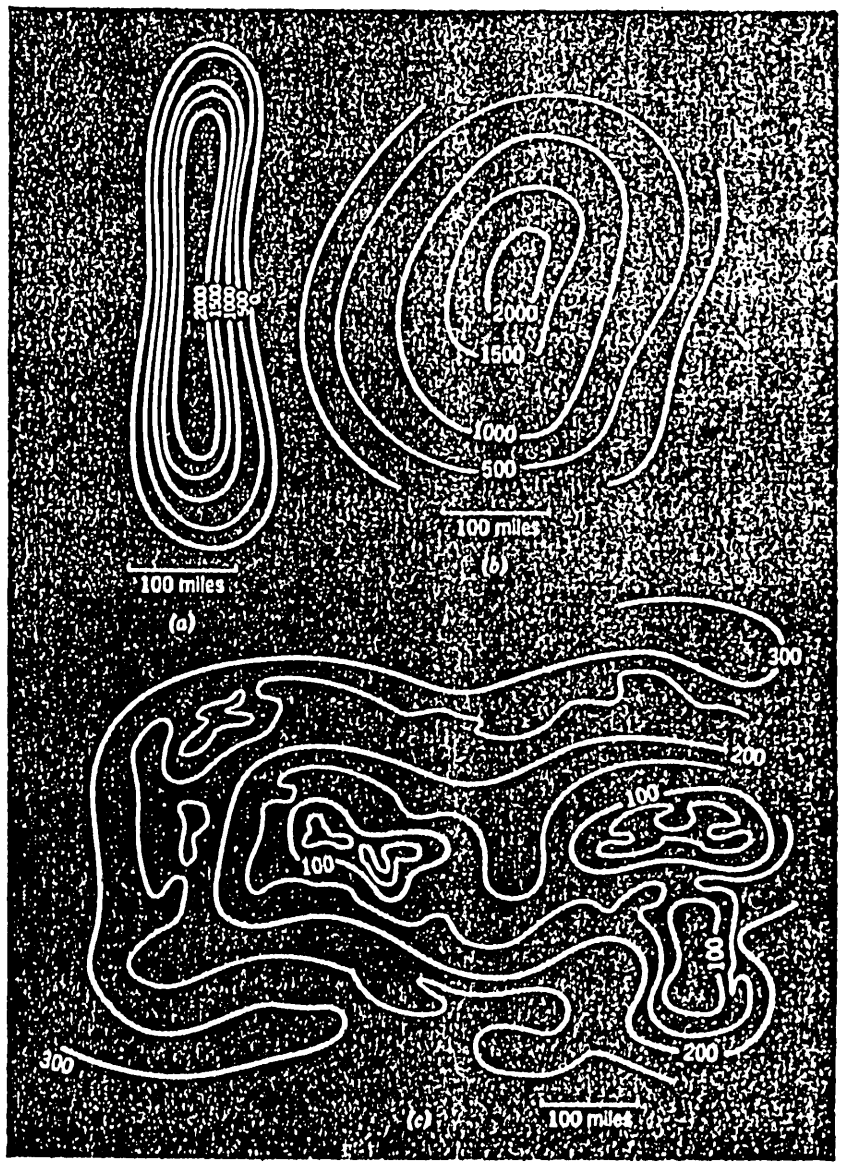


Fig. 6.1 Diagrammatic contour patterns for isopach maps of regional negative areas. (*a*) Geosyncline. (*b*) Intracratonic basin. (*c*) Shelf.
(After Bishop,1960)

6.2.1 Principles of Interpretation

A basin is a depressed region of the earth's surface which has been filled with sediments. A sedimentary basin could be formed as a result of:

1. folding, where the syncline forms the basin and the anticline forms an uplift (ridge);

2. block faulting, where the sedimentary basin is bounded by nearly vertical faults;

3. curved strike-slip faulting with regional extent where the "hole" becomes a sedimentary basin (Fig. 6.3a);

4. thrust faults where the upthrust block forms a structurally high area, mountain ranges and the sedimentary basin forms over the downthrust block (Fig. 6.3b);

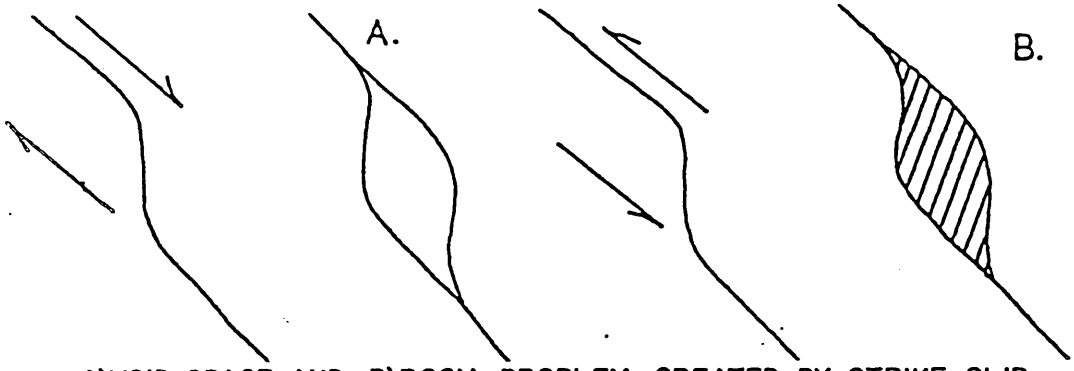
5. thermal subsidence where the surface cooling causes subsidence as the basement rocks cool and contract (Turcotte and Schubert, 1982).

The difference in thickness shown on isopach maps could be attributed to both tectonic and non-tectonic factors, such as:

1. Folding

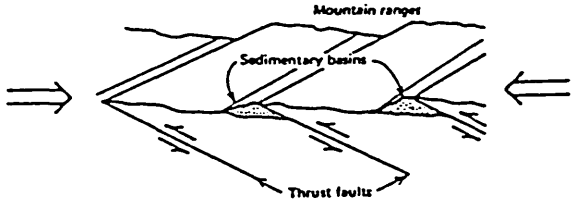
a. Supratenuous folding

In such folds, the sediments usually thin towards the crest. The ratio of the thickness of the crest relative to the limbs is a measure of the differential compaction as well as the rate of subsidence of the crust on the arch of the fold and beyond it.



A)VOID SPACE AND B)ROOM PROBLEM CREATED BY STRIKE-SLIP MOVEMENT ON A NON-PLANAR BASEMENT FAULT

(After Price)



Horizontal compression resulting in continental collision and a series of thrust faults. Each uplifted block creates a mountain range and each downdropped block a sedimentary basin.

(After Turcotte and Schubert,1982)

Fig. 6.3 Possible development of sedimentary basins.

Detailed study of the distribution of thicknesses often helps to reveal signs of migration of the arches over an area where the thickness of the sediments is thin. These supratenuous folds are most probably controlled by the displacement caused by underlying faults..

b. Buckle folding

The axes of the buckle folds usually run parallel to the trend of the thickness contours. In such folds, any change in the thickness is most usually not caused by the original conditions of accumulation of the sediments, but through secondary flow of the materials of its layer during deformation. These folds take place in certain zones, mainly as a result of horizontal stresses.

Unlike the supratenuous folds, the buckle folds are mainly post-sedimentary. They are formed after the strata involved have already been deposited and usually before fresh strata were laid down on the erosional surface. Angular unconformity truncate these folds.

c. Diapir or injection folding

In this folding, the rocks of high ductility and low density at a certain depth below the surface in a sedimentary series may be squeezed out of one place and injected into others. The injection process depends initially on the thickness of the ductile rocks and their mobility. Sometimes the ductile materials form small undulations which are unable to deform and pierce the

overlying rocks. Injection folds develop gradually over long periods in the same way as supratenuous folds.

2. Faulting

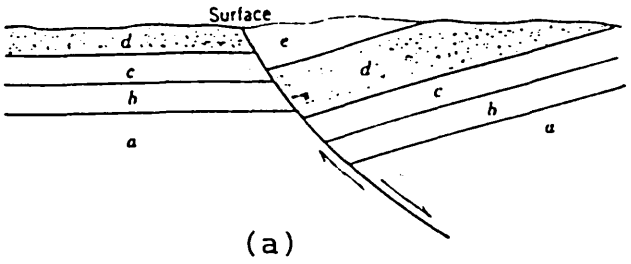
Faulting affects the thickness of the isopach maps whether the deposition was concurrent with faulting or as it occurred after or before deposition of sediments, as shown in Figs. 6.4 and 6.5.

3. A regional dipping surface which causes an increase in the thickness of the sediments in the direction of dip during deposition of such sediments (Fig. 6.6a);

4. Uplift and the subsequent erosion lead to decrease in the thickness or absence of an original rock layer, or layers, which have been eroded before being covered by subsequent deposition (Fig. 6.6b);

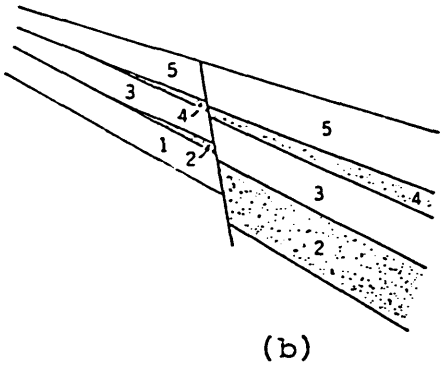
5. Topographic relief or the deposition on an irregular surface causes variation in the thickness of the layer, which has been deposited (Fig. 6.6c).

As long as the compaction factor is not taken into consideration, an isopach map is a relative, but not a direct measure of the amount of subsidence. However, differential compaction of a mud layer may develop minor irregularities in thickness or tends to emphasize dips in the initial layers by decreasing the thickness of the shale, but not greatly affecting the sands within the



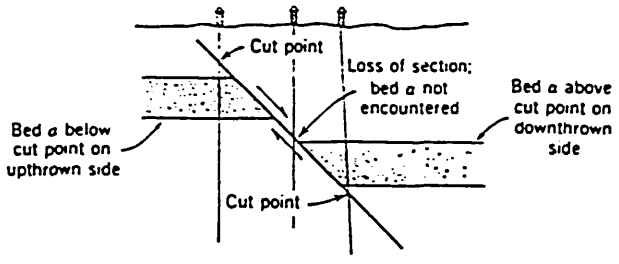
(a)

(*a*) In isopach contours on bed *e*, note rapid thickening along fault. Bed absent on upthrown side because of erosion. Bed *d* is present on the upthrown side but thin because of erosion.

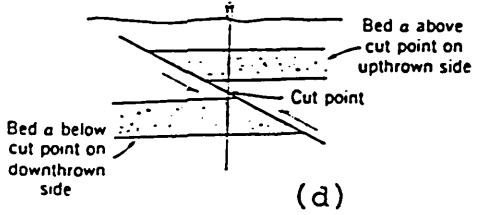


(b)

(*b*) In isopach contours on bed 2, note rapid thickening along the downthrown side of the fault. Deposition concurrent with faulting.



(c)



(d)

(c) Normal fault with loss of bed. (d) Reverse fault with repetition of beds.

Fig. 6.4 Effects of faulting on the thickness of the deposits.

(After Bishop,1960)

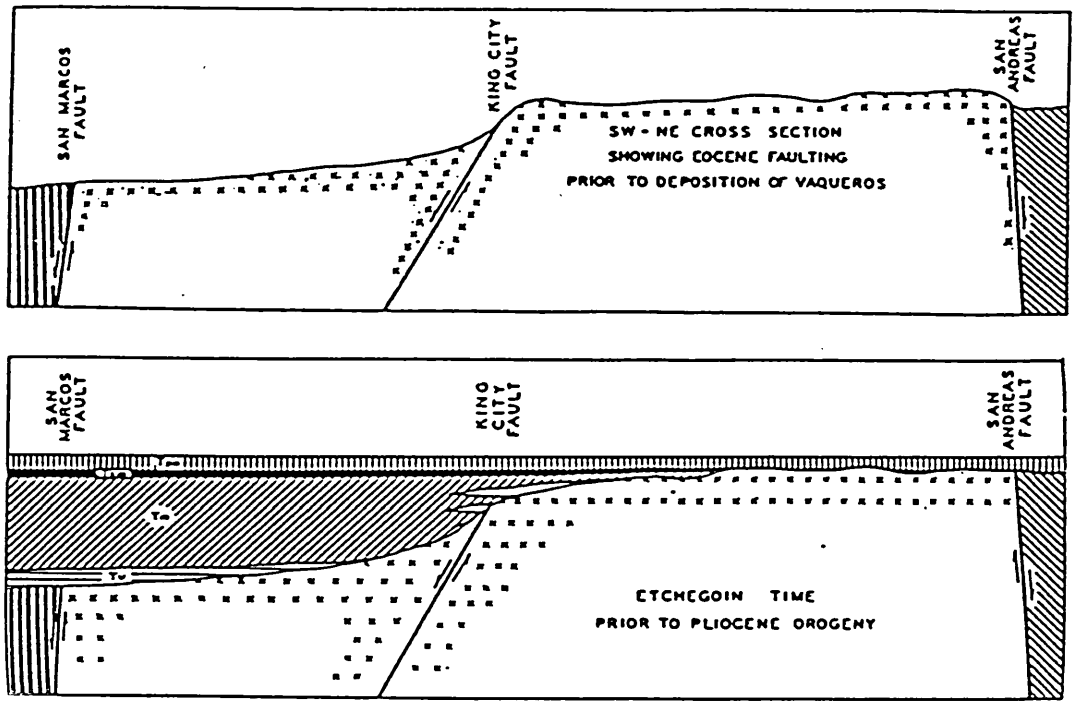


Fig. 6.5 Shows deposition after faulting

(After Kilkenny,1948)

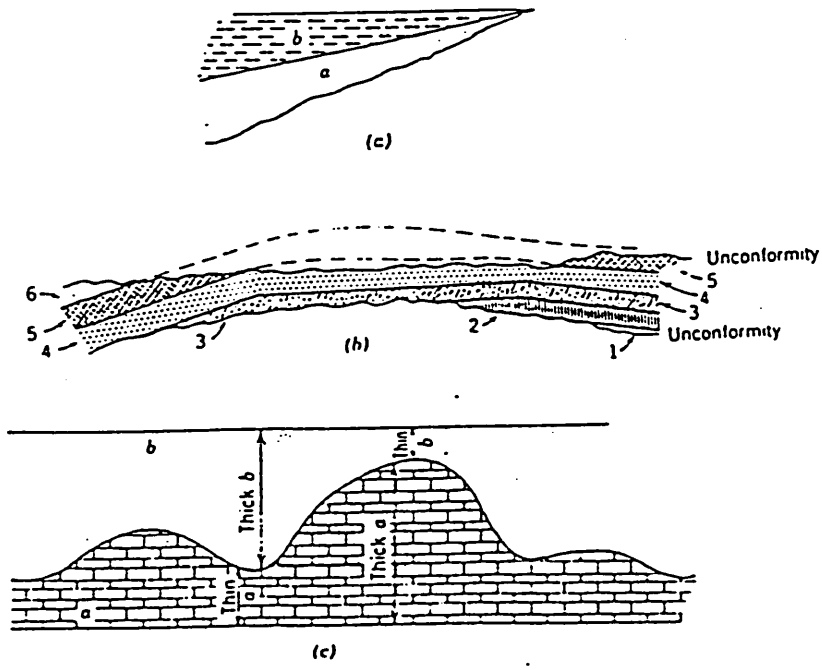


Fig. 6.6 Effects of regional dip (a), uplift (b) and topographic relief (c) on the thickness of deposits (after Bishop,1960).

basin. Inasmuch as sedimentation is thought often to continue until the upper surface of depositon becomes level, the effect of compaction may be minimized in isopach studies if this level surface can be identified and used as the upper boundary of the mapping unit.

Generally, the area of maximum thickness indicates the position of the axis of depositon. The location of positive regions within or bordering the basin is recognized in areas where the unit thins or disappears completely. So, changes in the positions of the axes of positive and deposition regions are reflected by changes in the areal distribution of the minimum and maximum thickness zones of successive stratigraphic units.

6.2.2 The Basement Relief or Structure Contour Map

The basement structure contour map (Fig. 6.7) is based on the depths encountered in the deep wells and the available geophysical measurements or estimations. Thus, this map reflects the regional features of the basement.

Some subsurface lineaments or fractures were interpreted (Fig. 6.7 overlay) according to what has been mentioned earlier in this chapter and Bishop, 1960. These subsurface lineaments or fractures were compared as trends with the main sets of surface lineament, which have been mentioned in Chapter V and appear here between brackets, in order to find out if those surface lineaments or fractures have or have not basement control.

The main features of this map (Fig. 6.7) are:

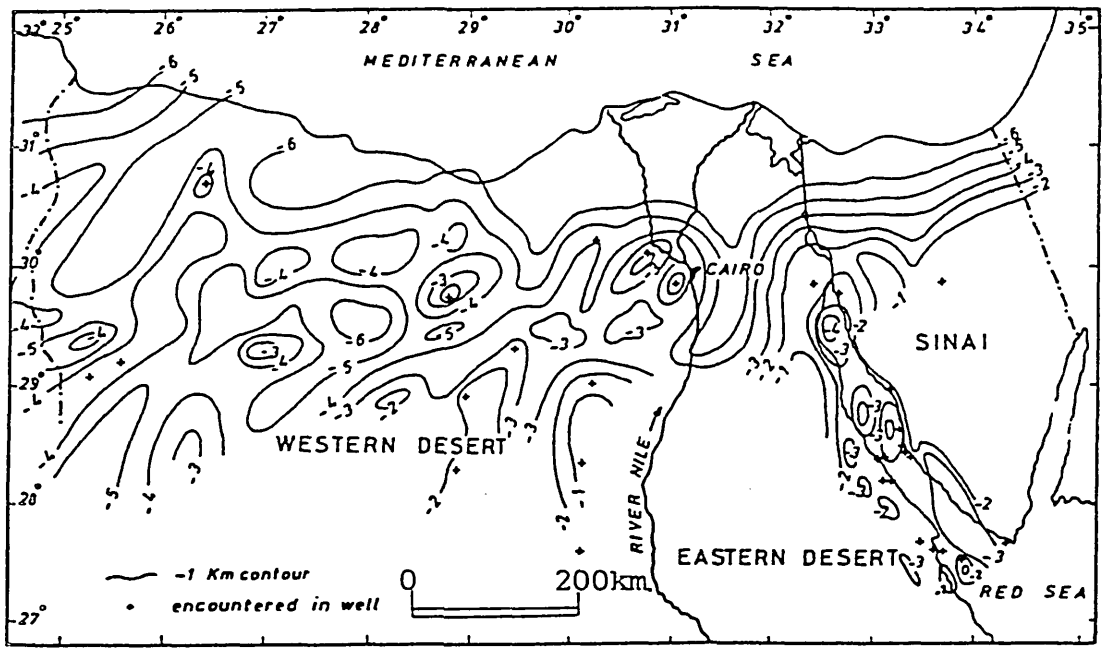


Fig. 6.7 Northern Egypt depth map of top of Basement (El Gezeery *et al.*, 1975).

(After El Shazly,1977)

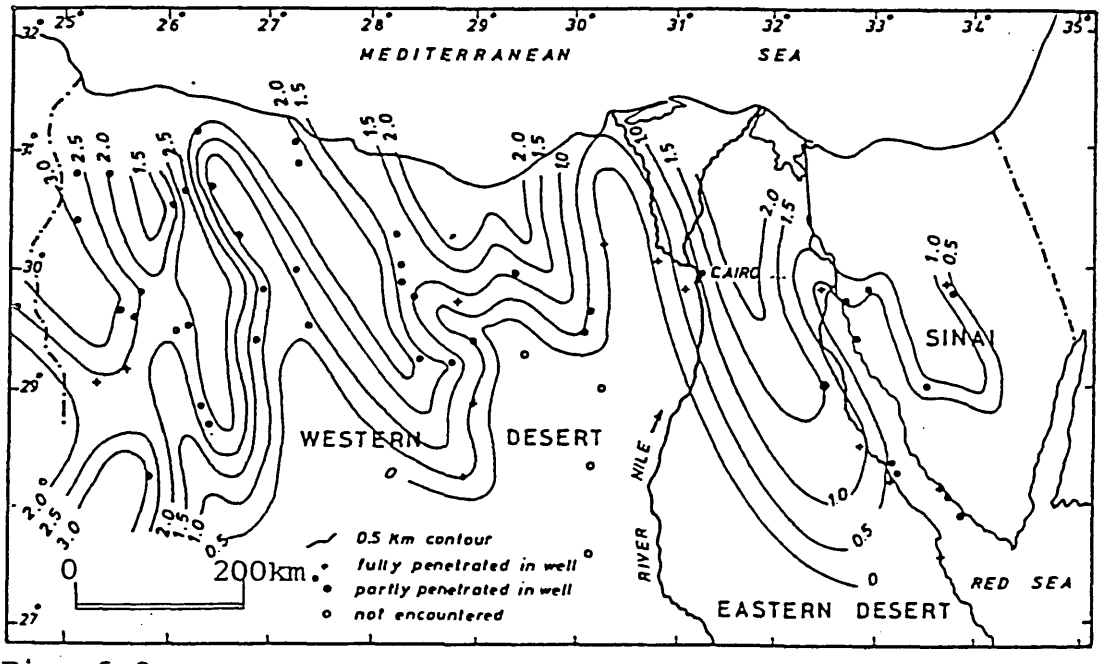


Fig. 6.8 Northern Egypt isopach map of the Paleozoic (El Gezeery *et al.*, 1975).

(After El Shazly,1977)

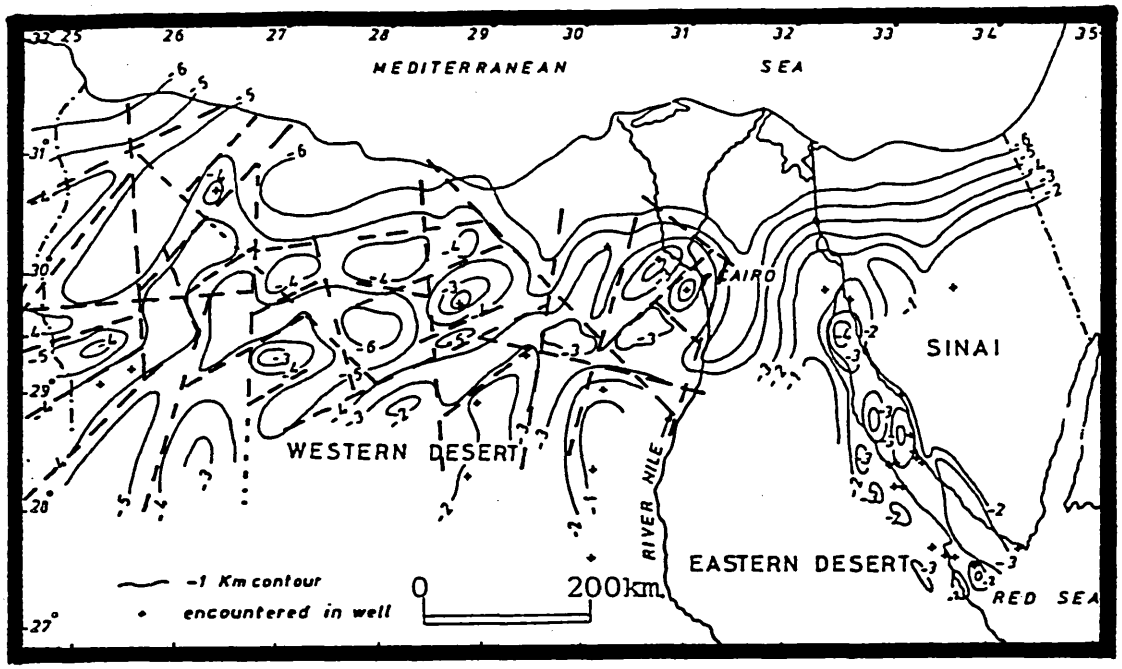


Fig. 6.7 Northern Egypt depth map of top of Basement (El Gezeery *et al.*, 1975).

(After El Shazly,1977)

OVERLAY TO FIG. 6.7

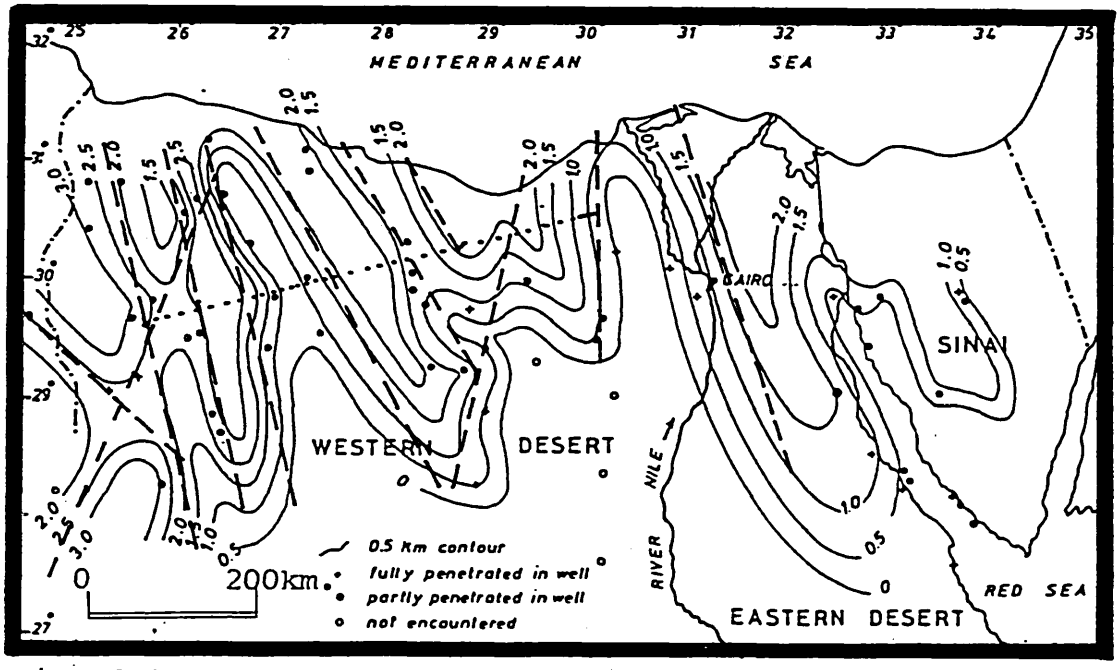


Fig. 6.8 Northern Egypt isopach map of the Paleozoic (El Gezeery *et al.*, 1975).

(After El Shazly,1977)

OVERLAY TO FIG. 6.8

1. The trends of the interpreted subsurface lineaments or fractures are as follows:

a. $N5^{\circ}W$ - $N5^{\circ}E$ (nearly N - S) which swings a few degrees up to 5° degrees to either side (possibly or in part Set 2, surface lineaments);

b. $N60^{\circ}$ - $70^{\circ}E$, ENE, (Set 1);

c. $N85^{\circ}W$- $N85^{\circ}E$, nearly E - W, (Set 5);

d. $N65^{\circ}$ - $70^{\circ}W$, WNW, (Set 4);

e. $N40^{\circ}$ - $50^{\circ}E$, NE, (Set 7);

f. $N15^{\circ}$ - $20^{\circ}E$, NNE, (Set 2);

g. $N15^{\circ}$ - $25^{\circ}W$, NNW, (Set 3);

h. $N40^{\circ}$ - $50^{\circ}W$, NW, which swings a few degrees towards the west (Set 6).

2. These subsurface lineaments enclose between each other structurally low and high areas, basins and uplifts which trend ENE, E - W, NE, NNE, nearly N - S and NNW.

3. Except at the SW corner of the contoured areas, the southern structures are relatively higher than the northern ones.

4. The maximum depth represented on this map (Fig. 6.7) is 6 km.

The basement rocks of the studied area are segmented by fractures of different trends which could be reactivated and/or propagated into the surface and appear as surface lineaments on Landsat images.

6.2.3 Palaeozoic Isopach Map

The Palaeozoic isopach map (Fig. 6.8) demonstrates the following:

a. alternating N10° - 30°W (NNW) basins and uplifts except at the western borders, where the basins and uplifts appear to have nearly N45°W (NW) and N23°E (NNE) trends;

b. These basins and uplifts can be interpreted as having been controlled by N10° - 30°W, N - S, N47°W and N10° - 25°E (NNE) lineament. Also, most of these basins and uplifts are disturbed by N77°E (ENE) lineaments. These lineaments have been identified during the course of this study.

c. The maximum thickness of the Palaeozoic section as shown in Fig. 6.8 is 3 km.

d. The interpreted subsurface lineaments, which trend N10° - 30°W, N10° - 25°E, N47°W and N77°E, are comparable with some of the different surface lineament sets, which have been interpreted from the Landsat images (see the previous chapter).

e. The stratigraphic cross section (Fig. 6.10), (where the top of the Palaeozoic has been taken here as a datum) shows that the Palaeozoic basins and uplifts were established as a result of basement block faulting.

f. The non-parallel uplifting during late Palaeozoic, (see Fig. 6.10) at wells El Nashfa, Wadi Natrun and Khatatba, caused NNW fractures within the Palaeozoic section (see Price, 1974 and Fig. 5.16). These or some of these fractures are most probably

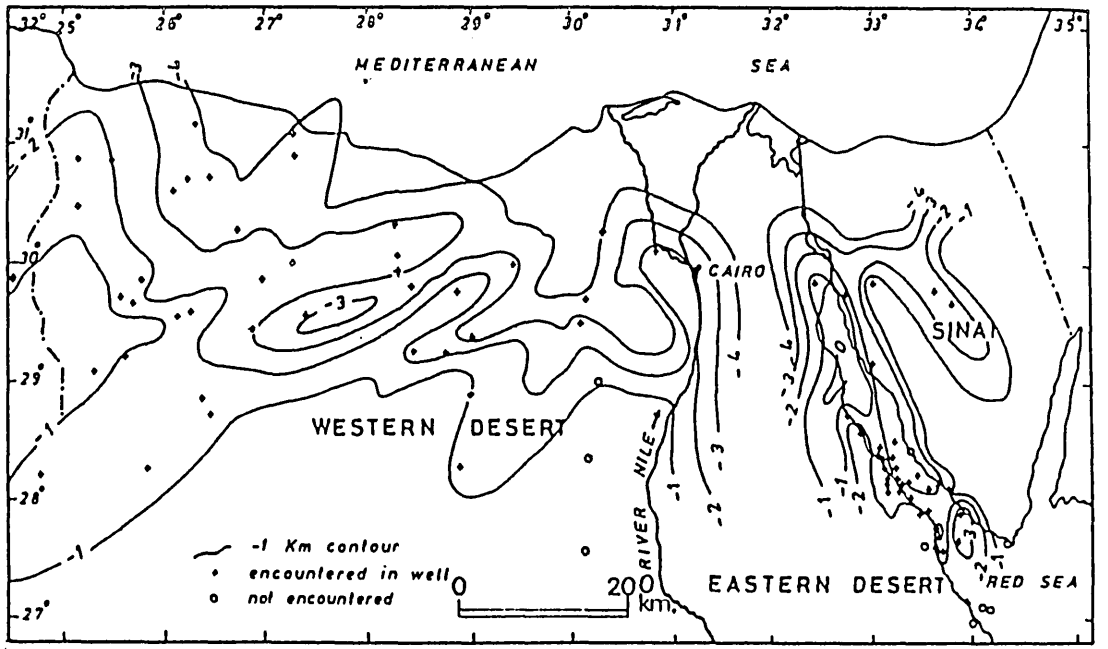


Fig. 6.9 Northern Egypt depth map of top of Paleozoic (El Gezeery *et al.*, 1975).

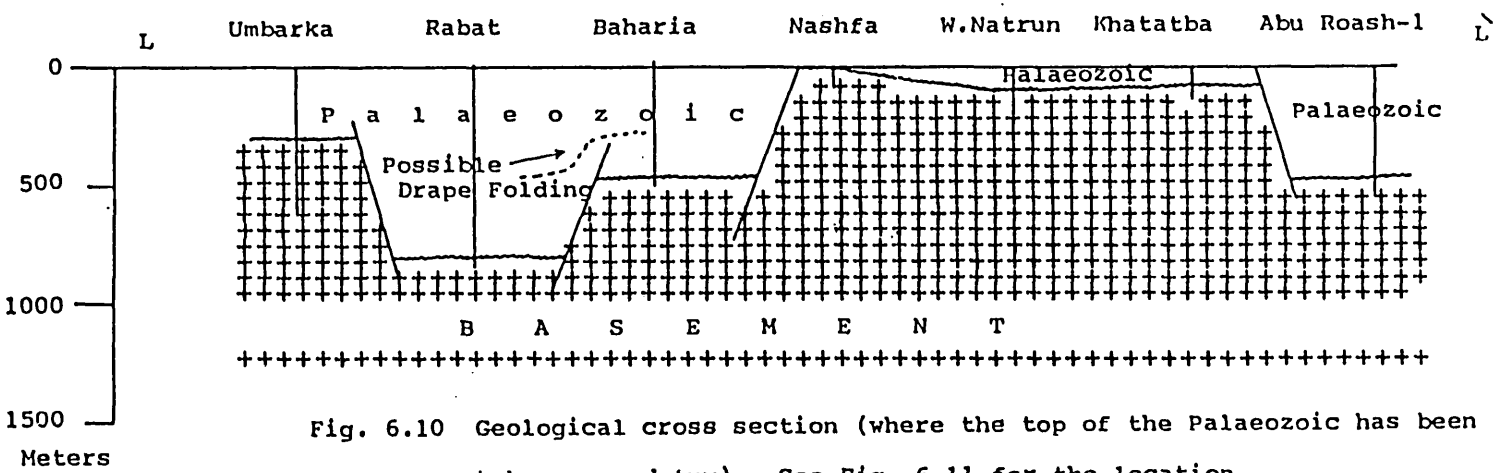


Fig. 6.10 Geological cross section (where the top of the Palaeozoic has been taken as a datum). See Fig. 6.11 for the location.

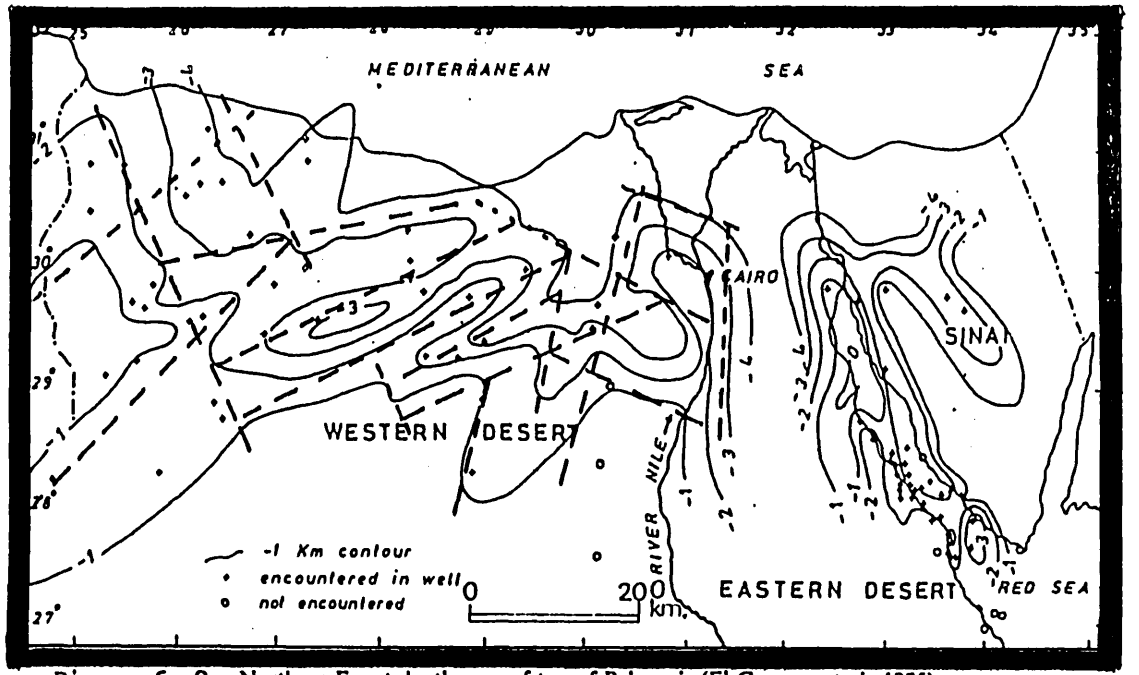


Fig. 6.9 Northern Egypt depth map of top of Paleozoic (El Gezeery *et al.*, 1975).

OVERLAY TO FIG. 6.9

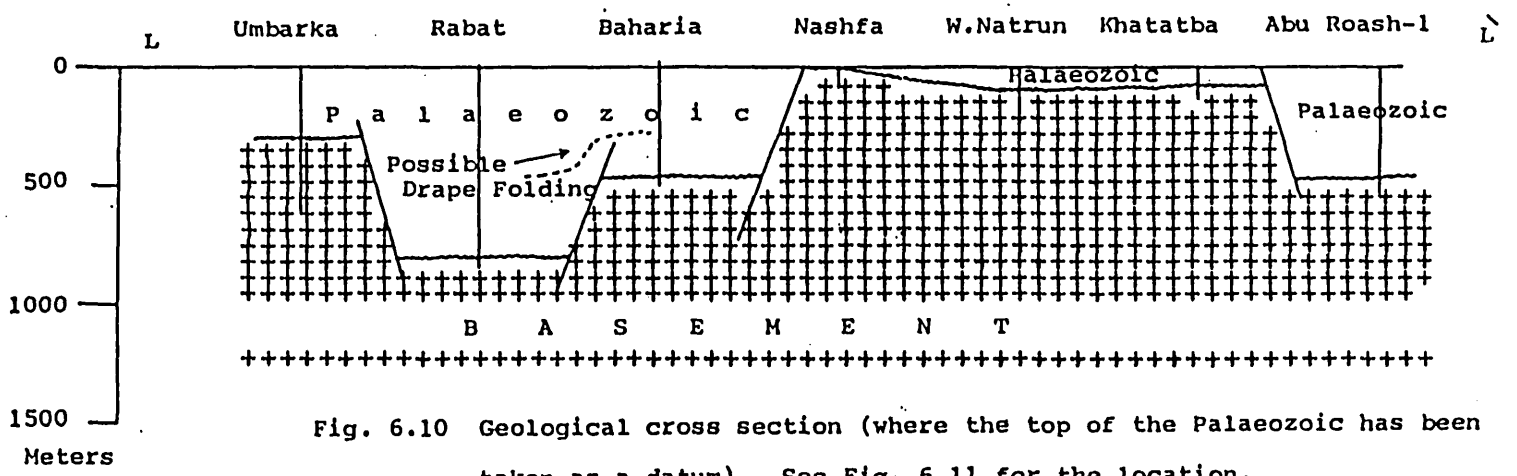


Fig. 6.10 Geological cross section (where the top of the Palaeozoic has been taken as a datum). See Fig. 6.11 for the location.

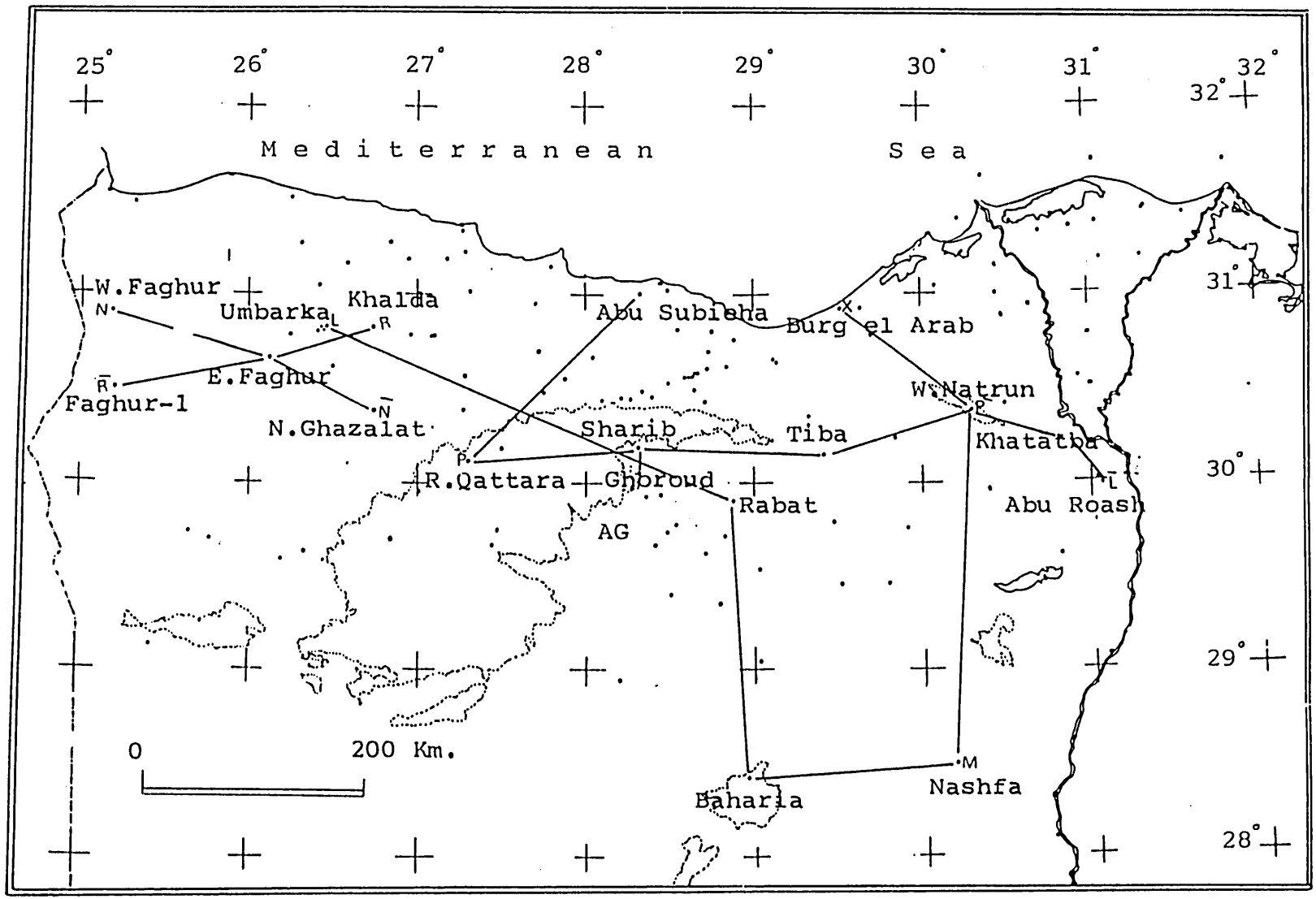


Fig. 6.11 Location map of the geological cross sections.

basement faults which developed or reactivated during the end of the Palaeozoic.

g. The interpreted subsurface lineaments, (Fig. 6.9) of top Palaeozoic [which trend N60 - 78E, (ENE), N40-50E (NE), N15°E (NNE), N3°E (nearly N - S), N60 - 70W (WNW) and N20° - 30°W (NNW)] have been recognized from the surface lineament sets.

h. Palaeozoic folding

Said (1962) mentioned that the Palaeozoic section has been affected by N - S folds. In fact, the trends of such fold as shown in Fig. 2.29 are ranging from N20°W to N20°E. The mechanics of these folds have been completely ignored.

In light of the previously mentioned points, the Palaeozoic section is controlled by basement tectonics.

The basement rocks in the Northern Western Desert of Egypt deform by faulting and rigid-block rotation. These faults at the interface between the sedimentary and crystalline basement rocks can be anything from low-angle reverse faults to normal faults (Fig. 6.12). Thus, the Palaeozoic sedimentary layers deformed primarily by block faulting, where vertical movements seem more likely to dominate than horizontal movements and possibly by block rotation.

The final geometry of the product of block faulting (such as folding, monoclines (Figures 6.13 and 6.14) demand some seismic cross sections (see Fig. 6.15) to give a clear cut picture of the basement - Palaeozoic

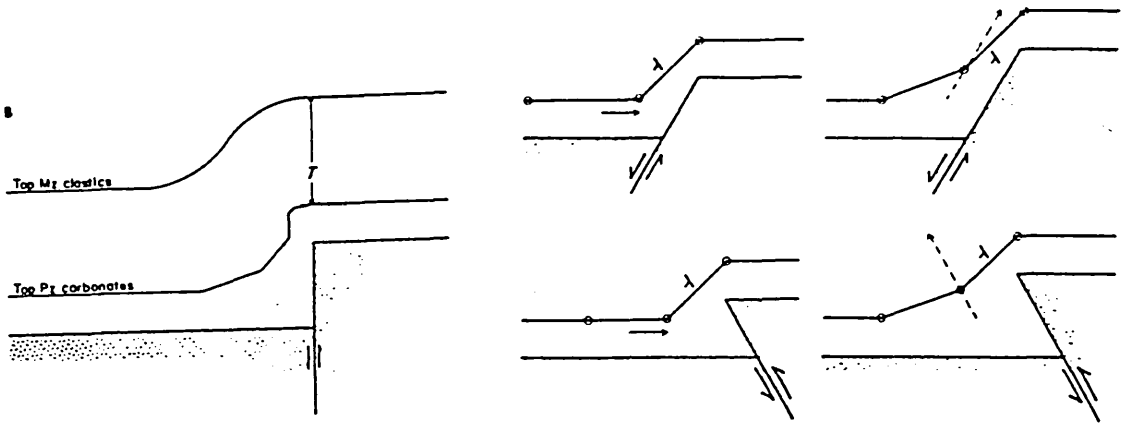


Fig. 6.12 Possible basement faults and their effects on the overlying sediments(after Weinberg,1978).

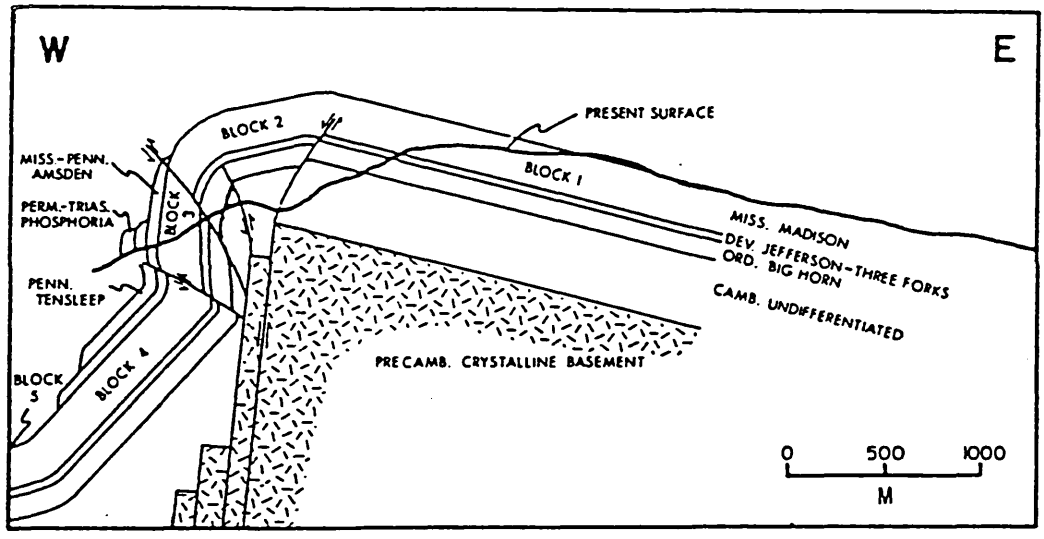
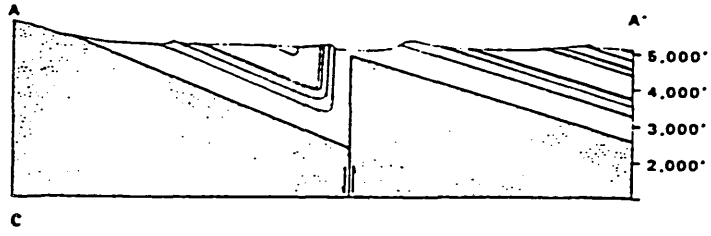
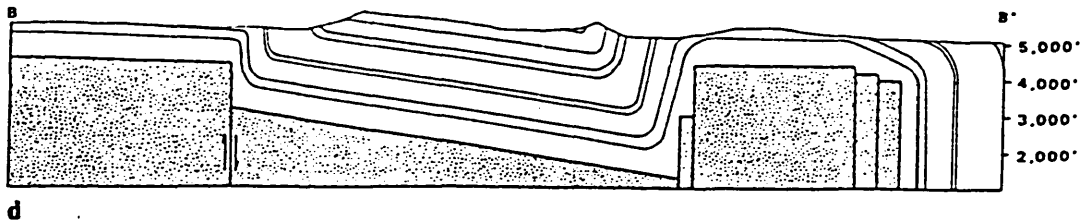


Figure Geologic cross-section of Rattlesnake Mountain (modified from Stearns, 1971, Fig. 5, p. 131).

(After Weinberg,1978)





(After Matthews and Work,1978)

Fig. 6.13 Some drape folds.

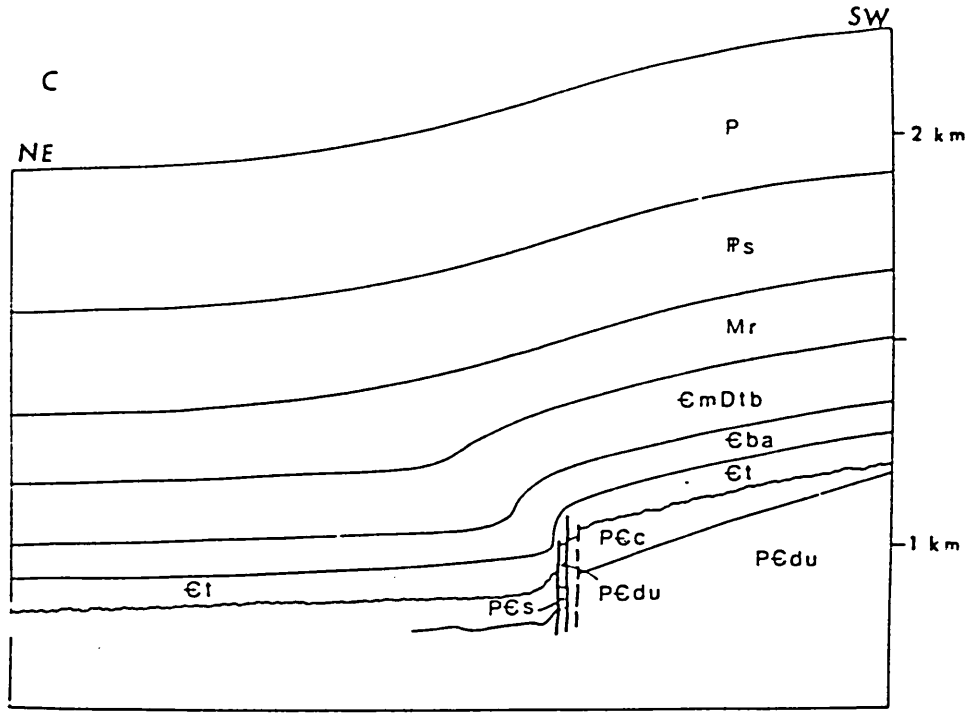


Fig. 6.14 A monocline structure
(After Reches and Johnson,1978)

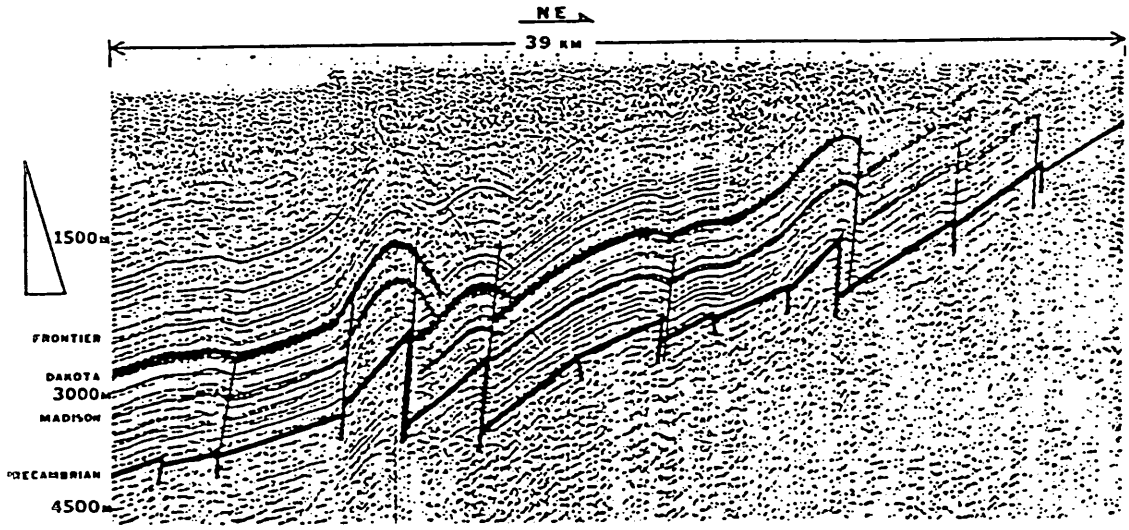


Fig. 6.15 Seismic section, northern Bighorn Basin, Wyoming.
(After Sacrison,1978)

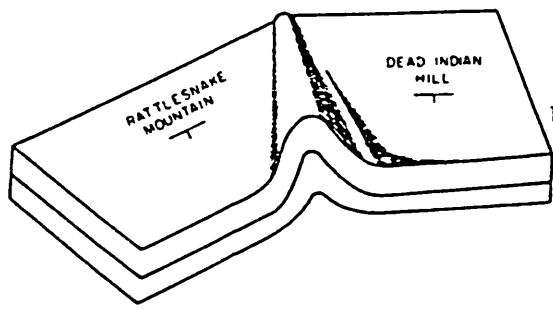


Fig. 6.16
Unforced fold structure
(after Stearns,1978).

structures. However, in the absence of such seismic cross sections, the present writer put forward the following as possible mechanics for the development of the Palaeozoic folding:

1. Basement block faulting (Figs. 6.13 and 6.15);

2. Rotation of blocks in the same general direction, but along different axes of rotation, which result in the development of folds (Fig. 6.16) from an excess of material in layered rocks, where the two blocks join one another;

3. Gravity tectonics, as a result of the rotation of blocks which causes an increase of the regional dip of one block and decreases in the regional dip of the other block (ramp structure). The gravitational sliding may be coupled with tearing as indicated in Fig. 6.17.

6.2.4 Jurassic Isopach Maps

The isopach map (Fig. 6.18) represents the thickness contour of the total Jurassic sediments from the bottom of Eghei (which uncomformably overlies the Palaeozoic sediments) to the top of Masajid formations. The main features of such a map are:

1. Rabat uplift, which trends N50E (NE) and plunges in both NE and SW;

2. Agnes-Cairo embayment with a trend that varies from N90^{o}E (E - W) at Cairo to nearly N60^{o}E to the east;

3. Betty-Marzouk embayment which borders Rabat uplift from the west. Its trend is N25^{o}E (NNE) and sediments become thicker in the same direction;

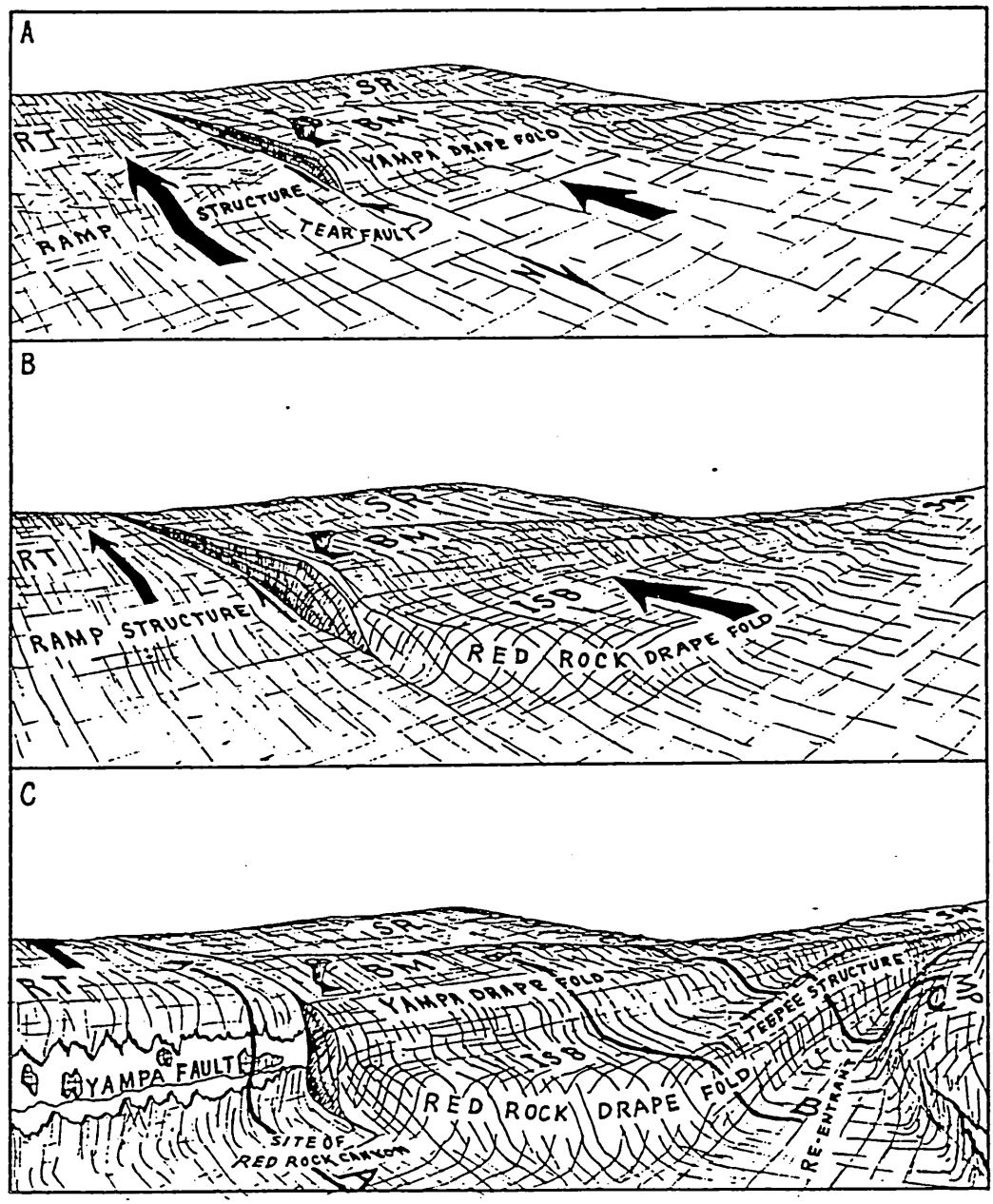


Fig. 6.17 Drawing illustrating sequential movements and deformation envisioned for Dinosaur National Monument(after Cook,1978).

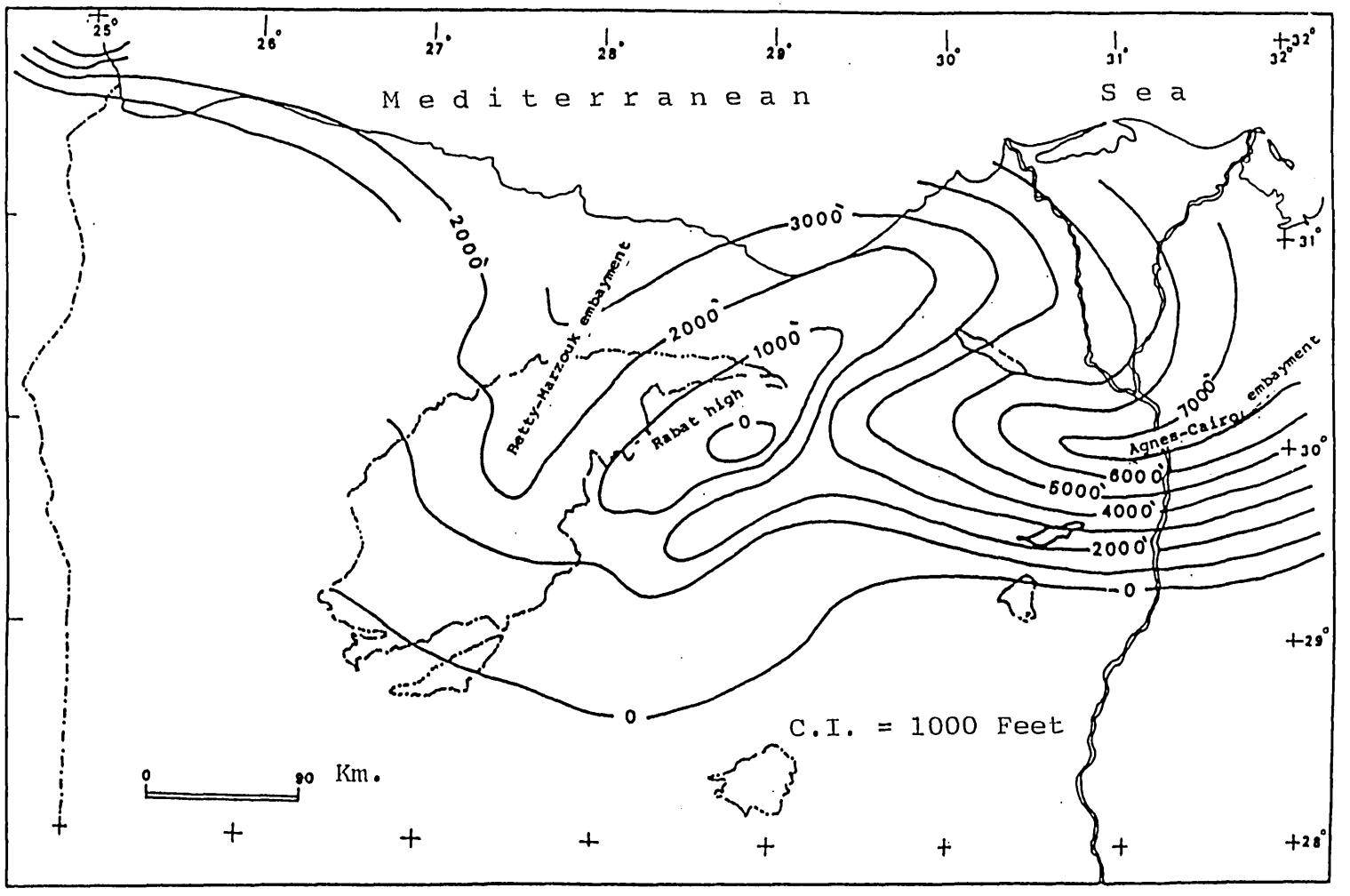


Fig. 6.18 Jurassic isopach map (after Khalid,1975).

4. The maximum thickness of the Jurassic sediments is 7000 feet or 2133 meters;

5. The geologic cross sections which are represented in Figs. 6.19 to 6.21, where the top of the Jurassic has been taken as a datum, demonstrate the following:

a. The thickness is controlled by basement faults in a form of horsts and grabens, as indicated in Figs. 6.19 and 6.20.

b. The area was tectonically active, especially during the deposition of Khatatba and Masajid formations where some faults, which have downthrow sides toward the north, were developed, possibly as a result of downwarping (see Price, 1974). This structural activity caused an increase in the thickness of Khatatba and Masajid formations towards the north (Fig. 6.21).

c. The subsurface criteria of lineaments are in conformable relation with the interpreted surface lineaments from Landsat images, as shown in Fig. 6.22. Accordingly, some of the surface lineaments are earlier structures which were reactivated during the Jurassic.

d. The western and southern borders of the studied area were structurally high during the Jurassic (Figs. 6.18 and 6.23).

e. It is quite clear from Fig. 6.18 that the faults which bounded the Agnes-Cairo embayment and Rabat uplift from the southern and southeast sides, respectively, are more steep than the other sides.

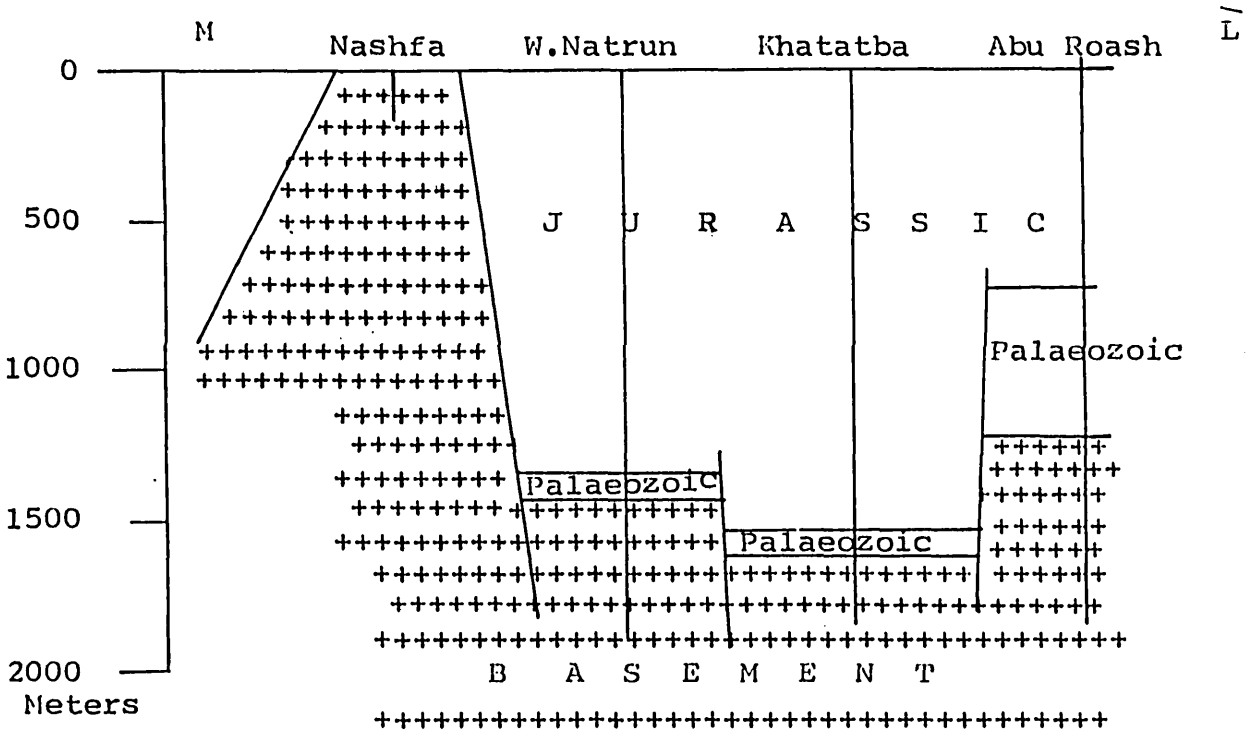


Fig. 6.19 Geological cross section M - L

(where the top of the Jurassic has been taken as a datum)

(See Fig. 6.11 for the location)

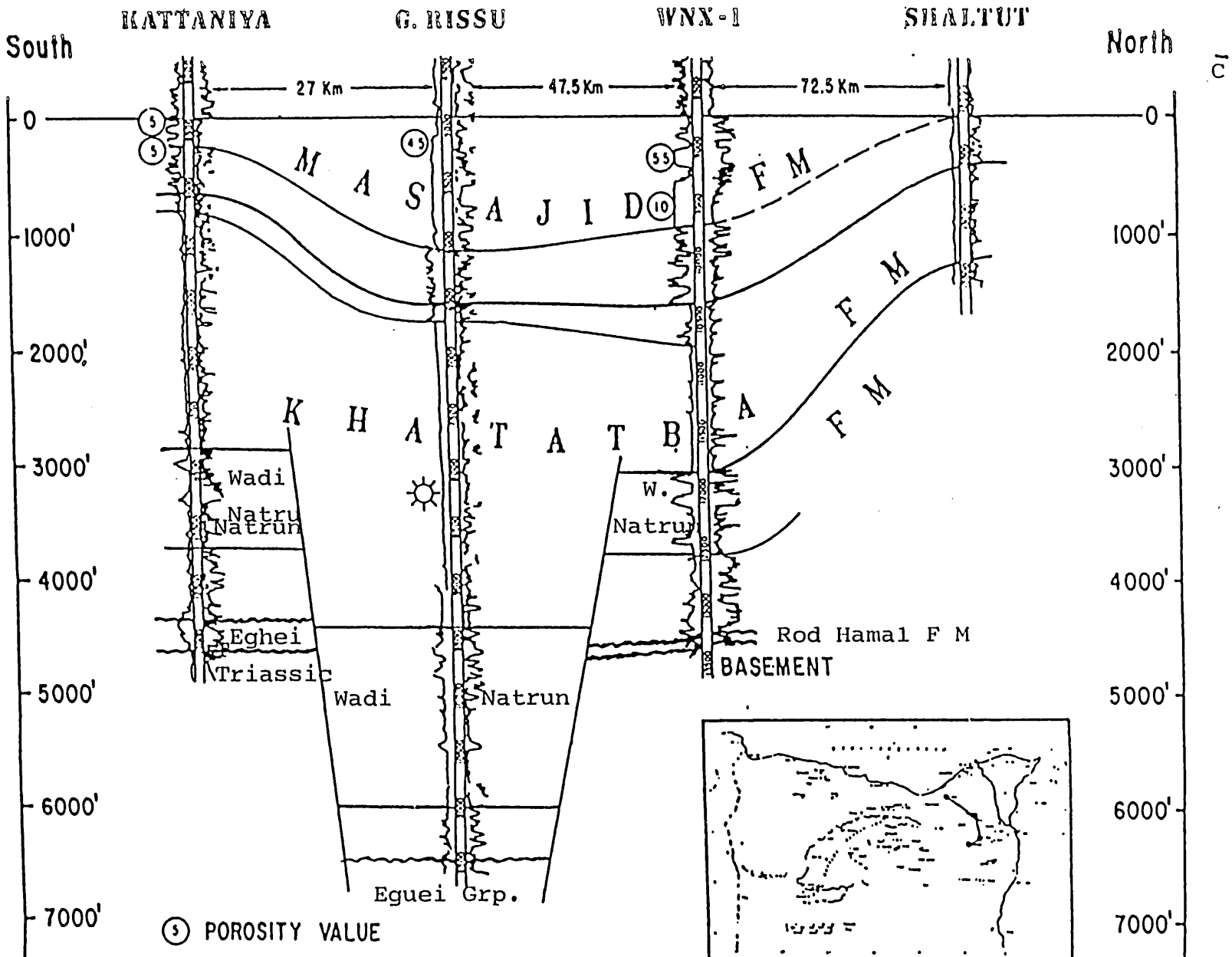


Fig. 6.20 Geological cross section C - $\bar{C}$, where the top of the Jurassic has been taken as a datum(modified by the present author after Khalid,1975).

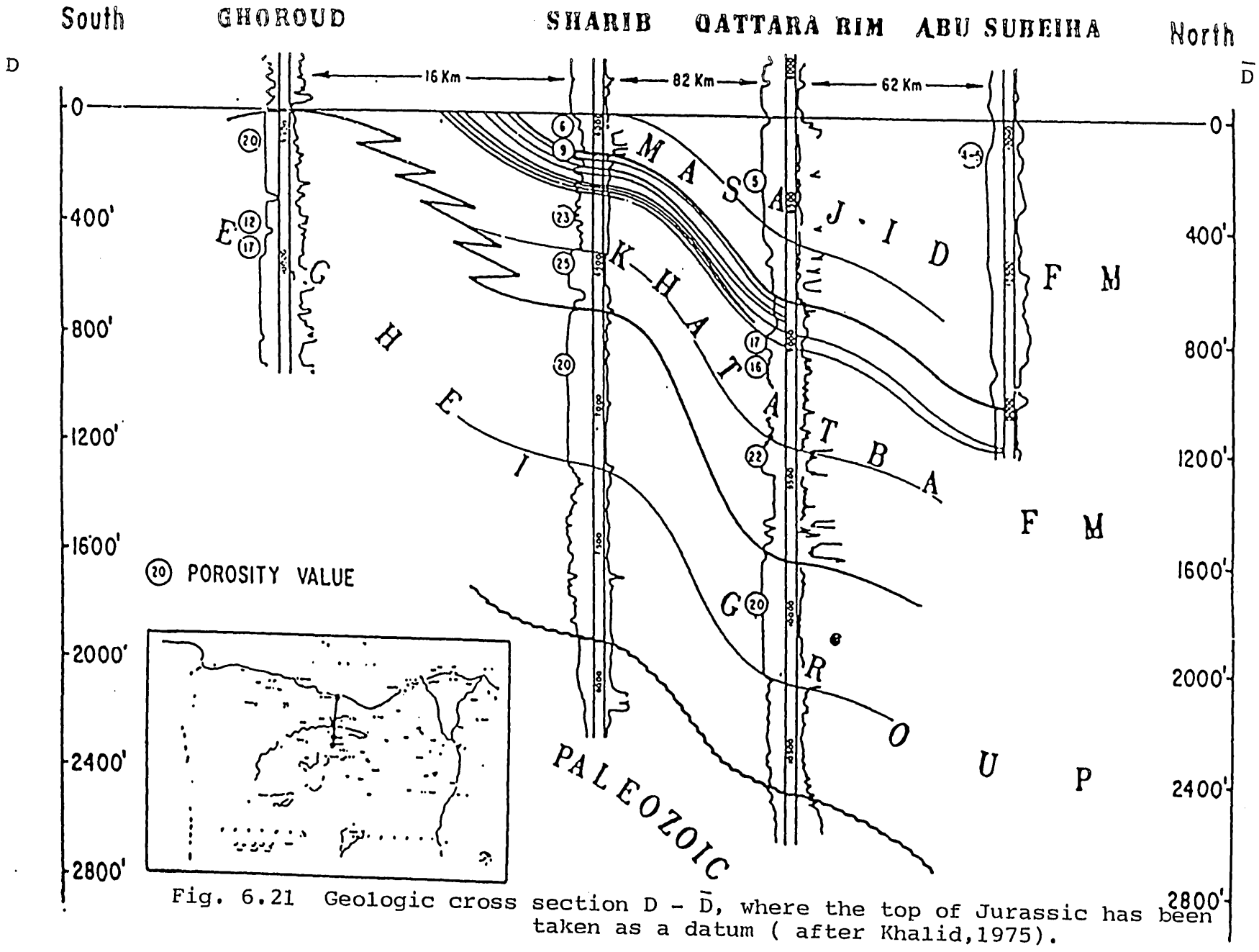


Fig. 6.21 Geologic cross section D - D̄, where the top of Jurassic has been taken as a datum (after Khalid,1975).

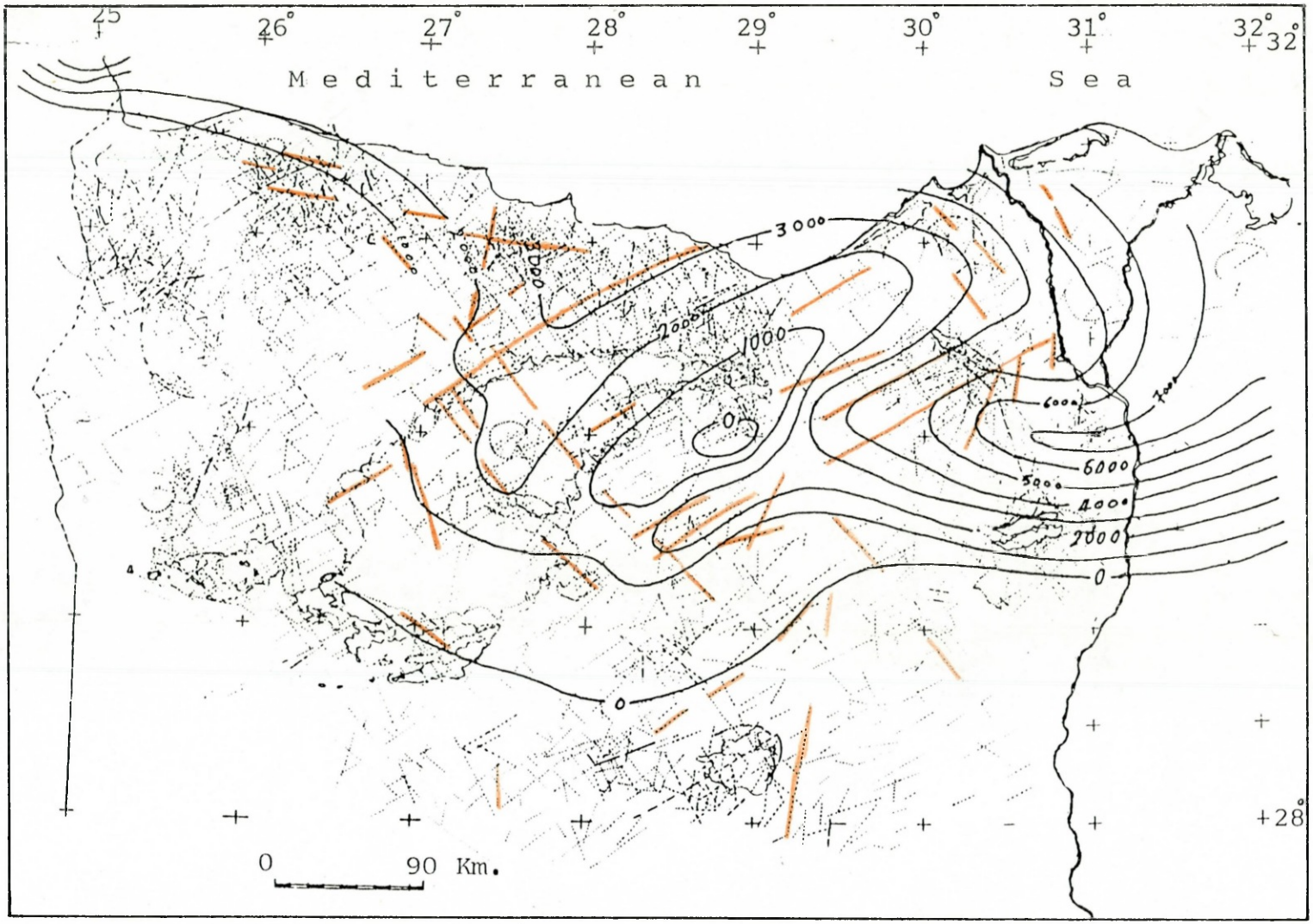


Fig. 6.22 Compiled Jurassic isopach and lineament (I.R. Colour composite) map.

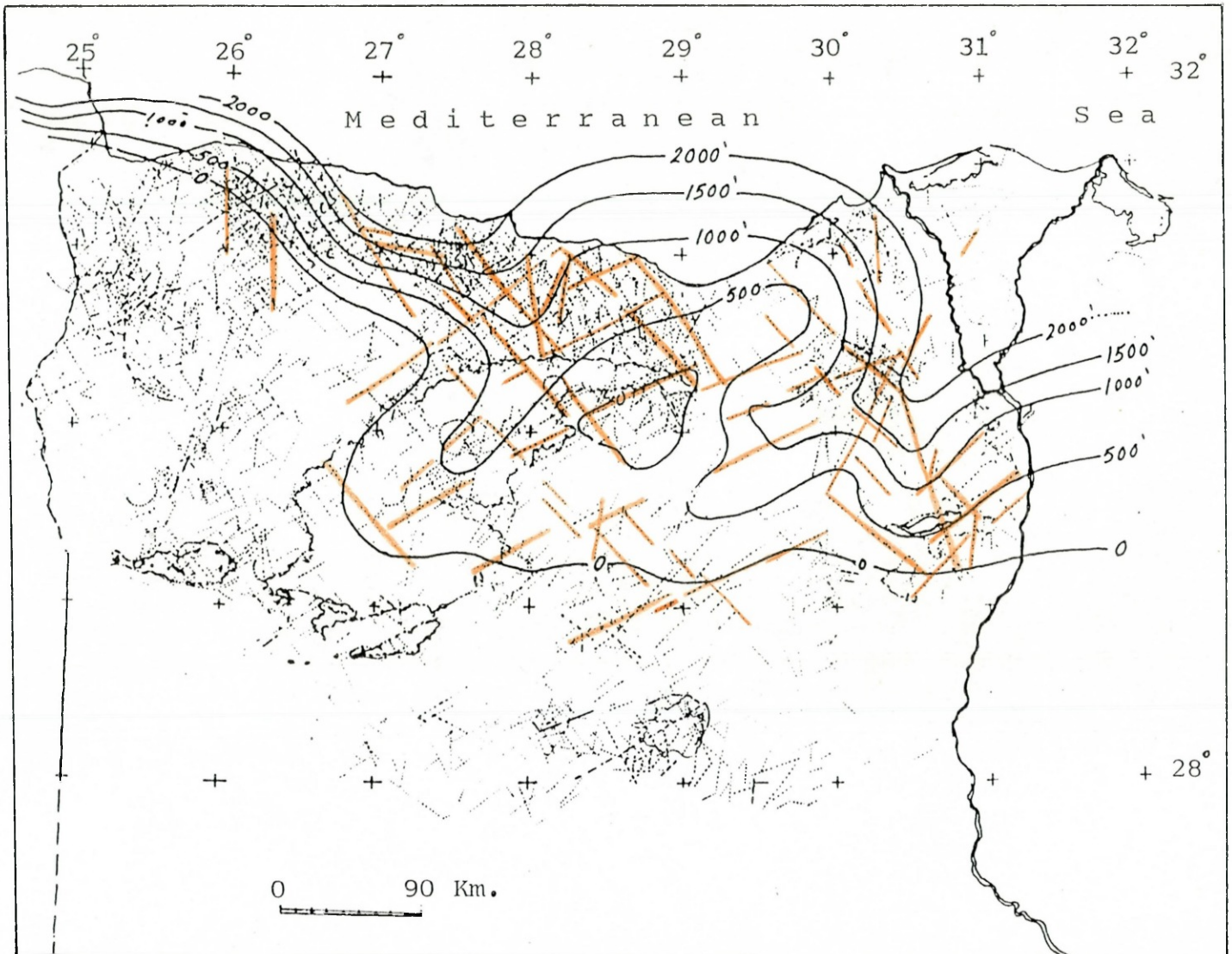


Fig. 6.23 Compiled Masajid formation isopach and lineament (I.R. Colour composite) map.

f. The studied area was tilted towards the north during the deposition of the Masajid formation (upper - middle to upper Jurassic) (see Figs. 6.22 and 6.23).

g. The effects of the nearly N50W faults on the Masajid formation become evident as indicated in Fig. 6.23. These faults may be developed as shear fractures, but their effects are not apparent here. The evidence of such shears is clear in the Albian-Cenomanian isopach map (Fig. 6.24) which will be discussed later.

In conclusion, the analysis of the Jurassic isopach maps indicates the following:

1. In the studied area, the thickness of the Jurassic sediments changes where it increases towards the north and from west to east.

2. The structures of the studied area, such as uplifts and embayments, could be attributed to basement tectonics, which played a major role during this period.

3. Some of the NE or ENE faults developed as a result of downwarping, while others along with nearly N50W and may be nearly N - S, developed as a result of non-parallel uplift by the end of the Jurassic.

4. This non-parallel uplift caused the tilting of the studied area towards the north.

5. The lineaments in Figs. 6.22 and 6.23 may have a structural and stratigraphical significance, although they are disconnected and seem to be of limited length. This discontinuity of the lineaments could be attributed to many factors, such as the nature of the terrain and

the absence of any digital enhancement of the Landsat images.

6.2.5 Albian-Cenomanian Isopach Map

The Albian-Cenomanian isopach map (Fig. 6.24) consists mainly of an alternative series of N65-70E (ENE) basins and uplifts. It has been deduced by the present writer that these basins and uplifts were subsequently dislocated by nearly N50°W (NW) fault, as dextral strike-slip fault, as indicated in Fig. 6.24. This fault divided Abu Gharadig basin into two sub-basins. The other main features of the map are:

1. Umbarka-Mideiwar basin, which is divided into:
   a. Abu Tunis sub-basin and
   b. East Umbarka sub-basin;
2. North Siwa-Khadem/Obayed Allah uplift;
3. Western Abu Gharadig sub-basin;
4. Baharia uplift;
5. El-Minya, or Nile basin;
6. Eastern Abu Gharadig sub-basin, which is divided by a relatively high block, Wadi Khadis block, into two parts;
7. Rabat-North Dillingat uplift;
8. El-Dabaa basin;
9. The maximum thickness is 5500 feet, or about 1676 meters. Specifically, the thickness contour map (Fig. 6.24) represents the thickness contours of the Cenomanian as the lower part of the upper Cretaceous, the Albian and the uppermost part of the Aptian, as the upper

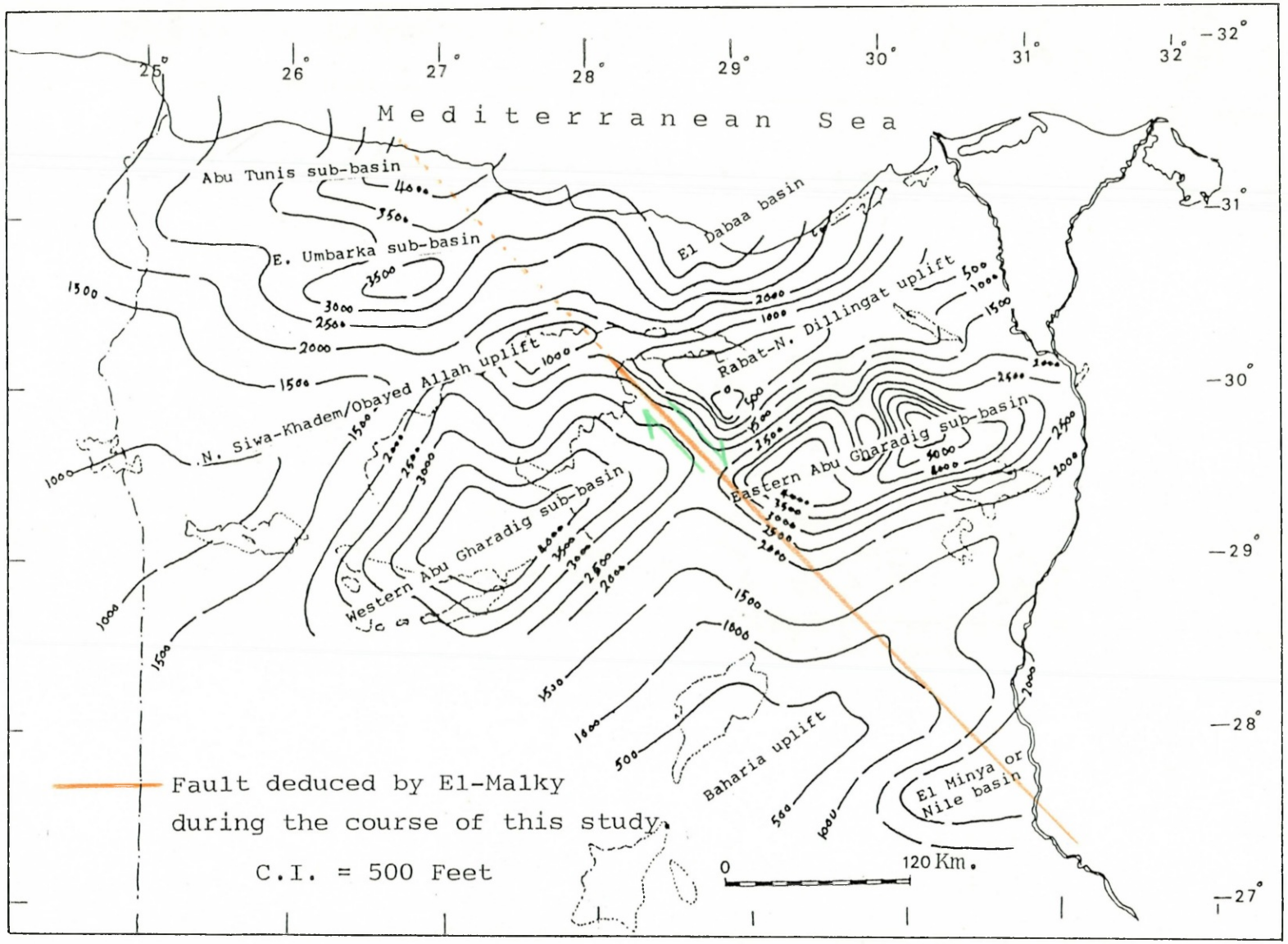


Fig. 6.24 Isopach map of Albian-Cenomanian (top Alamein-top Abu roash) (After Aadland and Hassan,1972)

part of the lower Cretaceous. The geological cross sections (Figs. 6.25 to 6.28) demonstrate the following:

a. The thickness variations of the lower Cretaceous are controlled by basement block faulting.

b. The thickness of the Cenomanian sediments show no remarkable effects as a result of the lower Cretaceous differential block faulting movements.

Hence, the Albian-Cenomanian isopach map (Fig. 6.24) reflects the block faulting of the lower Cretaceous and Jurassic in a form of basins and uplifts. This is clearly shown on Fig. 6.24 by the strong ENE and NW lineation of the thickness contours.

10. The deduced NW dextral strike-slip fault matches a major NW lineament.

11. Some of the surface lineaments (Fig. 6.29) are in alignment with the subsurface lineaments or criteria. This means that these surface lineaments may have subsurface structural control and in turn, stratigraphical control.

6.2.6 Turonian Isopach Map

The Turonian isopach map (Fig. 6.30) is composed of an alternating series of nearly N50-90E (NE to E - W) trending basins and uplifts which are narrower than those of the Albian-Cenomanian (Fig. 6.24). During the course of the analysis, two nearly N50W (NW) faults, F_1-F_1 and F_2-F_2, have been deduced and located (Fig. 6.30). One of these NW faults, F_1-F_1, is taken to be a continuation of

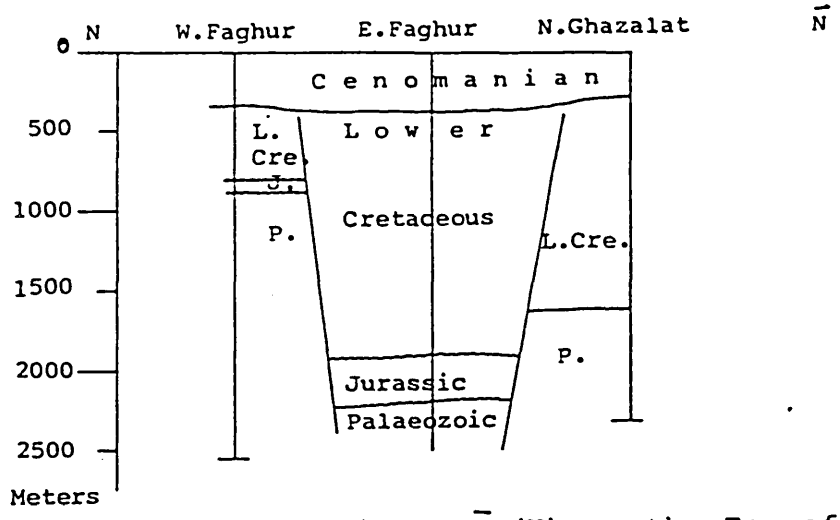


Fig. 6.25 Geologic Cross Section N-$\bar{N}$ (Where the Top of Cenomanian Has Been Taken As a Datum)

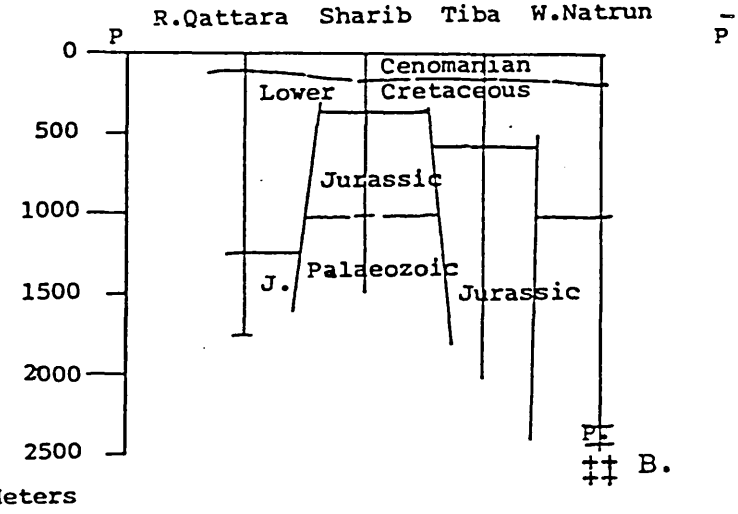


Fig. 6.26 Geological Cross Section P-$\bar{P}$ (Where the Top of Cenomanian is a Datum

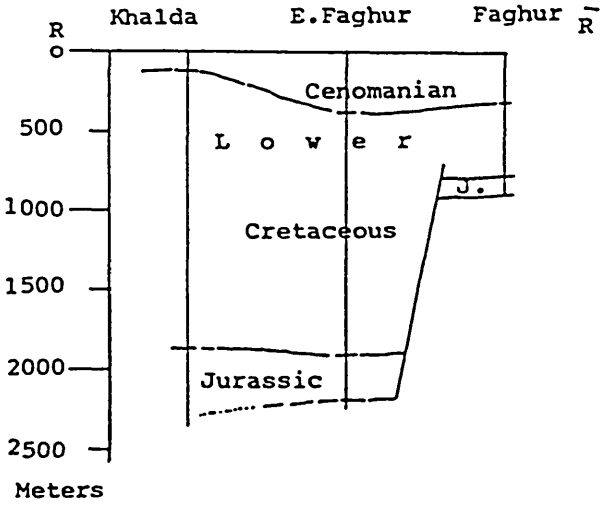


Fig. 6.27 Geological Cross Section R-$\bar{R}$ (Where the Top of Cenomanian is a Datum)

(See Fig. 6.11 for the location of these sections)

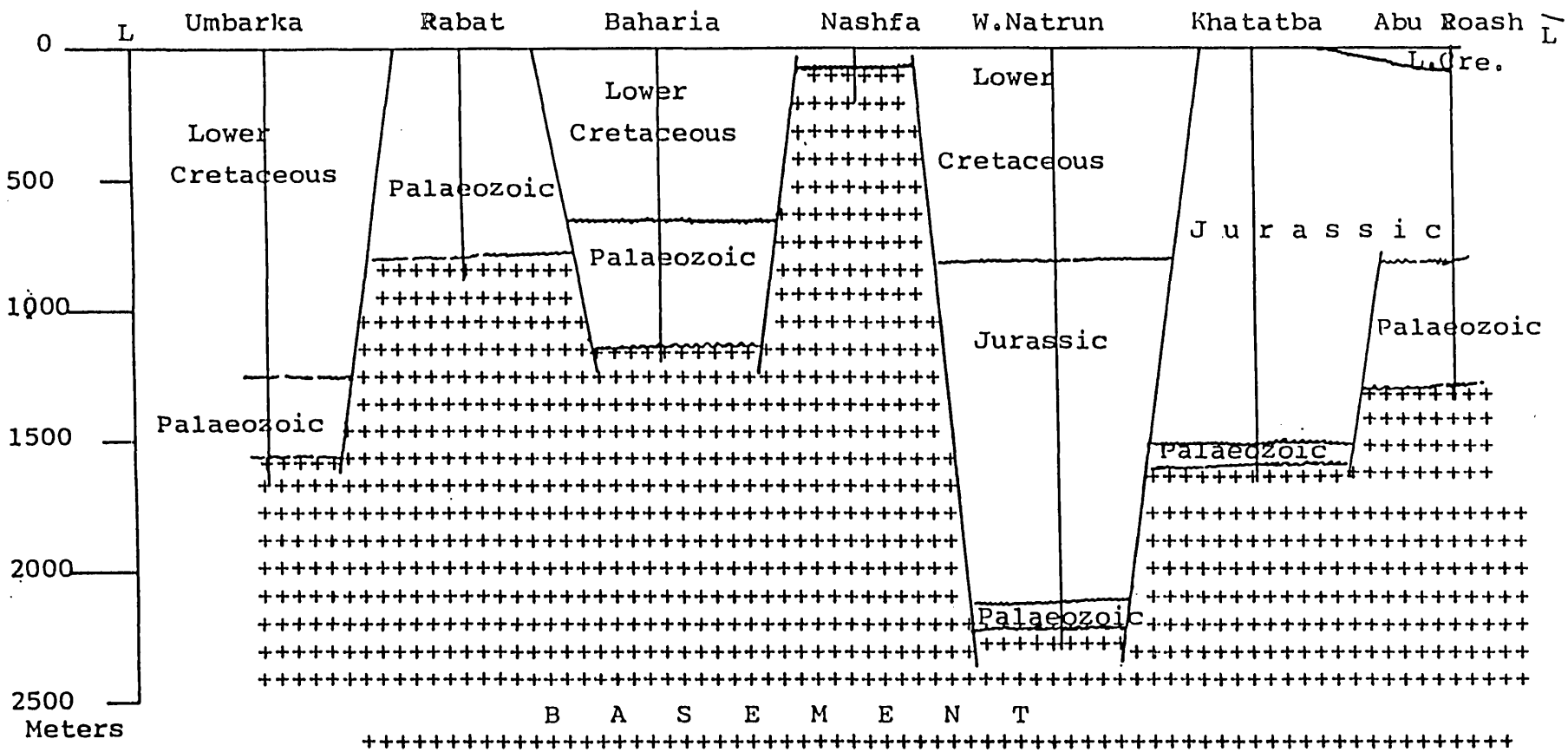


Fig. 6.28 Geological cross section L - $\bar{L}$ (where the lower Cretaceous is a datum).

(See Fig. 6.11 for the location)

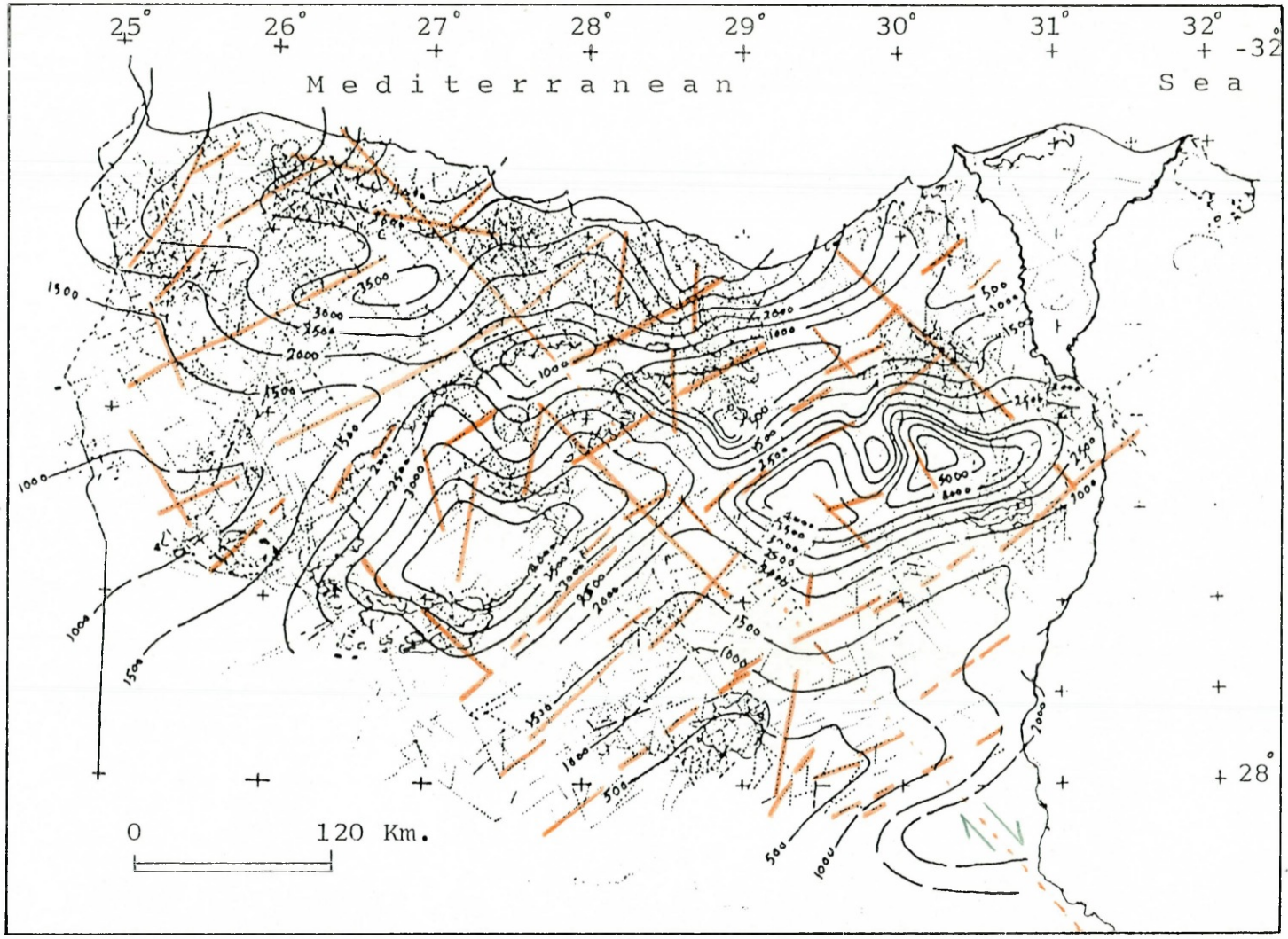


Fig. 6.29 Compiled Albian-Cenomanian isopach and lineament (I.R. Colour composite) map.

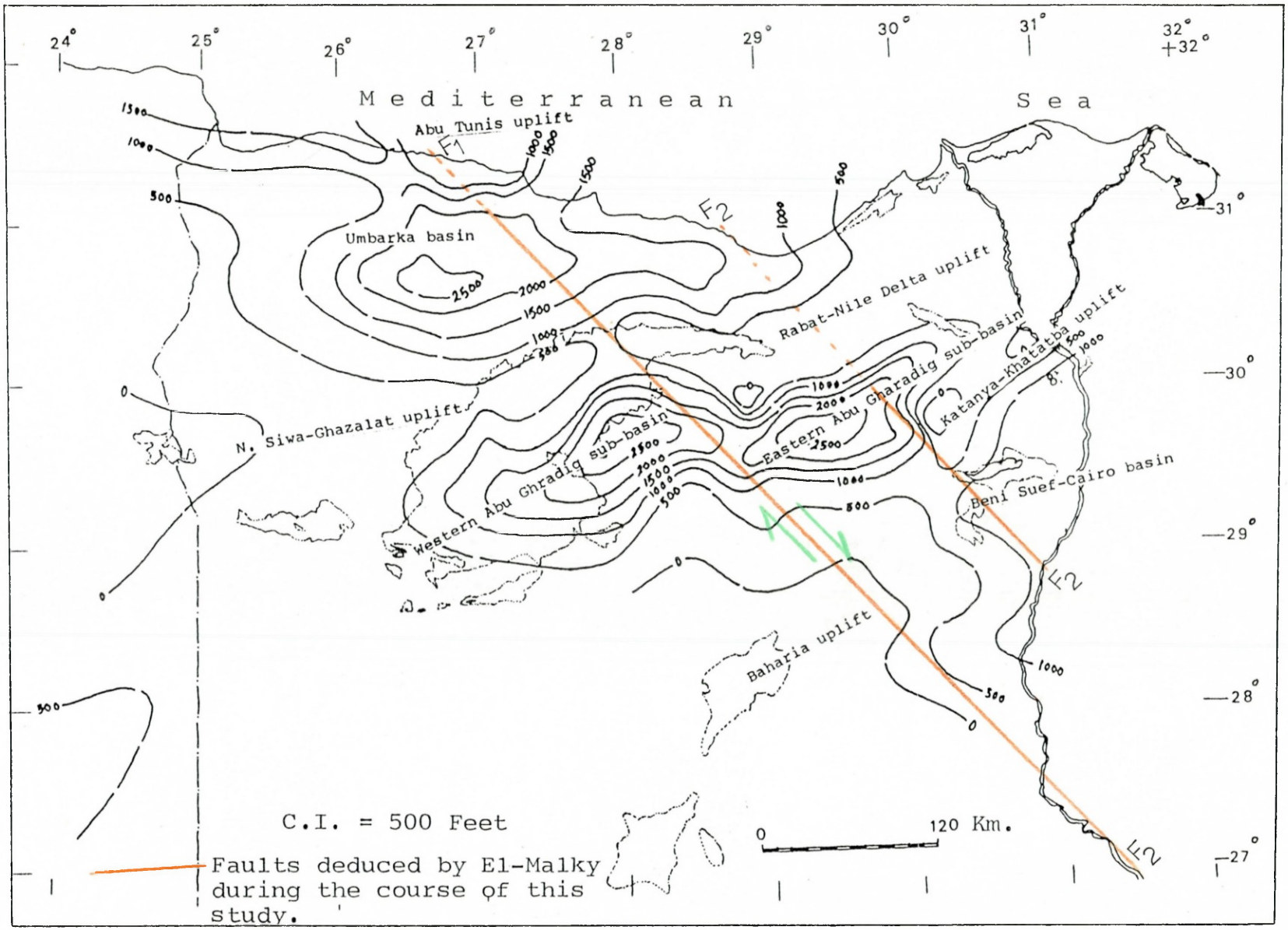


Fig. 6.30 Isopach map of Turonian (after Aadland and Hassan,1972).

the dextral strike-slip fault, which dislocated the Albian-Cenomanian basins and uplifts (Fig. 6.24). The main features of the Turonian isopach map (Fig. 6.30) are:

1. Abu Tunis uplift (N80^{o}E);
2. Umbarka basin (N87^{o}E);
3. N. Siwa-Ghazalat uplift (N75^{o}E);
4. Western Abu Gharadig sub-basin (N70^{o}E);
5. Baharia uplift (N57^{o}E);
6. Beni-Seuef - Cairo basin (N56^{o}E);
7. Katanya-Khatatba uplift (N50^{o}E);
8. Eastern Abu Gharadig sub-basin (N57^{o}E);
9. Rabat-Nile Delta uplift (N60^{o}E);
10. The maximum thickness is 2500 feet or about 750 meters
11. The narrowing of the Turonian basins and uplifts, relative to Albian-Cenomanian basins and uplifts, could be attributed to the upper Cretaceous folding where their sedimentary fill buck-led, as indicated in Figs. 6.31 to 6.33.

Studying the isopach map of the Turonian in conjunction with the interpreted surface lineaments, as shown in Fig. 6.34, indicates that some of the lineaments almost certainly have structural and stratigraphical control upon the thickness contours.

Based on the Cretaceous thickness contours and the geological cross sections, one can conclude the following:

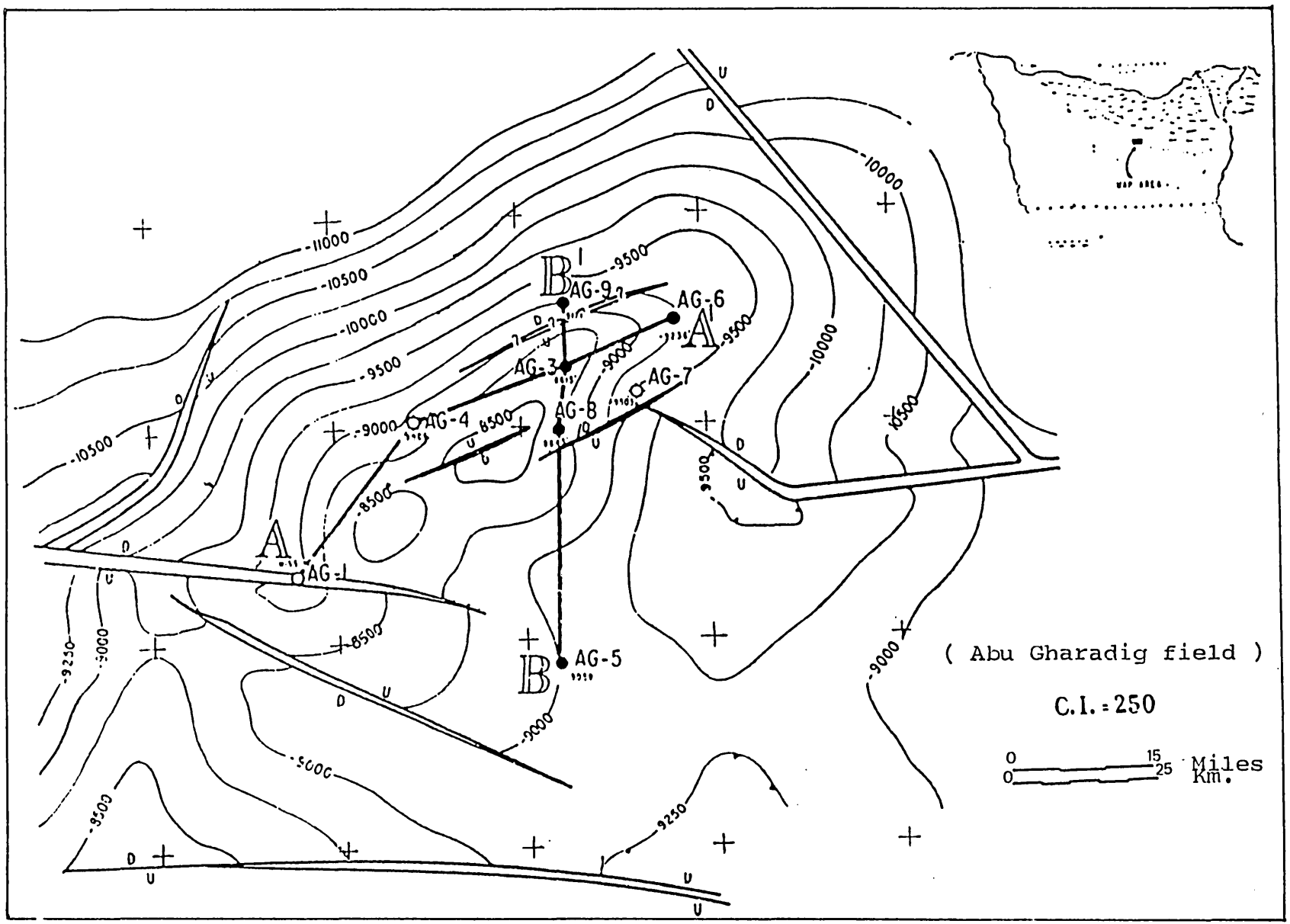


Fig. 6.31 Top Abu Roash "C" unit structural contour map(after Aadland and Hassan,1972).

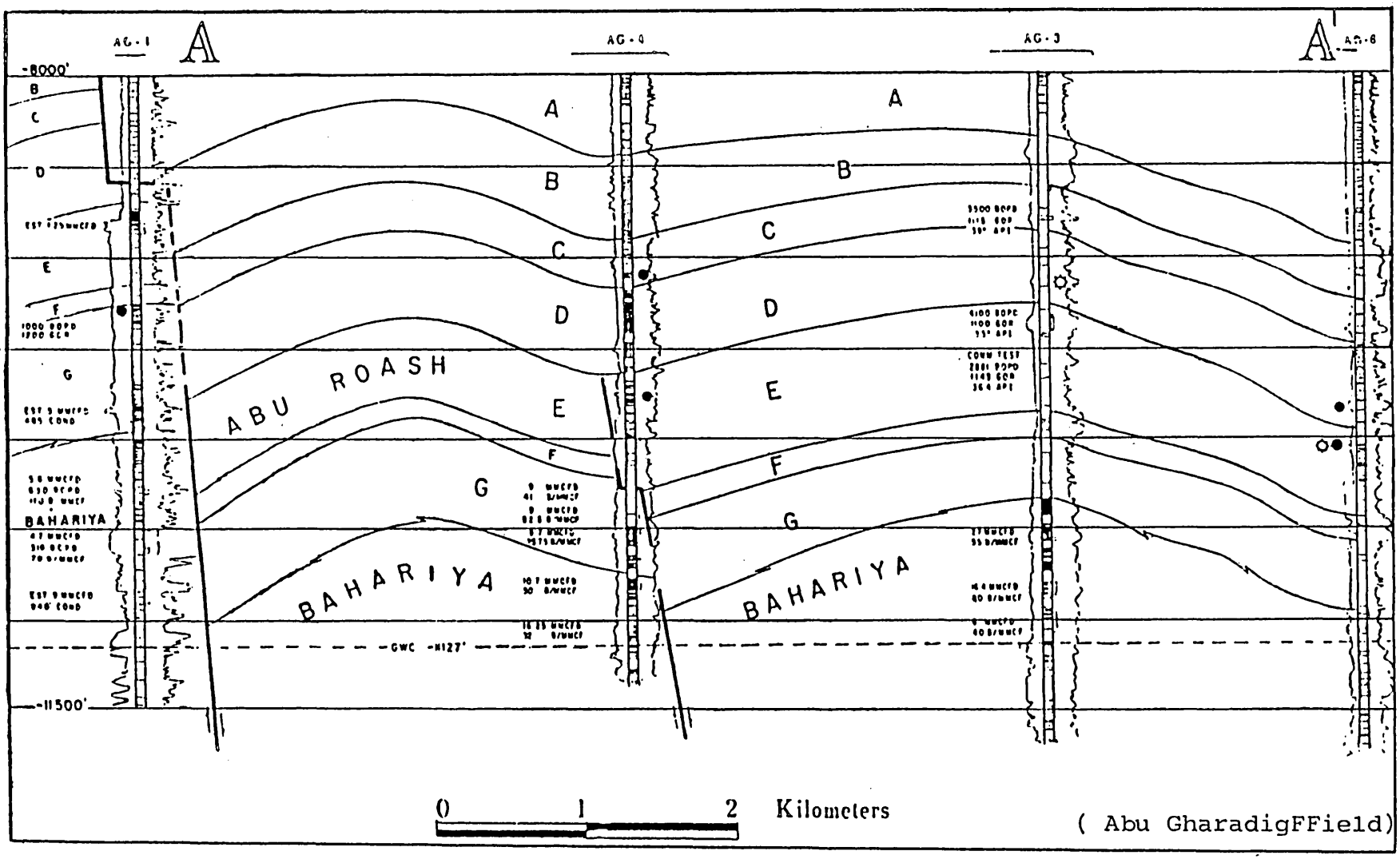


Fig. 6.32 Structural cross section A - A , Abu Gharadig Field.
(After Aadland and Hassan,1972)

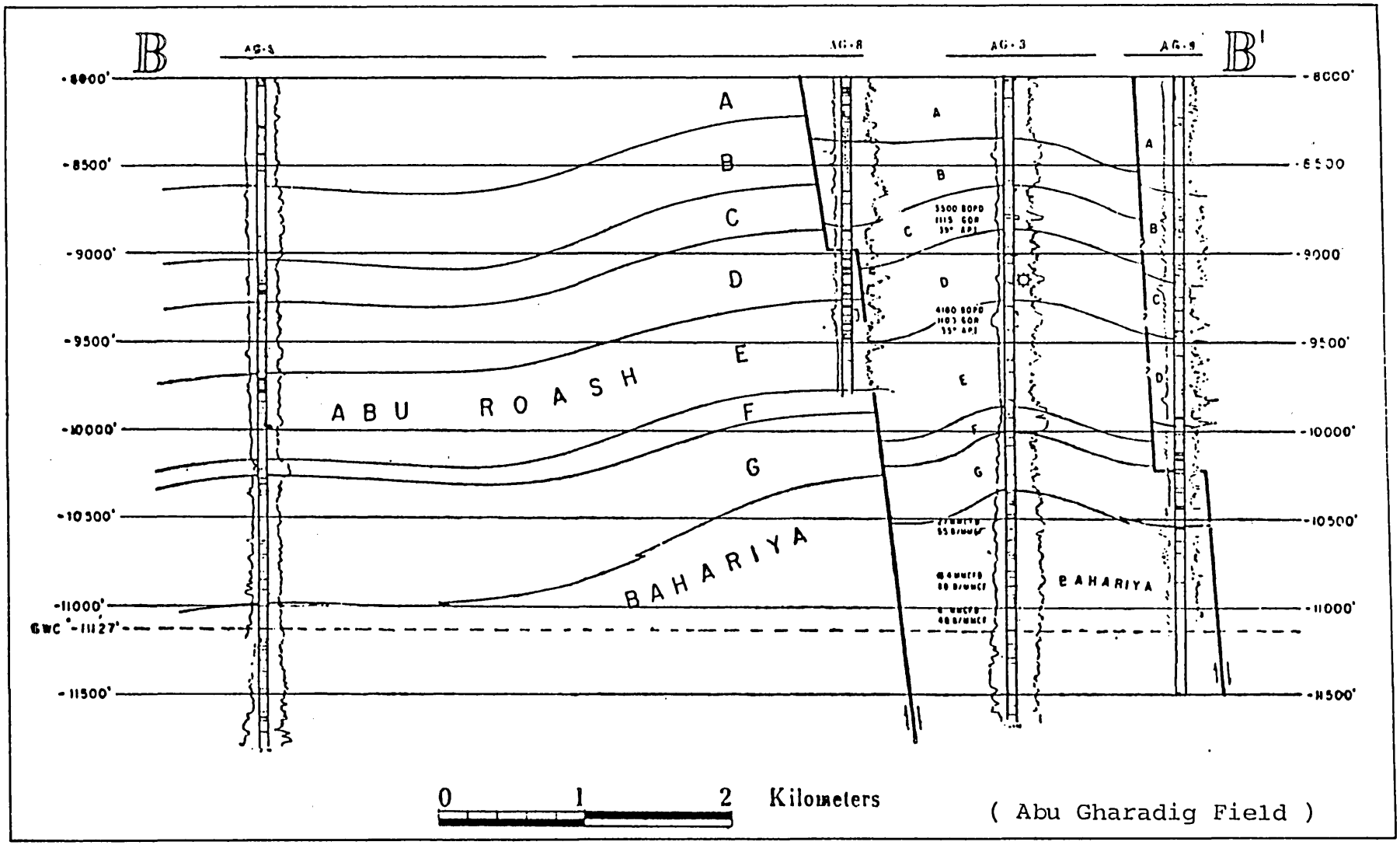


Fig. 6.33 Structural cross section B - B , Abu Gharadig Field (after Aadland and Hassan,1972)

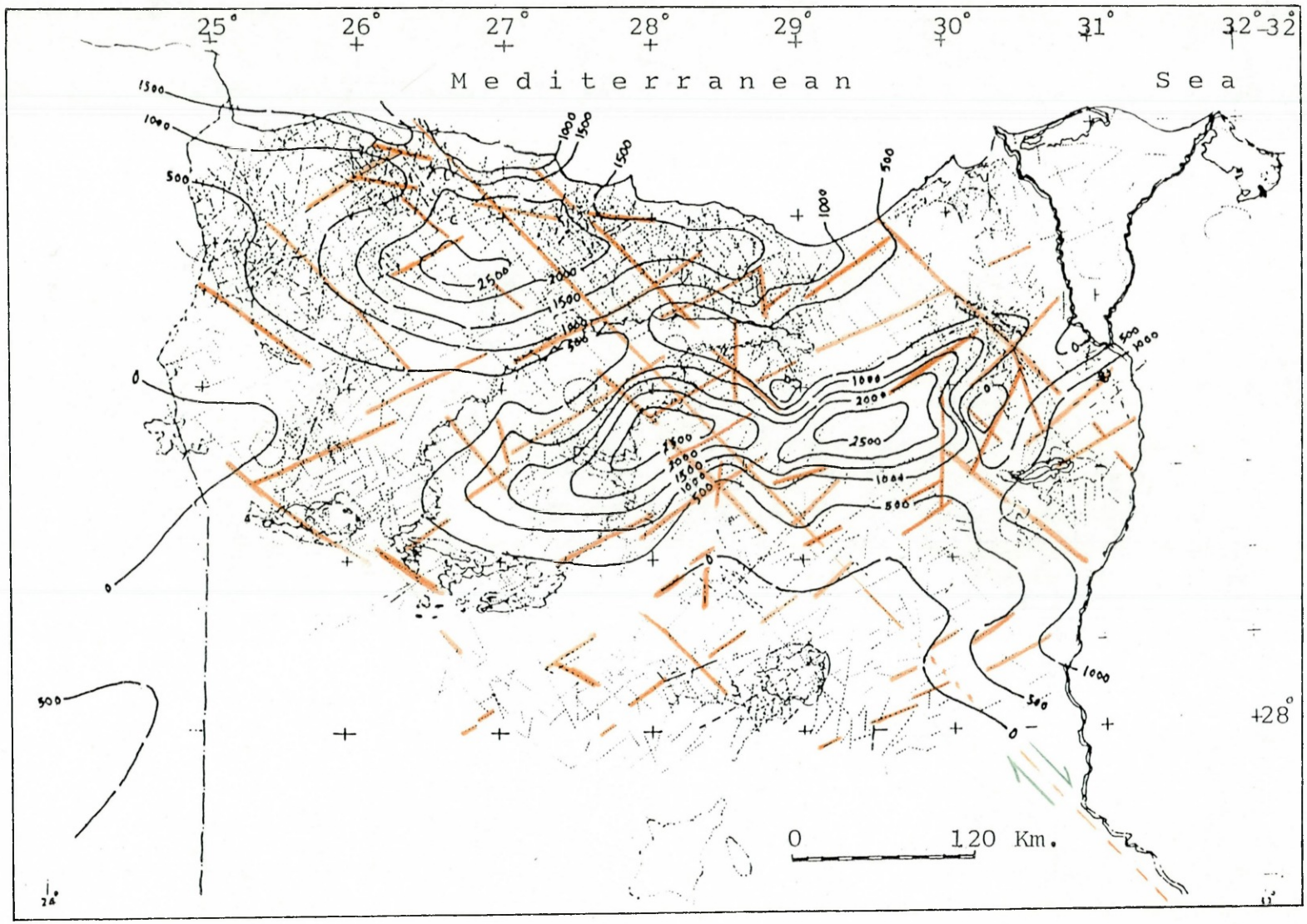


Fig. 6.34 Compiled Turonian isopach and lineament (I.R. Colour composite) map.

A. The Cretaceous basins and uplifts were subsequently dislocated by nearly N50°W (NW) dextral strike-slip faults. One of these faults, F_1-F_1 (Fig. 6.30) is a continuation of the Albian-Cenomanian fault.

B. The basins and uplifts of the Albian-Cenomanian, most probably developed as a result of block faulting.

C. The Turonian basins and uplifts became narrow, most probably as a result of buckle folding.

D. Some of the interpreted lineaments have structural and/or stratigraphic control upon the Cretaceous thickness contours.

E. The alignment of the subsurface dextral strike-slip fault, F1-F1 (Fig. 6.30) (in the Albian-Cenomonian and Turonian) with a surface lineament, indicates that this fault is likely a basement controlled fault which is reactivated and became apparent during these periods.

6.2.7 Middle Eocene - Palaeocene Isopach Map

In this isopach map (Fig. 6.35), most of the basins and uplift axes trend nearly N50-70E (ENE) except at the north western corner of the mapped area where the axes of Sidi Barrani uplift and Faghur basin might have nearly N70°W (WNW) trend. The nearly N50°W (NW) dextral strike-slip fault which dislocated the Cretaceous basins and uplifts, still has the same effect on the basins and uplifts of middle Eocene - Palaeocene isopach map, as indicated in Fig. 6.35. This fault was reactivated during Middle Eocene - Palaeocene. Also, the

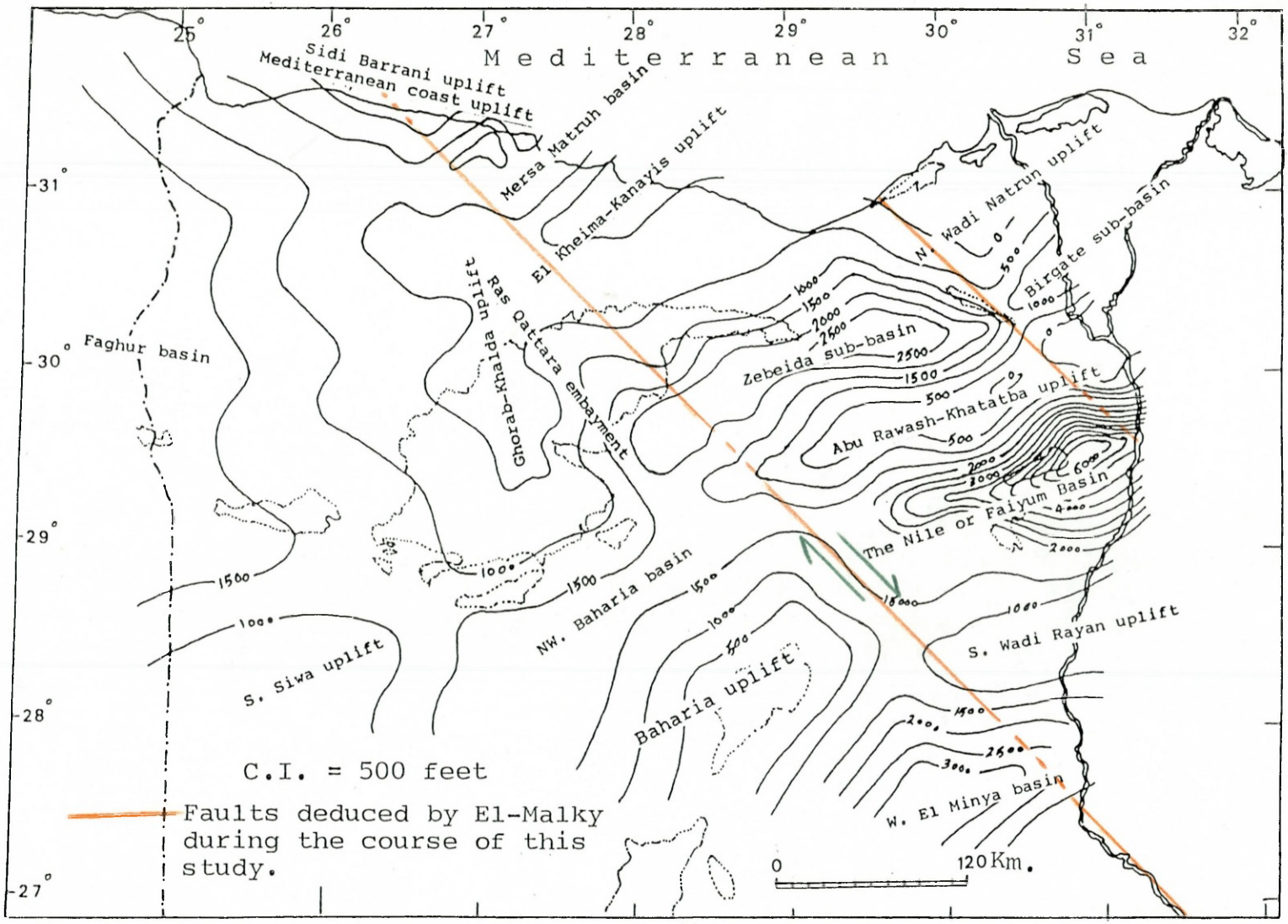


Fig. 6.35 M. Eocene-Palaeocene isopach map (after Aadland and Hassan,1972).

configurations of the basins and uplifts in Fig. 6.35 are quite different from those of the Cretaceous isopach maps. The main features of such isopach map (Fig. 6.35) are:

a. Faghur basin (might have N70°W [WNW] trend);

b. South Siwa uplift (N58°E or ENE);

c. North west Baharia basin (N50°E or NE);

d. Baharia uplift (N55°E);

e. West Minya basin (N63°E or ENE);

f. South Wadi Rayan uplift (N70°E or ENE);

g. The Nile or Faiyum basin (N70°E or ENE);

h. Abu Rawash-Khatatba uplift (N70°E or ENE)

i. Zebeida sub-basin (nearly N75°E or ENE);

j. El Kheima-Kanays uplift (N50°E or NE);

k. Mersa Matruh basin (N50°E or NE);

l. Sidi Barrani uplift (N70°W or WNW);

m. North Wadi Natrun uplift (N50°E or NE);

n. Birgate sub-basin (nearly N60°E or ENE);

o. Ghorab-Khalda uplift (N15°W or NNW);

p. Ras Qattara embayment (nearly N55°W or NW);

q. The maximum thickness is 6000 feet or about 1,830 meters.

With respect of the Turonian isopach map (Fig. 6.30), the middle Eocene - Palaeocene isopach map (Fig. 6.35) shows:

I. Significant narrowing of the Baharia uplift and

II. of the Beni-Suef-Cairo basin, where it now occupies the Faiyum area;

III.The presence of West El Minya basin and south Rayan uplift in the same area, which was occupied by Beni-Suef-Cairo basin as shown in Fig. 6.35.

The above mentioned points indicate the continuation of the buckle folding during the Palaeocene-middle Eocene, which started at the Turonian (see Fig. 6.32 and 6.33.

The analysis of the middle Eocene-Palaeocene isopach map (Fig. 6.35), in light of the interpreted surface lineaments, show that some lineaments have structural and stratigraphical control on the thickness contours as indicated on the transparent overlay (Fig. 6.36). But the contouring of such a regional isopach map (Fig. 6.35) resulted in a more or less minor misfit along the NW dextral strike-slip fault (see Fig. 6.36), which may be caused either by the interpolation or extrapolation process as a possible expected error.

IV.The nearly N50W (NW) dextral strike-slip fault is almost certainly a basement fault that reactivated more than once during different geological periods throughout its geological history. Thus, this fault has an additive horizontal displacement through geological time. The regional character of the isopach maps, as well as the limited subsurface data, may cause the deduction of the horizontal movement along some nearly $N50^{o}W$ (NW) strike-slip faults completely obscured.

V. Lineaments in a folded area such as the studied area often reflect two different fractures: 1) earlier (basement) fractures and 2) fractures resulted from the

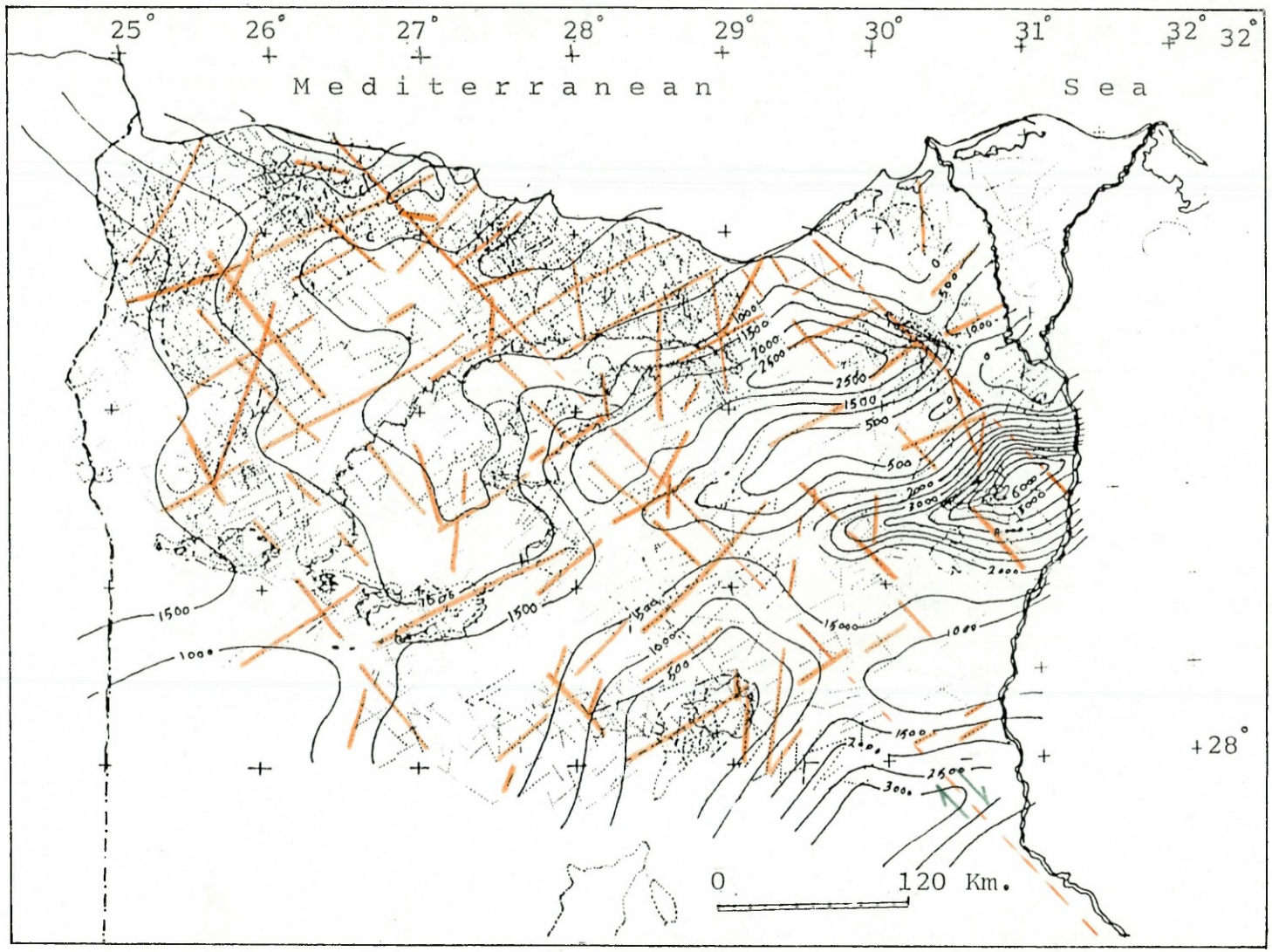


Fig. 6.36 Compiled M. Eocene-Palaeocene isopach and lineament (I.R. Colour composite) map.

process of folding. Under these circumstances, it is difficult to visualize the real structure of the basins or uplifts especially in the absence of seismic cross sections. However, in light of the cross sections (Figs. 6.32 and 6.33), one can say that during the Turonian, the studied area was folded into buckled anticlines and synclines.

VI. Some mechanics of the upper Cretaceous buckle folding (Syrian Arc System of ENE folds) have been assumed by former authors (see Chapter II). However, the present writer gives some other possible mechanics which may lead to the development of the upper Cretaceous folds in the area under study, especially if one considers that the deformation pattern of the underlying pre-Cambrian basement in the Northern Western Desert of Egypt area is one of differential block faulting and rotation of rigid blocks (see Fig. 6.10). These mechanics are:

1) Tilting of two blocks in opposite directions should create a state of compression in the strata between them, which may lead to compressional structures between these blocks.

2) Tilting of one or more of the underlying blocks which was accompanied by gravitational gliding of the overlying strata.

3) Rotation of blocks in the same general direction but along different axes of rotation, as mentioned early in this chapter (see Fig. 6.16).

4) Reverse faulting or thrust in the underlying rocks.

5) Shearing in the underlying rocks which may cause drag folds in the overlying rocks (as a result of simple shear mechanism).

6.2.8 Eocene Isopach Map

The Eocene isopach map (Fig. 6.37) represents a cumulative isopach map of the whole Eocene section encountered in the Western Desert of Egypt. Most of the alternating basins, embayments, uplifts and/or ridges have N40° - 65°E (NE to ENE) trend, while the Mediterranean coast uplift and Burg El-Arab embayment have N70°W (WNW) trend.

With respect to the previous isopach map (Fig. 6.35), the Eocene isopach map (Fig. 6.37) shows no indication of Wadi Rayan uplift and west El-Minya basin which lies south of the Nile, or Faiyum basin (in Fig. 6.35), although the Wadi Rayan uplift represents a surface NE anticline in the Eocene formations (Shata, 1953). Instead, the Nile basin (here in Fig. 6.37) occupies the whole area. This can probably be attributed to the deficiency of the data which affects the process of the contouring in this particular area and, in turn, possibly masks the effects of the NW strike-slip fault of the previous isopach map (Fig. 6.35).

The main elements of this map (Fig. 6.37) are:

i. Salum basin N62°E (ENE)

ii. Faghur ridge N40°E (NE)

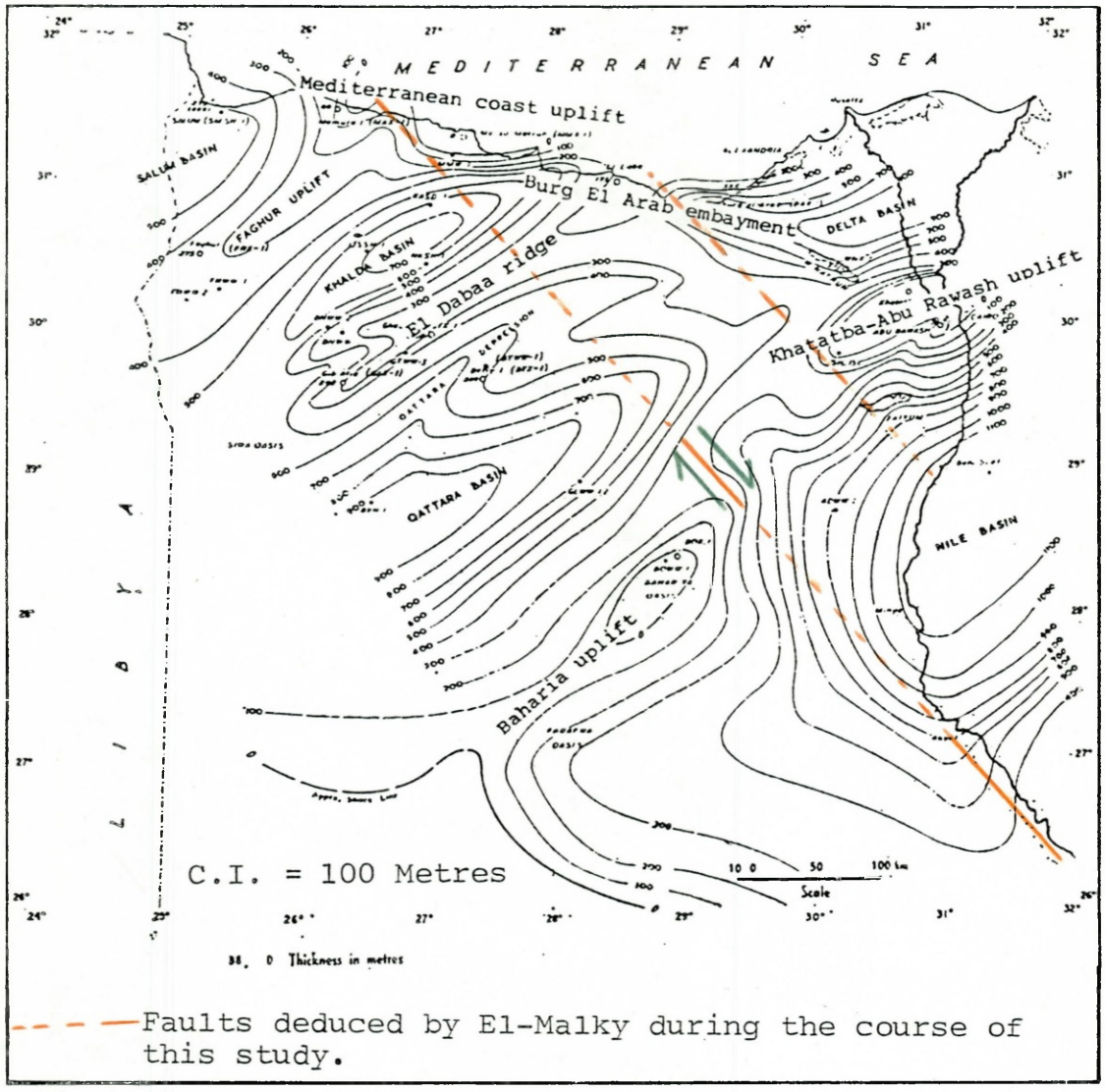


Fig. 6.37 Isopach map of Eocene, Western Desert.
(After Kostandi, 1963)

iii. Khalda basin N56°E (nearly NE);

iv. El-Dabaa ridge N60°E (ENE);

v. Qattara basin N60°E (ENE);

vi. Baharia uplift N51°E (NE);

vii. Nile basin N50°E (NE);

viii. Khatatba-Abu Rawash uplift N57°E;

ix. Nile Delta basin N65°E (ENE);

x. Burg El Arab embayment N70W (WNW)

xi. Mediterranean coast uplift N70W (WNW);

xii. the maximum thickness is 1100 meters.

The most interesting feature of this map is the narrowing of basins, embayments, ridges and uplifts, especially Baharia uplift, with respect to the previous isopach map (Fig. 6.35).

Comparing this map with the lineaments, as indicated in Fig. 6.38, shows that some of the lineaments have structural and/or stratigraphical control on the thickness contours. These lineaments seem to be disconnected because of the lack of any digital enhancement, but on the overlay (Fig. 6.38) they appear as probable long lineaments because these disconnected lineaments have the same trend.

Studying the Palaocene - Eocene isopach maps demonstrates the following:

1. There are pre-Eocene structures which are not preserved in the Eocene, such as the eastern and western Abu Gharadig sub-basins.

2. The general trend of the subsurface basins and uplifts is N50° - 70°E (ENE), which is in alignment with

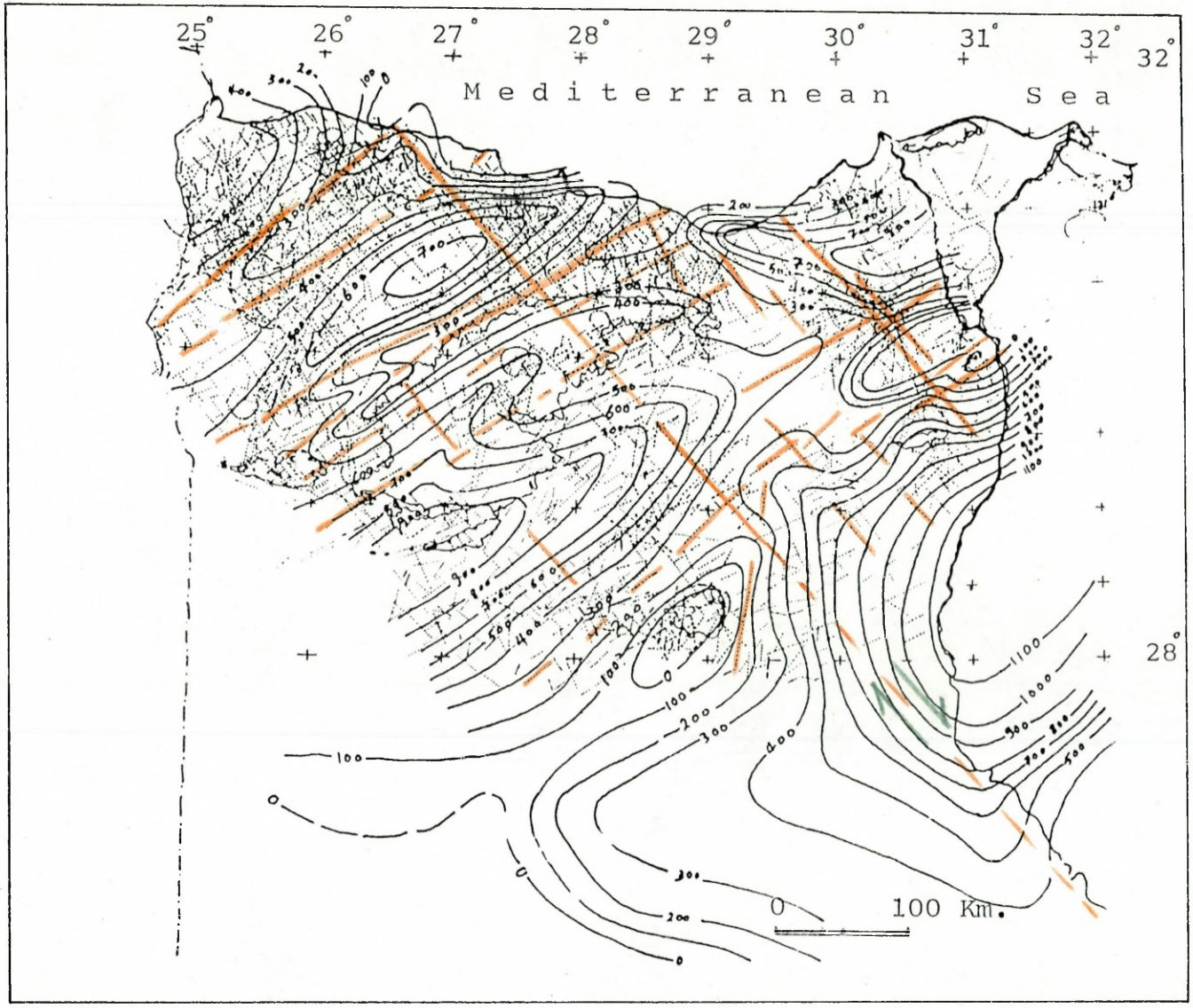


Fig. 6.38 Compiled Eocene isopach and lineament (I.R. Colour composite) map.

the folding of Abu Rawash, field study, and north Sinai Syrian Arc trend or System.

3. The narrowing of the basins and uplifts during the Eocene indicates that the upper Cretaceous folding (see Figs. 6.32 and 6.33) continued during this period.

4. The zero thickness contour lines represent erosional surfaces or unconformities over the anticlines or uplifts, while continuous sedimentation are present in the basins between anticlines.

5. The Mediterranean Coast uplift, with N70^{o}W (WNW) of pre-Eocene is manifest as a result of the decrease in the thickness of Eocene deposits. These uplifts have been attributed to a regional thrust at the bottom of the Mediterranean Sea (Sigaev, 1967).

6. It seems likely that the N20^{o} - 30°W (NNW) maximum compression (S_1), which worked on the studied area during the Cretaceous caused the development of the upper Cretaceous N60 - 70E (ENE) folding, which continued during the Palaeocene - Eocene, and subsequently the nearly N50^{o}W shears. This indicates that Price's explanations of the development of relatively small fractures or joints as a result of post tectonic uplift (1966) are still working on regional scale, taking into consideration that the upper Cretaceous folding ended by uplifting during late Eocene - Oligocene.

7. Some of the surface lineaments have structural and/or stratigraphical control.

8. Some of the basement faults were rejuvenated during the late Eocene-Oligocene uplifting, as indicated in Fig. 5.40.

In conclusion, the analysis of the available isopach maps and subsurface data were very useful in demonstrating the following:

1. The contour pattern of the various isopach maps and the thickness of the rock units suggest that the studied area lies within the unstable shelf zone. This zone includes the transitions between the stable shelf in the south, where the sedimentary section becomes thin and the more strongly and deeply developed basins at the north.

2. The main structural elements of the Palaeozoic, Jurassic and lower Cretaceous could be attributed to basement block faulting and block rotation.

3. The Palaeozoic folding could be attributed to basement block faulting as drape folds and/or block rotation.

4. The upper Cretaceous folding (ENE or Syrian Arc System of folds) is represented in the studied area by buckle folds (see Figs. 6.32 and 6.33).

5. These buckle folds (ENE) of the upper Cretaceous could be established as a result of either pure shear or simple shear mechanisms (see Chapter VIII).

6. The late Eocene - Oligocene uplifting was accompanied most probably by the development of shear fractures, especially the nearly N50^{o}W dextral

strike-slip fault, which dislocated the Cretaceous basins and uplifts and Gaa-Abu Rawash village pericline.

7. The ENE and NNW extension fractures which gave way to the outpouring of the Oligocene basalts and hydrothermal solutions, as a result of volcanic activity could be attributed to:

a. post-tectonic uplifting, where the tectonic stresses were directed $N20^{\circ}$ - $30^{\circ}W$;

b. the process of the upper Cretaceous folding and

c. as basement fractures, which had been reactivated at that time.

8. Price's explanation of the development of relatively small fractures or joints as a result of post-tectonic uplifting could be applied to explain the development of regional fractures or lineaments.

9. Some of the surface lineaments have structural and/or stratigraphical control.

10. The basement rocks are segmented by fractures of different trends. Some, or all, of these fractures could be reactivated and/or propagated into the surface as surface lineaments.

11. It seems likely that some of the basement faults change the relative sense of their movements along their fault planes throughout geological time, as indicated in Figs. 6.10 and 6.28 at Rabat and Abu Rawash-1 wells.

CHAPTER SEVEN

GEOPHYSICAL STUDY

CHAPTER SEVEN

Geophysical Study

7.1 Introduction

Gravity and magnetic methods are both used to seek anomalies in natural force fields of the earth, caused by changes in physical properties of subsurface rocks.

Variations of the gravitational field over an area depend only upon lateral heterogeneity of the earth's material density contrast. Anomalies of the magnetic field are generated by lateral variations in the direction or amplitude of magnetic polarisation of earth materials; in particular, igneous and metamorphic rocks.

These two methods are useful in detecting concealed structural trends, which often determine the trends of gravity and magnetic anomalies, and locating hidden masses of interest.

In this study, gravity and magnetic fields have been analysed over the studied area or some parts of the studied area, in order to locate the trends of the concealed geological structures, as well as any obvious horizontal movements along these trends.

In the previous chapters, the structural trends have been mapped and analysed on different scales, but the relationship between these trends and those of deeper structures has not yet been well established. The importance of this present study is that such relationships can be established.

Studying potential fields requires their resolution into their components; regional component caused by deeper structures or sources and local component generated by shallower features or sources having limited horizontal dimension. Generally, local component, residual anomaly, is superimposed on the regional component, but is frequently camouflaged by it.

Several techniques have been used in this study for analysing the gravity and magnetic fields into their components. Low-pass filtering and upward continuation techniques have been used to bring out anomalies associated with large scale structures, i.e. the regional component, of both gravity and magnetic fields. Local anomalies have been delineated by the production of high-pass filter, second vertical derivative maps.

Reduction to the pole technique has been applied to reduce or eliminate the distortion in the magnetic field caused by the magnetic field inclination. To convert the magnetic field into pseudogravity field, which represents only the effects of the magnetic rocks, pseudogravity technique was employed.

This study throws much light on the nature of Landsat imagery lineaments and, in turn, on the tectonic framework of the Northern Western Desert of Egypt.

7.2 Previous Geophysical Work

In this section, previous geophysical work is reviewed briefly in order to enhance some points which

are going to be considered later in this chapter, or which are out of the scope of this study.

Shereef (1972), in his geophysical study on the Nile Delta area, concluded the following:

a. The general increase of the gravity and magnetic fields towards the Mediterranean Sea was attributed to variations in the basement rocks from granites to metavolcanics northwards.

b. The Oligocine-Miocene basaltic sheet, which lies underneath Miocene deposits, varies considerably in thickness from 50 m. to more than 300 m.

c. The depth to the top of the basement is about 6000 ft (1829 m.) at the south and increases to more than 25,000 feet (7620 m.) at the north.

Nakhla and Podbelova (1973), during their aeromagnetic study on the western borders of the Western Desert of Egypt, mentioned that the most prominant trend is sublatitudinal in the northern part of the area which has been studied by them, but this trend swings to NW (in the central area) and NE (in the southern area). Relatively, the submeridional trend is less dominant. They claimed that sublatitudinal and NE trends are the oldest relative to the NW and submeridional.

Riad (1977) interpreted some NW shears (Fig. 7.1) directly from the Bouguer anomaly (gravity) map. On the basis of previous work, these shears were classified as right lateral (Riad, 1977).

In fact, Riad's work in 1977 could be criticized for the following reasons:

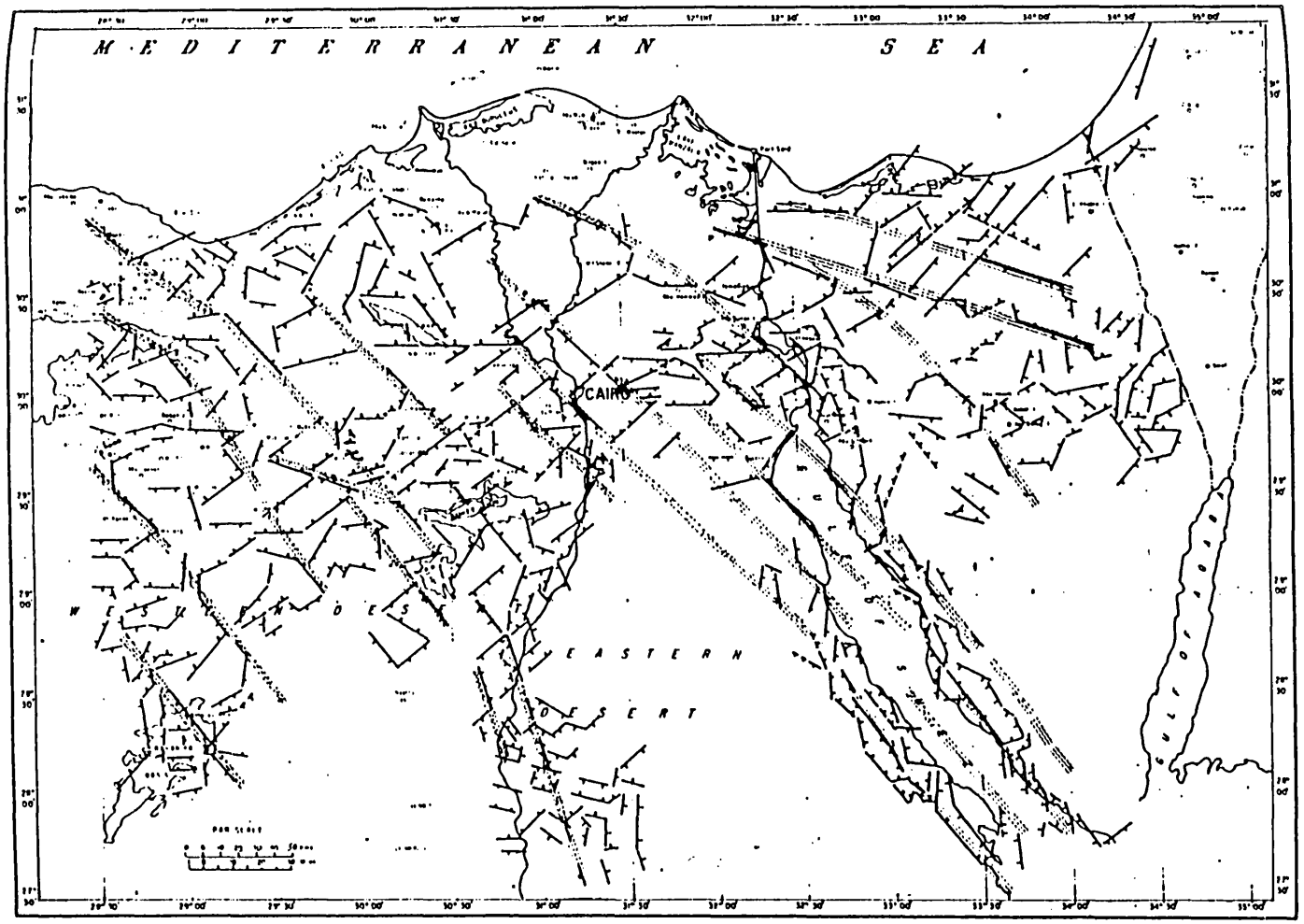


Fig. 7.1 Possible shear zones interpreted from gravity anomalies.

(After Riad,1977)

a. The Bouguer anomaly map was used directly without any attempt to separate the local anomalies, shallow, from the regional background.

b. Some shears, especially in the Eastern and Western Desert, as shown in Fig. 7.1, seem to be not real, because the distance between two successive faults, which define the shear, is relatively quite long.

Abdel Rahman (1979), in his geophysical study (gravity) on the Northern Western Desert of Egypt, located some N - S, NNE, NE, NW and nearly E - W faults. Also, the same author mentioned that the NE trend is a shear direction.

Sabri and Abdel Hady (1979), in their gravity study of the North Western Desert of Egypt, (approximately the central part of the present studied area), located the following:

a. ENE and nearly E - W faults from the Bouguer map;

b. NE, E - W and NNE shallow faults from the second derivative map;

c. E - W, WNW, nearly N - S and NE faults from downward continuation map.

7.3 Preparation of the Geophysical Data

In this study, digitization of the geophysical data was carried out by projecting a grid tracing paper on the field contour maps and readings were taken at irregular intervals. Then, these data were typed, or punched, checked and stored in the computer under file names.

By using the USGS program No. W9322 (FIXD), 1968, these irregular data were interpolated into a regular grid at intervals 5 km. (gravity field) and 2.5 km. (magnetic field). The program is based on the following:

$$G(i,j) = \frac{\sum_{k=1}^{n} X(k) * 1/d^2(k)}{\sum_{k=1}^{n} 1/d^2(k)}$$

where

G (i,j) = grid value or the output;

X(k) = original value or the input;

d(k) = is the distance between the original values and the grid (i,j) in grid units, so that

$(i-1) \leq dk \leq (i+1)$ in x direction;

$(j-1) \leq dk \leq (j+1)$ in y direction.

When the distance between the original data points is greater than the grid interval (sparsely distributed data), the average of the nearest 4 points was used to give the values of the field at these missing grids.

To minimize or get rid of any noise introduced during the process of interpolation or due to instrumental effects, a 9 by 9 filter operation was applied. This filter operator, based on low pass filtering technique, passes any wavelength lower than 7.5 km. (gravity field) and 3.75 km. (magnetic field), is represented in Table 7.1.

Table 7.1

Noise Filter Coefficients (Fourth Quadrant)

0.05500	0.04755	0.02981	0.01174	0.00102
0.04755	0.04109	0.02568	0.01006	0.00087
0.02981	0.02568	0.01591	0.00612	0.00051
0.01174	0.01006	0.00612	0.00227	0.00018
0.00102	0.00087	0.00051	0.00018	0.00001

Thus the raw data were contoured using the Contouring Package (ICCC) and became available either for qualitative interpretation or further analysis.

7.4 Geophysical Data Used in the Study

A. Gravity Data

The Bouguer anomaly map of the Northern Western Desert of Egypt was compiled by the Egyptian General Petroleum Corporation in 1967, with contour interval of 1 mgal., after it had been reduced. These data were published by Riad (1977) and Abdel Rahman (1979).

For a reasonable presentation in this study, the Bouguer gravity map was digitized, replotted and contoured with intervals of 5 mgal. (Fig. 7.2). For the moment, the reader is asked to take as valid first lineaments represented in Figs. 7.2 to 7.4. The criteria on which such interpretations and citing of lineaments are based are discussed at length later in this chapter.

The main trends, as indicated on Fig. 7.2, are ENE, nearly N - S to NNE, NW, WNW and E - W. Also, gravity

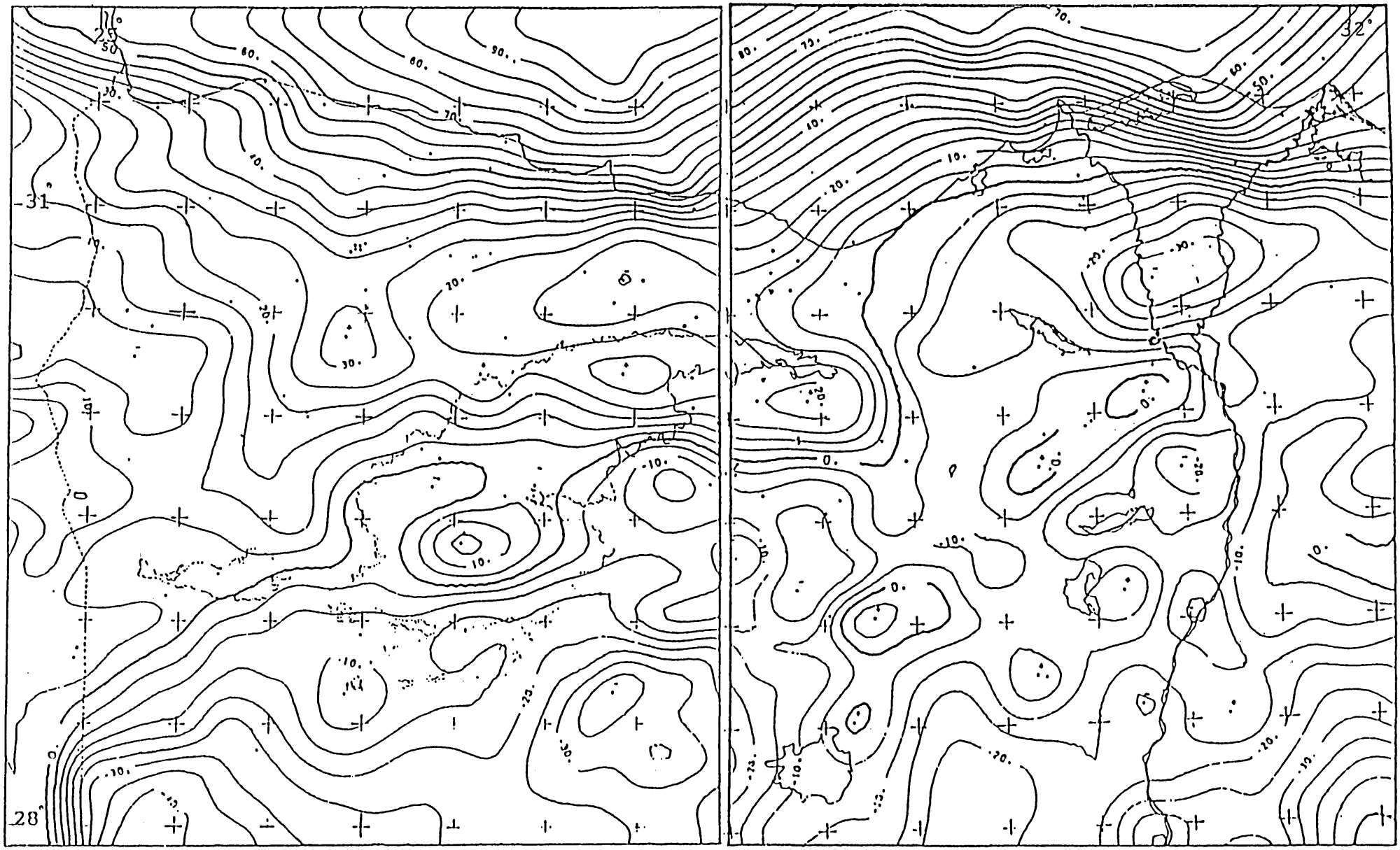


Fig. 7.2 Smoothed gravity map of the studied area (C.I. = 5 mgal).

0 50 km.

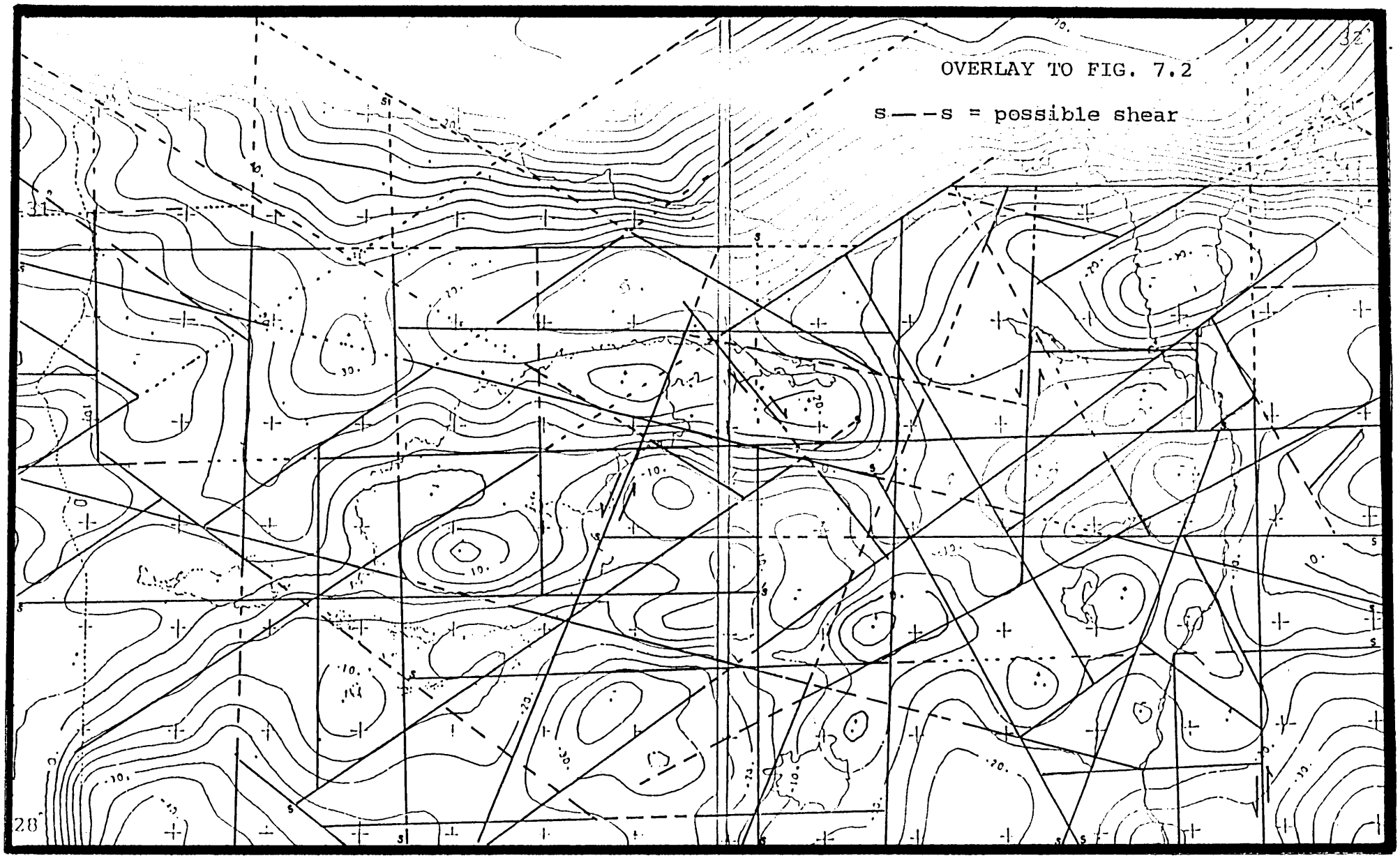


Fig. 7.2 Smoothed gravity map of the studied area (C.I. = 5 mgal).

0 50 km.

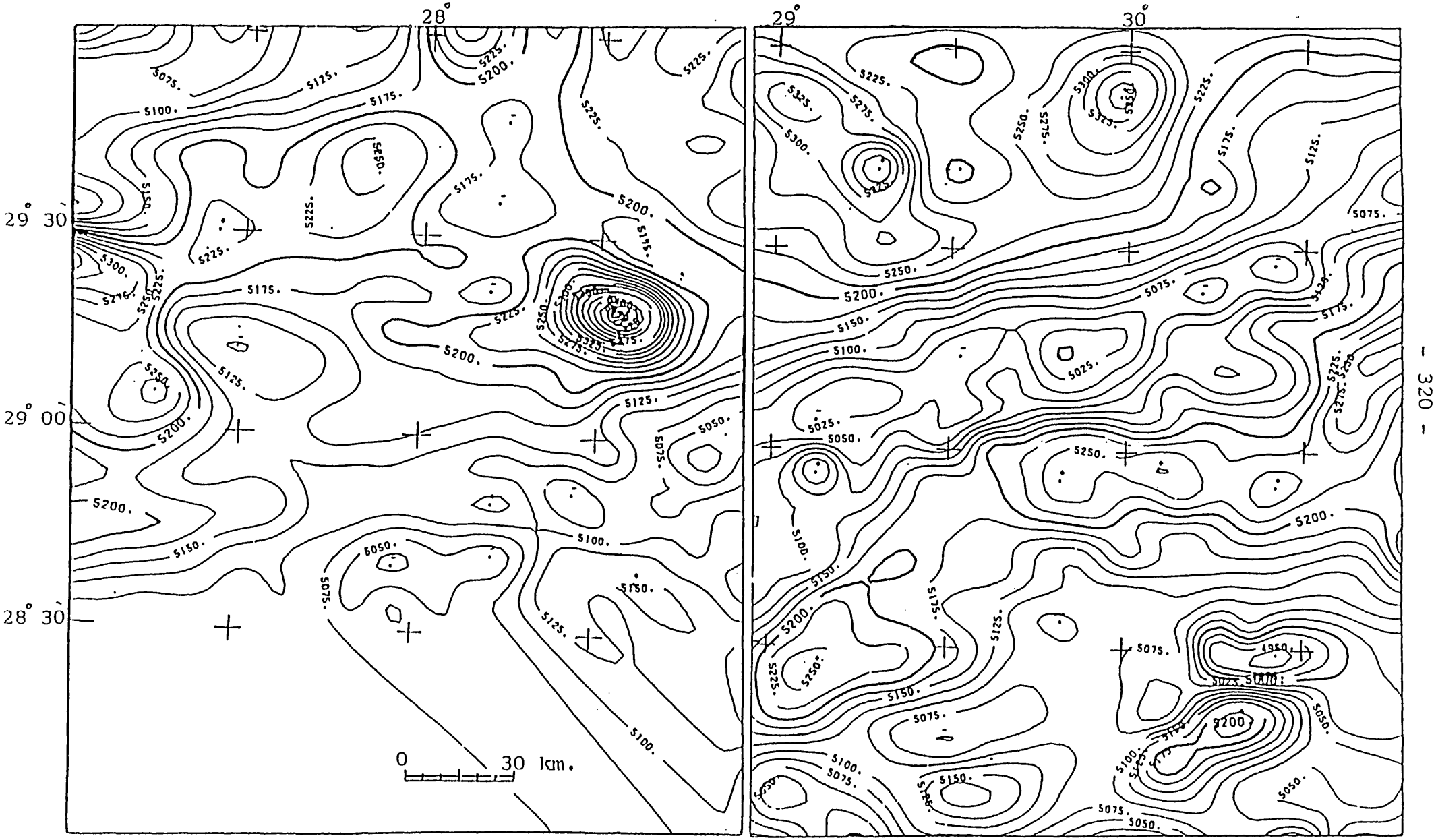


Fig. 7.3 Smoothed aeromagnetic map of the Western Desert of Egypt (C.I. = 25 gamma).

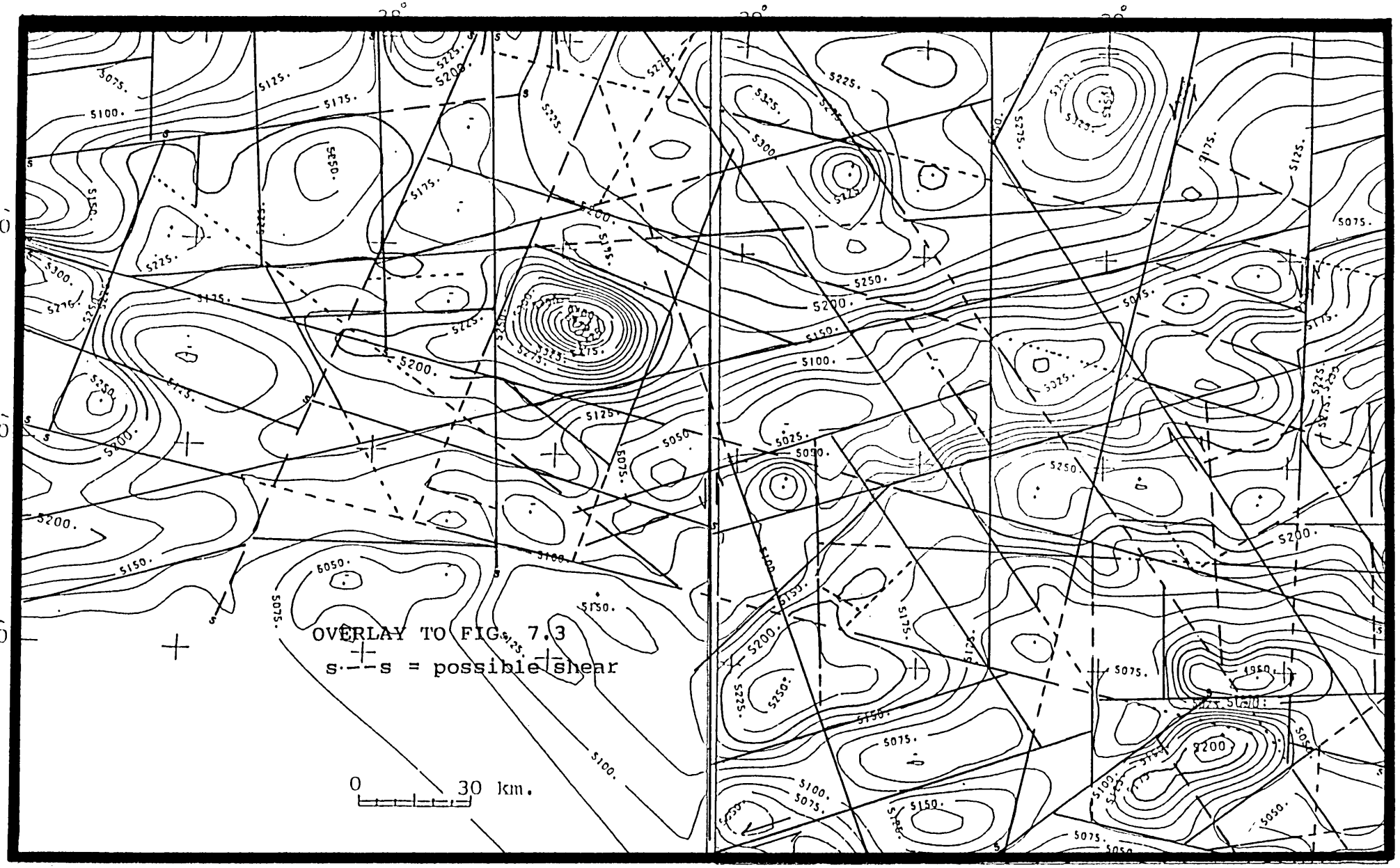


Fig. 7.3 Smoothed aeromagnetic map of the Western Desert of Egypt (C.I. = 25 gamma).

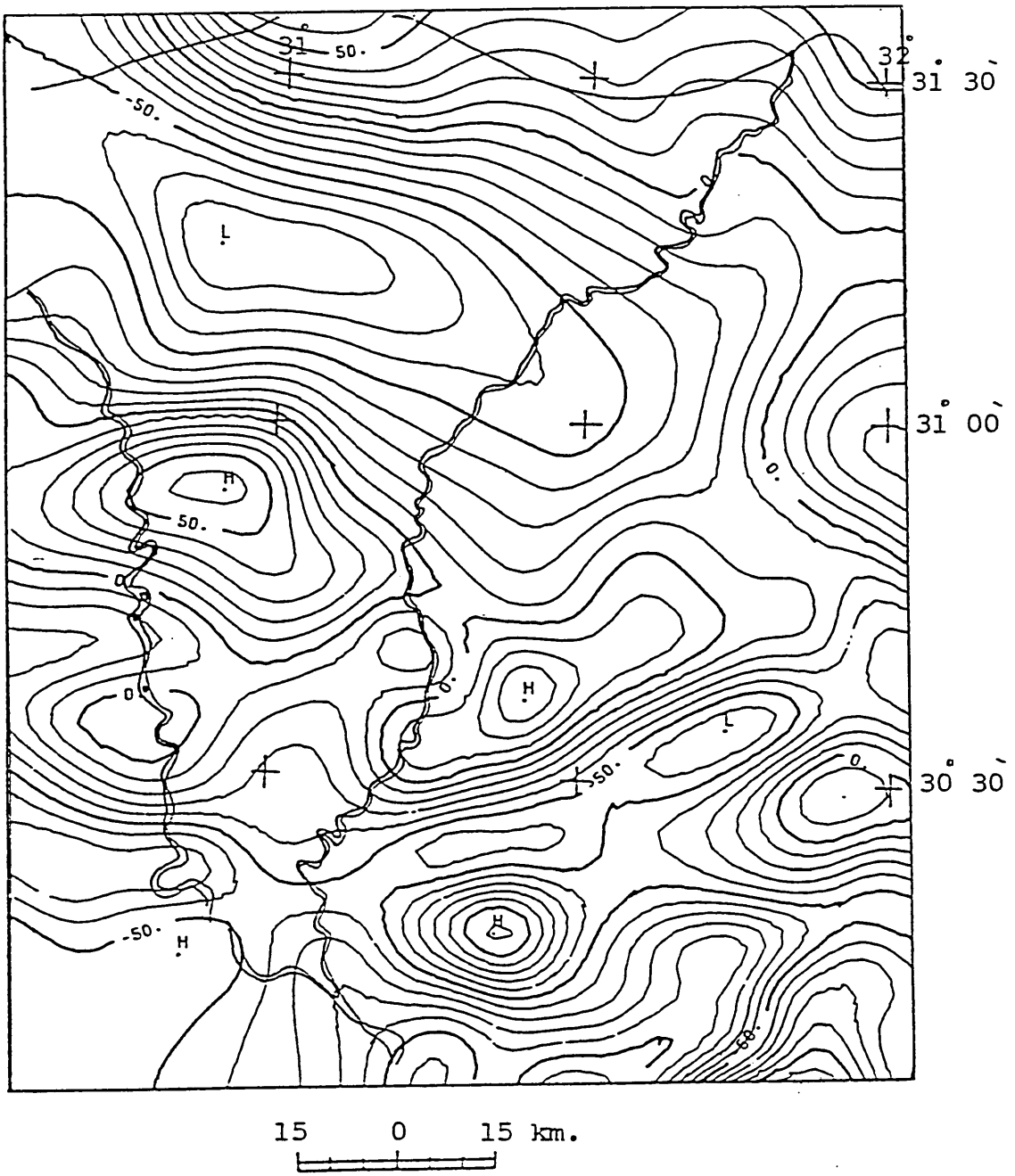


Fig. 7.4 Smoothed aeromagnetic map of the Nile Delta (C.I. = 10 gamma).

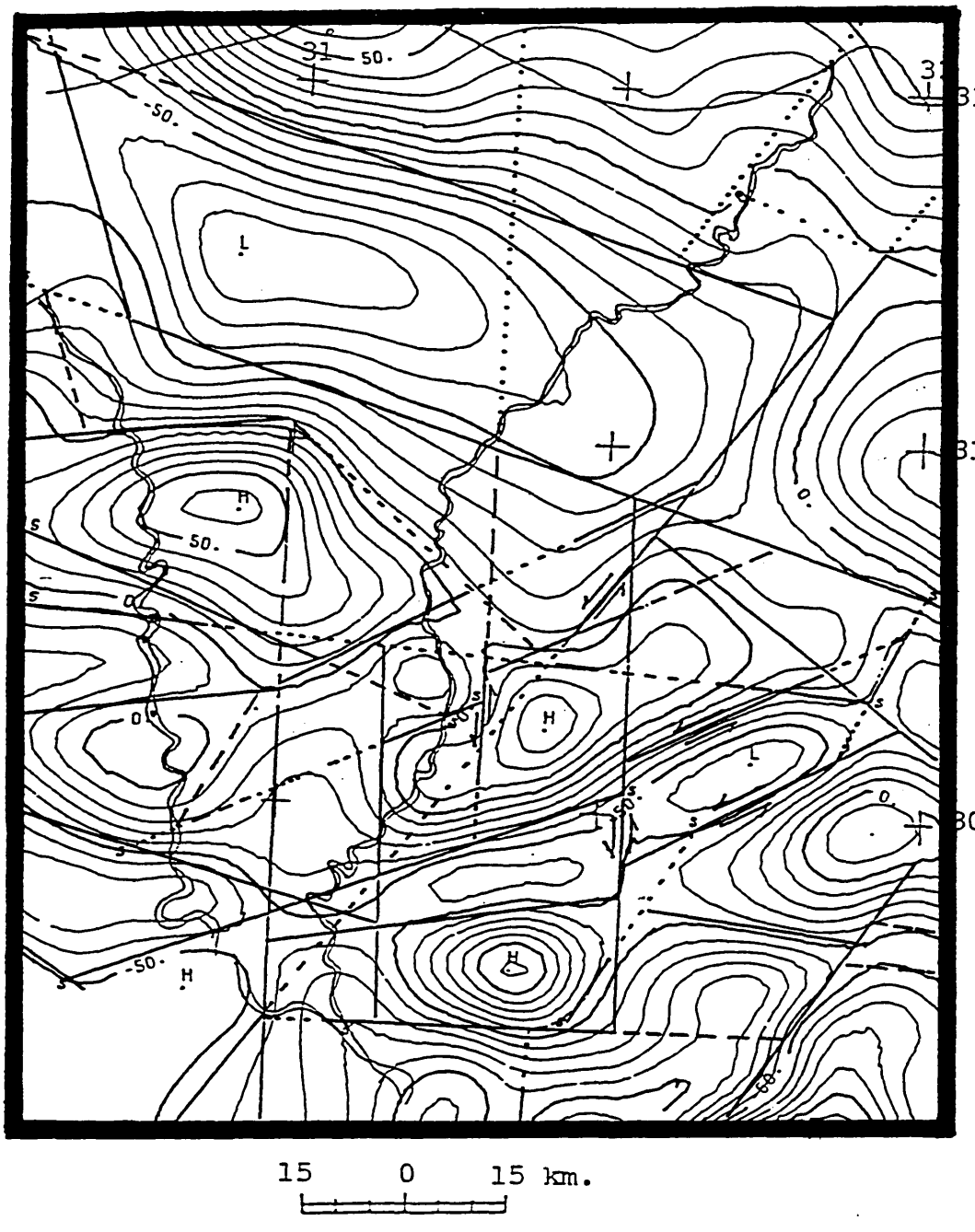


Fig. 7.4 Smoothed aeromagnetic map of the Nile Delta (C.I. = 10 gamma).

OVERLAY TO FIG. 7.4

s- - - - - s = possible shear

anomalies with positive, negative and different amplitudes have trends like those mentioned before. The amplitudes of such anomalies range from -50 mgal. to +30 magal. or more (as it seems over the Mediterranean). Some of the trends represent possible strike-slip faults, as shown in Table 7.2.

Table 7.2

Trends of the Gravity Map of the Northern Western Desert

Gravity Map Fig. 7.2	Possible Shears
ENE	NNE (L.L.)
N-S	N-S (L.L.)
NNE	NW (R.L.)
NW	nearly E-W
WNW	WNW
E-W	
NNW	

L.L. = Left Lateral

B. Magnetic Data

Magnetic data used in this study are represented by two aeromagnetic maps. These magnetic data have been reduced and broad effects caused by the earth's main magnetic field were removed.

The first map, part of the studied area, was produced by AMOCO Oil Company of Egypt in 1964, with a contour interval of 5 gamma. The second one (of the Nile

Delta) has been produced by Geological Survey and Mineral Research Department, Ministry of Petroleum, Egypt and published by Shereef (1972), with contour intervals of 10 gamma.

For satisfactory representation, the two maps were digitized, replotted and contoured with contour intervals of 25 and 10 gamma, respectively (Figs. 7.3 and 7.4).

a. Western Desert Aeromagnetic Map

The Western Desert aeromagnetic map (Fig. 7.3) covers approximately the fourth quadrant of the studied area. The essential lineament trends of this map are ENE, NW, WNW, N - S to NNE and E - W. Magnetic anomalies, with amplitudes ranging from 4925 to 5550 gamma, have the same trends of lineaments. Some of the interpreted lineaments exhibit strike-slip movements (see Fig. 7.3), where some lineaments show clear horizontal displacements; others do not show the sense of the relative horizontal movements but have the characteristics of the strike-slip lineaments as indicated in Table 7.3.

b. The Nile Delta Aeromagnetic Map

This map (Fig. 7.4) occupies most of the Nile Delta. The prominant lineaments have WNW, E - W, ENE, N - S to NNE and NW trends. Magnetic anomalies with amplitude ranges from -110 to +60 gamma have the same trends. Few lineaments are most probably strike-slip faults as indicated in Table 7.3.

Table 7.3

Trends of the Aeromagnetic Data

Trends of the smoothed aeromagnetic of the N.W.D.		Trends of the smoothed map of aeromagnetic map of the Nile Delta	
Aeromagnetic Map (Fig. 7.3)	Possible Shears	Aeromagnetic Map (Fig. 7.4)	Possible Shears
ENE	N-S (L.L.)	WNW	ENE (L.L.)
NW	NNE (L.L.)	E-W	NNE (L.L.)
WNW	NW (R.L.)	ENE	N-S (L.L.)
N-S	ENE (L.L.)	N-S	WNW
NNE	WNW	NNE	
E-W		NNW	
NNW		NW	

L.L. = Left Lateral

7.5 Analytical Techniques Used in this Study

1. Filtering Techniques

a. Low Pass Filter

The aim of any analytical technique is to extract as much useful information as possible from the available data. However, gravity and magnetic maps usually contain some features which are superimposed on each other. These features may be composed of regional and local anomalies. So, the main target of filtering technique is to separate anomalies of different ranges of

wave length from each other. This means the separation of shallow sources or local anomalies, with short wave length and high intensity, from deep geological sources or regional anomalies, with long wave length and low intensity.

Low pass filtered maps bring out the regional anomalies or regional geological trends of the entire area in a very noticeable way.

Filter operators used in this study were based on the following equation (after Baranov, 1975):

$$f(x) = F(x) * \frac{\sin(\pi x/Q)}{\pi x}$$

This equation is used to replace the function F (x), with arbitrary spectrum, by a function f (x) whose spectrum does not exceed π/Q in absolute value.

To calculate the two dimensional filtered function f (x,y) at single point X = y = 0 in terms of k, n and q, the following equation was used:

$$f(0,0) = \sum_k \sum_n F(kq,nq) \frac{\sin(\pi kq/Q)}{k\pi} * \frac{\sin(\pi nq/Q)}{n\pi}$$

$$= \sum_k \sum_n F(kq,nq) * C(k,n)$$

where the filter operators $C(k,n) = \frac{\sin(\pi kq/Q)}{\pi k} * \frac{\sin(\pi nq/Q)}{\pi n}$

and q is the grid spacing.

b. High Pass Filter

For high pass filtering, no calculation of the filter operator has been made. Instead, the residuals of low pass filtering have been obtained to represent the high pass filtering, because the residual should preserve all spectra higher than π/Q in the data.

2 Continuation Technique

The technique of field continuation to higher or lower levels than the plane of observation can be used to map subsurface geological structures by interpreting the output of this technique.

Continuation, as it has been defined by Baranov (1975), is a linear integral transformation, which is applied either to gravity or magnetic field, or to derivatives of the field. Accordingly, if U (x,y,o) or simply U (x,y) is an arbitrarily sampled function on a plane Z = o, downward or upward continuation can be continued at (x,y) to altitude Z, using the following equation (Baranov, 1975):

$$U(x,y,z) = \sum_k \sum_n U(k,n) \frac{1}{4\pi^2} \iint_{-\pi}^{\pi} e^{-\gamma z+(k-x)\alpha i+(n-y)\beta i} d\alpha d\beta$$

where x and y are expressed in terms of the grid intervals as k and n respectively.

Letting x = y = 0, then,

$$U(0,0,z) = \sum_k \sum_n U(k,n) \frac{1}{4\pi^2} \iint e^{-\gamma z+k\alpha i+n\beta i} d\alpha d\beta$$

where $U(k,n) = U(k,n,0)$

We then have $U(0,0,z) = \sum_k \sum_n U(k,n)\ C(k,n)$

where

$$C(k,n) = \frac{1}{4\pi^2} \iint_{-\pi}^{\pi} e^{-\gamma z + k\alpha i + n\beta i} \, d\alpha d\beta$$

is the filter function of continuations, and z could be negative or positive for upward or downward continuation coefficients, respectively.

In this study, upward continuation was used to simplify the appearance of gravity and magnetic maps by supressing local features. In this sense, the upward continuation can be regarded as a filtering operation, such as a low pass filter, which smooths out the disturbances owing to local features, without impairing the main regional features.

3 Reduced to the Pole Technique

The reduced to the pole method of analysis, which was introduced by Baranov (1957), transforms the total magnetic intensity field or map to a vertical field situation as if it were at the north magnetic pole. This means that this technique results in reducing the distortion in the pattern of magnetic anomalies caused by obliquity of the measured total magnetic field and non-vertical polarisation vectors in magnetic bodies. Thus, if the magnetic anomalies are mainly caused by induced magnetization, only the reduction to the pole will end up with a symetrical anomalies located above the causative bodies.

The advantage of this technique is the removal of any shifting caused by the obliquity of the total field,

so that comparison of the transformed map with geological maps becomes much easier. Comparison of the reduced to the pole map with gravity map need not to be close, because of the differences in the source of the anomalies.

Calculations for the reduction to the pole operators were given by Baranov (1975) as follows:

$$T_0(0) = \sum_k \sum_n T(k,n) \frac{1}{4\pi^2} \iint e^{k\alpha i + n\beta i} \frac{\gamma^2}{AB} d\alpha d\beta$$

$$= \sum_k \sum_n T(k,n)C(k,n)$$

where the coefficients $C(k,n) = \frac{1}{4\pi^2} \iint e^{k\alpha i + n\beta i} \frac{\gamma^2}{AB} d\alpha d\beta$

$$-\pi < \alpha,\beta < \pi$$

where $A = \lambda_3\gamma + \lambda_1\alpha_i + \lambda_2\beta_i$

$$B = v_3\gamma + v_1\alpha_i + v_2\beta_i$$

and $\lambda_1,\lambda_2,\lambda_3$ and v_1,v_2,v_3 are directions cosins of $\bar{\lambda}$ (unit vector of inducing field) and $\bar{v}$ (magnetization vector), respectively.

4 Pseudogravity Technique

Further transformation has been made to convert the magnetic field into gravity field, or pseudogravity field, which represents only the effects of the magnetic rocks. This transformation is called pseudogravity, so that the anamolies deduced from this technique are not true gravimetric anomalies; they are still magnetic

anomalies, but are computed on the assumption that the magnetization vector is vertical. Thus, the pseudogravity map shows anomalies that lie vertically over the magnetized masses and do not depend on the inclination of the normal field, nor the direction of magnetization. So, any further computations on such anomalies become very simple as their directional factors need no longer to be taken into account.

The coefficients used in this study were obtained using the following equation, after Park (1983):

$$g_0(0) = \sum_k \sum_n T(k,n) \frac{1}{4\pi^2} \iint e^{k\alpha i + n\beta i} \frac{\gamma}{AB} \, d\alpha d\beta$$

$$= \sum_k \sum_n T(k,n) \, C(k,n)$$

where the operators $C(k,n) = \frac{1}{4\pi^2} \iint e^{k\alpha i + n\beta i} \frac{\gamma}{AB} \, d\alpha d\beta$

$$-\pi < \alpha, \beta < \pi$$

and A, B are the same as in the reduced to the pole operators.

5 Second Vertical Derivative Technique

Second vertical derivative of the potential fields has been widely used as a method for qualitative interpretation. Second derivative tends to locate and emphasize the smaller anomalies of shallow origin and to give a better resolved picture (Peter, 1949; Henderson and Zietz, 1949; Elkins, 1951; and Rosenbach, 1953) or the method acts as a linear filter which accentuates the

local features at the expense of the regional components (Dean, 1958). However, the method does not eliminate the ambiguity of the interpretation. The operators used to bring out the second derivative, often introducing fictitious anomalies simulating local geological features which do not in fact exist (Fajklewicz, 1965) and mislead the interpretation of such maps.

Various methods to compute the second derivatives of gravity and magnetic fields are of the form

$$\frac{\partial^2 g}{\partial z^2} = \frac{1}{s^2}\left[W_0 . \bar{g}(r_0) + W_1 . \bar{g}(r_1) + \ldots\ldots + W_n . \bar{g}(r_n)\right]$$

where $r_o = o$, $\bar{g}(r_n)$ is the average field values over circles of radii r_n, W_n are the weights and s is the grid spacing.

In the present study, second derivative operators were calculated, using the following equation, after Agarwal and Lal (1972):

$$G(\rho) = \frac{1}{s^2} \sum_{r=0}^{M} w(r_n)\, J_0(\rho r_n)$$

where J_o is the Bessel function of zero order of first kind;

$\rho = \sqrt{u^2+v^2}$ is the radial frequency;

$G(\rho) = \rho^2 \exp(-\lambda\rho^2)$

and λ is smoothing parameter.

The simultaneous equations obtained were solved for the weights W_n with different smoothing parameters.

A review of the techniques or methods mentioned in

this section has been discussed by El-Malky (1974) and Park (1983).

7.6 Geophysical Data Processing

The operators of the previously mentioned techniques have been designed using a package of routines kindly supplied by Mr. Rark. These operators are shown in Appendix II.

1. Low Pass Filter Operators

These filter operators have been designed for the purpose of smoothing, as mentioned before, and low pass filtering. In low pass filtering, operators were designed as 11 by 11 to pass frequencies lower than 0.3 cycle/5km. (for gravity map) and 0.3 cycle/2.5 km. (for magnetic maps). This was equivalent to cut off wave length of approximately 16,600 m. and 8,300 m., respectively.

2. Continuation Operators

These operators have been designed as 13 by 13 to obtain an upward continued map at 20 km. (h=4) and 10 km. of gravity and magnetic maps, respectively, in order to enhance the regional trends.

3. Reduced To the Pole and Pseudo Gravity Operators

In this study, these operators were designed as one pair of 21 by 21. The first set belongs to the Western Desert aeromagnetic map where the inclination and declination of the total magnetic field are 39.6^{o} and 0.2^{o} degrees, respectively, while the second set was designed for the Nile Delta aeromagnetic map where the inclination and declination of the total magnetic field are 44.5^{o} and 1.9^{o} degrees, respectively.

During the calculation of these operators, it has been assumed that the magnetization vector of the total field is the same as that of the induced field.

4. Second Vertical Derivative Operators

These operators were designed as two sets of 7 by 7, with smoothing parameters of 0.1 and 0.2 for Western Desert and Nile Delta aeromagnetic maps, respectively.

The digital convolution of the different operators designed in this study, with the geophysical maps (Figs. 7.1, 7.2 and 7.3) is as follows:

$$Z(x,y) = \sum_{x=0}^{a-1} \sum_{y=0}^{b-1} X(x - \tau, y - \lambda)\, F(\tau,\lambda)$$

where $X(x,y)$ is the input data, $F(\tau,\lambda)$ is the lagged operator and $Z(x,y)$ is the output. a and b are the operator windows in x and y directions consequently.

The convolution process was carried out utilizing a program modified by Park (1983), after Robinson (1971).

The output at each stage was contoured with different contour intervals as shown in Figs. 7.9 to 7.24.

Because of technical difficulties, the gravity and the Western Desert aeromagnetic maps were divided into two halves during the process of contouring.

7.7 Principles of Interpretation

There are different approaches by which the geophysical data can be interpreted. However, in order to achieve the aim of this study, these geophysical data have been inspected for mapping possible fractures or dislocations present at both regional and local scales. These dislocations or lineaments could be defined as breaks or disruption of the map contours. The criteria for the recognition of such features on the potential field maps (Gay, 1972) are:

a. Termination of highs (Fig. 7.5a);

b. Termination of lows (Fig. 7.5b);

c. Changing gradients (Fig. 7.5c).

Changing gradients or steepening and flattening gradients define highs or lows anomalies of shorter wave length and lower amplitude than the anomaly responsible for the primary gradient, so it could be one of the features for the recognition of dislocations or lineaments.

d. Linear contour patterns (Fig. 7.5d).

This criterion may be associated with occasional alignment of highs and/or lows.

Detection of horizontal movements or shearing along

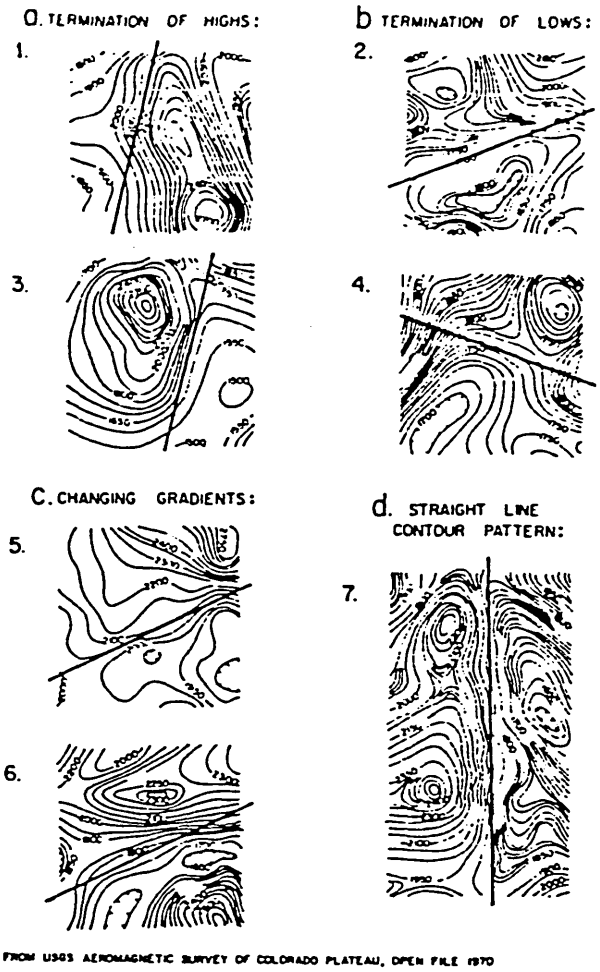


Fig. 7.5 Some features of aeromagnetic maps which define aeromagnetic lineaments.

(After Gay,1972)

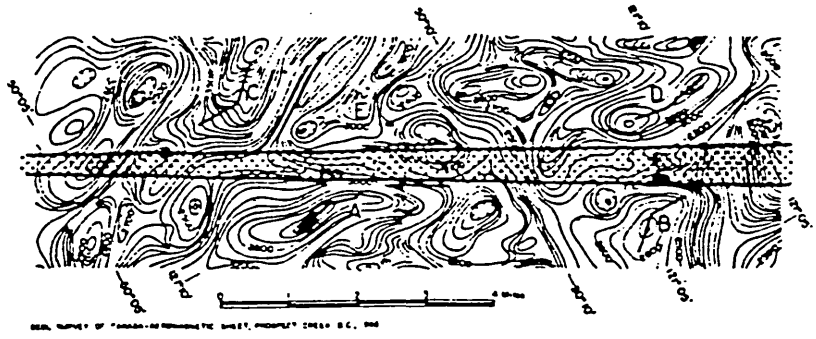


Fig. 7.6 Prominent aeromagnetic lineament cutting rocks adjacent to the coastal batholith in British Columbia. Note prominent drag features at A, B, C, D, and E, which indicate direction of strike-slip movement.

(After Gay,1972)

these fractures or lineaments requires the inspection of the gravity and magnetic maps for one of the following possible features:

i. offsets of the anomalies;

ii. offsets of lineaments or dislocations;

iii. drag features (Fig. 7.6);

iv. alignment of alternating positive and negative anomalies with different signs on both sides of the dislocation. This criterion, from the structural point of view, means that if a dislocation cutting across the axes of fold structures or faulted area, in a form of horsts and grabens, then any horizontal or shear movement along this dislocation may lead to a synclinal axis facing an inticlinal axis, as indicated in Figs. 7.7b and 7.8, or a graben facing a horst. These features could be noticed on the surface (Figs. 7.7a) and also could be present in the subsurface.

In geophysical interpretation of gravity and magnetic anomalies, shearing movement along any dislocation cutting across folded or faulted area, in a form of grabens and horsts, may cause a structurally high area or positive anomaly, axis of anticline, facing a structurally low area or negative anomaly, axis of syncline (Fig. 7.7c).

7.8 Results

Based on the principles of interpretation, as have been indicated in Figs. 7.6, 7.7 and 7.8, probable dislocations or lineaments were located, as shown in

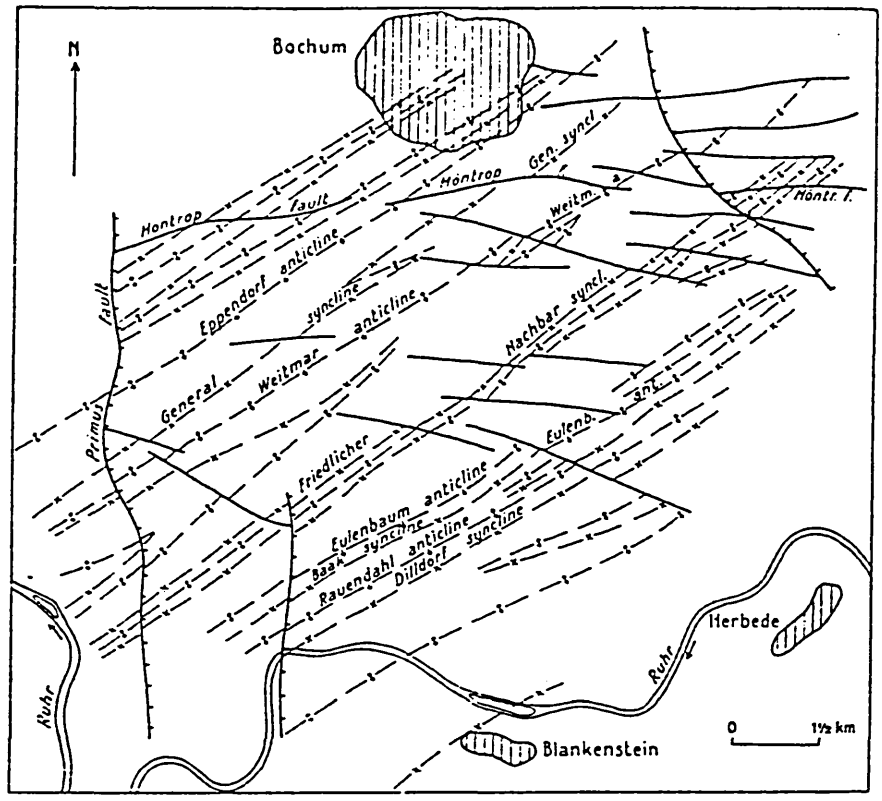


Fig. 7.7a The wrench-faults of the Bochum area of the Ruhr coalfield. *(After Kukuk, Geologie der Niederrheinisch-Westfälischen Steinkohlengebiete. Published by permission of Springer-Verlag, Berlin.)*

(After De Sitter,1964)

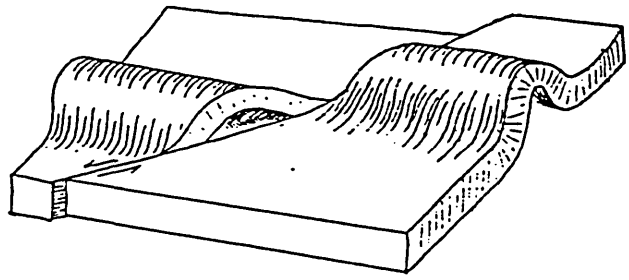
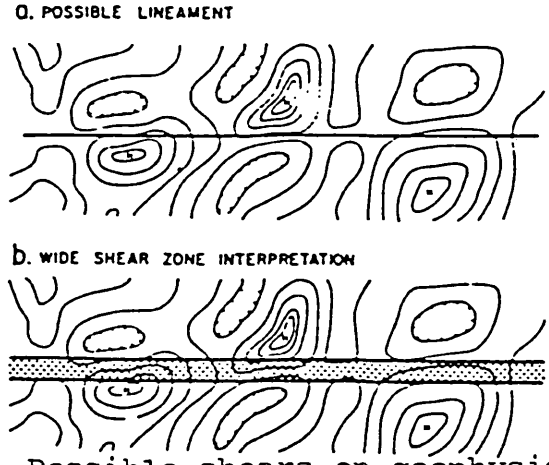


Fig. 7.7b Shearing of a fold structure.



(After Gay,1972)

Fig. 7.7c Possible shears on geophysical map (magnetic)

Fig. 7.8 Shearing of folded and faulted regions.

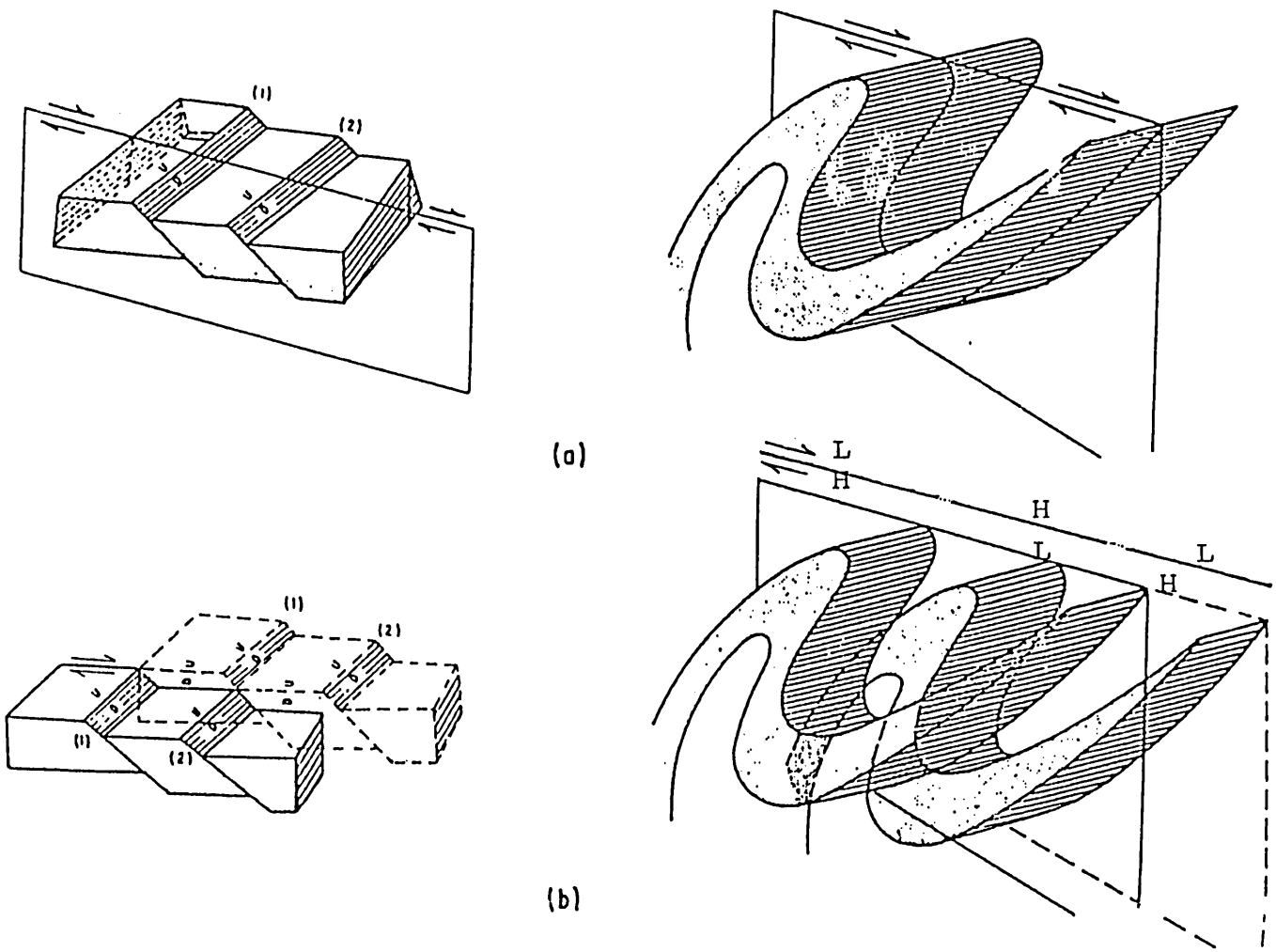


Fig. 7.8 . Shearing of folded and faulted rocks.
(Modified by the auther after Riad,1977)

Figs. 7.2 to 7.4 and Figs. 7.9 to 7.24, on both regional and local scales.

Some of these dislocations, which show drag features (Fig. 7.6) along these dislocations, were classified as shears where the small arrows demonstrate the relative movements along these fractures.

By careful study of other dislocations or lineaments, in light of the criterion of horizontal movement across folded or faulted area (Figs. 7.8 and 7.9), it becomes relatively easy to locate other shears shown as continuous or dashed lines.

In the following tables, the main trends of each map are given and their orientations will be briefly discussed.

A. Gravity Map

The main trends of this map (Fig. 7.2), are discussed earlier in this chapter and shown on Table 7.2.

The regional and local trends are represented in the following tables:

Table 7.4

Regional Trends of the Gravity Map

Low Pass Filter Map (Fig. 7.9)	Possible Shears	Upward Continuation Map (Fig. 7.10)	Possible Shears
ENE	N-S (L.L.)	ENE	N-S (L.L.)
NE	NNE (L.L.)	NNE	NNE (L.L.)
NNE	WNW (R.L.)	N-S	WNW (R.L.)
N-S	ENE	NW	ENE (L.L.)
WNW	NW (R.L.)	WNW	NW (R.L.)
NW		NE	
nearly E-W		nearly E-W	
NNW			

R.L. = Right Lateral
L.L. = Left Lateral

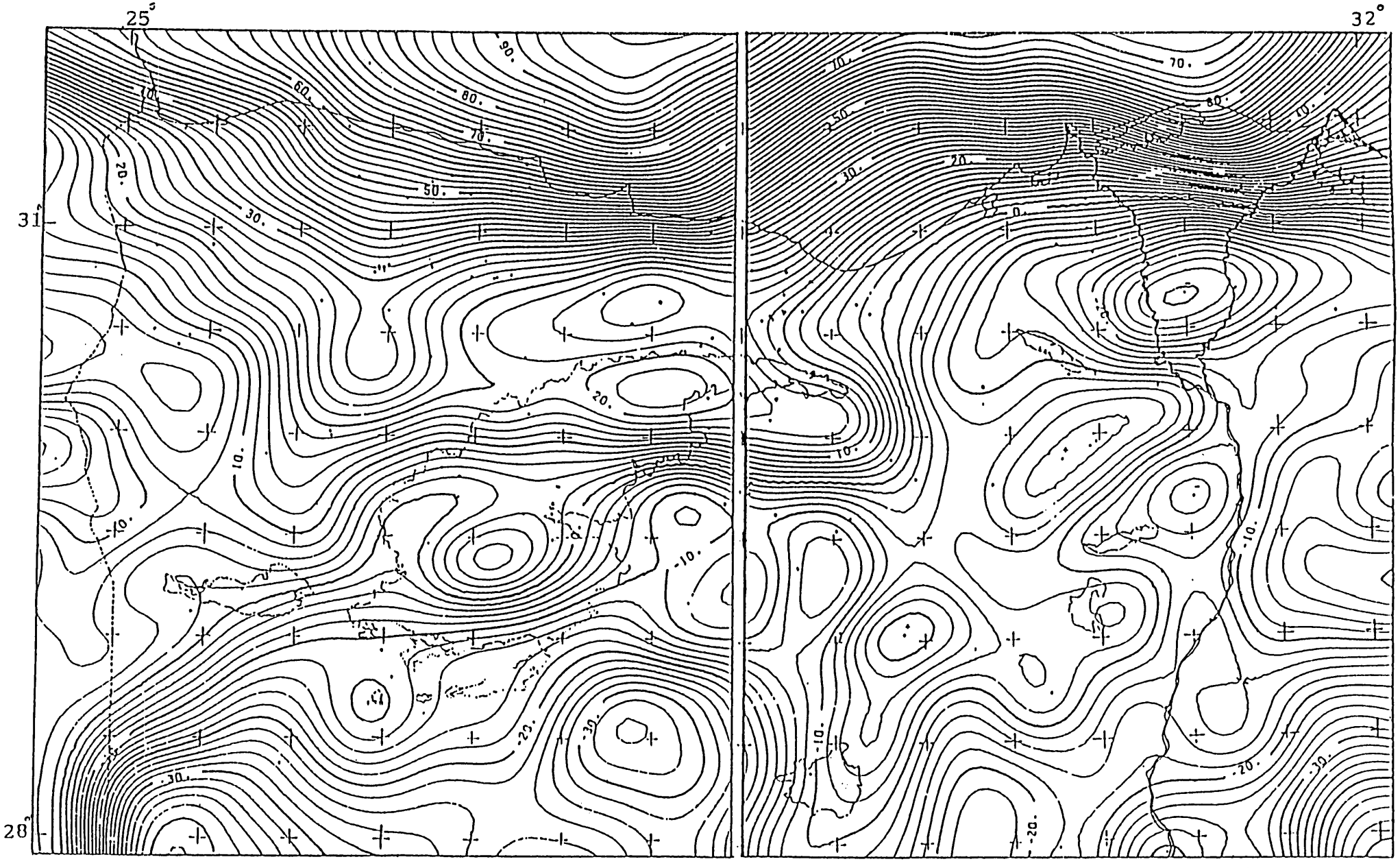


Fig. 7.9 Lowpass filtered gravity map of Western Desert of Egypt (C.I.=2)

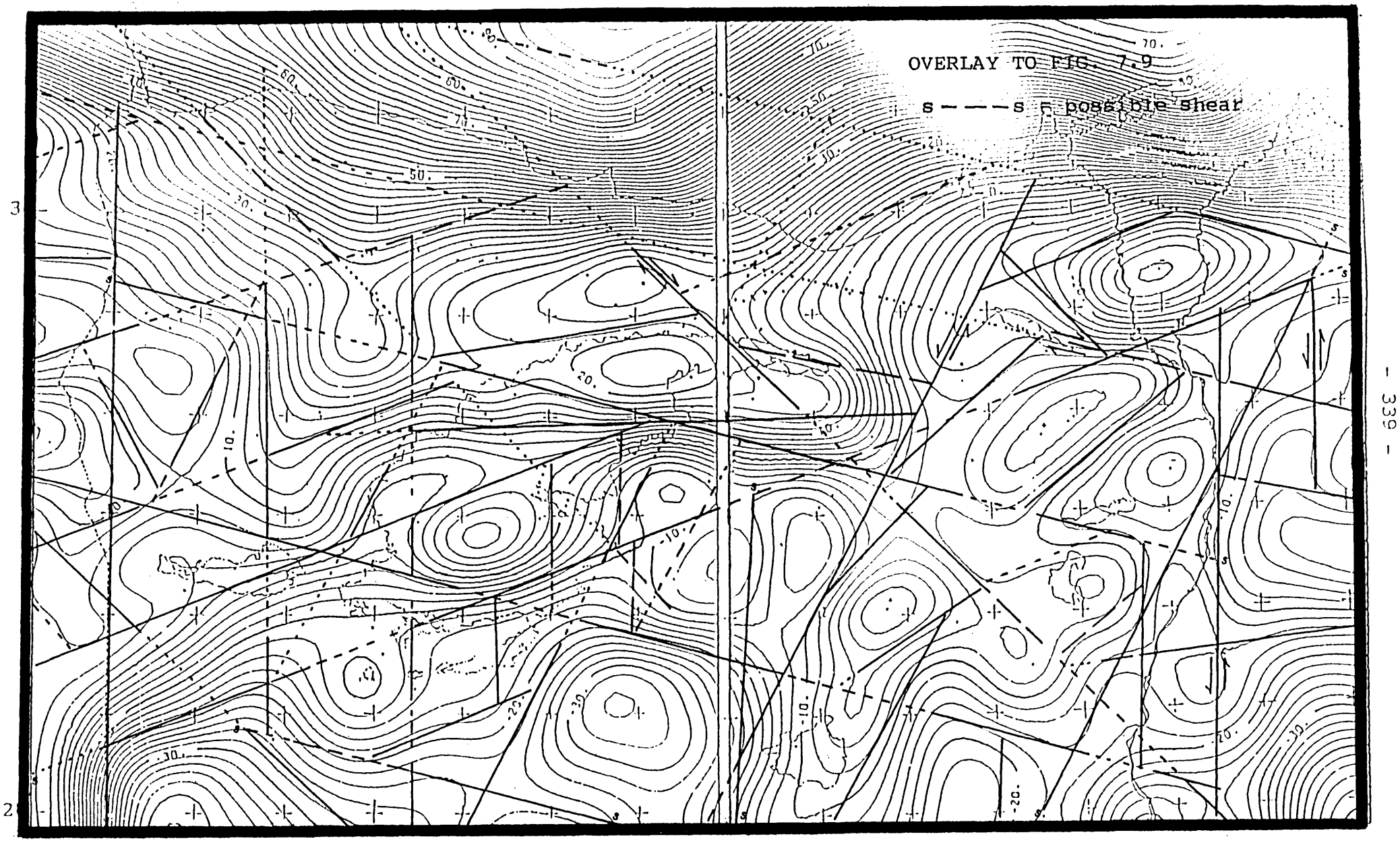


Fig. 7.9 Lowpass filtered gravity map of Western Desert of Egypt (C.I.=2)

0 50 km.

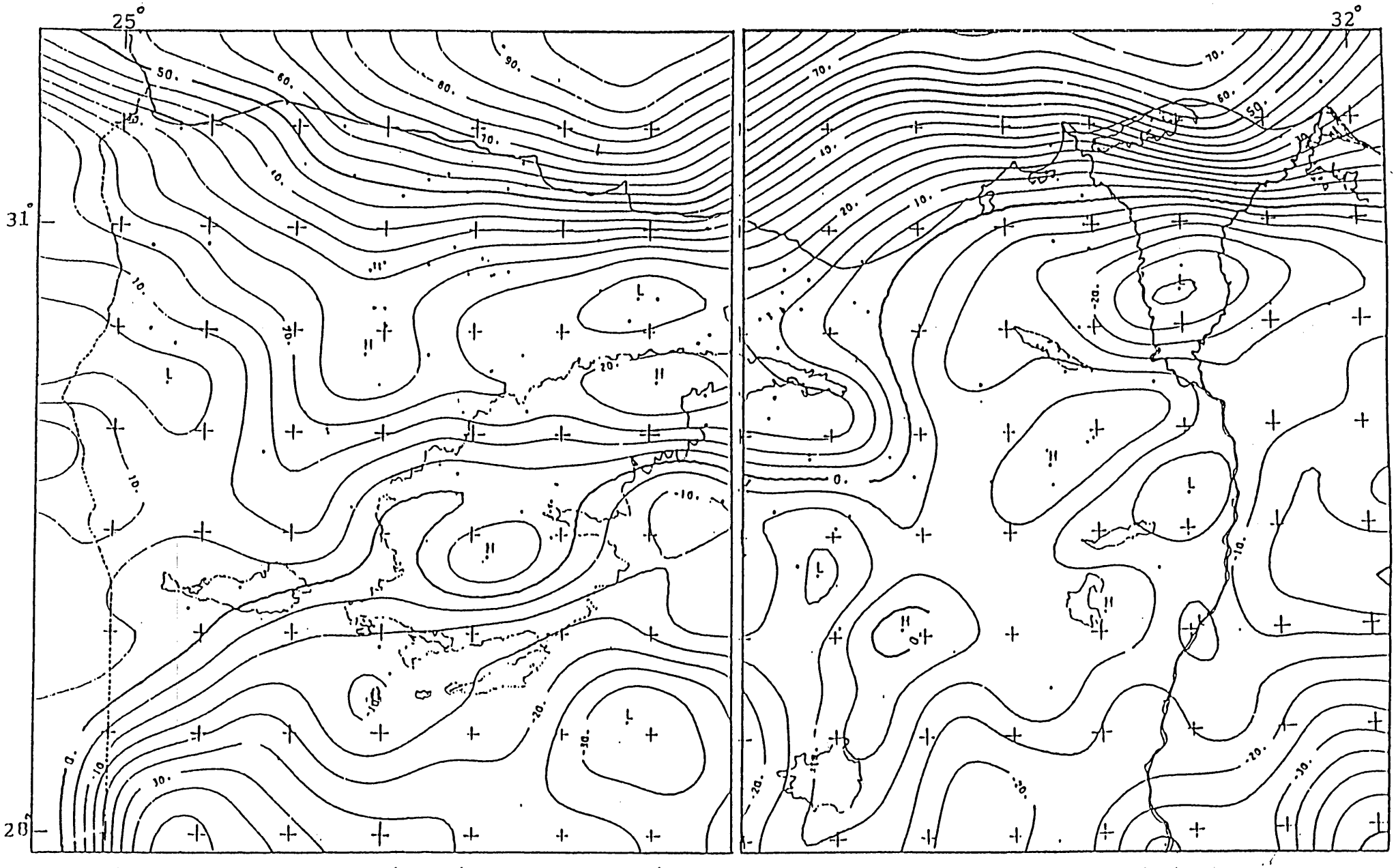


Fig. 7.10 Upward continuation of the gravity map of the Western Desert (C.I.=5).

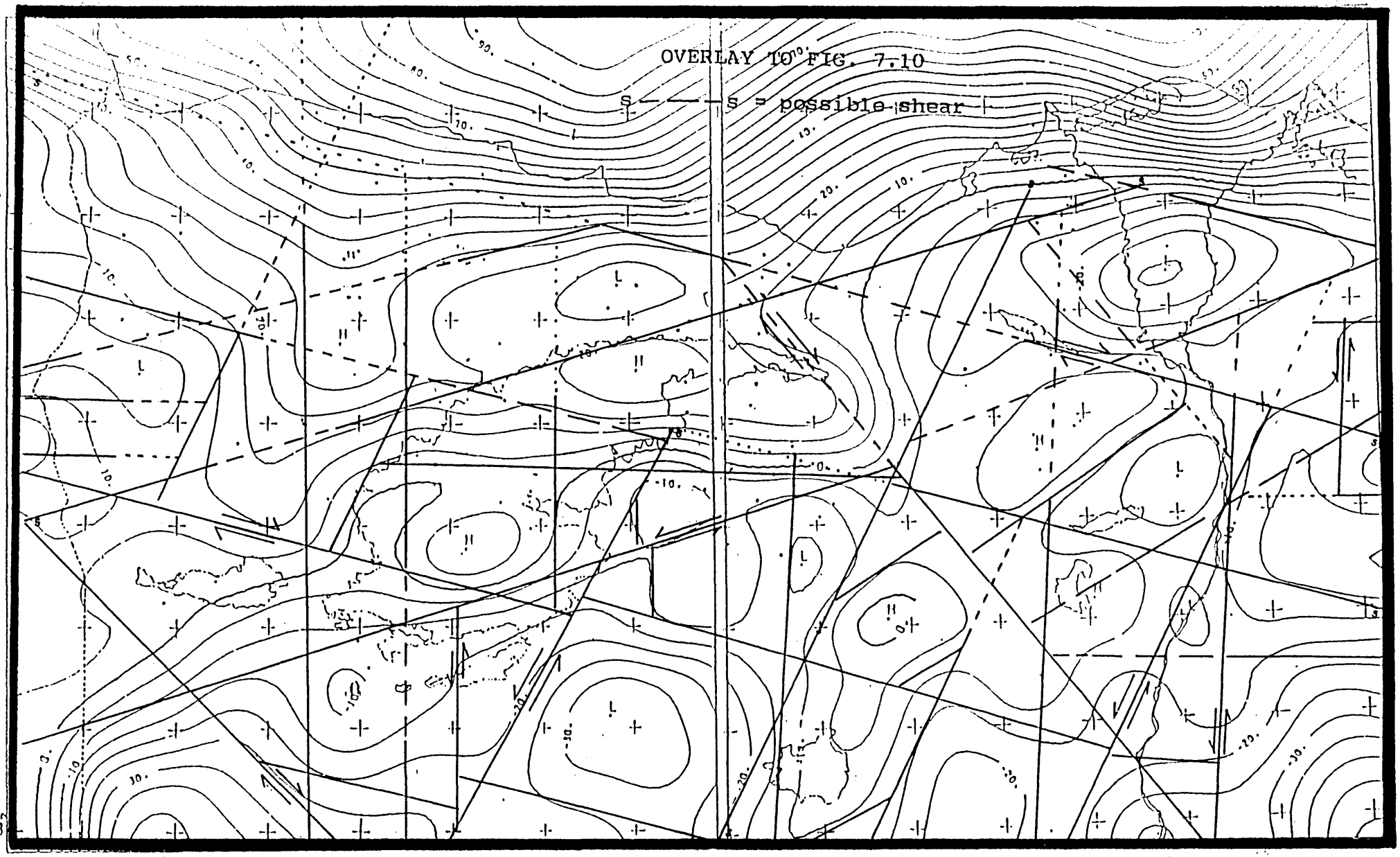


Fig. 7.10 Upward continuation of the gravity map of the Western Desert (C.I.=5).

Table 7.5

Local Trends of the Gravity Map

High Pass Filter map (Fig. 7.11)	Possible Shears	Second Vertical Derivative Map (Fig. 7.12)	Possible Shears
ENE	ENE (L.L.)	N-S	N-S (L.L.)
NE	NNE (L.L.)	ENE	WNW
WNW	WNW (R.L.)	WNW	ENE
NW	NW (R.L.)	NW	NNE
nearly N-S	N-S (L.L.)	NE	NW (R.L.)
NNW	≈ E-W (R.L.)	NNE	
nearly E-W		NNW	
NNE		nearly E-W	

B. Aeromagnetic Maps of the Western Desert

The main trends of these maps are represented in Table 7.6, as well as the following Tables.

Table 7.6

Trends of Filtered Aeromagnetic Maps of the W.D.

Reduced to the Pole Map (Fig. 7.13)	Possible Shears	Pseudo Gravity Map (Fig. 7.14)	Possible Shears
ENE	N-S (L.L.)	ENE	N-S (L.L.)
NE	NNE (L.L.)	NNE	NNE (L.L.)
NNE	WNW (R.L.)	N-S	WNW (R.L.)
N-S	ENE (L.L.)	WNW	ENE (L.L.)
WNW	NW (R.L.)	NW	NW (R.L.)
NW	E-W (R.L.)	nearly E-W	nearly E-W (R.L.)
nearly E-W		NE	
NNW		NNW	

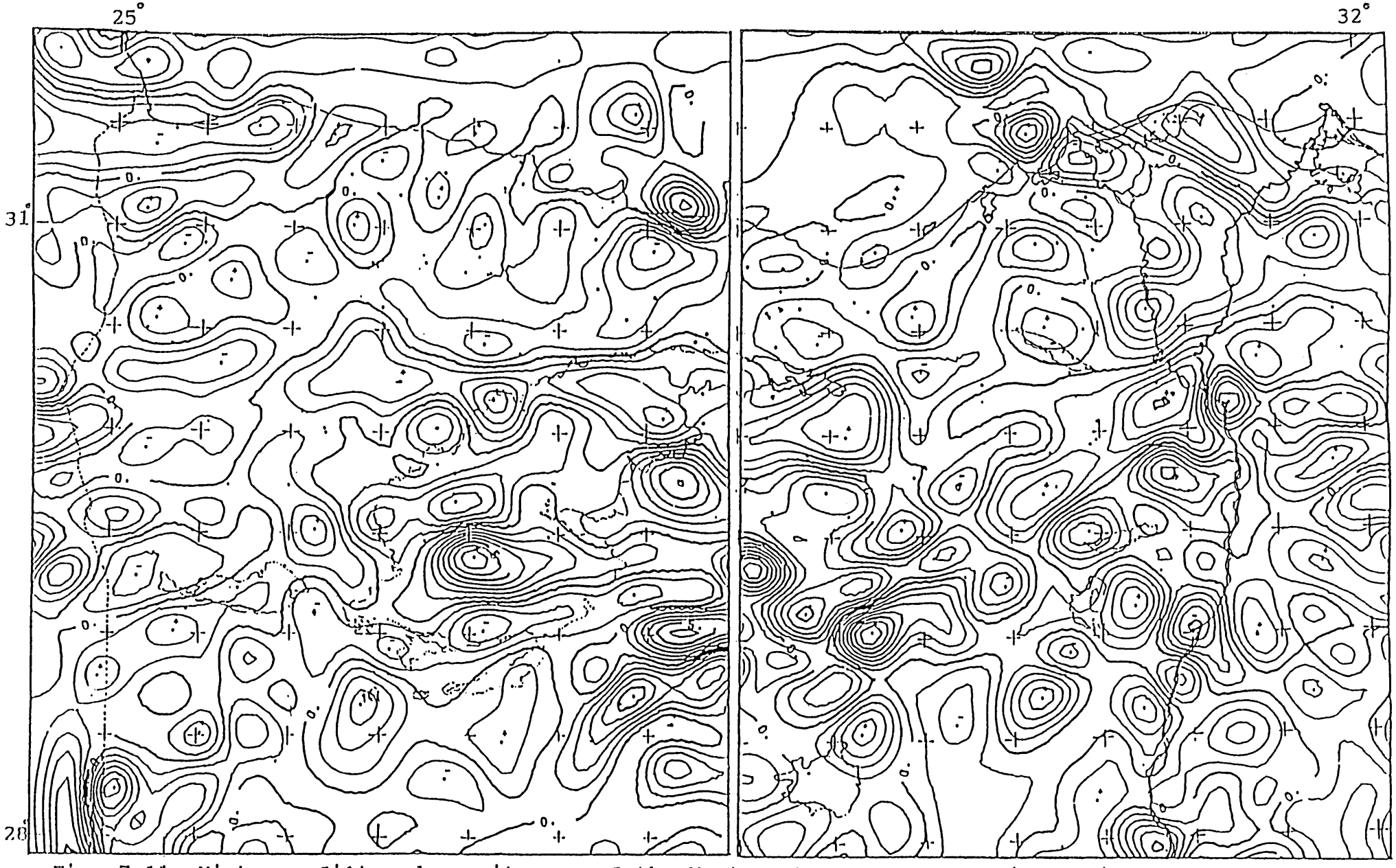


Fig. 7.11 Highpass filtered gravity map of the Western Desert of Egypt (C.I.=1).

OVERLAY TO FIG. 7.11

s— — —s = possible shear

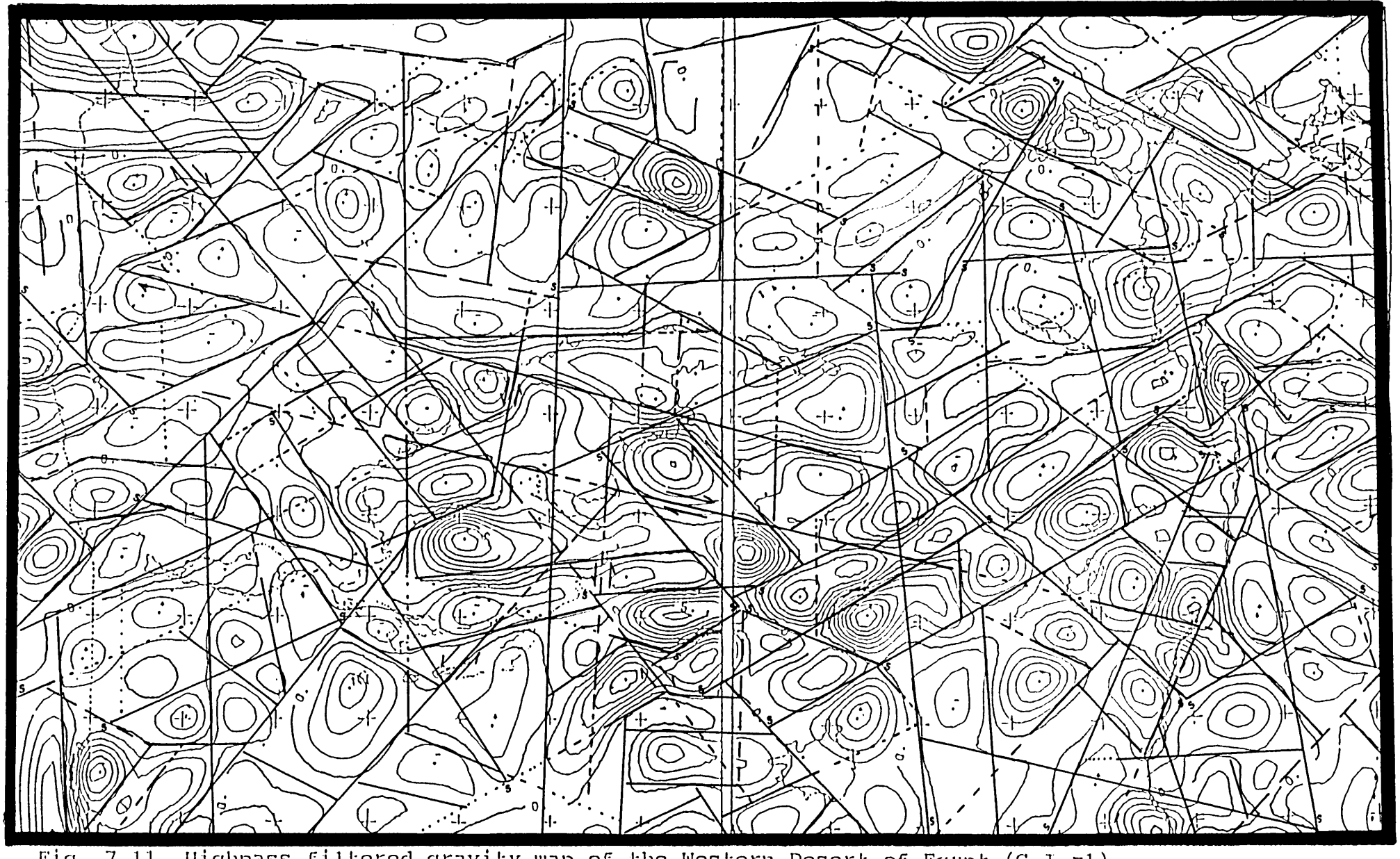


Fig. 7.11 Highpass filtered gravity map of the Western Desert of Egypt (C.I.=1).

0 50 km.

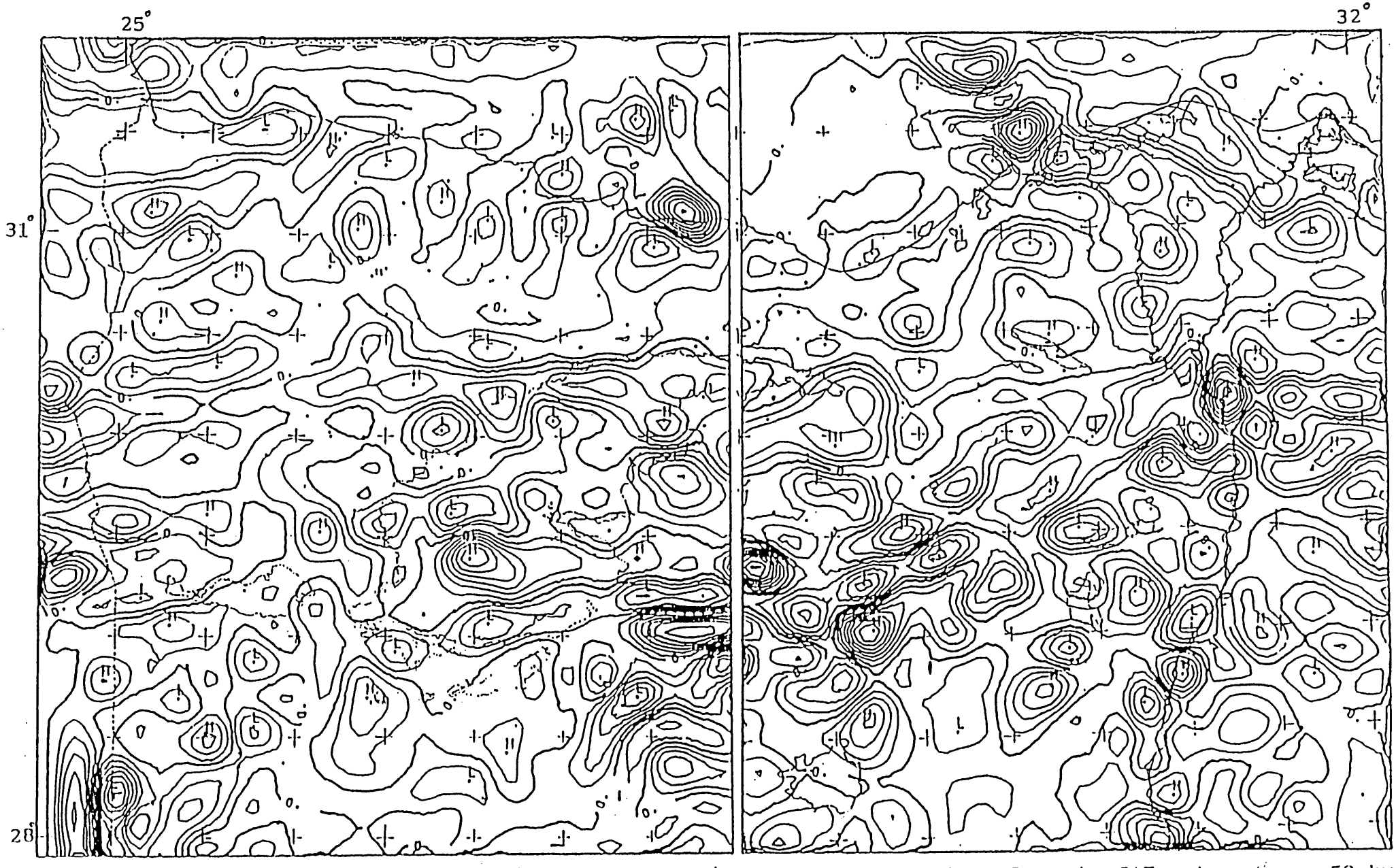


Fig. 7.12 Second vertical derivative of the gravity map of the Western Desert of Egypt. 0 50 km.
(C.I.=0.5)

OVERLAY TO FIG. 7.12

s——s = possible shear

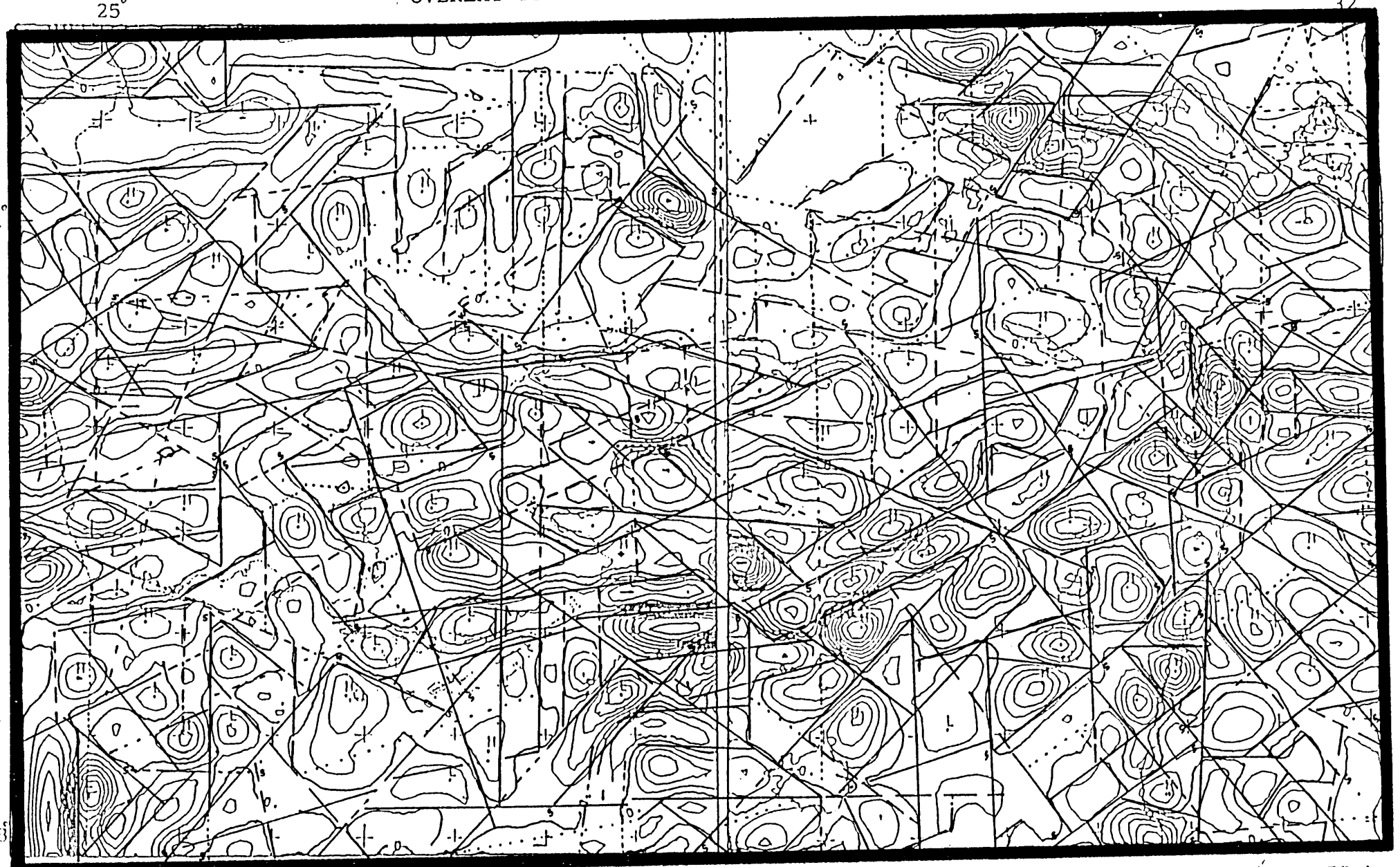


Fig. 7.12 Second vertical derivative of the gravity map of the Western Desert of Egypt. 0 50 km.

(C.I.=0.5)

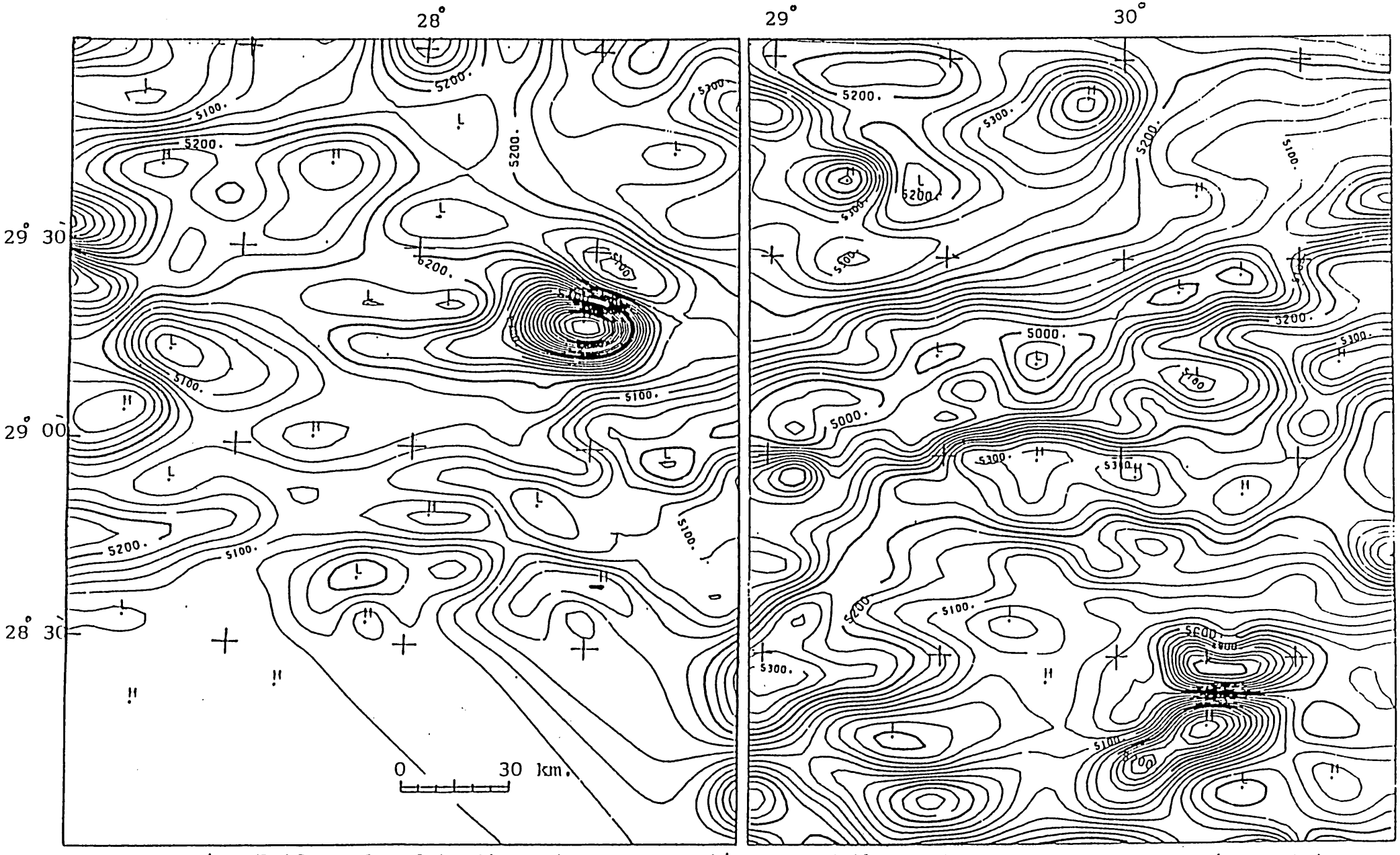


Fig. 7.13 Reduced to the pole aeromagnetic map of the Western Desert of Egypt (C.I.=25).

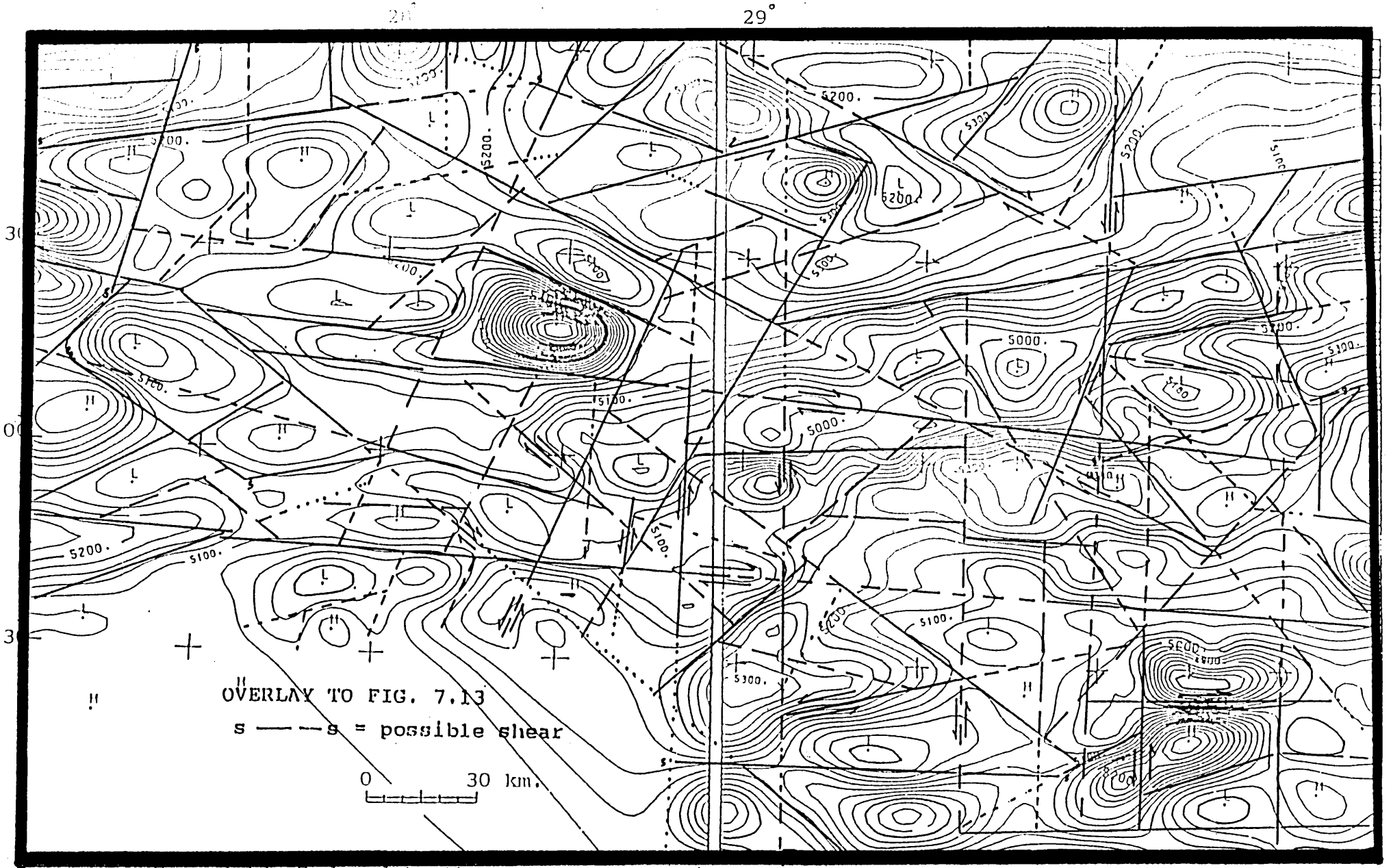


Fig. 7.13 Reduced to the pole aeromagnetic map of the Western Desert of Egypt (C.I.=25).

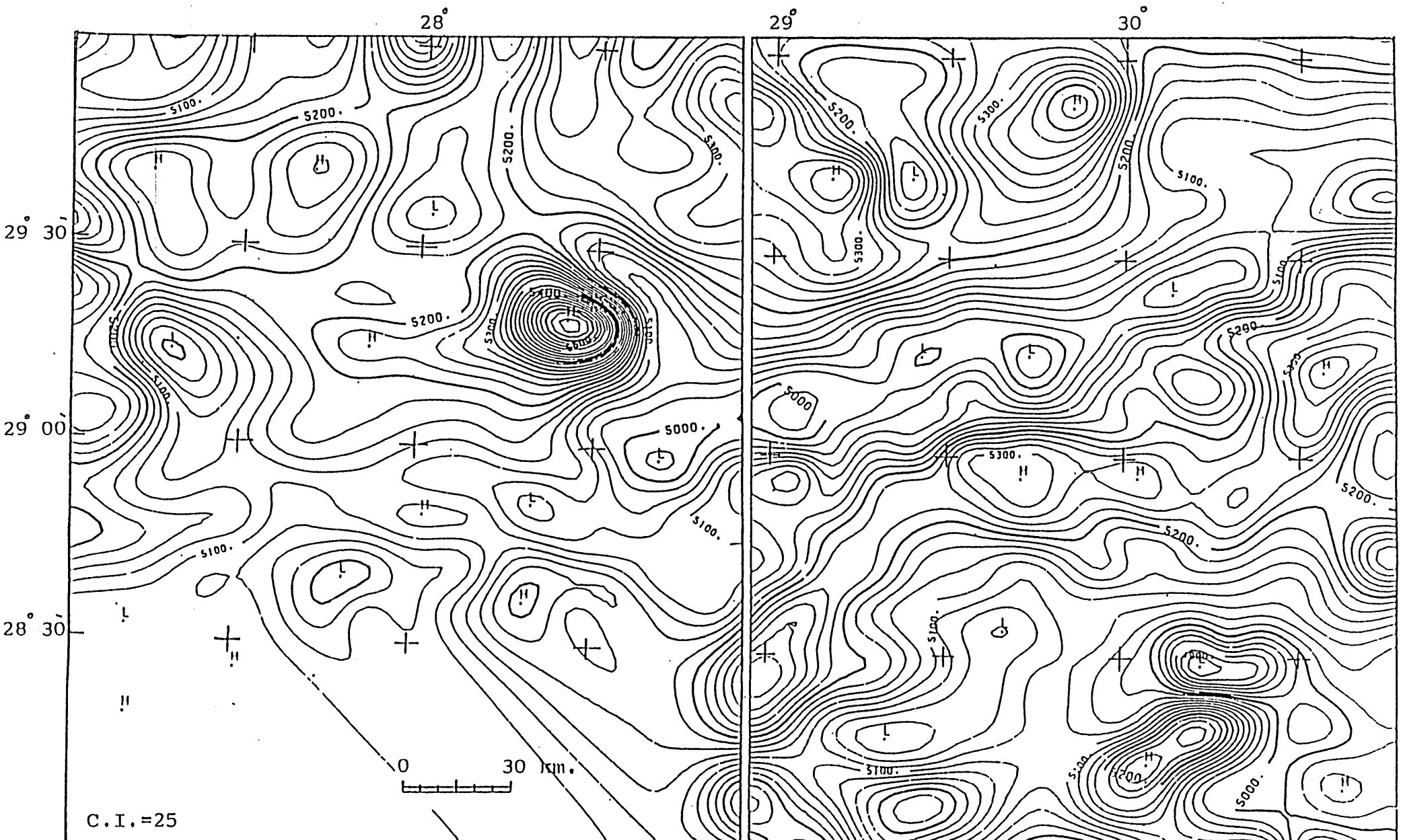


Fig. 7.14 Pseudogravity map of the Western Desert of Egypt.

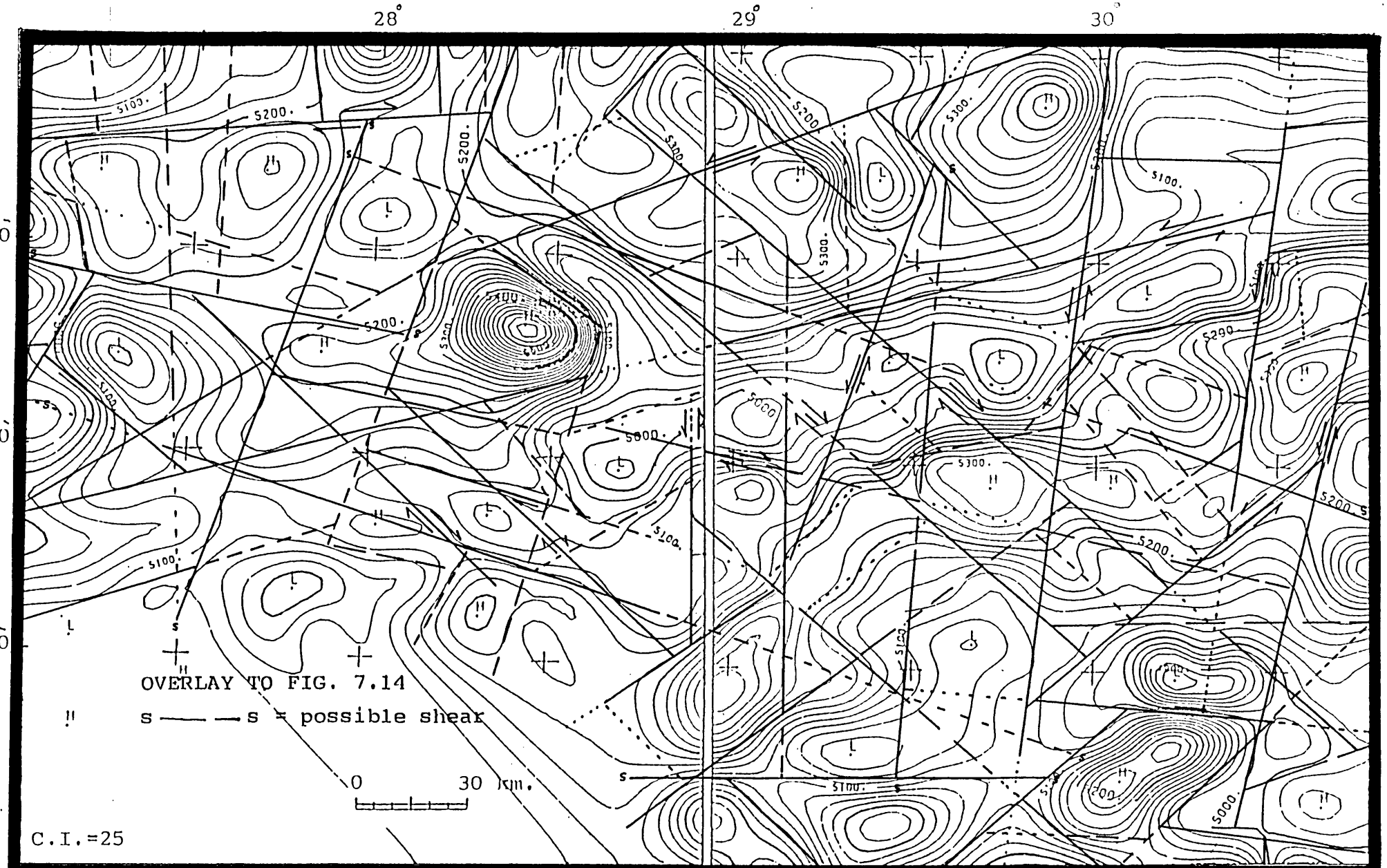


Fig. 7.14 Pseudogravity map of the Western Desert of Egypt.

Table 7.7

Regional Trends of the Aeromagnetic Maps of the W.D.

Low Pass Filter Map (Fig.7.15)	Possible Shears	Upward Continuation Map (Fig. 7.16)	Possible Shears
nearly N-S	N-S (L.L.)	NW	NW (R.L.)
ENE	ENE	ENE	ENE
NW	NNE (L.L.)	NNE	NNE (L.L.)
WNW	WNW (R.L.)	NE	WNW (R.L.)
NE		WNW	N-S (L.L.)
NNE		nearly E-W	
nearly E-W		N-S	
		NNW	

Table 7.8

Local Trends of the Aeromagnetic Maps of the W.D.

High Pass Filter Map (Fig. 7.17)	Possible Shears	Second Vertical Derivative Map (Fig. 7.18)	Possible Shears
nearly E-W	WNW (R.L.)	ENE	ENE (L.L.)
nearly N-S	ENE (L.L.)	NNE	N-S (L.L.)
NNE	NW (R.L.)	nearly E-W	NNE (L.L.)
WNW	N-S (L.L.)	NW	nearly E-W (R.L.)
NE	E-W (R.L.)	WNW	WNW
ENE	NNE	NE	NW (R.L.)
NW		NNW	
NNW			

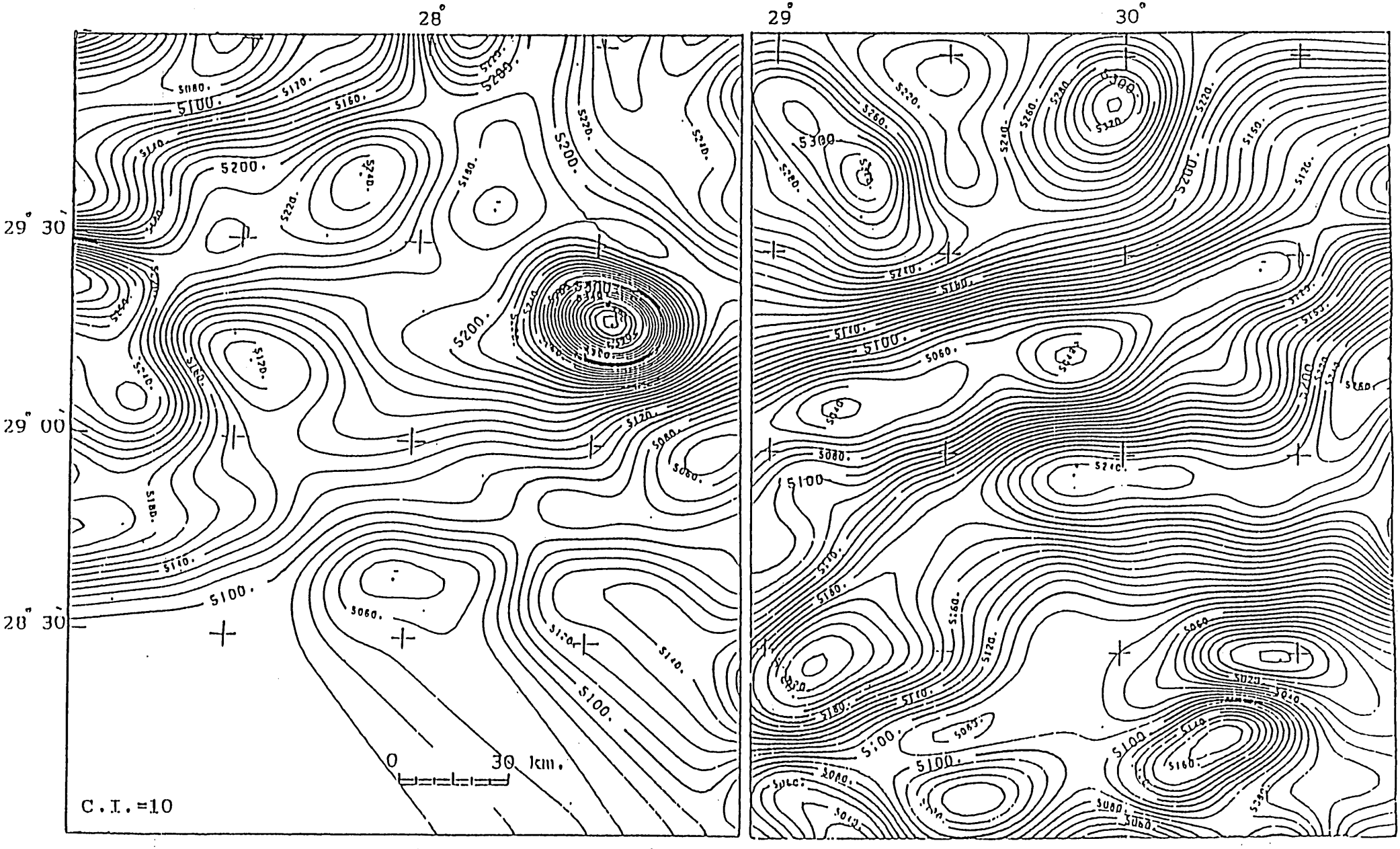


Fig. 7.15 Lowpass filtered aeromagnetic map of the Western Desert of Egypt.

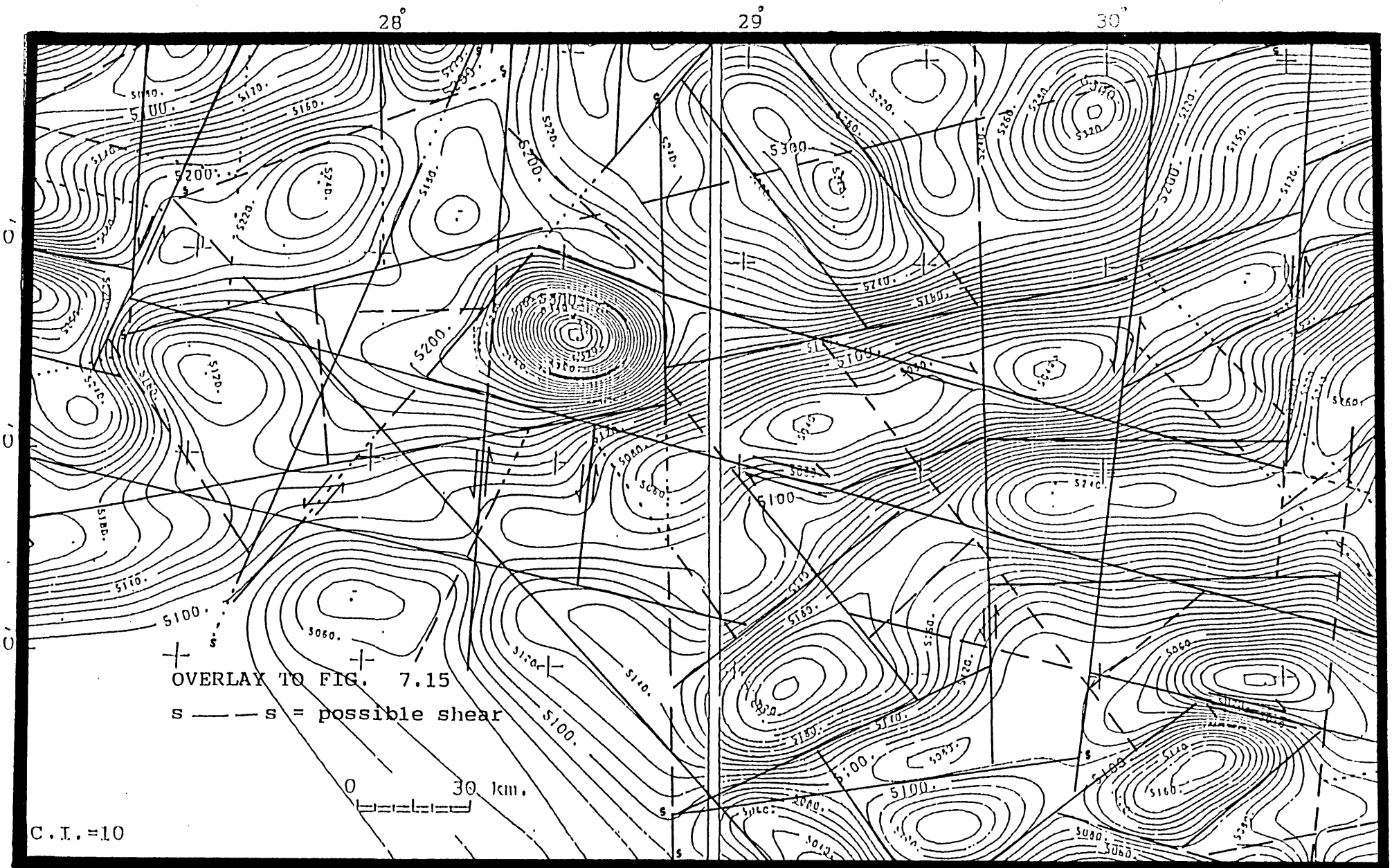


Fig. 7.15 Lowpass filtered aeromagnetic map of the Western Desert of Egypt.

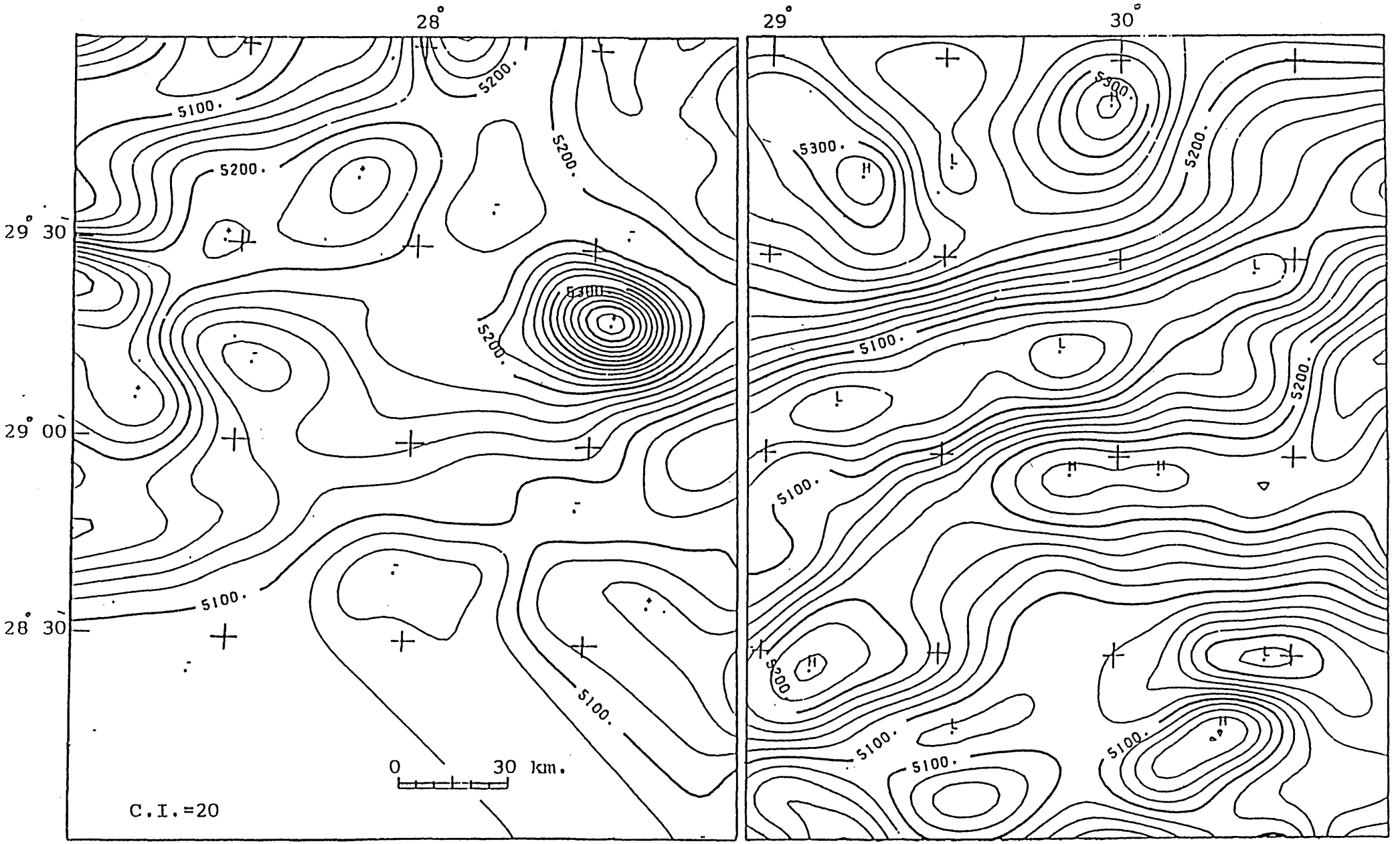


Fig. 7.16 Upward continuation of the aeromagnetic map of the W.D. of Egypt.

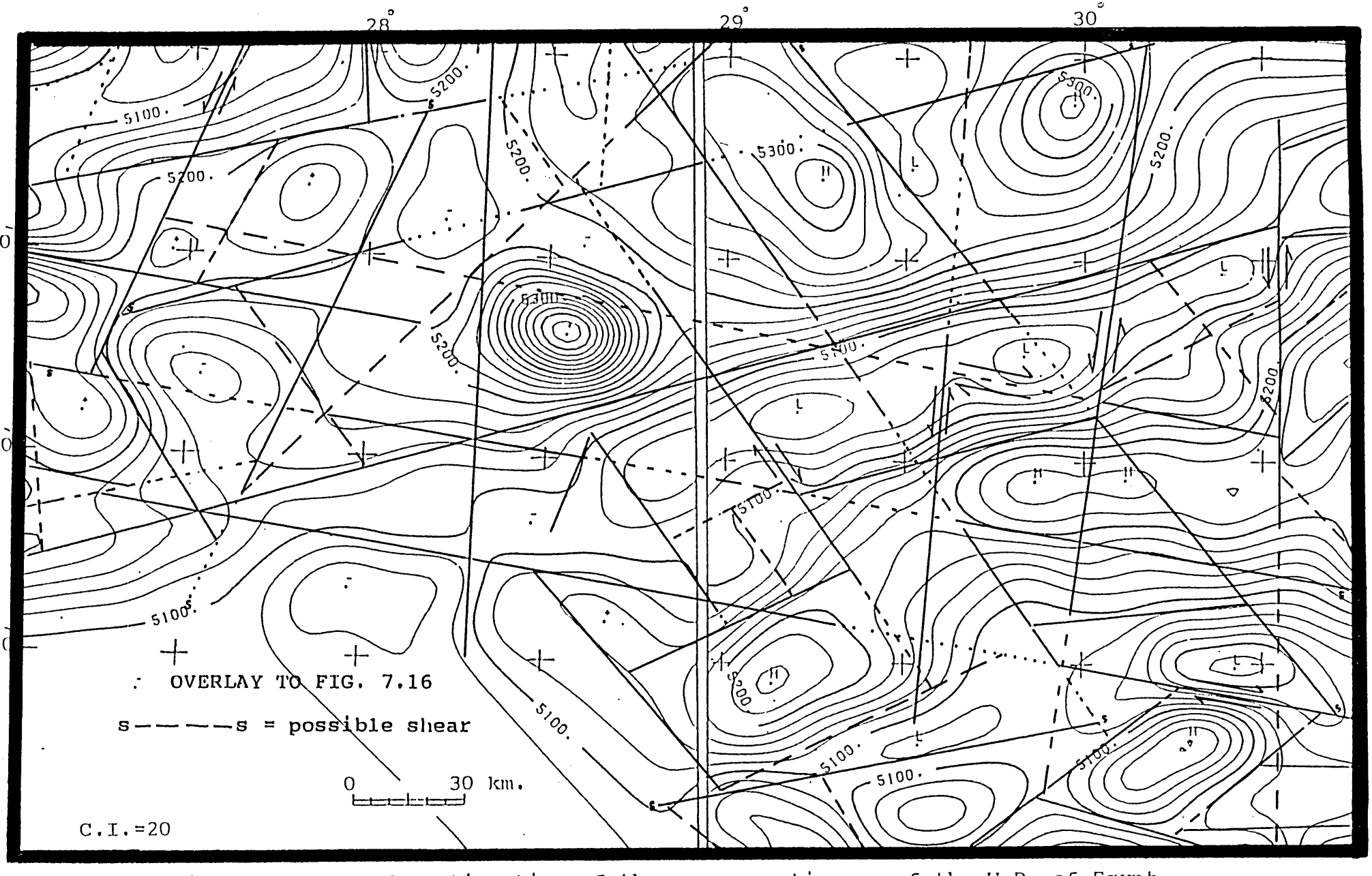


Fig. 7.16 Upward continuation of the aeromagnetic map of the W.D. of Egypt.

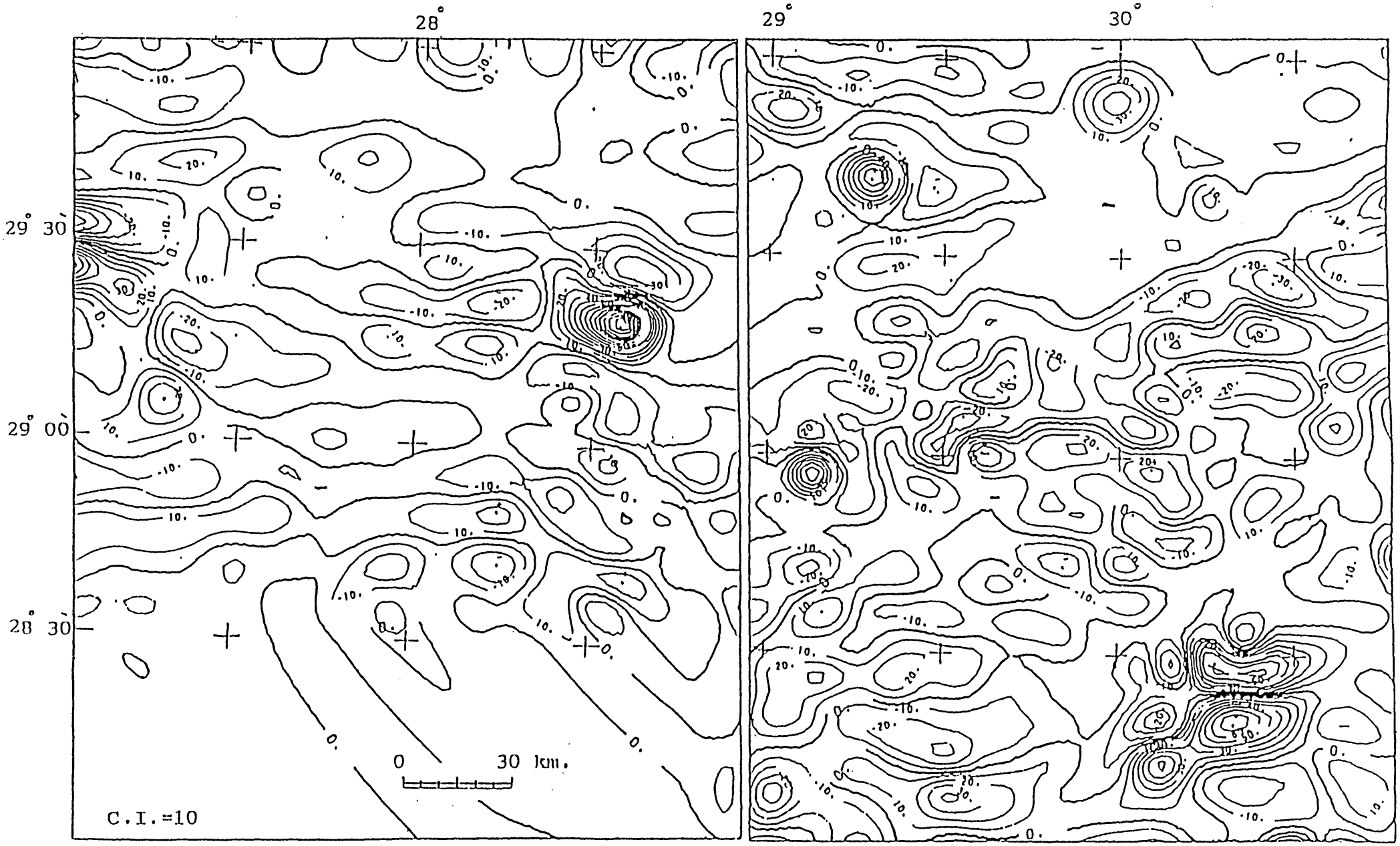


Fig. 7.17 Highpass filtered aeromagnetic map of the Western Desert of Egypt.

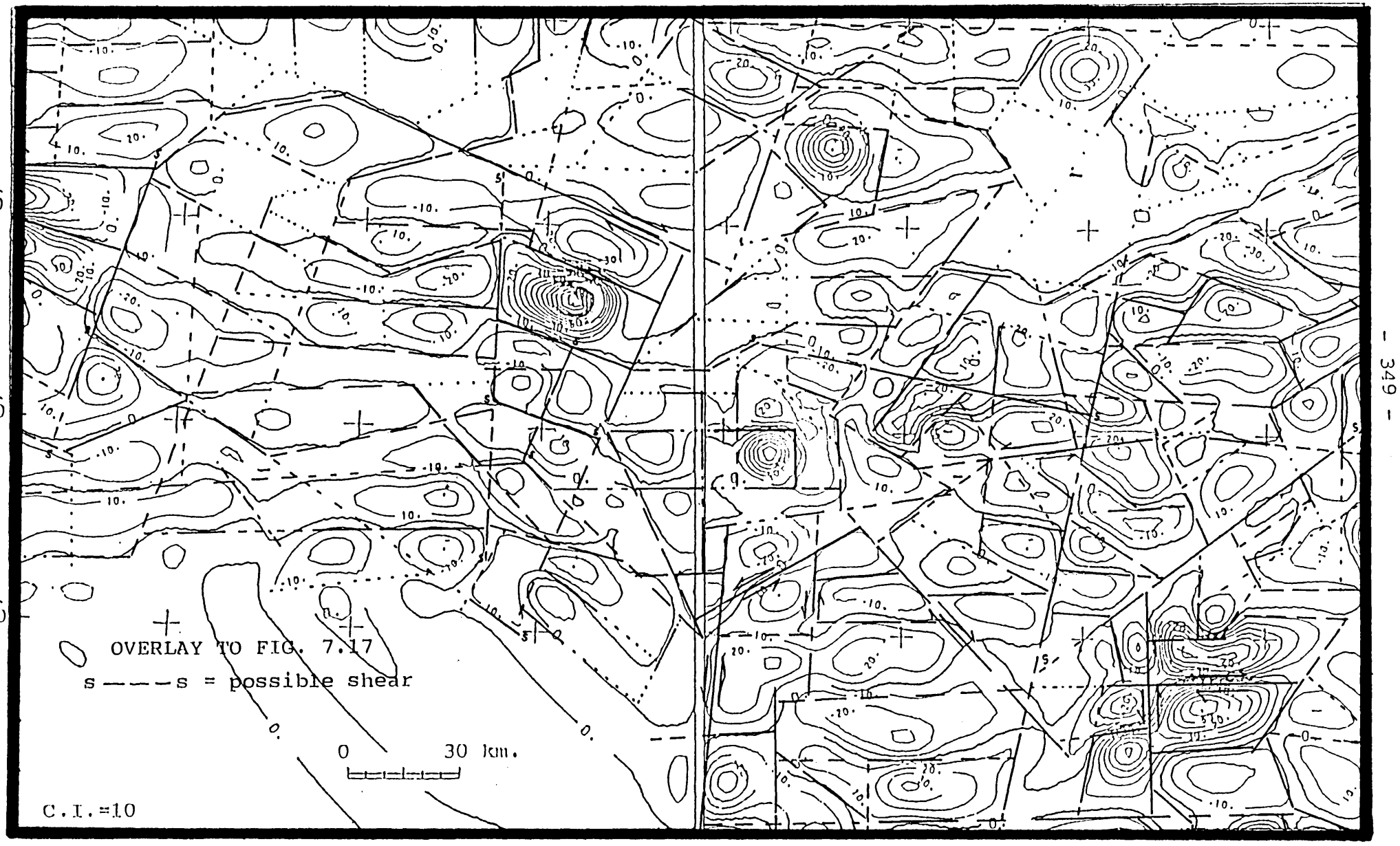


Fig. 7.17 Highpass filtered aeromagnetic map of the Western Desert of Egypt.

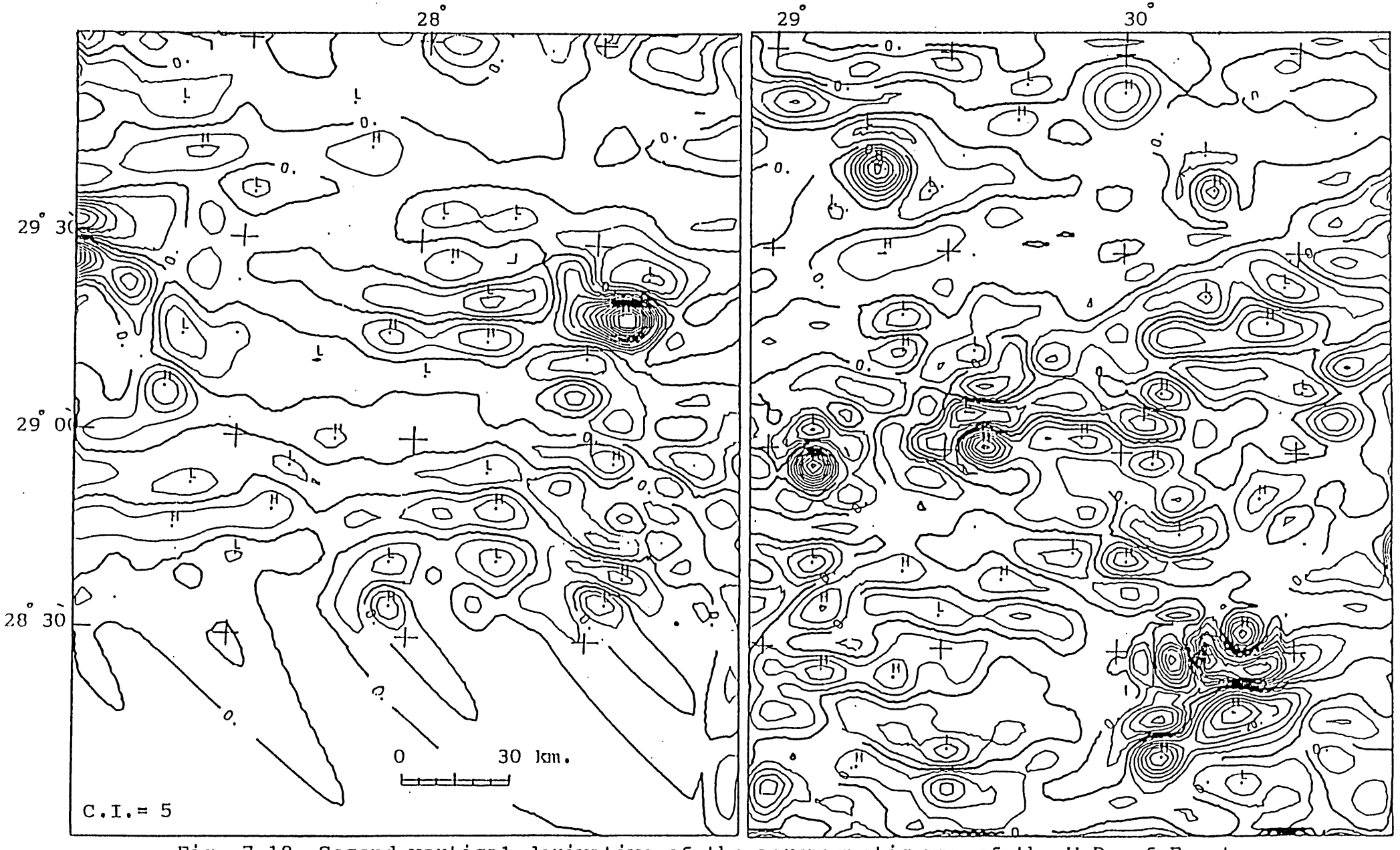


Fig. 7.18 Second vertical derivative of the aeromagnetic map of the W.D. of Egypt.

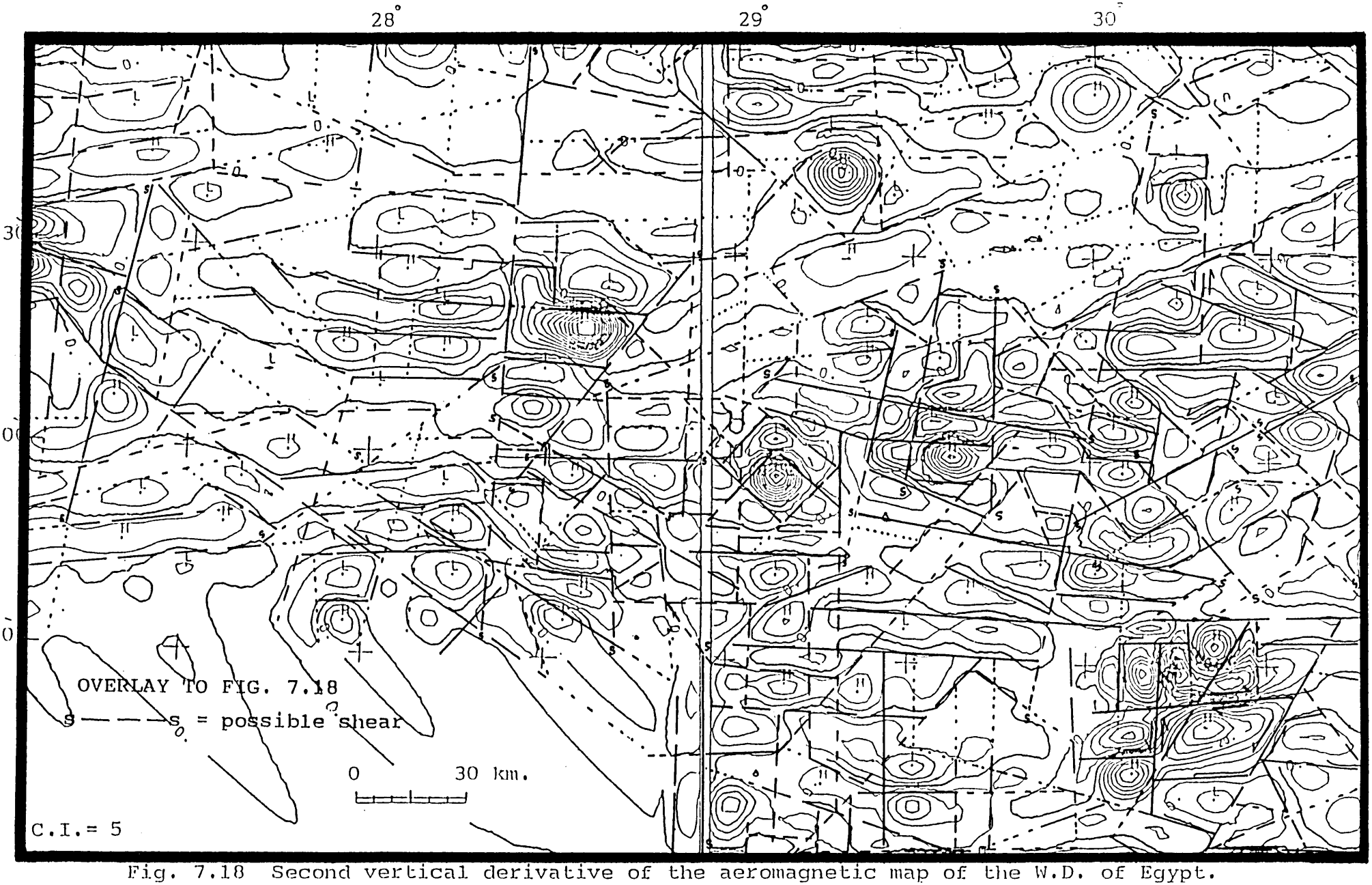


Fig. 7.18 Second vertical derivative of the aeromagnetic map of the W.D. of Egypt.

C. Aeromagnetic Maps of the Nile Delta

The trends of these maps as well as the regional and local trends are demonstrated in Table 7.3 and the following tables:

Table 7.9

Trends of the Filtered Aeromagnetic Maps of the Nile Delta

Reduced to the Pole Map (Fig. 7.19)	Possible Shears	Pseudogravity map (Fig. 7.20)	Possible Shears
WNW	ENE (L.L.)	WNW	ENE (L.L.)
ENE	N-S (L.L.)	ENE	N-S (L.L.)
NNW	NNE (L.L.)	nearly N-S	NNE (L.L.)
NNE	WNW	NNW	WNW
N-S		nearly E-W	nearly E-W
nearly E-W			

Table 7.10

Regional Trends of the Aeromagnetic Maps of the Nile Delta

Low Pass Filter Map (Fig. 7.21)	Possible Shears	Upward Continuation Map (Fig. 7.22)	Possible Shears
WNW	WNW	WNW	WNW
ENE	ENE	ENE	ENE
NNE	NNE	NNE	NNE
NNW		NNW	
N-S		N-S	
nearly E-W			

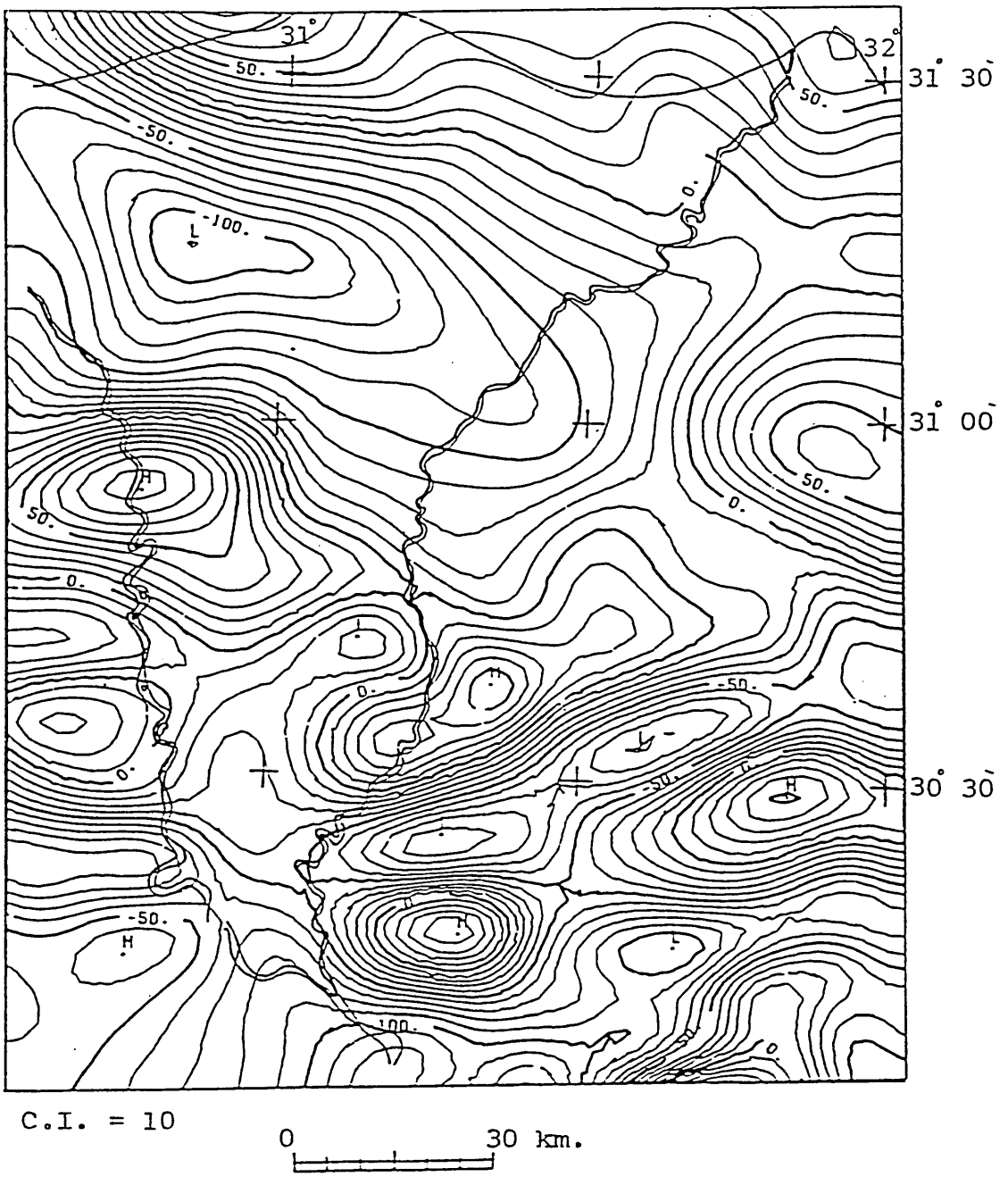


Fig. 7.19 Reduced to the pole aeromagnetic map of the Nile Delta.

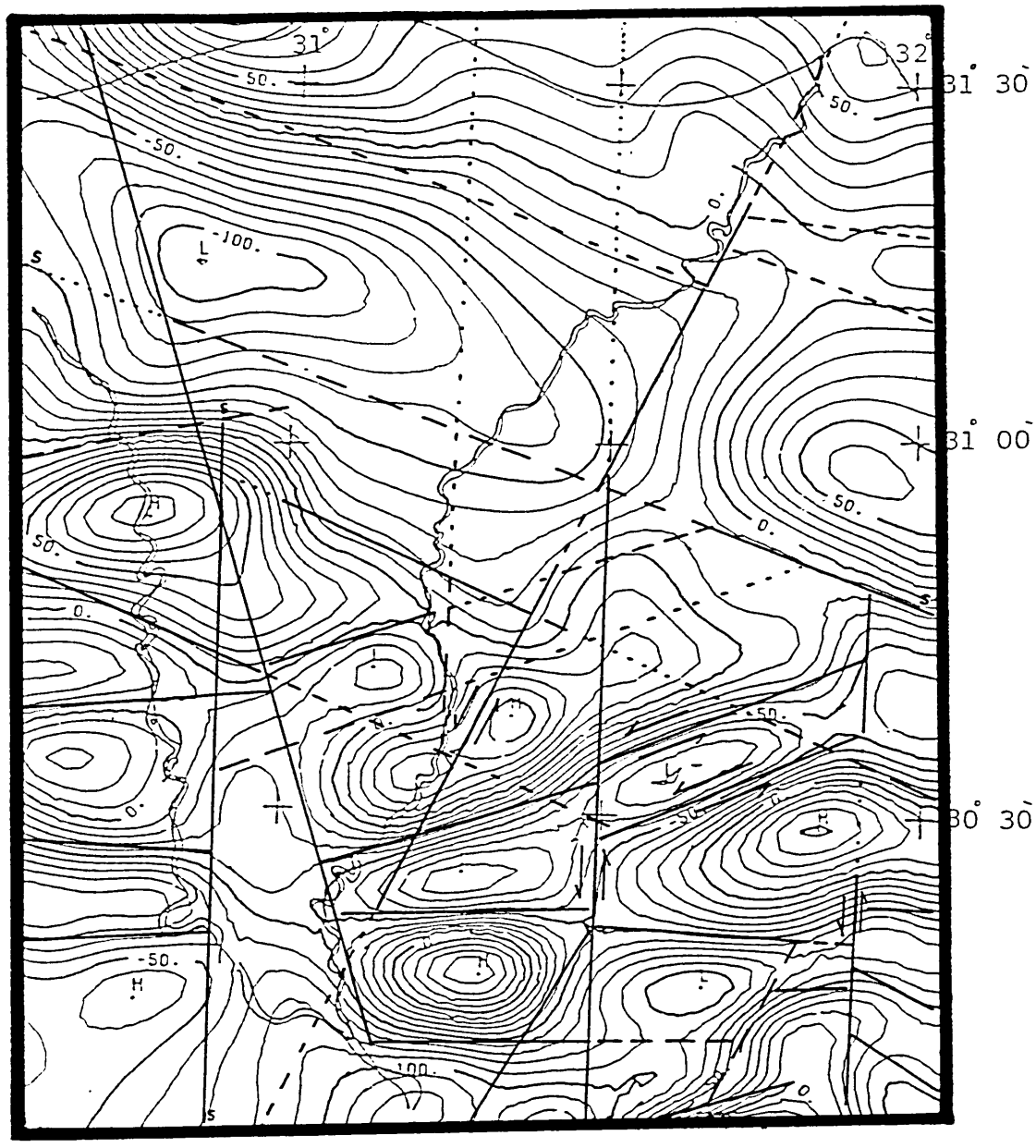


Fig. 7.19 Reduced to the pole aeromagnetic map of the Nile Delta.

OVERLAY TO FIG. 7.19

s —— —— s = possible shear

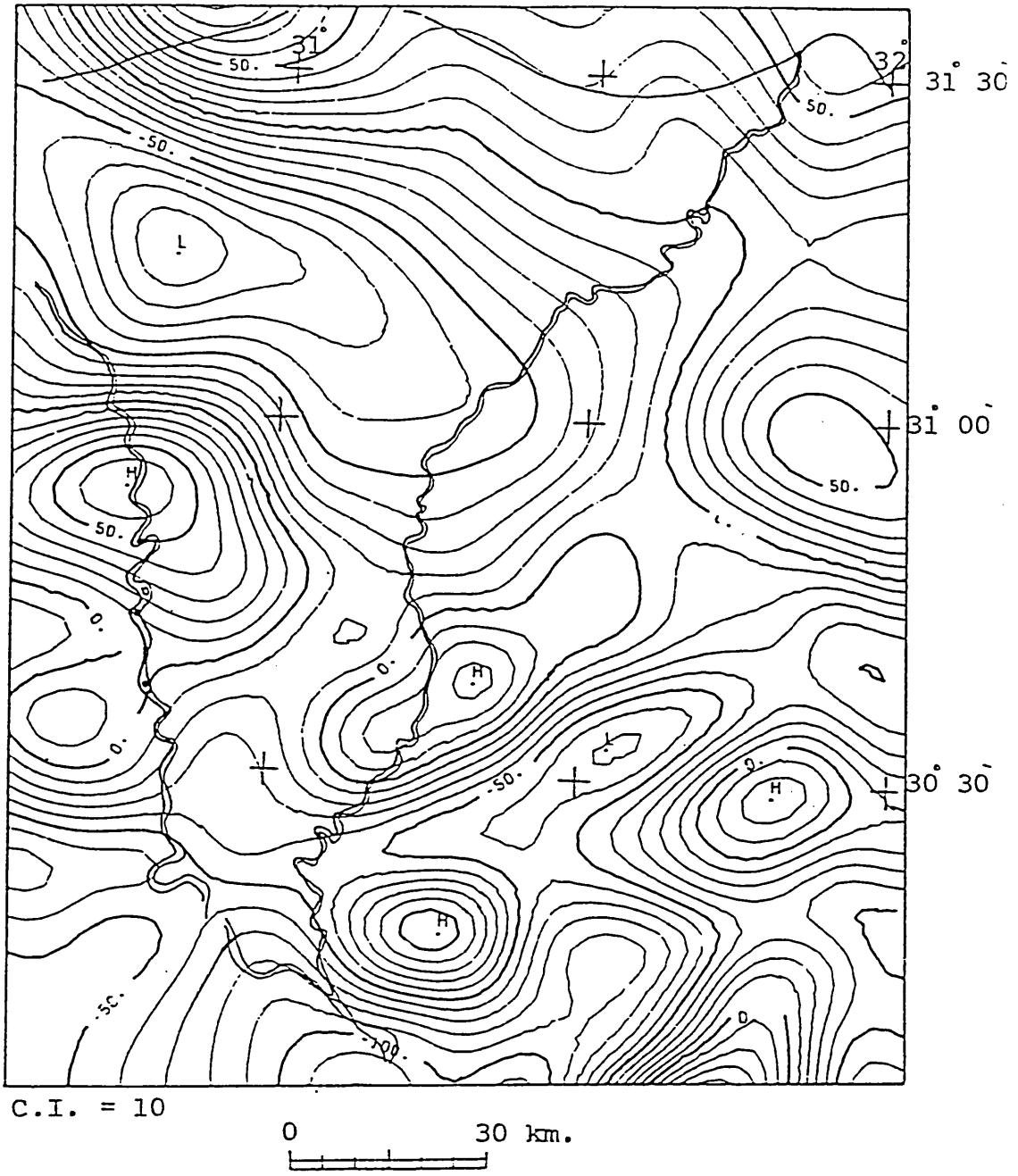


Fig. 7.20 Pseudogravity of the aeromagnetic map of the Nile Delta.

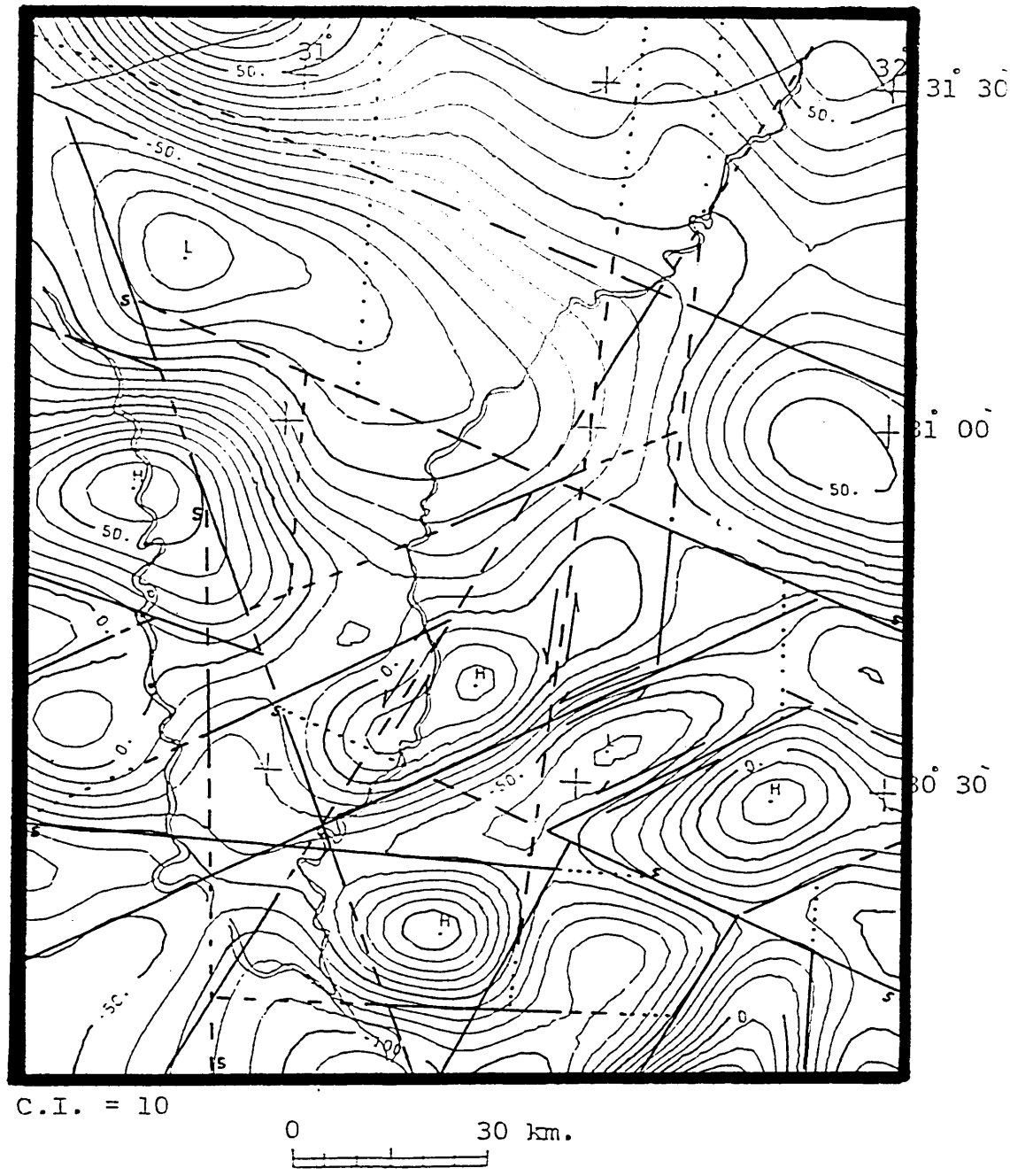


Fig. 7.20 Pseudogravity of the aeromagnetic map of the Nile Delta.

OVERLAY TO FIG 7.20

s —— — — s = possible shear

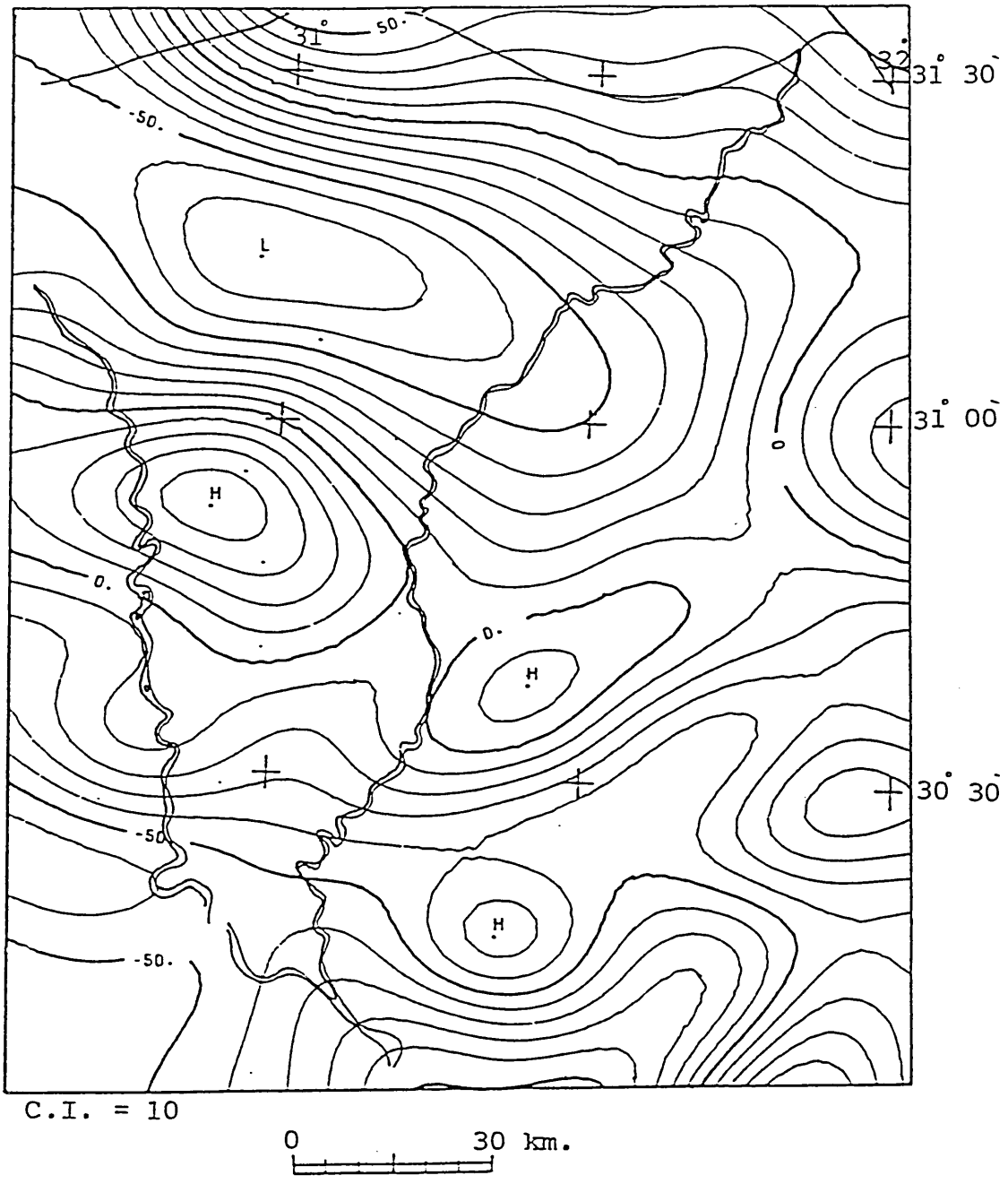


Fig. 7.21 Lowpass filtered aeromagnetic map of the Nile Delta.

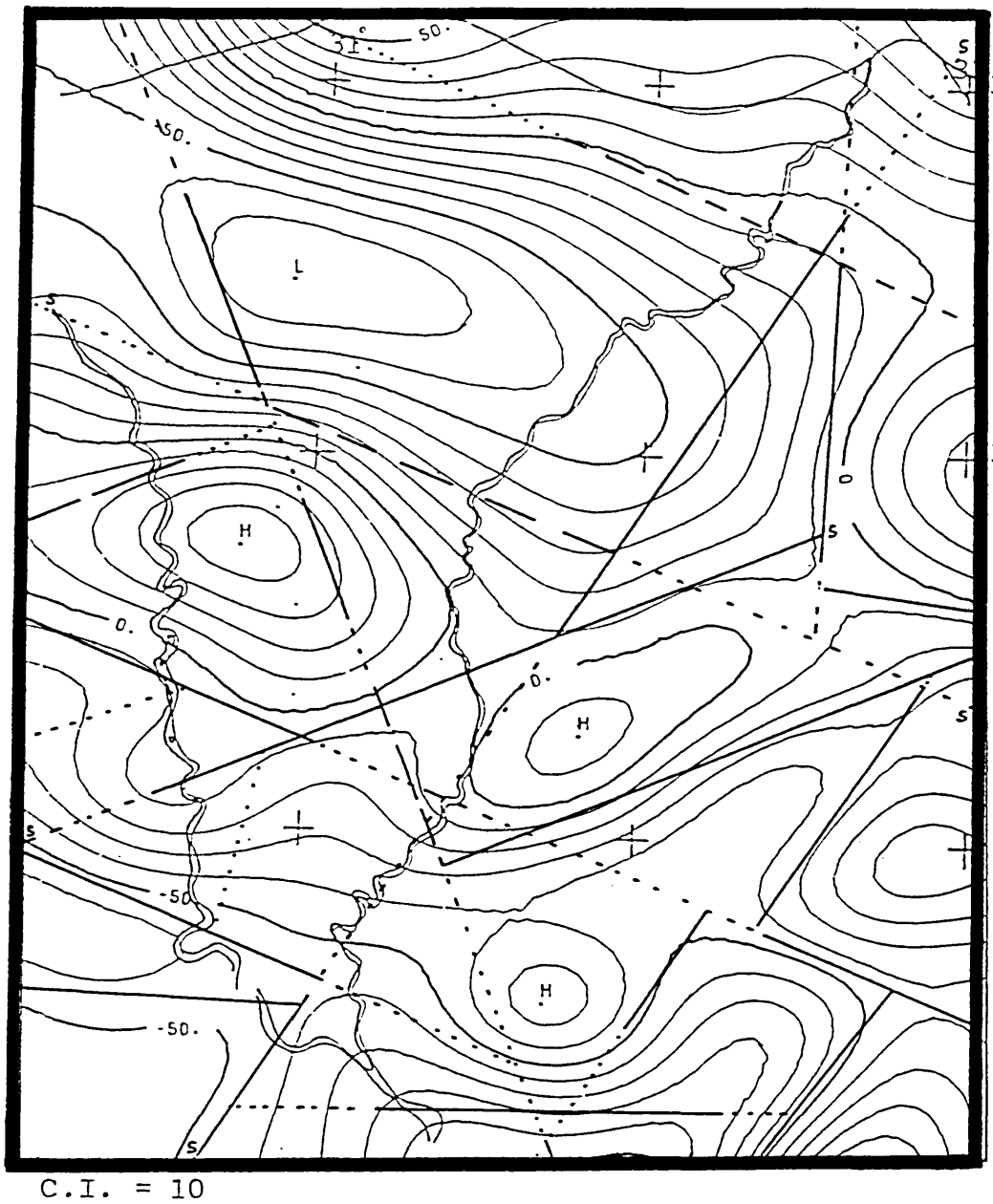


Fig. 7.21 Lowpass filtered aeromagnetic map of the Nile Delta.

OVERLAY TO FIG.7.21

s — — — — s = possible shear

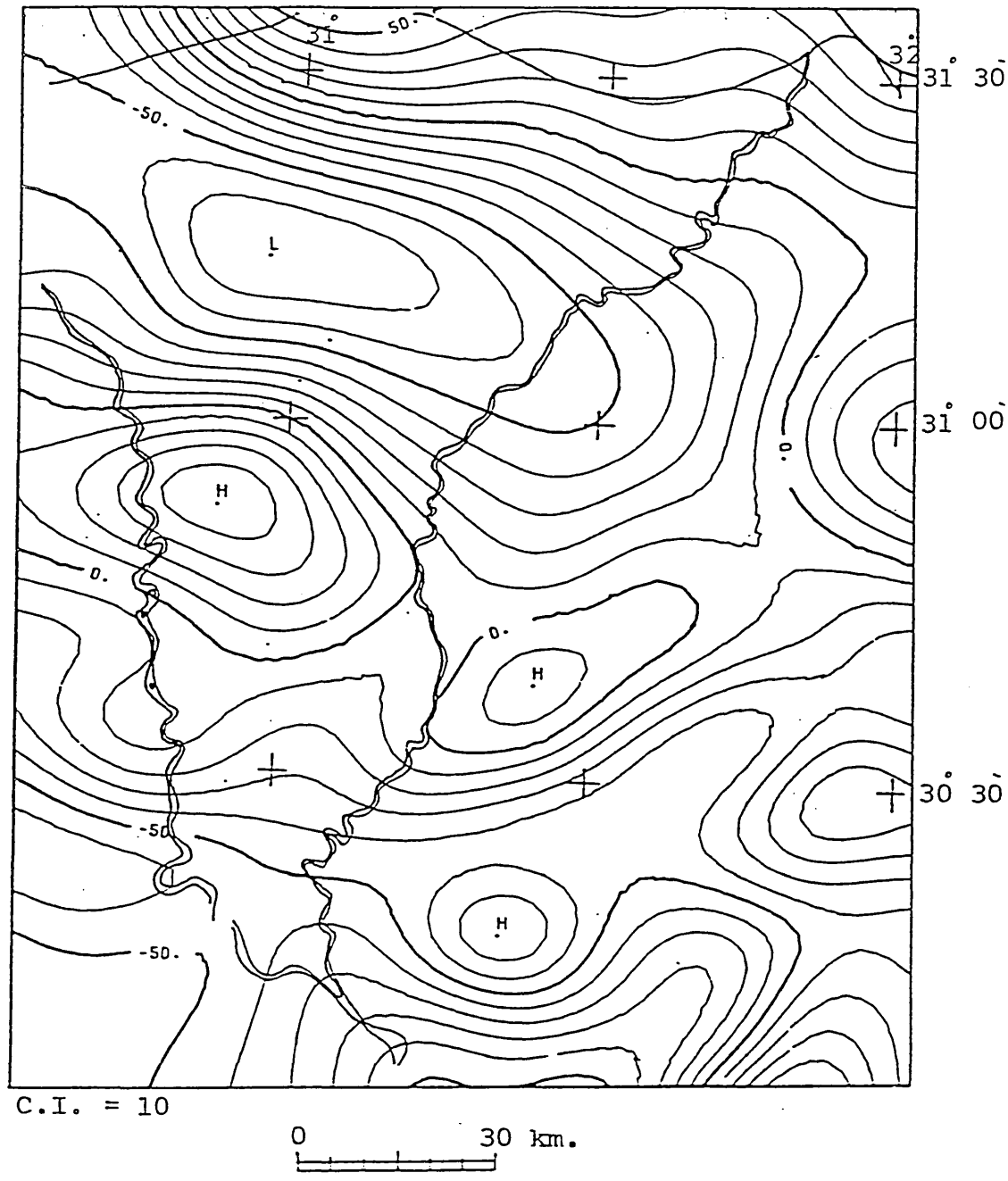


Fig. 7.22 Upward continuation of the Nile Delta aeromagnetic map.

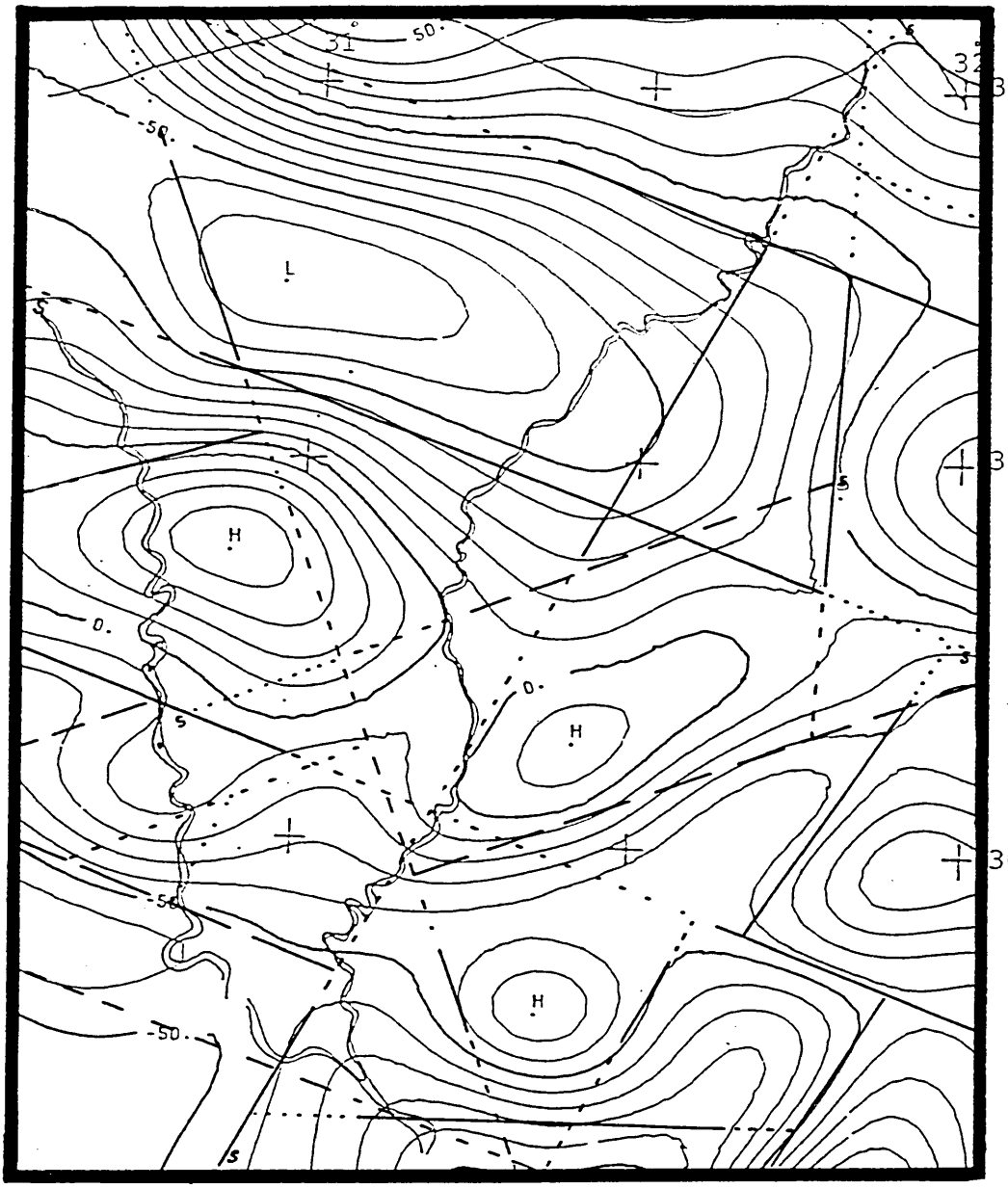


Fig. 7.22 Upward continuation of the Nile Delta aeromagnetic map.

OVERLAY TO FIG. 7.22

s— — — —s = possible shear

Table 7.11

Local Trends of the Aeromagnetic Maps of the Nile Delta

High Pass Filter Map (Fig. 7.23)	Possible Shears	Second Vertical Derivative Map (Fig. 7.24)	Possible Shears
ENE	ENE (L.L.)	ENE	ENE (L.L.)
nearly N-S	≈N-S (L.L.)	N-S	N-S (L.L.)
NNE	NNE (L.L.)	WNW	WNW (R.L.)
WNW	NW	NW	NW
nearly E-W		nearly E-W	NNE
NW		NNE	
NNW		NNW	

In conclusion:

1. The present study is very useful in locating some possible shears on both local and regional scales as indicated in Fig. 7.25 and the following Table:

Table 7.12

Possible Shears On Local and Regional Scales

Gravity		Magnetic (W.D.)		Magnetic (The Nile Delta)	
Regional	Local	Regional	Local	Regional	Local
N-S (L.L.)	N-S(L.L.)	N-S (L.L.)	N-S (L.L.)	WNW	NNE (L.L.)
NNE (L.L.)	ENE(L.L.)	NNE (L.L.)	ENE (L.L.)	ENE	N-S (L.L.)
WNW (R.L.)	WNW(R.L.)	WNW (R.L.)	NNE (L.L.)	NNE	WNW (R.L.)
ENE (L.L.)	E-W(R.L.)	NW (R.L.)	≈E-W(R.L.)		ENE (L.L.)
NW (R.L.)	NW (R.L.)	ENE	WNW (R.L.)		NW
	NNE(L.L.)		NW (R.L.)		

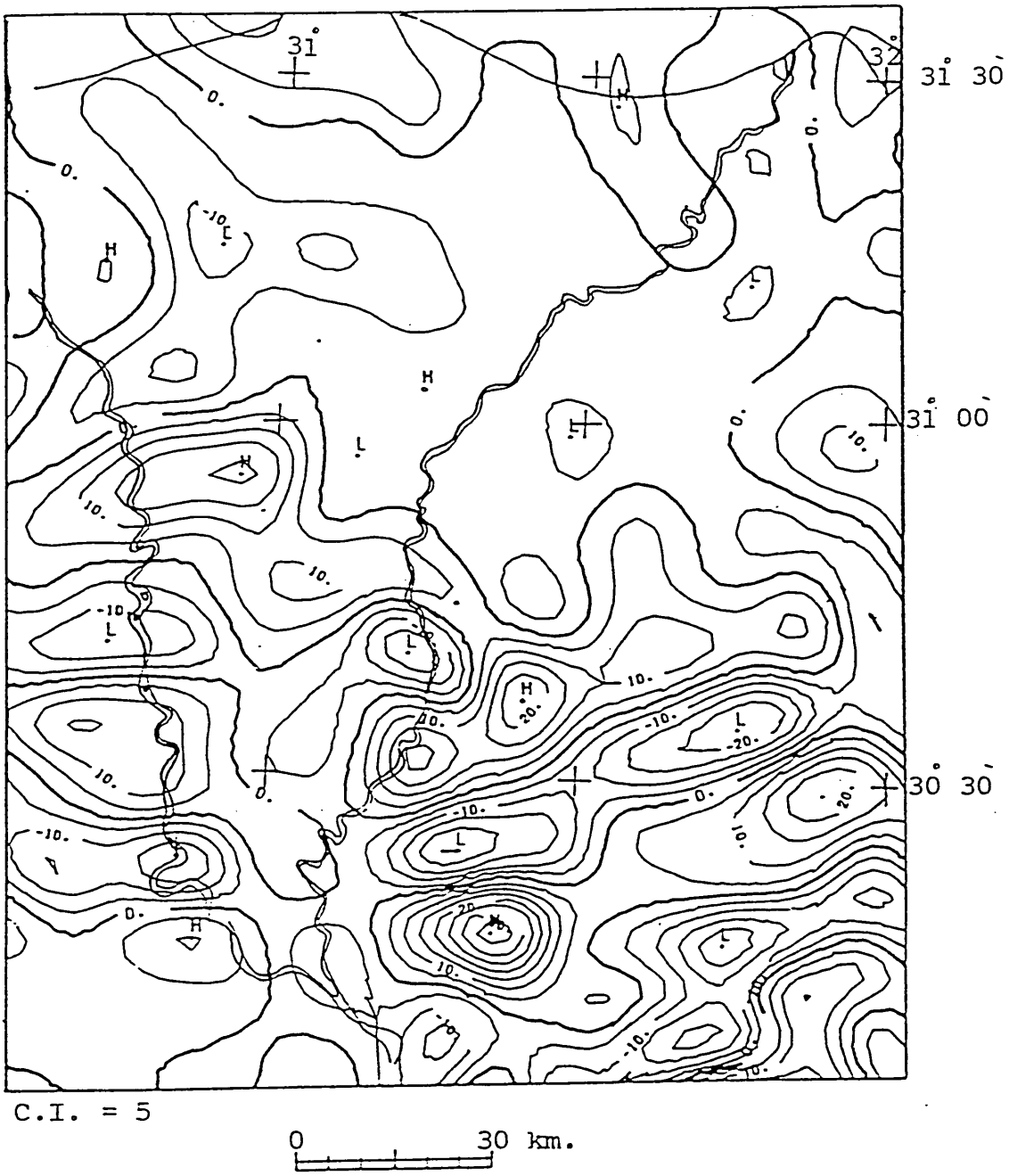


Fig. 7.23 Highpass filtered aeromagnetic map of the Nile Delta.

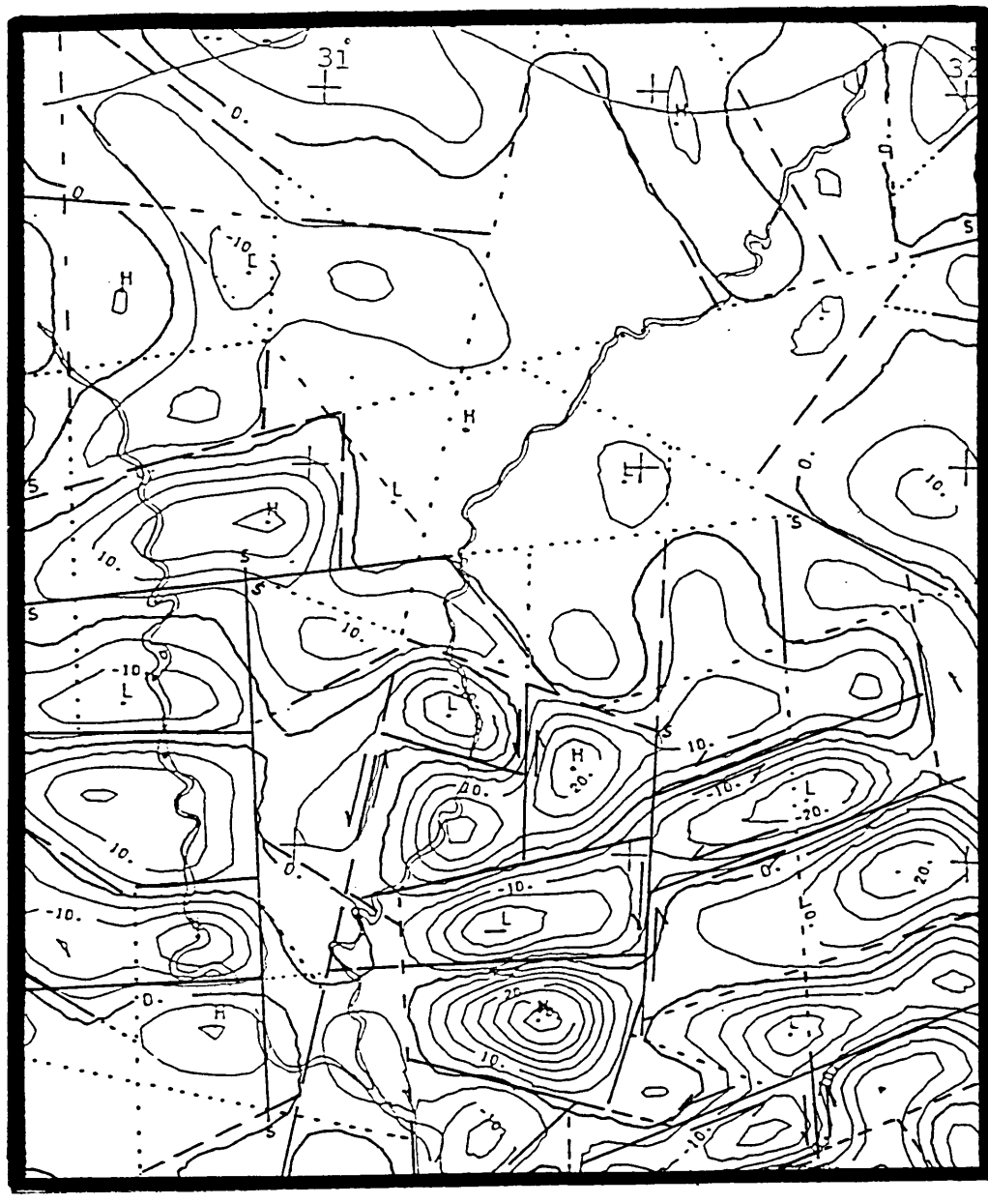


Fig. 7.23 Highpass filtered aeromagnetic map of the Nile Delta.

OVERLAY TO FIG. 7.23

s——— s = possible shear

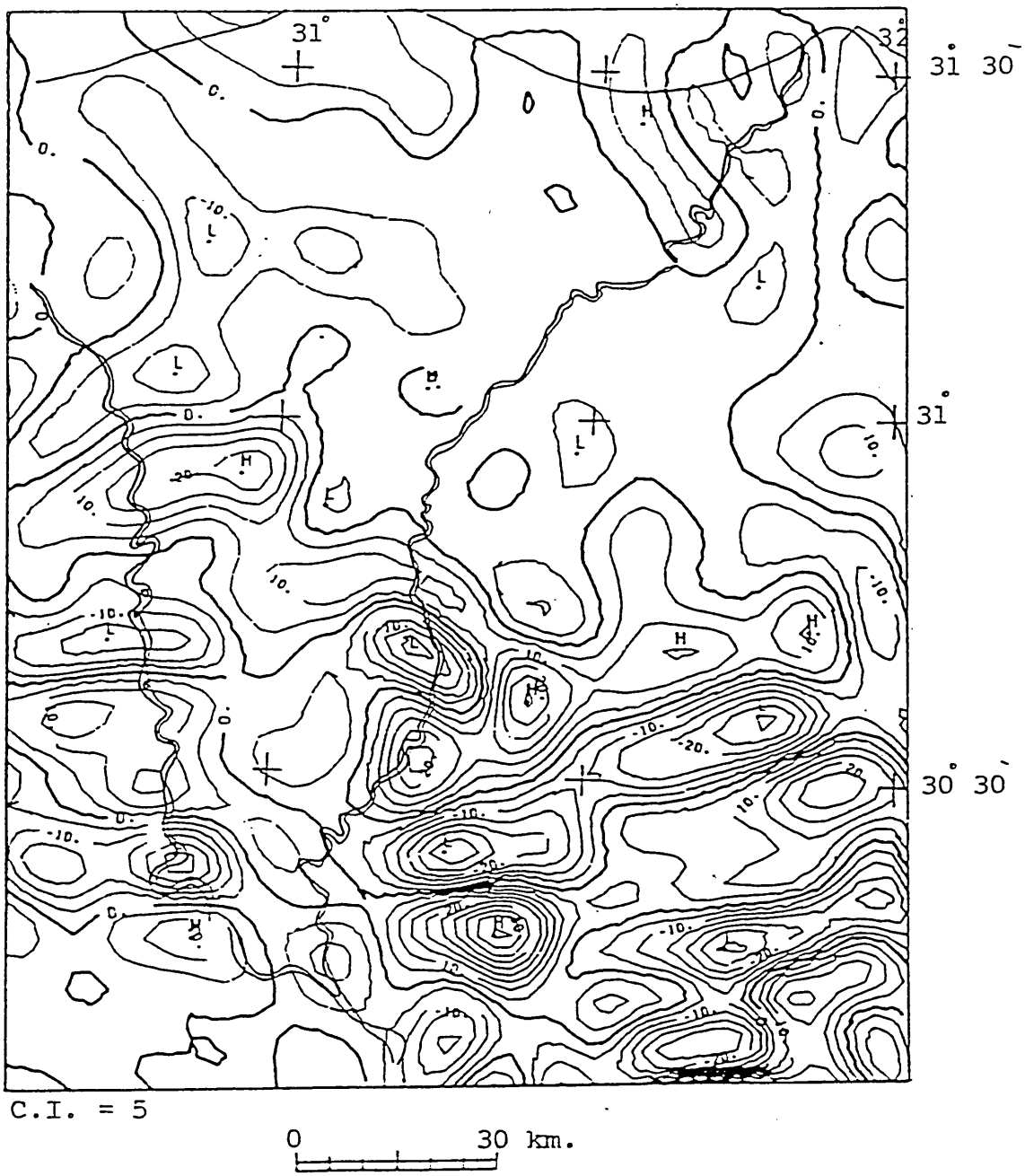


Fig. 7.24 Second vertical derivative of the aeromagnetic map of the Nile Delta.

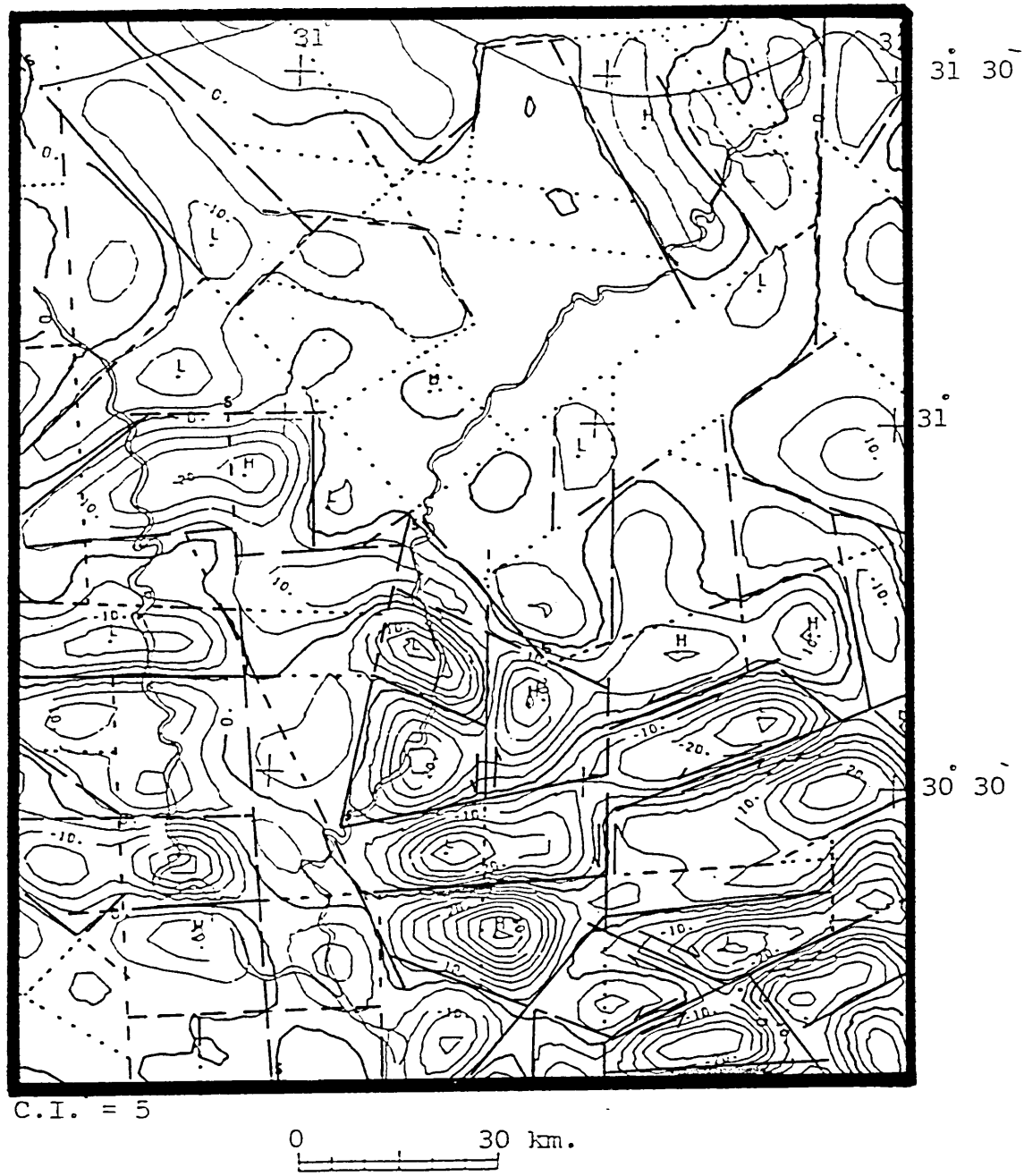
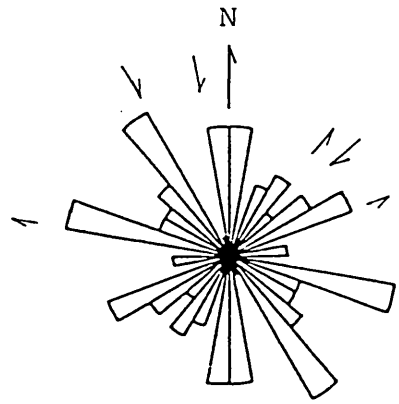


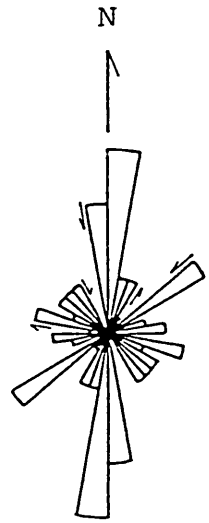
Fig. 7.24 Second vertical derivative of the aeromagnetic map of the Nile Delta.

OVERLAY TO FIG. 7.24

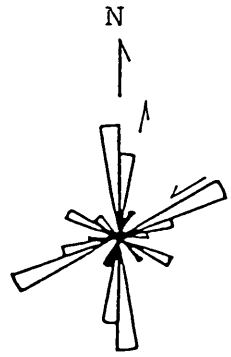
s — — — s = possible shear



A) Gravity maps



B) Aeromagnetic maps (W.D.)



C) Aeromagnetic maps (Nile Delta)

Fig. 7.25 Rose diagrams of possible geophysical regional and local shears.

2. Some shears, such as WNW, have the same sense of lateral movements as those detected from the field, aerial photographs and palaeotectonic studies.

3. It seems likely that movements along some shears, such as ENE and nearly N-S occurred or rejuvenated during Miocene time (where the basaltic sheet appears to be disclosed as a result of these shearing movements) as indicated in Figs. 7.23 and 7.24 (which show local trends) in comparison with Figs. 7.21 and 7.22 (which demonstrate regional trends).

4. On both the pseudogravity and gravity maps of the Nile Delta (Figs. 7.20 and 7.2, respectively), the shears have more or less the same trend and most probably the same sense of the horizontal lateral movements.

5. The possible shears on the unfiltered gravity and magnetic maps are relatively few with respect to the filtered ones.

CHAPTER EIGHT

SYNTHESIS

CHAPTER EIGHT

Synthesis

8.1 Introduction

The preceding chapters have documented a variety of results and conclusions which are concerned either with local or regional structures of the Northern Western Desert of Egypt. Here, an attempt is made to integrate those results in some maps which are amenable to further structural analysis in conjunction with the structures mapped by former authors. This analysis will attempt to assess the validity and significance of surface lineaments (especially the disconnected ones which may reflect old and deep structures whose identity are commonly concealed by younger deposits or later tectonics). In addition, an explanation of the development of ENE and WNW folds as well as the NNW undulations is given in light of the deduced tectonic stresses and a postulated pure shear mechanism. An attempt is also made to establish a block or lineament framework by which it is suggested, one can probably infer the relationship between deep seated structures, surface lineaments and other structures present in the studied area.

To establish a lineament framework, evidence of relative movements along these lineaments should be sought. Because of the nature of the study area and lack of any digital enhancement of the Landsat images, direct

evidence of such relative movements has not been found. Fortunately, however, the geophysical results fill this gap and provide evidence of such relative movements which permits one to define lineament or block framework. The significance of this block framework is examined in light of the mapped structures and laboratory model experiments carried out by Thomas (1974) and Ramos (1977).

8.2 Analysis of Lineament Shear Patterns

The objectives of this section are to determine the probable orientations of the maximum principal stresses which were obtained in the study area, as revealed from the relative lateral movement along some geophysical lineaments. The relationships of these stresses to the folds which occur in the study area are also considered. The directions of the geophysical shear-lineaments of known displacement are presented in Figures 8.1, 8.2 and 8.3. These geophysical shear-lineaments have been used to achieve the aims of this section, (See Chapter VII and Figs. 8.1 to 8.3).

From the sense of the relative lateral movements along these geophysical shear-lineaments, as indicated in Fig. 8.4, two main orientations of the maximum principal stresses have been deduced (see Fig. 8.4). These orientations are:

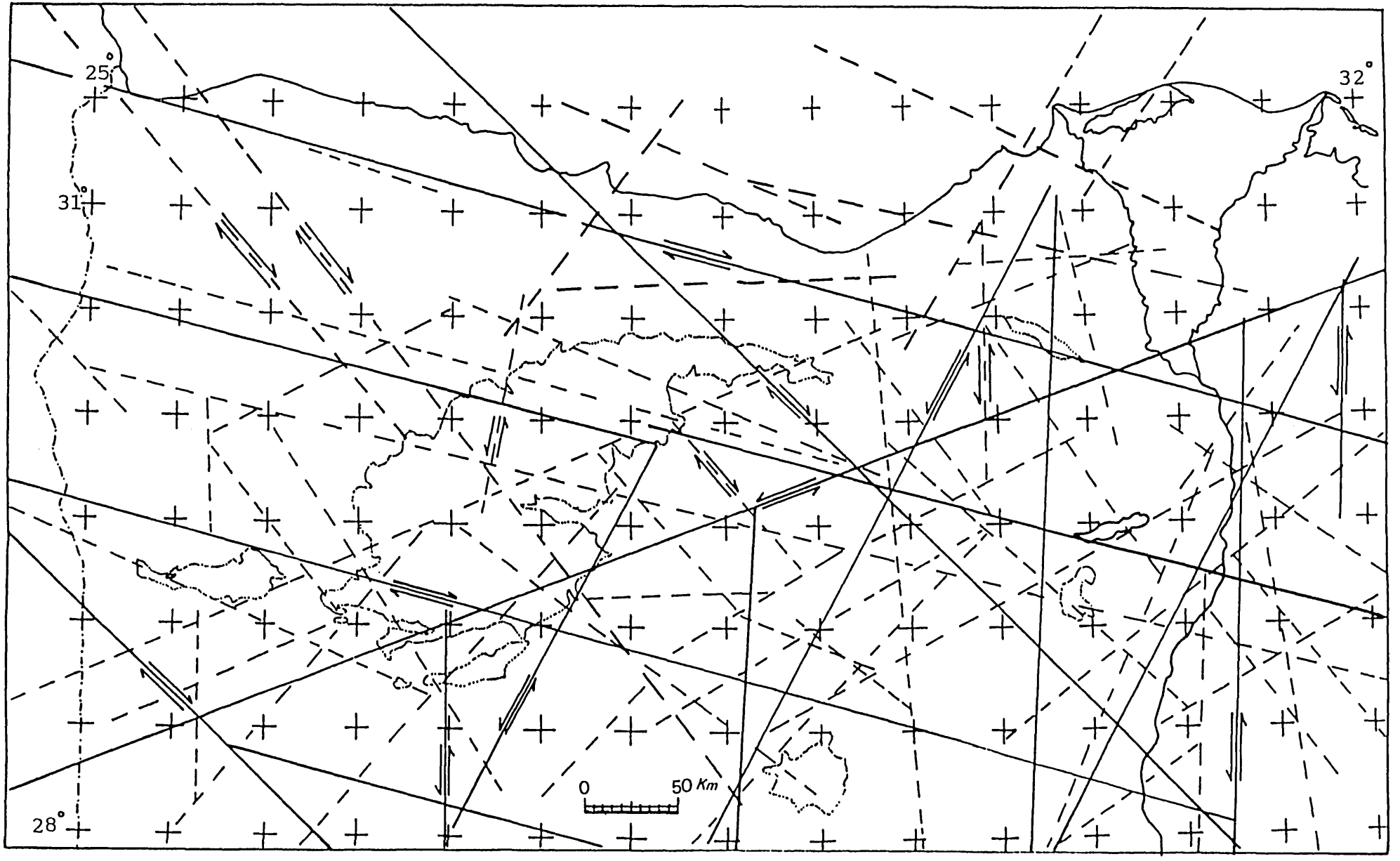


Fig. 8.1 Regional and local shears interpreted from the filtered gravity maps.

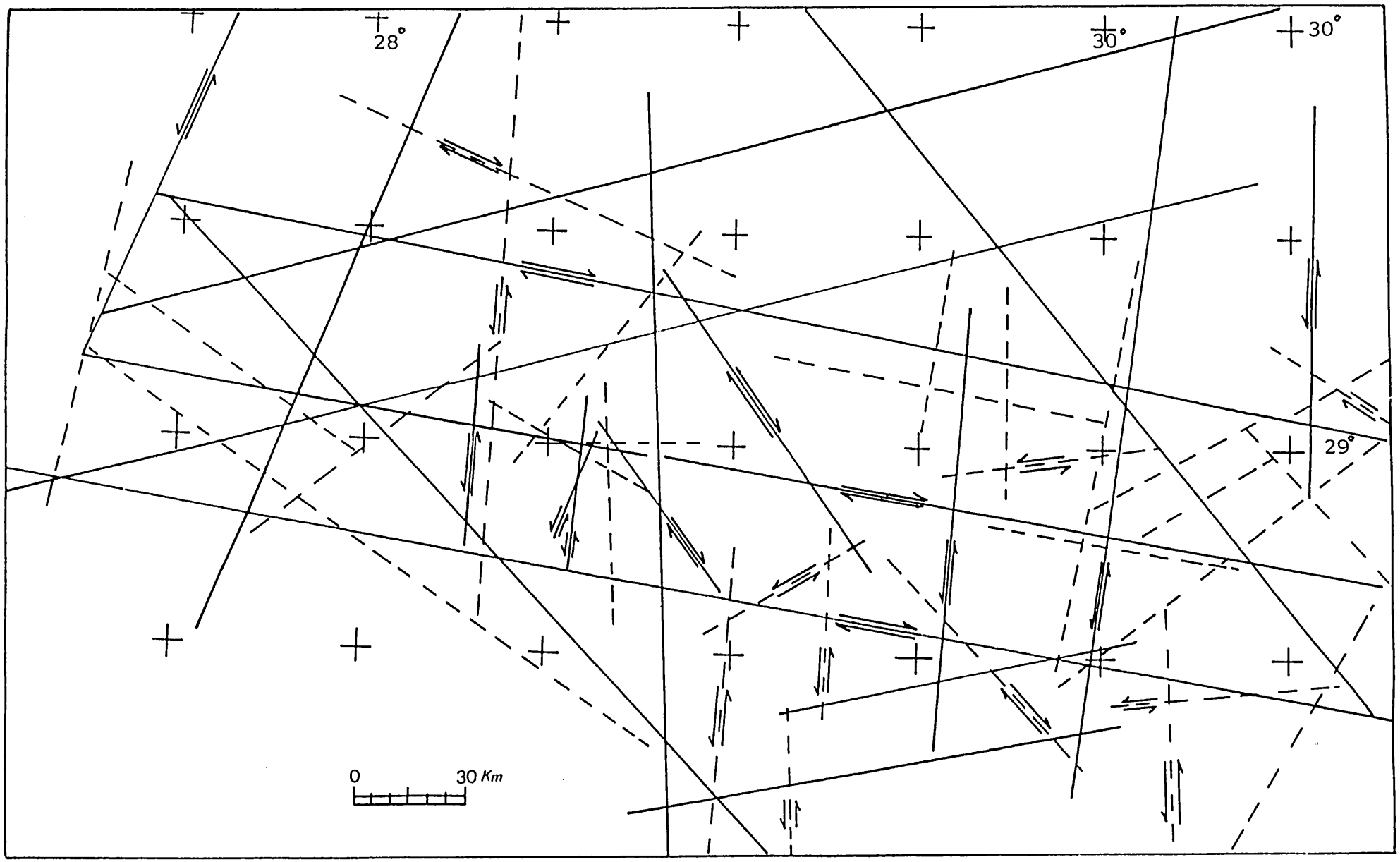


Fig. 8.2 Regional and local shears interpreted from the filtered aeromagnetic maps of the Western Desert.

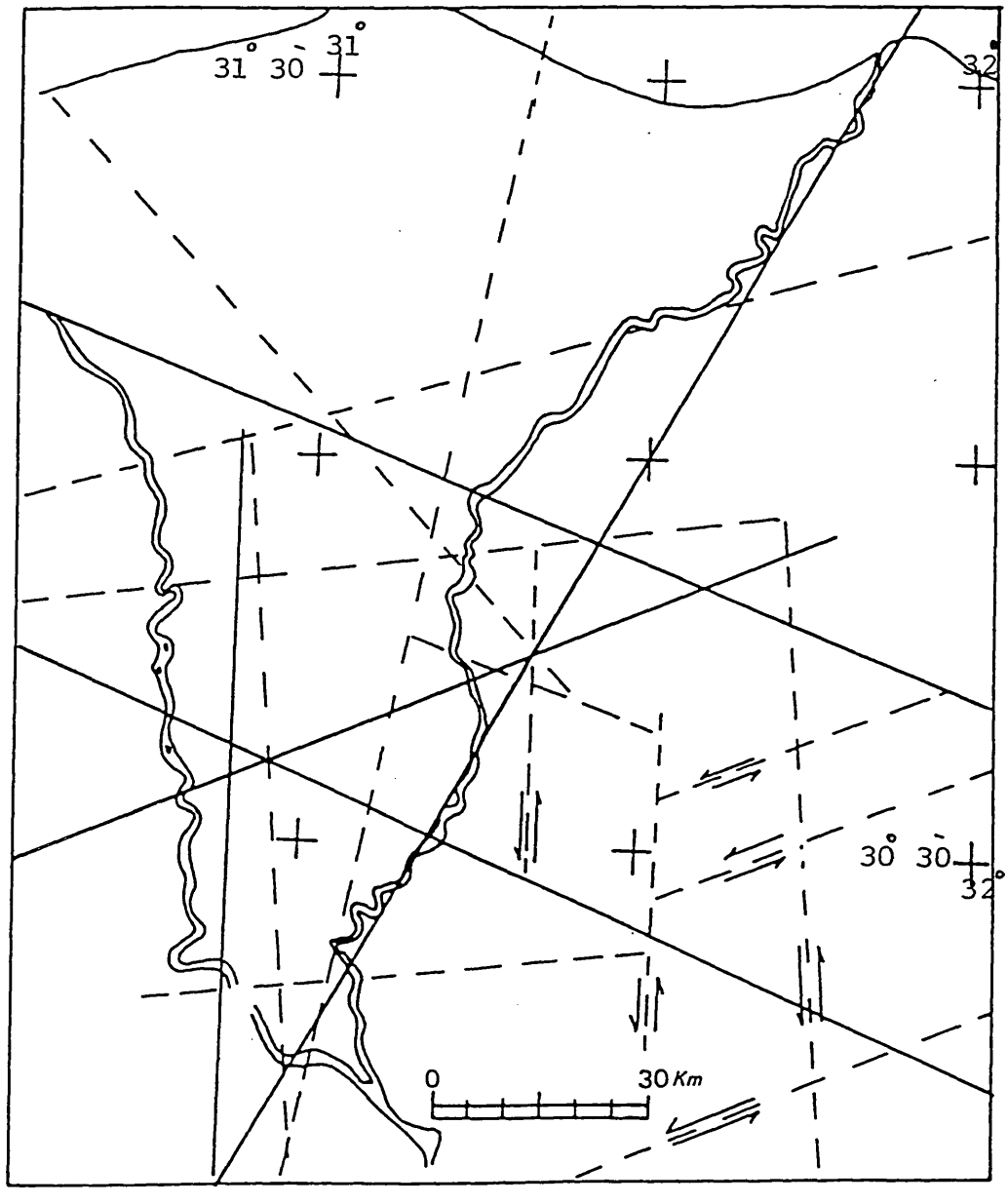
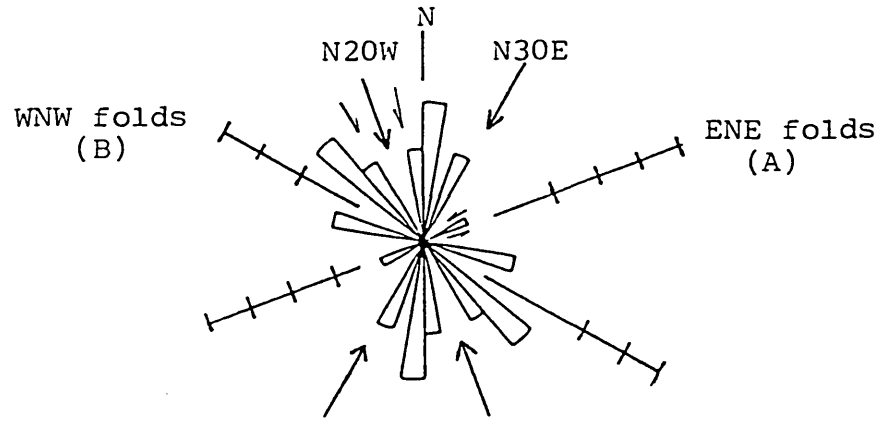
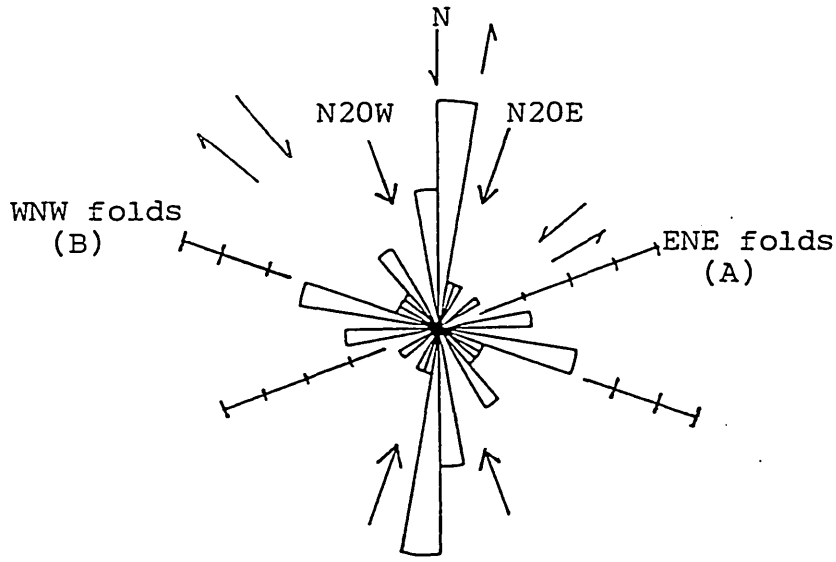


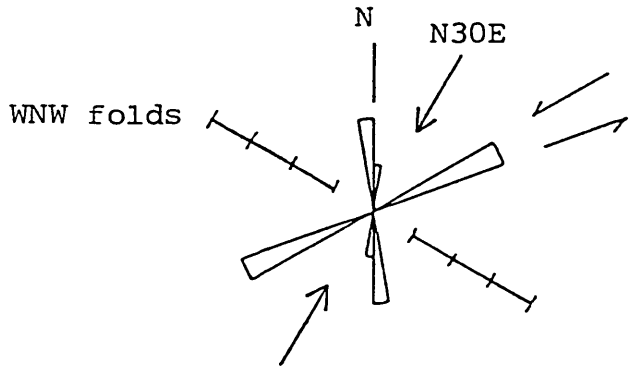
Fig. 8.3 Regional and local shears interpreted from the filtered aeromagnetic maps of the Nile Delta.



a) Gravity map shears



b) Aeromagnetic map (W.D.) shears



c) Aeromagnetic map (Nile Delta) shears

Fig. 8.4 Rose diagrams of interpreted geophysical shears and possible maximum compressions.

1. $N20^{\circ} - 30^{\circ}W$

The $N20^{\circ}$-$30^{\circ}W$ trend is the oldest tectonic stress which has been deduced during this study and has probably worked on the study area since the Palaeozoic up to or even later than the Oligocene (see Chapters V and VI and will also be discussed later in this chapter).

2. $N20^{\circ} - 30^{\circ}E$

This tectonic stress has been deduced on the basis of $N50^{\circ} - 70^{\circ}E$ sinistral lateral shears. Unfortunately, right lateral movements along the other complementary set of shears (nearly N - S) have not been detected. The lack of evidence for right lateral movements along the nearly N - S shears may be attributed to later reactivation of the $N20^{\circ} - 30^{\circ}W$ tectonic stress (as indicated in Figs. 7.19, 7.23 and 7.24). The basaltic sheet of Oligocene (or Oligocene - early Miocene) age is dislocated along $N60^{\circ} - 70^{\circ}E$ sinistral strike-slip faults (see Figs. 7.19, 7.23 and 7.24). Hence it can be inferred that the $N20^{\circ} - 30^{\circ}E$ tectonic stress was active during Miocene - early Pliocene.

Pure Shear Mechanism and Development of ENE and WNW Folds

It is evident (Fig. 8.4) that the $N20^{\circ} - 30^{\circ}W$ compression of the maximum tectonic stress suits the development of the $N60^{\circ} - 70^{\circ}E$ (ENE) folds and that the $N20^{\circ} - 30^{\circ}E$ compression gave rise to $N60^{\circ} - 70^{\circ}W$ (WNW) trending folds. The age relationships of the stress systems already noted is further approved by the fact

that the N60° - 70°E (ENE) or Syrian Arc System of folds was established during the upper Cretaceous while the N60° - 70°W (WNW) folds were developed during Miocene - early Pliocene.

At the Northern Western Desert of Egypt, a structural feature occurs which has been described as a series of NNW undulations, which decreases in magnitude towards the west (Shata, 1953), while on both sides of the Gulf of Suez, Shukri (1954) described this structural feature as anticlinal and synclinal structure of clysmic (NNW) trend, (see Fig. 2.30). An explanation regarding the development of this structural feature is given below.

Mechanisms of the N20° - 30°W (NNW) folds or undulations

The NNW undulations have been attributed to an anticlinal bulge, occurring at the close of Eocene, which decreases in intensity westwards (Shata, 1953), while Shukri (1954) referred these structural features to rifting.

In the Cairo-Suez district, the clysmic faulting is considered of late Oligocene (Blankenhorn, 1921; Shukri, 1953 and Shukri and Akmal, 1953), quoted by Shukri (1954).

The present writer suggests that the possible mechanism controlling the development of these undulations is:

a. Block faulting along old N20° - 30°W (NNW) faults (see Fig. 2.22) as well as regional stresses developed as a result of displacement of the basement

blocks (Fig. 8.5). The relative vertical movements of these blocks decrease towards the west but their width increases westwards (see Figs. 2.22 and 8.5). In the Northern Western Desert of Egypt (where the sedimentary section is relatively thick), N20° - 30°W (NNW) undulations were established as a result of the block faulting and regional stresses, while on both sides of the Gulf of Suez (where the sedimentary section is relatively thin or there is no sedimentary section) N20° - 30°W (NNW) fault blocks were developed.

The outcomes of this mechanism are in agreement with what have been noted in the field by Shata (1953) and Shukri (1954). Also, the regional stresses which were associated with the block faulting most probably caused minor thrusts, (as indicated in Chapter III, Page 101), and the cross warping of the Gaa-Abu Rawash village pericline, (see Plate 3.2 and Fig. 8.6).

8.3 Block or Lineament Framework

It seems likely from the palaeotectonic study that some lineaments have stratigraphical and structural control. Thus, if one considers this control is the result of weakness zones in the basement, as indicated in the previous two chapters, this means that the paleotopographic conditions were the result of paleostructures generated along the weakness zones and within blocks by tectonic reactivation. So, it is thought apposite to define the block framework, in an attempt to establish its structural and in turn its

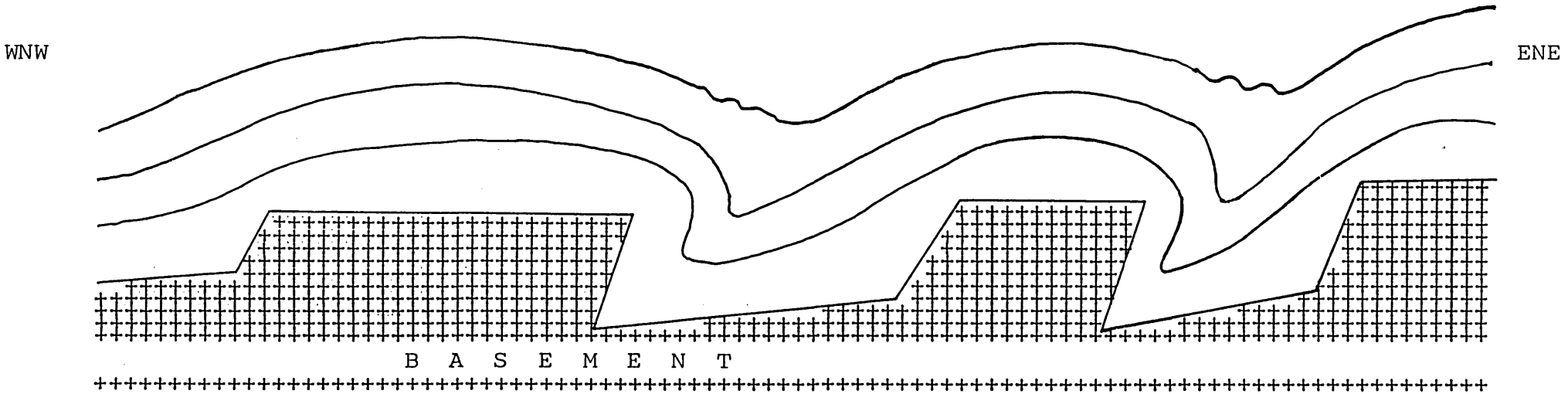


Fig. 8.5 Diagrammatic cross section showing possible development of NNW undulations.

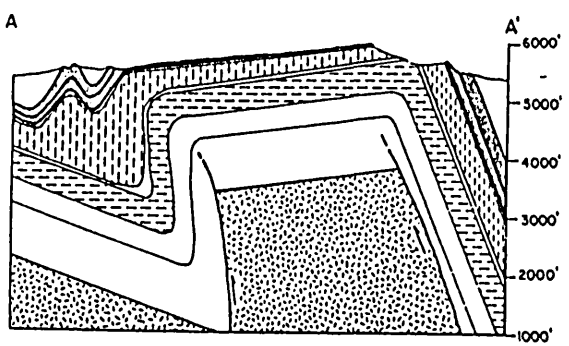


Fig. 8.6 Cross section showing development of undulations as a result of basement block faulting.
(After Matthews and Work, 1978)

stratigraphical significance. Here, the block framework has been defined according to geophysical results obtained during this study, (see Chapter VII) (where the sense of the relative movements along ENE and WNW have been recognized). These two trends are present on the structure contour map of top Cenomanian (Fig. 8.7) (which is based on both seismic and well control), as well as on Fig. 2.33.

Structural Significance of the Block Framework

The structural significance of block framework has been discussed by Thomas (1974) and Ramos (1977), where mapped structures (at different areas) have been related to theoretical and experimental fold and fault results which have been obtained by them and other authors, such as Wilcox et al (1973), Harding (1974) and Koide and Bhattacharji (1977), as a result of simple shear mechanism (Fig. 8.8, b and c).

According to Thomas (1974), if the basement is segmented by many zones of weakness, the orogenic forces would constantly be deflected by the weakness zones. Lateral adjustments on basement weakness zones produce coupling in the blocks defined by these zones. The relative sense of the simple shear adjustment is controlled by the direction of horizontal stresses relative to the trend of weakness zones (Fig. 8.9). The structural results of this mechanism are similar to those produced by pure shear mechanism except for the following:

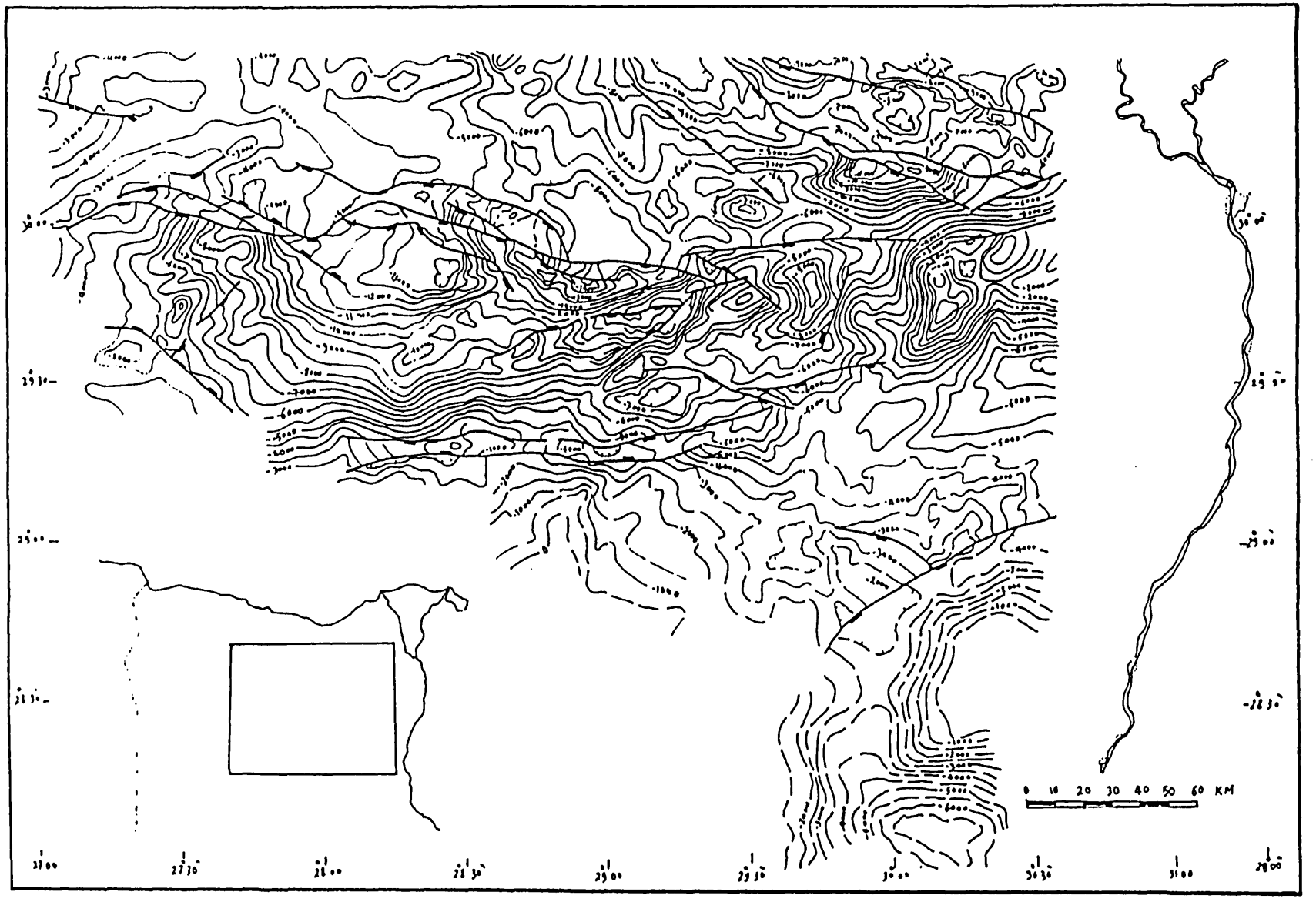


Fig. 8.7 Structure contour map (Top Cenomanian). After Aadland and Hassan (1972)

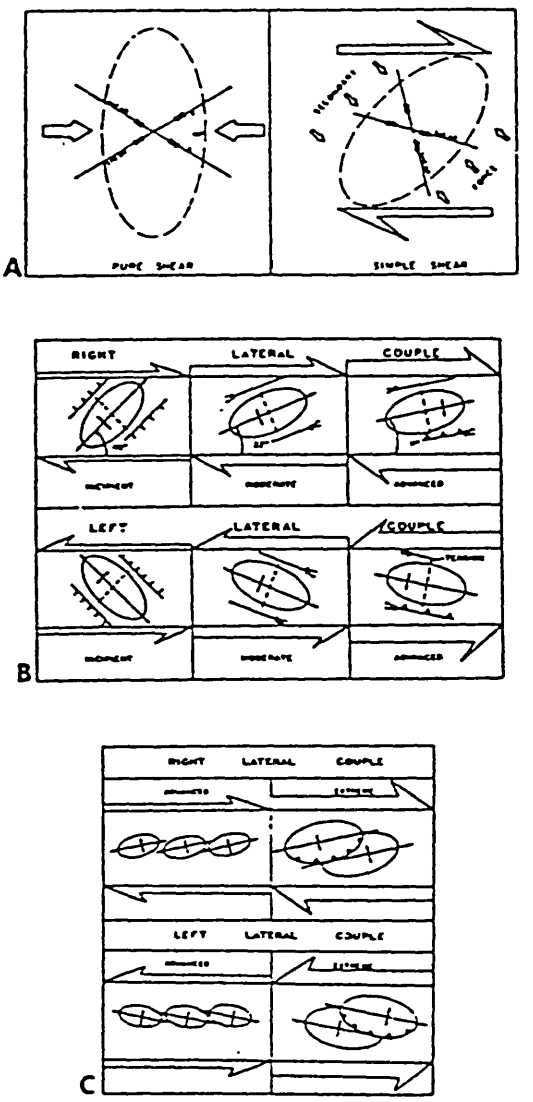


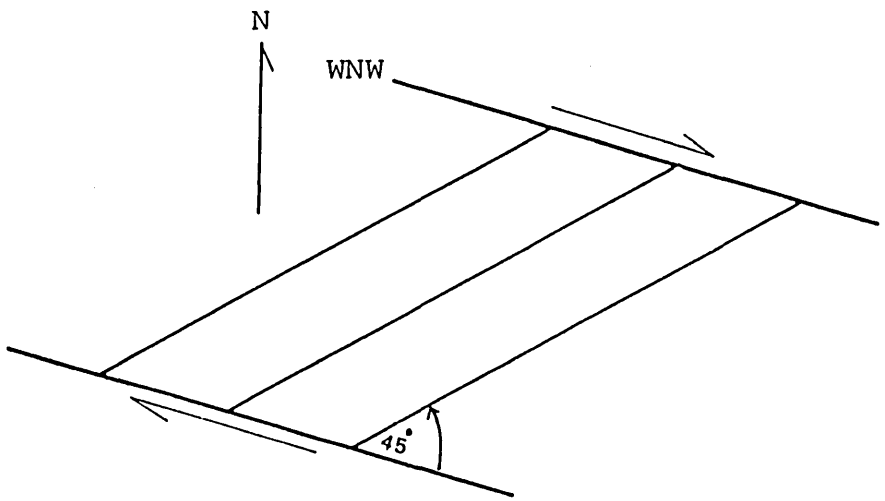
Fig. 8.8 —Comparison between pure-shear and simple-shear mechanics (A). Various phases of simple shear mechanics (B, C).

A. Pure shear characterized by inline compression; simple shear by differential horizontal movement.

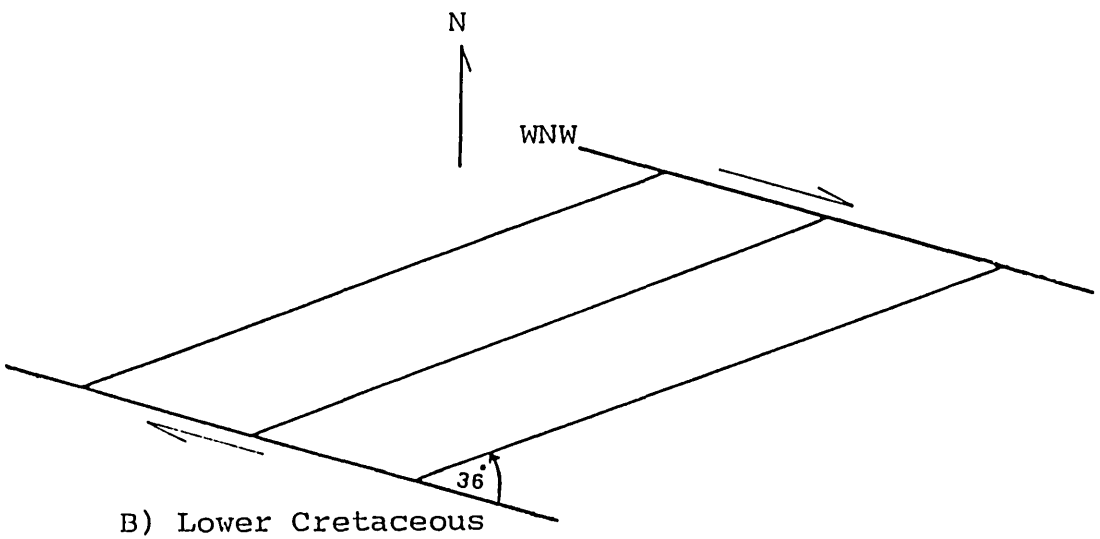
B. Lineament simple shear produces block coupling which results in drag-fold uplifts with associated flank faults and crossfold tension. Phases of coupling classified as to degree of drag-fold rotation.

C. En echelon drag folds, characteristic of advanced phase, overthrust one another in extreme phase.

(After Thomas, 1974)

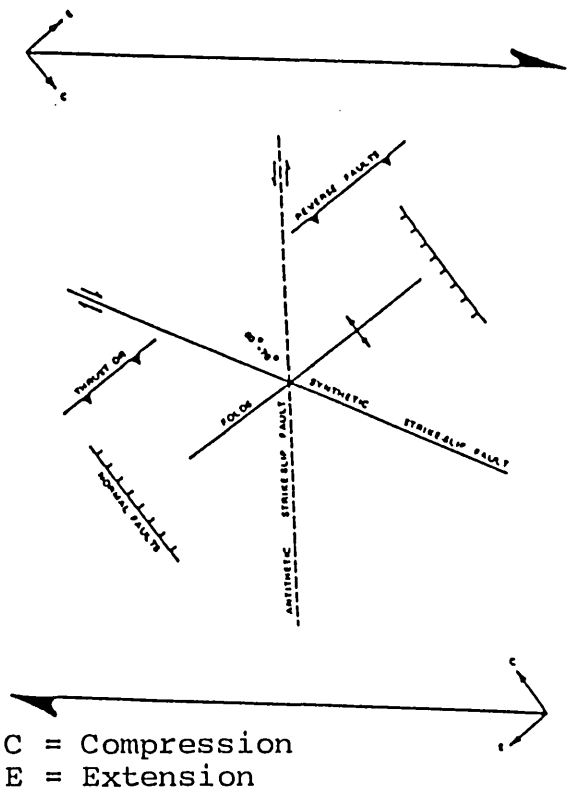


A) Palaeozoic - Jurassic



B) Lower Cretaceous

Fig. 8.10 Geometrical relationship between subsurface WNW Shears and Palaeozoic-lower Cretaceous basins and uplifts.



C = Compression
E = Extension

Fig. 8.9 Forces and composite of structures that can result from wrenching deformation. (After Harding,1974).

1. Block coupling produces en echelon arrangement of drag folds either within the block or along the bounding simple-shear zones.

2. At later stages the folds, which developed along the bounding simple-shear zones, may become shattered. As movement of crustal blocks continues over long priods of the geologic time, the half folds on one block can be offset or removed completely from the area.

3. As simple-shear (along the block weakness zones) increases, drag folds and associated faults tend to rotate in the direction of the shear couple (Fig. 8.8b). This rotation can cause subsequent weakness zones, such as flank faults and normal faults, to become shear zones and even high angle reverse faults in the later phases of orogeny.

According to the acute angle of drag folds with the weakness zones, which reflects the intensity of simple-shear, the stages of simple shear were classified (Thomas, 1974) into:

a. initial (incipient);

b. moderate; and

c. advanced

as indicated in Fig. 8.8b.

4. Rotation of the drag folds clockwise, right lateral, or counterclockwise, left lateral, can cause one fold to override the next (Fig. 8.8c).

The previously mentioned points are concerned with areas of rigid basement with sedimentary cover (see Ramos, 1977). But, in areas of rigid basement with or

without a thin sedimentary cover, a set of blocks are formed with flank faults of uplifted areas which make a different angle, such as the drag folds (see Fig. 8.8b), with the main lineament according to the intensity of the couple (see Ramos, 1977). At the moderate stage, lateral adjustment occurs at previously formed flank faults. But at the advanced stage, these flank faults become upthrusts.

Let us now review the structural development of the study area in light of the block framework.

A. During Palaeozoic to pre-Cenomanian

It has been shown in Chapter VI that the main structural element of the Palaeozoic to pre-Cenomanian sedimentary section (predominantly clastic with interfingering calcareous sediments [Said, 1962]) is block faulting.

As regards the development of the (Palaeozoic - pre-Cenomanian) basins and uplifts, the author follows Ramos (1977). During this period, faulting is dominant, as shown in Chapter VI. Accordingly, the subsurface lineaments or criteria, which border the basins and uplifts, are related to a block framework where faulting is dominant (rigid basement with or without thin cover), (Ramos, 1977).

Because of the scale problem of the different maps, it is convenient to express the relationship between the block framework and subsurface lineaments or criteria, which bound the basins and/or uplifts of the

Carboniferous, Jurassic and lower Cretaceous isopach maps (see Figs. 5.16, 6.22 and 6.24) as angles (Fig. 8.10), as follows:

1. The WNW dextral strike-slip geophysical lineaments, which defines the block framework, trend $N75^{o}W$.

2. The Carboniferous and Jurassic subsurface criteria or lineaments (Figs. 5.16 and 6.22), which limit the basins and/or uplifts trend $N60^{o}E$.

3. The lower Cretaceous subsurface criteria or lineaments (Fig. 6.24), which border the basins and uplifts trend $N70^{o}E$.

According to Ramos' model (1977), the lineaments which limit the basins and/or uplifts during Carboniferous up to lower Cretaceous possibly developed as a result of $N75^{o}W$ dextral couple (see Fig. 8.9).

From the geometrical relationship, one can see that the angles between the lineaments, which border the basins and/or uplifts, and the $N75^{o}W$ dextral strike-slip shears is 45° degrees (during the Palaeozoic - Jurassic period). While the same angle becomes 36° degrees during lower Cretaceous, (Fig. 8.10). This decrease in the angle during lower Cretaceous means that the intensity of the $N75^{o}W$ (WNW) couple became more effective during lower Cretaceous, (see Thomas, 1974; Ramos, 1977 and Fig. 8.8b).

B. During upper Cretaceous

A comparison of the Syrian Arc System of folds of the upper Cretaceous with the block framework as defined by geophysical lineaments of the area (Figs. 8.9, 8.10 and 8.11, for aeromagnetic maps and gravity map, respectively), permits one to suggest that the block framework has structural significance. It seems likely from this comparison that simple-shear coupling mechanism could be considered as another possible mechanism responsible for producing the Syrian Arc System of folds in the Northern Western Desert of Egypt. This means that the movements along the dextral N75° - 80°W (WNW) were reactivated during the upper Cretaceous, where the sedimentary section becomes relatively thick with limestones as control beds, and the intensity of the couple, as indicated by the intersection angles of folds with the WNW lineaments (Figs. 8.11, 8.12 and 8.13), was moderate.

Criteria which are in favour of this mechanism are:

a. the alignment of the Syrian Arc System of folds which show en echelon arrangement;

b. the missed and/or eroded parts of fold structures in the Abu Rawash area (see Figs. 4.8 and 4.9).

c. The WNW (N73°W) and nearly N50°W dextral strike-slip faults which have been detected during the course of this study, at Abu Rawash area (see Fig. 4.8).

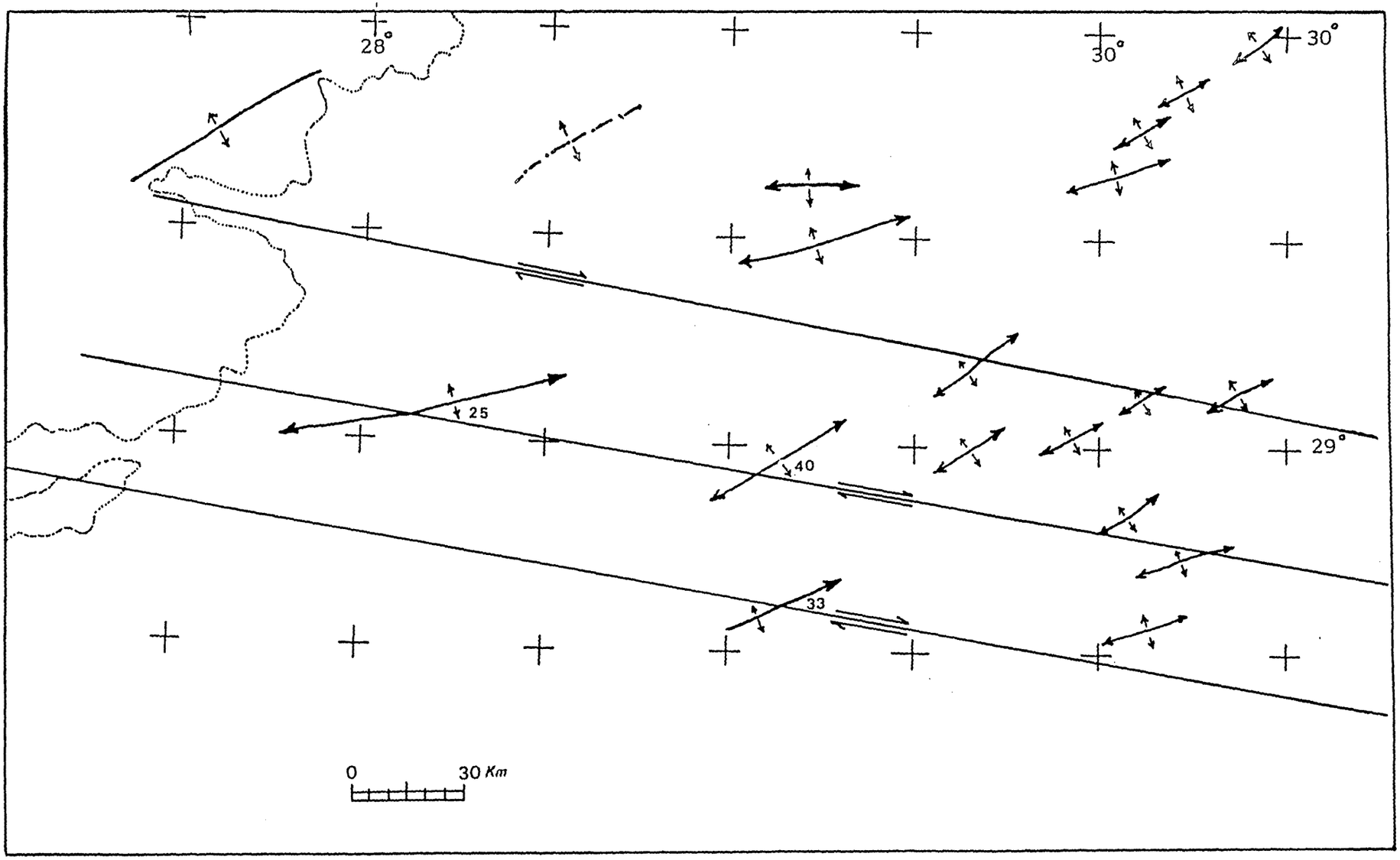


Fig. 8.11 Compiled map of WNW aeromagnetic shears and ENE fold structures (Western Desert).

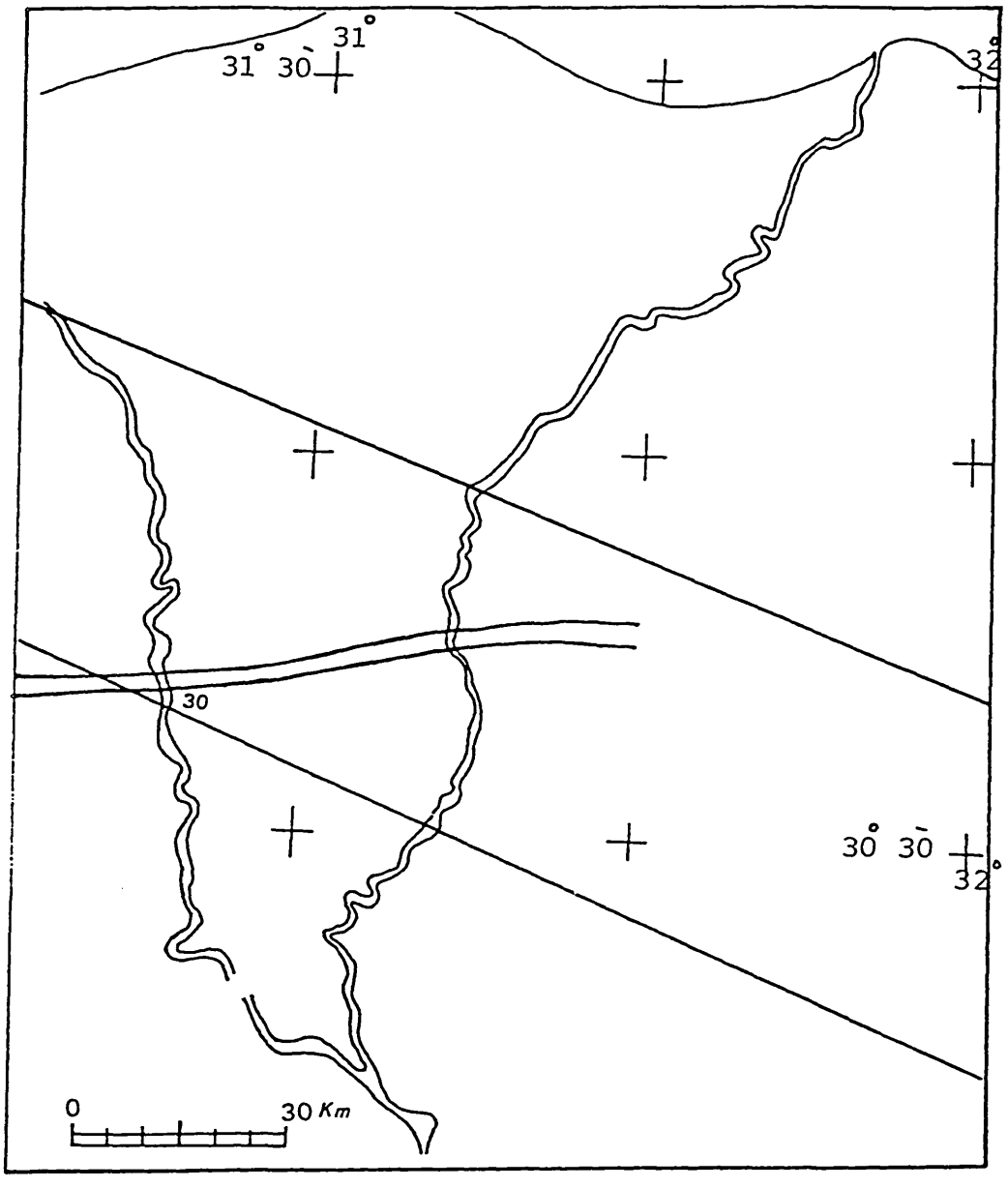


Fig. 8.12 Compiled map of WNW aeromagnetic shears and ENE fold structure (the Nile Delta).

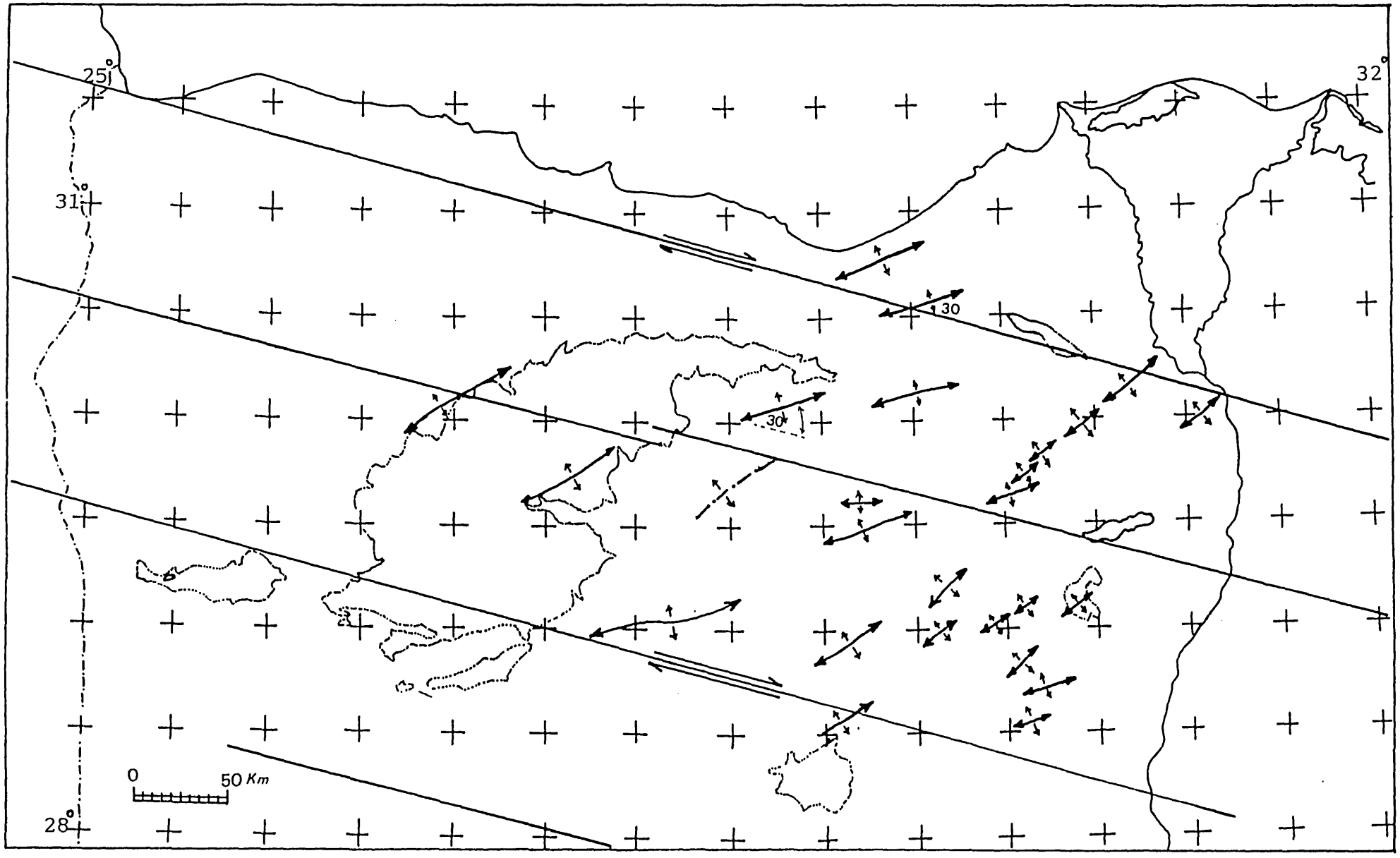


Fig. 8.13 Compiled map of WNW gravity shears and ENE fold structures (the study area).

C. During late Miocene - early Pliocene

Folds with N60° - 70°W (WNW) trend were recognized and considered to be of secondary importance (Shata, 1953). These folds, which have attracted little or no attention, affect Oligocene and younger sediments and are represented on the surface and in the subsurface (see Fig. 2.28).

In conjunction with the geophysical study, it is evident that the basaltic sheet of Oligocene age is dislocated along N60° - 70°E (ENE) sinstral strike-slip fault (see Figs. 7.19, 7.23 and 7.24). Applying the theoretical results (Thomas, 1974), for block coupling, it seems that this later folding was developed, as another possibility, by left lateral (incipient or initial) simple shear, as indicated from the intersection angles of such folds with the N60° - 70°E (ENE) geophysical lineaments (Figs. 8.14 and 8.15). This suggests that the block framework also has structural significance.

The en echelon arrangement of the WNW folds in the studied area is evidence which supports such simple shear mechanism.

As mentioned earlier in this chapter, it is quite difficult to detect any lateral movements through the analysis of Landsat images. However, the surface lineaments (which have been interpreted from Landsat images, Chapter V, (see Figs. 5.5 and 5.6) coupled with the geophyusical evidences for shear were used to define the WNW and ENE block framework (Figs. 8.16 and 8.17).

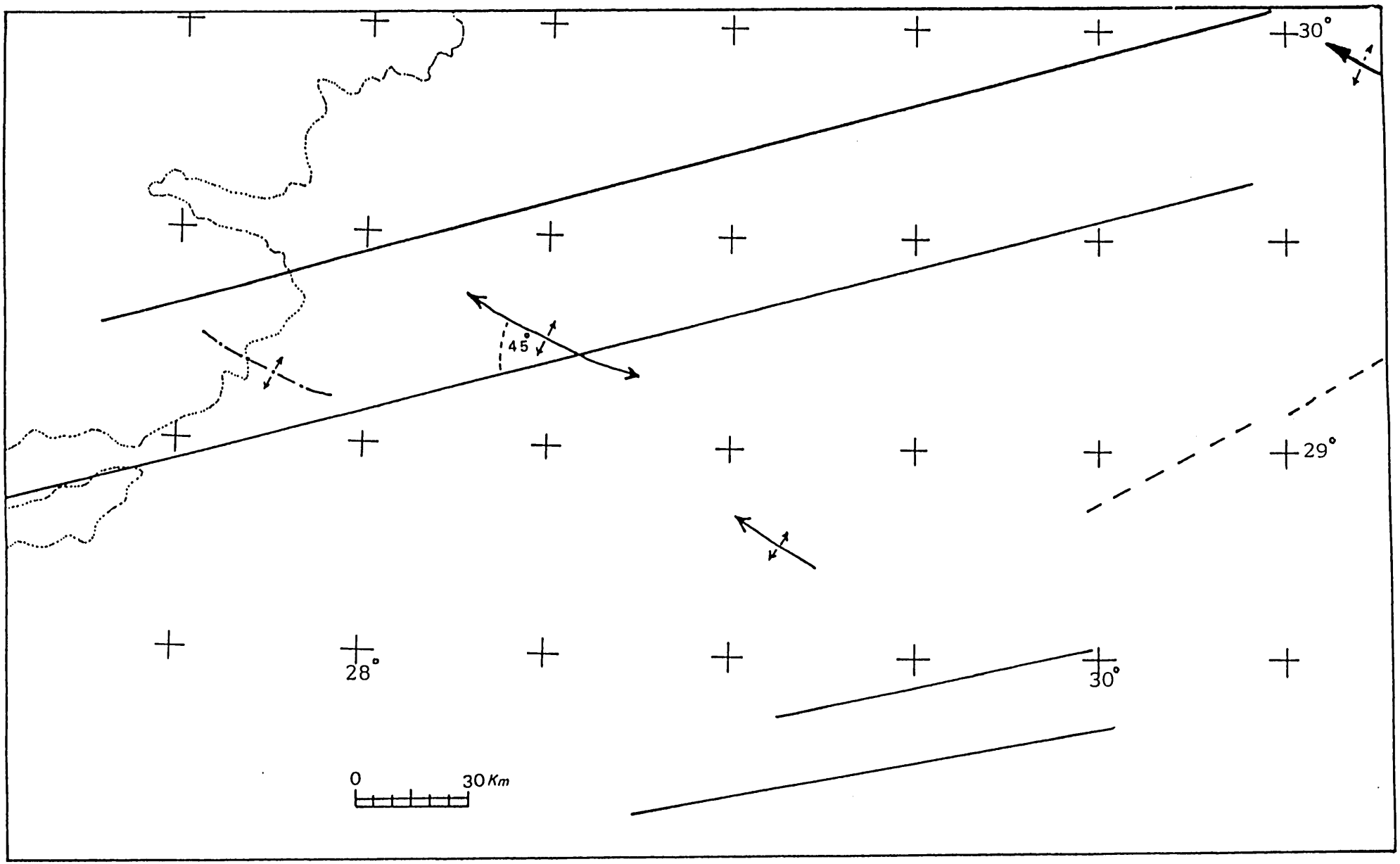


Fig. 8.14 Compiled map of ENE aeromagnetic shears and WNW fold structures.

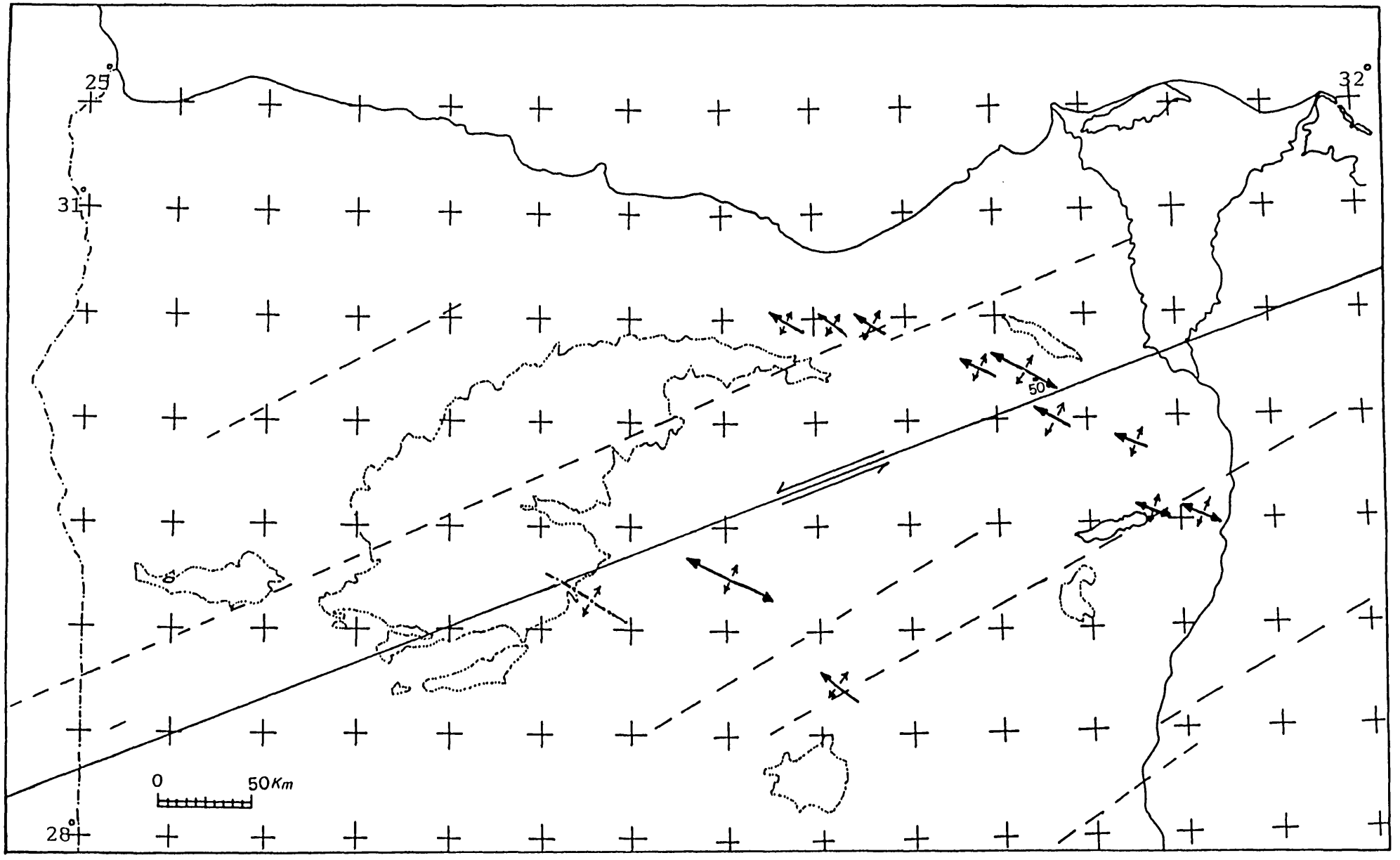


Fig. 8.15 Compiled map of ENE gravity shears and WNW fold structures.

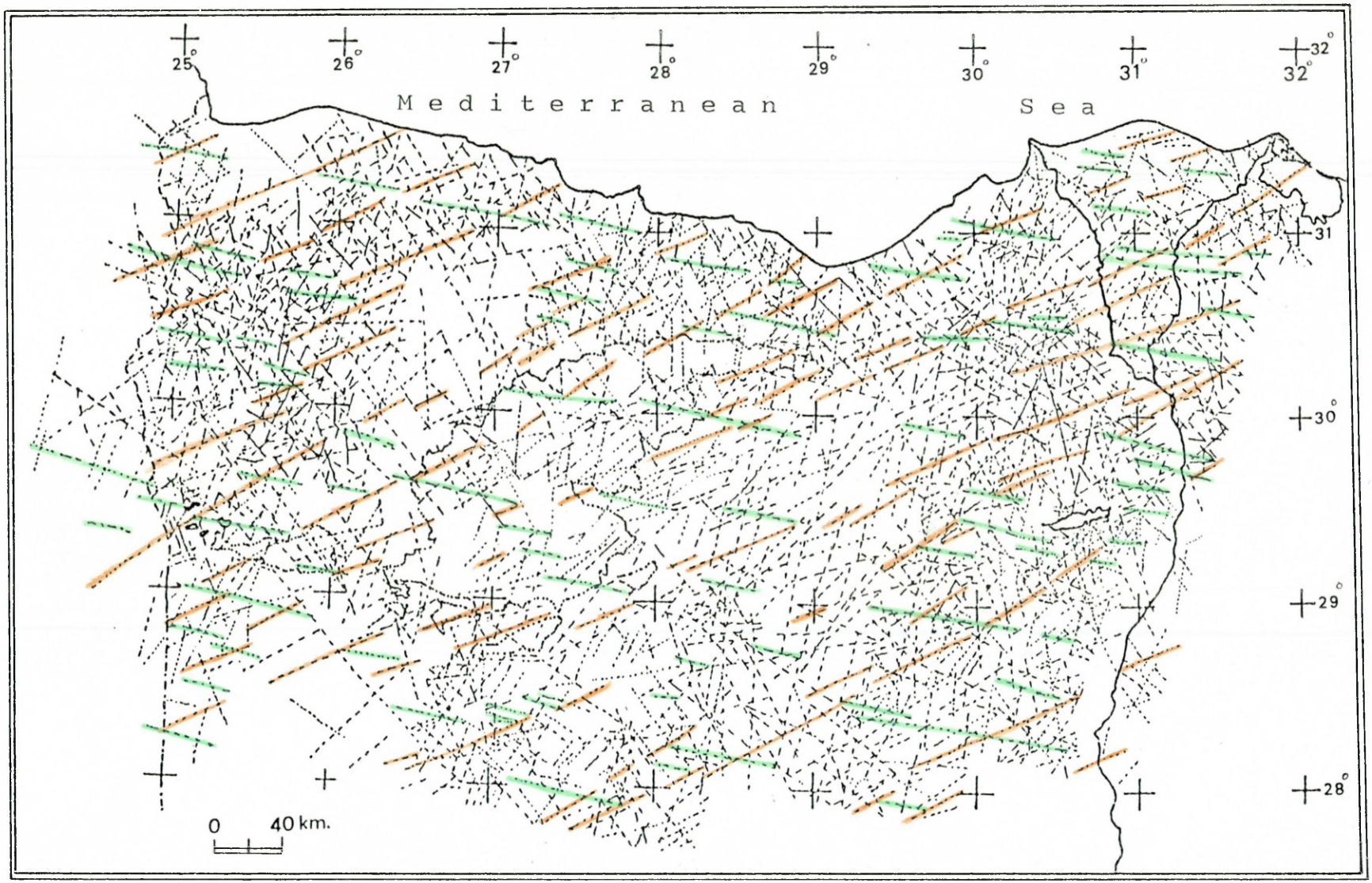


Fig. 8.16 Block framework defined from interpreted surface lineaments (Band 7).

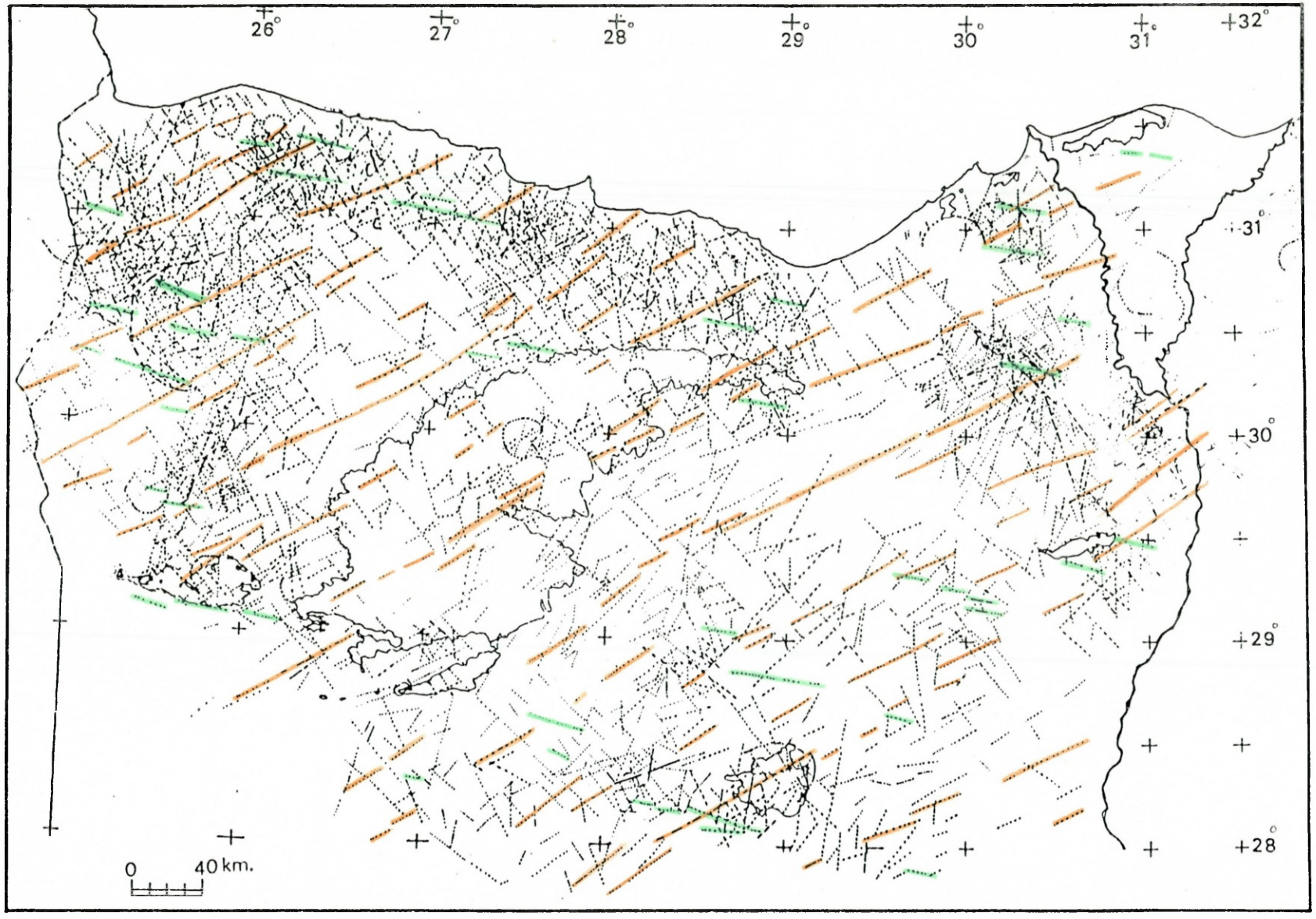


Fig. 8.17 Block framework defined from interpreted surface lineaments (Infra-Red false colour composite).

It is likely, therefore, from Figs. 8.16 and 8.17, that these disconnected surface lineaments (Chapter V) are structurally significant. Also, the information content of Band 7 is much better than that of the Infra-Red false colour composites.

8.4 Structural Conclusion

From the former structural analysis, the following conclusions can be drawn:

1. Identification of lineaments through the interpretation of Landsat images, coupled with subsurface data (such as isopach and/or structure contour maps as well as deep wells data) can be used for recognition of basement segmentation.

2. A complete structural picture of the studied area is vital for a conclusion to be drawn. So, subsurface mapping, as well as geophysical data are essential to get this picture.

3. Price's explanations of the development of small fractures or joints during post-compressional uplift can be applied for regional fractures or lineaments (see Fig. 8.4).

4. The rotation of blocks during uplifting causes changes in the shear angles between two conjugate sets (see Theoretical Model, Chapter III).

5. A fracture may be formed as a normal fault at an early stage by extension, but when stress increases, subsequent lateral adjustment might take place and eventually might be reactivated as a reverse fault..

6. During Palaeozoic-lower Cretaceous, block faulting was dominant and led to the development of Palaeozoic folding (see Chapter VI).

7. (Pure shear), the mechanism which was proposed by Moody and Hill (1956), have been used to explain the development of ENE and WNW fold structures in light of shears interpreted during the course of this study.

8. It is possible to infer that the WNW folds are secondary drag folds, developed as secondary effects of the N20° - 30°W tectonic stress particularly as a result of right lateral movements along nearly N50°W shears (Moody and Hill, 1956).

9. The lateral movements along shear lineaments, particularly nearly N50°W and nearly N - S, are additive.

10. The block framework of the studied area have been defined in light of geophysical shear lineaments and mapped structures, particularly ENE and WNW folds.

11. Comparison of the block framework with surface lineaments interpreted from Landsat images indicate that:

a. The information content of Band 7 Landsat images is much better than that of infra-red false colour composites.

b. The disconnected surface lineaments have structural significance which can not be detected easily on the images.

12. The structural significance of the block framework has been evaluated in light of a simple-shear model of deformation (Thomas, 1974 and Ramos, 1977).

13. The block framework seems to be active during almost all the geologic time, but the outcomes of its tectonics changed with time, such as:

a. From Palaeozoic up to lower Cretaceous, where the sedimentary cover was relatively thin, block faulting was the predominant structural element in the studied area, which resulted from WNW right lateral couple. Consequently, the stable shelf of Egypt, where the sedimentary section is relatively thin, is characterized by block faulting during almost all its geologic history. This block faulting controls the folds present in this shelf, such as the ENE fold structure of Wadi Araba (Eastern Desert of Egypt).

b. During upper Cretaceous up to Eocene, where the sedimentary section becomes relatively thick, ENE drag folds were developed as a result of WNW right lateral couple.

c. During late Miocene - early Pliocene, WNW drag folds were established as a result of ENE left lateral couple.

14. The intensity of the couple can be recognized from the angle between the drag fold axes and weakness zones or lineaments which becomes smaller as the intensity of lateral movements increased (see Thomas, 1974). Thus, the ENE folds were developed as a result of moderate WNW right lateral couple, while the WNW folds were established by initial or incipient ENE left lateral couple.

15. The NNW (N20° - 30°W) undulations were possibly developed as a result of basement block faulting, along N20°-30°W faults (see Figs. 8.5 and 8.6).

16. It seems likely that paleotopography was the result of paleostructures generated along the weakness zones by tectonic reactivation.

17. From the simple-shear model of deformation, it is clear that the intensity of deformation increases from Palaeozoic to lower Cretaceous.

18. The Mediterranean Coast uplift (N70W), most likely developed as a result of regional thrust at the bottom of the Mediterranean Sea (see Chapter VI).

REFERENCES

REFERENCES

Aadland, A.J. and Hassan, A.A. (1972). "Hydrocarbon Potential of the Abu Garadig Basin in the Western Desert, Arab Republic of Egypt." Eighth Arab Petroleum Congress, Algiers, Paper no. 81 (B-3).

Abdel Gawad, M. (1969). "New Evidence of Transcurrent Movements in Red Sea Area and Petroleum Implications." Amer. Assoc. Petrol. Geol. Bull., 53, (7): pp. 1466-1479.

Abdel Gawad, M. (1970). "Interpretation of Satellite Photographs of the Red Sea and Gulf of Aden". Phil. Trans. Roy. Soc. London, A.267. PP. 23-40.

Abdel Gawad, M. (1970). 'The Gulf of Suez: A Brief Review of Stratigraphy and Structure." Phil. Trans. Roy. Soc. London, A.267. pp. 41-48.

Abdel Rahman, E.M. (1979). "Analytical Evaluation of Gravity Data As a Means For Emphasizing Subsurface Structures in the Northern Western Desert of Egypt." Unpublished Ph.D. Thesis, Charles University, Prague, p. 121.

Agarwal, R.G. and Lal, T. (1972). "A Generalized Method of Computing Second Derivative of Gravity Field." Geophys. Prosp., 20, pp. 385-394.

Albers, J.P. (1967). "Belt of Sigmoidal Bending and Right-Lateral Faulting in the Western Great Basin." Geol. Soc. Amer. Bull, vol. 78: pp. 143-156.

Al-Khatieb, S.O. (1981). "Detection of Surface Evidence of Sub-Surface Structures by Interpretation Methods of Landsat Imagery in the Sedimentary Rocks of Central Saudi Arabia". Unpublished Ph.D. Thesis, University of London.

Amin, M.S. (1961). "Subsurface Features and Oil Prospects of the Western Desert, Egypt, U.A.R." Third Arab Petroleum Congress. Alexandria, 8PP.

Attia, A.I. (1955). "Topography, Geology and Iron Ore Deposits of the District East of Aswan." Geol. Survey Egypt. Cairo, p. 262pp.

Ball, J. and Beadnell, H.J.L. (1903). "Baharia Oasis; Its Topography and Geology". Geol. Survey of Egypt. Cairo.

Ball, J. (1939). Contributions to the Geography of Egypt. Cairo: Egypt. Survey Dept.

Barakat, M.G. (1970). "A Stratigraphical Review of the Jurassic Formations in Egypt and Their Oil Potentialities." Kuwait: Seventh Arab Petrol. Congr., paper no. 58 (B-3).

Baranov, W. (1957). "A New Method for Interpretation of Aeromagnetic Maps, Pseudogravity Anomalies." Geophys.22. pp. 357-383.

Baranov, W. (1975). "Potential Fields and Their Transformations in Applied Geophysics." Geoexpl. Monographs 1(6), p. 121.

Bayoumi, A.I. and Wadie, N. (1965). "Susceptibility Measurements on Some of the Egyptian Basement Complex. Cairo: Fifth Arab Petrol. Congr.

Beadnell, H.J.L. (1902). "The Cretaceous Region of Abu Roash, Near the Pyramids of Guiza." Cairo: Geol. Survey.

Beadnell, H.J.L. (1905). "The Relations of the Eocene and Cretaceous Systems in the Esna-Aswan Reach of the Nile Valley." Quart. J. Geol. Soc. London, vol. 61, pp. 667-678.

Beckman, J.P. (1967). "Stratigraphy and Regional Geology of the Northern Western Desert." Cairo: The Geol. Soc. Egypt

Belcher, D.J. and Schepis, E.L. (1965). "Exploration Theory Can Aid Oil Hunters." The Oil and Gas Journal, 63(48), pp. 108-113.

Bishop, M.S. (1960). Subsurface Mapping. John Wiley & Sons, Inc.

Blanchet, P.H. (1957). "Development of Fracture Analysis As Exploration Method." Amer. Assoc. Petrol. Geol. Bull. 41(8).

Boyed, W.R. (1947). "A Preliminary Note on a Geological Reconnaissance Survey of the Qattara-Natrun Area, Western Desert, Egypt." Unpublished report. General Petroleum Co., Egypt.

Chukwu-Ike, I.M. (1977). "Regional Photogeological Interpretation of the Tectonic Features of the Central Nigerian Basement Complex: A Satellite Imagery Based Study." Unpublished Ph.D. Thesis, University of London.

Cohenour, R.E. and Sharp, B.F. (1968). "The Impact Theory: Asteroids and the Earth-Moon System." Geo-Science News, 1(3), pp. 9-12.

Condie, K.C. (1982). Plate Tectonics & Crustal Evolution, 2nd. Edition. Pergamon Press Inc.

Cook, R.A. (1978). "A Relationship Between Strike-Slip Faults and the Process of Drape Folding of Layered Rocks." Geol. Soc. Amer. Memoir, 151, pp. 197-214.

Critchley, M.F. (1981). "Structure and Formation Mechanisms of Vein-Fracture System in the North Pennine Orefield." Unpublished Ph.D. Thesis, University of London.

Davis, J.C. (1973). Statistics and Data Analysis in Geology. John Wiley & Sons, Inc.

Dean, W.C. (1958). "Frequency Analysis For Gravity and Magnetic Interpretation." Geophysics, 23(1), pp. 97-127.

De Sitter, L.U. (1964). Structure Geology. New York: MacGraw-Hill.

Dolivo-Dobrovol'sky, A.V. and Strel'nikov. (1976). "The Remote Sensing Study of the Largest Lineaments and Their Systems With Reference to Some Regions of Eurasia." Proc. First International Conf. on the New Basement Tectonics, Utah Geol. Assoc. Publication no. 5, pp. 349-353.

El-Etr, H.A. et al. (1976). "Airphoto lineations of the Southern Part of the Gulf of Suez Region, Egypt." Proc. First International Conf. on the New Basement Tectonics, Utah Geol. Assoc. Publication no. 5, pp. 309-326.

El-Etr, H.A. (1976). "Proposed Terminology For Natural Linear Features." Proc. First International Conf. on the New Basement Tectonics, Utah Geol. Assoc. Publication no. 5, pp. 480-489.

El-Etr, H.A. and El-Baz, F. (1979). "Utilization of ASTP Photographs in the Study of Small Structures in Abu Rawash and Wadi el Natrun, Egypt." Apollo-Soyuz Test Project, Summary Science Report, Vol. II: Earth Observations and Photography, Smithsonian Institute, pp. 107-118.

Elkins, T.A. (1951). "The Second Vertical Derivative Method of Gravity Interpretation." Geophys., vol. 16, pp. 29-50.

El-Malky, M.G. (1974). "Geophysical Study on the Area Soutwest of Wadi El-Natrun, Northern Western Desert of Egypt." Unpublished M.Sc. Thesis, Ain Shams University, Cairo.

El-Shazly, E.M. et al. (1974). "Geology of Sinai Peninsula From ERTS-1 Satellite Images." Remote Sensing Research Project, Academy of Scientific Research and Technology, Cairo.

El-Shazly, E.M. et al. (1975). "Geologic Interpretation of Landsat Satellite Images for West Nile Delta Area, Egypt." Remote Sensing Research Project, Academy of Scientific Research and Technology (Cairo, Egypt) and Oklahoma State University (U.S.A.).

El-Shazly, E.M. et al. (1976). "Geologic Interpretation of Landsat Satellite Images for the Qattara Depression Area, Egypt." Remote Sensing Center, Academy of Scientific Research and Technology, Cairo, Egypt.

El-Shazly, E.M. (1977). "The Geology of the Egyptian Region" in The Eastern Mediterranean, vol. 4A, The Ocean Basins and Margins. (Narin, A.E.M. et al, Eds). New York: Plenum Press, pp. 379-444.

Fajklewicz, Z.T. (1965). "Fictitious Anomalies of Higher Vertical Derivatives of Gravity." Geophys., vol. 30, pp. 1094-1107.

Faris, M.I. (1946). "The Cretaceous Rocks of Abu Rauwash District." Unpublished Ph.D. Thesis, Fouad I. University, Cairo, Egypt.

Faris, M.I. (1947). "The Contact of the Cretaceous and Eocene Rocks in the Tramsa-Tukh Area (Quena, Upper Egypt)." Bull. Inst. Egypte, no. 28, pp. 73-85.

Freund, R. (1965). "A Model of the Structural Development of Israel and Adjacent Areas Since Upper Cretaceous Times." Geol. Mag., 102(3), pp. 189-205.

Freund, R. et. al. (1970). "The Shear Along the Dead Sea Rift." Phil. Trans. Roy. Soc. London. A.267, pp. 107-130.

Fyfe, W.S., Price, N.J. and Thompson, A.B. (1978). Fluids in the Earth"s Crust. Amsterdam: Elsevier Scientific Publishing Company.

Gallagher, J.J. and McGuire, M.J. (1979). "Structure and Stratigraphy Revealed by Lineaments." Proc. Second International Conf. on Basement Tectonics, Basement Tectonics Committee, Inc., publication no. 2, Denver, Colorado, pp. 392-405.

Gallant, R.L.C. (1963). "Meteorite Impacts, Lunar Maria Lopoliths and Ocean Basins." Nature, vol. 197, pp. 38-39.

Garfunkel, Z. and Bartov, Y. (1977). "The Tectonics of the Suez Rift." Geol. Surv. Israel Bull., no. 71, pp. 1-44.

Gay, S.P., Jr. (1972). Aeromagnetic Lineaments: Their Geological Significance and Their Significance to Geology. Salt Lake City: American Stereo Map Company, p. 94.

Gindy, R.A. and Elaskary, M.A. (1969). "Stratigraphy, Structure and Origin of Siwa Depression, Western Desert of Egypt." Amer. Assoc. Petrol. Geol. Bull., 53(3), pp. 603-625.

Griggs, D.T. and Handin, J. (1960). "Observations on Fracture and a Hypothesis of Earthquakes." Geol. Soc. Amer. Memior, 79, pp. 347-364.

Gol'braykh, I.G., Mirkin, G.R. and Zabaluyer, V.V. (1966). "Tectonic Analysis of Megajointing." Int. Geol. Rev., 8(9), pp. 1009-1016.

Haman, P.J. (1961). Lineament Analysis on Aerial Photographs. West Camden Research Publication, No. 1, Series 2, 22p.

Haman, P.J. (1964). "Geomechanics Applied to Fracture Analysis on Aerial Photographs." West Canadian Research Publication, Series 2, no. 2..

Hancock, P.L. and Atiya, M.S. (1979). "Tectonic Significance of Mesofracture Systems Associated with the Lebanese Segment of the Dead Sea Transform Fault." J. Structural Geology, Vol. 1, No. 2, pp. 143 - 153.

Harding, T.P. (1974). "Petroleum Traps Associated With Wrench Faults." Amer. Assoc. Petrol. Geol. Bull., 58(7), pp. 1290-1304.

Harris, J.F., Taylor, G.L. and Walper, J.L. (1960). "Relation of Deformational Fractures in Sedimentary Rocks to Regional and Local Structures." Amer Assoc. Petrol. Geol. Bull, 44(12), p. 1853.

Henderson, R.G. and Zietz, I. (1949). "The Computation of Second Vertical Derivatives of Geomagnetic Fields." Geophys., 14, pp. 517-534.

Henson, R.R.S. (1951). "Observations on the Geology and Petroleum Occurrences in the Middle East." Proc. Third World Petrol. Congr., Sect. I. Leiden: E.J. Brill, pp. 118-140.

Hobbs, W.H. (1904). "Lineaments of the Atlantic Border Region." Geol. Soc. Amer. Bull., vol. 15, pp. 483-506.

Hobbs, W.H. (1911). "Repeating Patterns in the Relief and in the Structure of the Land." Geol. Soc. Amer. Bull., vol. 22, pp. 123-176.

Hodgson, R.A. (1961). "Classification of Structures on Joint Surfaces". Amer. J. Sci., 259, 493.

Hodgson, R.A. (1961). "Regional Study of Jointing in Comb Ridge Navajo Mountain Area: Arizona and Utah." Amer. Assoc. Petrol. Geol. Bull., 45(1).

Horsfield, W.T. (1977). "An Experimental Approach to Basement Controlled Faulting." Geol. Mijnbouw, 56, pp. 363-370.

Hume, W.F. (1911). "The Effects of Secular Oscillation In Egypt During the Cretaceous and Eocene Periods." Quart. J. Geol. Soc. London, 67, pp. 118-148.

Hume, W.F. (1925). Geology of Egypt, Vol. I: The Surface Features of Egypt, Their Determining Causes and Relation to Geological Structure. Cairo: Egypt. Survey Dept.

Huntington, J.F. (1969). "Methods and Applications of Fracture Trace Analysis in the Quantification of STructural Geology." Geol. Mag., 106(5).

Huntington, J.F. (1975). "A Photogeological Study of Fracture Trace Patterns Using Data Processing Techniques." Unpublished Ph.D. Thesis, University of London.

Huntington, J.F., and Raich, A.P. (1978). "A Multi-Attribute Method for Comparing Geological Lineament Interpretation." Remote Sensing of Environment, 7, pp. 145-161.

Jux, U. (1954). "Zur Geologie des Kreidegebietes von Abu Roasch bei Kairo." Neues Jahrb. Geol. u. Palaontol, Abhandl., 100, pp. 159-207.

Katterfeld, G.N. (1976), "Global and Regional Systems of Lineaments on the Earth, Mars and the Moon." Proc. First International Conf. on New Basement Tectonics. Utah Geol. Assoc., publ. no. 5, pp. 369-378.

Khalid, A.D. (1975). "Jurassic Prospects in the Western Desert, Egypt." Ninth Arab Petrol. Congr., Dubai, Paper no. 100 (B-3).

Kilkenny, J.E. (1948). "Geology and Exploration For Oil in Salinas Valley, California." Amer. Assoc. Petrol. Geolog. Bull., 32(12), pp. 2254-2268.

Knetsch, G. and Yallouze, M. (1955). "Remarks on the Origin of the Egyptian Oasis Depression." Bull. Soc. Geogr. Egypte, 28, pp. 21-33.

Knetsch, G. (1957). "Eine Strukturelle-Skizze Aegyptens Und Einiger Seiner Nachbargebiete." Geol. Jb., Band 74, pp. 75-86.

Knetsch, G. (1958). "Germanotype Deformationbilder aus Aegypten." Geologie, 7, pp. 440-447.

Koide, H. and Bhattacharji, S. (1977). "Geometric Patterns of Active Strike-Slip Faults and Their Significance As Indicators For Areas of Energy Release. In Energetics in Geological Processes, Saxena, S., and Bhattachatji, S., eds. New York: Springer Verlag, pp. 46-66.

Kostandi, A.B. (1963). "Eocene Facies Maps and Tectonic Interpretation in the Western Desert, U.A.R." Revue de L'Institut Francais Du Petrole, XVIII (10), pp. 1331-1343.

Ladeira, F.L. (1978). "Relationship of Fractures to Other Geological Structures in Various Crustal Environments." Unpublished Ph.D. Thesis, University of London.

Ladeira, F.L. and Price, N.J. (1981). "Relationship Between Fracture Spacing and Bed Thickness." J. Structural Geology, vol. 3, No. 2, pp. 179 - 183.

Lattman, L.H. (1958). "Techniques of Mapping Geologic Fracture Traces and Lineaments On Aerial Photographs". Photogrammetric Engineering, vol. 24, pp. 568-572.

Le Pichon, X. (1968). "Sea-Floor Spreading and Continental Drift." J. Geophys. Res., 73, pp. 3661-3697.

Le Pichon, X., Francheteau, J., and Bonnin, J. (1976). Plate Tectonics, second edition. Developments in Geotectonics 6. Elsevier.

Longwell, C.R. (1948). "Low Angle Normal Faults in the Basin and Range Province." Amer. Geophys. Union Trans., vol. 26, pt. 1, pp. 107-118.

Makin, J.Y. (1960). "Structural Significance of Tertiary Volcanic Rocks in Soutwestern Utah". Amer. Jour. Sci., 258(2), pp. 81-131.

Marzouk, I. (1970). Rock Stratigraphy and Oil Potentialities of the Oligocene and Miocene in the Western Desert, U.A.R. Kuwait: Seventh Arab Petroleum Congress, paper no. 54 (B-3).

Matthews, V. and Work, D.F. (1978). "Laramide Folding Associated with Basement Block Faulting Along the Northeastern Flank of the Front Range, Colorado." Geol. Soc. Amer. Memoir, 151, pp. 101-124.

Mckenzie, D.P. (1970). "The Plate Tectonics of the Mediterranean Region." Nature, 226, 239.

Mckenzie, D.P., Molnar, P., and Davis, D. (1970). "Plate Tectonics of the Red Sea and East Africa." Nature, 226, 243.

Mckenzie, D.P. (1972). "Active Tectonics of the Mediterranean Region." Royal Astronomical Society, Geophysical Journal, vol. 30, pp. 109-185.

Meshref, W.M., and El-Sheikh, M.M. (1973). "Magnetic Tectonic Trend Analysis in Northern Egypt." Egypt. Jour. Geol., vol. 17, pp. 179-184.

Mollard, J.D. (1957). "Aerial Mosaics Reveal Fracture Patterns on Surface Materials in Southern Saskatchewan and Manitoba." Oil in Canada, 9(40), pp. 26-48.

Moody, J.D. and Hill M.J. (1956). "Wrench Fault Tectonics." Geol. Soc. Amer. Bull., vol. 67, pp. 1207-1246.

Moody, J.D. (1966). "Crustal Shear Patterns and Orogenesis." Tectonophysics, vol. 3, pp. 479-522.

Nakhla, A.F. and Podbelova, E.A. (1973). "Qualitative and Quantitative Analysis of the Aeromagnetic Survey Over the Western Part of the Western Desert." J. Geol. Egypt, no. 2, pp. 185-194.

Norman, J.W. (1968). "Photogeology of Linear Features in Areas Covered With Superficial Deposits." Trans. Inst. Min. Metall., Section B., vol. 77, pp. 60-77.

Norman, J.W. (1968). "The Air Photograph Requirements of Geologists." Photogramm. Records 6, p. 133.

Norman, J.W., Price, N.J., and Chukwu-Ike, M.I. (1977). "Astrons The Earth's Oldest Scars?" New Scientist, vol. 73, pp. 689-691.

Norman, J.W., and Partridge, T.C. (1978). "Fracture Analysis in the Determination of Sub-Unconformity Structure: A Photogeological Study." J. Petrol. Geol., 1(1), pp. 43-63.

Norman, J.W. (1980). 'Causes of Some Old Crustal Failure Zones Interpreted from Landsat Images and Their Significance in Regional Mineral Exploration." Trans. Inst. Min. Metall., Section B, 89, pp. 63-72.

Norman, J.W. (1980). "Regional Tectonic Structures of Cover Rocks." Open File Report CRC/IC5: Ministry of Petroleum and Mineral Resources, Jeddah, Saudi Arabia.

O'Leray, D.W., Friedman, J.D., and Pohn, H.A. (1979). "Lineament and Linear: A Terminological Reappraisal." Denver, Colorado: Proc. Second International Conf. on Basement Tectonics, Basement Tectonic Committee Inc., pub. no. 2, pp. 571-577.

Omara, S. (1953). "The Structural Features of the Giza Pyramids Area." Unpublished Ph.D. Thesis, Cairo University.

Omara, S. (1964). "Diapiric Structures in Egypt and Syria." Amer. Assoc. Petrol. Geol. Bull., 48(7), pp. 1116-1125.

Park, J.N. (1983). "Pattern Recognition Techniques for Integration of Geophysics, Remote Sensing, Geochemistry and Geology. Unpublished Ph.D. Thesis, University of London.

Patton, F.D. (1966). "Multiple Modes of Shear Failure in Rock and Related Materials." Unpublished Ph.D. Thesis, University of Illinois.

Peters, L.J. (1949). "The Direct Approach to Magnetic Interpretation and its Practical Application." Geophys., vol. 19, pp. 341-342.

Peterson, R.M. (1976). "Curvilinear Features Visible on Small Scale Imagery as Indicators of Geologic Structures." Proc. First International Conf. on the New Basement Tectonics. Utah Geol. Assoc. Pub. no. 5, pp. 618-625.

Picard, L. (1937). "On the Structure of the Arabian Peninsula." Bull. Geol. Dept., Hebrew Univ., Jerusalem, vol. 1, pp. 1-12.

Picard, L. (1943). "Structure and Evolution of Palestine." Bull. Geol. Dept., Hebrew Univ., Jerusalem, 4(2-4), 134pp.

Picard, L. (1970). "On Afro-Arabian Graben Tectonics." Geologische Rundschan, Band 59, Heft 2, p. 337-381.

Podwysocki, M.H. and Gold, D.P. (1979). "Some Possible Surface Expressions of a Regular Fracture Grid Deformed by Subsurface Structures." Proc. Second International Conf. on Basement Tectonics. Denver, Colorado: Basement Tectonics Committee Inc. publ. no. 2, pp. 542-553.

Price, N.J. (1959). "Mechanics of Jointing in Rocks." Geol. Mag., 1(96), pp. 149-167.

Price, N.J. (1966). Fault and Joint Development in Brittle and Semi-Brittle Rock. Oxford: Pergamon Press.

Price, N.J. (1969). "A Dynamic Mechanism for the Development of Second Order Faults." Canada Geol. Surv., Papers 68-52, pp. 49-71.

Price, N.J. (1974). "The Development of Stress Systems and Fracture Patterns in Undeformed Sediments." Proc. Third Congr. Int. Soc. Rock Mech., 1-A, pp. 487-496.

Price, N.J. (1975). "Fluids in the Crust of the Earth." Sci. Prog., Oxf., 62, pp. 59-87.

Price, N.J. (1977). "Aspects of Gravity Tectonics With Special Reference to the Development of Listric Faults." J. Geol. Soc. London, 103, pp. 311-327.

Ragan, D.M. (1968). Structural Geology. (An Introduction to Geometrical Techniques. New York: John Wiley & Sons.

Ramos, V.A. (1977). "Basement Tectonics From Landsat Imagery in Mining Exploration." Geol. Mijnbouw, 56, pp. 243-252.

Ray, R.G. (1960). "Aerial Photographs in Geologic Interpretation and Mapping". U.S. Geol. Survey Prof. Paper No. 373, 230pp.

Reches, Z. and Johnson, A. (1978). "Development of Monoclines: Part II Theoretical Analysis of Monoclines." Geol. Soc. Amer. Memoir, 151. pp. 273 - 311.

Riad, S. (1977). "Shear Zones in North Egypt Interpreted From Gravity Data." Geophysics, 42(6), pp. 1207-1214.

Rittmann, A. (1954). "Remarks on Eruption Mechanism of the Tertiary Volcanoes of Egypt." Bull. Volcanol., Ser. 2, 15, pp. 109-117.

Robinson, J.E. and Ellis, M.J. (1971). "Spatial Filters and Fortran IV Program for Filtering Geologic Maps." Geocom. Programs 1, 21p.

Rosenbach, O. (1953). "A Contribution to the Computation of the Second Derivative From Gravity Data." Geophysics, vol. 18, pp. 894-912.

Sabins, F.F. Jr. (1978). Remote Sensing: Principles and Interpretation. W.H. Freeman and Co., 426pp.

Sabri, A.M. and Abdelhady, Y.E. (1979). "Qualitative and Quantitative Analysis of Gravity Data in Northern Western Desert". Desert Inst. Bull., A.R.E. 28(1), pp. 59-89.

Sacrison, W.R. (1978). "Seismic Interpretation of Basement Block Faults and Associated Deformation." Geol. Soc. Amer. Memior, 151, pp. 39-49.

Said, R. (1961). "Tectonic Framework of Egypt and its Influence on Distribution of Foraminifera." Amer. Assoc. Petrol. Geol. Bull., vol. 45, pp. 198-218.

Said, R. (1962). The Geology of Egypt. Elsevier Publ. Co.

Said, R. (1971). "Explanatory Notes to Accompany the Geological Map of Egypt." The Geological Survey of Egypt, No. 56.

Salem, R. (1976). "Evolution of Eocene-Miocene Sedimentation Patterns in Parts of Northern Egypt." Amer. Assoc. Petrol. Geol. Bull., 60(1), pp. 34-64.

Sander, J.J. (1981). "Structural Evolution of the Mediterranean Region During the Mesozic." In Tethys the Ancestral Mediterranean. Sonnenfeld, P., ed. Benchmark Papers in Geology/53, pp. 100-189.

Saunders, D.F. (1969). "Airborne Sensing As An Oil Reconnaissance Tool in Unconventional Methods in Exploration for Petroleum and Natural Gas." Beray, W.B., Ed. Inst. For Study of Earth and Man. Dallas, Texas: Southern Methodist University, pp. 105-125.

Schurmann, H.M.E. (1974). The Pre-Cambrian in North Africa. Leiden, Netherlands: E.J. Brill.

Secor, D.T. (1969). "Mechanics of Natural Extension Fracturing at Depth in the Earth's Crust." Canada Geol. Surv., Paper 68-52, pp. 3-48.

Shata, A. (1953). "New Light On the Structural Development of the Western Desert of Egypt." Egypt. Bull. Inst. du Desert d'Egypte, Tome III, No. 1, pp. 101-106.

Shata, A. (1955). "An Introductory Note On the Geology of the Northern Portion of the Western Desert of Egypt." Egypt. Bull. Inst. du Desert d'Egypte, Tome 5, No. 2, pp. 96-104.

Shereef, M.R.A. (1972). "A Geophysical Study On the Nile Delta Area for Petroleum Prospection." Unpublished Ph.D. Thesis, Cairo University.

Shukri, N.M. (1954). "Remarks on the Geological Structure of Egypt." Soc. Geogr. d'Egypte Bull., t. 27, pp. 65-82.

Shukri, N.M. (1954). "The Geology of Shadwan Island, Northern Red Sea." Soc. Georgr. d'Egypte Bull., t. 27, pp. 83-92.

Shul'ts, S.S. (1971). "Planetary Fractures and Tectonic Deformation." Geotectonic 4, Academy of Science, U.S.S.R., pp. 203-207.

Sigaev, N.A. (1967). "The Main Tectonic Features of Egypt." Geol. Surv. Egypt. Cairo: Paper No. 39, 26 p.

Smith, A.G. (1971). "Alpine Deformation and the Oceanic Areas of the Tethys, Mediterranean and Atlantic." Amer. Geol. Soc. Bull., vol. 82, pp. 2039-2070.

Smith, M.R. (1976). "Arcuate Structural Trends and Basin and Range Structures Based on a Study of ERTS-1 Imagery." Proc. First International Conf. on New Basement Tectonics. Utah Geol. Assoc., Publ. No. 5, pp. 626-634.

Soliman, S.M. and El Fetouh, M. (1970). "Carboniferous of Egypt: Isopach and Lithofacies Maps." Amer. Assoc. Petrol. Geol. Bull., vol. 54, pp. 1918-1930.

Stearns, D.W. (1978). "Faulting and Forced Folding in the Rocky Mountains Foreland." Geol. Soc. Amer. Memior 15, pp. 1-37.

Swartz, D.H. and Arden, D. (1960). "Geologic History of Red Sea Area." Amer. Assoc. Petrol. Geol. Bull., 44(10), pp. 1621-1637.

Thomas, G.E. (1974). "Lineament - Block Tectonics: Williston-Blood Creek Basin." Amer. Assoc. Petrol. Geol. Bull., 58(7), pp. 1305-1322.

Tosson, S. (1954). "The Rennebaum Volcano in Egypt." Bull. Volcanol. (Ser. 2), 15, pp. 99-108.

Tromp, S.W. (1949). "Block Folding Phenomena in the Middle East." Geologie en Mijnbouw, 11e Jaargang No. 9, pp. 273-278.

Tromp, S.W. (1950). "The Age and Origin of the Red Sea Graben." Geol. Mag, vol. 87, pp. 385-392.

Turcotte, D.L. and Schubert, G. (1982). Geodynamics: Applications of Continuum Physics to Geological Problems. John Wiley & Sons.

Weeks, L.G. (1952). "Factors of Sedimentary Basin Development that Control Oil Occurrence." Am. Assoc. Petrol. Geol. Bull., vol. 36, pp. 2071-2124.

Weinberg, D.M. (1978). "Some Two-Dimensional Kinematic Analysis of the Drape-Fold Concept." Geol. Soc. Amer. Memior, 151, pp. 51-78.

Wertz, J.B. (1976). "Detection and Significance of Lineaments and Lineament Intersections in Parts of the Northern Cordillera." Proc. First International Conf. on New Basement Tectonics. Utah Geol. Assoc., Publ. No. 5, pp. 42-53.

Wilcox, R.E., Harding, T.P., and Seely, D.R. (1973). "Basic Wrench Tectonics." Amer. Assoc. Petrol. Geol. Bull., Vol. 57, pp. 74-96.

Windley, B.F. (1977). The Evolving Continents. John Wiley & Sons.

Wisser, E. (1960). "Relationship of Ore Deposition To Doming In the North American Cordillera." Geol. Soc. Amer. Mem. 77

Yallouze, M., and Knetsch, G. (1954). "Linear Structures In and Around the Nile Basin." Bull. Soc. Geogr. Egypte, vol. 27, pp. 153-207.

Youssef, M.I. (1968). "Structural Pattern of Egypt and Its Interpretations." Amer. Assoc. Petrol. Geol. Bull., 52(4), pp. 601-614.

Zein, El Din, M.Y., and Marzouk, M.A. (1974). "Geology and Hydrocarbon Prospects of the Nile Delta." "Egyptian General Petroleum Company Report."

Zwain, J.A. (1976). "Analysis From Air Photographs of Fracture Trace in Northern Iraq: A Structural Geology Study With Reference to Oil Exploration." Unpublished Ph.D. Thesis, University of London.

APPENDIX I

SOME RESULTS

OF

LANDSAT IMAGES STUDY

APPENDIX ONE

SOME RESULTS OF LANDSAT IMAGES STUDY

Table A

Dominant Trends of Some Rose Diagrams of the Colour Composite Images

False Colour(IR) Frame No.70 Sun Azimuth 124° Sun Elevation 54°

R.F.F.	%	R.F.L.	%	R.F.E.	%	R.Av.F.L.	%	Int.Tech.	%
N30-40E	12.2	N30-40E	12.4	N30-40E	24.2	N20-30W	9.3	N30-40E	14.9
N50-60E	12.2	N50-60E	11.8	N50-60E	21.9	N70-80W	9.1	N50-60E	13.4
N10-30E	20.4	N40-50E	10.6	N40-50E	14.5	N30-50W	17.6	N40-50E	10.4
N40-50E	10.2	N60-70E	9.3	N60-70E	9.1	N60-70E	6.9	N20-30E	9.0
N60-70E	8.2	N30-40W	9.0	N20-30E	7.7	N80-90E	6.9	N10-20E	7.5
N80-90W	8.2	N20-30E	7.7	N10-20E	7.4	N 0-10E	6.2	N60-70E	7.5
N30-40W	6.1	N10-20E	7.5	N30-40W	6.3	N40-50E	6.2	N80-90W	7.5
		N80-90W	6.2			N30-40E	6.1	N30-40W	7.5
		N40-50W	6.0			N50-60E	5.8	N20-30W	6.0

False Colour(IR) Frame No.71 Sun Azimuth 105° Sun Elevation 60°

N 0-10W	21.7	N 0-10W	18.8	N 0-10W	51.3	N50-60E	20.1	N 0-10W	24.1
N30-40W	17.4	N20-30E	13.6	N30-40W	16.9	N70-80W	13.1	N30-40W	12.1
N 0-10E	8.7	N40-50E	12.7	N20-30E	10.8	N20-30E	12.0	N20-30E	12.1
N20-30E	8.7	N30-40W	12.1	N40-50E	9.4	N40-50W	11.9	N40-50E	12.1
N40-50E	8.7	N50-60E	11.4			N40-50E	11.2	N50-60E	8.6
N10-20W	8.7	N 0-10E	7.8			N 0-10E	6.9	N 0-10E	6.9
		N70-80W	7.4					N70-80W	6.9
		N40-50W	6.8						

False Colour(IR) Frame No.72 Sun Azimuth 150° Sun Elevation 35°

N30-40W	17.2	N30-40W	20.7	N30-40W	38.8	N30-40E	17.6	N30-40W	19.6
N50-60E	16.1	N50-60E	19.2	N50-60E	31.3	N40-50E	10.3	N50-60E	17.6
N40-50W	13.8	N40-50E	14.7	N40-50W	15.7	N30-40W	10.0	N40-50W	13.7
N10-20E	10.3	N20-30W	11.3	N20-30W	7.0	N50-60E	9.9	N20-30W	10.8
N20-30W	10.3	N10-20E	8.2			N20-30W	9.1	N10-20E	8.8
N 0-10W	9.2	N40-50E	7.1			N40-50W	8.9	N40-50E	6.9
								N 0-10W	5.9

False Colour(IR) Frame No.73 Sun Azimuth 140° Sun Elevation 35°

R.F.F.	%	R.F.L.	%	R.F.E.	%	R.Av.F.L.	%	Int.Tech.	%
N30-40W	16.1	N30-40W	22.6	N30-40W	69.7	N30-40W	9.0	N30-40W	19.4
N20-30E	9.8	N60-70E	11.3	N60-70E	10.6	N70-80E	8.8	N60-70E	9.7
N60-70E	9.8	N50-60E	9.0			N50-60W	7.4	N50-60E	8.3
N50-60E	8.0	N20-30E	6.7			N60-70E	7.3	N20-30E	6.9
N30-40E	7.1	N30-40E	5.8			N70-80W	7.3	N30-50E	11.2
N 0-10E	6.3	N40-50E	5.5			N50-60E	7.1	N40-50W	5.6
N80-90W	6.3					N10-20W	7.0	N10-30W	11.2
						N40-50E	6.5		
						N40-50W	6.5		

False Colour(IR) Frame No.74 Sun Azimuth 144° Sun Elevation 31°

R.F.F.	%	R.F.L.	%	R.F.E.	%	R.Av.F.L.	%	Int.Tech.	%
N30-40W	18.9	N30-40W	19.1	N30-40W	46.7	N20-30W	11.8	N30-40W	22.6
N50-60E	16.8	N50-60E	17.5	N50-60E	34.8	N30-40E	8.9	N50-60E	17.0
N60-70E	9.5	N20-30E	10.0	N20-30E	5.0	N20-30E	8.4	N10-30E	15.0
N10-20E	8.4	N10-20E	8.0			N40-50W	7.0	N60-70E	7.5
N20-30E	7.4	N60-70E	7.8			N 0-10W	6.8	N 0-10E	5.7
N 0-10E	6.3	N40-50W	7.1			N50-60E	6.4	N 0-10W	5.7
N40-50W	6.3	N20-30W	6.0			N60-70W	6.3	N20-30W	5.7
						N10-20E	6.2	N40-50W	5.7
						N30-40W	6.2		
						N40-50E	5.7		

False Colour(IR) Frame No.80 Sun Azimuth 110° Sun Elevation 61°

N50-60E	16.8	N50-60E	16.1	N50-60E	49.7	N 0-10E	8.7	N50-60E	18.5
N30-40W	11.7	N60-70E	9.7	N30-40W	11.7	N70-80E	8.4	N30-40W	9.2
N10-20E	8.6	N30-40W	9.4	N60-70E	8.5	N60-70E	8.1	N10-20E	7.7
N60-70E	7.9	N10-20E	8.7	N10-20E	7.4	N20-30E	7.4	N60-70E	7.7
N40-50W	7.9	N40-50W	8.2			N40-50W	6.9	N40-50W	7.7
N40-50E	7.2	N40-50E	7.1			N10-20E	6.7	N 0-10E	6.2
N20-30W	6.5	N20-30E	6.9			N40-50E	6.5	N20-30E	6.2
N20-30E	6.2					N10-20W	6.5	N40-50E	6.2
N10-20W	6.2					N50-60E	6.3	N10-30W	12.4
						N 0-10W	6.2		
						N20-30W	6.1		
						N50-60W	6.0		

False Colour(IR) Frame No.81 Sun Azimuth 132° Sun Elevation 51°

N60-70E	26.3	N60-70E	29.0	N60-70E	82.7	N40-50W	10.0	N60-70E	29.8
N50-60E	10.5	N40-50W	12.1			N70-80E	9.4	N20-30E	10.5
N20-30E	9.6	N20-30E	12.0			N20-30E	8.1	N40-50W	10.5
N30-40W	9.6	N50-60E	10.9			N 0-10E	7.5	N50-60E	8.8
N40-50W	7.9					N10-20E	7.4	N30-40W	7.0
						N60-70E	7.2	N40-50E	5.3
						N50-60E	6.7	N 0-20E	4.0
						N40-50E	6.5	N70-80E	3.5
								N20-30W	3.5
								N50-60W	3.5

False Colour (IR) Frame No.82 Sun Azimuth 150° Sun Elevation 36°

N50-70E	43.2	N50-60E	28.6	N50-60E	62.0	N50-60E	11.0	N50-60E	23.8
N30-40W	9.5	N60-70E	20.0	N60-70E	30.3	N50-60W	10.5	N60-70E	17.5
N40-50W	7.8	N40-50W	9.5			N40-50W	10.2	N10-30E	15.8
N30-40E	6.9	N30-40W	7.7			N20-30E	10.0	N40-50W	7.9
						N 0-10W	8.5	N30-40E	6.3
						N10-20E	7.9	N30-40W	6.3
						N60-70E	7.7	N 0-10W	6.3
						N40-50E	6.7	N10-20W	4.8
						N30-40W	6.7		
						N30-40E	6.2		

False Colour(IR) Frame No.83 Sun Azimuth 147° Sun Elevation 29°

R.F.F.	%	R.F.L.	%	R.F.E.	%	R.Av.F.L.%		Int.Tech.%	
N50-60E	16.7	N60-70E	16.4	N30-40W	25.4	N60-70E	9.8	N60-70E	15.7
N30-40W	16.1	N40-50W	15.2	N40-50W	24.0	N20-30W	7.4	N30-50W	31.4
N40-50W	13.5	N30-40W	14.3	N50-60E	23.1	N40-50W	6.6	N50-60E	13.7
N60-70E	9.9	N50-60E	13.4	N60-70E	20.6	N70-80E	6.3	N40-50E	5.9
N10-30E	12.6					N50-60W	6.3		
N40-50E	6.3					N30-40E	6.1		
						N40-50E	5.9		
						N80-90W	5.7		
						N 0-10W	5.7		

False Colour(IR) Frame No.84 Sun Azimuth 147° Sun Elevation 29°

N50-60E	19.8	N50-60E	18.3	N50-60E	37.5	N 0-10W	9.6	N50-60E	22.5
N60-70E	15.5	N60-70E	16.2	N60-70E	22.8	N20-30W	8.1	N60-70E	15.0
N30-40W	15.0	N30-40W	16.1	N30-40W	21.9	N40-50W	8.1	N30-40W	15.0
N40-50W	11.6	N40-50W	14.1	N40-50W	13.0	N 0-10E	7.6	N40-50W	12.5
N40-50E	8.2					N30-40W	7.1	N40-50E	7.5
N10-20E	6.3					N50-60E	6.1	N 0-30E	15.0
						N50-60W	6.1	N 0-10W	5.0
						N20-30E	6.0		

False Colour(IR) Frame No.85 Sun Azimuth 150° Sun Elevation 35°

N30-40W	15.5	N60-70E	15.6	N60-70E	37.7	N10-20W	7.7	N60-70E	50.0
N60-70E	14.4	N30-40W	14.7	N30-40W	36.1	N80-90E	7.6	N30-40W	37.5
N40-50W	8.8	N40-50W	9.4	N40-50W	8.4	N 0-10E	6.7	N40-50W	12.5
N50-60E	7.4	N10-20W	7.8			N70-80W	6.2		
N40-50E	6.3	N50-60E	7.2			N60-70E	6.0		
N20-30E	6.0	N40-50E	5.7			N40-50W	5.9		
N30-40E	5.6	N20-30E	5.5			N60-70W	5.7		
N10-30W	11.2	N20-30W	5.3			N50-60E	5.4		
						N30-40W	5.3		
						N 0-10W	5.2		
						N20-30E	5.1		
						N50-60W	5.1		
						N20-30W	5.1		
						N40-50E	5.0		
						N70-80E	5.0		

False Colour(IR) Frame No.90 Sun Azimuth 120° Sun Elevation 55°

N50-70E	25.0	N60-70E	17.2	N60-70E	31.5	N60-70E	9.7	N60-70E	15.0
N30-50W	25.0	N40-50W	14.8	N40-50W	23.3	N40-50W	8.4	N30-50W	24.2
N 0-10E	10.9	N30-40W	12.4	N30-40W	16.3	N50-60W	8.2	N50-60E	11.2
N40-50E	7.8	N50-60E	12.1	N50-60E	15.6	N70-80W	7.6	N 0-10E	7.5
N20-30E	4.7	N40-50E	8.2	N 0-10E	4.9	N40-50E	7.4	N40-50E	7.5
N80-90W	4.7	N 0-10E	7.2	N40-50E	4.4	N80-90W	7.4	N80-90W	6.5
N 0-10W	4.7	N50-60W	5.4			N 0-10W	7.3	N50-60W	5.6
N50-60W	4.7					N30-40W	7.0	N 0-10W	4.7
						N50-60E	6.8		
						N10-20W	6.3		
						N10-20E	5.7		
						N20-30E	5.2		

False Colour(IR) Frame No.91 Sun Azimuth 130° Sun Elevation 51°

R.F.F.	%	R.F.L.	%	R.F.E.	%	R.Av.F.L.	%	Int.Tech.	%
N50-60E	15.5	N50-60E	15.6	N50-60E	39.5	N70-80E	7.2	N50-70E	34.0
N60-70E	15.1	N60-70E	14.5	N60-70E	33.3	N 0-10W	6.9	N 0-10E	8.5
N 0-10E	10.0	N 0-10E	8.9	N 0-10E	8.4	N40-50W	6.8	N40-50E	8.5
N40-50E	7.3	N40-50E	8.7			N40-50E	6.7	N30-40W	6.4
N30-40W	6.4	N30-40W	6.2			N20-30W	6.2		
N10-20E	5.5	N40-50W	6.0			N80-90E	6.1		
N30-40E	5.5	N80-90W	5.6			N50-60E	5.7		
N80-90W	5.5	N20-30W	5.5			N80-90W	5.7		
N40-50W	5.0	N10-20E	5.3			N50-60W	5.6		
N20-30W	5.0					N30-40W	5.5		
						N60-70E	5.4		
						N10-20E	5.4		
						N60-70W	5.3		
						N30-40E	5.1		

False Colour(IR) Frame No.92 Sun Azimuth 149° Sun Elevation 37°

N40-50W	13.9	N40-50W	14.7	N40-50W	32.7	N30-40E	6.8	N40-50W	16.4
N50-60E	13.3	N60-70E	12.2	N50-60E	21.1	N70-80E	6.8	N50-70E	26.8
N60-70E	12.0	N50-60E	12.1	N60-70E	19.6	N80-90E	6.6	N40-50E	10.4
N40-50E	10.1	N40-50E	9.8	N40-50E	10.7	N50-60W	6.5	N30-40W	7.5
N30-40W	8.9	N30-40W	8.2	N30-40W	6.4	N10-20E	6.3	N20-30E	6.0
N20-30E	6.3	N20-30E	6.6			N70-80W	6.2	N50-60W	4.5
N20-30W	6.3	N20-30W	5.5			W 0-10E	6.0	N20-30W	4.5
		N10-20E	5.0			N40-50W	5.8		
						N20-30E	5.7		
						N60-70E	5.6		
						N40-50E	5.3		
						N30-40W	5.1		
						N50-60E	5.0		
						N20-30W	4.8		
						N10-20W	4.7		

False Colour(IR) Frame No.93 Sun Azimuth 146° Sun Elevation 30°

N50-60E	23.3	N50-60E	21.7	N50-60E	49.1	N80-90E	10.2	N60-70	20.7
N60-70E	18.6	N60-70E	21.2	N60-70E	37.4	N10-20E	8.1	N50-60E	19.0
N30-40W	10.1	N30-40W	10.7	N30-40W	5.2	N40-50W	7.9	N30-40W	8.6
N40-50W	8.5	N40-50W	9.9			N60-70E	7.7	N40-50E	6.9
N40-50E	7.8					N50-60W	7.4	N20-30W	6.9
N20-30W	6.2					N20-30W	7.3	N40-60W	13.8
N 0-10W	6.2					N30-40W	7.2	N 0-10W	5.2
						N70-80W	6.9		
						N50-60E	6.3		
						N10-20W	5.7		

Table B

Dominant Trends of Some Rose Diagrams of Band 7 Images

Band 7	Frame No. 4			Sun Azimuth 124°		Sun Elevation 54°			
R.F.F.	%	R.F.L.	%	R.F.E.	%	R.Av.F.L.	%	Int.Tech.	%
N80-90W	14.3	N80-90W	11.8	N80-90W	34.7	N60-70W	12.0	N80-90W	29.4
N30-40W	10.5	N70-80E	10.2	N70-80E	12.2	N50-60W	8.2	N30-40W	11.8
N50-60E	8.6	N50-60W	8.9	N30-40W	10.4	N70-80E	8.0	N50-60E	11.8
N30-40E	7.6	N50-60E	7.9	N50-60E	9.3	N40-50W	8.0		
N70-80E	6.7	N30-40W	7.5	N50-60W	7.9	N20-30W	7.1		
N 0-10W	5.7	N40-50W	7.3			N60-70E	6.4		
N50-60W	5.7	N10-20W	6.4			N10-20W	5.8		
N10-20W	5.7	N 0-10W	6.3			N20-30E	5.1		
		N60-70E	5.8			N 0-10W	4.9		
		N30-40E	5.7			N50-60E	4.8		
		N 0-10E	5.0			N 0-10E	4.6		

Band 7	Frame No. 8			Sun Azimuth 105°		Sun Elevation 60°			
N20-30E	22.2	N20-30E	18.1	N20-30E	46.2	N40-50W	26.6	N20-30E	29.6
N80-90W	16.7	N40-50E	14.4	N10-20E	16.1	N70-80E	12.4	N40-50E	14.8
N10-20E	13.9	N10-20E	13.5	N40-50E	14.7	N60-70E	10.5	N80-90W	14.8
N40-50E	11.1	N60-70E	12.6	N80-90W	9.2	N40-50E	9.1	N10-20E	11.1
N50-70E	16.6	N40-50W	10.6	N60-70E	8.4	N10-20E	6.8	N60-70E	11.1
		N80-90W	9.3			N80-90E	6.4	N40-50W	7.4
						N30-40E	6.0		
						N50-60E	4.9		
						N 0-10E	4.6		

Band 7	Frame No. 12			Sun Azimuth 150°		Sun Elevation 35°			
N 0-10E	13.5	N10-20E	13.5	N 0-10E	27.0	N20-30W	13.1	N 0-10E	13.5
N10-20E	10.8	N 0-10E	12.4	N10-20E	26.0	N80-90W	10.3	N10-20E	12.0
N30-40W	10.8	N20-30W	10.7	N30-40W	14.4	N 0-20W	18.2	N30-40W	10.5
N20-30E	8.1	N30-40W	10.1	N20-30W	8.1	N60-70E	8.4	N20-30W	9.8
N40-60E	16.2	N80-90W	8.4	N80-90W	5.0	N10-20E	8.3	N80-90W	7.5
N40-50W	8.1	N10-20W	7.4			N70-80W	7.4	N10-20W	6.8
		N60-70E	6.8			N30-40E	6.9		
		N30-40E	5.6			N30-40W	6.2		
		N50-60E	5.6			N 0-10E	6.1		

Band 7 Frame No. 16 Sun Azimuth 140° Sun Elevation 35°

R.F.F.	%	R.F.L.	%	R.F.E.	%	R.Av.F.L.	%	Int.Tech.	%
N30-40W	18.3	N20-40W	33.6	N30-40W	36.2	N60-70E	10.4	N30-40W	18.6
N20-30W	16.7	N10-20E	13.4	N20-30W	32.6	N40-50W	10.1	N20-30W	16.9
N10-20E	11.7	N60-70E	12.4	N10-20E	14.6	N30-40E	9.4	N10-20E	15.3
N50-70E	16.6	N50-60E	7.9	N60-70E	8.9	N70-80W	9.2	N60-70E	11.9
		N30-40E	6.7			N10-20E	8.1	N50-60E	6.8
						N20-30W	7.1		
						N70-80E	7.0		
						N50-60E	6.6		
						N30-40W	6.5		
						N80-90W	5.4		
						N50-60W	5.2		
						N40-50E	5.1		

Band 7 Frame No. 20 Sun Azimuth 98° Sun Elevation 60°

N40-50E	13.6	N60-70E	13.3	N60-70E	28.6	N80-90W	12.7	N40-50E	14.3
N60-70E	12.3	N40-50W	12.0	N40-50E	25.2	N 0-10W	10.7	N60-70E	14.3
N 0-10E	8.6	N40-50E	11.9	N40-50W	14.0	N40-50W	9.8	N40-50W	11.1
N20-30E	8.6	N20-30E	8.6	N20-30E	8.5	N70-80W	7.9	N 0-10E	7.9
N50-60E	8.6	N 0-10E	7.6	N 0-10E	6.5	N60-70E	6.5	N20-30E	7.9
N10-20E	7.4	N 0-10W	6.6			N10-20W	6.3	N10-20E	6.3
N40-50W	7.4	N10-20W	6.4			N20-30E	6.0	N50-60E	6.3
N10-30W	12.4	N10-20E	6.3			N 0-10E	5.3	N 0-20W	12.6
		N50-60E	6.0			N40-50E	5.3		
						N10-20E	5.2		

Band 7 Frame No. 27 Sun Azimuth 110° Sun Elevation 61°

N60-70E	9.4	N30-40W	10.5	N30-40W	19.4	N60-70W	8.2	N60-70E	10.3
N20-30E	9.0	N60-70E	9.9	N60-70E	19.2	N30-40W	6.9	N30-40W	9.0
N30-40W	8.5	N20-30E	9.1	N20-30E	15.2	N50-60E	6.8	N20-30E	8.3
N10-20E	8.1	N10-20E	8.2	N10-20E	7.4	N40-50W	6.7	N10-20E	7.6
N80-90W	7.2	N40-50W	7.5	N80-90W	7.4	N70-80E	6.4	N80-90W	6.2
N 0-10E	6.3	N80-90W	7.1	N40-50W	7.2	N50-60E	5.9	N40-50W	6.2
N40-50W	6.3	N50-60E	6.0			N10-30E	11.4	N 0-10E	5.5
N30-40E	5.4	N 0-10E	5.7			N10-20W	5.6	N50-60E	5.5
N10-20W	5.4	N10-20W	5.4			N50-60W	5.6	N70-80E	5.5
N50-60E	4.9	N70-80E	5.1			N80-90W	5.5	N70-80W	4.8
N70-80W	4.9					N40-50E	5.3	N10-20W	4.8
						N 0-10E	5.0		

Band 7 Frame No. 31 Sun Azimuth 132° Sun Elevation 51°

R.F.F.	%	R.F.L.	%	R.F.E.	%	R.AV.F.L.	%	Int.Tech.	%
N60-70E	12.6	N10-20E	13.6	N10-20E	24.5	N10-20E	7.4	N10-20E	11.9
N50-60E	12.1	N50-60E	12.8	N50-60E	23.8	N30-40E	7.3	N50-60E	10.4
N10-20E	11.0	N60-70E	11.4	N60-70E	19.8	N20-30W	7.2	N60-70E	8.9
N30-40E	8.2	N30-40E	10.0	N30-40E	10.0	N50-60E	6.4	N30-40E	8.1
N40-50W	8.2	N40-50W	8.5	N40-50W	7.3	N70-80E	6.4	N 0-10E	7.4
N 0-10E	7.1	N 0-10E	7.5	N 0-10E	4.8	N 0-10E	6.3	N40-50W	6.7
N80-90W	7.1	N20-30W	6.5			N40-50W	6.3	N20-30W	6.7
N70-80E	5.5	N70-80E	5.9			N80-90E	5.9	N70-80E	5.9
N20-30W	5.5	N80-90W	5.5			N60-80W	11.8	N70-90W	10.4
						N40-50E	5.5		
						N60-70E	5.4		
						N80-90W	4.7		

Band 7 Frame No. 35 Sun Azimuth 147° Sun Elevation 29°

N50-60E	17.4	N50-60E	16.0	N50-60W	36.9	N50-60W	21.9	N50-60E	19.6
N60-70E	13.2	N60-70E	13.6	N60-70E	20.1	N70-80W	7.2	N60-70E	13.0
N10-20E	12.1	N10-20E	11.8	N10-20E	14.0	N30-40E	6.5	N10-20E	13.0
N30-40W	11.1	N30-40W	11.4	N30-40W	12.0	N70-80E	6.2	N40-50E	10.9
N40-50E	9.5	N40-50E	10.3	N40-50E	8.4	N40-50E	6.0	N30-40W	10.9
N 0-10E	7.9	N70-80W	8.3					N 0-10E	6.5
N70-80W	6.3	N20-30W	6.2					N70-80W	6.5
N20-30W	6.3	N 0-10E	5.7					N20-30W	6.5

Band 7 Frame No. 39 Sun Azimuth 150° Sun Elevation 36°

N50-60E	15.5	N50-60E	17.1	N50-60E	50.8	N 0-10W	10.5	N50-60E	19.1
N60-70E	10.7	N 0-10W	11.5	N 0-10W	10.1	N30-40E	8.1	N60-80E	17.6
N70-80E	8.7	N60-80E	17.2	N60-70E	8.8	N20-30W	7.8	N 0-10W	8.8
N10-20E	7.8	N20-30W	8.6	N70-80E	7.3	N50-60E	6.8	N10-20E	7.4
N40-50W	7.8	N40-50W	8.4			N40-50W	6.7	N30-40E	7.4
N20-30W	6.8					N40-50E	6.5	N40-50W	7.4
N 0-10W	6.8					N30-40W	6.5	N20-30W	7.4
N20-40E	11.6					N80-90E	6.4		
N10-20W	4.9					N 0-10E	5.5		
N80-90W	4.9					N10-20E	5.4		
						N70-80W	5.1		
						N60-70E	5.0		

Band 7 Frame No. 43 Sun Azimuth 139° Sun Elevation 36°

R.F.F.	%	R.F.L.	%	R.F.E.	%	R.AV.F.L.	%	Int.Tech.	%
N30-40W	15.1	N30-40W	17.2	N30-40W	56.0	N60-70W	7.7	N30-40W	22.9
N10-20E	8.3	N10-20E	9.2	N10-20E	8.8	N80-90E	7.0	N10-20E	8.6
N50-60E	8.3	N60-70E	8.6	N60-70E	7.1	N30-40W	6.4	N60-70E	8.6
N60-70E	7.8	N50-60E	8.1	N50-60E	6.8	N10-20E	6.2	N20-60E	22.8
N20-30E	6.8	N40-50W	7.0			N60-70E	6.2	N40-50W	5.7
N40-50W	6.8	N20-30E	6.7			N30-40E	6.1	N 0-10W	5.7
N20-30W	6.8	N20-30W	6.3			N40-50W	5.8		
N 0-10W	6.8	N 0-10W	6.1			N 0-10E	5.6		
N40-50E	6.3	N40-50E	5.7			N20-30E	5.6		
N70-80E	6.3					N50-60E	5.5		
N 0-10W	6.8					N40-50E	5.2		
						N20-30W	5.2		
						N50-60W	5.1		
						N 0-10W	5.0		

Band 7 Frame No. 48 Sun Azimuth 150° Sun Elevation 35°

N10-20E	15.1	N10-20E	13.5	N10-20E	42.7	N10-20W	6.7	N10-20E	17.5
N40-50E	9.8	N20-30E	9.7	N20-30E	13.5	N50-60E	6.6	N20-30E	9.5
N20-30E	9.3	N40-50E	8.5	N40-50E	10.8	N70-80E	6.5	N40-50E	9.5
N30-40W	8.3	N10-20W	8.5	N10-20W	7.5	N60-70W	6.4	N30-40W	7.9
N10-20W	6.8	N30-40W	7.6	N30-40W	7.4	N80-90E	6.1	N10-20W	7.9
N70-80E	6.3	N70-80E	6.6			N60-70E	6.0	N70-80E	6.3
N20-30W	5.9	N70-80W	6.4			N 0-10E	5.7	N70-80W	6.3
N70-80W	5.4	N60-70E	5.4			N20-30E	5.7		
		N50-60E	5.3			N50-60W	5.7		
						N70-80E	5.6		
						N 0-10W	5.3		
						N30-40E	5.1		
						N40-50W	5.1		
						N30-40W	5.0		

Band 7 Frame No. 52 Sun Azimuth 107° Sun Elevation 61°

N60-70E	13.6	N10-20E	14.3	N60-70E	30.9	N60-70W	10.0	N10-20E	18.8
N10-20E	12.7	N60-70E	13.9	N10-20E	30.5	N70-80W	6.9	N60-70E	18.8
N50-60E	12.3	N50-60E	11.8	N50-60E	20.2	N10-20E	6.4	N50-60E	15.6
N30-40W	7.5	N30-40E	7.0	N30-40E	4.1	N10-20W	6.2	N30-40E	6.3
N30-40E	7.0	N30-40W	6.7			N 0-10W	6.1	N30-50E	12.6
N 0-10W	6.1	N 0-10W	6.7			N20-30E	6.0		
N 0-10E	5.7	N80-90W	4.8			N60-70E	5.8		
N40-50W	5.3	N40-50W	4.6			N30-50E	11.4		
N80-90W	4.8	N10-20W	4.3			N20-30W	5.6		
N80-90W	5.6								

Band 7 Frame No. 57 Sun Azimuth 130° Sun Elevation 51°

R.F.F.	%	R.F.L.	%	R.F.E.	%	R.AV.F.L.	%	Int.Tech.	%
N60-70E	15.0	N60-70E	13.2	N60-70E	34.5	N60-70W	9.0	N10-20E	30.0
N10-20E	14.3	N10-20E	12.5	N10-20E	29.3	N 0-10E	8.2	N60-70E	25.0
N70-80E	8.6	N70-80E	9.3	N70-80E	9.8	N40-50E	7.7	N70-80E	10.0
N20-30W	7.1	N40-50E	8.0	N40-50E	4.8	N30-40E	6.6		
N50-60E	6.4	N50-60W	7.5	N50-60W	4.7	N50-60W	6.4		
N70-90E	12.8	N50-60E	7.0			N50-60E	6.0		
N50-60W	6.4	N20-30W	6.9			N70-80E	6.0		
		N80-90W	5.6			N20-30E	5.8		
		N70-80W	5.3			N20-30W	5.3		
						N40-50W	5.0		

Band 7 Frame No. 61 Sun Azimuth 149° Sun Elevation 37°

N10-20E	14.4	N50-60E	13.8	N50-60E	33.8	N 0-10E	7.5	N50-60E	14.1
N50-60E	14.4	N10-20E	13.3	N10-20E	31.4	N70-80E	7.3	N10-20E	12.9
N20-30E	8.3	N20-30E	9.2	N20-30E	8.7	N30-40W	6.5	N20-30E	9.4
N60-70E	8.3	N60-70E	8.4	N60-70E	7.2	N30-40E	6.4	N60-80E	14.2
N50-60W	6.6	N70-80E	7.1			N40-50W	6.4	N80-90W	5.9
N80-90W	6.1	N30-40E	6.3			N20-30E	6.3	N50-60W	5.9
N30-40E	5.5	N30-40E	6.3			N40-50E	6.1	N20-40W	11.8
N70-80E	5.5	N40-50W	6.2			N60-70W	5.8		
N20-30W	5.5	N50-60W	6.0			N60-70E	5.7		
N40-50W	5.5	N30-40W	5.8			N50-60E	5.4		
		N80-90W	5.6			N20-30W	5.3		
		N20-30W	5.1			N10-20E	5.2		
						N80-90W	5.2		
						N50-60W	5.1		
						N 0-10W	5.0		

Band 7 Frame No. 65 Sun Azimuth 146° Sun Elevation 30°

N60-70E	20.9	N60-70E	21.1	N60-70E	58.9	N40-50W	19.6	N60-70E	50.0
N10-20E	18.6	N10-20E	13.9	N10-20E	22.6	N20-30E	8.0	N10-20E	30.0
N50-60E	11.6	N30-40W	10.1			N30-40W	7.5	N50-60E	10.0
N30-40W	8.1	N50-60E	8.6			N20-30W	7.4	N30-40W	10.0
N10-20W	7.0	N40-50W	7.6			N50-60W	7.2		
N70-80E	5.8	N10-20W	7.2			N40-50E	6.8		
N70-80W	5.8	N70-80W	6.4			N70-80W	6.7		
						N10-20W	6.2		
						N60-70E	6.1		

Band 7 Frame No. 69 Sun Azimuth 138° Sun Elevation 37°

N50-60E	13.6	N50-60E	19.3	N50-60E	51.3	N70-80E	16.6	N50-60E	21.4
N10-20E	12.3	N20-30E	10.2	N10-20E	12.2	N80-90W	11.6	N10-20E	10.7
N70-80W	11.1	N70-80W	9.9	N70-80W	11.1	N50-60E	8.0	N20-30E	8.9
N20-30E	9.9	N80-90W	7.6	N20-30E	10.4	N30-40W	6.6	N70-80W	8.9
N30-40E	8.6	N60-70W	7.5			N20-30E	5.8	N30-40E	7.1
N60-70E	7.4	N30-40E	7.0			N40-50W	5.8	N60-70E	7.1
N10-20W	6.2	N30-40W	5.8			N60-70E	5.7	N70-80E	5.4
N30-40W	4.9					N20-30W	5.3	N80-90W	5.4
						N70-80W	5.0	N30-40W	5.4
						N 0-10W	5.0		

Table C

Dominant Trends of Some Rose Diagrams of Band 6 Images

Band 6 Frame No. 3
Sun Azimuth 124° Sun Elevation 54°

R.F.F.	%	R.F.E.	%	Int. Tech.	%
N50-60E	11.9	N50-60E	31.8	N50-60E	12.1
N70-80E	10.2	N70-80E	20.2	N30-40W	11.2
N20-30W	8.5	N30-40W	14.7	N70-80E	10.3
N40-50E	6.8	N80-90W	8.4	N80-90W	8.4
N70-90W	13.6			N 0-10E	6.5
				N40-50W	6.5
				N70-80W	5.6
				N50-60W	5.6
				N20-30W	5.6

Band 6 Frame No. 7
Sun Azimuth 105° Sun Elevation 60°

N20-30E	12.2	N20-30E	35.0	N20-30E	15.5
N30-40E	9.8	N80-90W	13.8	N80-90W	10.7
N80-90W	9.8	N30-40W	13.8	N30-40W	10.7
N50-60E	7.3	N70-80W	9.6	N30-40E	8.3
N70-90E	14.6	N30-40E	8.2	N70-80W	8.3
N70-80W	7.3	N50-60E	6.1	N50-60E	7.1
N30-40W	7.3			N70-80E	6.0
N10-20W	7.3			N10-20W	6.0

Band 6 Frame No. 11
Sun Azimuth 150° Sun Elevation 35°

N20-30W	21.6	N10-20E	58.5	N10-20E	23.0
N10-20E	18.9	N20-30W	28.3	N20-30W	20.3
N 0-10E	10.8	N60-70E	5.2	N60-70E	9.5
N30-40E	8.1			N 0-10E	8.1
N50-60E	8.1			N30-40E	6.8
N60-70E	8.1			N50-60E	6.8
				N30-40W	6.8
				N80-90W	5.4

Band 6 Frame No. 15
Sun Azimuth 140° Sun Elevation 35°

N30-40W	20.9	N30-40W	65.9	N30-40W	21.3
N50-60E	11.9	N50-60E	13.7	N50-60E	12.0
N10-30W	20.8			N10-30W	18.6
				N20-30E	6.7
				N60-70E	6.7
				N70-80W	5.3

Band 6 Frame No. 19
Sun Azimuth 98° Sun Elevation 60°

R.F.F.	%	R.F.E.	%	Int. Tech.	%
N10-20E	16.7	N40-50E	38.7	N40-50E	24.4
N40-50E	16.7	N10-20W	21.5	N10-20W	18.6
N60-70E	16.7	N40-50W	17.6	N40-50W	17.4
N40-50W	16.7	N60-70E	15.0	N60-70E	15.1
N10-20W	16.7			N10-20E	11.6
				N70-80E	7.0
				N30-40W	5.8

Band 6 Frame No. 26
Sun Azimuth 134° Sun Elevation 36°

N10-20E	7.8	N50-60E	12.6	N40-50E	9.2
N40-50E	7.8	N10-20E	11.7	N 0-10E	7.7
N60-80E	15.6	N40-50E	11.3	N50-70E	15.4
N50-60E	7.2	N70-80E	10.8	N80-90W	7.7
N80-90W	6.6	N60-70E	9.6	N10-20E	6.2
N30-40W	6.6	N 0-10E	7.5	N30-40E	6.2
N20-30W	6.0	N80-90W	6.2	N70-80W	6.2
N 0-10E	5.4	N30-40W	5.5	N30-40W	6.2
N70-80W	5.4	N70-80W	5.2		
N 0-10W	5.4	N20-30W	5.2		

Band 6 Frame No. 30
Sun Azimuth 132° Sun Elevation 51°

N10-20E	16.0	N60-70E	41.5	N10-20E	23.5
M60-70E	14.9	N10-20E	37.6	N60-70E	17.6
N30-40E	8.6	N30-40E	6.9	N30-40E	8.8

Band 6 Frame No. 34
Sun Azimuth 147° Sun Elevation 29°

N60-70E	14.1	N60-70E	37.2	N60-70E	14.2
N50-60E	12.2	N50-60E	31.2	N50-60E	13.0
N10-20E	9.3	N10-20E	10.2	N10-20E	9.5
N40-50W	7.8			N40-50W	7.1
N 0-10E	7.3			N20-30E	6.5
N40-50E	7.3			N70-80W	5.9
N70-80W	5.4			N 0-10E	5.3
				N40-50E	5.3
				N80-90W	5.3
				N20-30W	5.3

Band 6 Frame No. 38
Sun Azimuth 150° Sun Elevation 36°

R.F.F.	%	R.F.E.	%	Int. Tech.	%
N50-60E	17.4	N50-60E	59.7	N50-60E	18.1
N70-80E	9.6			N40-50W	8.3
N30-40E	7.8			N40-50E	8.3
N30-40W	7.8			N 0-10E	6.9
N40-50E	7.0			N30-40E	6.9
N40-50W	7.0			N70-80E	6.9
				N30-40W	6.9
				N 0-10W	6.9
				N20-30E	5.6
				N20-30W	5.6

Band 6 Frame No. 42
Sun Azimuth 139° Sun Elevation 36°

N30-40W	11.4	N30-40W	36.6	N30-40W	18.2
N20-30E	8.4	N20-30W	9.3	N20-30W	9.1
N60-70E	7.8	N50-60E	7.2	N 0-10W	9.1
N20-30W	7.8	N20-30E	6.7	N 0-10E	6.8
N40-50E	6.6			N20-30E	6.8
N 0-10E	6.0			N50-70E	13.6
N30-40E	6.0			N40-50W	6.8
N40-50W	6.0			N30-50E	9.0
N 0-10W	6.0			N50-60W	4.5
				N70-80E	4.5

Band 6 Frame No. 47
Sun Azimuth 150° Sun Elevation 35°

N40-50E	10.9	N40-50E	22.3	N 0-10E	16.0
N10-30E	20.6	N 0-10E	19.8	N40-50E	16.0
N 0-10E	9.2	N10-20E	13.9	N10-30E	24.0
N30-40E	6.9	N20-30E	11.6	N30-40E	8.0
N60-70E	5.7	N60-70E	9.3	N60-70E	8.0
N70-80W	5.7				
N70-80E	5.2				
N40-50W	5.2				
N20-30W	5.2				

Band 6 Frame No. 51
Sun Azimuth 107° Sun Elevation 61°

N60-70E	11.7	N60-70E	31.8	N60-70E	17.2
N10-20E	9.3	N10-20W	16.2	N10-20E	13.8
N10-20W	8.5	N10-20E	10.6	N10-20W	13.8
N50-60E	8.1	N30-40W	8.2	N40-60E	13.8
N40-50W	7.7	N40-50W	7.2	N30-50W	13.8
N30-40W	6.0				

Band 6 Frame No. 56
Sun Azimuth 130° Sun Elevation 51°

R.F.F.	%	R.F.E.	%	Int. Tech.	%
N10-20E	12.7	N10-20E	32.0	N10-20E	33.3
N60-70E	10.3	N60-70E	15.0	N60-70E	25.0
N80-90W	10.3	N40-50E	13.8	N40-50E	16.7
N40-50E	9.1	N80-90W	11.1	N80-90W	16.7
N70-80E	6.7	N50-60W	7.7	N50-60E	8.3
N50-60W	6.7	N50-60E	6.4		

Band 6 Frame No. 60
Sun Azimuth 149° Sun Elevation 37°

N60-70E	14.0	N60-70E	56.9	N60-70E	18.1
N20-30E	11.0	N20-30E	22.7	N20-30E	12.0
N 0-10E	7.5			N30-40E	6.0
N30-40E	7.5			N70-80E	6.0
N70-80E	7.5			N20-30W	6.0
N10-20E	6.0				
N20-30W	6.0				

Band 6 Frame No. 64
Sun Azimuth 146° Sun Elevation 30°

N60-70E	15.8	N60-70E	58.6	N60-70E	19.1
N20-30E	9.5	N40-50W	18.5	N40-50W	11.2
N40-50W	9.5			N20-30E	7.9
N10-20E	7.4			N20-30W	7.9
N50-60E	7.4			N10-20E	6.7
N30-40W	7.4			N30-50E	13.4
N30-50E	12.6				

Band 6 Frame No. 68
Sun Azimuth 138° Sun Elevation 37°

N50-70E	20.8	N50-60E	47.0	N50-60E	16.7
N30-40E	9.1	N60-70E	16.8	N80-90W	11.9
N70-90W	15.6	N80-90W	11.0	N60-70E	9.5
N10-20W	7.8			N50-60W	7.1
N10-30E	13.0			N10-20W	7.1
N 0-10W	6.5				

Table D

Dominant Trends of Some Rose Diagrams of Band 5 Images

Band 5 Frame No. 2
Sun Azimuth 124° Sun Elevation 54°

R.F.F.	%	R.F.E.	%	Int. Tech.	%
N40-50W	14.8	N40-50W	60.7	N40-50W	19.4
N80-90E	11.1	N80-90E	8.1	N 0-20E	16.2
N10-20E	11.1			N70-90E	16.2
N 0-10E	7.1			N20-30W	8.1
N60-80E	14.8			N50-70E	13.0
N80-90W	7.4			N80-90W	6.5
N20-30W	7.4				

Band 5 Frame No. 6
Sun Azimuth 105° Sun Elevation 60°

N10-30E	44.4	N20-30E	28.6	N10-20E	21.2
N40-70E	33.3	N10-20E	25.2	N20-30E	17.3
N70-80W	11.1	N70-80W	17.1	N70-80W	17.3
N 0-10W	11.1	N40-50E	11.0	N40-50E	13.5
		N 0-10W	9.5	N 0-10W	12.5
				N60-70E	9.6
				N50-60E	8.7

Band 5 Frame No. 10
Sun Azimuth 150° Sun Elevation 35°

R.F.F.	%	R.F.E.	%	Int. Tech.	%
N20-30W	25.0	N20-30W	80.9	N20-30W	31.3
N30-40W	12.5	N60-70E	7.0	N50-70E	20.8
N60-70E	12.5			N80-90W	8.3
N50-60W	9.4			N50-60W	8.3
N50-60E	9.4			N30-40W	8.3
				N10-20E	6.3

Band 5 Frame No. 14
Sun Azimuth 140° Sun Elevation 35°

N10-20E	12.5	N30-40W	18.4	N50-60E	14.5
N60-70E	12.5	N50-60E	18.4	N30-40W	11.3
N40-50W	12.5	N60-70E	17.8	N10-20E	9.7
N30-40W	11.1	N40-50W	16.4	N60-70E	9.7
N50-60E	9.7	N10-20E	12.3	N70-80W	9.7
N20-30W	6.9	N70-80W	9.3	N40-50W	9.7
N10-20W	5.6			N20-30W	6.5
N70-80W	5.6				

Band 5 Frame No. 18
Sun Azimuth 144° Sun Elevation 31°

R.F.F.	%	R.F.E.	%	Int. Tech.	%
N60-70E	20.4	N60-70E	43.9	N60-70E	17.8
N50-60E	13.0	N50-60E	23.9	N50-60E	16.4
N30-40E	11.1	N30-40W	14.4	N30-40W	12.3
N30-40W	11.1	N30-40E	7.1	N30-40E	8.2
N20-30W	9.3			N20-30W	8.2
				N 0-10W	8.2
				N70-80W	6.8

Band 5 Frame No. 24
Sun Azimuth 110° Sun Elevation 61°

N10-20E	12.8	N60-70E	26.1	N10-20E	15.2
N40-50E	11.8	N10-20E	24.2	N40-50E	13.0
N60-70E	11.3	N40-50E	17.1	N60-70E	13.0
N 0-10E	8.2	N30-40W	9.1	N30-40W	8.7
N30-40W	6.7			N 0-10E	6.5
				N50-60E	6.5
				N70-80W	6.5

Band 5 Frame No. 29
Sun Azimuth 132° Sun Elevation 51°

N50-60E	16.3	N50-60E	56.9	N50-60E	33.3
N10-20E	9.4	N60-70E	8.9	N 0-20E	22.2
N 0-10E	8.9			N60-80E	22.2
N60-70E	8.9			N80-90W	5.6
N50-60W	8.9			N30-60W	16.8
N70-80E	7.9				
N30-40W	7.9				
N80-90W	5.9				

Band 5 Frame No. 33
Sun Azimuth 147° Sun Elevation 29°

N60-70E	15.9	N60-70E	32.9	N10-20E	18.5
N10-20E	14.9	N10-20E	24.3	N60-70E	14.8
N30-40W	12.3	N30-40W	21.0	N30-40W	13.0
N40-50E	11.3	N50-60E	8.5	N40-60E	18.6
N50-60E	10.3			N30-40E	5.6
N 0-10E	5.6			N70-80W	5.6
N30-40E	5.6				
N70-80W	5.6				

Band 5 Frame No. 37
Sun Azimuth 150° Sun Elevation 36°

R.F.F.	%	R.F.E.	%	Int. Tech.	%
N50-60E	12.8	N50-60E	28.7	N50-60E	13.2
N30-40E	12.1	N30-40E	22.5	N30-40E	11.6
N60-70E	11.3	N60-70E	16.2	N60-70E	9.9
N40-50E	9.2	N40-50E	9.2	N40-50E	9.1
N 0-10E	6.4	N30-40W	6.9	N30-40W	8.3
N30-40W	6.4			N 0-10W	6.6
N20-30E	5.7			N20-30W	5.8
N40-50W	5.7			N10-30E	10.0
N 0-10W	5.7			N80-90W	5.0

Band 5 Frame No. 41
Sun Azimuth 139° Sun Elevation 36°

N60-70E	12.5	N60-70E	36.1	N60-70E	14.8
N10-20E	9.6	N40-50W	14.4	N40-50W	9.9
N30-50W	19.2	N30-40W	12.8	N10-20E	8.6
N 0-20W	16.2	N50-60E	8.3	N50-60E	8.6
N20-30E	7.4	N10-20E	8.0	N30-40W	8.6
N50-60E	6.6			N 0-10W	7.4
				N20-30E	7.4
				N10-20W	6.2

Band 5 Frame No. 45
Sun Azimuth 150° Sun Elevation 36°

N10-20E	12.9	N10-20E	39.1	N10-20E	14.8
N30-40W	9.3	N30-40W	26.0	N30-40W	14.8
N40-50E	7.1	N50-60E	5.9	N10-20W	7.4
N30-40E	6.4			N 0-10E	5.6
N50-60E	6.4			N30-70E	22.4
N10-20W	6.4			N60-70W	5.6

Band 5 Frame No. 50
Sun Azimuth 107° Sun Elevation 61°

N50-60E	14.7	N50-60E	33.2	N50-60E	27.8
N10-20E	12.0	N10-20E	26.0	N10-20E	22.2
N30-40W	10.1	N30-40W	12.6	N30-40W	16.7
N60-70E	8.5	N40-50W	9.2	N80-90W	11.1
N40-50W	8.1	N60-70E	6.7	N40-50W	11.1

Band 5 Frame No. 55
Sun Azimuth 130° Sun Elevation 51°

N50-60E	16.7	N50-60E	62.2	N50-60E	43.8
N10-20E	11.1	N40-50E	9.3	N10-20E	18.8
N 0-10E	7.9	N10-20E	8.4	N 0-10E	12.5
N40-50E	7.9				

Band 5 Frame No. 59
Sun Azimuth 149° Sun Elevation 37°

R.F.F.	%	R.F.E.	%	Int. Tech.	%
N70-80E	13.6	N70-80E	43.3	N70-80E	21.9
N50-60E	11.2	N50-60E	23.8	N50-60E	15.6
N20-30E	10.7	N20-30E	8.2	N20-30E	12.5
N30-40E	9.5	N30-40W	7.7	N30-40E	9.4
N30-40W	8.3			N10-20E	6.3
				N60-70E	6.3
				N70-80W	6.3
				N30-40W	6.3

Band 5 Frame No. 63
Sun Azimuth 146° Sun Elevation 30°

N10-20E	12.4	N10-20E	36.5	N10-20E	13.5
N30-40E	10.5	N60-70E	14.1	N30-40W	9.0
N50-60E	8.6	N30-40E	11.1	N30-40E	8.1
N60-70E	7.6	N50-60E	8.3	N50-70E	16.2
N40-50W	7.6	N50-60W	7.0	N50-60W	8.1
				N20-30W	6.3

Band 5 Frame No. 67
Sun Azimuth 138° Sun Elevation 37°

N50-60E	16.7	N50-60E	74.9	N50-60E	20.8
N10-20E	7.6			N30-40E	7.5
N30-40E	7.6			N60-70W	7.5
N30-40W	7.6			N80-90W	7.5

Table E

Dominant Trends of Some Rose Diagrams of Band 4 Images

Band 4 Frame No. 1
Sun Azimuth 124° Sun Elevation 54°

R.F.F.	%	R.F.E.	%	Int. Tech.	
N60-70E	15.9	N60-70E	51.3	N60-70E	19.2
N20-30W	13.6	N20-30W	19.5	N20-30W	14.1
N30-40W	11.4	N80-90W	11.4	N80-90W	10.3
N80-90W	9.1			N30-40W	9.0
N 0-10E	6.8			N70-80W	7.7
N10-40E	13.5			N40-50W	6.4
N70-80E	4.5			N70-80E	5.1
N70-80W	4.5				
N40-60W	9.0				
N10-20W	4.5				

Band 4 Frame No. 5
Sum Azimuth 105° Sun Elevation 60°

N80-90W	17.6	N80-90W	35.6	N80-90W	18.7
N20-30E	11.8	N40-50W	27.9	N40-50W	18.7
N50-60E	11.8	N20-30E	22.5	N20-30E	15.4
N40-50W	11.8	N50-60E	6.5	N50-60E	9.9
				N30-40W	7.7
				N 0-10W	6.6

Band 4 Frame No. 9
Sun Azimuth 150° Sun Elevation 35°

N10-20E	19.5	N10-20E	64.5	N10-20E	26.5
N10-20W	12.2	N10-20W	12.8	N10-20W	11.8
N20-30W	9.8			N60-70E	8.8
N30-40E	7.3			N30-40W	8.8
N50-70E	14.6			N30-40E	5.9
				N50-60E	5.9
				N50-60W	5.9
				N20-30W	5.9

Band 4 Frame No. 13
Sun Azimuth 150° Sun Elevation 35°

N30-40W	23.8	N30-40W	82.6	N30-40W	28.9
N10-20E	11.1			N50-60E	10.5
N20-30W	9.5			N 0-10E	7.9
N 0-10E	7.9			N20-30W	7.9

Band 4 Frame No. 17
Sun Azimuth 98° Sun Elevation 60°

R.F.F.	%	R.F.E.	%	Int. Tech.	%
N20-30W	14.1	N50-60E	28.8	N50-60E	13.8
N50-60E	12.0	N20-30W	26.9	N20-30W	13.0
N50-60W	10.9	N60-70E	12.7	N50-60W	10.1
N60-70E	9.8	N50-60W	11.5	N60-70E	9.4
N10-20E	8.7	N10-20E	6.6	N10-20W	8.7
				N10-20E	8.0
				N20-30E	7.2
				N70-80W	5.1

Band 4 Frame No. 23
Sun Azimuth 110° Sun Elevation 61°

N50-60E	16.0	N50-60E	40.6	N50-60E	17.7
N40-50W	12.2	N10-20E	26.5	N10-20E	11.3
N10-20E	10.7	N40-50W	18.2	N40-50W	11.3
N60-70E	9.9	N60-70E	7.2	N60-70E	9.7
N20-30W	6.1			N20-30E	4.8
				N70-80E	4.8
				N80-90W	4.8
				N10-30W	9.6
				N50-60W	4.8

Band 4 Frame No. 28
Sun Azimuth 132° Sun Elevation 51°

N10-20E	16.1	N10-20E	40.2	N10-20E	20.5
N70-80E	11.7	N70-80E	17.8	N70-80E	11.4
N50-60E	8.8	N50-60E	9.0	N40-70E	20.4
N40-50E	8.0	N40-50E	7.9	N10-30W	13.6
N10-20W	8.0			N70-80W	6.8

Band 4 Frame No. 32
Sun Azimuth 147° Sun Elevation 29°

N60-70E	16.8	N50-60E	33.7	N60-70E	27.8
N50-60E	15.2	N60-70E	33.2	N50-60E	22.2
N10-20E	12.0	N10-20E	16.5	N10-20E	16.7
N 0-10E	9.4	N40-50W	3.5	N 0-10E	5.6
N40-50E	8.4			N70-90W	11.2
N30-50W	12.6			N30-50W	11.2

Band 4 Frame No. 36
Sun Azimuth 150° Sun Elevation 36°

R.F.F.	%	R.F.E.	%	Int. Tech.	%
N50-70E	21.2	N50-60E	19.3	N60-70E	12.7
N40-50E	9.3	N60-70E	16.3	N50-60E	11.1
N 0-20E	17.2	N40-50E	15.4	N40-50E	9.5
N30-40E	7.3	N10-20E	9.5	N 0-10E	7.9
N20-30E	6.6	N 0-10E	8.9	N30-40E	7.9
N20-30W	6.6	N30-40E	8.1	N30-40W	7.9
N30-40W	6.0	N20-30W	6.7	N10-20E	6.3
N80-90E	5.3	N30-40W	6.5	N70-80E	6.3
				N20-30W	6.3

Band 4 Frame No. 40
Sun Azimuth 139° Sun Elevation 36°

N20-30E	15.1	N20-30E	35.9	N20-30E	26.9
N30-40W	13.0	N30-40W	34.2	N30-40W	23.1
N 0-10W	8.2	N60-70E	5.9	N 0-10E	7.7
N60-70E	7.5	N 0-10W	5.5	N60-80E	15.4
				N 0-10W	7.7

Band 4 Frame No. 44
Sun Azimuth 150° Sun Elevation 35°

N20-30E	10.1	N10-20E	20.8	N40-50E	12.9
N40-50E	10.1	N40-50E	20.2	N10-20E	11.3
N20-30W	10.1	N20-30W	13.5	N20-30W	11.3
N10-20E	9.5	N70-80W	9.9	N20-30E	8.1
N70-80W	8.3	N20-30E	9.0	N50-60E	8.1
N10-20W	7.1			N70-80W	8.1
N50-60E	6.5			N30-40W	6.5
				N10-20W	6.5

Band 4 Frame No. 49
Sun Azimuth 107° Sun Elevation 61°

N40-50W	10.6	M40-50W	22.5	N10-20E	16.7
N10-20E	10.1	N40-50E	16.8	N40-50W	16.7
N 0-10E	9.6	N10-20E	12.3	N40-50E	12.5
N60-70E	9.1	N 0-10E	11.5	N60-70E	12.5
N40-50E	8.7	N80-90W	11.0	N80-90E	12.5
N80-90W	8.7	N60-70E	8.9	N 0-10E	8.3
N50-60E	7.7			N10-20W	8.3
N30-40E	6.7				
N10-20W	6.7				

Band 4 Frame No. 54
Sun Azimuth 130° Sun Elevation 51°

R.F.F.	%	R.F.E.	%	Int. Tech.	%
N50-60E	11.8	N50-60E	30.2	N50-60E	13.1
N70-80E	10.1	N70-80E	17.7	N70-80W	13.1
N60-70E	8.4	N50-60W	13.2	N10-20E	8.2
N50-60W	8.4	N60-70E	9.6	N60-70E	8.2
N 0-10E	7.6	N10-20E	8.0	N50-60W	8.2
N30-40E	7.6			N 0-10E	6.6
N70-80W	5.9			N30-40E	6.6
N30-40W	5.9			N30-40W	6.6

Band 4 Frame No. 58
Sun Azimuth 149° Sun Elevation 37°

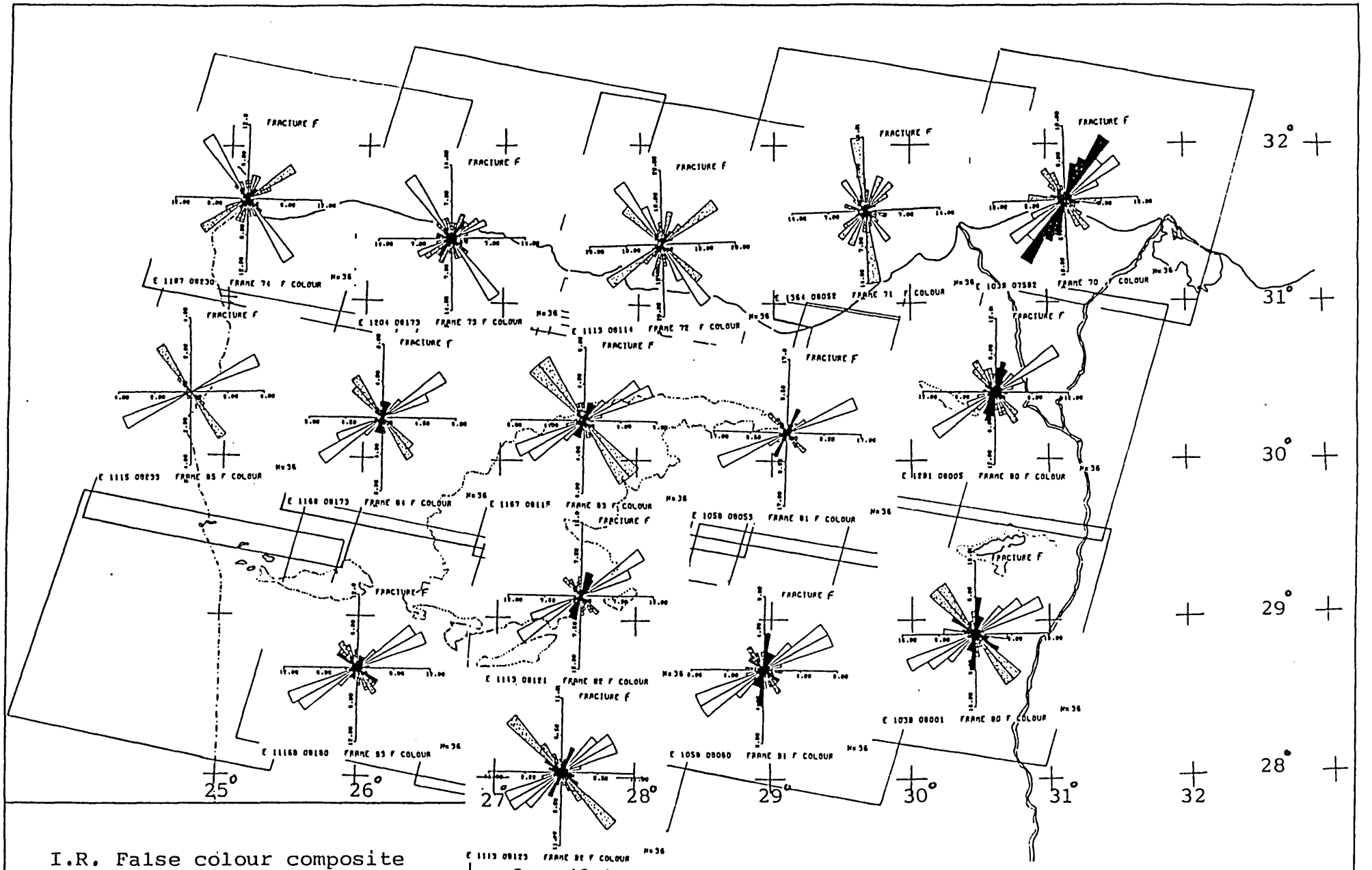
N70-80E	13.0	N70-80E	32.8	N70-80E	16.7
N10-20E	11.4	N10-20E	25.1	N10-20E	12.5
N30-40E	8.9	N20-30E	9.5	N20-30E	8.3
N20-30W	8.1	N40-50W	8.2	N30-40E	6.9
N 0-10E	6.5			N40-50W	6.9
N20-30E	7.3			N20-30W	6.9
N40-50W	7.3			N 0-10E	5.6
N80-90W	6.5			N50-70E	11.2
N30-40W	6.5			N80-90W	5.6
N60-70E	5.7				

Band 4 Frame No. 62
Sun Azimuth 146° Sun Elevation 30°

N60-70E	20.0	N60-70E	71.7	N60-70E	25.4
N10-20E	13.3	N50-60E	11.2	N50-60E	11.1
N50-60E	12.0			N10-20E	9.5
N40-50W	9.3			N40-50W	7.9
				N70-80E	6.3
				N30-40W	6.3
				N 0-10W	6.3

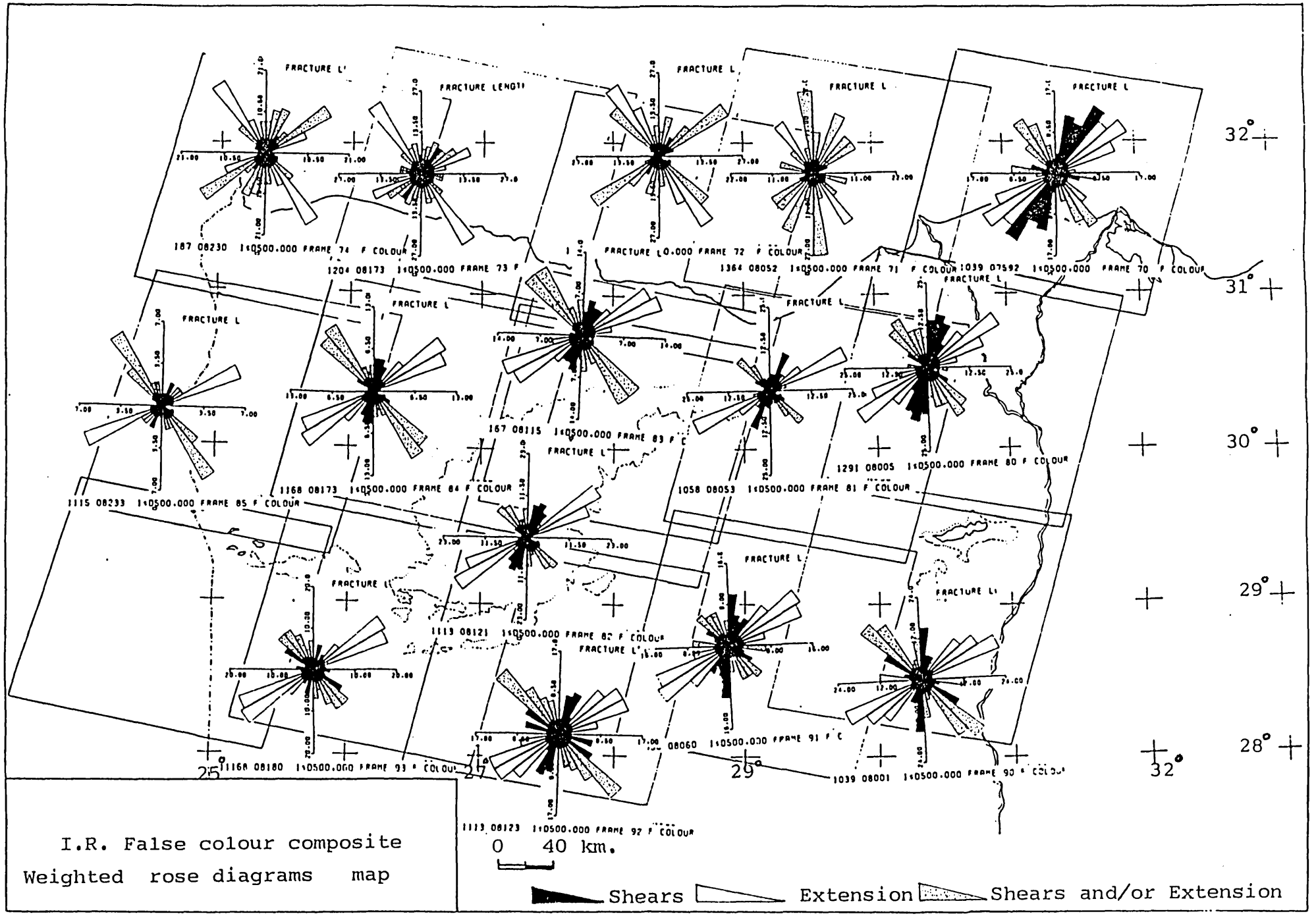
Band 4 Frame No. 66
Sun Azimuth 138° Sun Elevation 37°

N60-70E	16.9	N60-70E	73.9	N60-70E	22.9
N20-30E	11.7			N20-30E	10.0
N50-60E	10.4			N50-60E	8.9
N10-20E	9.1			N70-80E	7.1
N 0-10W	7.8			N40-50W	7.1
N40-50W	6.5			N20-30W	7.1
N20-30W	6.5			N10-20E	5.7
				N70-80E	5.7

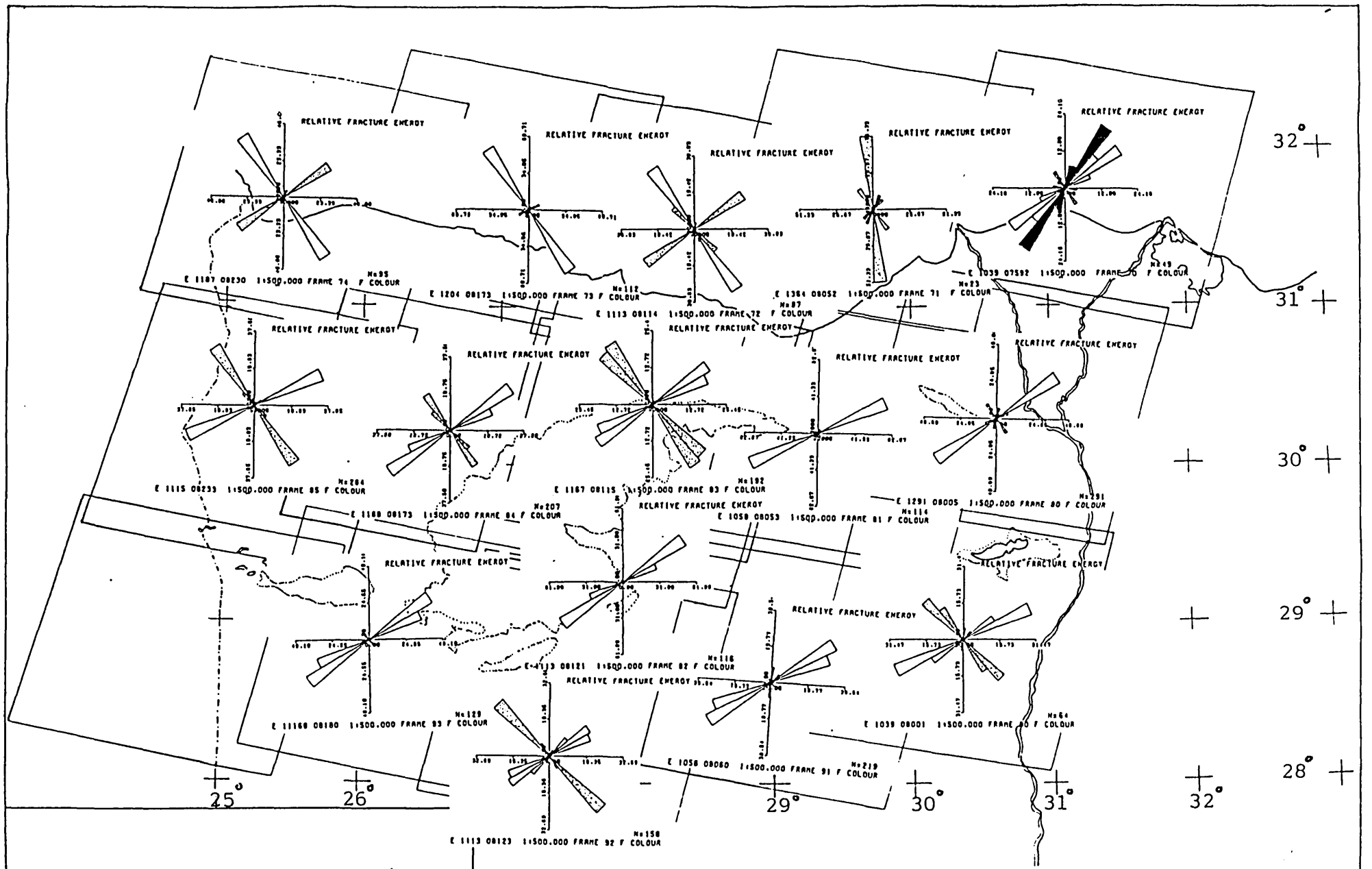


I.R. False colour composite

Integrated rose diagrams map

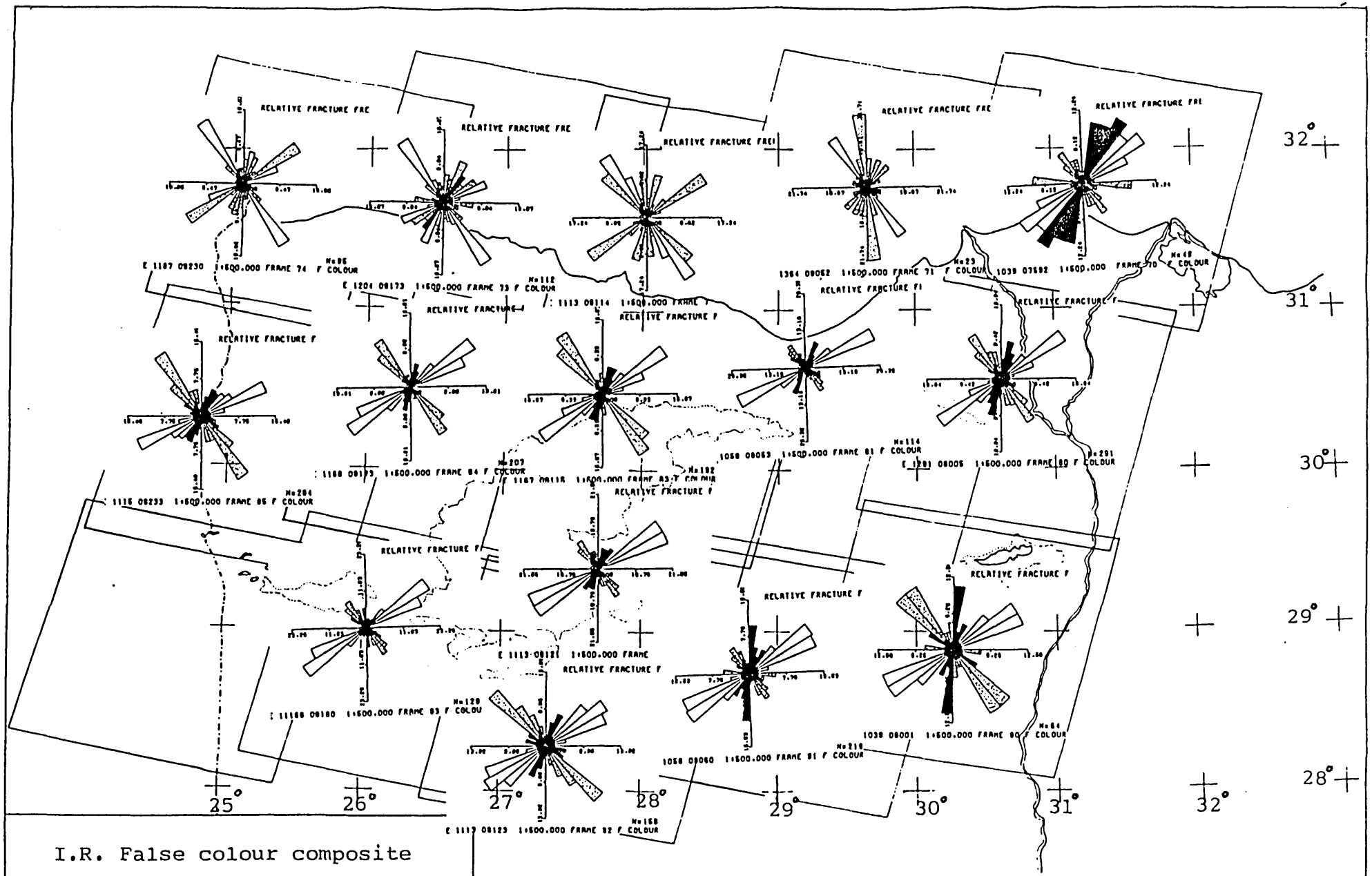


I.R. False colour composite
Weighted rose diagrams map



I.R. False colour composite

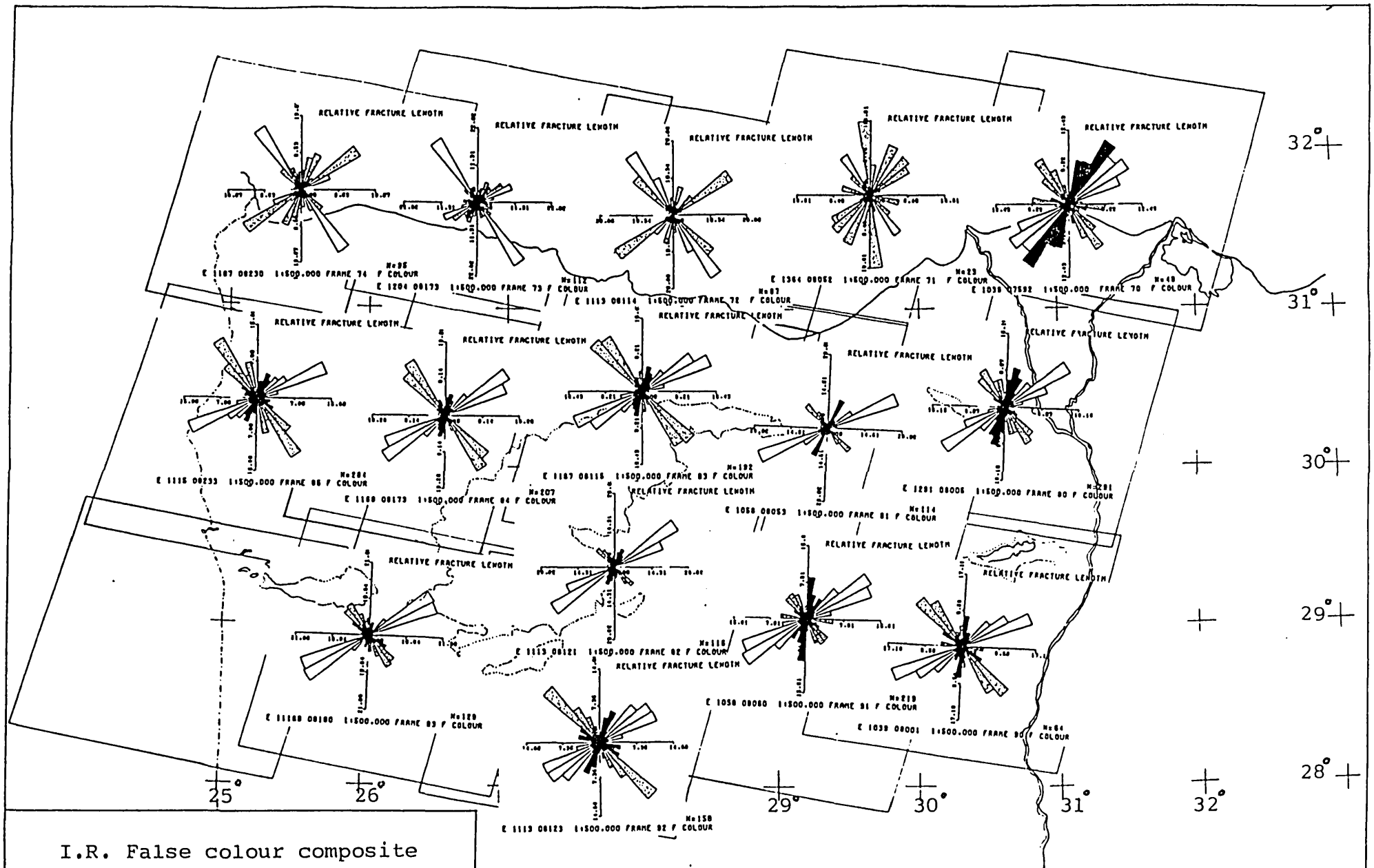
Relative fracure energy rose diagrams map.



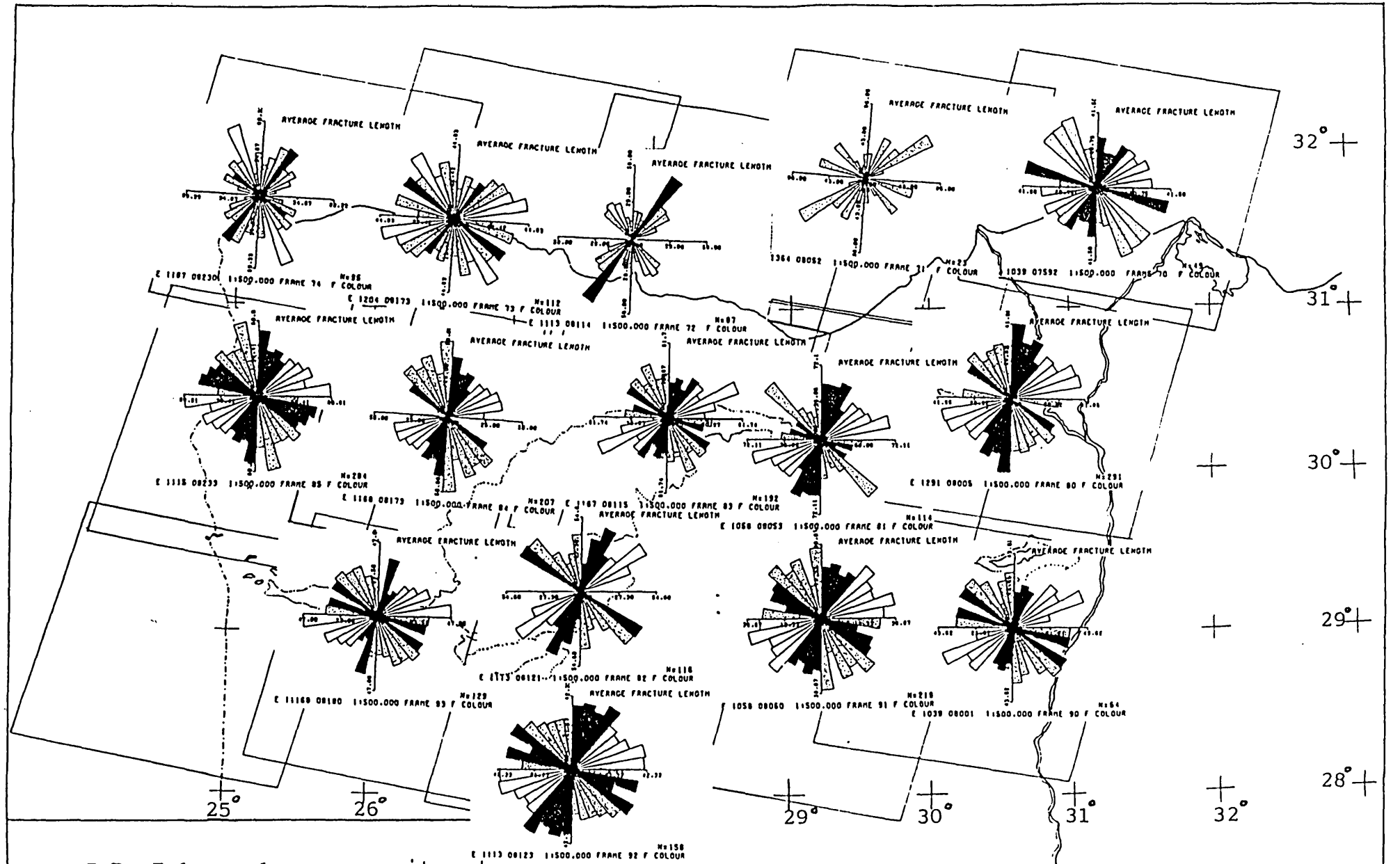
I.R. False colour composite
Relative fracture frequency rose diagrams map.

0 40 km.

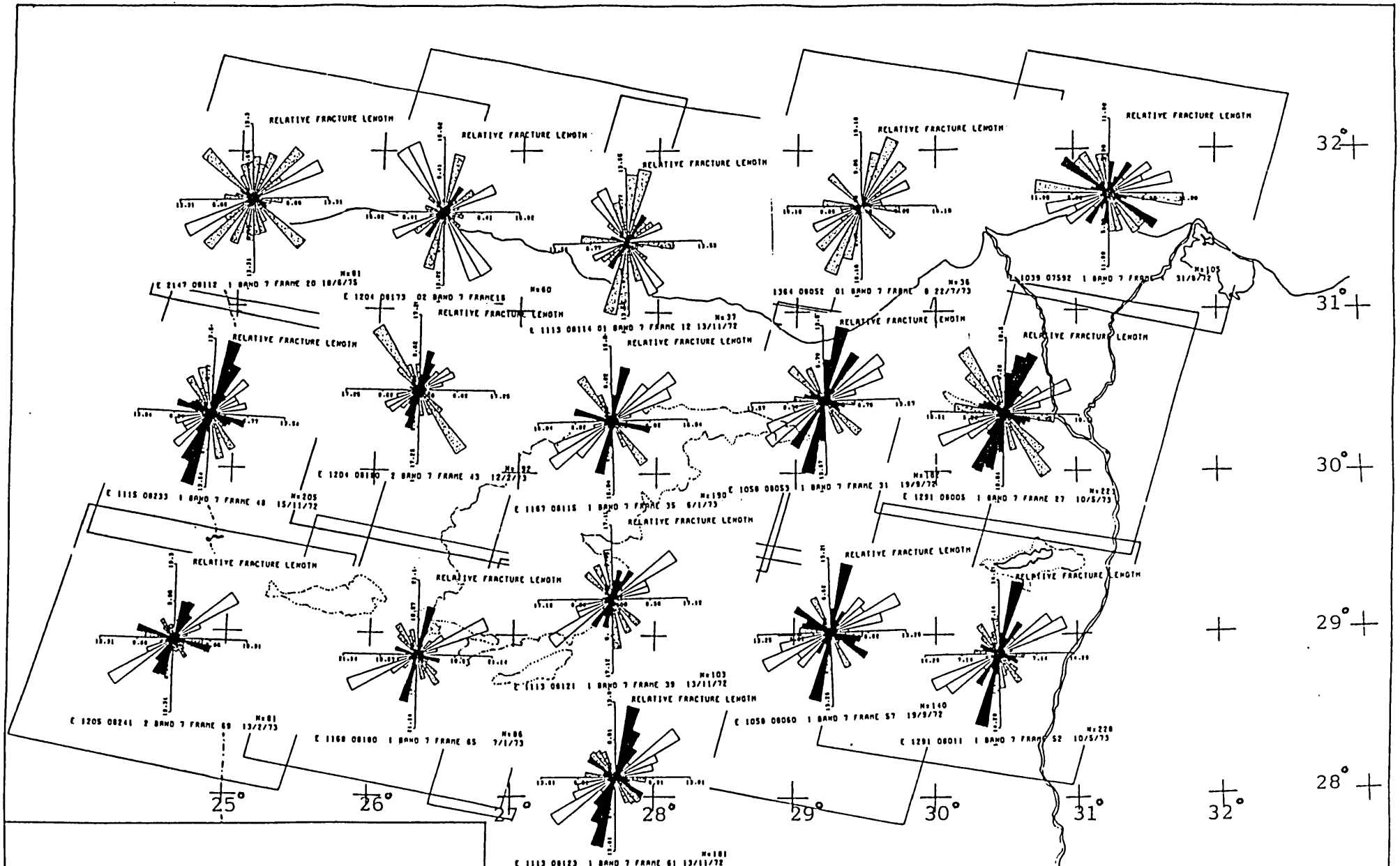
Shears Extension Shears and/or Extension



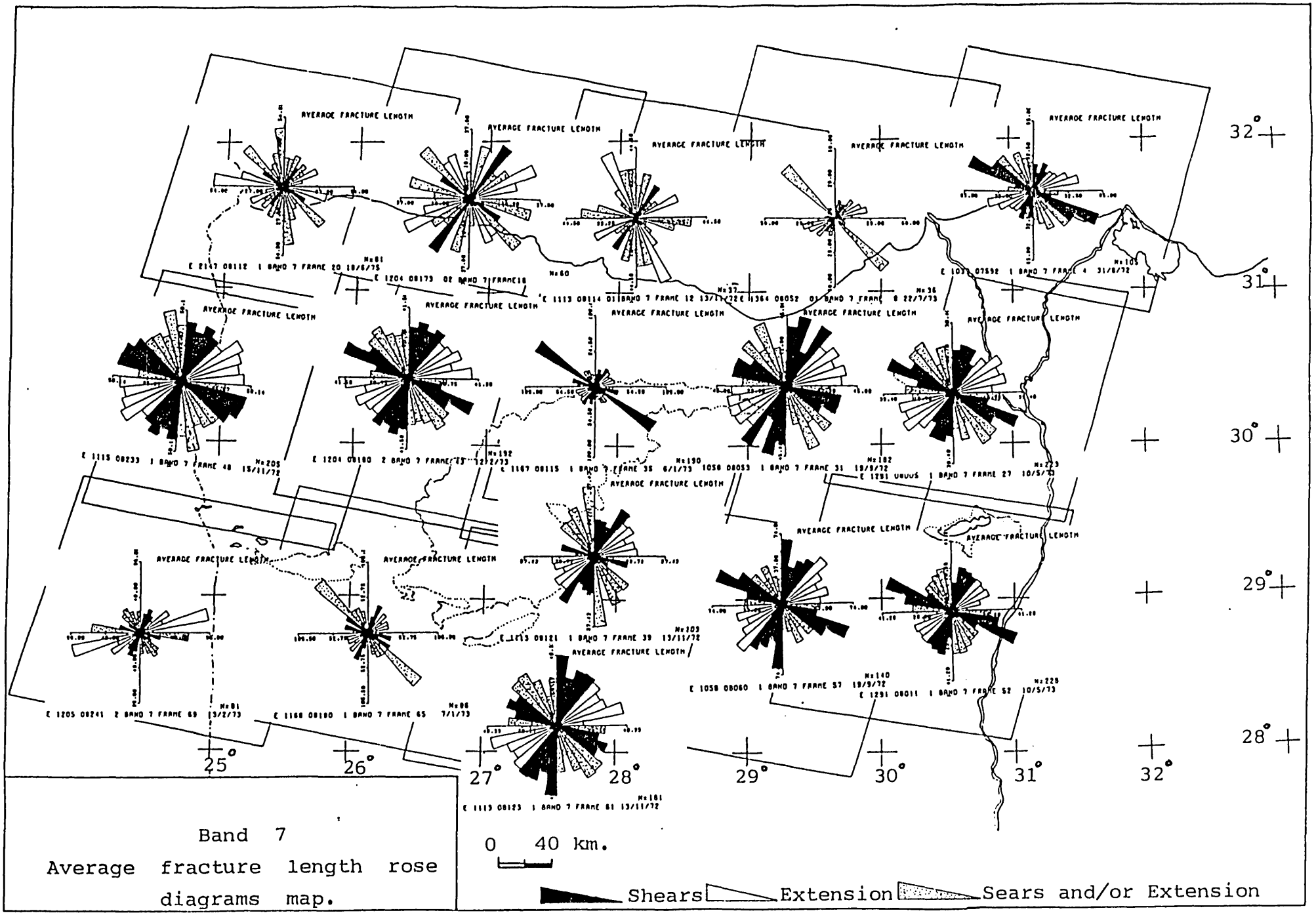
I.R. False colour composite
Relative fracture length rose
diagrams map.



I.R. False colour composite Average fracture length rose diagrams map.

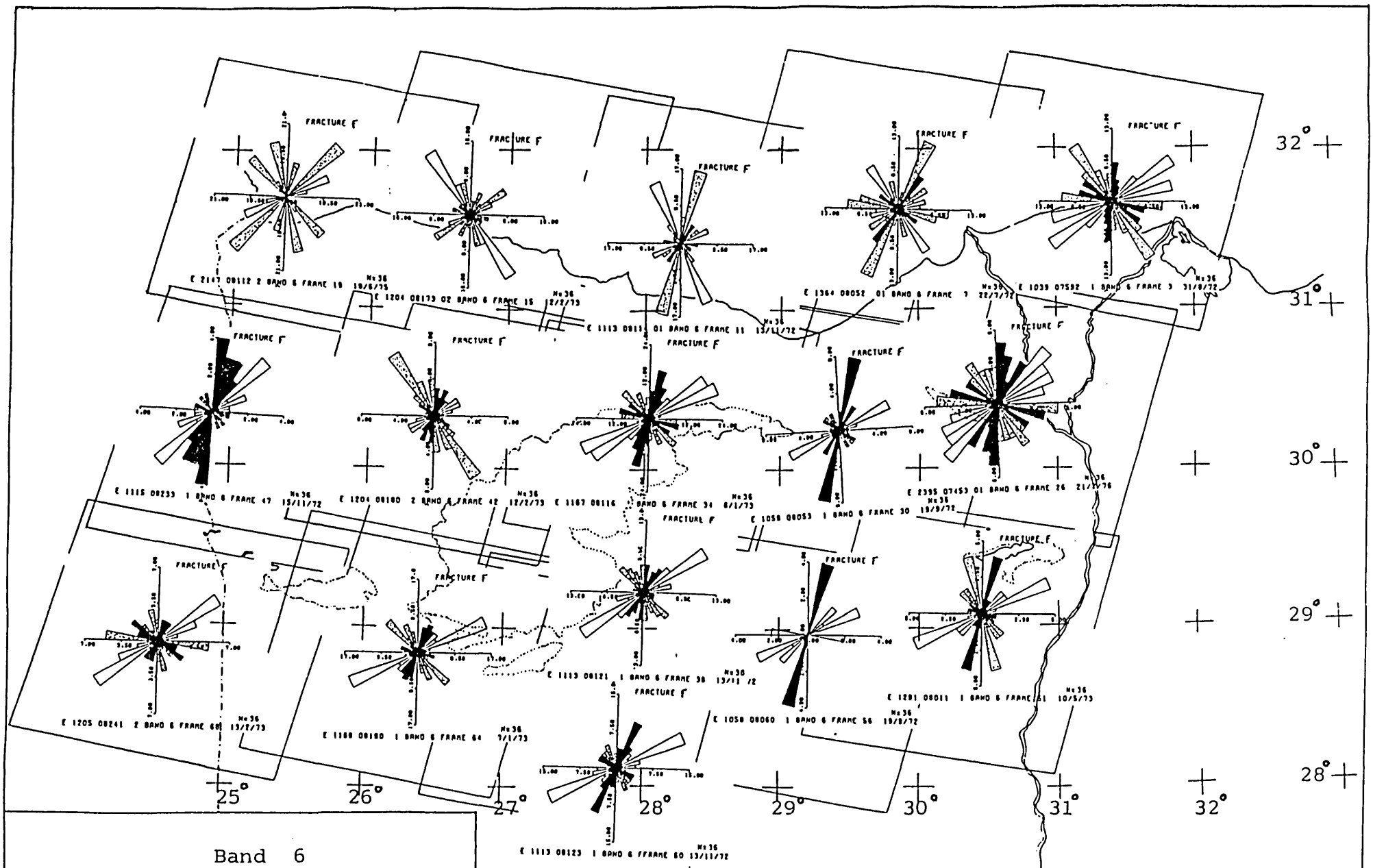


Band 7
Relative fracture length rose diagrams map.



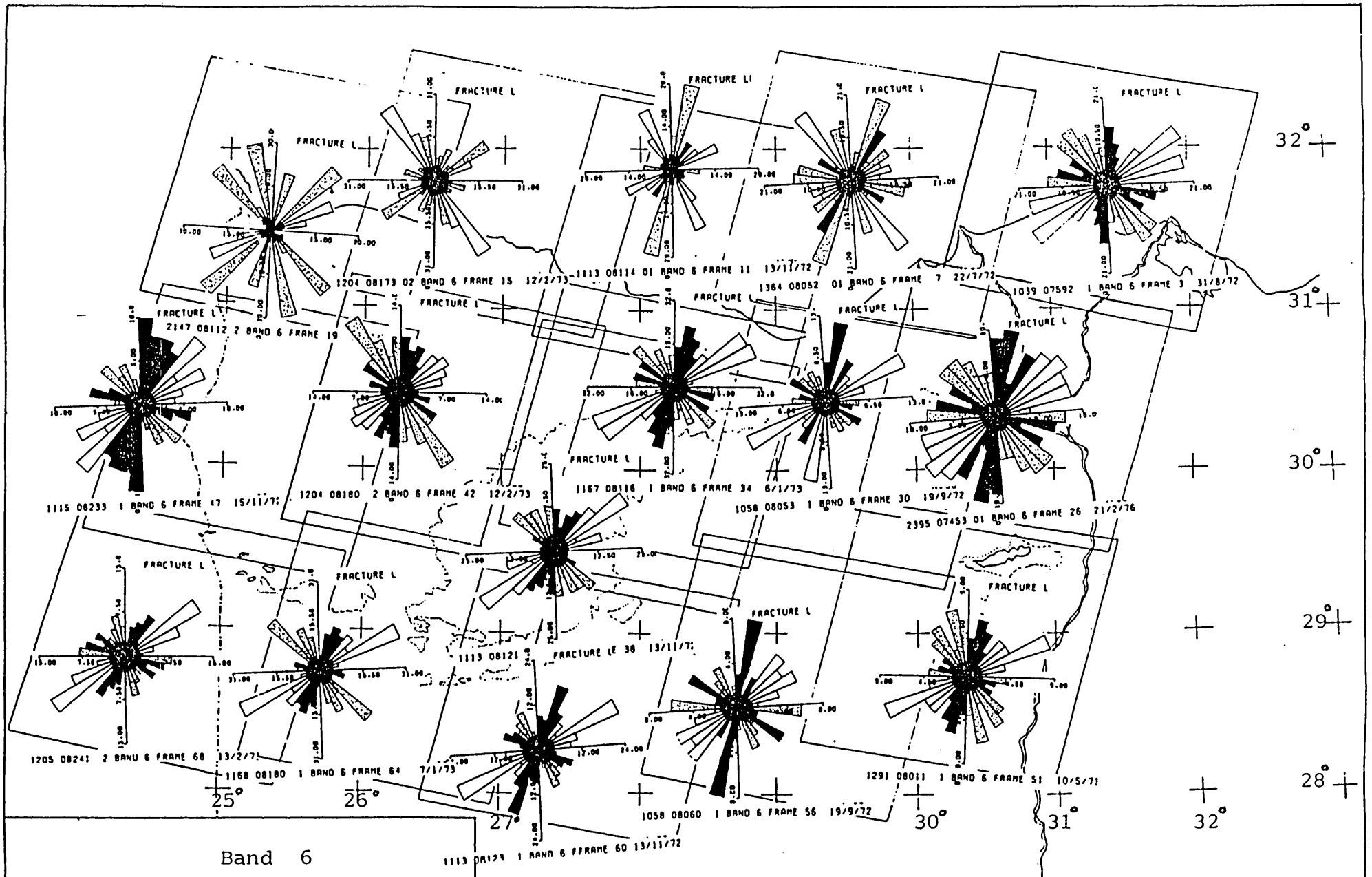
Band 7

Average fracture length rose diagrams map.



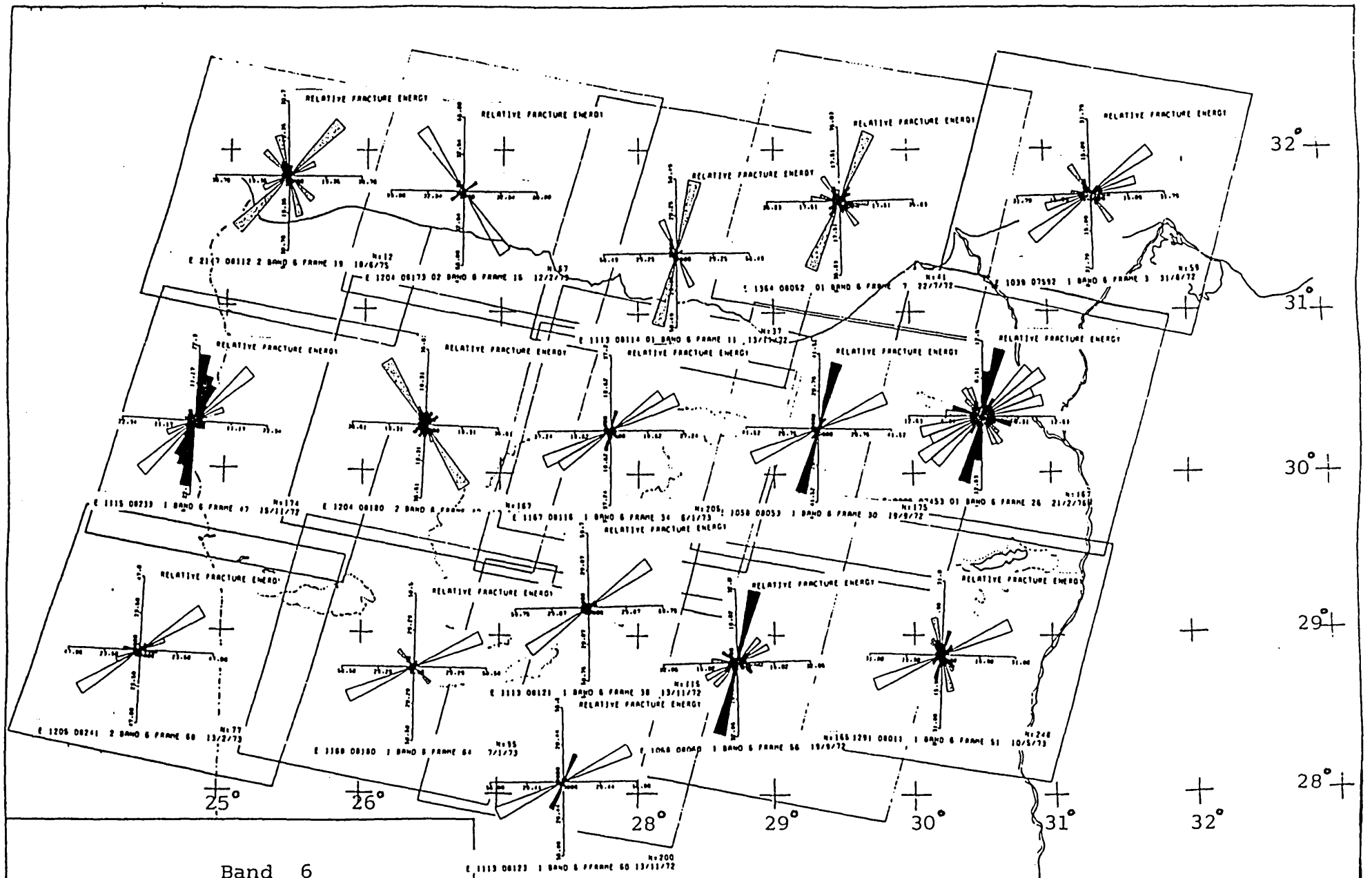
Band 6

Integrated rose diagrams map.



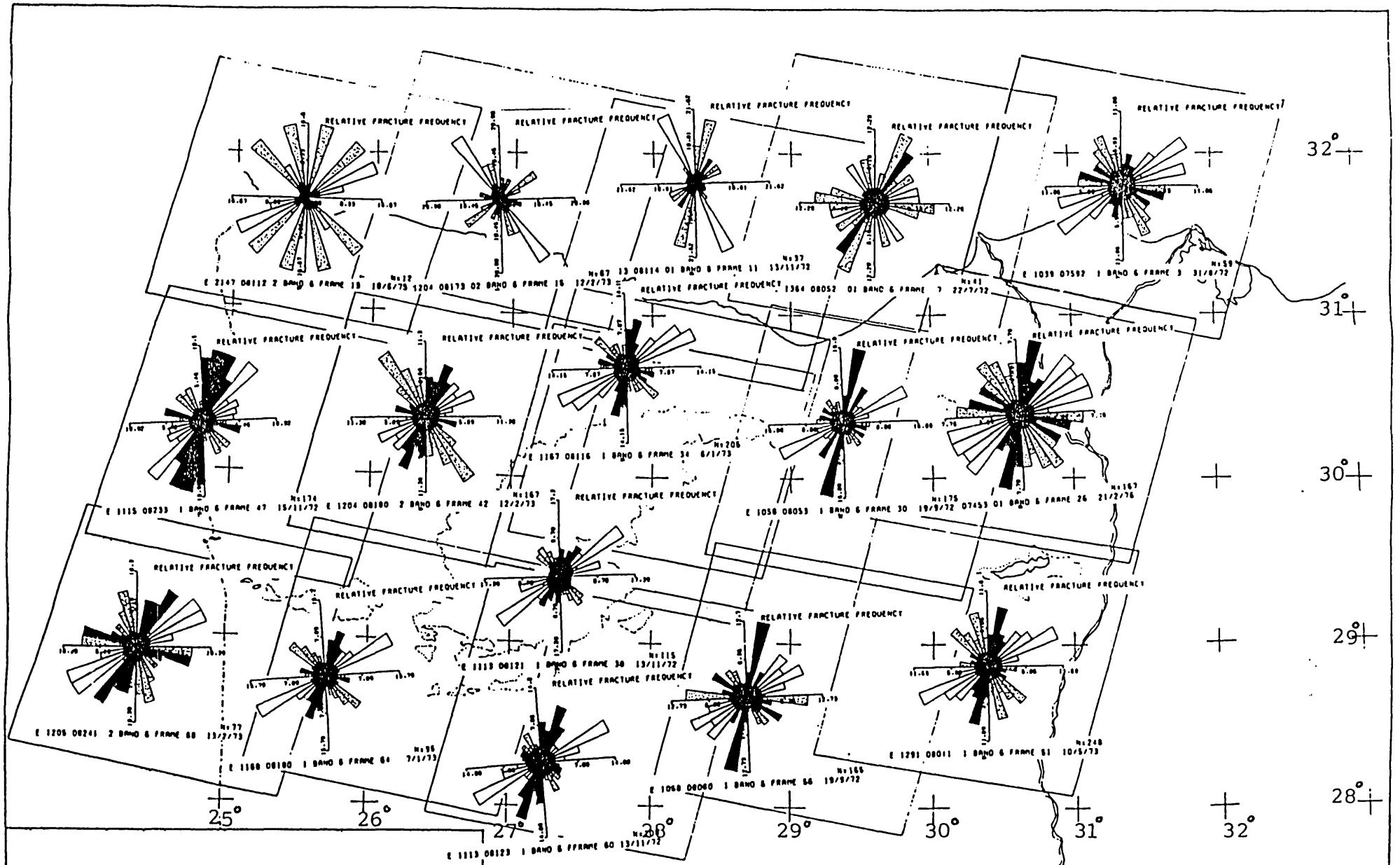
Band 6

Weighted rose diagrams map.



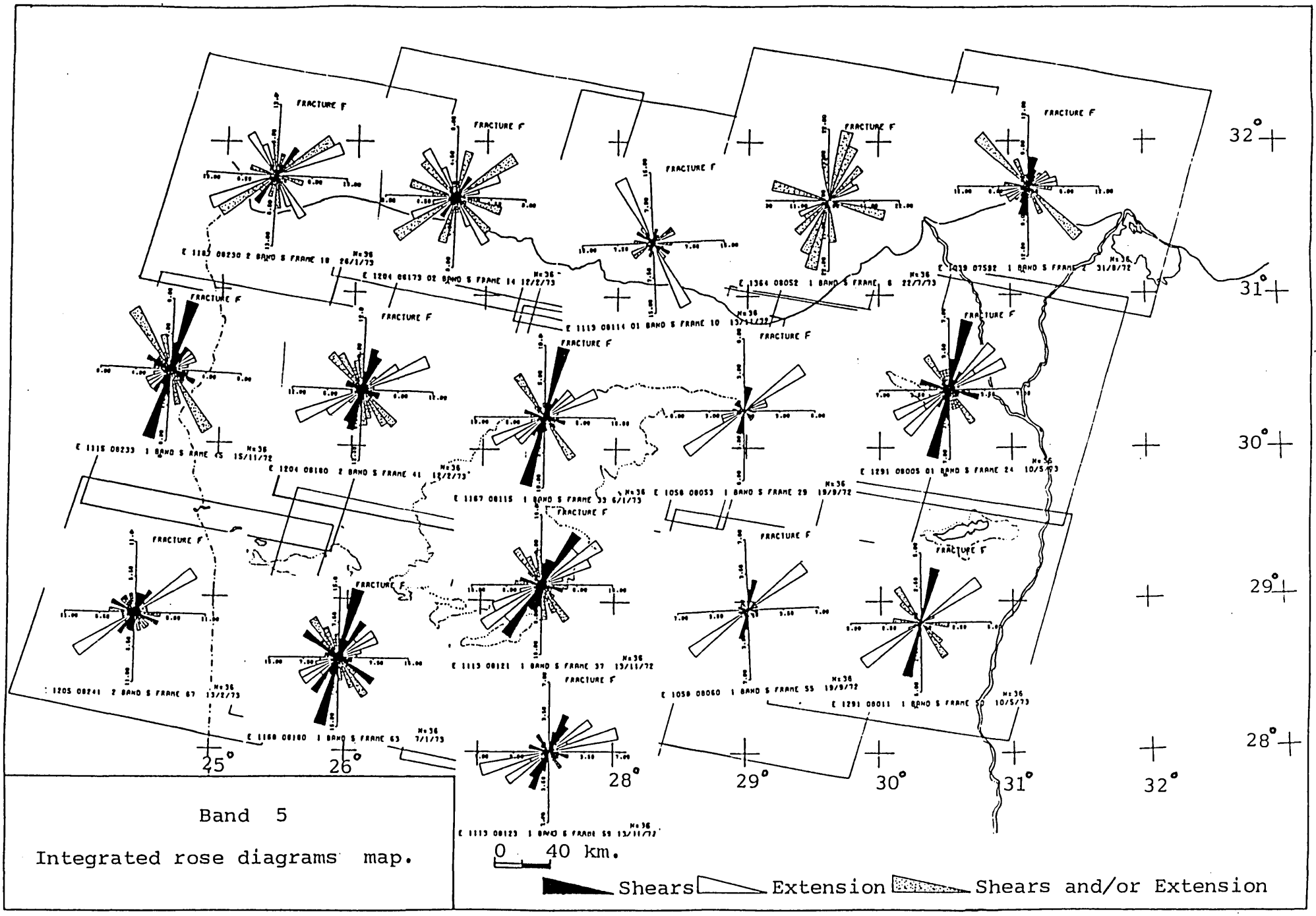
Band 6

Relative fracture energy rose diagrams map.



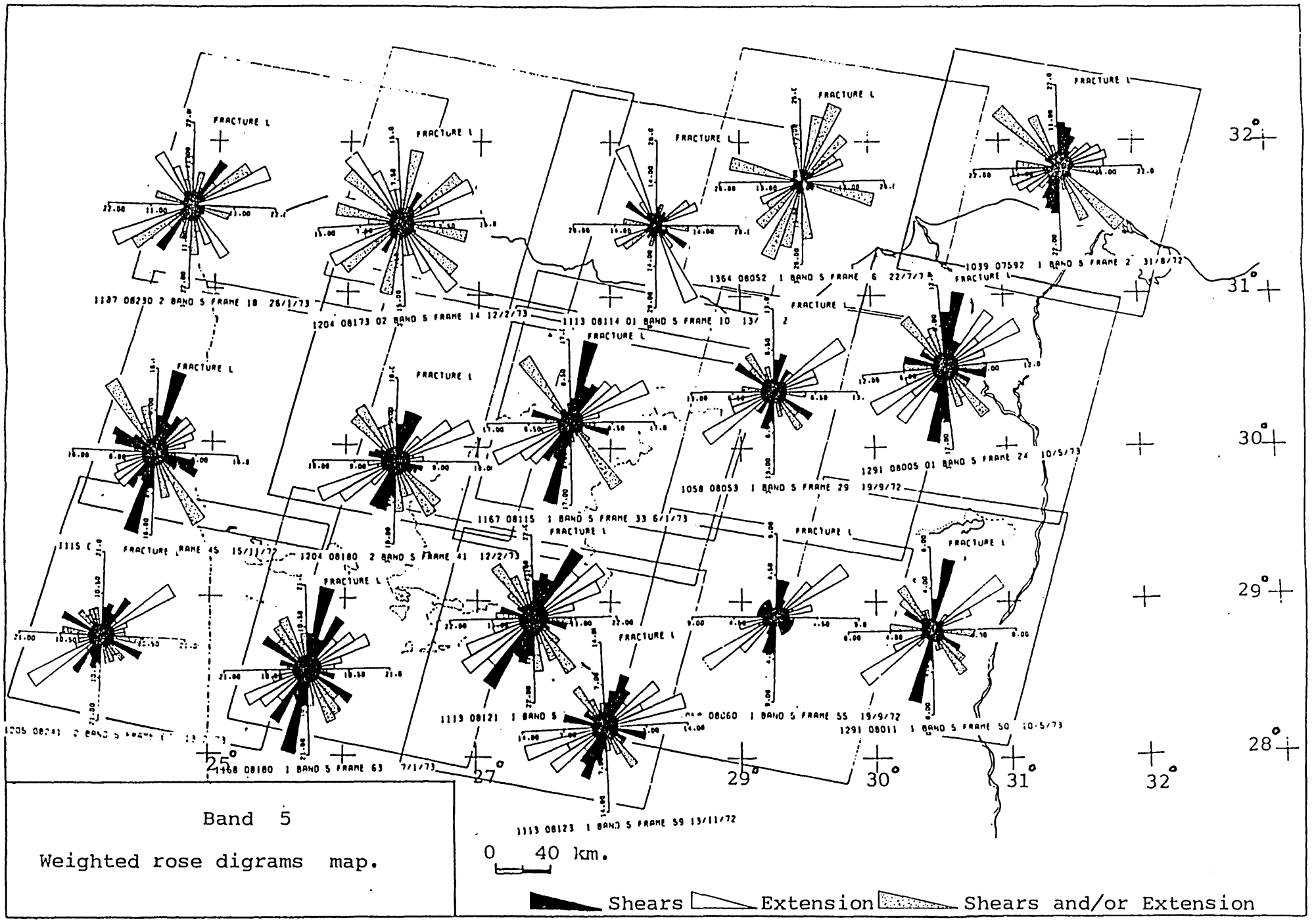
Band 6

Relative fracture frequency rose diagrams map.



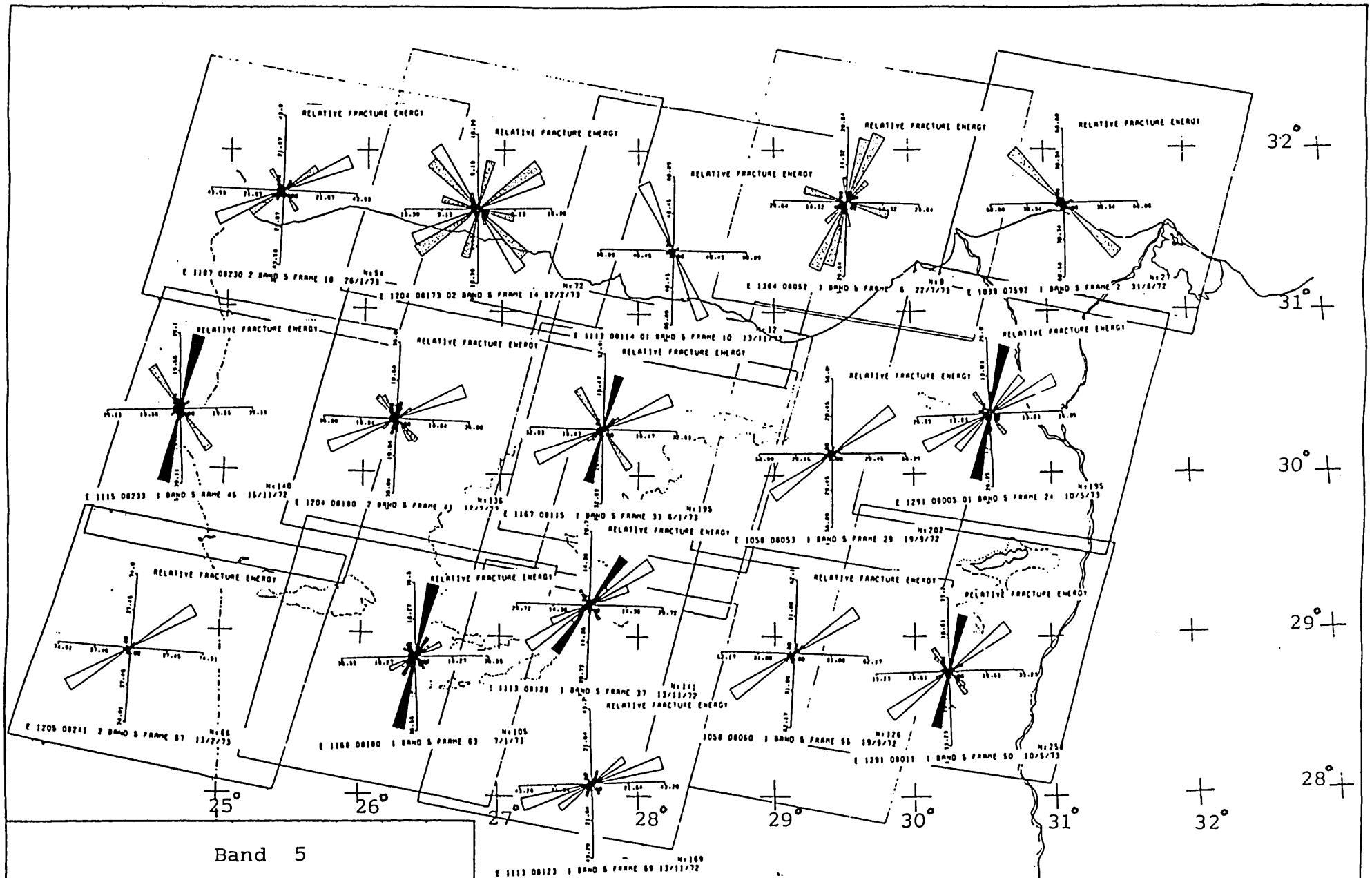
Band 5

Integrated rose diagrams map.



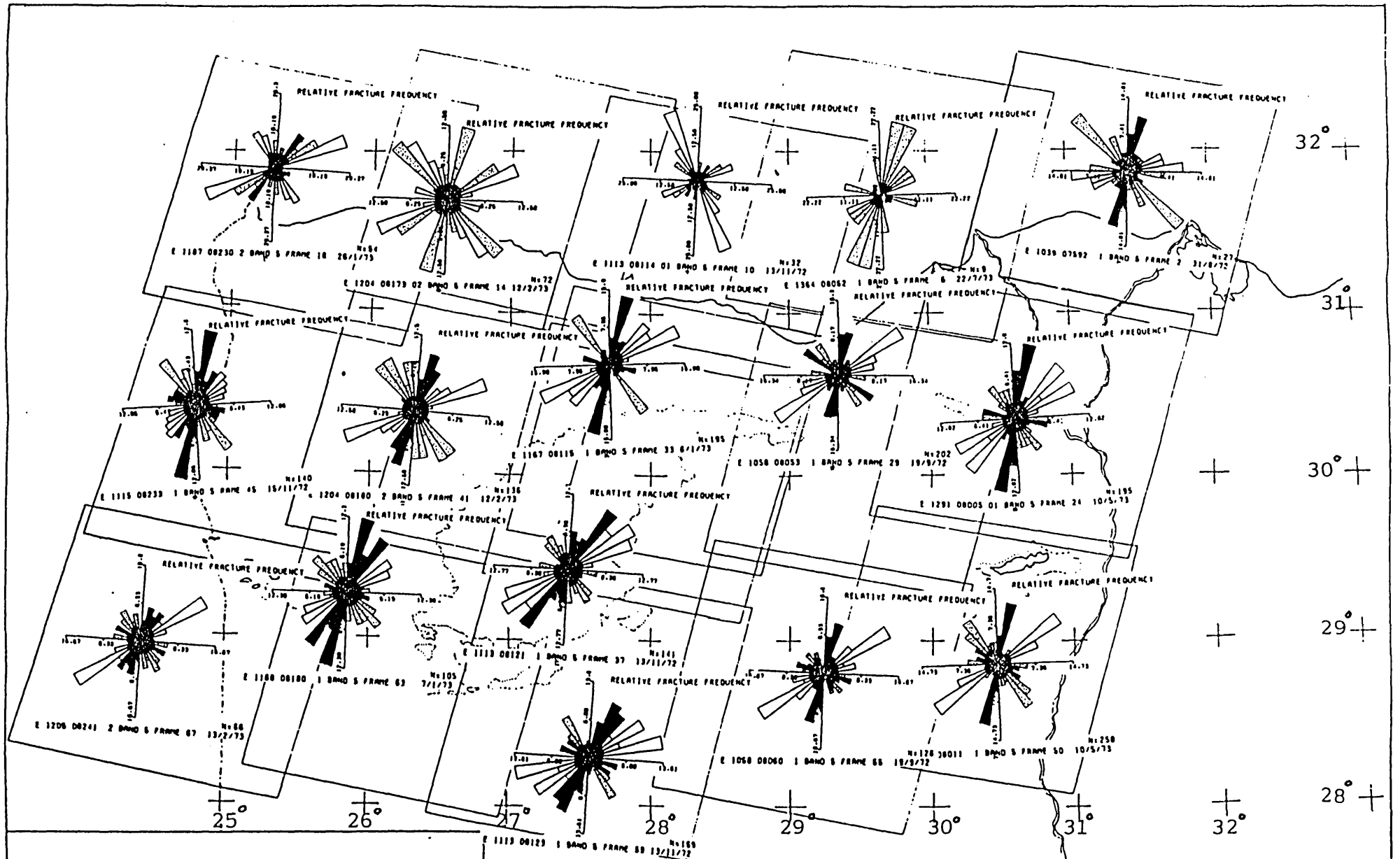
Band 5

Weighted rose digrams map.



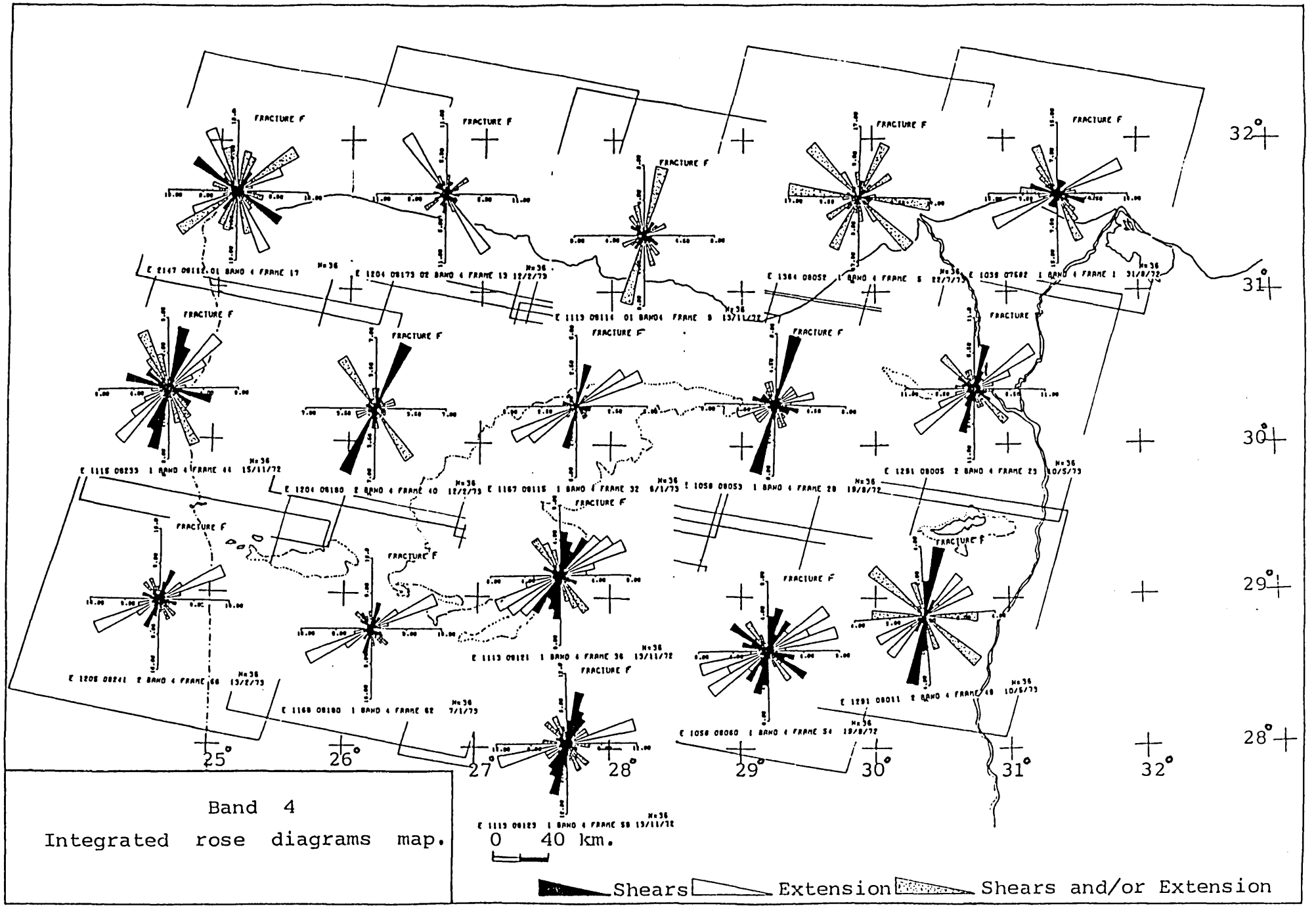
Band 5

Relative fracture energy rose diagrams map.



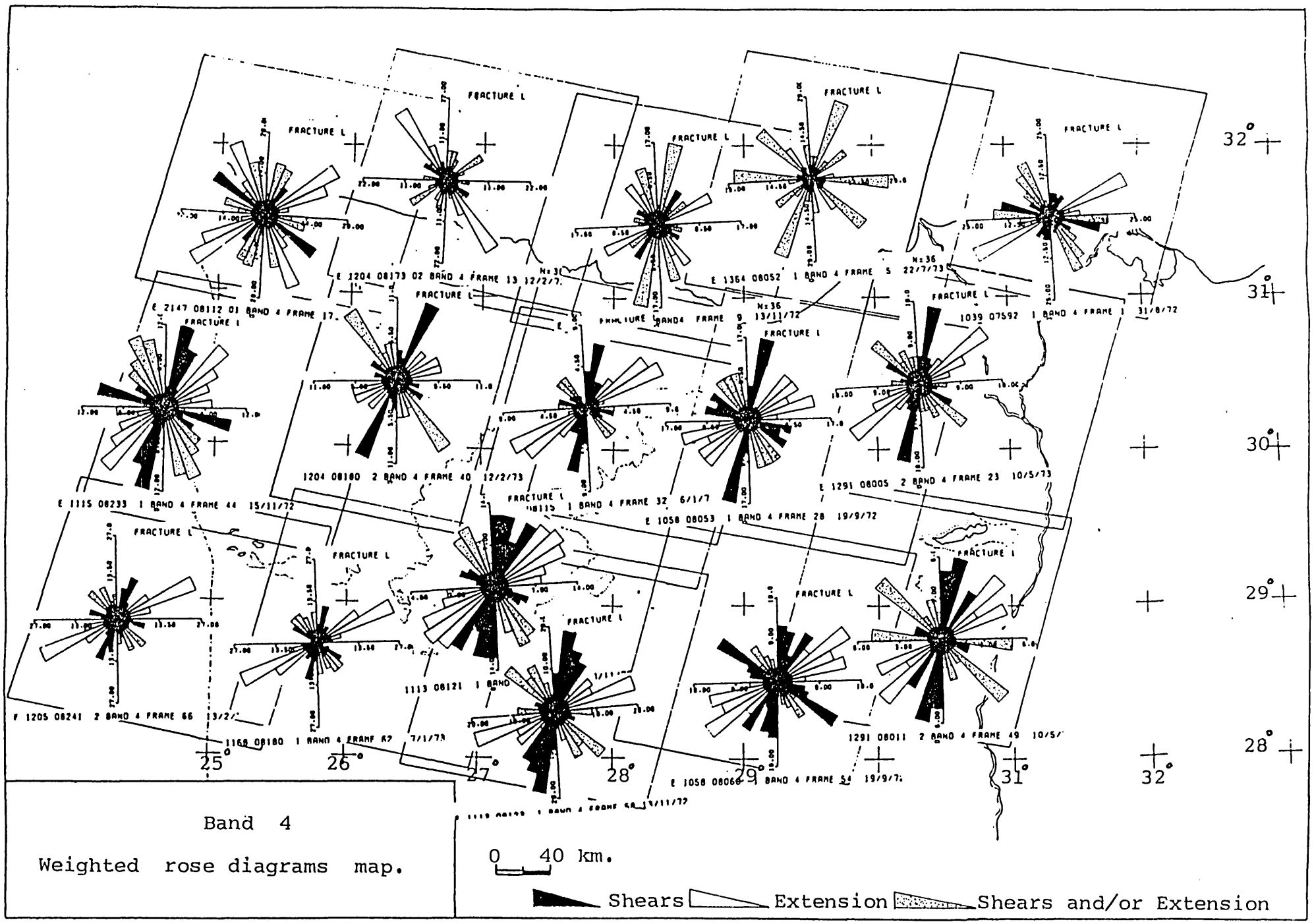
Band 5

Relative fracture frequency rose diagrams map.



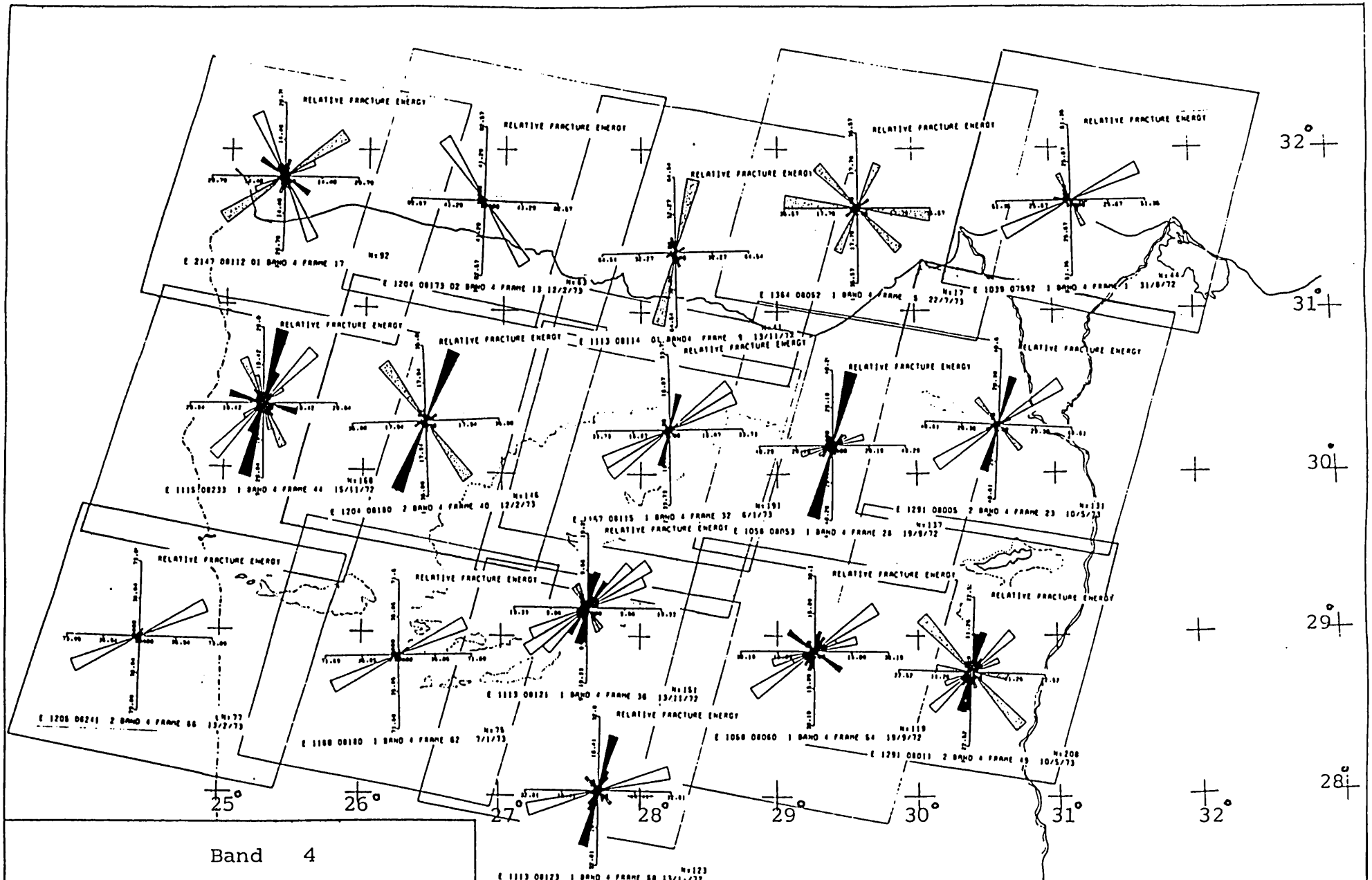
Band 4

Integrated rose diagrams map.



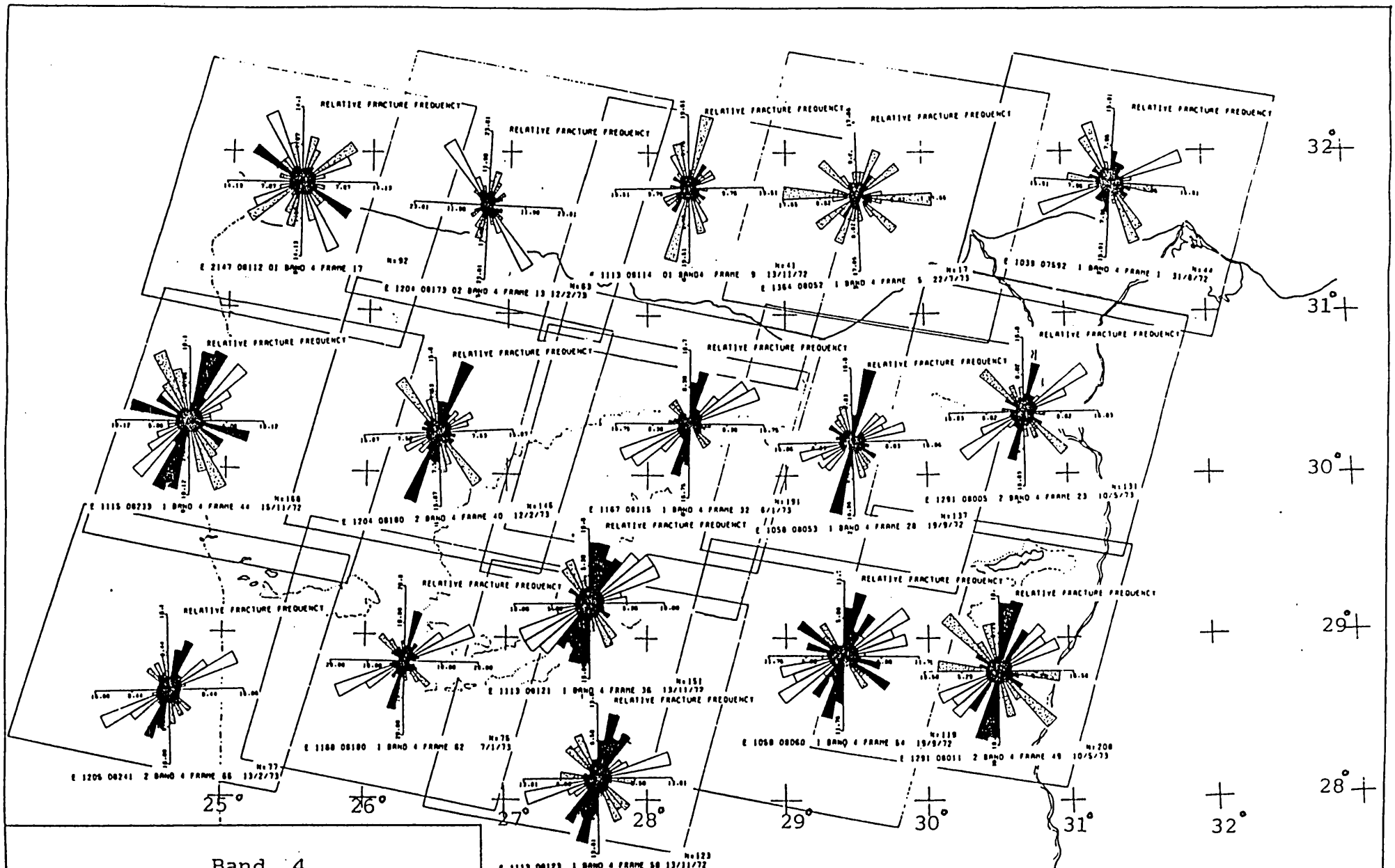
Band 4

Weighted rose diagrams map.



Band 4

Relative fracture energy rose diagrams map.



Band 4

Relative fracture frequency rose diagrams map.

APPENDIX II

FILTER COEFFICIENTS
OF
GEOPHYSICAL DATA

APPENDIX TWO

FILTER COEFFICIENTS OF GEOPHYSICAL DATA

Lowpass filter (11 x 11)

.00060	.00148	.00260	.00373	.00455	.00486	.00455	.00373	.00260	.00148	.00060
.00148	.00305	.00494	.00676	.00807	.00855	.00807	.00676	.00494	.00305	.00148
.00260	.00494	.00765	.01021	.01203	.01269	.01203	.01021	.00765	.00494	.00260
.00373	.00676	.01021	.01342	.01569	.01652	.01569	.01342	.01021	.00676	.00373
.00455	.00807	.01203	.01569	.01829	.01922	.01829	.01569	.01203	.00807	.00455
.00486	.00855	.01269	.01652	.01922	.02020	.01922	.01652	.01269	.00855	.00486
.00455	.00807	.01203	.01569	.01829	.01922	.01829	.01569	.01203	.00807	.00455
.00373	.00676	.01021	.01342	.01569	.01652	.01569	.01342	.01021	.00676	.00373
.00260	.00494	.00765	.01021	.01203	.01269	.01203	.01021	.00765	.00494	.00260
.00148	.00305	.00494	.00676	.00807	.00855	.00807	.00676	.00494	.00305	.00148
.00060	.00148	.00260	.00373	.00455	.00486	.00455	.00373	.00260	.00148	.00060

Upward continuation (h = 4)

.00011	.00029	.00057	.00092	.00129	.00157	.00168	.00157	.00129	.00092	.00057	.00029	.00011
.00029	.00066	.00120	.00191	.00267	.00327	.00350	.00327	.00267	.00191	.00120	.00066	.00029
.00057	.00120	.00218	.00350	.00497	.00620	.00669	.00620	.00497	.00350	.00218	.00120	.00057
.00092	.00191	.00350	.00576	.00845	.01083	.01180	.01083	.00845	.00576	.00350	.00191	.00092
.00129	.00267	.00497	.00845	.01289	.01706	.01884	.01706	.01289	.00845	.00497	.00267	.00129
.00157	.00327	.00620	.01083	.01706	.02324	.02597	.02324	.01706	.01083	.00620	.00327	.00157
.00168	.00350	.00669	.01180	.01884	.02597	.02917	.02597	.01884	.01180	.00669	.00350	.00168
.00157	.00327	.00620	.01083	.01706	.02324	.02597	.02324	.01706	.01083	.00620	.00327	.00157
.00129	.00267	.00497	.00845	.01289	.01706	.01884	.01706	.01289	.00845	.00497	.00267	.00129
.00092	.00191	.00350	.00576	.00845	.01083	.01180	.01083	.00845	.00576	.00350	.00191	.00092
.00057	.00120	.00218	.00350	.00497	.00620	.00669	.00620	.00497	.00350	.00218	.00120	.00057
.00029	.00066	.00120	.00191	.00267	.00327	.00350	.00327	.00267	.00191	.00120	.00066	.00029
.00011	.00029	.00057	.00092	.00129	.00157	.00168	.00157	.00129	.00092	.00057	.00029	.00011

Second vertical derivative (λ = 0.1, normalized)

0	0	-.00119	0	-.00119	0	0
0	.02163	-.09443	.47823	-.09443	.02163	0
-.00119	-.09443	-.71977	-.60361	-.71977	-.09443	-.00119
0	.47823	-.60361	4.05905	-.60361	.47823	0
-.00119	-.09443	-.71977	-.60361	-.71977	-.09443	-.00119
0	.02163	-.09443	.47823	-.09443	.02163	0
0	0	-.00119	0	-.00119	0	0

Second vertical derivative (λ = 0.2, normalized)

0	0	-.00131	0	-.00131	0	0
0	.00592	-.13888	.01956	-.13888	.00592	0
-.00131	-.13888	-1.22671	1.13447	-1.22671	-.13888	-.00131
0	.01956	1.13447	1.38857	1.13447	.01956	0
-.00131	-.13888	-1.22671	1.13447	-1.22671	-.13888	-.00131
0	.00592	-.13888	.01956	-.13888	.00592	0
0	0	-.00131	0	-.00131	0	0

Reduction to the pole (21 x 21)

Inclination = 39.6°

Declination = 0.2°

-.00001 -.00002 -.00004 -.00007 -.00010 -.00016 -.00020 -.00029 -.00033
-.00044 -.00017 -.00049 -.00067 -.00055 -.00052 -.00043 -.00036 -.00025
-.00017 -.00009 -.00004
-.00002 -.00004 -.00007 -.00011 -.00018 -.00023 -.00035 -.00042 -.00059
-.00063 -.00128 -.00093 -.00073 -.00091 -.00084 -.00077 -.00061 -.00047
-.00031 -.00018 -.00009
-.00003 -.00007 -.00011 -.00018 -.00024 -.00038 -.00048 -.00070 -.00081
-.00113 -.00048 -.00138 -.00185 -.00155 -.00148 -.00123 -.00102 -.00074
-.00051 -.00030 -.00016
-.00006 -.00009 -.00017 -.00023 -.00038 -.00049 -.00076 -.00093 -.00137
-.00154 -.00321 -.00233 -.00195 -.00244 -.00223 -.00200 -.00152 -.00113
-.00071 -.00042 -.00020
-.00007 -.00015 -.00020 -.00035 -.00046 -.00075 -.00095 -.00149 -.00180
-.00267 -.00126 -.00376 -.00492 -.00411 -.00377 -.00294 -.00226 -.00145
-.00090 -.00044 -.00019
-.00011 -.00016 -.00030 -.00039 -.00069 -.00087 -.00147 -.00187 -.00303
-.00371 -.00825 -.00611 -.00541 -.00648 -.00544 -.00433 -.00275 -.00167
-.00074 -.00027 .00003
-.00011 -.00024 -.00029 -.00059 -.00071 -.00132 -.00166 -.00299 -.00392
-.00670 -.00371 -.01176 -.01463 -.01112 -.00857 -.00506 -.00278 -.00085
-.00001 .00057 .00059
-.00019 -.00019 -.00048 -.00049 -.00112 -.00126 -.00263 -.00339 -.00691
-.01006 -.02694 -.02123 -.01795 -.01672 -.00890 -.00374 .00040 .00185
.00263 .00218 .00180
-.00007 -.00042 -.00024 -.00097 -.00071 -.00223 -.00219 -.00588 -.00821
-.02138 -.01778 -.06193 -.05443 -.01719 -.00096 .00914 .00936 .00923
.00660 .00516 .00318
-.00093 .00091 -.00203 .00157 -.00405 .00215 -.00837 .00097 -.02316
-.02691 -.26281 -.14784 .05135 .04943 .05910 .03251 .03032 .01517
.01399 .00634 .00576
.01072 -.01464 .02245 -.02889 .04186 -.05390 .07670 -.10831 .16159
-.37906 .61007 1.31228 .20080 .30889 .01799 .11961 -.00707 .05530
-.00795 .02550 -.00497
-.00091 .00088 -.00199 .00150 -.00397 .00201 -.00821 .00068 -.02282
-.02785 -.26149 -.13932 .05719 .05317 .06088 .03372 .03085 .01560
.01415 .00649 .00580
-.00008 -.00040 -.00027 -.00093 -.00077 -.00216 -.00230 -.00574 -.00848
-.02107 -.01947 -.06610 -.05515 -.01685 -.00006 .00985 .01001 .00959
.00689 .00529 .00329
-.00018 -.00020 -.00047 -.00052 -.00108 -.00131 -.00257 -.00350 -.00680
-.01041 -.02623 -.01912 -.01758 -.01646 -.00875 -.00342 .00067 .00214
.00280 .00233 .00187
-.00011 -.00024 -.00030 -.00057 -.00073 -.00129 -.00172 -.00294 -.00405
-.00655 -.00438 -.01346 -.01509 -.01134 -.00853 -.00503 -.00265 -.00076
.00012 .00065 .00066
-.00011 -.00016 -.00029 -.00040 -.00067 -.00090 -.00144 -.00192 -.00297
-.00388 -.00786 -.00502 -.00520 -.00641 -.00548 -.00430 -.00274 -.00161
-.00070 -.00022 .00006
-.00007 -.00014 -.00021 -.00035 -.00047 -.00074 -.00098 -.00147 -.00187
-.00259 -.00161 -.00464 -.00515 -.00423 -.00378 -.00297 -.00224 -.00145
-.00088 -.00042 -.00018
-.00006 -.00009 -.00017 -.00024 -.00038 -.00051 -.00075 -.00096 -.00134
-.00163 -.00300 -.00173 -.00183 -.00240 -.00225 -.00200 -.00153 -.00112
-.00071 -.00041 -.00020
-.00003 -.00007 -.00011 -.00018 -.00025 -.00038 -.00049 -.00069 -.00084
-.00108 -.00066 -.00184 -.00197 -.00161 -.00149 -.00125 -.00102 -.00074
-.00050 -.00030 -.00015
-.00002 -.00004 -.00007 -.00011 -.00018 -.00024 -.00034 -.00043 -.00057

-.00068 -.00117 -.00062 -.00067 -.00089 -.00085 -.00077 -.00061 -.00046
-.00031 -.00018 -.00009
-.00001 -.00002 -.00004 -.00007 -.00010 -.00016 -.00021 -.00028 -.00034
-.00042 -.00026 -.00070 -.00072 -.00058 -.00052 -.00044 -.00036 -.00026
-.00017 -.00009 -.00004

Pseudogravity (21 x 21)
Inclination = 39.6°
Declination = 0.2°

```
-.00008 -.00017 -.00000 -.00048 -.00000 -.00087 -.00000 -.00123 -.00000
-.00137 -.00131 -.00129 -.00000 -.00056 -.00000  .00004 -.00000  .00015
-.00000  .00012  .00007
-.00017 -.00033 -.00053 -.00078 -.00105 -.00134 -.00161 -.00185 -.00201
-.00207 -.00194 -.00143 -.00109 -.00063 -.00004  .00015  .00028  .00034
 .00034  .00029  .00019
-.00000 -.00053 -.00081 -.00114 -.00000 -.00190 -.00000 -.00263 -.00000
-.00292 -.00278 -.00272 -.00000 -.00070 -.00000  .00039 -.00000  .00070
 .00070  .00061 -.00000
-.00047 -.00076 -.00112 -.00156 -.00205 -.00259 -.00312 -.00363 -.00397
-.00413 -.00380 -.00245 -.00153 -.00020  .00042  .00087  .00120  .00136
 .00134  .00116  .00088
-.00000 -.00102 -.00000 -.00203 -.00267 -.00338 -.00000 -.00483 -.00000
-.00555 -.00529 -.00509 -.00000  .00019 -.00000  .00183  .00233  .00253
-.00000  .00208 -.00000
-.00084 -.00129 -.00185 -.00253 -.00333 -.00428 -.00528 -.00637 -.00721
-.00779 -.00698 -.00322 -.00030  .00115  .00256  .00373  .00441  .00454
 .00419  .00351  .00265
-.00000 -.00155 -.00000 -.00302 -.00000 -.00519 -.00664 -.00813 -.00000
-.01041 -.01007 -.00907 -.00000  .00311  .00575  .00750 -.00000  .00791
-.00000  .00562 -.00000
-.00119 -.00179 -.00252 -.00351 -.00464 -.00619 -.00795 -.01039 -.01280
-.01551 -.01348  .00025  .00429  .00921  .01314  .01491  .01469  .01314
 .01089  .00842  .00605
-.00000 -.00194 -.00000 -.00380 -.00000 -.00686 -.00000 -.01235 -.01760
-.02171 -.02404 -.01126  .01315  .02523 -.00000  .02819 -.00000  .02015
-.00000  .01158 -.00000
-.00142 -.00208 -.00298 -.00411 -.00556 -.00764 -.01017 -.01500 -.02089
-.04030 -.03437  .04771  .07438  .06921  .05824  .04603  .03588  .02706
 .02006  .01425  .00974
 .00087 -.00870  .00182 -.01708  .00342 -.03154  .00633 -.06174  .01364
-.18565  .15286  .30944  .14553  .12407  .06771  .06314  .03612  .03406
 .01915  .01731  .00908
-.00141 -.00210 -.00296 -.00414 -.00552 -.00770 -.01010 -.01512 -.02072
-.04068 -.03243  .04980  .07608  .07042  .05900  .04656  .03620  .02729
 .02020  .01435  .00979
-.00000 -.00193 -.00000 -.00378 -.00000 -.00683 -.00000 -.01230 -.01770
-.02154 -.02464 -.01225  .01353  .02586 -.00000  .02872 -.00000  .02044
-.00000  .01172 -.00000
-.00119 -.00180 -.00252 -.00352 -.00463 -.00621 -.00793 -.01043 -.01275
-.01560 -.01293  .00066  .00457  .00955  .01350  .01529  .01501  .01341
 .01108  .00857  .00615
-.00000 -.00154 -.00000 -.00301 -.00000 -.00518 -.00666 -.00810 -.00000
-.01032 -.01033 -.00967 -.00000  .00323  .00595  .00771 -.00000  .00809
-.00000  .00573 -.00000
-.00084 -.00129 -.00184 -.00254 -.00333 -.00429 -.00527 -.00639 -.00718
-.00782 -.00670 -.00256  .00001  .00124  .00267  .00386  .00454  .00467
 .00430  .00359  .00271
-.00000 -.00102 -.00000 -.00203 -.00268 -.00337 -.00000 -.00482 -.00000
-.00550 -.00543 -.00543 -.00000  .00023 -.00000  .00190  .00241  .00260
-.00000  .00213 -.00000
-.00047 -.00076 -.00112 -.00156 -.00205 -.00260 -.00312 -.00364 -.00395
-.00415 -.00365 -.00211 -.00138 -.00007  .00046  .00092  .00125  .00141
 .00138  .00119  .00090
-.00000 -.00053 -.00081 -.00113 -.00000 -.00190 -.00000 -.00262 -.00000
-.00289 -.00286 -.00290 -.00000 -.00066 -.00000  .00041 -.00000  .00073
 .00073  .00062 -.00000
-.00017 -.00033 -.00053 -.00078 -.00105 -.00134 -.00161 -.00185 -.00200
-.00208 -.00187 -.00126 -.00102 -.00057  .00000  .00017  .00029  .00036
 .00036  .00030  .00020
-.00008 -.00017 -.00000 -.00048 -.00000 -.00087 -.00000 -.00123 -.00000
-.00135 -.00135 -.00137 -.00000 -.00055 -.00000  .00005 -.00000  .00016
-.00000  .00012  .00007
```

Reduction to the pole (21 x 21)

Inclination = 44.5°

Declination = 1.9°

```
-.00001 -.00002 -.00004 -.00008 -.00009 -.00017 -.00018 -.00031 -.00027
-.00050  .00015  .00016 -.00049 -.00040 -.00044 -.00033 -.00028 -.00018
-.00012 -.00006 -.00003
-.00002 -.00004 -.00008 -.00010 -.00019 -.00021 -.00037 -.00037 -.00063
-.00047 -.00161 -.00169 -.00078 -.00086 -.00065 -.00062 -.00043 -.00034
-.00020 -.00012 -.00005
-.00003 -.00008 -.00010 -.00020 -.00023 -.00041 -.00044 -.00074 -.00069
-.00123  .00018 -.00001 -.00138 -.00115 -.00121 -.00089 -.00076 -.00048
-.00034 -.00017 -.00009
-.00007 -.00009 -.00019 -.00022 -.00042 -.00046 -.00081 -.00084 -.00144
-.00123 -.00376 -.00373 -.00197 -.00218 -.00167 -.00151 -.00101 -.00074
-.00040 -.00024 -.00008
-.00007 -.00016 -.00019 -.00039 -.00044 -.00082 -.00090 -.00158 -.00161
-.00284 -.00010 -.00107 -.00368 -.00298 -.00286 -.00196 -.00149 -.00080
-.00048 -.00016 -.00006
-.00013 -.00015 -.00034 -.00037 -.00075 -.00084 -.00158 -.00175 -.00317
-.00318 -.00897 -.00834 -.00507 -.00531 -.00373 -.00286 -.00149 -.00084
-.00019 -.00000  .00018
-.00010 -.00027 -.00028 -.00065 -.00069 -.00144 -.00162 -.00318 -.00368
-.00692 -.00166 -.00612 -.01067 -.00744 -.00558 -.00261 -.00124  .00009
 .00042  .00072  .00055
-.00021 -.00018 -.00053 -.00049 -.00122 -.00125 -.00283 -.00334 -.00722
-.00931 -.02695 -.02326 -.01460 -.01140 -.00427 -.00113  .00173  .00202
 .00235  .00171  .00139
-.00008 -.00044 -.00026 -.00102 -.00076 -.00235 -.00230 -.00615 -.00837
-.02158 -.01411 -.04139 -.03325 -.00591  .00311  .00877  .00738  .00695
 .00464  .00365  .00214
-.00078  .00062 -.00173  .00098 -.00350  .00104 -.00740 -.00115 -.02137
-.03247 -.23465 -.10596  .04875  .03687  .04269  .02165  .02099  .00978
 .00960  .00402  .00395
 .01034 -.01428  .02163 -.02819  .04029 -.05265  .07371 -.10607  .15458
-.37647  .69859 1.11535  .09443  .24626 -.01084  .09846 -.01639  .04681
-.01153  .02202 -.00627
-.00056  .00024 -.00125  .00023 -.00261 -.00032 -.00576 -.00366 -.01789
-.04153 -.21738 -.04024  .08342  .05929  .05126  .02856  .02312  .01226
 .01009  .00496  .00403
-.00021 -.00026 -.00053 -.00066 -.00129 -.00169 -.00331 -.00496 -.01078
-.01873 -.02933 -.06821 -.03251 -.00175  .01077  .01298  .01140  .00874
 .00635  .00428  .00278
-.00014 -.00030 -.00038 -.00073 -.00093 -.00171 -.00232 -.00431 -.00624
-.01233 -.02002 -.00879 -.01311 -.00880 -.00269  .00181  .00358  .00398
 .00335  .00262  .00178
-.00015 -.00020 -.00040 -.00051 -.00093 -.00118 -.00209 -.00273 -.00478
-.00561 -.00774 -.01751 -.01225 -.00832 -.00461 -.00201 -.00004  .00090
 .00133  .00120  .00098
-.00010 -.00021 -.00027 -.00050 -.00062 -.00108 -.00135 -.00226 -.00269
-.00463 -.00527 -.00090 -.00449 -.00473 -.00389 -.00232 -.00122 -.00029
 .00014  .00041  .00038
-.00009 -.00013 -.00025 -.00032 -.00057 -.00069 -.00115 -.00135 -.00218
-.00210 -.00324 -.00700 -.00453 -.00363 -.00269 -.00204 -.00121 -.00069
-.00023 -.00003  .00010
-.00005 -.00011 -.00016 -.00028 -.00035 -.00060 -.00070 -.00112 -.00118
-.00199 -.00172  .00035 -.00162 -.00189 -.00186 -.00139 -.00104 -.00060
-.00035 -.00013 -.00004
-.00004 -.00006 -.00013 -.00017 -.00029 -.00035 -.00057 -.00062 -.00099
-.00083 -.00148 -.00312 -.00180 -.00149 -.00115 -.00099 -.00069 -.00049
-.00027 -.00015 -.00005
-.00002 -.00005 -.00007 -.00013 -.00017 -.00028 -.00031 -.00050 -.00049


-.00085 -.00056  .00042 -.00059 -.00071 -.00076 -.00058 -.00048 -.00031
-.00020 -.00010 -.00005
-.00001 -.00002 -.00005 -.00007 -.00012 -.00015 -.00024 -.00025 -.00040
-.00030 -.00064 -.00131 -.00068 -.00056 -.00042 -.00038 -.00026 -.00019
-.00011 -.00006 -.00002
```

Pseudogravity (21 x 21)
Inclination = 44.5°
Declination = 1.9°

-.00005	-.00011	-.00000	-.00028	-.00000	-.00046	-.00000	-.00056	-.00000
-.00043	-.00005	.00005	-.00000	.00014	-.00000	.00024	-.00000	.00023
-.00000	.00013	.00007						
-.00011	-.00020	-.00032	-.00045	-.00060	-.00071	-.00083	-.00084	-.00082
-.00059	-.00054	-.00012	.00014	.00025	.00036	.00043	.00046	.00045
.00039	.00029	.00018						
-.00000	-.00033	-.00049	-.00069	-.00000	-.00107	-.00000	-.00129	-.00000
-.00098	-.00013	.00012	-.00000	.00044	-.00000	.00076	-.00000	.00080
.00071	.00056	-.00000						
-.00030	-.00048	-.00071	-.00095	-.00124	-.00148	-.00172	-.00179	-.00178
-.00131	-.00102	.00005	.00043	.00074	.00107	.00129	.00140	.00137
.00123	.00099	.00071						
-.00000	-.00066	-.00000	-.00128	-.00163	-.00202	-.00000	-.00258	-.00000
-.00205	-.00033	.00027	-.00000	.00131	-.00000	.00220	.00235	.00228
-.00000	.00164	-.00000						
-.00056	-.00084	-.00120	-.00161	-.00211	-.00260	-.00315	-.00347	-.00361
-.00287	-.00175	.00042	.00140	.00234	.00322	.00375	.00392	.00370
.00322	.00258	.00188						
-.00000	-.00103	-.00000	-.00198	-.00000	-.00331	-.00403	-.00478	-.00000
-.00442	-.00091	.00075	-.00000	.00442	.00581	.00650	-.00000	.00586
-.00000	.00386	-.00000						
-.00080	-.00119	-.00169	-.00230	-.00307	-.00399	-.00510	-.00631	-.00733
-.00709	-.00281	.00254	.00600	.00911	.01097	.01125	.01041	.00893
.00719	.00545	.00386						
-.00000	-.00131	-.00000	-.00255	-.00000	-.00456	-.00000	-.00795	-.01079
-.01128	-.00411	.00439	.01453	.02012	-.00000	.01887	-.00000	.01275
-.00000	.00716	-.00000						
-.00090	-.00150	-.00188	-.00296	-.00350	-.00550	-.00634	-.01074	-.01255
-.02722	.00122	.03965	.05080	.04461	.03622	.02833	.02180	.01644
.01210	.00862	.00586						
.00073	-.00828	.00153	-.01623	.00287	-.02990	.00530	-.05824	.01138
-.17117	.12744	.20737	.08741	.07732	.03987	.03916	.02126	.02111
.01128	.01073	.00535						
-.00079	-.00166	-.00165	-.00328	-.00305	-.00609	-.00550	-.01190	-.01062
-.03034	.00562	.05176	.05917	.05033	.03956	.03066	.02316	.01744
.01267	.00904	.00607						
-.00000	-.00122	-.00000	-.00238	-.00000	-.00425	-.00000	-.00733	-.01144
-.00911	-.00834	.00380	.01766	.02383	-.00000	.02147	-.00000	.01410
-.00000	.00777	-.00000						
-.00077	-.00123	-.00162	-.00239	-.00293	-.00413	-.00481	-.00654	-.00657
-.00737	.00069	.00500	.00780	.01132	.01315	.01334	.01210	.01027
.00814	.00612	.00428						
-.00000	-.00099	-.00000	-.00191	-.00000	-.00315	-.00412	-.00441	-.00000
-.00318	-.00273	.00013	-.00000	.00547	.00717	.00783	-.00000	.00689
-.00000	.00443	-.00000						
-.00054	-.00085	-.00116	-.00164	-.00202	-.00264	-.00295	-.00349	-.00309
-.00284	.00028	.00154	.00202	.00307	.00400	.00463	.00474	.00445
.00381	.00303	.00219						
-.00000	-.00064	-.00000	-.00123	-.00164	-.00192	-.00000	-.00232	-.00000
-.00131	-.00129	-.00056	-.00000	.00167	-.00000	.00273	.00290	.00277
-.00000	.00195	-.00000						
-.00029	-.00048	-.00068	-.00095	-.00118	-.00147	-.00159	-.00176	-.00144
-.00124	.00013	.00063	.00071	.00104	.00136	.00164	.00174	.00169
.00149	.00119	.00085						
-.00000	-.00032	-.00049	-.00066	-.00000	-.00100	-.00000	-.00112	-.00000
-.00056	-.00064	-.00049	-.00000	.00058	-.00000	.00096	-.00000	.00099
.00087	.00068	-.00000						
-.00011	-.00020	-.00031	-.00045	-.00056	-.00070	-.00074	-.00080	-.00063
-.00054	.00006	.00026	.00026	.00037	.00047	.00056	.00059	.00056
.00048	.00036	.00022						
-.00005	-.00010	-.00000	-.00026	-.00000	-.00043	-.00000	-.00047	-.00000
-.00022	-.00029	-.00028	-.00000	.00019	-.00000	.00031	-.00000	.00029
-.00000	.00015	.00008						